Assimilation of Dolomite by Bushveld Magmas in the Flatreef; Implications for the Origin of Ni-Cu-PGE Mineralization and the Precambrian Atmosphere

Katherine E. L. Abernethy

School of Earth and Ocean Sciences

Cardiff University

Submitted in the partial fulfilment of the requirements for the degree of:

Doctor of Philosophy (PhD)

September 2019

Acknowledgments

geochronology, measuring multiple samples as well as providing detailed feedback and advice during the write-up no matter what time or day! I would also like to the thank Adrian Wood also at the BGS for his guidance in crushing and separating zircon and providing much needed entertainment while I undertook this. Thanks are also due to Dr Reid at the University of Cape Town for providing a sample of Merensky Reef material from the Northam Platinum Mine for U-Pb zircon geochronology.

Mg isotopic work would not have been possible without guidance from Philip Pogge von Strandmann, who provided valuable discussion throughout the early stages. Thanks are also due to Tim Elliot for allowing me to use the isotope labs in Bristol, even in the wake of a major fire, to carry out the work and providing useful and challenging discussion on the data I collected. None of this would have been possible without the hard work and dedication of Xiaoning Liu, a fellow PhD student at Bristol University, who taught me the Mg-isotope column chemistry and oversaw all my lab work and helped run sample analyses.

There are multiple others at Cardiff University who have aided and supported this research. I would like to thank Tom Blenkinsop, my project convenor, who challenged my research aims and plans throughout helping to focus my work and identify key plan-B options! In addition, I would like to thank Duncan Muir for his support on everything SEM related, Tony Oldroyd for his impeccable production of thin and thick sections and Morten Anderson for helping me run my samples for trace element data in Bristol. I am also grateful to Sarah-Jane Barnes and the group at LabMaTer, including Dany Savard and Audrey Lavoie for providing PGE and whole rock geochemistry analysis, and to Ben Buse at Bristol University for teaching me how to undertake electron microprobe analyses.

I have been fortunate enough to travel the world during this PhD for numerous conferences and field trips including South Africa, USA, Finland and Canada not to mention multiple trips around the UK and Europe as a demonstrator on undergraduate fieldtrips. Along the way I have met numerous geologists whose own research and discussions have inspired me throughout.

Next I would like to thank my fellow PhD students who have made life as a PhD student both bearable and enjoyable. This mostly manifested itself in numerous cups of tea. My thanks in particular go to fellow tea addicts, past and present, including Michael Hodge, Bob Gooday, James Panton, Joanna Brims, Matt Price and Liam Hoare. I probably would have finished sooner without the tea but it would have been a lot less enjoyable! I would also like to thank my year-group, a lot has changed as a group not to mention the engagements, weddings, babies, secondments to government postings and IODP cruises but we have remained supportive of each other throughout for which I am always grateful. In particular, thanks are

Abstract

The formation of the Platreef in the northern limb of the Bushveld Complex remains unresolved, as does the stratigraphic correlation of the northern limb to that in the wider Bushveld Complex. This is largely due to intense contamination by country rocks modifying the stratigraphy. However, the Flatreef, located down-dip of the Platreef, is relatively less contaminated and offers an opportunity to evaluate the potential correlation between the different limbs of the Bushveld Complex.

The present study, focussing on 2 drill cores intersecting the Flatreef (UMT081 and UMT094), has utilised geochemical, isotopic and geochronological data to characterise the Flatreef. Modelling the Flatreef using Mg-Nd-O isotopes indicates that the lower portions of the Flatreef in particular have been affected by contamination. The upper portions have been much less affected, showing important lithological and compositional similarities to the UCZ of the WBC.

The present study has also provided the first high-precision U-Pb single-zircon geochronology data for the Flatreef, with ages of purported Merensky Reef overlapping with those of the WBC. In addition, the geochronological data show that the Bastard and UG2 reefs are younger than their hangingwall rocks, supporting a model of out-of-sequence sill emplacement in the Flatreef.

The origin of PGE mineralization in the Flatreef remains less clear. Well mineralized sills such as the Bastard Reef imply sulphides were entrained in magmas prior to emplacement. However, elevated grade where the northern limb intrudes dolomitic floor rocks suggests contamination by calcareous sediments and mineralization are linked. In addition, it is likely that the assimilation of calcareous sediments by Flatreef magmas in addition to devolatization of calcareous sediments and dolomites in the wider metamorphic aureole of the Bushveld Complex released significant volumes of CO_2 into the Precambrian atmosphere and potentially played a role in the global Shunga Event, whose age coincides with that of the Bushveld Complex.

Contributions

I would like to note the following contributions to this thesis:

- Chapter 3 – Methodology for geochronological work undertaken at the BGS was supplied by Simon Tapster
- Chapter 7 and 8 – Samples were analysed for whole rock composition of lithophiles and PGE at the LabMaTer, Chicoutimi, Université du Quebec by Dany Savard and Audrey Lavoie
- Chapter 9 – Oxygen isotopes were analysed by ed Ripley at the University of Indiana
- Chapter 10 – Laboratory processing and analysis of zircons for geochronological work was undertaken by Simon Tapster at the BGS
- Additional assay and lithophile data was supplied by Ivanhoe from across the Flatreef (referenced in text)

Publication

I would like to note the following publication that has been submitted and currently in review:

Abernethy, K.E.L., Maier, W.D., Grobler, D.F., Barnes, S.-J. (submitted) Lithogeochemistry of the Flatreef and its floor rocks, and comparison to the Platreef and Upper Critical Zone of the western Bushveld Complex. Mineralium Deposita.

This paper was written by myself (Abernethy) using some of the data presented in this thesis (whole rock lithophile and chalcophile element data and mineral compositional data). Maier provided feedback and discussion on this paper. Grobler provided drill core samples and some access to the wider Flatreef database. Barnes facilitated the analysis of whole rock samples. Whilst some similar figures have been used in both the paper and this thesis, no text from this paper has been repeated here and the ideas presented in this thesis are conceived myself (Abernethy).

Table of Contents

List of Figures

Chapter 6

Chapter 7

Chapter 8

Chapter 9

List of Tables

Abbreviations

BAR	Bastard Reef
BCU	Bastard Cyclic Unit
CA-ID-TIMS	Chemical Abrasion Isotopic Dilution Thermal Ionisation Mass Spectrometry
CL	Cathodoluminescence
EBC	Eastern Bushveld Complex
FAZ	Footwall Assimilation Zone
GMA	Giant Mottled Anorthosite
GNPA	Grasvally Norite Pyroxenite Member
ICP-MS	Inductively Coupled Plasma Mass Spectrometer
IPGE	Iridium Group PGE (e.g. Os, Ir, Ru)
JD	Johannesburg Dome
LA-ICP-MS	Laser Ablation Inductively Coupled Plasma Mass Spectrometry
LCZ	Lower Critical Zone
LMI	Layered Mafic Intrusion
LOI	Loss On Ignition
LPX	Lower Pyroxenite
LUU	Lower Ultramafic Unit
LZ	Lower Zone
MC-ICP-MS	Multi Collector Inductively Coupled Mass Spectrometry
MgZ	Marginal Zone
MQ	Milli-Q water
MR	Merensky Reef
MCU	Merensky Cyclic Unit
MFU	Merensky Footwall Unit
MZ	Main Zone
PAL	Present Atmospheric Level
PCA	Principle Component Analyses
PGE	Platinum Group Elements
PNZ	Pyroxenite Norite Zone
PPGE	Palladium Group PGE (e.g. Rh, Pt, Pd)
RLS	Rustenburg Layered Suite
SEM	Scanning Electron Microscope
SEM	Secondary Electron Multiplier
TML	Thabazimbi Murchison Lineament
UCZ	Upper Critical Zone
UG2	Upper Group 2 Chromitite
UG2 CU	UG2 Cyclic Unit
UG2 FU	UG2 Footwall Unit
UPX	Upper Pyroxenite
UZ	Upper Zone
WBC	Western Bushveld Complex

1 Introduction

1.1 Context of this research project

The Bushveld Complex is the world's largest layered mafic-ultramafic intrusion (LMI) covering approximately 65,000 km^2 in sub-surface outcrop and containing a globally important resource of PGE, Cr, Ni, Cu, V and Ti (Eales and Cawthorn, 1996; Lee, 1996). Its immense size lends itself as a natural laboratory in which many traditional concepts of petrology and ore genesis can be tested. Despite this, many features of the Bushveld Complex, including the lithological layering and enrichment of PGE, remain unresolved. The petrogenesis of the northern limb of the Bushveld Complex has been particularly difficult to unravel due to significant contamination of the intruding magmas by sedimentary and carbonate country rocks. This has disrupted geochemical, isotopic and lithostratigraphic marker horizons that are used to correlate layers of the various limbs with each other (McDonald and Holwell, 2011).

The northern limb is also more mineralized than the remainder of the Bushveld Complex, with PGE reefs that are up to several tens of meters in thickness. In addition, the enrichment of Pd in mineralized reefs in the northern limb relative to the remainder of the Bushveld Complex has resulted in the former becoming a focus for exploration. Global demand for Pd is increasing, largely in response to its use in petrol engine catalytic converters, while demand for diesel cars, which use Pt-based catalytic converters, is falling (Rowling et al., 2019). This is expressed in a broad decline of the Pt price over the last decade, whereas the price of Pd has risen exponentially (Figure 1.1) (www.infomine.com).
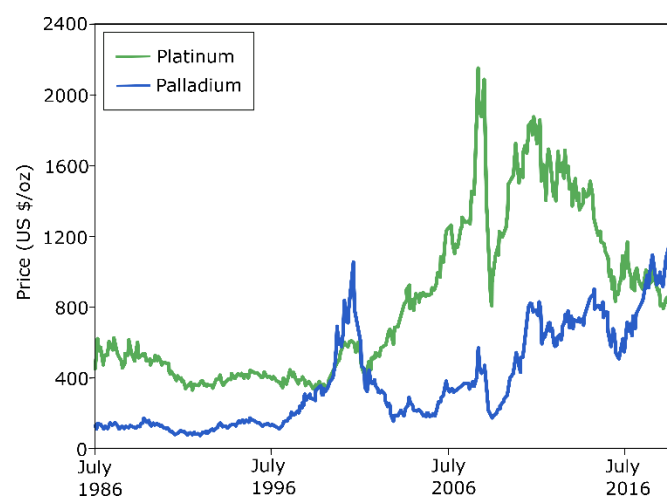
Figure 1.1 Graph showing comparative price (USD/oz) of Pt and Pd over the last 33 years. Modified after (www.infomine.com).

An extensive drilling campaign undertaken by Ivanhoe Mines over the last decade has discovered high grade mineralisation downdip of the outcropping Platreef in the northern limb, termed the Flatreef (Grobler et al., 2018). Understanding the mechanisms by which the Flatreef deposit formed is crucial to inform future exploration projects both in the Bushveld Complex and other layered mafic intrusions.

1.2 Research aims

The PGE rich Flatreef in the northern limb of the Bushveld Complex is the focus of the present study. Magmas that form the Flatreef and the up-dip Platreef in the central portion of the northern limb have shown extensive interaction with footwall country rocks, most notably thick packages of calcareous sediments. These areas display anomalous stratigraphy and mineralization styles relative to the remainder of the Bushveld Complex and suggest these calcareous sediments could play an important role in formation of the northern limb.

Within the context of the ongoing debates over the formation of the Bushveld Complex the main aims of the present project are listed below:

1) Characterise the Flatreef deposit by means of a detailed study of 2 drill cores.
2) Assess the similarities and differences between the Flatreef and the remainder of the Bushveld Complex to determine whether the Flatreef can be correlated to the western and eastern limbs of the Bushveld Complex.
3) Investigate the impacts of contamination of the Flatreef magmas by the country rocks and attempt to quantify this contamination.
4) Estimate the potential impact of interaction between the Flatreef magma and country rocks on the Precambrian atmosphere.
5) Evaluate models for the formation of the Flatreef and determine which is most useful in exploration and mining.

This thesis will first provide an introduction to the geological setting of the Bushveld Complex, with special focus on the northern limb and the Flatreef, as well as presenting models previously proposed in the literature to explain the formation and mineralization of these igneous bodies. Next, the methods used and data generated in this study will be presented. This is followed by extensive comparisons between the Flatreef, the Platreef and the Upper Critical Zone (UCZ) of the western limb leading to a discussion over whether the Flatreef is correlative to the remainder of the Bushveld Complex. Models assessing the extent of contamination are also presented. Next, a critical appraisal of models proposed for the formation of the Bushveld Complex and its mineralization, in both the western and northern limbs, is undertaken. Finally, a genetic model for the formation of the Flatreef is proposed.

2 Geological Setting of the Bushveld Complex

The vast size of the Bushveld Complex coupled with the abundance of academic studies on the intrusion and its host rocks warrants a review of the relevant literature and outlining of the key unanswered questions in research in layered mafic intrusions. This chapter seeks to contextualize the Flatreef of the northern limb with both the wider Bushveld Complex and its host rocks.

2.1 Introduction

The Bushveld Complex was emplaced around 2.05 Myr ago (Scoates and Friedman, 2008) into the Kaapvaal Craton, in what is now South Africa. It is the world's largest known layered mafic intrusion with a sub-surface footprint between approximately 65,000 km^2 and thickness of up to 9 km (Eales and Cawthorn, 1996). The layered suite is broadly comprised of an upwardly evolving sequence from an ultramafic base to a felsic top, with spectacular layering in the lower portions which can be traced hundreds of km along strike. The Bushveld Complex also forms the world's largest ore district, hosting globally important resources of PGE, Cr, V, Ni, Fe, F, Sn, Cu and andalusite (Lee, 1996). Most notably, it is the largest global deposit of PGE, supplying over 75% of global demand, with new world class reserves still being discovered (Grobler et al., 2018; Maier et al., 2013). The Bushveld Complex provides a natural laboratory in which many petrological theories have been tested, and often rejected, challenging classical models as increasingly sophisticated data are added to the vast volume of published works on the Complex. At present, debate continues over several important aspects of the Bushveld Complex including its age, size, emplacement style, parental magma compositions and layering mechanisms.

2.2 Structure and Composition of the Bushveld Complex

The Bushveld Complex was emplaced into the central portion of the Kaapvaal craton, possibly exploiting a trans-lithospheric suture zone, the Thabazimbi Murchison Lineament (TML) (Good and DeWit, 1997). The TML formed at 2.96 Ga following the collision of the Pietersburg Block and the Kaapvaal Shield, creating the Kaapvaal Craton (Figure 2.1) (Silver et al., 2004). The region remained tectonically active throughout the Archean, expressed by the Limpopo orogeny at 2.7-2.6 Ga and the Magondi orogen at 2.0 Ga (Holzer et al., 1998; Silver et al., 2004). The Magondi orogen may have reactivated shear faulting along the TML during emplacement of Bushveld magmas and NW-SE compression within the cratons (Clarke et al., 2009; Silver et al., 2004). These tectonic events resulted in strong folding and formation of half-grabens in both the Archean basement and overlying sediments of the Transvaal Supergroup (Clarke et al., 2009).

Clarke et al. (2009) suggested that the Bushveld Complex was emplaced under localised extension in a back-arc subduction setting. In contrast Silver et al. (2004) favoured extension occurring in response to anisotropy in the mantle, while Olsson et al. (2011) preferred formation in response to delamination of the sub-continental lithospheric mantle (SCLM) and decompression melting of the asthenosphere following earlier magmatism. Palaeomagnetic modelling of magnetite (Clarke et al., 2009; Letts et al., 2009) suggests that the complex was emplaced sub-horizontally before subsiding into its present lopolithic structure, possibly coinciding with the cessation of plume activity and consequent subsidence of the crust (Olsson et al., 2011).
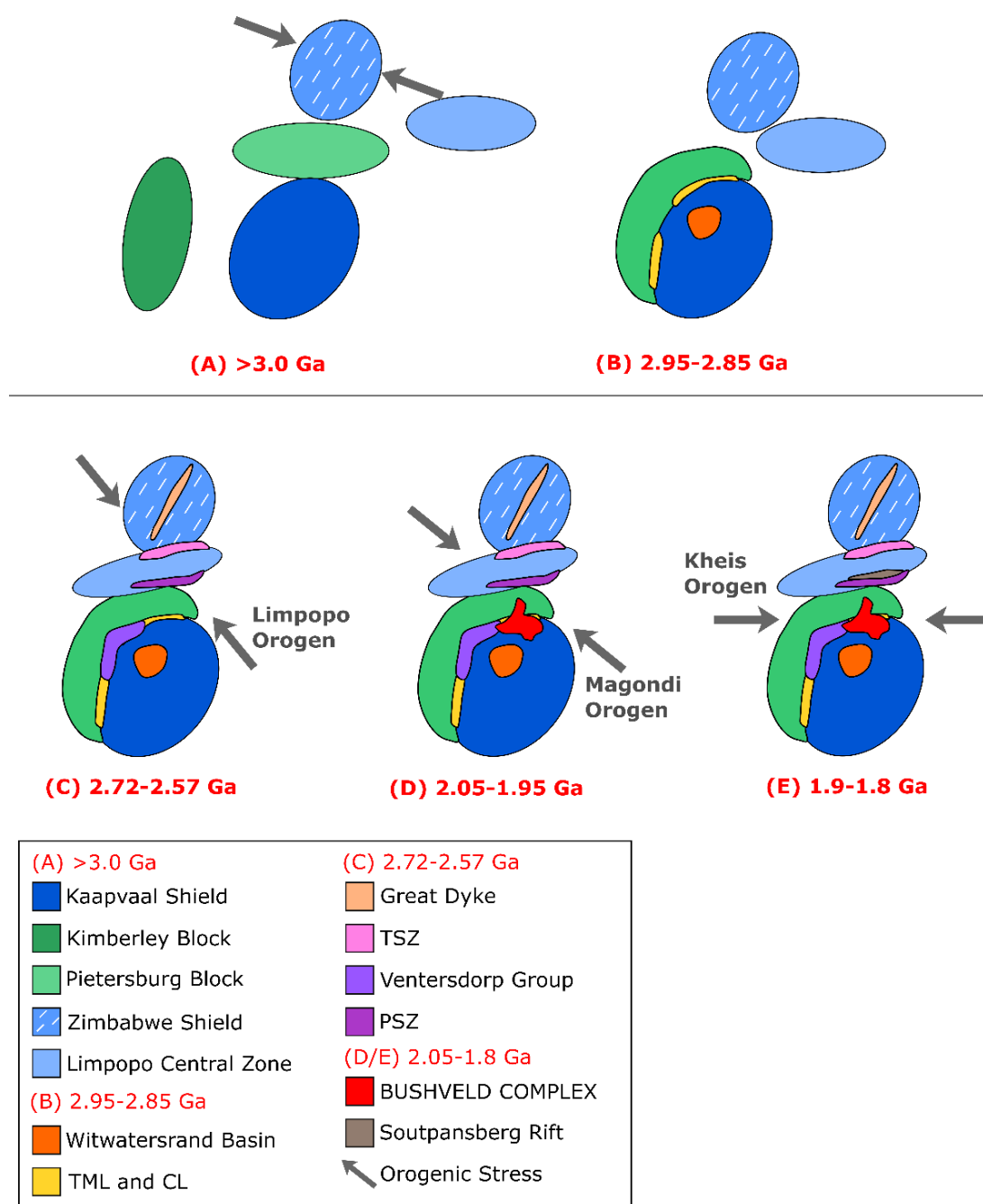
Figure 2.1: Block diagram of the assembly of the Kaapvaal Craton. Modified after McDonald and Holwell (2011) and Silver et al. (2004).

The location of the Bushveld Complex relative to the TML has led to suggestions that this suture may have played a central role in the emplacement of magmas in the Bushveld Complex serving as a magma conduit (Clarke et al., 2009; Good and DeWit, 1997). Other authors have suggested multiple feeder zones which are connected at depth and exploited the fabric and structures of prior tectonism (Kinloch, 1982; Sharpe et al., 1981). Another feeder zone has been proposed at Union Section in the western limb (Figure 2.2) based on lateral variation in the composition of Critical Zone rocks (Eales et al., 1988; Maier and Teigler, 1995).

The role of staging chambers below the main intrusion remains controversial. Some authors proposed these are critical to explain contamination and mineralization of Bushveld magmas (Harris et al., 2005; Maier et al., 2000; Naldrett et al., 2009), but until recently no conclusive evidence to support their existence has been found. Geophysical modelling by Cole (2018) has potentially identified several large staging chambers at the base of the crust.

The layered mafic-ultramafic rocks of the Bushveld Complex are grouped into the Rustenburg Layered Suite (RLS) which is preceded by mafic sills intruded into the upper crust and post-dated by more differentiated units including the Lebowa Granite Suite (Button and Cawthorn, 2015; Sharpe, 1981; Wabo, 2013; Walraven and Hattingh, 1993). The RLS is comprised of 5 limbs, the well exposed western, eastern and northern limbs as well as the far-western and Bethal limbs which are commonly covered by younger rocks, but detectable by gravity anomalies (Figure 2.2) (e.g. Webb et al., 2004). The northern limb lies to the north of the TML whereas the remaining limbs are located to the south. The full extent of the northern limb is still not known, with new discoveries such as the Waterberg project extending its geographical boundary northwards (Huthmann et al., 2016; Kinnaird et al., 2017; McDonald et al., 2017). Extensive geophysical investigation has suggested the northern limb may extend at depth up to 160 km west of the outcropping rocks, following the outcrop area of Bushveld Granites above (Cole, 2018; Finn et al., 2015; Willemse, 1964).
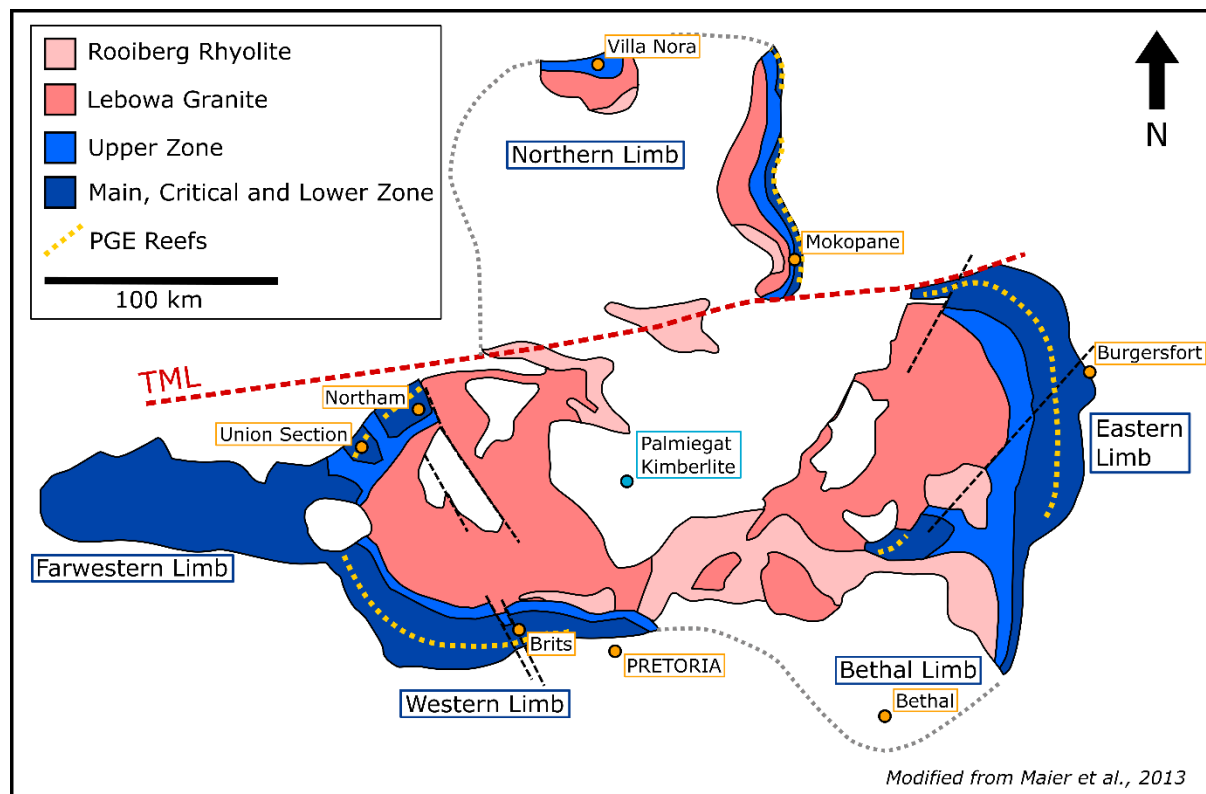
Figure 2.2: Geological Map of the Bushveld Complex. Modified after Maier et al. (2013). The TML trends WSW-ENE between the northern limb and the remainder of the Bushveld Complex. The far southern and northern extents of the Bushveld Complex are covered by younger rocks.

While the RLS was initially considered to represent a single intrusion, gravity data and consequent modelling in the latter half of the 20th century was used to suggest the eastern and western limbs represented separate intrusions of dipping magmatic sheets (Cousins, 1959; Du Plessis and Kleywegt, 1987). Later, modelling accounting for lithostatic flexure of the crust and MOHO in response to loading from the emplacement of the Bushveld Complex, suggested once again that these limbs are connected (Cawthorn et al., 1998; Cole et al., 2014; Webb et al., 2004) as was originally suggested (Hall, 1932a). This model is additionally supported by the discovery of Critical Zone xenoliths from kimberlite pipes in the centre of the intrusion and similar Sr isotope profiles of the eastern and western limbs (Kruger, 1994b; Webb et al., 2011).

2.2 Stratigraphy of the RLS

The RLS is subdivided into 5 zones (Hall, 1932b). From the base these are the Marginal Zone (MgZ), Lower Zone (LZ), Critical Zone (CZ), Main Zone (MZ) and Upper Zone (UZ) (Figure 2.3). These zones show an overall pattern of upward fractionation with a predominantly mafic-ultramafic base in the LZ and CZ, grading upwards into more evolved units of the, MZ and UZ (Figure 2.4). A Basal Ultramafic Series (BUS) has been documented in the eastern limb

beneath the marginal zone (Wilson, 2015). In total, the Bushveld Complex reaches a thickness of up to 9 km (Eales and Cawthorn, 1996). In addition, multiple sills are found intruding country rocks around the Bushveld Complex (Button and Cawthorn, 2015; Sharpe, 1981; Sharpe and Hulbert, 1985).
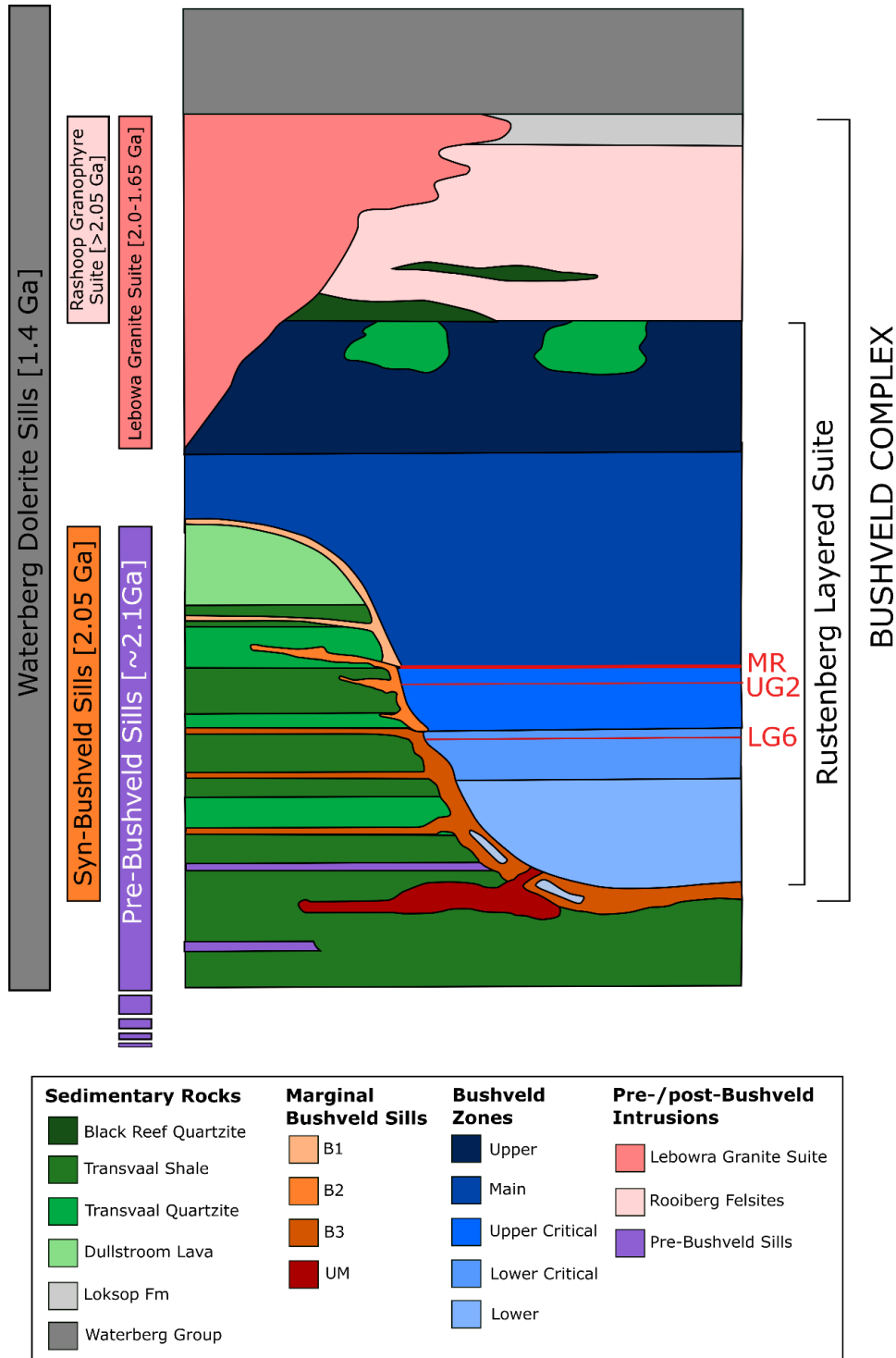
Figure 2.3: Schematic cross-section of the Bushveld Complex. Modified after Von Gruenewaldt et al. (1985). Note the marginal sills intruding country rock surrounding the main complex.

The Marginal Zone forms the lowermost zone and is laterally variable in thickness, being completely absent in places while attaining thicknesses of 800 m in the western limb (Eales and Cawthorn, 1996; Wilson, 2015). The MgZ is largely found as sill-like units intruding the country rocks associated with the complex (Sharpe, 1981). It is generally comprised of norites, pyroxenites and gabbronorites and locally contains anorthosite xenoliths suggesting the MgZ was intruded after the CZ (Wilson, 2015).

The Lower Zone is the least evolved zone comprising dunites, harzburgites and orthopyroxenites (Cameron, 1978; Teigler, 1990; Teigler and Eales, 1996; Yudovskaya et al., 2013). The Lower Zone is less laterally continuous than overlying rocks and has a maximum thickness around 1 km while being locally absent elsewhere, with thickness largely controlled by floor rock topography (Cameron, 1978; Eales and Cawthorn, 1996). Broadly the Lower Zone is thickest in the northern portion of the western and eastern limbs, in proximity to the TML and thinner towards the south (Karykowski and Maier, 2017). The thickness of individual layers of dunites, harzburgites and pyroxenites varies from several cm to ~40 m (Teigler and Eales, 1996). Cyclicity has been inferred to result from injections of new magma into the LZ, possibly forming a sill complex (Karykowski and Maier, 2017; Maier et al., 2013).

The Critical Zone is generally separated into 2 sections, named the Upper Critical Zone (UCZ) and Lower Critical Zone (LCZ), respectively. The Lower Critical Zone is 700-800 m thick and dominated by cumulus orthopyroxene. It is defined by either the onset of cumulus chromite (Scoon and Teigler, 1994), the increase in interstitial plagioclase from 2 to 6% (Cameron, 1978), or a sharp decrease in modal olivine (Teigler et al., 1992). Chromite can be locally concentrated to form chromitite seams, of which there are 9 major layers in the LCZ (Figure 2.4) (Scoon and Teigler, 1994). These chromitites can be economically important, including the Lower Group 6 (LG6) seam, hosting the world's largest chromitite reserve (Cousins and Feringa, 1964). Overall, the Critical Zone shows an upwards increase in intercumulus feldspar within orthopyroxenite layers although orthopyroxene composition remains broadly constant within much of the Lower, Lower Critical, and Upper Critical Zones (Cameron, 1978, 1980, 1982; Godel et al., 2011; Maier and Barnes, 1998; Teigler and Eales, 1996).
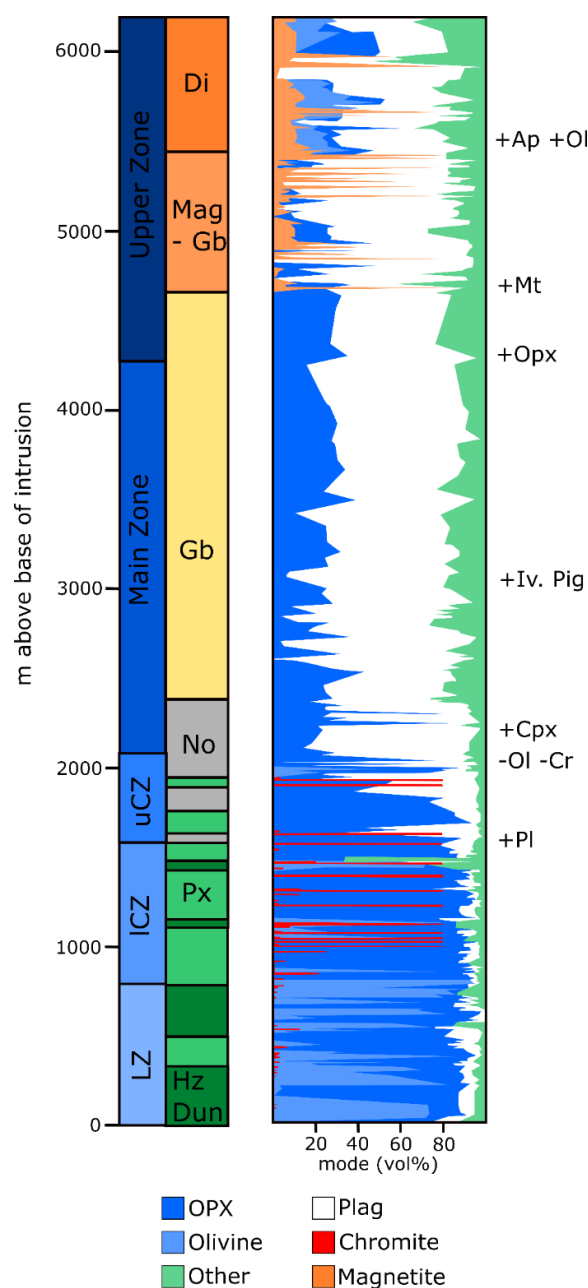
Figure 2.4: General Stratigraphy of the Bushveld Complex layered series showing the variation in modal mineralogy with height and characteristic compositions of the different zones. Modified after Maier et al. (2013).

The Upper Critical Zone is defined by the appearance of cumulus plagioclase although orthopyroxene remains the dominant cumulus phase (Eales and Cawthorn, 1996; Naldrett et al., 2009), except for areas distal to proposed feeder zones where cumulus plagioclase is dominant (Teigler et al., 1992). The UCZ is generally 0.5 km thick and hosts up to 5 main chromite seams including the MG3-4 and UG1-3 (Scoon and Teigler, 1994). Towards the top of the UCZ, norites and anorthosites form thick cyclic packages alongside orthopyroxenites (Cameron, 1982). The UCZ also hosts several PGE-rich reefs, namely the Merensky Reef and UG2 chromitite (Hiemstra, 1985; Maier and Barnes, 2008; Naldrett et al., 1986). The Merensky

Reef is located in the upper portions of the UCZ at the base of the Merensky Cyclic Unit. The reef is hosted by a pyroxenite layer but can locally extend into its noritic/anorthositic footwall rocks. The mineralized pyroxenite is locally pegmatoidal, up to 4 m thick and bounded by chromitite stringers along its upper and lower contact (Barnes and Maier, 2002a; Brynard et al., 1976). Generally, the highest PGE grade is found near the upper chromitite stringer (Barnes and Maier, 2002b). The Merensky Cyclic Unit is overlain by the Bastard Cyclic Unit, which resembles the Merensky Cyclic Unit but contains much lower grade. It is overlain by the uppermost layer of the CZ, a mottled anorthosite termed the Giant Mottled Anorthosite (GMA) in reference to its large pyroxene oikocrysts (De Klerk, 1992).

Above the Critical Zone is the Main Zone. This is significantly thicker than underlying units reaching 2-3 km in thickness. It is comprised of norites, gabbronorites, anorthosites and rare pyroxenite (Maier et al., 2001; Maier et al., 1996; Mitchell, 1990). The lower Main Zone is comprised of several 10s to 100s of metres of norite grading upwards into gabbronorite, which is capped by a Pyroxenite Marker horizon, above which more evolved gabbros and anorthosites of the Upper Main Zone are found (Cawthorn et al., 1991; Eales and Cawthorn, 1996; Kruger, 1994b; Mitchell, 1990; Molyneux, 1974).

The Upper Zone rests unconformably above the Main Zone, but where underlying units are absent the former can rest directly on floor rocks of the Transvaal Supergroup, such as in the so-called gap areas in the northern portion of the Western Bushveld Complex (WBC) (Wilson et al., 1994). The Upper Zone contains the most evolved rocks of the Bushveld Complex and is demarcated from the Main Zone by different authors as either, (1) the onset of cumulus magnetite, (2) the occurrence of the lowermost magnetite layer, or (3) the pyroxenite marker horizon (Kruger, 2005; Kruger et al., 1987; Wager and Brown, 1968). Magnetite is an abundant cumulus phase in much of the Upper Zone and can be concentrated to form magnetitite layers (Figure 2.4) (Eales and Cawthorn, 1996). Up to 26 such layers are documented in the UZ which individually can reach over 10 m in thickness constituting a significant resource of Ti and V (Reynolds, 1985). Cumulus plagioclase is the most abundant phase in the UZ, occurring within gabbro, diorite, troctolite and up to 45 anorthosite layers (Cawthorn and Ashwal, 2009; Reynolds, 1985). Country rock xenoliths are also documented throughout the UZ, especially in the northern limb (Ashwal et al., 2005; Tegner et al., 2006).

2.3 Geology of the Country Rocks

The magmatic rocks of the Bushveld Complex were intruded into the volcano-sedimentary Transvaal Supergroup, a sedimentary package up to 15 km thick (Figure 2.5) (Eriksson et al., 1993). The Transvaal Supergroup was unconformably deposited from 2.67-2.1 Ga on top of the Wolkberg Group and Archean basement; it also contains strata formed during the Great Oxidation Event (GOE) at 2.40-2.32 Ga, notably in the Duitschland Formation (Clendenin et al., 1991; Eriksson et al., 2001; Lyons et al., 2014). The RLS predominantly rests on the Magaliesberg quartzite, located in the upper half of the Transvaal sequence, while the northern limb is emplaced transgressively into formations below the Magaliesberg Quartzite (Cheney and Twist, 1991; du Toit, 1954; van der Merwe, 1976).

The Transvaal sedimentary basin, into which the Transvaal Supergroup was deposited, experienced thermal subsidence after regional rifting events, during which quartzites of the Black Reef Formation at the base of the Chuniespoort Group were deposited (Eriksson et al., 2001). Continued subsidence and formation of epicontinental seas allowed for the deposition of thick carbonate sequences that constitute the 2 km thick Malmani Subgroup (Figure 2.6) (Eriksson et al., 1993). The Malmani Subgroup is predominantly comprised of dolomite with a variable chert component and occasional oolite beds and stromatolite sequences (Eriksson and Truswell, 1974). Zones of limestone, unaffected by dolomitization are also documented (Button, 1973).

Above this, banded iron formation (BIF) of the Penge Formation are proposed to have formed in a deep, stratified epicontinental sea (Beukes, 1987; Klein and Beukes, 1989). Further rifting and fluctuating sea levels in the basin resulted in deposition of shale and carbonate sequences above the BIF, constituting the Pretoria Group, while sedimentary structures documented at Rooiberg suggest an additional fluvial input (Eriksson et al., 2001; Stear, 1977).
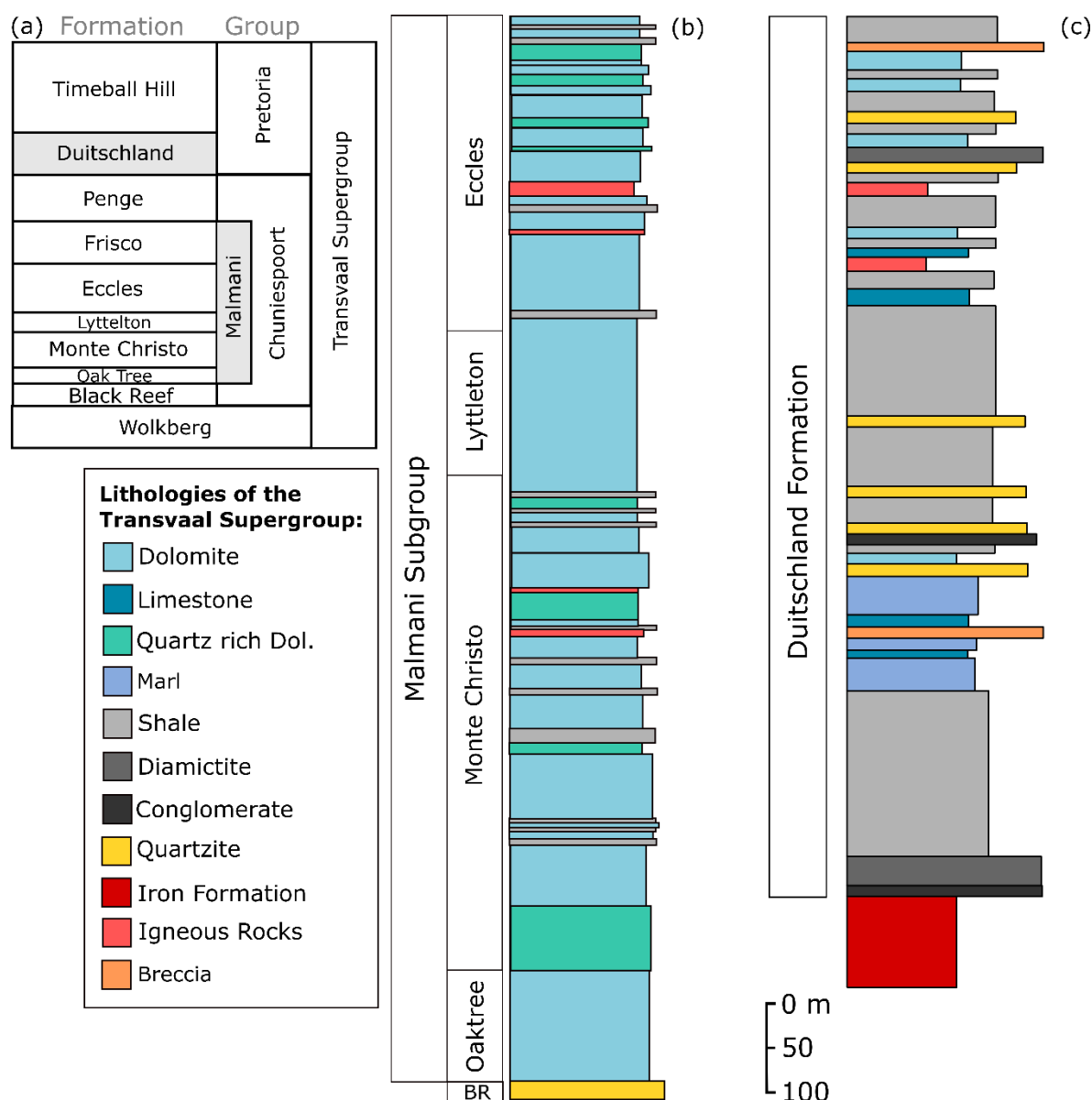
Figure 2.5: Stratigraphy of the country rocks that host the Bushveld Complex, modified after Bekker et al. (2001), Eroglu et al. (2015), Frauenstein et al. (2009). (a) General stratigraphy of the Transvaal Supergroup. (b) Detailed stratigraphy of the Malmani Subgroup recorded in the Transvaal Basin. (c) Stratigraphic section representative of the Duitschland Formation.

The lower portion of the Pretoria Group comprises the Duitschland Formation (Bekker et al., 2001). The Duitschland Formation is up to 1 km thick and was deposited from 2480 ± 6 Ma unconformably above the Penge Iron Formations (Bekker et al., 2001; Frauenstein et al., 2009). The lower section of the Duitschland Formation comprises a glacial diamictite and conglomerates, which are overlain by carbonaceous shale grading upwards into limestone, marl and dolomites (Bekker et al., 2001). This is interpreted to represent multiple cycles of sea level regressions upwards through the sequence, broadly in response to rifting and thermal subsidence events (Eriksson et al., 2001). Above the Duitschland Formation is the Timeball

Hill Formation comprised mostly of shales and an increasing sandstone component upwards through the succession. It is proposed to have formed from increasingly frequent episodic fluvial input into a deep-water depositional environment (Bekker et al., 2001; Eriksson et al., 2001).
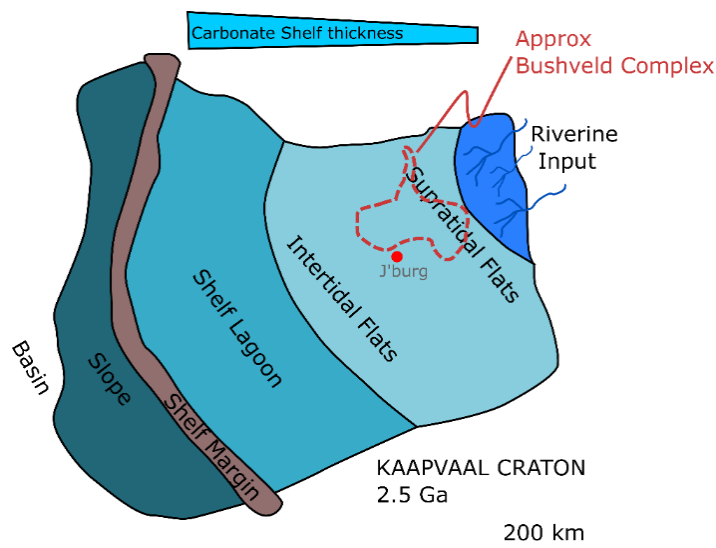
Figure 2.6: Schematic diagram showing the depositional environment of the Kaapvaal Craton that deposited the Transvaal Supergroup prior to intrusion of the Bushveld Complex, whose approximate location is marked. Fluctuations in sea level control the deposition of shales and carbonates and moderate the input of fluvial sediments. Modified after Beukes (1987) and Eroglu et al. (2015).

2.4 Parental Magmas to the Bushveld Complex

The nature of the parental magmas to the Bushveld Complex has remained controversial. Sharpe (1981) documented numerous sills marginal to the Bushveld Complex and proposed 3 potential magmatic suites, named Bushveld (B) 1-3. B1 is a siliceous high-Mg basalt, rich in both compatible elements (e.g. Ni and Cr) and incompatible elements. B2 and B3 are Al-rich tholeiitic basalts, with lower Mg than B1 with B3 magmas lower concentrations of incompatible elements (Barnes et al., 2010; Sharpe, 1981). Other authors have termed the B1 as U-type magma (Ultramafic) whilst B2 and B3 were termed A-type magmas (Anorthitic) (Irvine et al., 1983). B1 magmas are purported to be parental to the Lower and Lower Critical Zone, B2 to the Upper Critical Zone and B3 to the Main Zone. The parental magma to the UZ remains unclear. However, modelling B2 magmas does not produce the observed crystallisation sequence of the UCZ. Instead a mix of B1 and B2 magmas (60:40 ratio) has been proposed to satisfy the petrological evidence (Barnes et al., 2010). An ultramafic sill suite has also been identified comprising olivine-chromite rich B1 rocks, and was thus termed the B1-UM (Barnes et al., 2010; Godel et al., 2011).

The formation of the parental magmas is still debated, with geochemical and isotopic data suggesting the magmas were contaminated by crustal material prior to emplacement (Barnes et al., 2010; Harris et al., 2005; Kruger, 1994b; Maier et al., 2000; Sharpe, 1981). However, crustal contamination of a primitive melt does not explain the high PGE contents and Pt/Pd ratios seen in the Bushveld. To explain this, some authors have proposed a model of sub-lithospheric continental mantle (SCLM) melting as this has high Pt/Pd ratios (Maier and Barnes, 2004; Richardson and Shirey, 2008), but others prefer PGE enrichment to occur during assimilation of PGE rich sulphides in staging chambers (Naldrett et al., 2009).

2.5 Emplacement Styles of Bushveld Magmas

The emplacement of the Bushveld Complex continues to be a topic of vigorous debate within the LMI community. There is little consensus on the mechanisms or even relative timings of emplacement, largely due to the wide variety of cumulus textures. Traditionally, the Bushveld Complex was envisaged as a large convecting magma chamber in which basaltic magmas underwent fractional crystallisation and crystal settling, creating a cumulate pile (Wager and Brown, 1968). Repeating cyclic units are explained in this model by the episodic injections of fresh magma into the chamber which mixes with the resident melt. Repetitive magma replenishment has been used to explain the significant Cr and PGE contents throughout the CZ (Maier et al., 2013). Injections of new magmas have also been invoked to explain the transgressive contacts of units, e.g. the Merensky reef (Latypov et al., 2017a; Naldrett et al., 2009; Viljoen, 1999).

Whether magmas were intruded with or without a significant crystal load also remains unresolved. Magma mixing models mostly imply crystal free melts (Naldrett and Von Gruenewaldt, 1989), consistent with the fine grain size of most marginal sills (Sharpe, 1981). However, several authors have suggested the MZ magmas were emplaced as a crystal mush, citing the largely homogeneous nature of the MZ, deformation structures in MZ plagioclase crystals, low concentrations of incompatible elements and broadly constant Sr isotope values (Maier and Barnes, 1998; Roelofse and Ashwal, 2012; Roelofse et al., 2015).

However, other workers take issue with the model of a large magma chamber and prefer to view the intrusion to form by multiple sill injections. Sills have been documented intruding country rock around both the eastern and western limbs (Cawthorn et al., 1981; Sharpe, 1981). Recent geochronological work undertaken by Mungall et al. (2016) on several layers in the Western Bushveld Complex (WBC) in the UCZ and MZ, including major mineralized layers such as the Merensky Reef, have been interpreted to reflect intrusion of younger sills below older units. This directly contravenes the traditional model for the crystallisation of large layered intrusions from a convecting magma chamber (Wager and Brown, 1968). In the

northern limb there is clearer evidence of sill emplacement, with country rock layers separating discrete cumulate units in the Platreef, the MgZ and the LZ (Kinnaird et al., 2005; Manyeruke et al., 2005; Yudovskaya et al., 2013).

2.6 Geochronology

The Bushveld Complex was first dated in 1977 with a Rb-Sr age of 2095 ± 24 Ma (Hamilton, 1977). Subsequent advances in geochronological techniques have culminated in high-precision U-Pb analysis of zircon, with the Merensky Reef producing an initial crystallisation age of 2054.4 ± 1.3 Ma (Scoates and Friedman, 2008) and more recently published dates ranging between 2055.09 ± 0.36 (Zeh et al., 2015) and 2057.04 ± 0.55 Ma (Scoates and Wall, 2015). As precision and accuracy of geochronological data improves, more detailed relationships between emplacement of different units in the Bushveld Complex can begin to be unravelled (Mungall et al., 2016). The duration of Bushveld magmatism remains unresolved with estimates ranging between 1.02 ± 0.37 Myrs based on U-Pb zircon analysis (Zeh et al., 2015) and 75 Kyrs based on model calculations (Cawthorn and Walraven, 1998). However, such models are largely dependent on the size of the intrusion, which remains unknown, although estimates suggest the total volume of magma was in excess of 1 million km^3 (Cawthorn and Walraven, 1998).

2.7 Models of mineralization in the Bushveld Complex

Models for the formation of laterally extensive reefs such as the Merensky Reef in the Bushveld Complex and the J-M reef of the Stillwater Complex can be grouped into two categories, either envisaging a downwards concentration of PGE-rich phases (so-called "downer" models), usually in the form of immiscible sulphide melts, or the upward movement of PGE in a fluid or a melt (so-called "upper" models).

2.7.1 Downer Models

Downer models invoke downward percolation of an immiscible sulphide melt through a sulphur saturated magma column to the top of the cumulate pile. Many workers propose that sulphur saturation may be achieved through mixing of magmas with different compositions, assisted by contrasting magma densities and turbulent injection (Eales et al., 1986; Li et al., 2001; Naldrett et al., 1986; Naldrett and Von Gruenewaldt, 1989). Mixing could have resulted in high R factors (ratio of silicate to sulphide melt) to increase sulphide tenor (Campbell and Naldrett, 1979). However, other workers have refuted magma mixing as a viable mechanism to trigger sulphide saturation in the Bushveld Complex (Cawthorn, 2002; Maier et al., 2013; Seabrook and Cawthorn, 2005). Li and Ripley (2005) have shown that both magmas must be close to sulphide saturation to satisfy this model (Li and Ripley, 2005). In addition, magma mixing models largely rely on processes occurring within a large convecting magma chamber,

although more recently authors suggest these chambers are largely comprised of crystal mush with a relatively small melt component (Cashman et al., 2017).

The global occurrence of PGE reefs within the transition from ultramafic to mafic portions of layered intrusions suggests that fractionation is an important reef-forming process (Maier, 2005). Cawthorn (2005) invokes pressure change across the chamber, in response to additions of large volumes of magma such as the MZ, to instantaneously trigger sulphide saturation and PGE partitioning into sulphides simultaneously across the whole intrusion. However, sulphide settling through a magma column is still required in this model, albeit in a more quiescent environment than that of magma mixing.

Several authors favour instead a model whereby intruding Bushveld magmas already contained an immiscible sulphide melt component, removing the need for large magma columns above the Merensky Reef (Arndt et al., 2005). Sulphide entrainment has also been proposed for the formation of the Platreef in the northern limb (McDonald and Holwell, 2007). However, Barnes et al. (2010) found Bushveld magmas to be sulphur undersaturated, although some sulphides have been documented in sills surrounding the complex (Sharpe and Hulbert, 1985).

2.7.2 Upper Models

Boudreau and McCallum (1992) and Boudreau (2008) proposed a detailed model in which the Merensky Reef was recrystalised from ascending fluids carrying PGE. At the top of the mush pile, the fluids dissolved in the melt triggering sulphide saturation and deposition of the reef. The presence of hydrous phases such as biotite, hydrous melt- and fluid inclusions are used as evidence to support this model. A similar model was proposed by Nicholson and Mathez (1991), although they did not suggest large scale mobilization of PGE, while Boudreau's model derives PGE from the entire thickness of the cumulate pile. Pegmatoidal units beneath both the UG2 and Merensky Reef have also been proposed to form in response to fluid flux (Mathez et al., 1997; Mathez and Mey, 2005). More recently a model of sulphide melt redistribution by attaching to volatile-rich bubbles has been proposed (Mungall et al., 2015).

2.8 Introduction and General Geology of the Northern limb

The northern limb of the Bushveld Complex is located north of the TML with outcropping rocks extending 110 km north, although recent work on the Waterberg project has shown that Bushveld rocks continue for a further 30 km (Kinnaird et al., 2017; van der Merwe, 1976). The northern limb dips 15-45° to the west resulting in a package of outcropping rocks 4-15 km in thickness (van der Merwe, 1976). The country rocks to the northern limb have been intensely folded in response to regional tectonism (van der Merwe, 1976). The resultant fold structures strongly controlled emplacement of northern limb magmas, creating the sinuous outcrop pattern of the northern limb, compartmentalizing intrusions of magma into discrete sections at depth, and forming large-scale fold features such as the 'dolomite tongue' on the farm Sandsloot (McDonald and Holwell, 2011; Yudovskaya et al., 2013).

The magmas in the northern limb were mostly emplaced into stratigraphically lower Transvaal Supergroup rocks compared to the Bushveld Complex south of the TML, and the intrusion transgressed progressively deeper portions of the Transvaal Supergroup from south to north (Figure 2.7) (Cheney and Twist, 1991; van der Merwe, 1976). In view of the rapidly changing floor rocks, different sections of the northern limb are referred to by the farm name on which it occurs. The farms, in turn, are grouped into the southern, central and northern sectors (Kinnaird et al., 2005). In the southern sector of the northern limb, on the farms Grasvally, Rooipoort and Townlands the floor rocks comprise quartzites and shales, respectively (Maier et al., 2008; Manyeruke et al., 2005). On the farm Turfspruit, where the present study is located, the northern limb intrudes Duitschland Formation shales and dolomites (Kinnaird et al., 2005). In the central sector of the northern limb the magmas intruded dolomite of the Malmani Subgroup on the farms Tweefontein, Sandsloot and Zwartfontein (Holwell and Jordaan, 2006; Holwell et al., 2006). On the farms Overysel and Drenthe, the northern limb magmas intruded directly into or onto granite and gneiss of the Archean basement (Cawthorn et al., 1985; Gain and Mostert, 1982). Concurrent with this transgressive footwall relationship the lower portions of the RLS pinch out northwards (Buchanan 1981). For example, in the southern sector the Platreef is up to 445 m thick (Kinnaird et al., 2005), thinning northwards to 35 m on the farm Overysel (Holwell and McDonald, 2006) and locally absent in the far north (Maier et al., 2008).
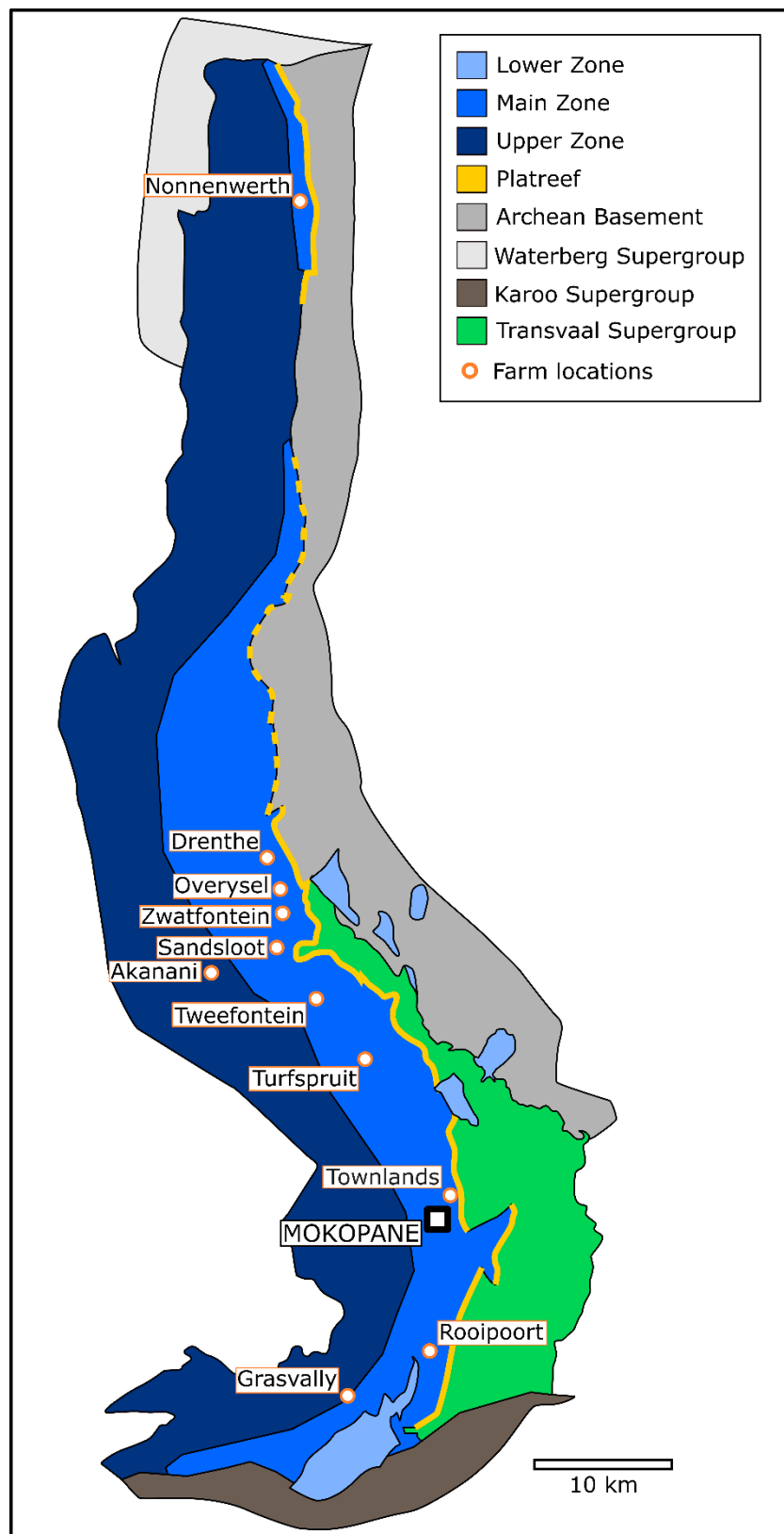
Figure 2.7: Geological map of the northern limb of the Bushveld Complex illustrating the transgressive nature of Bushveld magmas relative to the underlying country rock. Modified after Maier et al. (2008).

The northern limb is significantly more contaminated by its floor rocks than the rest of the Bushveld Complex, particularly where the footwall contains shales and dolomites. Contamination is expressed by abundant xenoliths and rafts of country rocks. In addition, abundant contaminated magmatic units occur, to which the prefix 'para-' is commonly attached (Armitage et al., 2002; Kinnaird, 2005; Kinnaird et al., 2005; Manyeruke et al., 2005). This intense contamination can obliterate magmatic layering and has resulted in ongoing debate over the formation of the northern limb and its correlation to the rest of the Bushveld Complex.

2.9 Stratigraphy of the northern limb

2.9.1 Characteristics of the Lower and Marginal Zones in the Northern limb

In the northern limb, the Lower Zone reaches thicknesses in excess of 770 m and is comprised of dunite, harzburgite and subordinate pyroxenite (Grobler et al., 2018; Yudovskaya et al., 2013). It is intruded into floor rocks of the Transvaal Supergroup, which separate the LZ from overlying magmatic rocks. Similar to the rest of the complex, the LZ in the northern limb is strongly controlled by structures in the country rock, with the LZ forming discrete compartments (Yudovskaya et al., 2013). Within the LZ, cyclic units are generally marked by basal chromitite seams. In the far southern section of the northern limb, on the farm Grasvally, the LZ carries significant PGE grade in the Volspruit and Drummondlea subzones which are not documented elsewhere in the Bushveld Complex (Hulbert and Vongruenewaldt, 1982; Tanner et al., 2019). Here the LZ can attain thicknesses up to 1600 m, with 37 cyclic units documented (Hulbert and Vongruenewaldt, 1982).

The noritic rocks of the MgZ are documented intruding between the LZ and overlying magmatic rocks, either along the upper contact of the LZ with country rocks, at the base of the Platreef/Flatreef or within the Platreef/Flatreef (Kinnaird et al., 2005; Yudovskaya et al., 2013). This is in contrast to the eastern and western limbs, where MgZ is situated stratigraphically below the LZ, or intruding into it (Engelbrecht, 1985; Wilson, 2012; Yudovskaya et al., 2013).

2.9.2 Characteristics of the Platreef and Flatreef in the Northern Limb

2.9.2.1 Platreef

The Platreef is defined as comprising magmatic rocks between Transvaal/Archean floor rocks below and the Main Zone rocks above, which contain Ni-Cu-PGE mineralization (Kinnaird and McDonald, 2005). The Platreef is broadly comprised of orthopyroxenite with lesser norites, gabbros, anorthosites and, less commonly, harzburgite that is largely serpentinised (Kinnaird et al., 2005; Kinnaird and Nex, 2015). In addition, significant contamination by country rocks produced a wide range of exotic lithologies including wehrlite, lherzolite and clinopyroxenite, the latter of which is colloquially termed parapyroxenite (McDonald and Holwell, 2011). Traditionally, the Platreef was categorized into A, B and C units from the base to the top

(White, 1994), although this terminology has been widely abandoned due to the strong lateral heterogeneity of the Platreef which is interpreted to result from contamination (Kinnaird et al., 2005). For example, on the farm Sandsloot, extensive interaction of the Platreef with dolomitic and BIF floor rocks resulted in replaced Fe-rich Platreef and hybrid rocks, as well as abundant calc-silicate xenoliths (Buchanan et al., 1981; McDonald et al., 2005). Isotopic and geochemical data from across the Platreef also indicate a significant (5-18%) country rock contamination with shale, dolomite and Archean basement rocks (Barton et al., 1986; Cawthorn et al., 1985; Harris and Chaumba, 2001; Holwell et al., 2007; Pronost et al., 2008; Reisberg et al., 2011).

Xenoliths of shale have been metamorphosed to cordierite-bearing hornfels and xenoliths of metamorphosed dolomite comprising clinopyroxene-olivine bearing calc-silicates (Kinnaird et al., 2005). Hornfels and calc-silicates are also documented to form elongate rafts within the Platreef (Kinnaird, 2005; Manyeruke et al., 2005). The xenolith population in any one portion of the Platreef is broadly representative of the local floor rocks. However, on the farm Nonnenwerth there are abundant dolomite xenoliths, despite the floor rocks comprising Archean basement (Manyeruke, 2007). Where xenolith composition differs to the immediate floor rocks they have been suggested to either have been transported northwards during emplacement of magmas or xenoliths derived from the roof rocks (Gain and Mostert, 1982; Holwell et al., 2007). Floor rock topography also has strong control on the thickness of the Platreef. Local topographic highs in the floor rocks can incur a local thinning of the Platreef down to several metres (Armitage et al., 2002).

At the southern end of the northern limb lies a mafic package termed the GNPA (Grasvally Norite Pyroxenite Anorthosite) which is interpreted to be the stratigraphic equivalent to the Platreef and was correlated with the Critical Zone by Hulbert and von Gruenewaldt (1985). It is separated from the rest of the northern limb by the Ysterberg-Planknet fault and bound to the south by the Zebediela fault (Figure 2.7). Similar to the Critical Zone the GNPA is comprised of multiple cyclic units comprising gabbronorite and pyroxenite. A UG2-like chromitite was also documented on the farm Grasvally (Hulbert and Vongruenewaldt, 1985)

The Platreef is so termed because of its significant PGE mineralization forming thick reefs (on the order of decimetres). This is in contrast to PGE mineralization in the eastern and western limbs, which is restricted to thin reefs (up to ~2 m). Where the footwall is dolomitic PGE grades in the Platreef exceed 4 g/t, while in the northern sector where the footwall is Archean basement grades are lower at 1-2 g/t (Hutchinson and Kinnaird, 2005). Sulphur isotope studies suggest only a small contribution of crustal sulphur to the Platreef, which is largely restricted to its lower portions (Holwell et al., 2007; Yudovskaya et al., 2017a).

The enrichment of PGE and S throughout the thickness of the Platreef remains unexplained and has precluded workers from correlating the Platreef with the UCZ of the eastern and western limbs. The Platreef is also unusual in its Pt/Pd ratio which is generally around 1, whereas in the eastern and western limbs it is mostly > 2 (McDonald and Holwell, 2011). This relative enrichment in Pd has been purported to result from fluid remobilization (Maier et al., 2019 In Press), although this remains controversial.

Several models have been proposed to explain the Platreef mineralization and can be largely grouped into whether sulphide saturation occurred pre- or post-emplacement. McDonald et al. (2007) suggested sulphides were entrained in a staging chamber prior to emplacement. Maier (2005) and Maier et al. (2008) also prefer a model of sulphide saturated magmas prior to intrusion, which then experienced variable cooling rates dependent on their proximity to cold country rocks upon emplacement, supressing formation of reef layers in favour of fast-cooling contact-style mineralization. Others prefer a model of contact-style mineralisation where sulphides segregated after emplacement of magmas into the northern limb in response to contamination by country rocks (Buchanan et al., 1981). Naldrett et al. (2009) proposed a 'pudding-basin' model whereby the Platreef represents residual UCZ magmas derived from the centre of the complex, squeezed out at the margin of the intrusion.

2.9.2.2 Flatreef

The Flatreef represents the deep extension of the Platreef (~700 m below surface) where the dip of the magmatic rocks shallow to become sub-horizontal (Figure 2.8) (Grobler et al., 2018). It is largely identified by an extensive drilling campaign on the farm Turfspruit by Ivanhoe Mines Ltd. and may possibly extend to the farm Akanani further north, downdip of the Platreef on the farm Sandsloot (Mitchell and Scoon, 2012). The Flatreef appears to be less contaminated than the Platreef, with magmatic layering broadly preserved, especially in its upper portion, which is located further from the floor rocks. It has been defined by Grobler et al. (2018) as an ultramafic-mafic package that hosts 3 mineralized reefs, the upper 2 being pyroxenitic and the lower being a chromitite. In the present study the definition of the Flatreef is extended to include all magmatic rocks between the MZ hangingwall and the footwall Transvaal sequence that hosts the LZ. This extended Flatreef can attain thicknesses in excess of 500 m. The 3 reefs at the top of the Flatreef have been correlated with the Bastard Reef, Merensky Reef and UG2 chromitite of the UCZ in the western and eastern limbs of the Bushveld Complex (Figure 2. 9) (Grobler et al., 2018). However, this model is not yet widely accepted and is largely based on litho-stratigraphic observations and limited geochemical data.
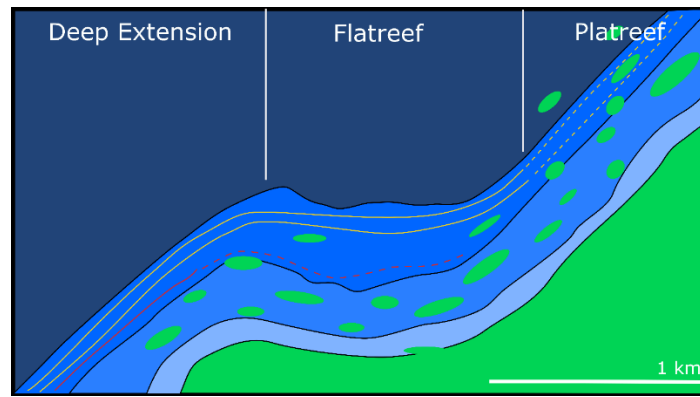
Figure 2.8: Schematic cross-section of farm Turfspruit looking northwards. Modified after Grobler et al.
(2018). At depth the Platreef shallows into the Flatreef, both are overprinted by abundant xenoliths.
Note the vertical scale is exaggerated.

As is the case for the Platreef, the Flatreef is strongly controlled by both footwall composition
and topography. Variable footwall topography can interrupt the otherwise well developed
layering (Figure 2. 9). On the farm Turfspruit the Flatreef was largely emplaced into the
Duitschland Formation of the Transvaal Supergroup (Grobler et al., 2018) and thus xenoliths
of hornfels and calc-silicate are abundant in lower portions of the Flatreef. In contrast, there is
little interaction with floor rocks in upper portions of the Flatreef. One exception is the abundant
granitic veins which cross-cut the Flatreef throughout its thickness. These granitic veins are
also documented in the Platreef (Kinnaird et al., 2005).
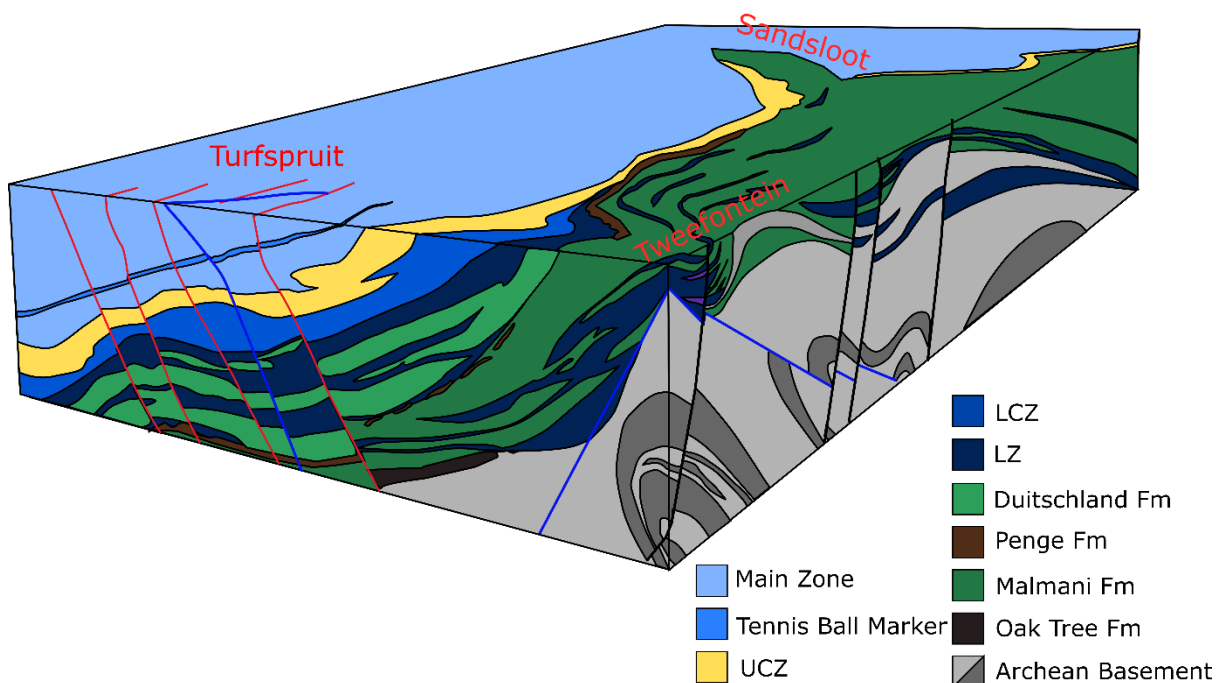
Figure 2. 9: Geological 3-D block diagram of the southern sector of the northern limb. Modified after
Grobler et al. (2018). Note the strong folding of the Archean basement, sedimentary country rock units
and Lower Zone intrusions.

Mineralization in the Flatreef contains features similar to both the Platreef and the UCZ of the WBC. Three relatively thin zones of significant PGE mineralization are documented in the Flatreef and can be traced across most of the Turfspruit property, similar to the reefs of the UCZ. However, in the Flatreef these zones commonly extend over several metres thickness, although peak mineralization is broadly confined to the upper ~1 m (Grobler et al., 2018; Yudovskaya et al., 2017b). The mineralized reefs can be traced up-dip and are seen to transgress into disseminated mineralization in the Platreef (Grobler et al., 2018). Notably, the silicate host rocks of the main reefs are also mineralized with reported intersections of 4.5 g/t Pt-Pd-Rh-Au over 90 m (Grobler et al., 2018).

2.9.3 Characteristics of the Upper and Main Zones in the Northern limb

The Main and Upper Zones of the northern limb show variable thickness along strike, unlike their counterparts south of the TML. Both zones are thickest in the central sector (2200 m MZ), with the upper portions of both zones largely absent further south (van der Merwe, 2008). To the north the various zones of the northern limb thin and pinch out resulting in the Main Zone resting directly on Archean basement on the farm Nonnenwerth (Maier et al., 2008; Manyeruke, 2007). Cross-cutting relationships at Sandsloot suggest a possible hiatus between crystallisation of the Platreef and intrusion of the Main Zone although this has not been observed elsewhere (Holwell et al., 2005). The Main Zone of the northern limb is largely comprised of gabbro, norite and anorthosite rocks with 2 pyroxenite marker layers, similar to that of the eastern and western limbs (Tanner et al., 2014). However, in addition, the MZ in the northern limb also contains a troctolite unit not documented elsewhere (van der Merwe, 1976). Mineral compositions evolve upwards through the stratigraphy (Ashwal et al., 2005; Tanner et al., 2014; van der Merwe, 1976). Cyclicity has also been observed in mineral compositional studies (Tanner et al., 2014) and extensive density and magnetic susceptibility studies (Ashwal et al., 2005).

The Upper Zone reaches a thickness exceeding 1180 m in the central sector and contains the most evolved mineral compositions of the RLS. The main lithologies comprise of pyroxenite, gabbro, norite and anorthosite, with variable amounts of olivine and magnetite (Ashwal et al., 2005; van der Merwe, 1976). The latter forms up to 32 massive magnetitite layers. Towards the top of the UZ, biotite, apatite, K-feldspar, quartz and amphibole become increasingly abundant forming ~20% of the modal mineralogy with exceptional enrichments up to 30 and 50% (Ashwal et al., 2005).

2.10 Formation of the Northern limb and its correlation with the wider Bushveld Complex

The emplacement of the RLS in the northern limb is thought to originate from a feeder zone identified by gravity anomalies to the west of Mokopane (Kruger, 2005; van der Merwe, 1976). Formation of the Platreef is proposed to result from the intrusion of multiple sills. This model is consistent with the presence of abundant country rock rafts within the Platreef and thick intervals of LZ within Transvaal Supergroup floor rocks (Kinnaird, 2005; Manyeruke et al., 2005; Yudovskaya et al., 2013). Other workers still envisage emplacement of magmas into chambers (McDonald and Holwell, 2011).

The significant contamination of magmas by country rock has overprinted magmatic layering, geochemical composition, and isotopic signatures of the RLS in the northern limb. In addition, the thick PGE reefs in the northern limb contrast with the thin strata-bound reefs of the remainder of the Bushveld Complex. The differing characteristics of the Platreef compared to the Critical Zone of the eastern and western limbs has led some authors to suggest the CZ is absent from the northern limb (Kruger, 2005; McDonald and Holwell, 2011; McDonald et al., 2005).

Other discrepancies between the lithostratigraphy of the northern limb relative to the eastern and western limbs include, (1) the presence of a thick troctolite marker in the northern limb, (2) the poor development of a pyroxenite marker separating the Main and Upper zones in the northern limb, and (3) the presence of PGE mineralization in the LZ at Grasvally (McDonald and Holwell, 2011). These discrepancies, in addition to the significant country rock contamination and the paucity of magmatic layering, have led many workers to reject the idea that the Platreef of the northern limb can be correlated directly to the UCZ of the eastern and western limbs (McDonald et al., 2005). However, the discovery and characterisation of the Flatreef has lent renewed support to the notion that the main PGE mineralized sequences within all Bushveld limbs can be stratigraphically correlated (Grobler et al., 2018; Yudovskaya et al., 2017b).

Chapter 3 - Methodology

In order to investigate the formation of the Flatreef, a range of analytical techniques have been used, including both traditional and more novel approaches. The former includes drill core logging, thin-section petrography, SEM analyses of silicate minerals and whole rock radiogenic isotope studies, namely Sr, Nd and Pb. More novel datasets include thin-section element maps and stable Mg isotopes. The following chapter provides a detailed account of the methods used. Data on standard materials can be found in the appendices.

3.1 Sampling Strategy

3.1.1 Drill Core Sampling

Two drill cores, UMT081 and UMT094, collared in the Main Zone on the Turfspruit property were selected for sampling (Figure 3.1). These drill cores are particularly long cores intersecting the deepest portions of the Flatreef and significant intervals of its sedimentary floor rocks. In total 66 samples were selected spanning the entire thickness of the Flatreef, its immediate footwall country rocks and the lower Main Zone hangingwall, a list of samples is provided in Appendix 1. These are quarter core samples with a core thickness of ~5 cm and are generally 10-15 cm in length. The data generated for these samples complement extensive analyses of samples (593 analyses in drill core UMT081 and 279 analyses in drill core UMT094) assayed for PGE, Au, Ni, Cu, Cr and S.
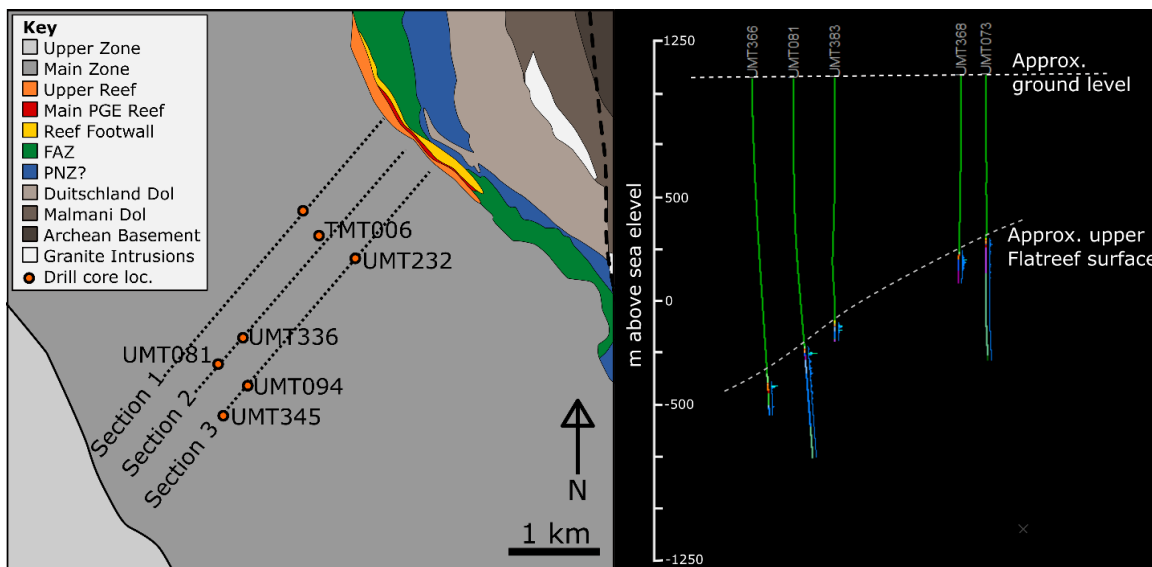
Figure 3.1: Plan view of drill cores localities overlain on a geological map. Section 2 is displayed in cross-section indicating the dip of the Flatreef and the enhanced depth of drill core UMT081 relative to surrounding drill cores. (a) Modified after Grobler et al., 2018, (b) supplied by Ivanhoe Ltd. (unpublished)

3.1.2 Outcrop Sampling

Six hand specimens of calcareous sediments were sampled from the Duitschland Formation and the Malmani Subgroup (labelled DUIT and MAL, respectively) approximately 16.5 km east of Mokopane. This was deemed sufficiently far from the magmatic contact of the northern limb to be outside the metamorphic aureole of the Bushveld Complex.

3.2 Mineral Chemistry

3.2.1 Petrology and Petrographic Micrographs

Petrological analysis was done on polished thin sections using a Microtec microscope with 2.5x to 60x magnification and reflected light capabilities. Micrograph images in transmitted and reflected light were taken on a Leica DM750P and captured using a Nikon camera using the Leica Application Suite software.

3.2.2 SEM

Mineral chemistry was obtained for all the main silicate phases present in the samples including orthopyroxene, clinopyroxene, plagioclase and olivine. Three analyses were taken in each grain to capture the range of compositions. These data were collected using the Zeiss Sigma HD Field Emission Gun Analytical Scanning Electron Microscope at Cardiff University. A beam energy of 20 kV was used with a 60 μm aperture at a working distance of 8.9 μm and counting time of 20 seconds. X-rays are acquired using dual 150 mm^2 Oxford Instruments X-Max Energy Dispersive Spectrometers using a 3 μs process time. Secondary standards used routinely for this work include plagioclase, chrome-rich clinopyroxene and olivine supplied by Astimex (block MINM25.53 + FC). Calibrations were performed at the beginning of each session and secondary standards are monitored throughout the sessions to monitor for drift. Average standard deviations based on secondary standards throughout the collection of SEM data are listed in Table 3.1. The full dataset of mineral compositions is reported in Appendix 2.

Plagioclase	O	Na	Mg	Al	Si	K	Ca	Fe	Total
Published Value	46.79	3.24	0.06	15.54	24.83	0.2	8.53	0.27	99.46
Average *(This study)*	46.73	3.21	0.04	15.74	24.54	0.30	8.70	0.33	99.60
Std Dev *(This study)*	0.26	0.05	0.02	0.11	0.17	0.04	0.07	0.02	0.53

n=105

Cr-diopside	O	Na	Mg	Al	Si	Ca	Ti	Cr	Fe	Total
Published Value	44.07	0.3	10.69	0.16	25.67	17.63	0.06	0.38	1	99.96
Average *(This study)*	44.18	0.31	10.63	0.20	25.84	17.39	0.05	0.38	1.04	100.03

| Std Dev *(This study)* | 0.26 | 0.03 | 0.11 | 0.03 | 0.19 | 0.14 | 0.02 | 0.09 | 0.04 | 0.56 |

n=126

Olivine	O	Mg	Si	Fe	Ni	Total
Published Value	44.09	30.74	19.45	5.64	0.29	100.2
Average *(This study)*	44.52	31.36	19.47	5.58	0.36	101.31
Std Dev *(This study)*	0.38	0.30	0.19	0.05	0.05	0.84

n=64

Table 3.1: Average standard deviation data from analytical runs for SEM data collection sessions.

Element maps were run with a 15 kV beam, 60 μm aperture and 5000 μs dwell time at roughly 100x magnification with a 10 μm pixel size allowing several thin sections to be mapped overnight. Typical input and output count rates of 60,000 cps were achieved with a 0.5 μs process time and dead time of 30%. These maps are used for textural studies and to quantify modal mineralogy. Mineralogical proportions within each rock type were largely deduced using whole thin section element mapping on the analytical SEM at Cardiff University and processing of these quantitative maps to determine mineral abundance.

3.2.3 Electron Microprobe

Olivine was analysed in part on a JEOL JXA8530F Hyperprobe at Bristol University. Olivine was analysed for Mg, Fe, Si, Ca, Ni and Mn with standard data presented in Table 3.2. Olivine standards SH11 and Nahavo Olivine were used. For analysis of olivine a beam energy of 20 keV with 200 nA current and 20 μm aperture was used. The spot size of analysis was 1.07 μm and this was rastered over a 300 nm area.

SH11	SiO_2	MgO	CaO	FeO	NiO	MnO
Standard avg	40.846	48.537	0.098	10.492	0.362	0.141
stdev	0.207	0.343	0.002	0.063	0.003	0.003
avg *(this study)*	40.482	48.530	0.098	10.522	0.361	0.145
std dev *(this study)*	0.299	0.224	0.001	0.051	0.004	0.003

n=3

Navaho	SiO_2	MgO	CaO	FeO	NiO	MnO
Standard avg	41.265	49.975	0.086	8.414	0.388	0.118
stdev	0.137	0.259	0.002	0.057	0.002	0.003
avg *(this study)*	40.854	50.118	0.085	8.422	0.388	0.121
std dev *(this study)*	0.252	0.146	0.000	0.037	0.002	0.002

n=3

Table 3.2 Average standard laboratory analyses and std dev, compared with standard deviation of standard analyses from this study for EPMA data.

3.3 Whole Rock Geochemistry

Representative samples of drill core were crushed at Cardiff University using a steel jaw crusher and milled with an agate lined planetary disc mill. Sand was milled between each sample to minimize cross-sample contamination. The resulting powders were then analysed at the LabMaTer [P2-4250], University of Quebec at Chicoutimi. 1g of rock powders was fused using Lithium Borate and then analysed by Laser Ablation Inductively Coupled Plasma Mass Spectrometer (LA-ICP-MS). Standard reference materials MGR-N (GeoPt19), OKUM and GSN (GeoPt36) were used and agree with assigned or working values. Duplicate analyses for samples was not undertaken but duplicate standards were run, the results of which are presented in the Appendix 3, Standards tab. In addition, a summary of standard measurements of major element oxides is reported in Table 3.3. Note that 2 standard error calculations for each standard measurement is supplied in Appendix 1 – Whole Rock Geochemistry, Standards tab. Maximum Limits of Detection (LOD) from data collection are also reported in the Appendix 3, LOD tab.

	Na_2O %	MgO %	Al_2O_3 %	SiO_2 %	P_2O_5 %	K_2O %	CaO %	TiO_2 %	MnO %	Fe_2O_3 %
OKUM WORKING VALUES	**1.14**	**21.29**	**7.97**	**44.14**	**0.03**	**0.04**	**7.85**	**0.38**	**0.18**	**11.81**
average from all runs	1.17	21.67	7.94	44.64	0.03	0.08	7.71	0.38	0.18	11.81
std deviation	0.01	0.53	0.10	0.21	0.01	0.01	0.24	0.01	0.00	0.15
max 2se on std measurements	0.05	1.09	0.13	1.89	0.01	0.02	0.24	0.02	0.01	0.27
average 2se on std measurements	0.03	0.51	0.10	1.06	0.01	0.01	0.19	0.01	0.00	0.20

n=6

Table 3.3: Measurements on standards throughout data collection showing agreement with published standards and reproducibility of measurements.

3.4 Platinum Group Element Analyses

Platinum Group Elements (PGE) were analysed from rock powders at the LabMaTer at Chicoutimi University, Canada using nickel-sulphide fire assay techniques (Savard et al., 2010). At least 15 g of sample powder was combined with silica, sodium tetraborate, sodium carbonate, silica and sulphur and fused at 1050°C to produce a Ni-S bead and analysed by ICP-MS after Te-Co-precipitation using a Thermo Elemental X7 series. A full methodology can be found in Savard et al. (2010) and estimates of accuracy and precision in Table 3.4. Data from samples and standards is presented in Appendix 4. Volatiles including sulphur were determined from infrared analysis after Bedard et al. (2008). Detection Limits (LOD) on data from this study are also presented in Table 3.4.

	Os	Ir	Ru	Rh	Pt	Pd	Au
	2.8 +/-	6.62 +/-	16.85	15.35	97.40 +/-	123.4	37.33 +/-
KPT (Working)	0.19	0.74	+/- 0.93	+/- 1.24	20.99	+/- 18.6	11.55
KPT (this study avg)	2.82	5.41	16.02	14.41	118.27	109.76	37.73
std dev.	0.26	0.32	0.74	0.77	18.94	6.85	12.34
RSD %	9.11	5.90	4.64	5.37	16.02	6.24	32.71
		0.99 +/-	4.25 +/-	1.40 +/-	11.0 +/-	11.7 +/-	1.49 +/-
Okum (OSG)	nd	0.07	0.30	0.13	0.6	0.5	0.16
Okum (this study avg)	0.71	0.89	3.79	1.21	11.09	10.67	1.43
std dev.	0.10	0.07	0.18	0.09	0.68	0.62	0.61
RSD %	13.80	8.37	4.87	7.16	6.16	5.77	42.62
LOD	0.07	0.03	0.12	0.08	0.08	0.47	0.48

Table 3.4: Data showing accuracy and precision of PGE data acquired for this study.

3.5 Isotope Analysis

A suite of samples from drill core UMT081 were analysed for a range of isotopic systems to provide insight into potential contaminants and magma provenance within a stratigraphic context. Calc-silicate samples from the floor rocks to the Flatreef in drill core UMT094 and samples of calcareous sedimentary rocks collected from outcrop, constituting the floor rocks to the Flatreef on the farm Turfspruit, were also analysed to quantify the contamination of the Flatreef magmas. Isotope data can be found in Appendix 5. All radiogenic isotope data from both the literature and the present study have been recalculated for an age of 2.05704 Ga, currently accepted as the most representative for the emplacement of the RLS (Scoates and Wall, 2015). This age was used alongside measured present day isotope ratios to determine initial isotope ratios using the equation below.

$$(1) \ \left(\frac{^{87}_{0}Sr}{^{86}_{0}Sr}\right)_m = \left(\frac{^{87}_{0}Sr}{^{86}_{0}Sr}\right)_0 + \left(\frac{^{87}_{0}Rb}{^{86}_{0}Sr}\right)_m \left(e^{\lambda t} - 1\right)$$

$$(2) \ T^{Nd}_{CHUR} = \frac{1}{\lambda}\left(\ln \frac{(^{143}_{0}Nd/^{144}_{0}Nd)_{sample,m} - (^{143}_{0}Nd/^{144}_{0}Nd)_{CHUR,m}}{(^{147}_{0}Sm/^{144}_{0}Nd)_{sample,m} - (^{147}_{0}Sm/^{144}_{0}Nd)_{CHUR,m}} + 1\right)$$

3.5.1 Nd Isotopes

Twenty samples from drill core UMT081, UMT094 and outcrop samples of calcareous sedimentary rocks as well as 2 standards and 2 procedural blanks were analysed for Nd

isotopes, following the procedure outlined by McCoy-West et al. (2017). The standard used was JB2 basalt. A mass of 0.1 g of powdered sample were digested in 500 µl hydrofluoric acid (HF) and 250 µl nitric acid (HNO_3) (~29 and 15 M, respectively) and fluxed overnight on a hotplate at 120°C. For carbonate rich samples a pre-treatment was required to remove volatiles. These were first dissolved in 600 µl of 0.2 M HCl, added in 2 steps of 200 µl then 400 µl, and fluxed to drive off CO_2. Following this, another 100 µl concentrated HCl was added to fully devolatise the carbonates. After CO_2 was liberated a digestion in 250 µl concentrated HF (~29 M) and 250 µl concentrated HNO_3 (~15 M) was carried out overnight. All samples were then dried down and fluxed in 5 ml 5.3 M HCl and dried down twice. Finally, samples were fluxed in 3 ml of 7.7 M HNO_3 before a final dry down.

Neodynium was separated from other elements and REE using a two-step procedure identical to that outlined by McCoy-West et al. (2017). Samples were dissolved in 2 ml of 1 M HCl and loaded on the first set of columns (polypropylene R1040 columns) containing 2.5 ml of BioRad AG50W-X8 cation exchange resin which had been cleaned and preconditioned. Samples were then washed with a 10 ml solution of 1 M HCl and 1 M HF before being washed with 12 ml of 2.5 M HCl and finally by 8 ml of 2 M HNO_3. After this REE were collected by eluting in 14 ml of 6 M HCl. These collected samples were then dried down and dissolved in 0.5 ml of 0.2 M HCl. For the second column (88 mm x 4 mm internal diameter) samples were loaded onto the columns of Ln-spec resin and washed with 6 ml of 0.2 M HCl. Nd was then collected in the following 6 ml of 0.2 M HCl.

Nd isotopes were then measured at Cardiff University on a nu-Plasma II Multi Collector Inductively Coupled Plasma Mass Spectrometer (MC-ICP-MS). JNd-i was used to calibrate the instrument and correct for instrumental drift during the analyses. Signal intensity for procedural blanks were tested against pure acids and a JNd-I solution of known concentration. They were found to be in line with long-term laboratory measurements of ≤20pg Nd with a voltage too low to measure the Nd isotope ratio and therefore negligible effect on isotopic measurements of samples. Duplicate samples of rock standard JB2, a basalt that is similar in composition to basaltic rocks of the Bushveld Complex, were within error of each other and within the published range of isotope ratios (Appendix 5).

3.5.2 Sr and Pb Isotopes

Sr-Pb are collected during the same column chemistry procedures so their methods will be described together here. To remove anthropogenic Pb a leaching stage is added before digestions. 200 mg sample were leached in 3 ml of 2.5 M HCl on the hotplate at 100°C for one hour, carbonate rich samples were leached in 0.2 M HCl. The samples were then centrifuged, and acids pipetted off and then repeated with Milli-Q (MQ) to remove residual acid. Samples

were then digested in 1 ml concentrated HF (~29 M) and 250 μl of concentrated HNO_3 (~15 M) and dried down before being fluxed three times in 10 ml of 5.25 M HCl to remove any fluorides before a final flux in 6 ml of 7.7 M HNO_3.

Resin for the first set of column chemistry was cleaned and preconditioned with 3 ml of 8 M HCl, then 6 ml of MQ and finally 600 μl of 8 M HNO_3. Samples were first dissolved in 1 ml of 8 M HNO_3 and loaded onto columns with 1 ml of Eichrom Sr-spec extraction chromatographic resin (columns comprised a standard 1ml pipette tip) (Charlier et al., 2006; Horwitz et al., 1992). Columns were washed with 1.3 ml of 8 M HNO_3 before Sr was eluted in 1.5 ml of 0.05 M HNO_3. The columns were then further washed in 200 μl of HCl before the Pb was collected in 900 μl of 8 M HCl.

Preliminary measurements of Pb isotopes suggested there were matrix elements still present that may interfere with the measurements. The Sr cut was also checked and was found to be clean of any interference matrix elements such as Rb. Pb isotopes were processed chemically a second time using the same column chemistry to remove residual matrix elements.

Sr and Pb isotopes were then measured at Cardiff University on a nu-Plasma II MC-ICP-MS. For Sr analysis a wet-plasma set up was used to reduce background interference. For Pb an Aridus was used to run a dry-plasma set up. During mass-spectrometry measurements for Sr NBS987 was used to calibrate the instrument and correct for instrumental drift during the analyses. For Pb analyses NBS981 was used. Similarly to Nd, the signal intensity for procedural blanks were tested against pure acids and standard solutions of known concentrations. These were found to be in-line with long-term laboratory blanks with a Sr or Pb concentration of ≤10 pg and thus too low to measure an isotopic ratio. This concentration has a negligible effect on sample measurements. Duplicate samples of standard JB2 were in error of each other and overlap with published ranges.

3.5.3 Trace elements for Radiogenic Isotope Corrections

Trace element measurements to age-correct radiogenic isotope ratios were carried out in Bristol on an Element HR-ICP-MS mass spectrometer. Rock powders were digested using the same techniques as for radiogenic isotope work. Standards used were JB2 and BCR2, see methods in Andersen et al. (2016). Trace element concentrations have an estimated error of 5-10%.

3.5.4 Mg Isotopes

Mg isotope samples were taken as a 10 μl aliquot from the Nd digestions. These were then dissolved in 0.2 ml 2 M HNO_3 and loaded onto Savillex columns containing 10 ml of BioRad AG50W-X12 cationic exchange resin with a high aspect ratio. Samples were then washed in 1 ml of 2 M HNO_3 followed by 7.5 ml of 0.5 M HF and 7 ml of 2 M HNO_3 before collecting Mg in 11

ml of 2 M HNO_3. 1 ml of the wash prior to the Mg collect and 1 ml following the Mg collect were kept to check yield. These samples were then dried down and fluxed in hydrogen peroxide (H_2O_2) and HNO_3 to remove any resin before being dissolved in 0.2 ml of 2 M HNO_3.

For the first set of samples these were then loaded onto a second smaller column with 250 µl of X-12 resin. The samples were loaded and immediately collected in 6 ml of 2 M HNO_3 and as before the following 1 ml of 2 M HNO_3 was also collected to check the yield, measured on an Element HR-ICP-MS at Bristol University.

Mg isotope ratios were then measured at Bristol University on a Neptune MC-ICP-MS using an ApexQ aspirator. JP1 and JB2 rock powder standards were digested and processed alongside my samples which have been characterised by Pogge von Strandmann et al. (2011). Blank-standard bracketing was used during analysis with DSM3 as the standard, a reference material characterised by Galy (2003). Yields for all samples exceeded 99%. Duplicate analyses are within error, here values with the lower uncertainty are used. For full results see appendix 3.

3.5.5 O isotopes

Multiple orthopyroxene and plagioclase grains were drilled from thick sections (300 µm) using a NewWave micromill at Bristol University, UK. These samples were then analysed for oxygen isotopes at Indiana University by Ed Ripley. Samples were reacted with bromine pentafluoride (BrF_5) at 650° to free the oxygen which forms CO_2 after reacting with a graphite disc (Clayton and Mayeda, 1963). The isotopic ratio was then measured on a Thermo-Fisher Delta-Plus stable isotope mass spectrometer with an analytical precision of ± 0.05 ‰. Results are reported relative to Vienna Standard Mean Ocean Water (VSMOW). In sample 81-1294 plagioclase and orthopyroxene were drilled separately to determine offset in oxygen isotope partitioning between these phases. NBS-28 quartz was used as the standard with a laboratory value of 9.6 ± 0.2 ‰ and Kanaga pyroxene with a value of 5.5 ± 0.2 ‰. Sample values given have an uncertainty of ± 0.2 ‰. Where duplicates were analysed an average is used. For full dataset see appendix 3.

3.6 Geochronology

3.6.1 Sample Collection

Four samples of the Flatreef were collected from drill cores UMT232 and UMT345. In addition, a sample of Merensky Reef from Northam platinum mine in the western limb was dated as detailed in Table 3.5.

Sample	Drill Core #	Depth (m)	Sample length (m)
Main Zone (MZ)	UMT232	740.3-741.2	0.9
Bastard Reef (BAR)	UMT232	804.7-805.9	1.2

Merensky Reef (M2)	UMT232	838-839	1
UG2	UMT345	1518-1519	1
Merensky Reef Northam (NORT)	7-5055	133.84-135.75	1.91 (smaller drill core size)

Table 3.3: Sample drill core and depths

3.6.2 Sample Preparation

Drill core samples were cleaned and cut to remove any detrital or vein material. Samples were crushed by jaw crusher and sieved to remove fractions > 500 µm. Density separation on a Rogers Table was used to separate heavy minerals (including zircons and rutile). The sample was then passed through a Franz magnetometer to remove magnetic phases and concentrate zircons and rutile in the final product. This concentrate was then separated using heavy liquid separation before individual zircon grains were picked for analysis. Selected zircon grains were annealed at 900°C for 72 hours.

3.6.3 CA-ID-TIMS

Chemical abrasion isotope dilution thermal ionisation mass spectrometry (CA-ID-TIMS) uranium-lead geochronology analysis was carried out at the NERC Isotope Geosciences Laboratory, British Geological Survey, Keyworth. Data is reported in appendix 6. Zircons were fluxed in Teflon beakers for 1-2 hours in 4 M HNO_3 at 90°C. Zircons were then ultrasonically cleaned and rinsed in MQ before being loaded into 300 µl Teflon microcapsules. Zircons were then leached inside a Parr vessel at 190-210°C in 2 or 3 2-7 hour steps totalling 12-14 hours to remove open-system or damaged parts of the zircon crystal that are affected by Pb loss (Mattinson, 2005). The HF containing leached portions of zircon was extracted and stored in Savillex beakers. The remaining zircon fraction was then rinsed in 4 M HNO_3 and 6 M HCl.

All zircon fractions were spiked with the mixed ^{202}Pb-^{205}Pb-^{233}U-^{235}U (ET2535) EARTHTIME tracer solution (Condon et al., 2015; McLean et al., 2015) and dissolved in 10-20 µl 4 M HNO_3 and ~ 200 µl 29 M HF at 220° in a Parr vessel for approximately 80 hours. Leachates from zircons were spiked with ^{205}Pb-^{233}U-^{235}U (ET535) EARTHTIME tracer solution. Both samples and leachates were evaporated and dissolved overnight in 3 M HCl at 180°C thus converting samples and leachates to chlorides. Samples and leachates were then loaded onto Teflon columns to separate U and Pb using HCl based anion exchange procedures (Krogh, 1973) and Bio-Rad AG-1 8x resin. ~10 µl of H_3PO_4 was added to the combined U-Pb fractions to dry the samples before being loaded in a silica gel matrix onto a zone-refined Re filament (Gerstenberger and Haase, 1997).

Measurements of isotope ratios were undertaken using a Thermo Triton thermal ionization mass-spectrometer (TIMS). For leachates, Pb was measured in dynamic (peak hopping) mode

using a single MassCom secondary electron multiplier (SEM). Repeated analyses of standards NBS 982, NBS 981 and U 500 were used to monitor dead time corrections and linearity on the SEM. U was run as an oxide (UO_2) and measured either on Faraday detectors with $10^{12}\Omega$ resistors in static mode, or on the SEM in dynamic mode. For zircon fractions, Pb was measured in full static mode. ^{202}Pb and $^{205-208}$Pb was measured on Faraday detectors equipped with $10^{12}\Omega$ resistors and ^{204}Pb measured on the SEM. Faraday detectors equipped with $10^{11}\Omega$ resistors monitored interferences from Tl and $BaPO_3$.

Tripoli software was used to filter the raw U and Pb data (Bowring et al., 2011). The U mass fractionation was calculated in real-time based on the isotopic composition of the double spiked 'ET535 v 3.0)' or 'ET2535 v 3.0' tracer. For zircon samples, the Pb mass fractionation was corrected using the isotopic composition of the double spike 'ET2535 v 3.0'. For ET535 leachate samples the Pb mass fractionation was attributed a value of 0.14 ± 0.02 %/amu. An ^{18}O/^{16}O value of 0.00205 was used to correct for isobaric interferences on uranium oxide measurements.

ET_Redux software was used for data reduction, date calculation, uncertainty propagation and graphical presentation (McLean et al., 2011) using U decay constants of Jaffey et al., (1971) and ^{230}Th decay constants of (Cheng et al., 2000). ^{238}U/^{235}U of 137.8185 (Hiess et al., 2012) was used and, as with Mungall et al. (2016), ^{238}U/^{235}U global uncertainty range was not propagated. Uranium blanks were assumed to be 0.1 ± 0.01 pb (1σ). Common Pb was attributed entirely to laboratory blank. This used a calculated Pb isotopic composition for the laboratory blank of ^{206}Pb/^{204}Pb = 18.10 ± 0.27%, ^{207}Pb/^{204}Pb = 15.55 ± 0.14% and ^{208}Pb/^{204}Pb = 37.82 ± 0.41 (1σ uncertainties). In addition, dates were corrected for initial ^{230}Th disequilibrium (Scharer, 1984) using a value of Th/U$_{[magma]}$ = 4.2 after Mungall et al. (2016).

3.6.4 Cathodoluminescence

A second set of representative zircon grains was picked and mounted in epoxy and polished for analysis by Cathodoluminescence (CL). Zircon populations for each sample were characterised at Cardiff University on the Analytical Scanning Electron Microscope using a Centaurus CL detector at a working distance of 20 mm with a 120 µm aperture and 10kv high current beam.

Chapter 4 – Stratigraphy of the lower Main Zone, Flatreef and sedimentary floor rocks

4.1 Introduction

It is important to document and understand the stratigraphy of the intrusion studied and relationships between the lithologies to inform models on formation of the Flatreef. In particular, the relationship between mafic and ultramafic rocks, thicknesses of these layers, and the location and abundance of sulphide and chromite rich layers are recorded. Understanding the stratigraphy of the Flatreef is essential for comparing the stratigraphy of the Flatreef with that of the Platreef in the northern limb and the remainder of the Bushveld Complex. In the following chapter two drill cores are documented in detail. Due to increased variability with depth, in part based on extensive contamination in lower sections of the Flatreef, the drill cores are described from the Main Zone downwards as these uppermost layers are most easily identifiable and can be correlated across the intrusion.

The Bushveld academic community traditionally do not use IUGS terminology when classifying rocks. Instead rocks are named based on the proportions of their cumulus phases (Irvine, 1982). This makes it easier to identify and separate out different units within the extreme thickness of the Bushveld Complex and correlate marker layers. Since the majority of academic research uses this cumulus terminology this practice is also adopted in the present description of drill cores UMT081 and UMT094 to enable easy comparison to other literature on the Bushveld Complex.

4.2 Drill Core UMT081

Drill core UMT081 was selected for this research as it is the longest drill core on the farm Turfspruit. It intersects all major units with clear evidence of contamination of magmatic intrusives by calcareous sediments, in the form of hybrid rocks and abundant dolomitic and calc-silicate xenoliths.

The uppermost 1293 m of the drill core is comprised of the MZ followed by a layered mafic-ultramafic package representing the Flatreef. The Flatreef becomes increasingly contaminated in its lower 200 m overlying the sedimentary footwall, which comprises calc-silicate and calcareous sedimentary rocks. Within and below the latter are several distinct mafic and ultramafic layers (Figure 4.1). The entire sequence has been intruded by two generations of granitic veins, cross cutting the core at high and low angles, reaching thicknesses up to four metres and generally exploiting lithological boundaries.

The uppermost rock analysed in the present study is Main Zone norite, forming a relatively homogeneous package nearly 1300 m thick (Figure 4.2a). Within this noritic package are marker layers that can be traced laterally across the farm Turfspruit, including the Tennis Ball Marker, located ~280 m above the base of the MZ (Grobler et al., 2018). The MZ underlain by an 8.5 m thick mottled anorthosite layer, named here as the "Upper Mottled Anorthosite" (UMA). The contact between MZ norite and the UMA is gradational with the pyroxene content of the MZ norite progressively decreasing downhole forming patches of leuconorite before transgressing into the UMA. The UMA is heterogeneous, with the mottles ranging in size between 1-8 cm and contains domains of leuconorite and pure anorthosite (10-15 cm in width) (Figure 4.2b).
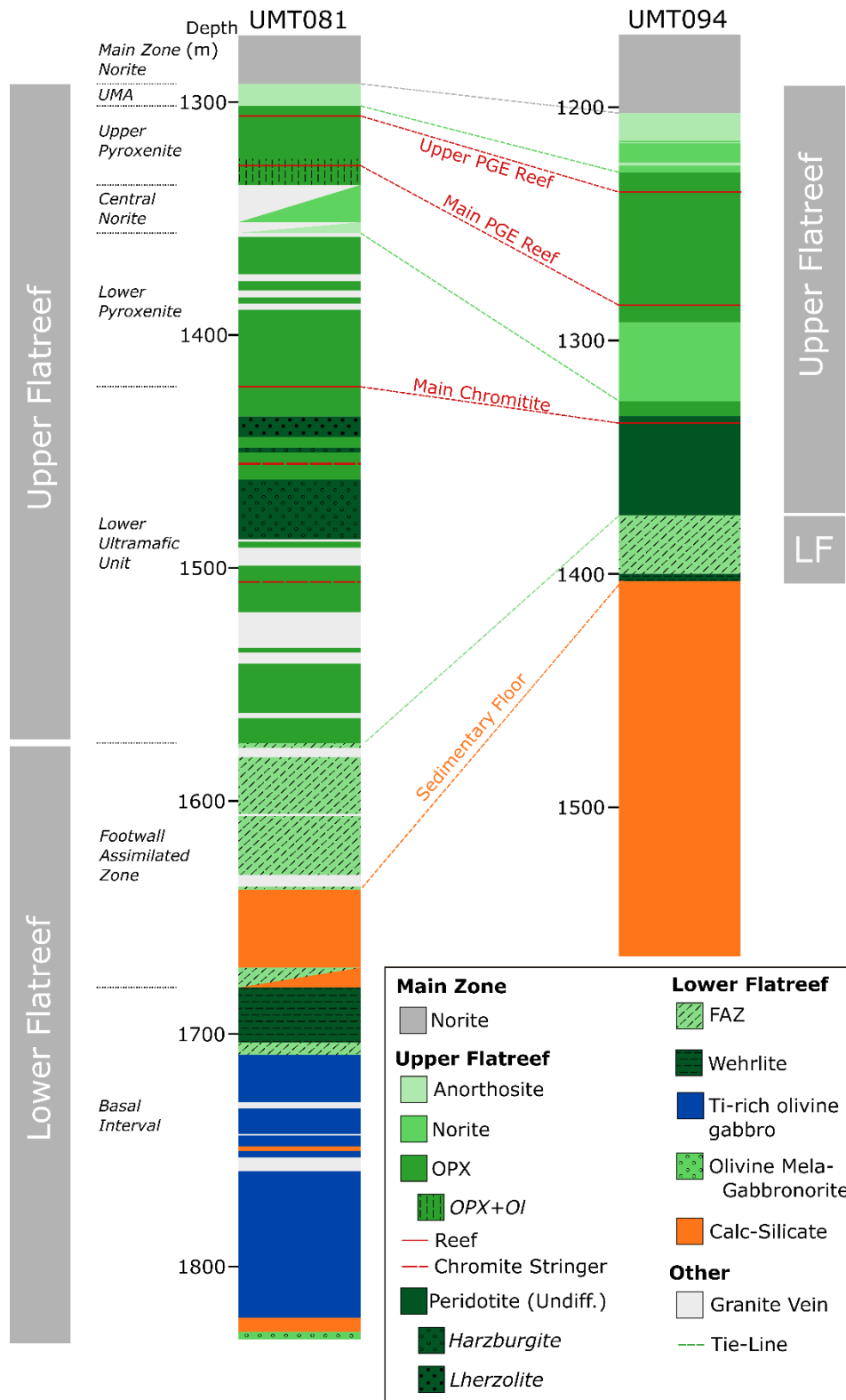
Figure 4.1: Stratigraphic log of drill holes UMT081 and UMT094. The Flatreef is broadly split into Upper and Lower sections. UMT081 is a deeper drill hole that extends into the footwall with several separate sill units at depth intruded into calc-silicates. UMT094 is drilled into a localised topographic high in the footwall resulting in a shorter magmatic stratigraphy. Drilling extends over 150 m into the calcareous sedimentary floor rocks. Granite veining is particularly prevalent in UMT081.
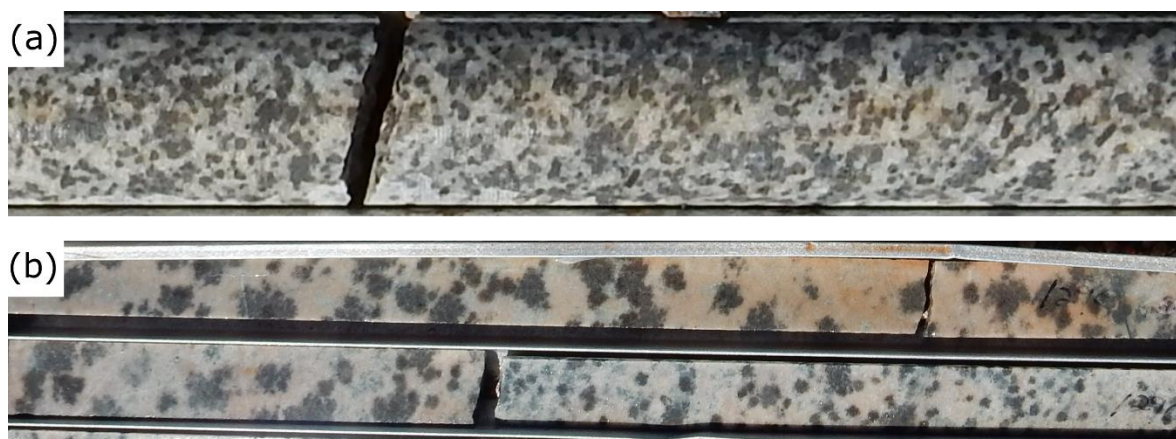
Figure 4.2: Drill core photographs taken from drill hole UMT081. Core is 5 cm wide (a) Massive norite from the Main Zone, (b) Upper Mottled Anorthosite that marks the top of the Flatreef, with mottles ranging in size up to 8 cm.

The base of the UMA is defined by a sharp magmatic contact with underlying feldspathic pyroxenite which is 23 m thick and is here termed the "Upper Pyroxenite" (Figure 4.3a). The upper portion of the Upper Pyroxenite (1301 to 1324 m) is comprised of fine to medium grained homogeneous feldspathic orthopyroxenite. Within the orthopyroxenite, between 1303 and 1309 m depth, PGE grade is elevated (up to 1.67 ppm Pt) and has been termed the "Upper PGE Reef" by Yudovskaya et al. (2017b). Pyroxenite hosting the reef remains unchanged throughout the mineralized interval. At 1324 m olivine begins to appear and the pyroxenite becomes coarser grained and contains thin (<1 mm) veins of serpentine. In addition, visible sulphides appear. The transition from feldspathic pyroxenite into feldspar-poor olivine-bearing pyroxenite is sharp and without evidence of tectonism along the contact. The pegmatoidal sulphide bearing pyroxenite contains thick (~5 cm) chromitite stringers between which PGE are concentrated and has been termed the "Main PGE Reef" by Yudovskaya et al. (2017b) (Figure 4.3b). A ~1 m thick interval of patchy chromitite marks the base of the Main PGE Reef.

The Main PGE Reef pegmatoidal olivine-bearing pyroxenite is underlain by a thick (approx. 15 m) norite package, here termed the "Central Norite", which is strongly overprinted by late-stage granite veining obliterating the upper contact with the pyroxenite hanging wall (Figure 4.3c) and lower contact with mottled anorthosite at 1351 m depth (Figure 4.3d). Here the mottled anorthosite which forms the lower portion of the Central Norite is also extensively overprinted by granite veins making it impossible to comment in more detail on the characteristics of the unit and its basal contact with a further orthopyroxenite unit at 1357 m. This orthopyroxenite unit is termed the "Lower Pyroxenite", containing a much lower feldspar component than the Upper Pyroxenite and is largely homogeneous over a thickness of 50 m. Rare pegmatoidal domains show diffuse contacts with the surrounding medium-grained orthopyroxenite.
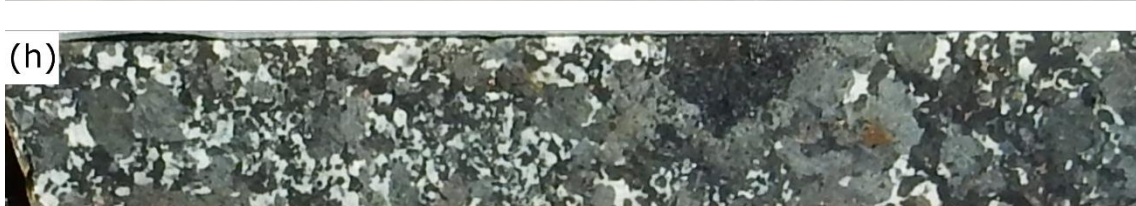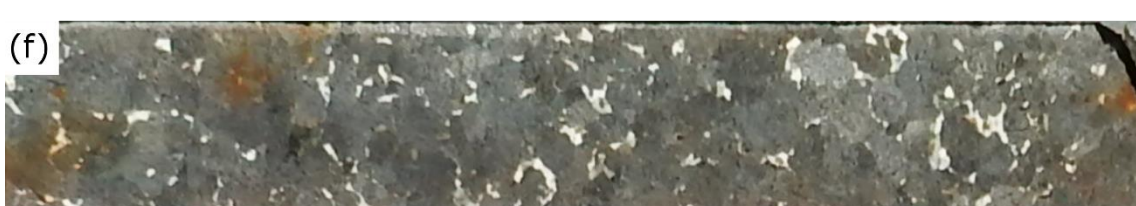
Figure 4.3: Drill core section photographs from UMT081. (a) Upper PGE Reef hosted in the Upper Pyroxenite (1305 m depth) comprising cumulus orthopyroxene with interstitial plagioclase seen in white (core is 4.76 cm wide). (b) Main PGE Reef olivine-bearing orthopyroxenite (1327 m depth). Black olivine can be seen in clusters within coarse to pegmatoidal pyroxenite (core is 2.38 cm wide). (c) Homogeneous norite with a single thick vein of serpentine cross-cutting norite from the Central Norite (depth 1339 m) (core is 4.76 cm wide). (d) Anorthosite with mottles of pyroxene from the lower portion of the Central Norite (1355 m depth). These mottles are generally smaller than those found in the Main Zone (core is 4.76 cm wide). (e) Main Chromitite with abundant chromite set in a pegmatoidal feldspathic orthopyroxenite (1422 m depth). Chromite rich zones have significant interstitial plagioclase component resulting in white "eyes" seen here (core is 5 cm wide). (f) Pegmatoidal orthopyroxenite with staining from oxidized sulphides from the Lower Ultramafic Unit (1432.2 m depth) (core is 4.76 cm wide). (g) Harzburgite from the LUU (1438.8 m depth) with abundant olivine (black) and large orthopyroxene crystals (grey) set in interstitial plagioclase (core is 2.38 cm wide). (h) Lherzolite from the LUU (1475.2 m depth) with abundant olivine and green-tinged pyroxene and significant interstitial plagioclase component (core is 2.38 cm wide).

At a depth of 1422 m a chromite-rich package, approximately one metre thick, is overlain by one metre of pegmatoidal orthopyroxenite. The pegmatoidal pyroxenite has a sharp magmatic contact with overlying pyroxenite of the Lower Pyroxenite. The chromitite is termed the "Main Chromitite" and is comprised of multiple chromite rich lenses interlayered with orthopyroxenite (Figure 4.3e). Interstitial plagioclase forms patchy oikocrysts within these chromite lenses.

Below the Main Chromitite is a 154 m thick sequence of ultramafic rocks, (pyroxenite, lherzolite and harzburgite) termed the "Lower Ultramafic Unit" (LUU). At the top of the unit is a pegmatoidal orthopyroxenite (approx. 1423 m depth), containing varying amounts of interstitial plagioclase, and layers of fine grained orthopyroxenite (Figure 4.3f). Next is an 8 m thick harzburgite package (1435-1443 m) that has a gradational lower contact with pegmatoidal feldspathic orthopyroxenite (Figure 4.3g). Within the latter there are layers of coarse grained harzburgite on the order of 1.5 m in thickness, with relatively sharp boundaries. At 1448 m depth is another ultramafic package but here clinopyroxene is the dominant pyroxene forming 2 thin (<1 m) layers of medium-coarse grained lherzolite (Figure 4.3h) with a thin (~10 cm) pegmatoidal pyroxenite sandwiched between. Below these lherzolite layers is an orthopyroxenite hosting irregular chromitite stringers (up to 5 cm thick) which in turn is underlain by another lherzolite layer that has a thickness of 26 m. It has a gradational lower contact with coarse-grained feldspathic orthopyroxenite (at 1488 m) that contains a 10 cm thick diffuse chromitite stringer.

Below this (at 1575 m depth) is the upper contact of the "Footwall Assimilated Zone" (FAZ), as termed by Ivanplats geologists. The FAZ contains several distinct packages of orthopyroxenite showing variable (fine to coarse) grain size. The contacts between these

packages are obscured by granite intrusions. The FAZ is defined here as consisting of magmatic rocks that have a significant component of contaminant material which, in drill-holes UMT081 and UMT094, is predominantly calcareous sediments (Figure 4.4). A notable increase in oxidized sulphide staining can distinguish contaminated FAZ rocks from their uncontaminated counterparts. It should be noted that changes in texture and a green tinge to the contaminated rocks and increased sulphide staining that are typical of the FAZ already begins to appear in the lower portions of the LUU (from ~1501 m depth), but is largely restricted to small localised patches (≤ 1.5 m wide) and represents < 5% of the rocks. The top of the FAZ denotes where these markers of contamination become the dominant feature of the rock.
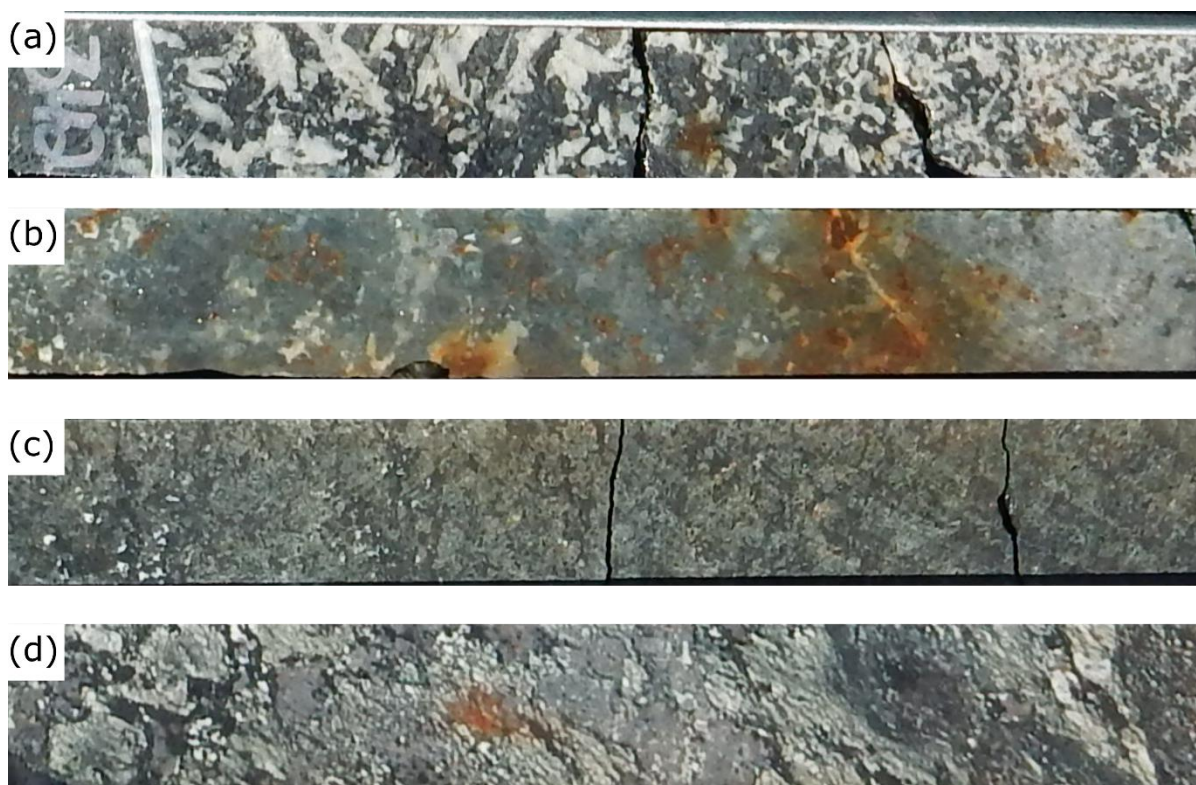
Figure 4.4: Core sample photographs of FAZ rocks, which contain both a magmatic and a significant floor rock component (all core 4.76 cm diameter). (a) Olivine-gabbronorite rock with coarse grained pyroxene and plagioclase laths visible in hand specimen. (b) Parapyroxenite dominated by green-tinged clinopyroxene and staining from sulphide oxidation. (c) Parapyroxenite with a significant olivine component. (d) Parapyroxenite containing abundant clinopyroxene and olivine.

From 1577 m depth onwards, granite veins interact and mingle more extensively with parapyroxenite. This heavily contaminated footwall zone extends to 1680 m and contains variable xenolith content. At 1680 m depth a 23 m thick layer of wehrlite is bounded by parapyroxenite with which it has noticeably diffuse boundaries (Figure 4.5a). Below the lower parapyroxenite (approx. 5 m thick) is a fine grained unit that does not contain any xenoliths or

other evidence of contamination. Based on geochemistry, its high TiO_2 content, it is termed here as the "Ti-rich olivine gabbro" (Figure 4.5b-d).
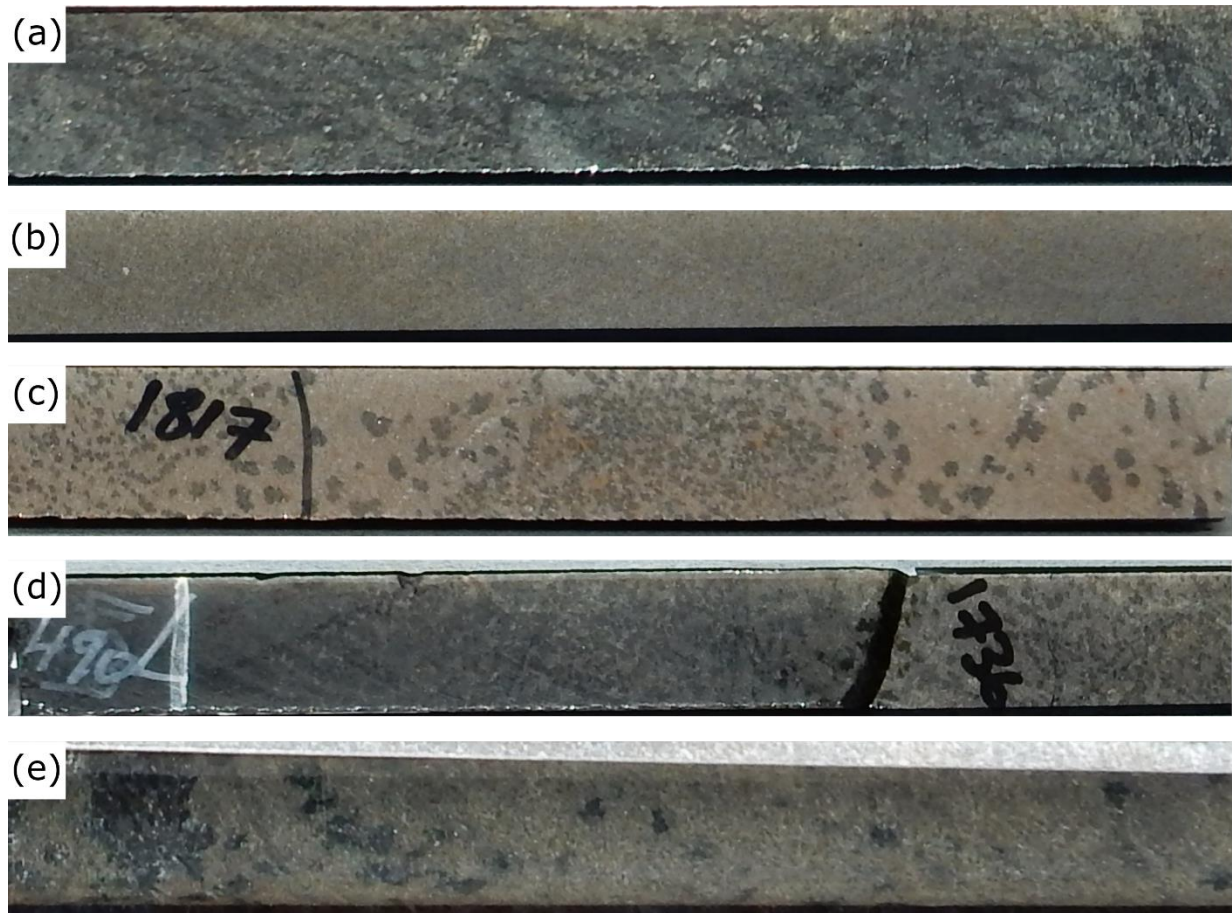
Figure 4.5: Core sample photographs of rocks forming the Lower Flatreef (all core 4.76 cm diameter). (a) Wehrlite with distinct green tinge from abundant clinopyroxene. (b) fine grained Ti-rich olivine gabbro found as fine grained homogeneous unit over 10s of metres. (c) Base of Ti-rich olivine gabbro becomes increasingly complex with cyclic layering of mini-mottles of olivine. (d) Sharp magmatic contact between spotted and fine-grained domains in the Ti-rich olivine gabbro in UMT081. (e) Olivine Mela-gabbronorite with mini-mottles of olivine within a plagioclase-pyroxene unit.

The Ti-rich olivine gabbro forms 121 m thick, fine grained, and homogeneous unit, particularly in its upper portions. The rocks are cross-cut by several coarse grained granitic veins. Sections of the Ti-rich olivine gabbro are characterised by a spotted texture. The small mottles, 1-2 cm wide, are present in variable concentrations, forming distinctive cycles, with mottle-rich bases grading upwards into fine-grained mottle-free sections (Figure 4.5c). Rarely, contacts between fine-grained and mottled units are preserved (Figure 4.5c, d). Towards the base of the unit granite veins become abundant, displaying undulating boundaries and rip-up clasts. Granite intrusions have a prominent black baked margin that can be up to 1 m wide.

At 1821 m depth the Ti-rich olivine gabbro abuts calcareous sedimentary floor rocks which display relict sedimentary bedding structures and appears relatively undisturbed by the magmatic intrusions. Finally, the lowermost metre of the drill core at 1828 m depth is a medium-grained olivine mela-gabbronorite which shows a sharp magmatic contact with the fractured sedimentary hangingwall (Figure 4.5e). The olivine mela-gabbronorite has a dark grey-brown colour and sugary texture with black mottles of olivine (1 cm) sparsely distributed throughout the rock.

4.3 Drill Core UMT094

Drill core UMT094 was drilled only a few hundred metres to the south-east from UMT081 and also intersects the MZ, Flatreef and calc-silicate floor rocks. The latter form a localised topographic high resulting in a significantly thinner Flatreef interval (~210 m) compared to that in drill core UMT081 (~530 m). This drill core therefore provides insight into the features of contact metamorphosed, variably devolatized, calcareous sediments which span a thickness of nearly 200 m. However, the lowermost lithologies in the Lower Flatreef seen in drill core UMT081 are not seen in UMT094.

Sampling for this research begins at the base of the homogeneous norite of the MZ. The boundary between the MZ and the Flatreef is harder to identify than in drill core UMT081, due to the presence of multiple mottled anorthosite units in drill core UMT094 but is assigned here at 1202.5 m depth. The UMA is underlain by a feldspathic orthopyroxenite forming the Upper Pyroxenite. It contains abundant decimetre scale adcumulate orthopyroxene domains with corresponding lower interstitial feldspar content. In addition, the pyroxenite occasionally contains small pegmatoidal patches on the order of 10 cm. At 1273 m the pyroxenite becomes pegmatoidal with an increased sulphide content. At ~1285 m depth the PGE grade is highest forming the Main PGE Reef. Olivine forms small crystals and is much lower in abundance than in the equivalent layer in UMT081. The pegmatoidal orthopyroxenite also contains sections of medium-grained pyroxenite with variable feldspar content. The reef is underlain by ~1 m of clinopyroxenite before transitioning back into pegmatoidal orthopyroxenite.

At 1292.5 m the pegmatoidal orthopyroxenite gives way to noritic rocks equivalent to the Central Norite found in UMT081 (Figure 4.6). Norite at this stratigraphic level tends to form cycles, controlled by varying proportions of pyroxene and plagioclase which commonly have knife-sharp lower and upper contacts. These cycles are well developed in UMT094 but not present in UMT081, possibly due to the abundant overprinting of granitic veins in the latter. Mottled anorthosites tend to occur at the top of individual norite cycles (Figure 4.6). With increasing depth these norite cycles become more orthopyroxene rich until the unit becomes essentially pyroxenitic. At 1325.6 m, after 33 m of norite cycles, is an 8 m thick orthopyroxenite

layer that overlies a 43 m thick package of largely undifferentiated peridotite, consisting primarily of lherzolite with lesser harzburgite forming the LUU. Peridotite is underlain by the ~25 m thick FAZ. Below this (at 1399.8 m) wehrlite forms a thin layer in direct contact with the uppermost portions the dolomitic floor (at 1404 m), although this is some 300 m higher stratigraphically than UMT081 (depths of approx. 1402 m and 1702 m respectively), making it difficult to correlate these units with any certainty.

Figure 4.6: Drill core interval from UMT094 showing the norite cycles with some development of mottled anorthosite and general increase in pyroxene content with depth (core is 4.76 cm wide). Norite cycles present in a variety of textures and thicknesses. Some cycles comprise pyroxenite layers with sharp contacts, others a normal grading with more plagioclase rich tops of varying thickness of cycles from 10 cm to 1 m.

The contact metamorphosed footwall to the Flatreef is well preserved in drill-hole UMT094, for a depth of 180 m below the magmatic contact with the footwall, providing unique exposures of carbonate units that have experienced varying intensities of contact metamorphism from overlying magma injections (Figure 4.7). The uppermost portion of the footwall (approx. 1405 m to 1452 m) is characterised by relict bedding and distinctive black and cream colouring with some strongly weathered sulphides (Figure 4.7a). At a depth of 1435 m, various carbonate

rocks are exposed including stromatolites (Figure 4.7b). Strongly magnetic bands are also present and can span several metres in thickness with a distinctive blue-black colouring (Figure 4.7c). Below this, the carbonates turn into 120 m of homogeneous marbles, pale cream in colour with black speckles and a sugary texture (Figure 4.7d).
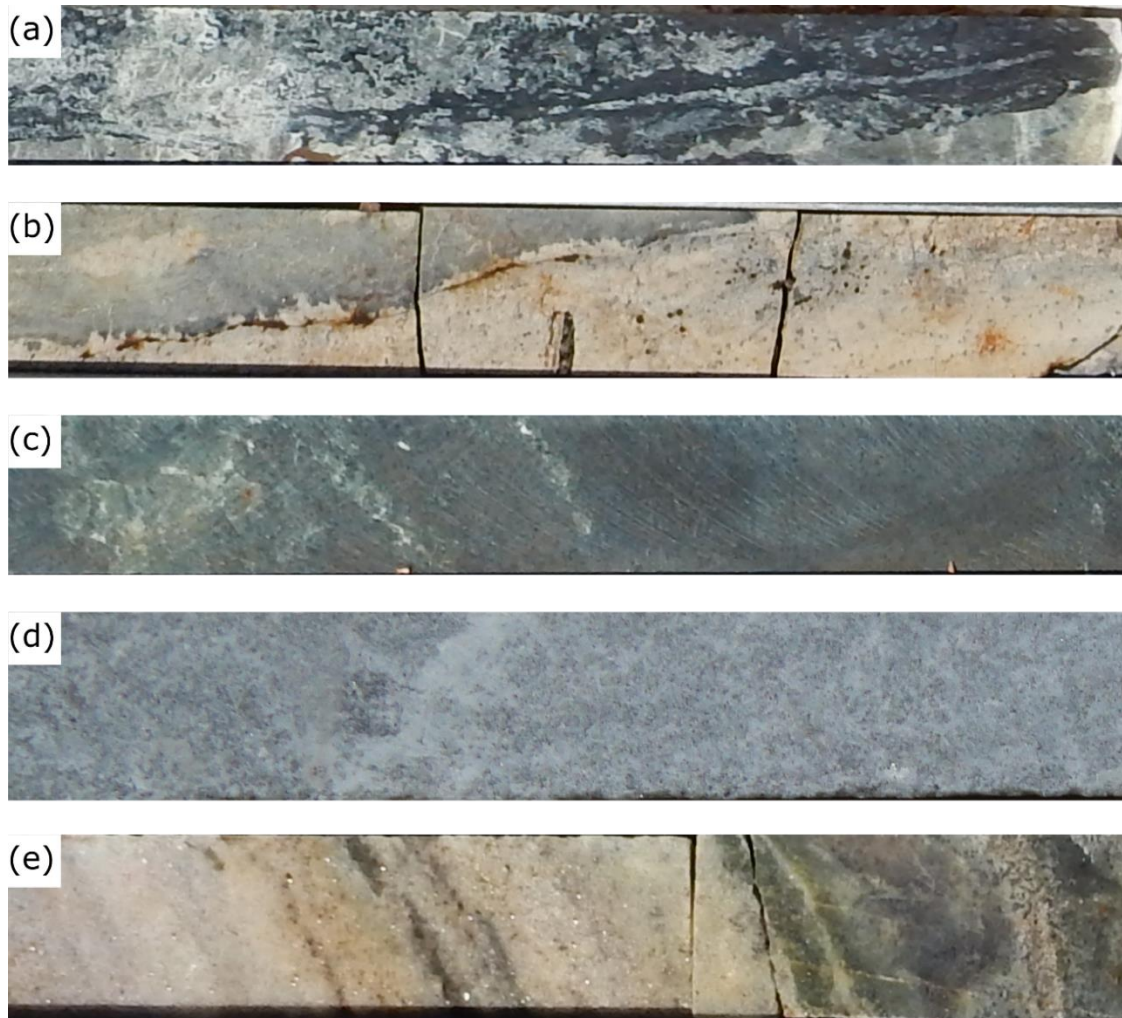
Figure 4.7: Core sample photographs showing the range of contact-metamorphosed footwall lithologies beneath drill cores UMT094 and UMT081. (a) Metamorphosed footwall unit consisting mainly of carbonates with a shale component (core is 4.76 cm wide). (b) Carbonate with stromatolite-like structures (core is 4.76 cm wide). (c) Magnetite dominated unit giving blue-grey colour to the unit (core is 4.76 cm wide). (d) Fine grained marble found over a thickness of several 10s of metres (core is 2.38 cm wide). (e) Marble near the base of drill core UMT081 that has been strongly metamorphosed but still retains conformable protolith layering (core is 4.76 cm wide).

Chapter 5 - Petrography of the lower Main Zone, Flatreef and sedimentary floor rocks

This chapter provides a detailed description of the petrographic features of the lithologies intersected by the drill cores studied, focussing on silicate, sulphide and oxide minerals. The alteration of these minerals is described as this may have important implications for interpreting the geochemical data.

5.1 Main Zone

Main Zone norite comprises abundant euhedral and subhedral plagioclase (74 modal %) and lesser amounts of subhedral orthopyroxene (21 modal %) as well as interstitial clinopyroxene (<5 modal %). The norite forms thick packages, spanning up to 1200 m, without significant petrological change. Plagioclase forms subhedral and euhedral laths and anhedral interstitial grains (Figure 5.1). Plagioclase laths are generally 2-3 mm in length with occasional smaller, more anhedral crystals around 0.5-1 mm in width, displaying well developed albite twinning and commonly simple twinning (Figure 5.2). The cumulus plagioclase shows faint compositional zoning with relatively Ca-rich cores and Na-rich rims. Plagioclase also forms small, rounded and embayed inclusions within orthopyroxene indicating textural disequilibrium. Minor quartz (<2%) is interstitial to plagioclase where clinopyroxene is absent.
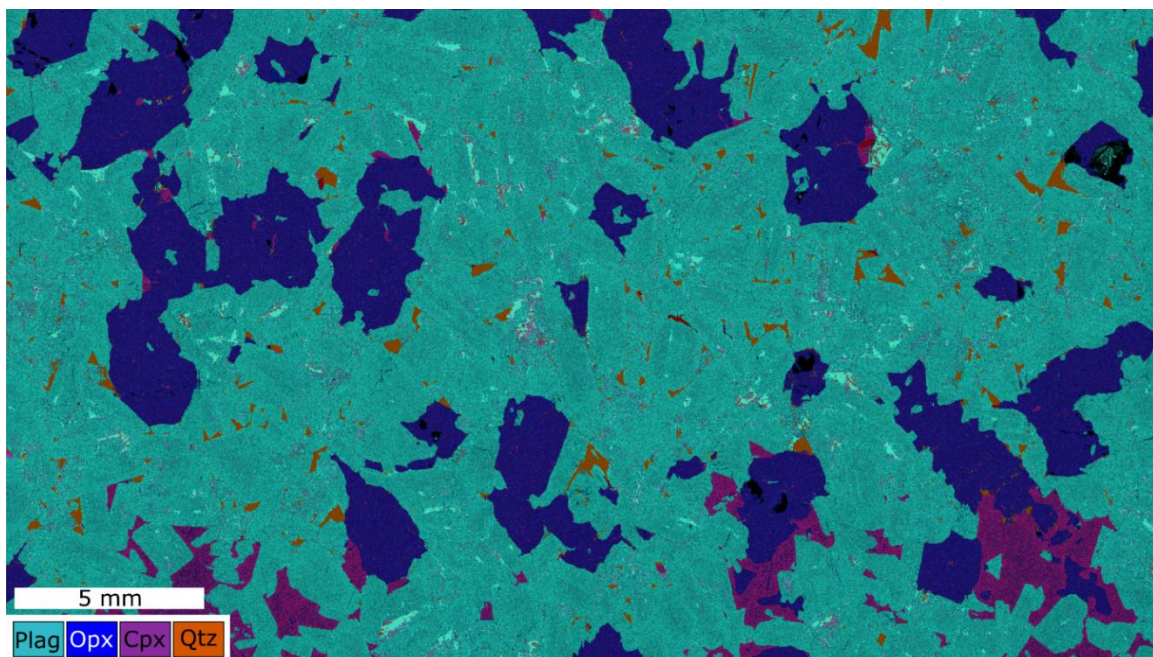
Figure 5.1: Element map of a thin section showing faint compositional zoning in euhedral cumulus plagioclase laths (sample 81-1238). Orthopyroxene crystals sometimes contain inclusions of small rounded plagioclase crystals. Clinopyroxene represents a minor interstitial phase and can be seen partially replacing larger orthopyroxene laths (bottom right).

Orthopyroxene can form long laths up to 8 mm in length or 101 crystal faces around 3 mm. It can contain minor exsolution of clinopyroxene in the cores of crystals. Grains show no obvious foliation. Clinopyroxene is a minor phase (4 % vol.) and locally found as a poikilitic phase with crystals up to 8 mm in diameter surrounding smaller plagioclase laths (0.25-1.5 mm) that display rounded edges and embayments. Clinopyroxene is commonly seen rimming anhedral orthopyroxene crystals with the central orthopyroxene rounded and embayed along its margins (Figure 5.2d). Subhedral magnetite is found as an interstitial phase and can have a thin corona of spinel. Trace amounts of fine disseminated chalcopyrite are observed as 'clouds' associated with sericite alteration of plagioclase. Sericite alteration forms localised patches within plagioclase crystals, although overall the norite is relatively unaltered.
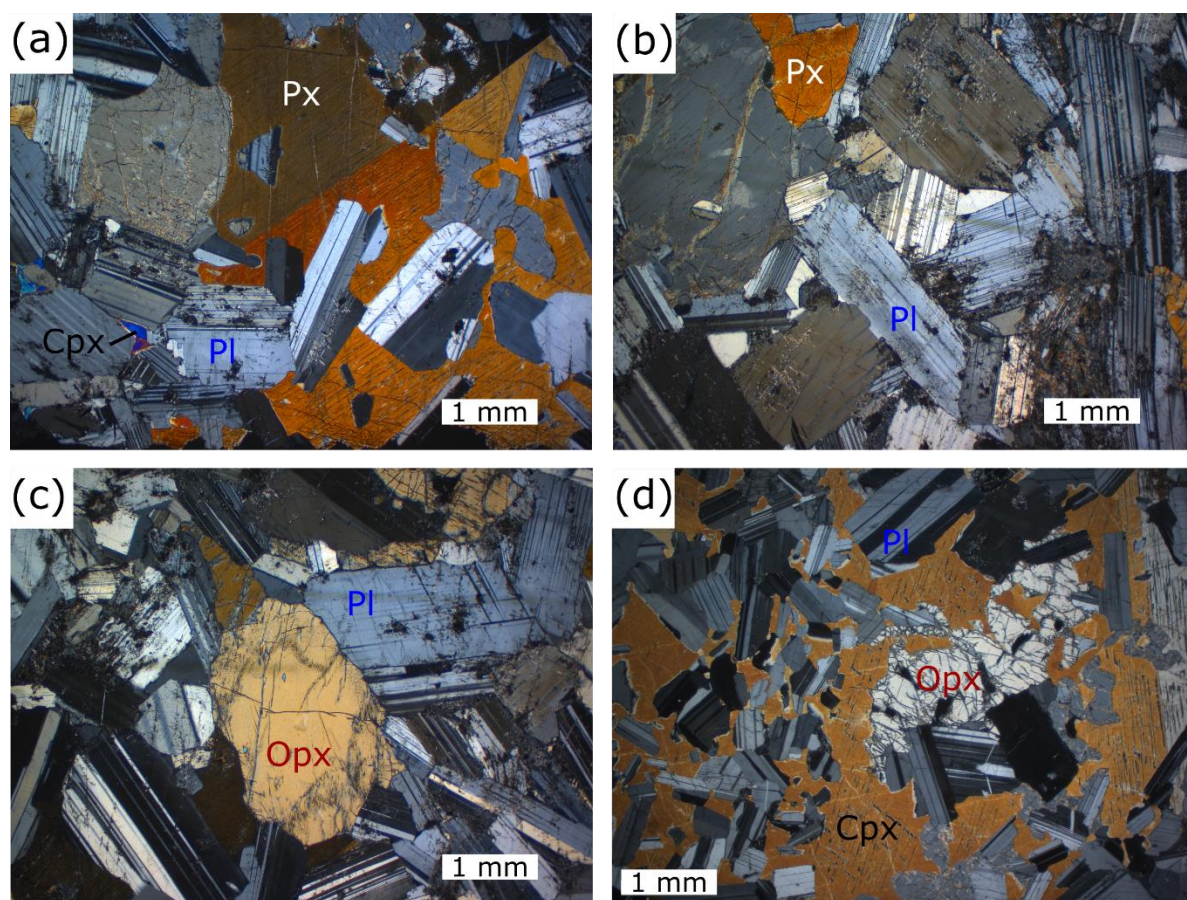
Figure 5.2: Photomicrographs of Main Zone norite. (a) Plagioclase laths with embayed grain boundaries hosted within large pyroxene oikocrysts (sample 81-1238). (b) Plagioclase forming subhedral laths with strongly developed albite twinning and interstitial phases where twinning is largely absent (sample 81-1238). (c) Orthopyroxene can form subhedral crystals alongside plagioclase laths (sample 81-1238). (d) Large clinopyroxene oikocryst with multiple plagioclase chadacrysts and strongly corroded orthopyroxene in the core of the oikocryst (sample 94-1177). Note the relatively small (≤ 1 mm) grain size of plagioclase crystals within the oikocryst core.

5.2 Upper Flatreef

5.2.1 Upper Mottled Anorthosite

The UMA is largely comprised of euhedral cumulus plagioclase, with laths measuring 1-2 mm in length, and well-defined albite twinning. Rare pericline twinning has also been observed. Plagioclase also forms anhedral interstitial crystals. Plagioclase is normally zoned with Ca-rich cores and Na-rich rims (Figure 5.3). In total, plagioclase accounts for 95% of the rock (Figure 5.3). Distinctive mottles, generally 5-7 cm across, are comprised of single oikocrysts of clinopyroxene containing rounded and embayed plagioclase chadacrysts with sizes of 0.1-1 mm. In the cores of clinopyroxene oikocrysts, small fragments of orthopyroxene oikocrysts can be found, although this is not ubiquitous and represent <1% of the modal mineralogy (Figure 5.4). Element maps indicate that the modal proportion of clinopyroxene is 4% (Figure 5.3). Minor sericite alteration is spatially restricted to fractures. Sulphide mineralization is generally rare, but some samples contain fine disseminated 'clouds' of chalcopyrite and pyrite spatially associated with sericite alteration of plagioclase. Trace amounts of small (0.15 mm) subhedral chromite are also present.
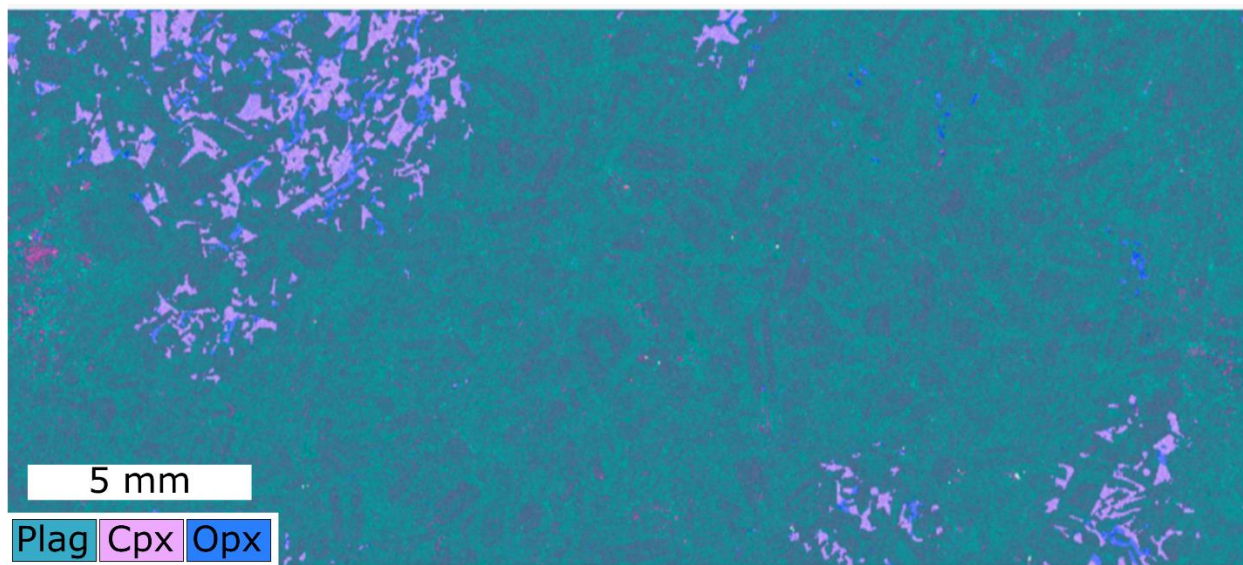
Figure 5.3: Element map of a thin section of Upper Mottled Anorthosite. Euhedral and subhedral normally zoned cumulus plagioclase is the predominant phase showing pink Ca-rich cores and blue Na-rich rims. Clinopyroxene and minor orthopyroxene form anhedral oikocrysts (sample 81-1294).
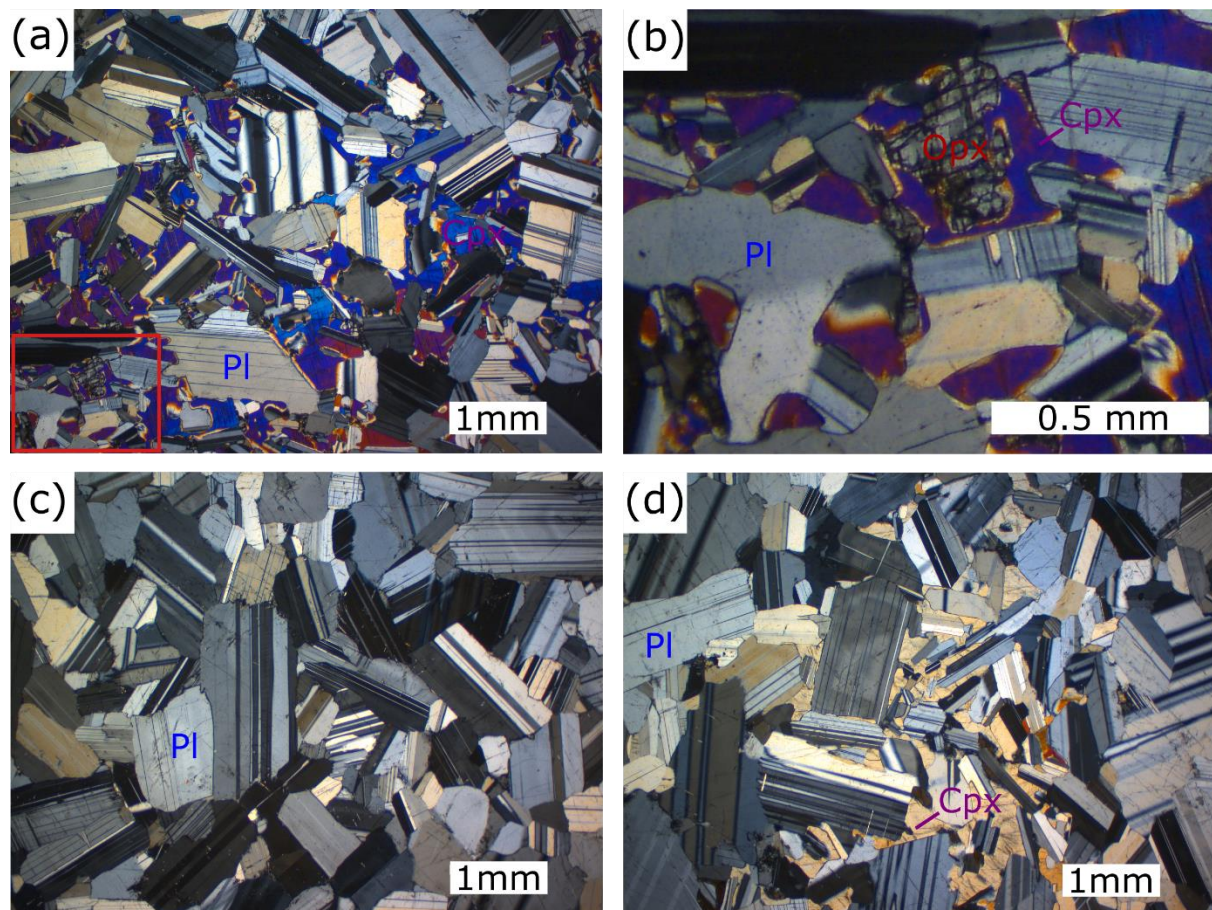
Figure 5.4: Photomicrographs of the Upper Mottled Anorthosite. (a) Subhedral and strongly embayed plagioclase chadacrysts within large clinopyroxene oikocryst (sample 81-1294). (b) Enlarged section of part of figure a, (see red box for location) showing remnant orthopyroxene oikocryst partially replaced by clinopyroxene (sample 81-1294). (c) Subhedral cumulus plagioclase in anorthosite (sample 81-1294). (d) Small clinopyroxene mottle with zoning in some plagioclase crystals (sample 81-1294).

5.2.2 Upper Pyroxenite

The Upper Pyroxenite is comprised largely of medium to coarse grained orthopyroxenite containing subhedral stubby orthopyroxene grains (75 modal %) and interstitial plagioclase (15 modal %) (Figure 5.5). Orthopyroxene grains range between 0.5-7 mm whereas plagioclase crystals can be > 10 mm and become oikocrystic (Figure 5.6). Well-defined albite twinning in plagioclase can be deformed (Figure 5.6c). Clinopyroxene can be present as a minor phase and rarely can become a major component (e.g. sample 94-1291) (Figure 5.6d). In addition, moderate alteration by amphibole and lesser phlogopite are also present occurring both within orthopyroxene crystals and along grain boundaries.
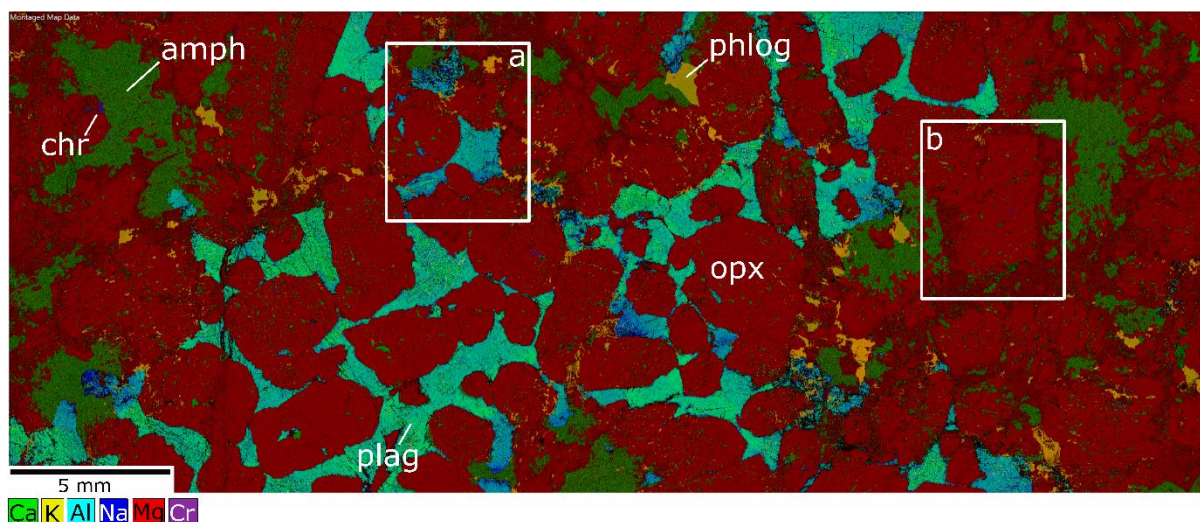
Figure 5.5: Coarse grained pyroxenite from the Upper Pyroxenite Unit (sample 81-1316). Orthopyroxene forms subhedral crystals showing no alignment of minerals. Amphibole and phlogopite occur largely along crystal boundaries. Note the more sodic patches of interstitial plagioclase as highlighted in box a, and Mg-rich orthopyroxene surrounded by alteration in box b.
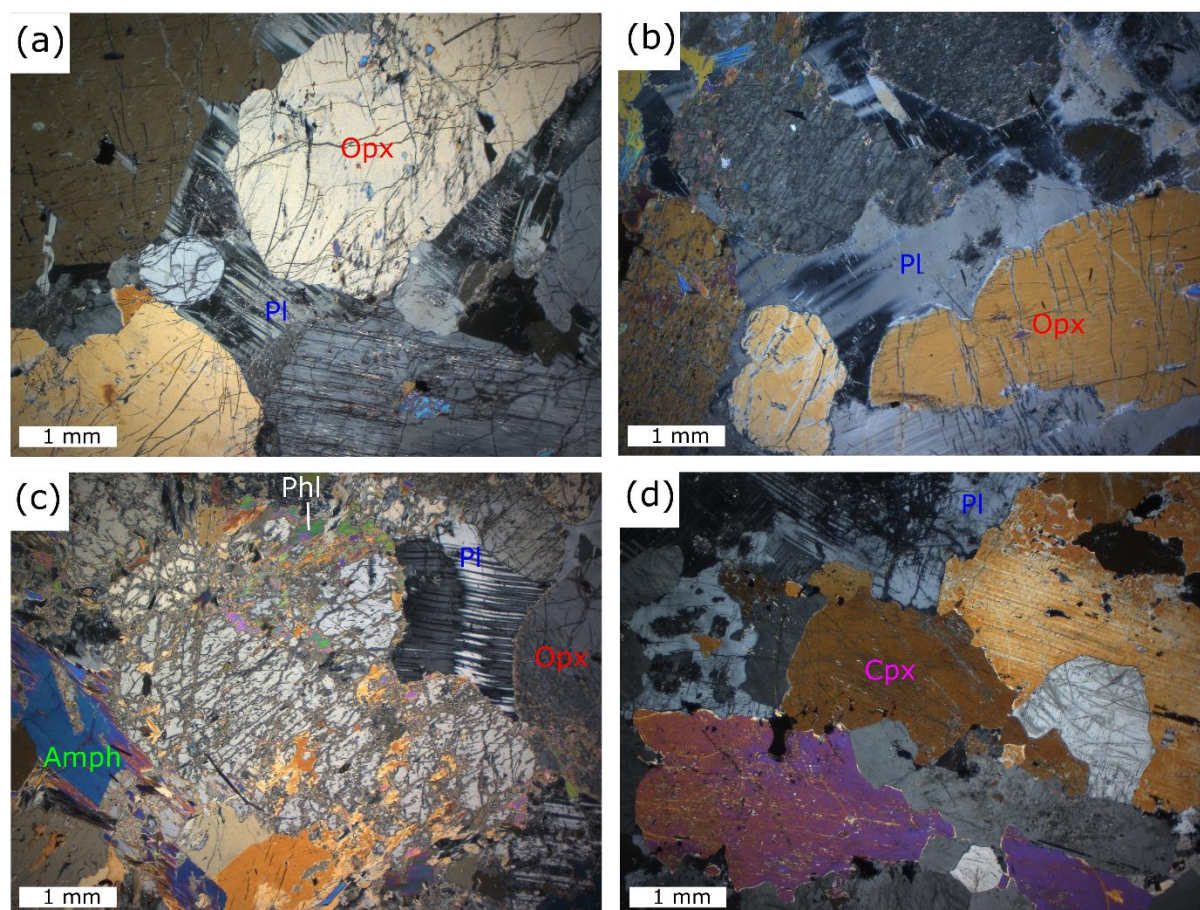
Figure 5.6: Petromicrographs of rocks in the Upper Pyroxenite Unit. (a) Coarse grained subhedral orthopyroxene (sample 94-1252). (b) Orthopyroxene crystals are hosted in a large plagioclase oikocryst (sample 81-1316). (c) Albite twinning of plagioclase can be deformed (sample 81-1316). (d) Anhedral clinopyroxene and interstitial plagioclase (sample 94-1291).

Rocks in the Upper Pyroxenite are generally sulphide poor. Sulphides are comprised of pyrrhotite, pentlandite and chalcopyrite and are interstitial to silicate minerals (Figure 5.7a). Chromite occurs as subhedral crystals concentrated in lenses hosted by pyroxene and plagioclase (e.g. sample 94-1281) (Figure 5.7b).
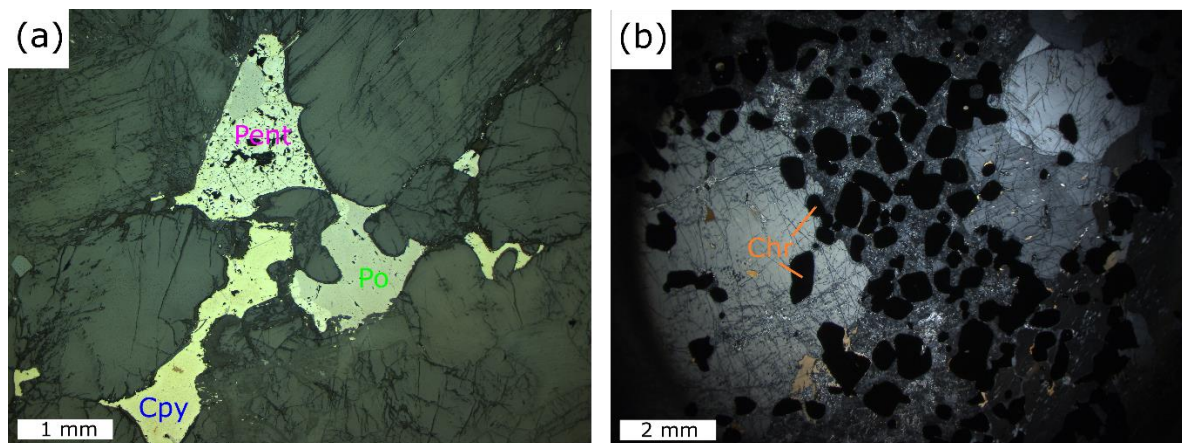
Figure 5.7: Reflected light petromicrographs of rocks in the Upper Pyroxenite. (a) Sulphide grain interstitial to silicate minerals containing chalcopyrite, pentlandite and pyrrhotite (sample 94-1239). (b) Lens of chromitite containing subhedral chromite grains (sample 94-1281).

5.2.3 Upper PGE Reef

The Upper PGE Reef is comprised of medium-grained orthopyroxenite that is largely unremarkable from hangingwall and footwall orthopyroxenites. Orthopyroxene is subhedral with elongate laths measuring up to 5 mm in length constituting 75 modal % of the rock (Figure 5.8). Plagioclase is interstitial and can form oikocrysts around orthopyroxene. The reef is somewhat altered by amphibole, and lesser phlogopite, that largely occurs on grain boundaries (Figure 5.9). The reef is generally sulphide poor, and where present occurs as small disseminated 'clouds'.
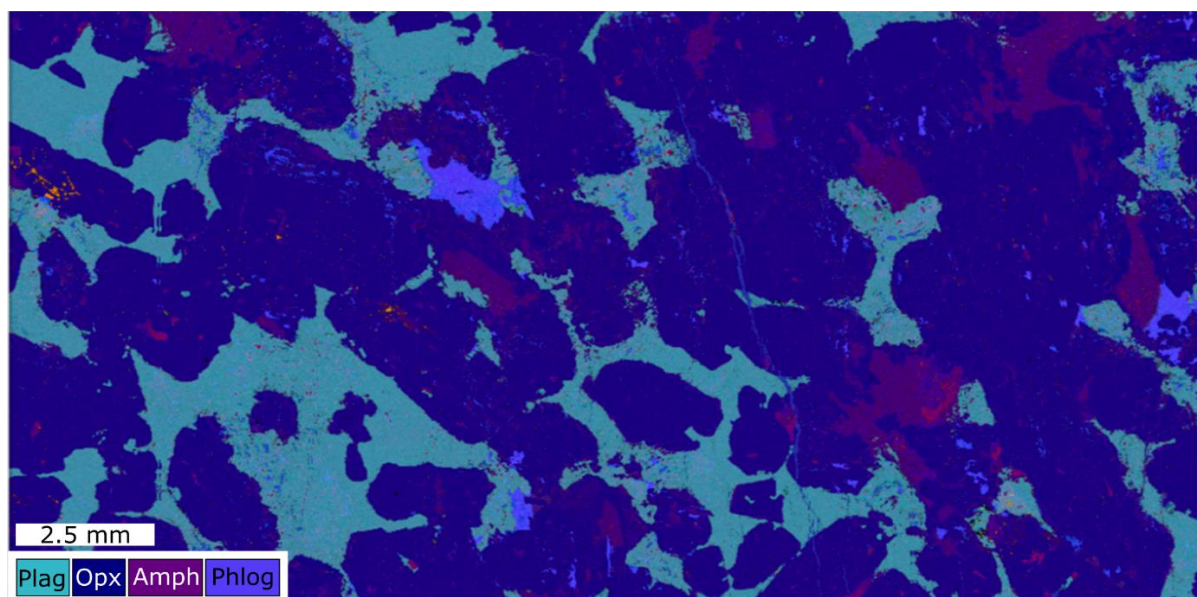
Figure 5.8: Element map of the Upper PGE Reef orthopyroxenite in the Upper Pyroxenite unit. Orthopyroxene in sample 81-1305 is coarse grained and hosted in interstitial plagioclase. Alteration is largely restricted to grain boundaries and pyroxene cleavage planes.
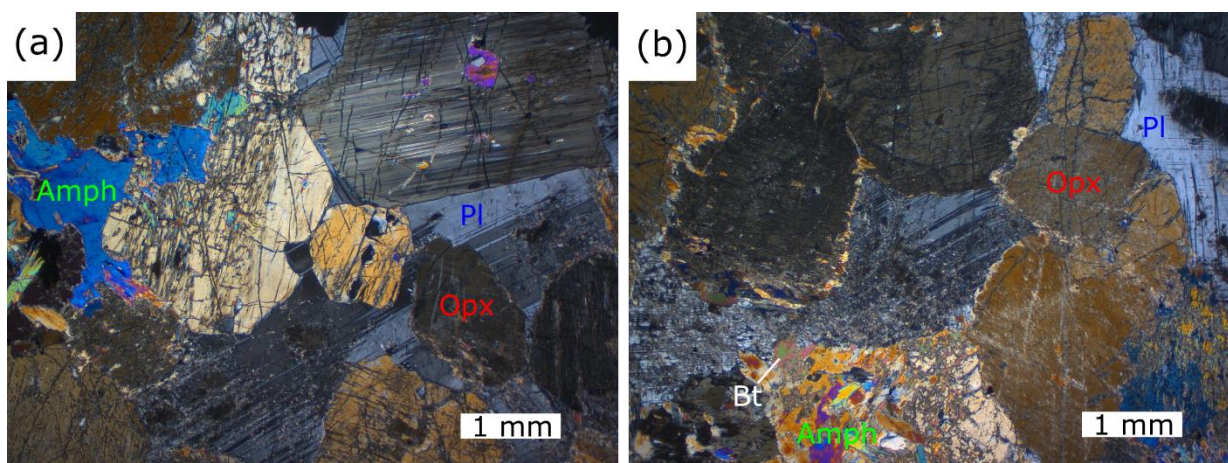
Figure 5.9: Petromicrographs of orthopyroxenites forming the Upper PGE Reef. (a) Subhedral orthopyroxene crystals within large plagioclase oikocrysts. Amphibole alteration partially overprints orthopyroxene (sample 81-1305). (b) Subhedral orthopyroxene showing thin alteration rims of amphibole. Biotite occurs with larger patches of amphibole (sample 81-1305).

5.2.3 Main PGE Reef

The lower portion of the Upper Pyroxenite contains elevated sulphide contents, associated with pegmatoidal pyroxenite layers. The pegmatoid itself comprises abundant pyroxene crystals (> 1 cm) that contain multiple inclusions of variably serpentinised anhedral olivine ranging from 1-5 mm in diameter (Figure 5.10, Figure 5.11). The rocks have undergone alteration resulting in subhedral phlogopite and amphibole growth along the rims and mineral cleavage planes of orthopyroxene. Some phlogopite crystals can be several mm in length and

are commonly found intergrown with sulphides. Fine grained phlogopite and muscovite is also found as an alteration phase.
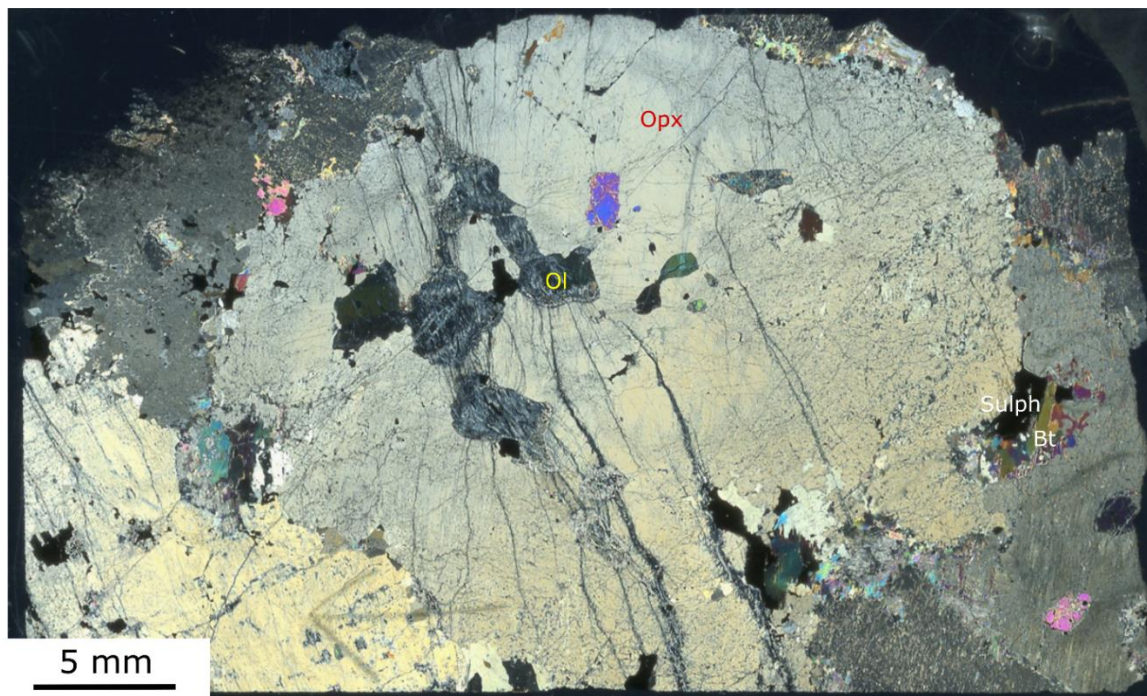
Figure 5.10: Photomicrograph of sample 81-1327 taken under crossed-polars (whole thin-section). Large anhedral orthopyroxene crystals contain inclusions of olivine with minor biotite-amphibole-sulphide alteration concentrated along grain boundaries. Some grains display undulose extinction.
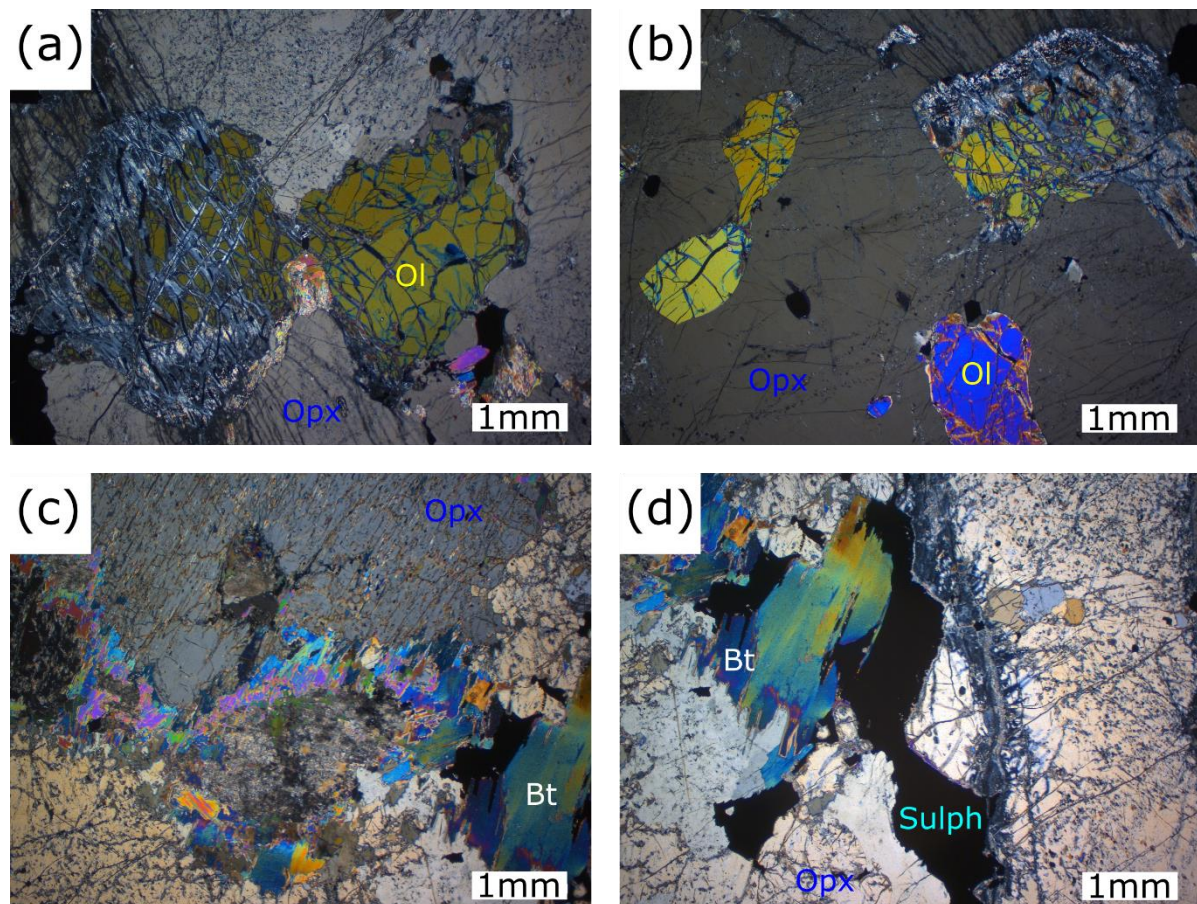
Figure 5.11: Photomicrographs of sulphide bearing samples from Upper Pyroxenite, sample 81-1327. (a+b) Large anhedral olivine with partial serpentinisation. The olivine crystals are enveloped in large orthopyroxene crystals. (c) Alteration by biotite and amphibole exploiting orthopyroxene grain boundaries. (d) Phlogopite crystals are commonly intergrown with sulphides.

Sulphides are generally comprised of equal proportions of chalcopyrite and pyrrhotite with minor pentlandite, although the proportions of the minerals vary between different grain aggregates (Figure 5.12). Domains of net-textured sulphides with pyrrhotite, pentlandite and chalcopyrite are also found (Figure 5.12b). Sulphides are also seen intergrown with biotite (Figure 5.11d), filling veins and associated with needles of amphibole, with chalcopyrite forming pseudomorphs of amphibole with distinctive 124-56° angles. Chromite is present as subhedral grains associated with sulphides or as inclusions in orthopyroxene crystals.
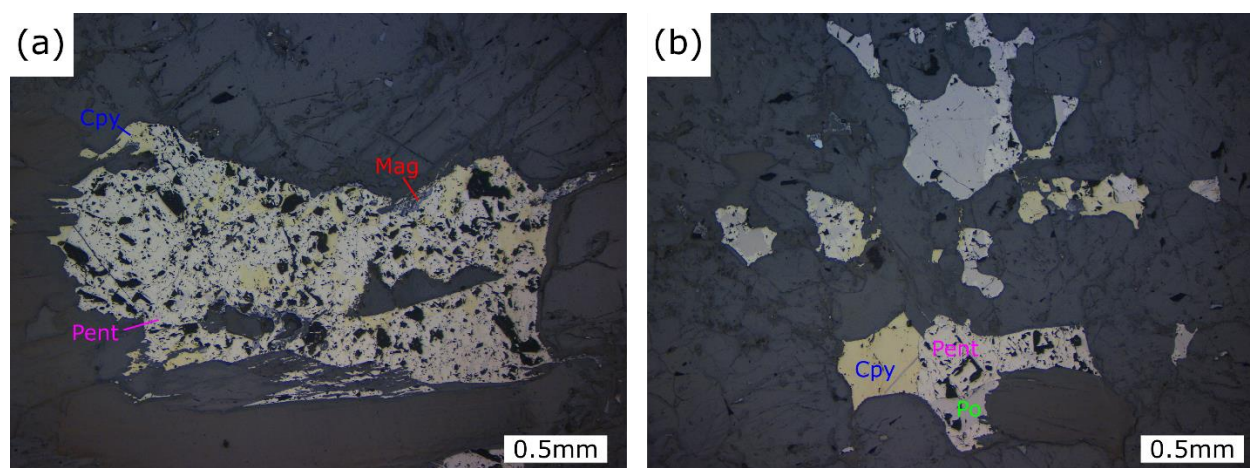
Figure 5.12: Reflected light photomicrographs of sulphides within the Main PGE Reef (sample 81-1327). (a) Irregular interstitial sulphide grain comprised of pentlandite and chalcopyrite intergrown with amphibole needles along its lower margins. (b) Net-textured sulphides of pyrrhotite, pentlandite and chalcopyrite.

5.2.5 Central Norite

5.2.5.1 Norite

Of the various lithologies in the Central Norite Unit, norite is the most abundant. The rocks consist mainly of cumulus orthopyroxene and plagioclase, whereas clinopyroxene occurs as an interstitial phase. As an example, sample 81-1338 (Figure 5.13) contains 14% orthopyroxene and 76% plagioclase. Orthopyroxene forms euhedral to subhedral grains (1-3 mm) whereas plagioclase forms mostly subhedral laths (0.5-2 mm in length), although plagioclase is also present as an intercumulus phase, alongside minor interstitial quartz (Figure 5.14). Most plagioclase grains show subtle normal zonation. Some larger orthopyroxene crystals can contain small, rounded, anhedral plagioclase crystals (0.1-0.6 mm in length; Figure 5.14c). Clinopyroxene is found as large oikocrysts measuring up to 3 cm diameter, forming typically ~10% of the rock type. The oikocrysts contain numerous subhedral plagioclase chadacrysts of varying size. In rare cases, plagioclase laths show deformed albite twinning. All norite samples are slightly altered showing patches of sericite in either the cores of plagioclase grains or along fractures. Minor amphibole alteration is also present, notably along pyroxene grain boundaries. Generally, the norites are free of sulphides. Chromite is present in trace proportions forming disseminated euhedral-subhedral grains found along grain boundaries as well as included in both orthopyroxene and plagioclase.

Ti Ca Si Al Na Mg
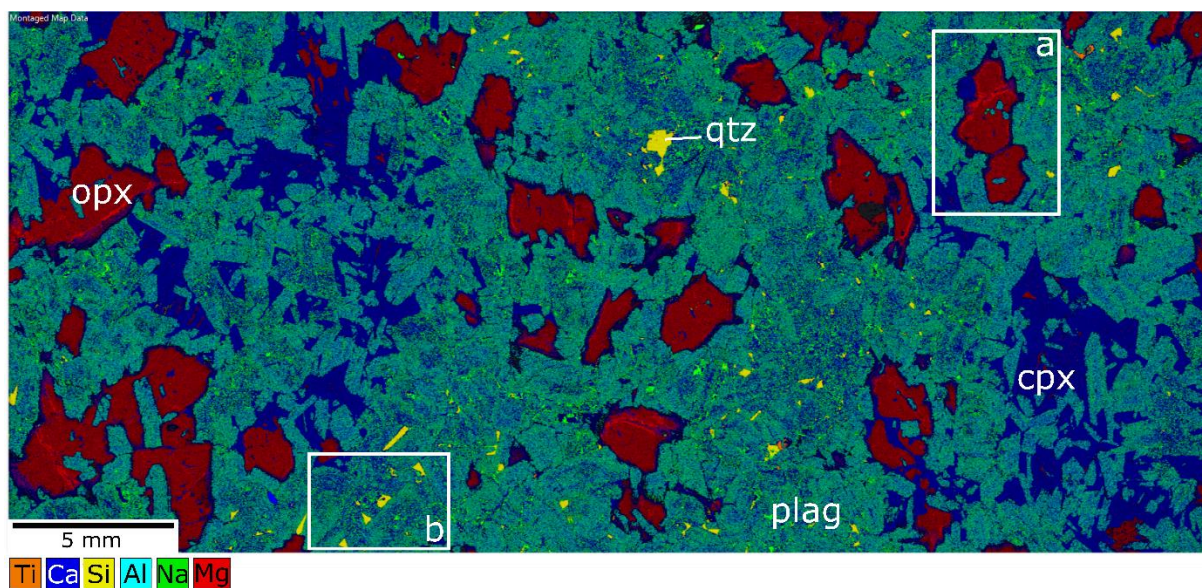
Figure 5.13: Element map of a norite (sample 81-1338) showing cumulus plagioclase and large anhedral to subhedral cumulus orthopyroxene grains and interstitial oikocrysts of clinopyroxene. Note the clinopyroxene rims around orthopyroxene cores highlighted in box a. Quartz, coloured yellow here is clearly interstitial to plagioclase as seen in box b.
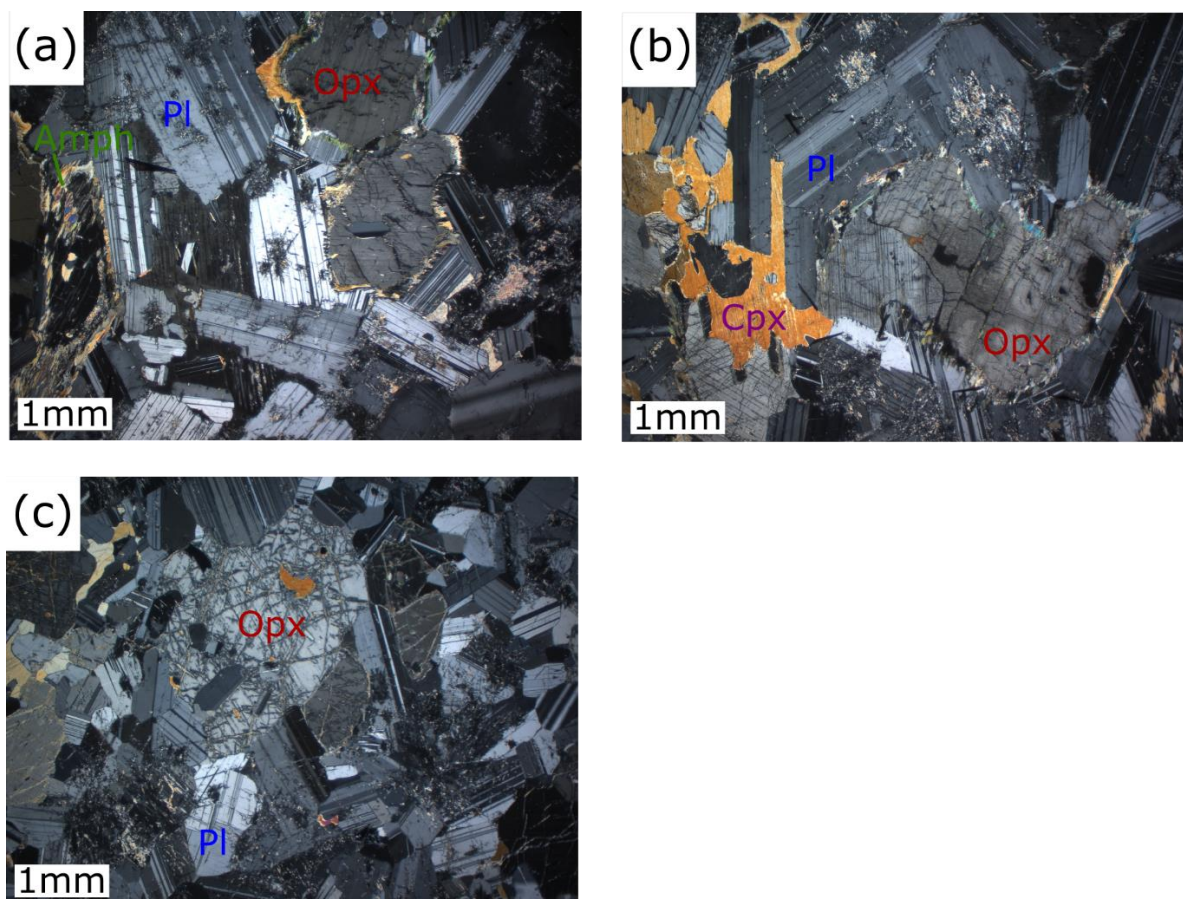
Figure 5.14: Photomicrographs of norite from the Central Norite Unit. (a) Cumulus orthopyroxene with minor plagioclase inclusions. Orthopyroxene is partially altered along its margins by hydrous phases (sample 81-1338). (b) Cumulus orthopyroxene and plagioclase, with the latter showing minor alteration and sericite. Clinopyroxene forms an oikocryst (sample 81-1338). (c) Anhedral orthopyroxene in a matrix of subhedral plagioclase (sample 94-1293).

5.2.5.2 Mottled Anorthosite

Mottled anorthosite forms the lowermost rock type of the Central Norite Unit. Anorthosite layers throughout the Critical Zone of the Bushveld typically have distinctive oikocrysts, colloquially known as mottles, formed by intercumulus pyroxene. According to IUGS nomenclature, many mottled anorthosites would have to be classified as leuconorites rather than anorthosites, but as is convention in the Bushveld geological community, cumulus terminology is used here and this rock is therefore named the "mottled anorthosite". The cumulus plagioclase in Flatreef anorthosite is generally more subhedral or anhedral in comparison to the commonly euhedral plagioclase laths observed in the Main Zone. Plagioclase laths generally display normal zoning with Ca-rich cores and Na-rich rims. Mottles of varying size are present comprising orthopyroxene and clinopyroxene (Figure 5.15). Plagioclase occurs as both a cumulus and intercumulus phase, constituting 78 modal % of the rock (Figure 5.16).

In sample 81-1355 a large orthopyroxene oikocryst has minor clinopyroxene along the outer margins of the orthopyroxene (Figure 5.16). Minor amphibole alteration is also present along the margins of the orthopyroxene. Orthopyroxene is the dominant pyroxene representing 21% of the rock. It tends to form substantial oikocrysts with small plagioclase chadacrysts. In comparison, clinopyroxene forms large skeletal oikocrysts with more abundant chadacrysts, representing around 1% in sample 81-1355. Plagioclase chadacrysts are not in textural equilibrium with their pyroxene host oikocrysts everywhere but can have rounded and embayed shapes. Rare euhedral chromite crystals are present interstitial to plagioclase. Elongate sulphides are found within the oikocryst exploiting cleavage planes within orthopyroxene.
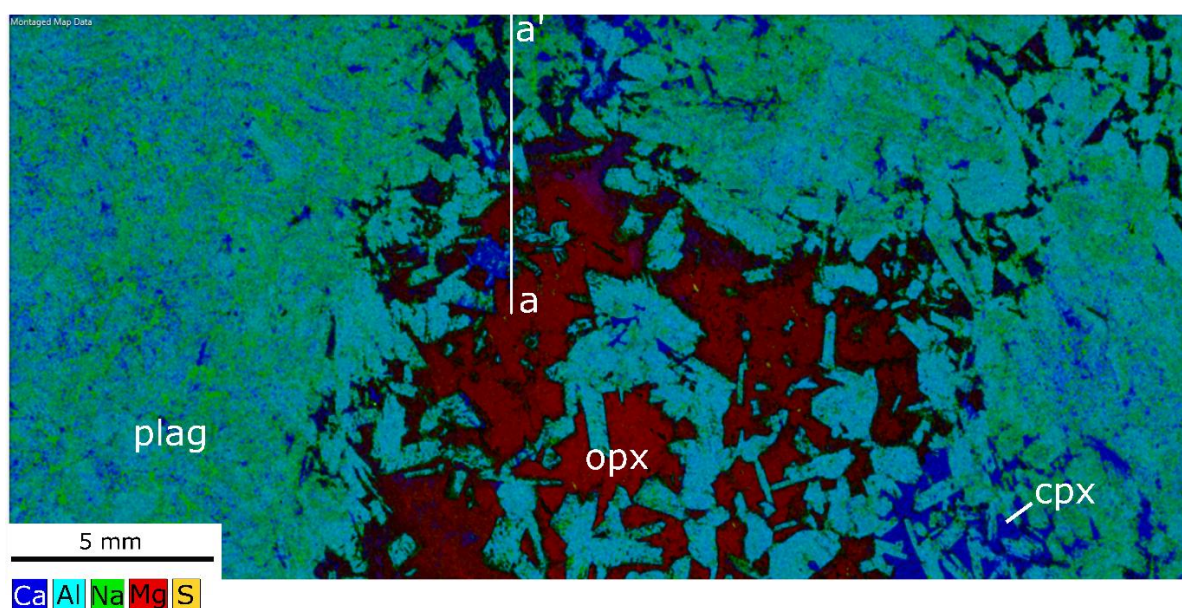
Figure 5.15: Element map of a mottled anorthosite showing a large pyroxene oikocryst in a matrix of cumulus plagioclase laths. The oikocryst is zoned with a relatively magnesian core and calcium rich

margin as shown along the section a-a' (sample 81-1355). A halo of interstitial clinopyroxene can be found around the mottle. Plagioclase laths show normal zoning with relatively sodic rims (blue) and calcium-rich cores (pink). Plagioclase within the oikocryst appears to lack zonation and appears less sodic.
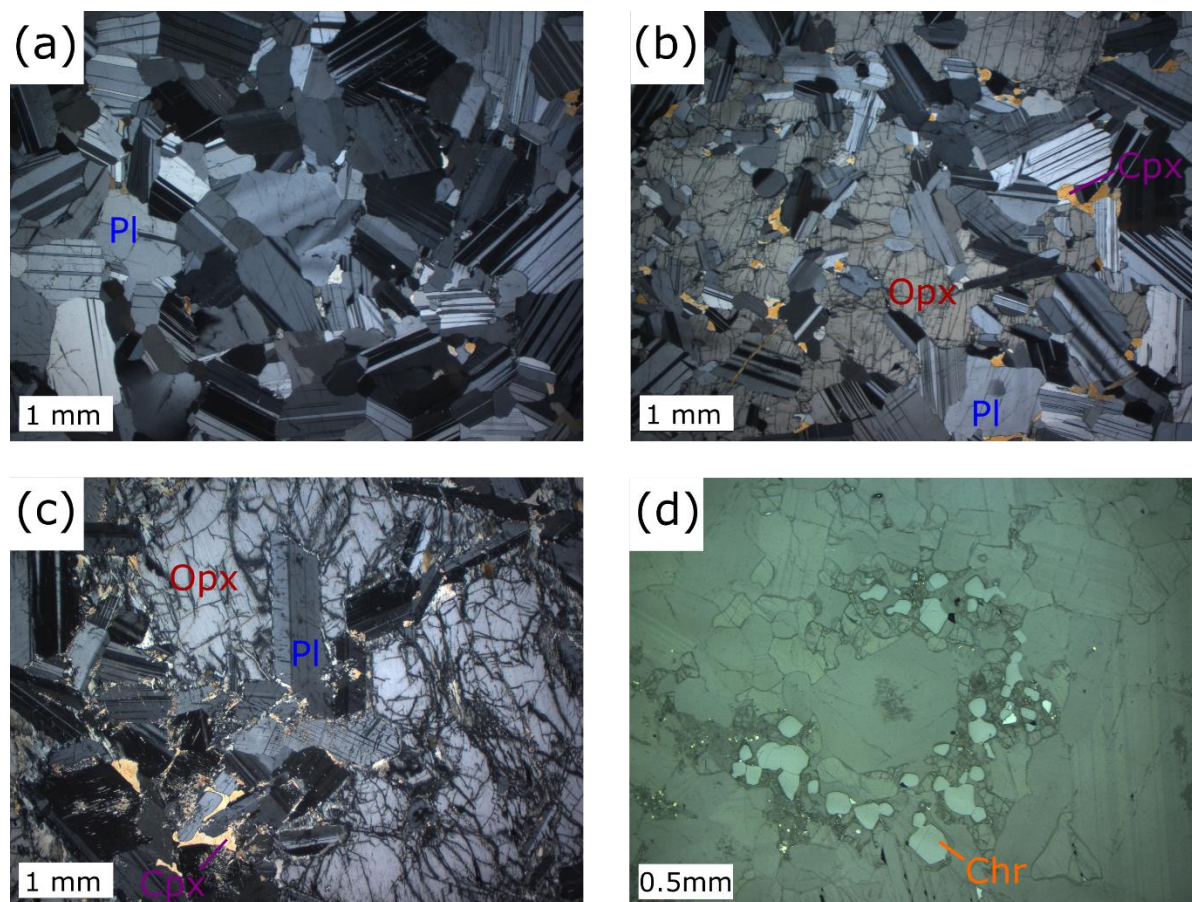
Figure 5.16: Photomicrographs of anorthosites in the Flatreef. (a) Typical anorthosite consisting of subhedral plagioclase with well-developed albite twinning (sample 94-1308). (b) Large orthopyroxene oikocryst with small rounded chadacrysts of plagioclase. Orthopyroxene is surrounded by interstitial clinopyroxene (sample 94-1308). (c) Orthopyroxene mottle containing subhedral plagioclase chadacrysts with a thin rim of clinopyroxene surrounding orthopyroxene (sample 81-1355). (d) Subhedral chromite clustered in a ring around a plagioclase crystal within the orthopyroxene oikocryst. Fine-grained recrystallised orthopyroxene surrounds the chromite crystals (sample 94-1308).

5.2.6 Lower Pyroxenite

The Lower Pyroxenite is largely homogeneous and medium to coarse grained consisting of subhedral to anhedral stubby orthopyroxene (0.5 – 5 mm) and interstitial plagioclase that can exceed 1 cm in diameter (Figure 5.17, Figure 5.18). Orthopyroxene accounts for 82 modal % of the rock with plagioclase < 8 modal %. In rare cases the well developed albite twinning in plagioclase is deformed. Minor clinopyroxene can form anhedral crystals of similar size to orthopyroxenite. Amphibole and phlogopite are large interstitial although amphibole is also

present along pyroxene cleavage planes. Generally, amphibole and phlogopite represent < 5% of the rock but locally can become a dominant phase (e.g. sample 81-1367) (Figure 5.18d).
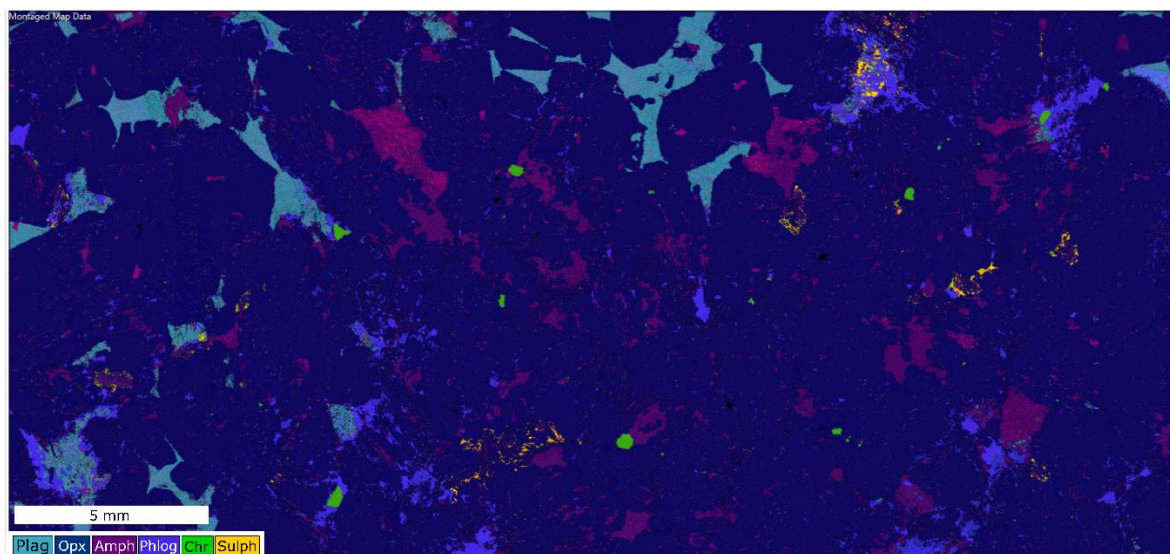
Figure 5.17: Element map of coarse grained orthopyroxene in the Upper Pyroxenite (sample 81-1405). Orthopyroxene is subhedral while plagioclase is interstitial.
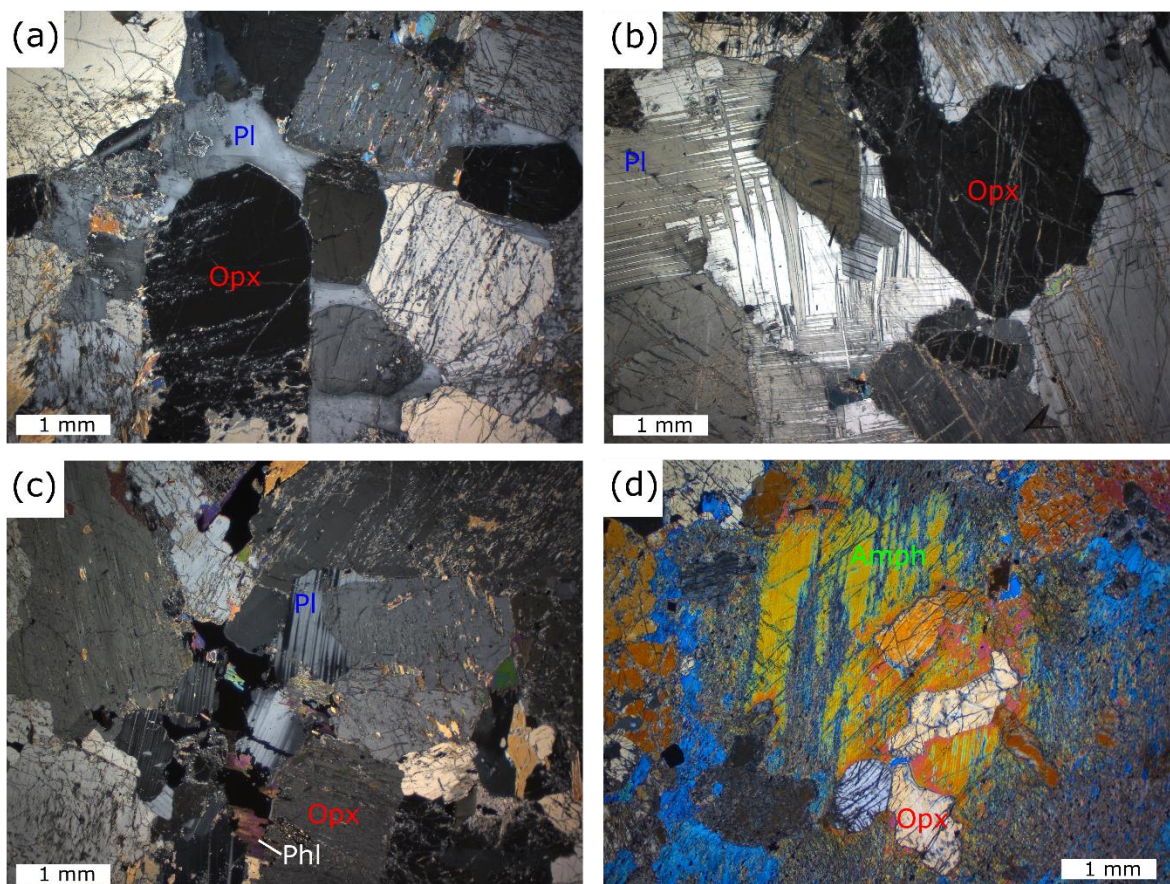
Figure 5.18: Petromicrographs of Lower Pyroxenite Unit rocks. (a) Coarse grained subhedral orthopyroxene hosted in plagioclase oikocrysts (sample 81-1405). Minor amphibole occurs along orthopyroxene grain boundaries and cleavage planes. (b) Interstitial plagioclase with deformed albite twins (sample 81-1393). (c) Orthopyroxenite with minor phlogopite and amphibole along silicate grain

boundaries and orthopyroxene cleavage planes (sample 81-1393). (d) Significant amphibole and anhedral orthopyroxene (sample 81-1367).

Sulphides grains are interstitial to silicate phases and commonly associated with amphibole and phlogopite (Figure 5.19a). Chromite is found both as interstitial phases, sometimes associated with sulphides where it is anhedral or as subhedral isolated crystals.
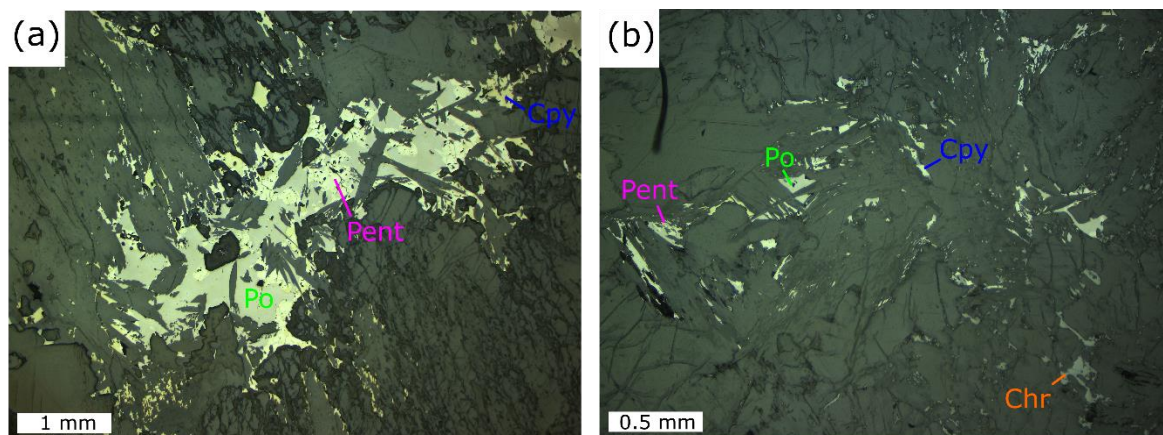
Figure 5.19: Reflected light petromicrographs of rocks in the Lower Pyroxenite Unit. (a) Sulphide grain is intergrown with amphibole crystals. Chalcopyrite is largely on the edge of sulphide grains (sample 81-1393). (b) Sulphide and anhedral chromite infilling interstitial space between silicate minerals (sample 81-1405).

5.2.7 Main Chromitite

The Main Chromitite is comprised of layers and lenses of chromitite hosted within pegmatoidal pyroxenite. The chromitite consists of subhedral and anhedral chromite grains within a matrix of interstitial plagioclase (Figure 5.20). In the pegmatoidal pyroxenite, the orthopyroxene crystals generally measure several centimetres and are variably altered, with amphibole altering margins of orthopyroxene crystals (Figure 5.21). Smaller anhedral orthopyroxene grains are also found along boundaries of larger pyroxene crystals, indicative of deformation. Biotite is found as an alteration phase concentrated on grain boundaries and intergrown with sulphides with amphibole. Trace carbonate is found in association with amphibole crystals.

Figure 5.20: image of drill-core sample from UMT081 (81-1422) with red box showing the location of thin-section (Figure 5.21). Note the interstitial plagioclase within chromitite. Chromitite forms cohesive layers displaying undulating contacts with pegmatoidal pyroxenite.
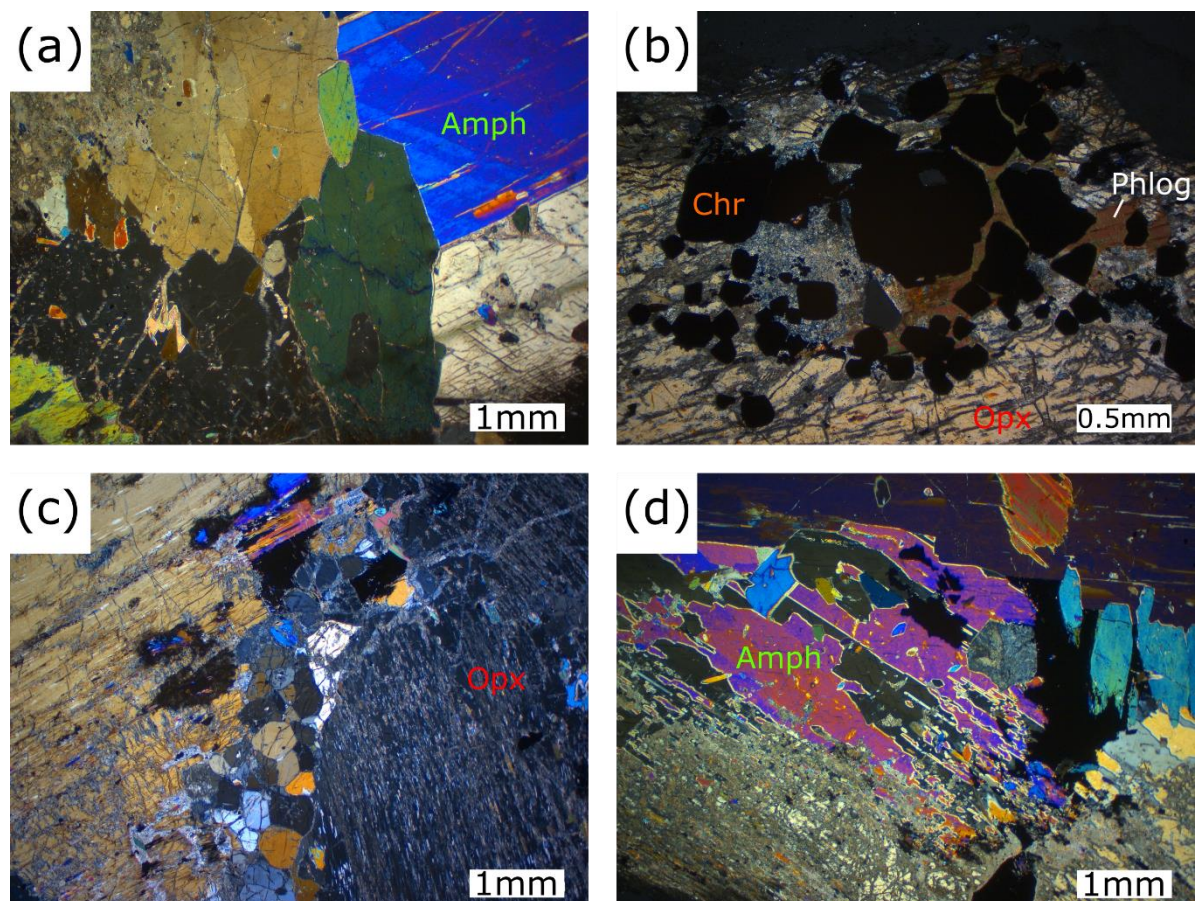
Figure 5.21: Photomicrographs of pegmatoidal pyroxenite associated with the Main Chromitite (sample 81-1422). (a) Altered pyroxenite showing amphibole overprinting most orthopyroxene. (b) Chromite grains are subhedral when large (< 0.75 mm) but tend to be euhedral when small. Phlogopite alteration is commonly found associated with clots of chromite. (c) Small grains of orthopyroxene (< 0.5 mm) are found along grain boundaries between larger orthopyroxene grains, suggesting deformation of the rock. (d) Amphibole alteration intergrown with sulphides.

Sulphides are comprised of pentlandite with lesser amounts of pyrrhotite and chalcopyrite (Figure 5.22). Sulphides generally form large composite grains 1-4 mm across that are interstitial to the main silicate phases, but closely associated with amphibole and biotite. Disseminated grains of pentlandite are found in close proximity to clots of euhedral chromite (Figure 5.22). Disseminated chromite grains within the pyroxenite footwall of the Main Chromitite are found in clots with interstitial biotite and commonly surrounded by sericite alteration. Larger chromite crystals (0.5-0.7 mm) tend to be subhedral whereas smaller crystals (0.1-0.15 mm) tend to be euhedral.
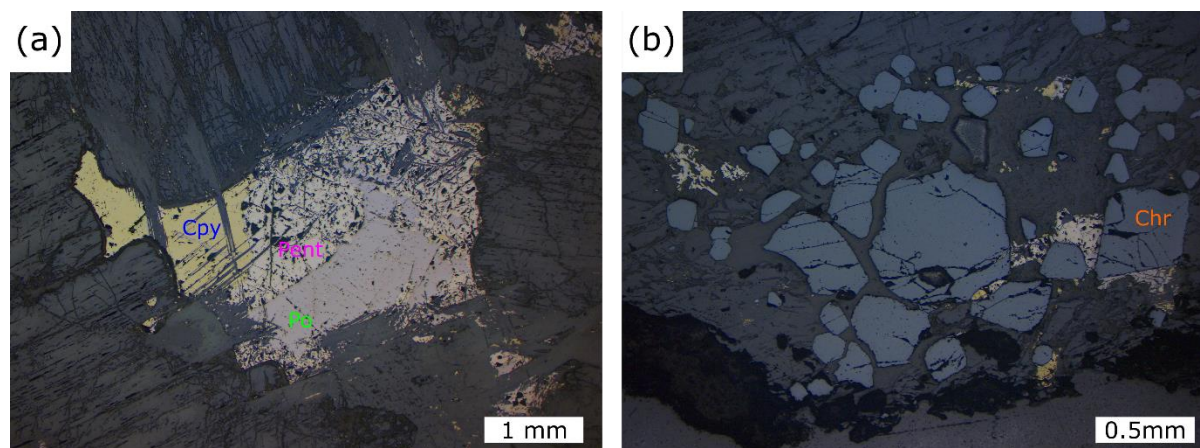
Figure 5.22: Reflected light photomicrographs of sulphides and oxides in the Main Chromitite host rocks. (a) Interstitial sulphide bleb with complex intergrowths with amphibole alteration (sample 81-1422). (b) Chromite is anhedral to subhedral and commonly annealed to nearby grains. Interstitial sulphides are commonly present with these clusters of chromite (sample 81-1422).

5.2.8 Lower Ultramafic Unit

5.2.8.1 Harzburgite

Harzburgites occur only in the Lower Ultramafic Unit. The rocks consist mainly of olivine (53%) which is 3-8 mm in width and orthopyroxene (18%) measuring up to 2 cm in width (sample 81-1438, Figure 5.23). Variable concentrations of clinopyroxene (0-6%) is also present. Olivine is generally amoeboidal and can display prominent kink-banding (Figure 5.24). The olivine is largely unaltered and contains only minor serpentine veins. Orthopyroxene is generally granular but can also form oikocrysts containing smaller olivine chadacrysts (3-4 mm). Where olivine is hosted by clinopyroxene, a thin partial corona of optically continuous orthopyroxene is present between the olivine and clinopyroxene (Figure 5.24). Plagioclase is present as an interstitial phase forming large crystals (up to 4 mm). There is minor sericite alteration, preferentially within core domains of plagioclase.
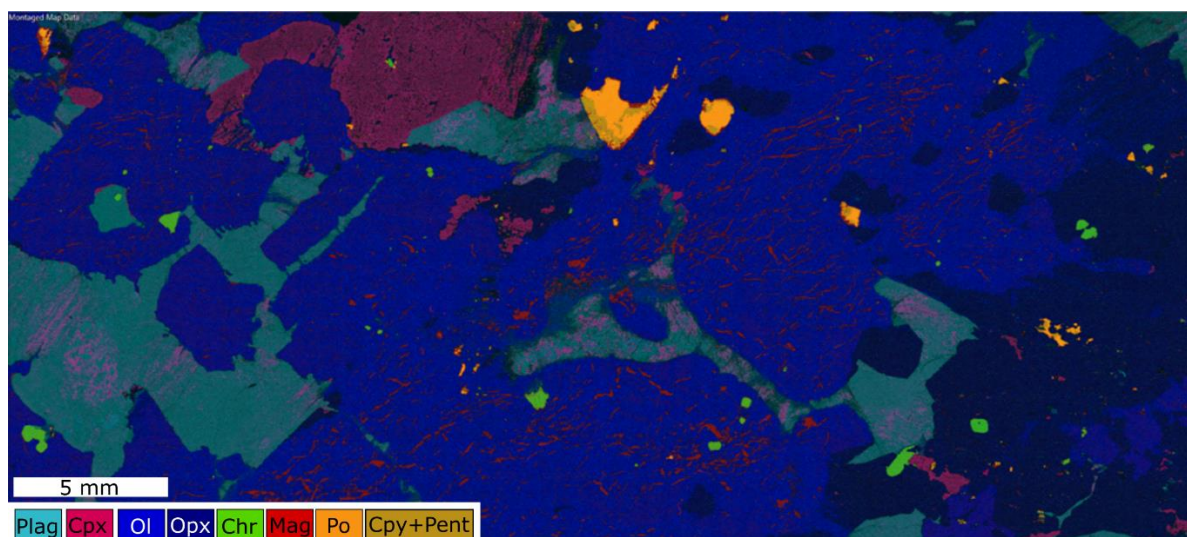
Figure 5.23: Element map of sample 81-1438 showing coarse-grained olivine and orthopyroxene set in interstitial plagioclase with minor clinopyroxene. Plagioclase contains some sericite alteration. Magnetite veins (red) cross-cut partially altered olivine, distinguishing it from darker blue orthopyroxenes in element maps.
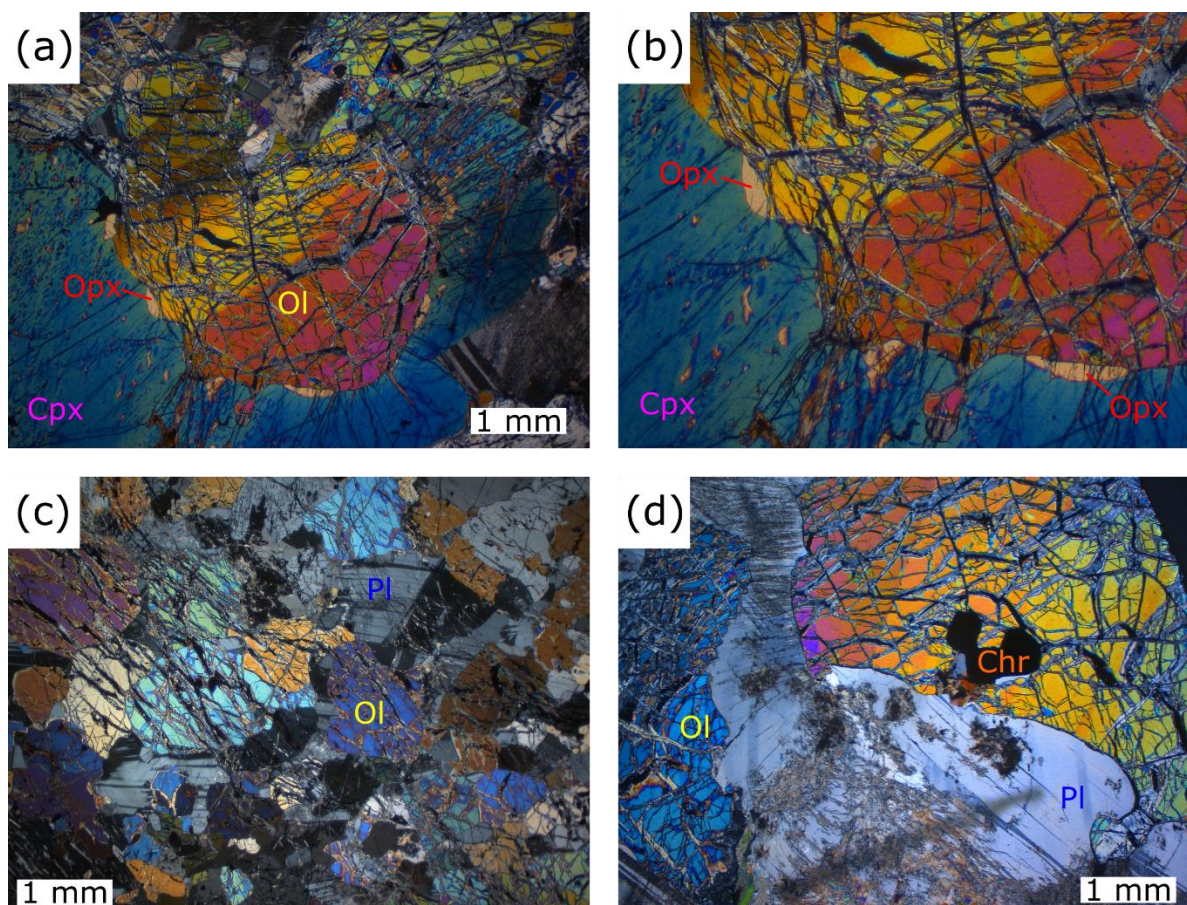
Figure 5.24: Photomicrographs of harzburgite occurrences in UMT081 and UMT094. (a) Kink-banded olivine surrounded by rare clinopyroxene. Note partial corona of orthopyroxene surrounding olivine (sample 81-1438). (b) Enlarged section of part of figure a. Orthopyroxene in optical continuity is found forming a fragmented corona along the boundary between olivine and clinopyroxene. (c) Amoeboidal

olivine and orthopyroxene within abundant interstitial plagioclase (sample 94-1337). (d) Kink-banded olivine with euhedral chromite inclusions and interstitial plagioclase (sample 81-1438).

Chromite is found as a euhedral phase within both silicate and sulphide minerals (0.2-1 mm). Occasionally, chromite is found rimmed by fine-grained phlogopite and can contain small inclusions of phlogopite. Sulphides comprise 0.45% by volume of harzburgite and consist mainly of pyrrhotite with less abundant pentlandite and trace amounts of chalcopyrite. Sulphides tend to form large fractionated grains that are interstitial to silicate phases and are sometimes associated with phlogopite and serpentine (Figure 5.25).
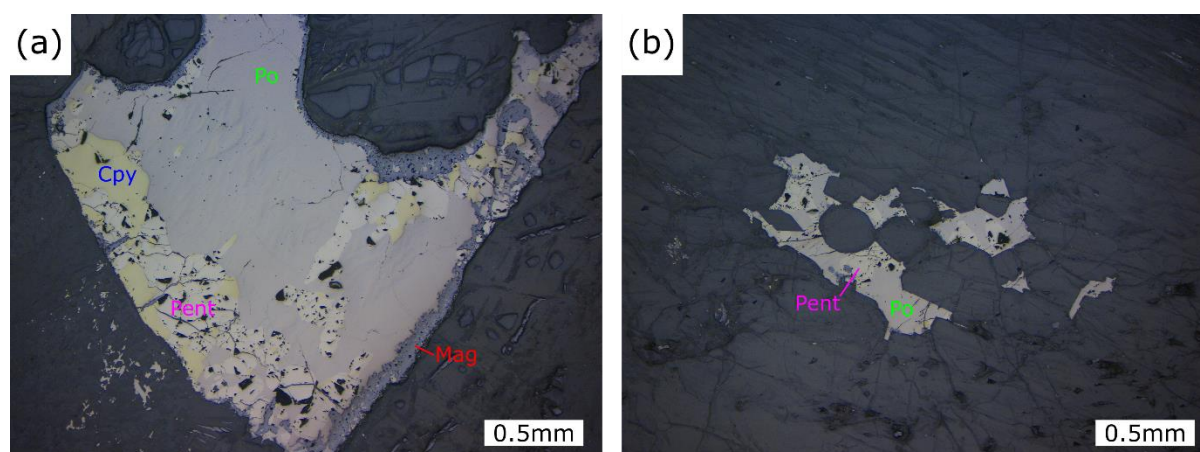
Figure 5.25: Photomicrographs of sulphide mineralization in harzburgite. (a) Large sulphide bleb comprised of pyrrhotite with less abundant pentlandite and chalcopyrite. Magnetite replacement is pervasive along all margins of the sulphide bleb (sample 81-1438). (b) Sulphides can also form smaller locally net-textured blebs, here comprised of pentlandite and pyrrhotite interstitial to silicate phases (sample 81-1438).

5.2.8.3 Lherzolite

Lherzolite is slightly finer grained than harzburgite and is dominated by cumulus olivine and clinopyroxene with plagioclase present as an interstitial phase (Figure 5.26). Olivine is anhedral, with a wide range of grain sizes (0.5-4 mm) and showing extensive serpentinisation of larger grains (Figure 5.27). Olivine in sample 81-1475 accounts for 64 modal % (including 8.9% serpentine associated with olivine). Smaller olivine crystals are usually subhedral, whereas larger olivine crystals are generally anhedral and are commonly amoeboidal. Clinopyroxene generally forms anhedral crystals, 2-5 mm in width, that can contain inclusions of olivine and have complex intergrowth patterns along boundaries with olivine. Clinopyroxene tends to form clusters comprised of several crystals and accounts for 20 modal % of the rock and is closely spatially associated with subordinate orthopyroxene (Figure 5.27). There is minor amphibole (<0.05%) that, like clinopyroxene, is interstitial to olivine. Plagioclase forms large interstitial crystals (3-6 mm) and is strongly altered to sericite, with alteration

concentrated within crystal cores and along fractures. Plagioclase accounts for 11 modal % of sample 81-1475. Trace phlogopite is also found forming relatively small crystals 0.3-0.4 mm.
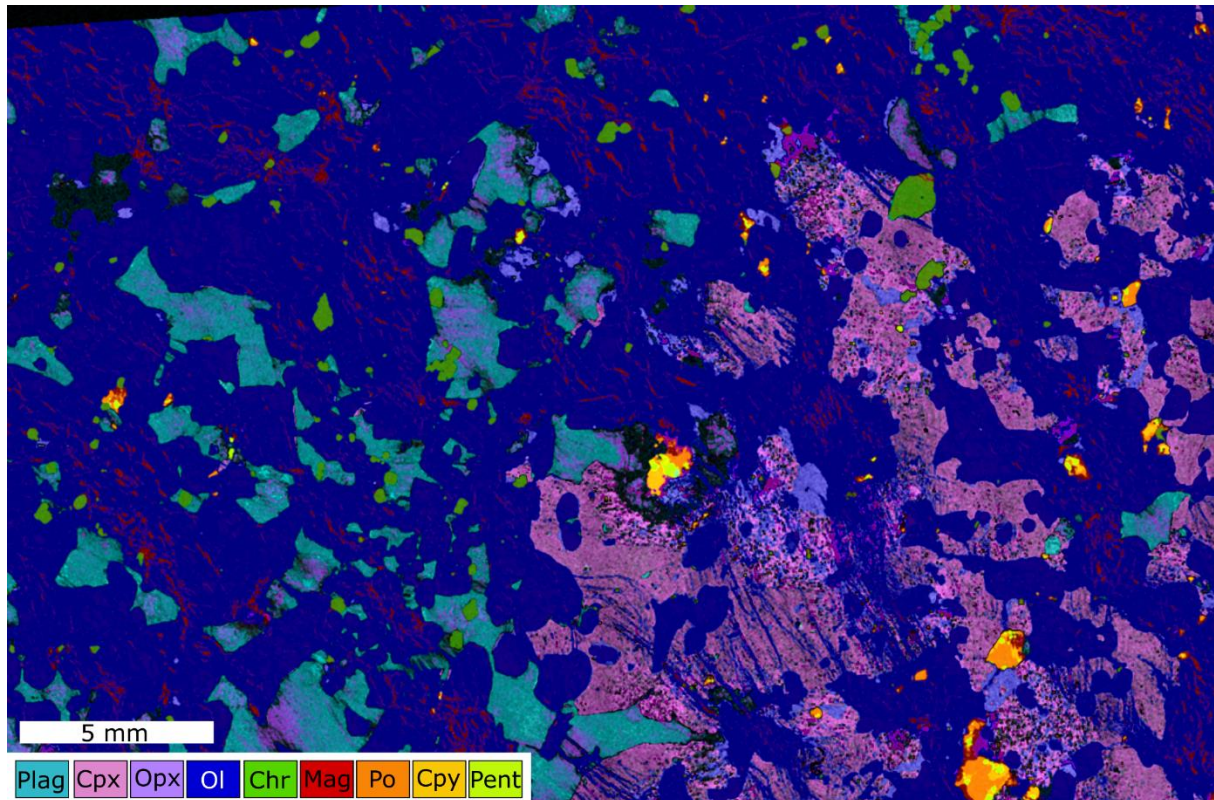
Figure 5.26: Element map of lherzolite (sample 81-1475). Olivine is seen as an abundant cumulus phase with large chromite crystals present throughout the sample. Clinopyroxene is found clustered in half of the image with plagioclase interstitial to olivine elsewhere.
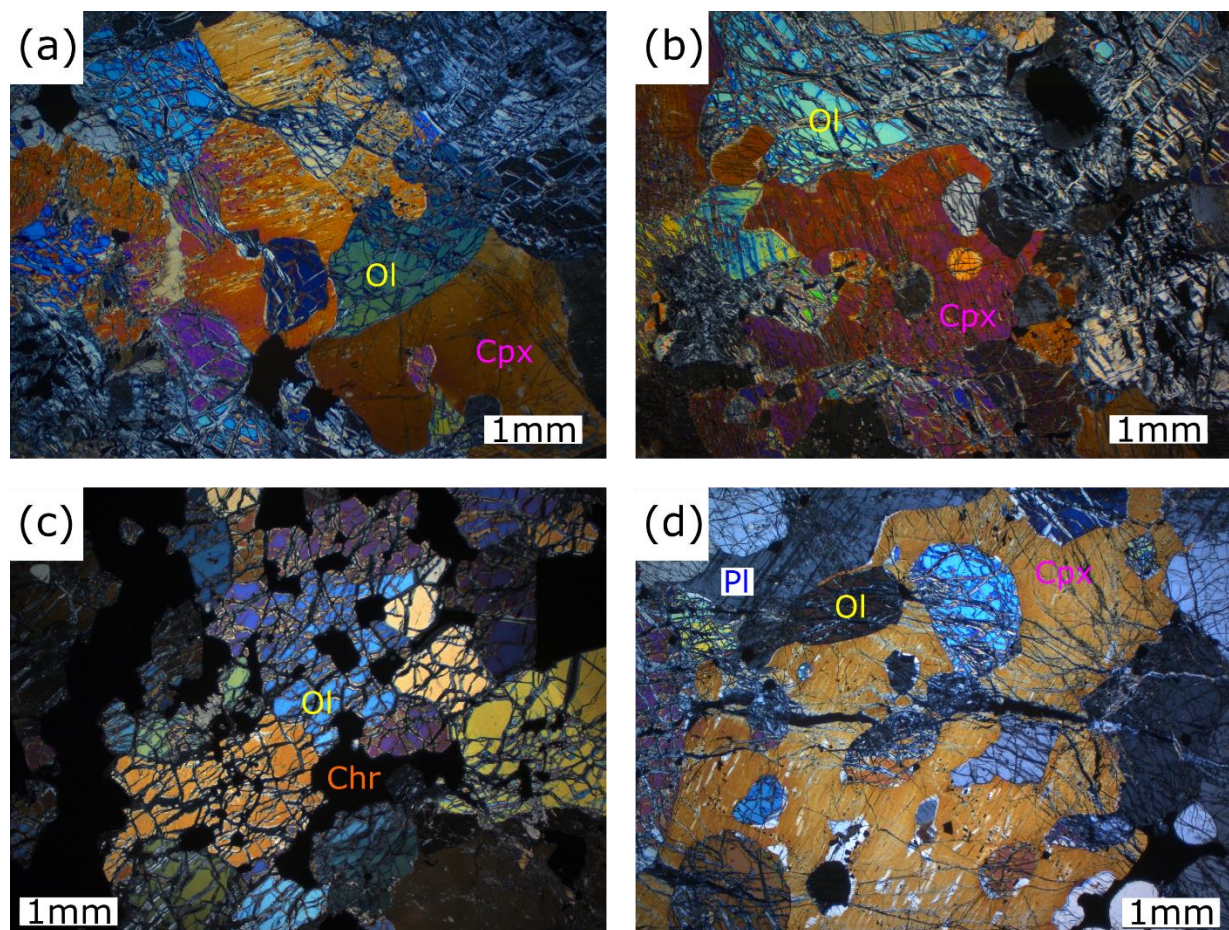
Figure 5.27: Photomicrographs of lherzolite rock types in the Lower Ultramafic Zone. (a) Amoeboidal olivine intergrown with larger clinopyroxene crystals. Olivine has been partially altered to serpentine and magnetite. Sulphides and chromite are generally found on grain boundaries (sample 81-1475). (b) Clinopyroxene can form oikocrysts with chadacrysts of olivine that are generally better preserved (sample 81-1475). (c) In drill-hole UMT094 abundant chromite is found as inclusions within olivine and occurring on grain boundaries (sample 94-1334). (d) A single large clinopyroxene crystal contains numerous inclusions of subhedral olivine of varying sizes (0.5-2 mm) (sample 94-1355).

Sulphides are rare, representing < 1% of modal mineralogy. They are mainly comprised of pyrrhotite as well as trace chalcopyrite and pentlandite, forming composite grains, interstitial to the silicate minerals, but occasionally remobilised to infill fractures in serpentinised olivine. Sulphides generally have a thin alteration rim of magnetite (Figure 5.28a). Large anhedral chromite grains (~1 mm) and smaller euhedral chromite (0.1-0.5 mm), found hosted in plagioclase and less commonly in olivine, account for nearly 1 modal % of the rock (Figure 5.28b). Euhedral chromite can be found as inclusions in both olivine, clinopyroxene and plagioclase. When hosted in pyroxene the chromite grains are commonly surrounded by a thin corona of plagioclase.
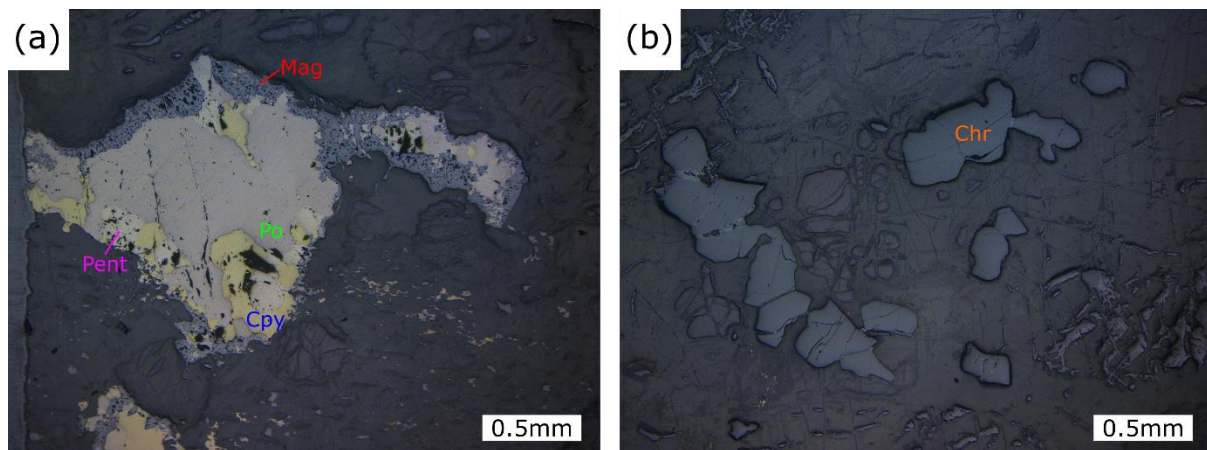
Figure 5.28: Reflected light photomicrographs of sulphides and oxides within lherzolite. (a) Interstitial sulphide bleb with pentlandite and chalcopyrite found on the edges of a pyrrhotite grain. The edges of this sulphide have been altered to magnetite (sample 81-1475). (b) Chromite is subhedral and annealed with neighbouring grains (sample 81-1475).

5.2.8.3 Pyroxenite

The pyroxenite rocks in the LUU show a wide range of grain sizes from fine grained (Figure 5.29) to pegmatoidal. In fine-grained rocks orthopyroxene is the predominant phase forming subhedral laths ranging between 0.2 to 1 mm in diameter. Plagioclase is interstitial and can form large oikocrysts within fine-grained rocks spanning several mm. Well developed albite twinning in plagioclase can be deformed, although this is not ubiquitous. In addition, minor anhedral clinopyroxene forms oikocrysts in which there are inclusions of embayed orthopyroxene (Figure 5.30b). These fine-grained pyroxenites are amongst the least altered pyroxenite rocks in the Flatreef. In pegmatoidal rocks orthopyroxene can exceed 15 mm in diameter and can contain minor alteration of pyroxene by amphibole and phlogopite and plagioclase by sericite (Figure 5.30c-d).
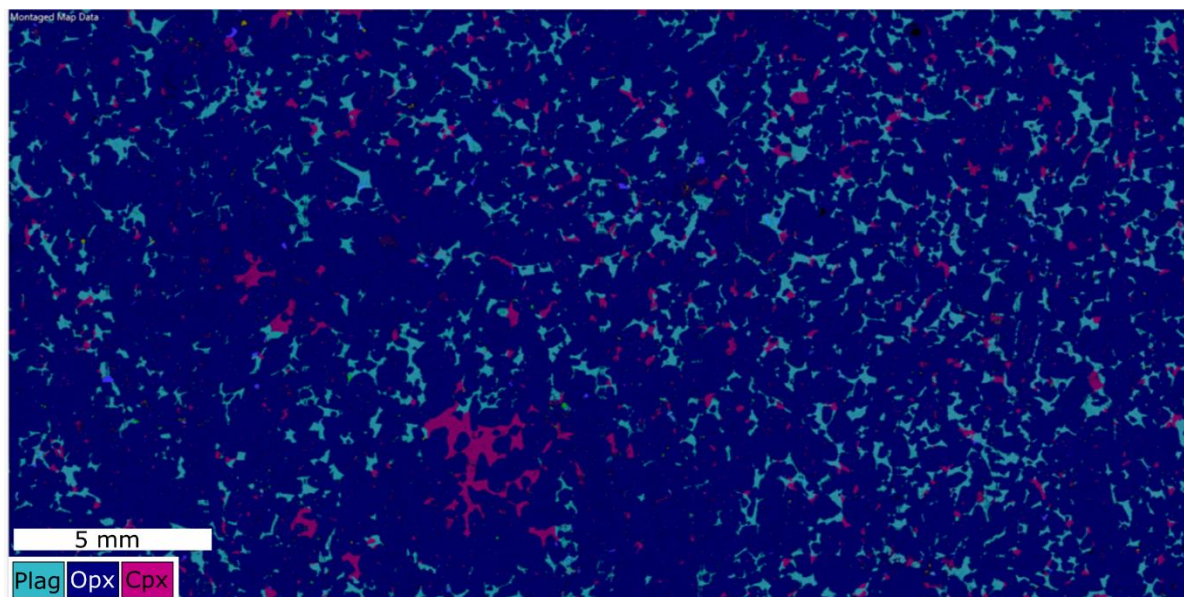
Figure 5.29: Element map of pyroxene in the Lower Ultramafic Unit (sample 81-1550). Orthopyroxene is subhedral within oikocrystic plagioclase and clinopyroxene.
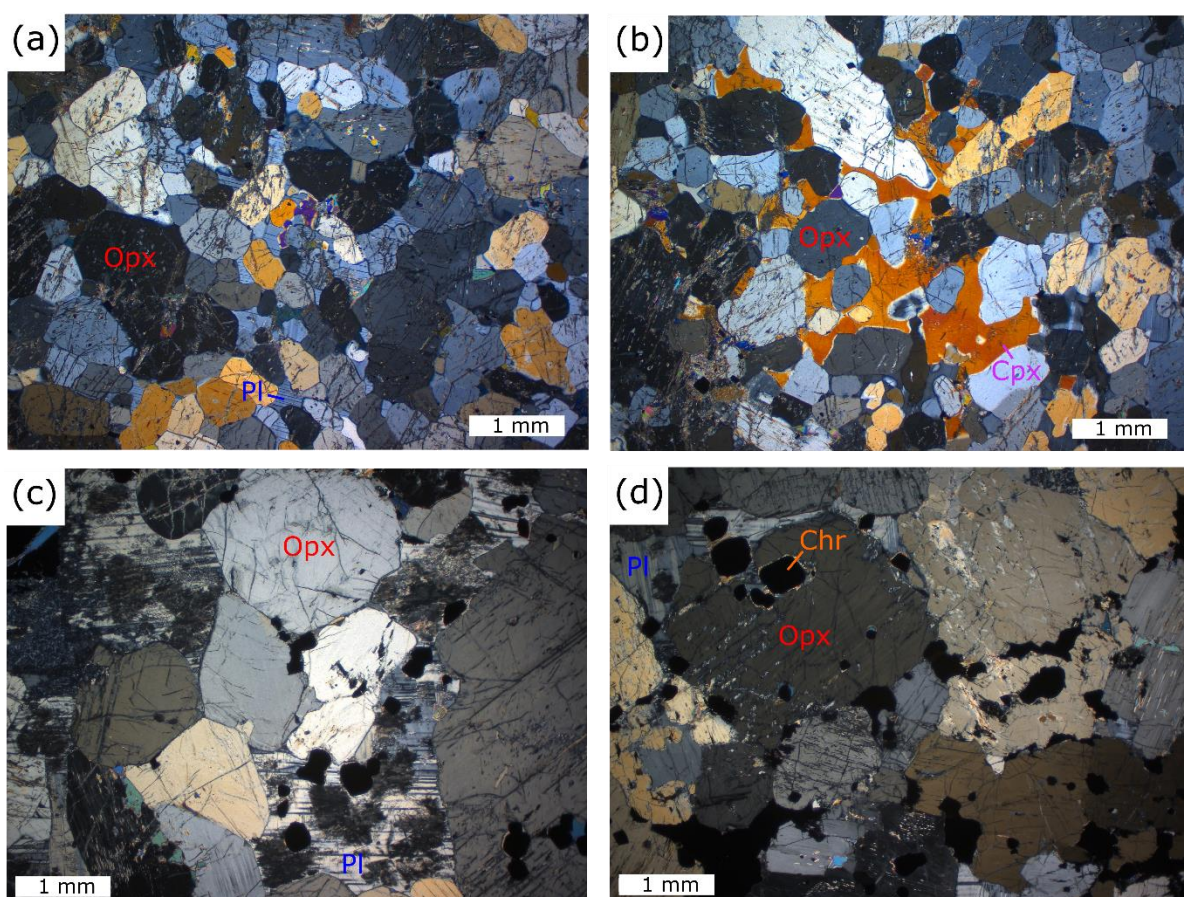
Figure 5.30: Petromicrographs of pyroxenite rocks in the LUU. (a) Fine grained orthopyroxenite with subhedral stubby orthopyroxene crystal (sample 81-1550). (b) Fine grained orthopyroxenite showing anhedral orthopyroxene chadacrysts within a clinopyroxene oikocryst (sample 81-1550). (c) Coarse grained orthopyroxenite containing subhedral to anhedral orthopyroxene and subhedral chromitite

largely hosted in plagioclase (sample 81-1468). (d) Coarse grained orthopyroxenite with a low interstitial feldspar content. Chromite can be surrounded by a rim of fine grained phlogopite (sample 81-1468).

The pyroxenite rocks in the LUU contain higher concentrations of sulphides than pyroxenites in the overlying units (up to 8% in pegmatoidal domains). These can form large composite grains interstitial to orthopyroxene and commonly intergrown with amphibole crystals (Figure 5.31b). Sulphide grains contain pyrrhotite with lesser pentlandite and chalcopyrite. The size of sulphide grains is largely related to the size of the silicate grains. Chromite is sometimes found as subhedral to anhedral grains within sulphide grains (Figure 5.31a) but largely occurs as subhedral crystals within or along silicate mineral grain boundaries. Chromite crystals can also be annealed and on occasion be surrounded by a thin rim of fine-grained mica or plagioclase.
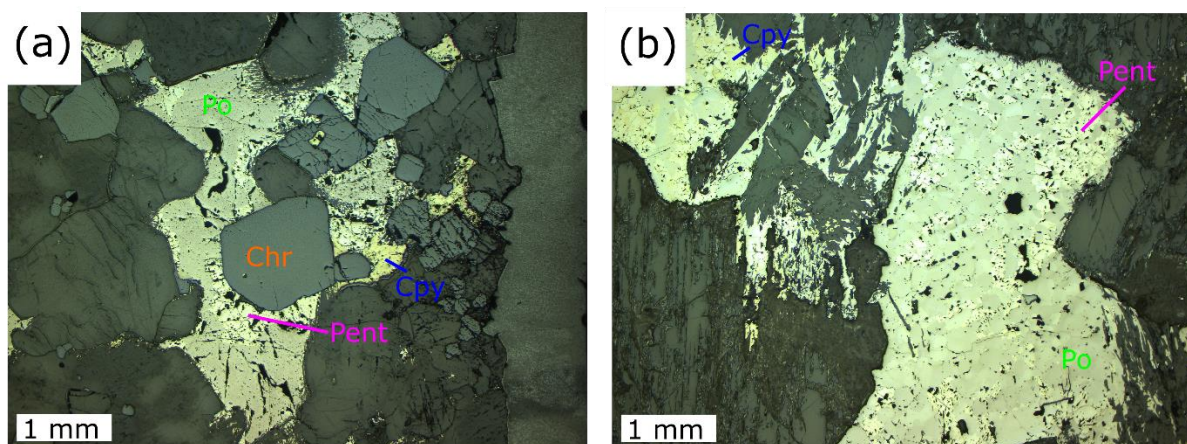
Figure 5.31: Reflected light petromicrographs of sulphide grains in pyroxenite rocks in the LUU. (a) Subhedral chromite grains of variable size partially contained in grains of sulphide. Sulphide is interstitial to silicate minerals (sample 81-1486). (b) Sulphide grains commonly *contain intergrowths of amphibole (sample 81-1452).*

5.3 Lower Flatreef

5.3.1 Footwall Assimilated Zone

Rocks of the FAZ display a wide range of textures and mineralogy dependent on the exact nature of the sedimentary lithology that has been assimilated, and the proportions of contaminant to magma (Figure 5.32; Figure 5.33). A key feature of all contaminated units is the abundance of clinopyroxene, giving the rock its distinctive green hue in drill core. The FAZ also contains 'parapyroxenites', a term introduced by previous workers to refer to rocks dominated by clinopyroxene of metamorphic origin (Kinnaird et al., 2005). Primary magmatic mineral assemblages include orthopyroxene, plagioclase and olivine in addition to abundant clinopyroxene. The rocks can be strongly overprinted by later fluid alteration forming phlogopite, sericite and amphibole. This alteration is most pronounced near the lower contact of the FAZ with the metamorphosed dolomitic footwall. Where alteration is locally absent,

cumulus phases can form triple junctions at 120°. Olivine and orthopyroxene are generally anhedral and commonly found as inclusions in single or multiple clinopyroxene crystals where they are rounded and partially replaced by amphibole, sericite and serpentine. It should also be noted that several thin (1-3 m) fine-grained orthopyroxenite layers occur in the uppermost portion of the FAZ (e.g. sample 81-1610) with broadly similar petrography to the fine-grained pyroxenite rocks in the Lower Ultramafic Unit.

A distinctive unit formed in the FAZ is a pegmatoidal olivine-bearing gabbronorite with large cumulus plagioclase laths (1-2 cm) (Figure 5.34). Olivine and clinopyroxene form anhedral grains or grain aggregates with undulating grain boundaries. They appear to have inclusions of plagioclase although optical continuity between these chadacrysts and surrounding plagioclase suggests these form part of a larger oikocryst. Olivine and clinopyroxene can be significantly smaller than plagioclase (3 mm) but can both form oikocrysts on the order of ~1 cm diameter.
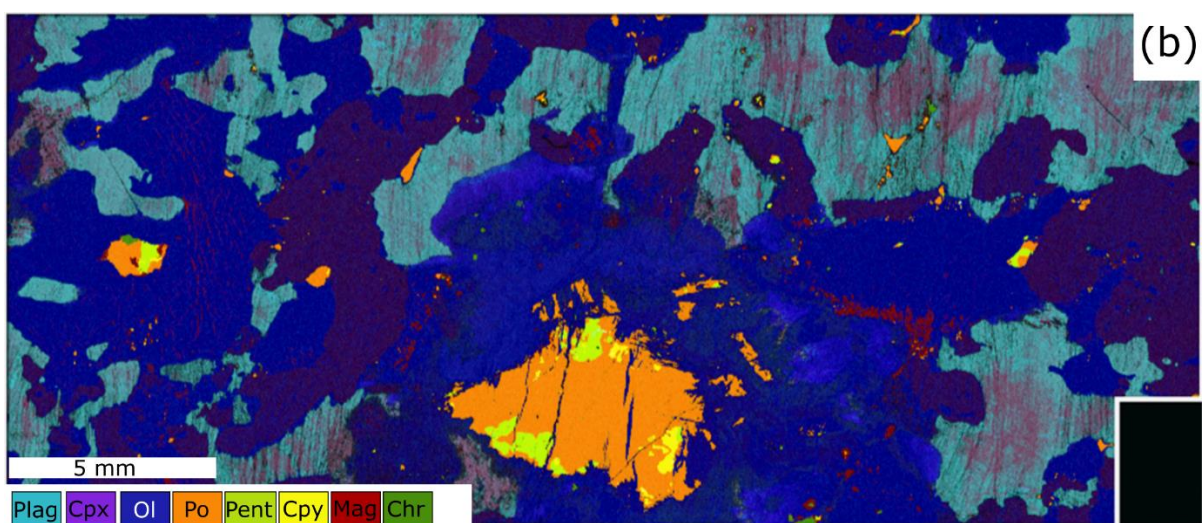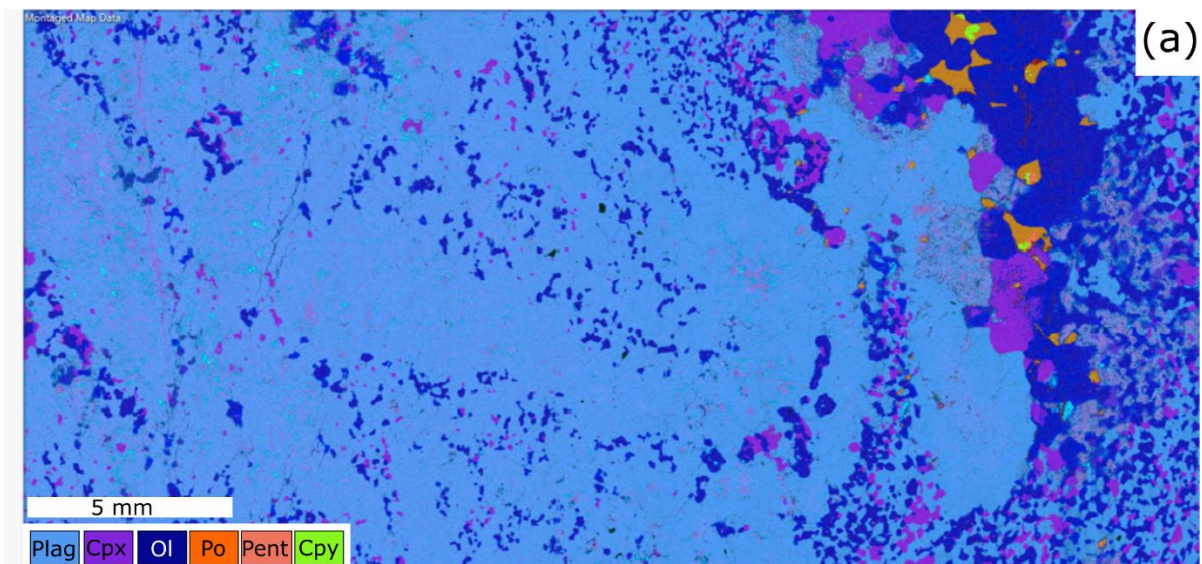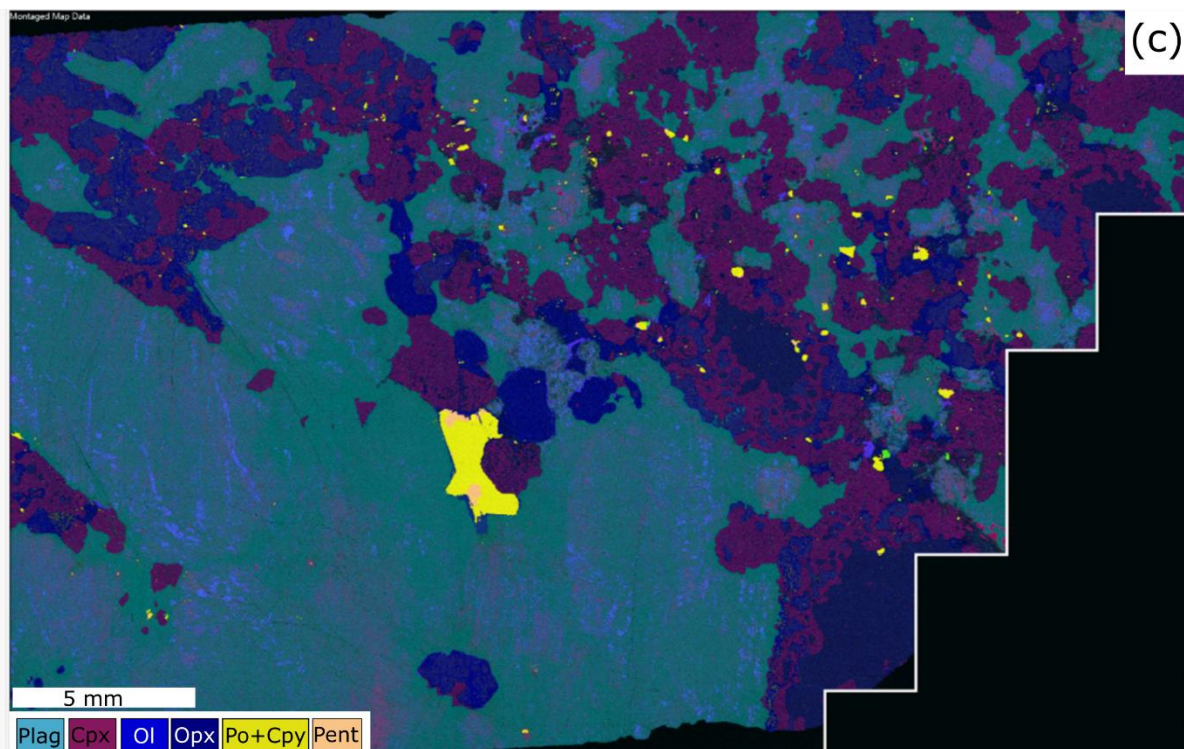
Figure 5.32: Element maps of thin sections showing a variety of FAZ lithologies in the Lower Flatreef. These rocks are strongly contaminated, and distinctive textures can help distinguish them from other lithologies. (a) Olivine gabbro containing locally net textured sulphides (sample 81-1628). (b) Olivine gabbro with abundant sulphides forming large blebs with complex intergrowths at their margins (sample 81-1618). (c) Element map of a whole thin section of olivine gabbronorite. Clinopyroxene forms complicated intergrowths on the outer margins of orthopyroxene with the texture suggesting clinopyroxenite alteration of orthopyroxene (sample 81-1597).
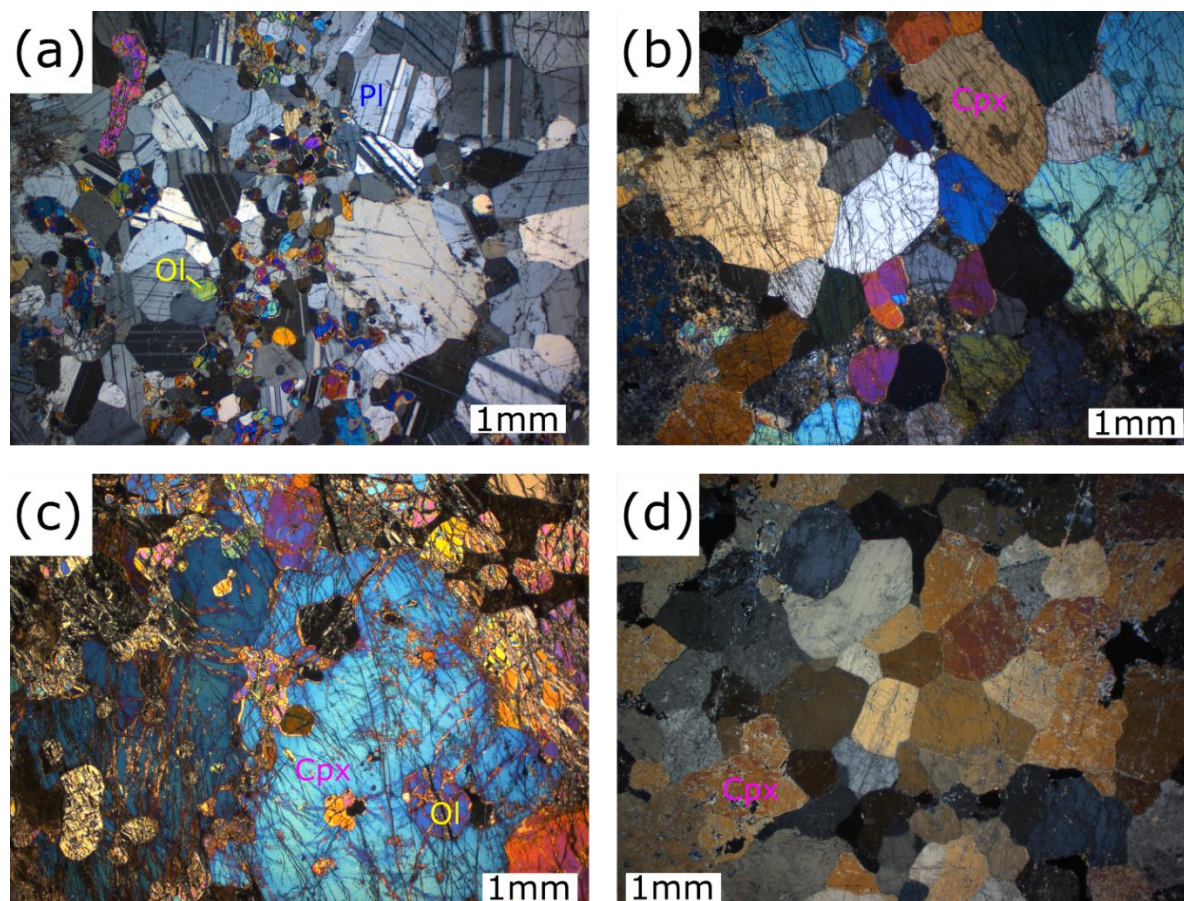
Figure 5.33: Photomicrographs of rocks of the Footwall Assimilated Zone showing the wide variety of lithologies present. (a) Olivine gabbro containing fine grained olivine within larger plagioclase crystals (sample 81-1628). (b) Clinopyroxene showing a variety of grain sizes with triple junctions suggesting recrystallisation (sample 94-1379). (c) Small (< 1 mm) subhedral olivine crystals embedded in large clinopyroxene crystals (sample 94-1391). (d) Clinopyroxenite/Parapyroxenite with low birefringence and a fairly uniform crystal size and triple junctions (sample 81-1654).
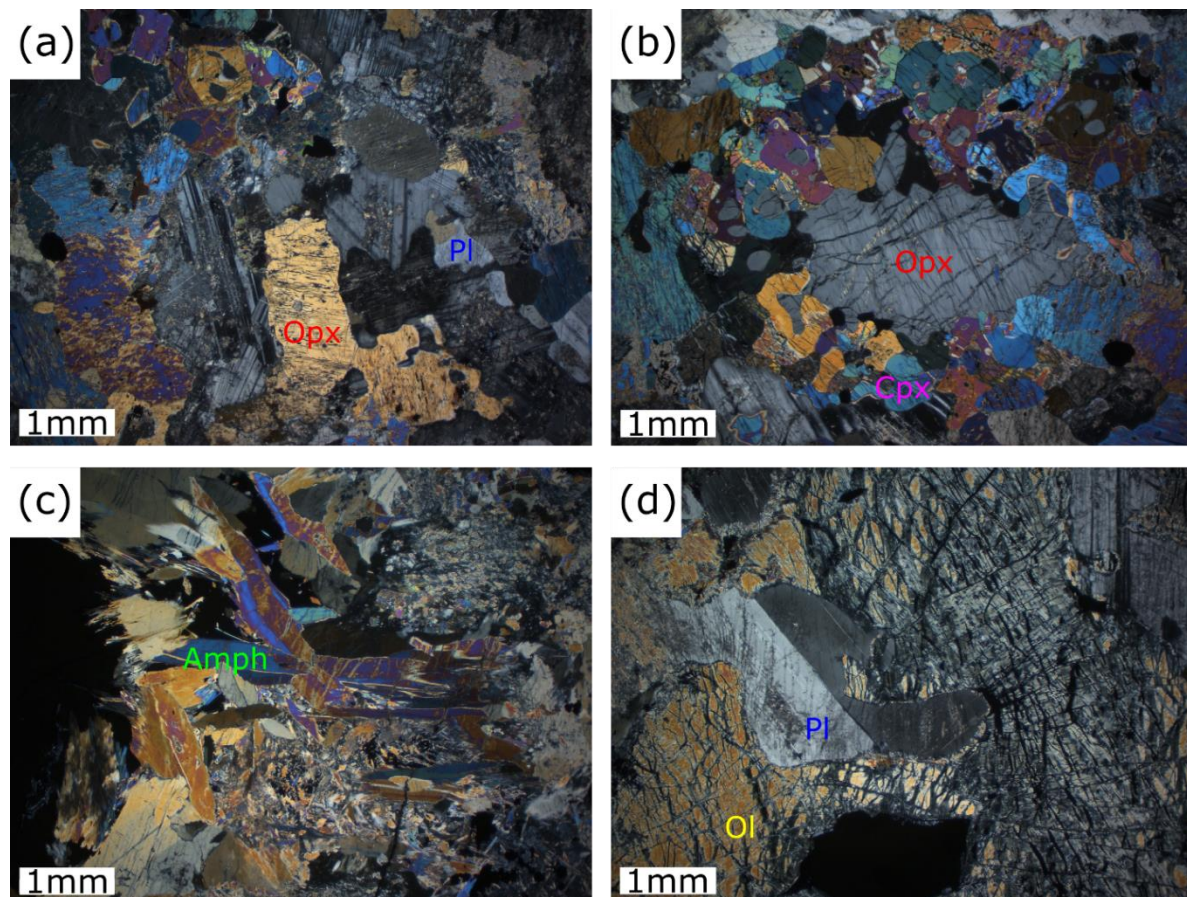
Figure 5.34: Photomicrographs of olivine-gabbronorite lithology within the Footwall Assimilated Zone. (a) Strongly altered olivine-gabbro with disequilibrium textures (sample 81-1597). (b) Complex intergrowths of clinopyroxene crystals surrounding an orthopyroxene crystal surrounded by large plagioclase and pyroxene crystals (sample 81-1597). (c) Alteration of fine-grained amphibole forming distinctive needles with sulphides infilling between amphibole (sample 81-1618). (d) Amoeboidal plagioclase inclusion within a larger olivine (sample 81-1618).

Sulphides tend to be more abundant and oxidized than in less contaminated magmatic units. Sulphides can form large composite grains as seen in samples 81-1618 to 81-1654 (Figure 5.32b). Sulphides are dominated by pyrrhotite, but the proportion of chalcopyrite relative to pentlandite and pyrrhotite is greater than in less contaminated Flatreef rocks. Pentlandite is generally rare and found in the form of small grains or as exsolved flames within pyrrhotite (sample 81-1654; Figure 5.35). Chalcopyrite is generally found on the margins of sulphide blebs or as disseminated grains in the immediate vicinity of larger sulphide blebs (e.g. sample 81-1654). In addition, it can also be found as exsolution in larger sulphide blebs and closely associated with pentlandite (sample 81-1618). Sulphides appear partly reworked along their margins and are intergrown with alteration phases, mainly amphibole. Minor magnetite alteration can be found along the boundaries of some larger sulphide grains. Rarely, subhedral chromite grains are embedded in sulphide blebs (sample 81-1618). Chromite can also be found as subhedral crystals within and along grain boundaries of silicate phases.
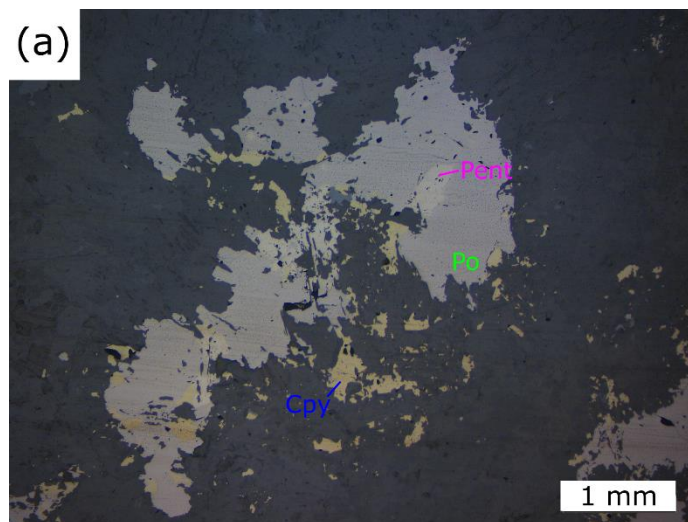
Figure 5.35: Reflected light photomicrograph of sulphides in the FAZ. Sulphides form large irregular grains consisting largely of pyrrhotite as well as minor pentlandite and chalcopyrite. Chalcopyrite tends to be concentrated on the edges of sulphide grains (sample 81-1654).

5.3.2 Wehrlite

The wehrlite is a medium grained rock comprised largely of clinopyroxene (57 modal %) and olivine (32 modal %), whereas plagioclase is not present. In addition, sulphides, magnetite and chromite form a major component of the rock with accessory apatite (Figure 5.36). Olivine and clinopyroxene form subhedral grains with sizes varying between 1-5 mm for olivine and 0.5-2.5 mm for clinopyroxene (Figure 5.37). Olivine commonly forms large anhedral grains that show complex interfingering along grain boundaries with smaller anhedral clinopyroxene crystals. Triple junctions at around 120° suggest recrystallisation. Apatite is present as a small accessory phase (0.4 mm width) found as clusters of several interstitial grains. Clinopyroxene crystal cores are slightly altered to serpentine exploiting mineral cleavage, olivine is unaltered.
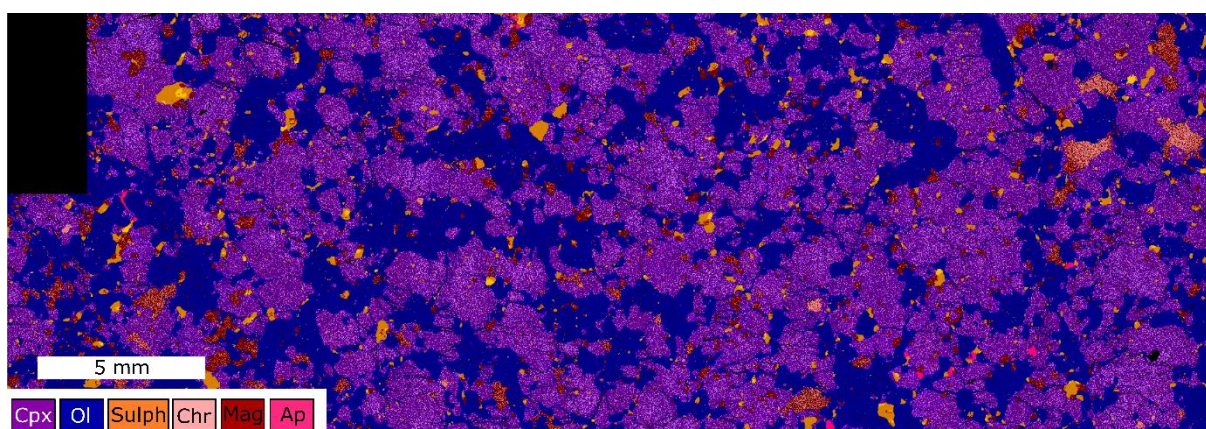
Figure 5.36: Phase map of wehrlite in thin section displaying abundant clinopyroxene and lesser amounts of olivine (sample 81-1702). Also note abundant net textured sulphides, magnetite and chromite.
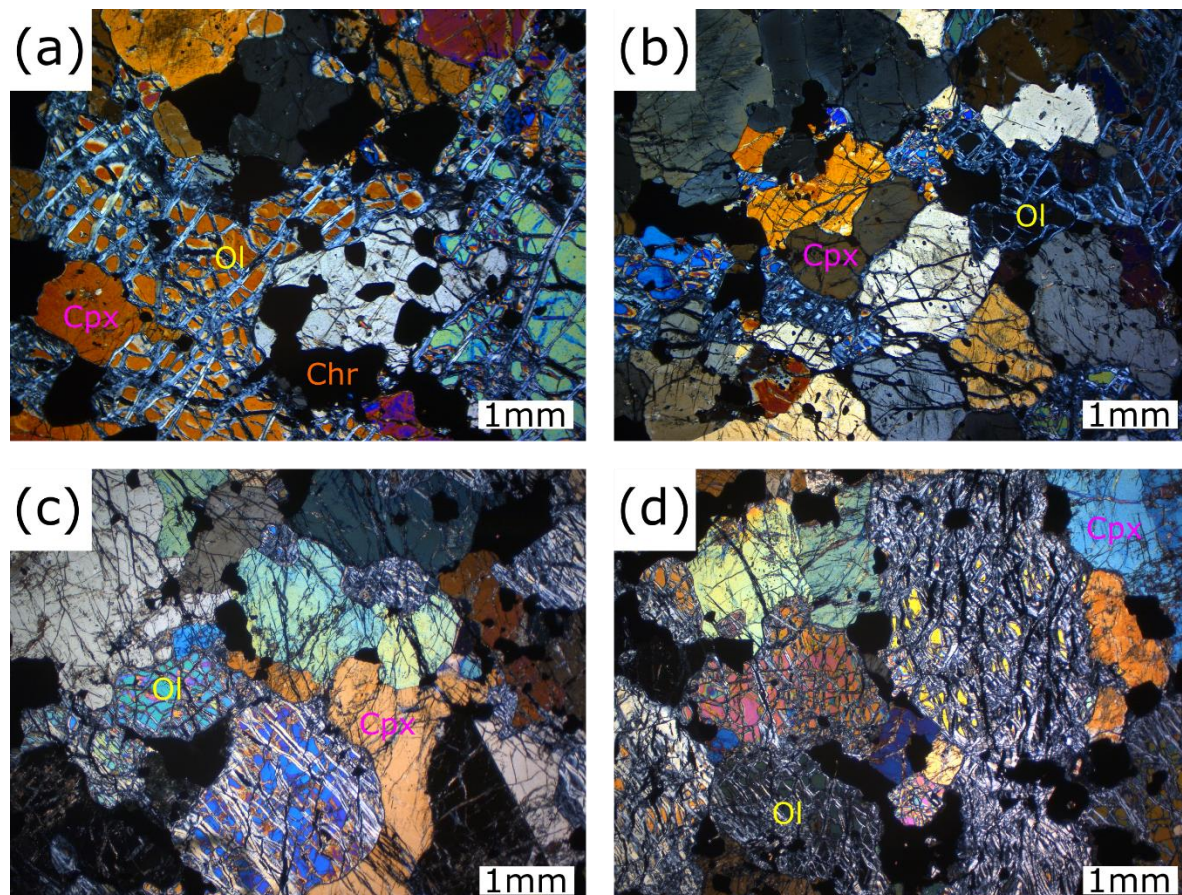
Figure 5.37: Photomicrographs of wehrlite. (a) Amoeboidal olivine with anhedral clinopyroxene and abundant chromite found as inclusions in both phases and on grain boundaries (sample 81-1702). (b) Wehrlite displays many 120° triple junctions suggesting recrystallisation (sample 81-1702). (c) Equigranular olivine and orthopyroxene, both anhedral, with complex interfingering of crystals (sample 94-1402). (d) Olivine partially altered to serpentine and magnetite (sample 94-1402).

The wehrlite rocks can be unusually rich in sulphides, chromite and magnetite (~3 modal % of the latter in sample 81-1702). The majority of the magnetite and chromite is found as subhedral to euhedral crystals in clinopyroxene. Grain sizes range from 0.1 mm where magnetite is included in clinopyroxene, to 0.4 mm where magnetite is located on grain boundaries. Sulphides consist of pyrrhotite, chalcopyrite and pentlandite. Most sulphides are found in intercumulus space and are dominated by pyrrhotite with lesser chalcopyrite and pentlandite (trace and 0.07% by volume respectively). These sulphides form complex amorphous blebs intergrown with silicates. Pyrrhotite may form small inclusions (0.89 modal %) in pyroxene. Many sulphides have been altered along their edges to magnetite.
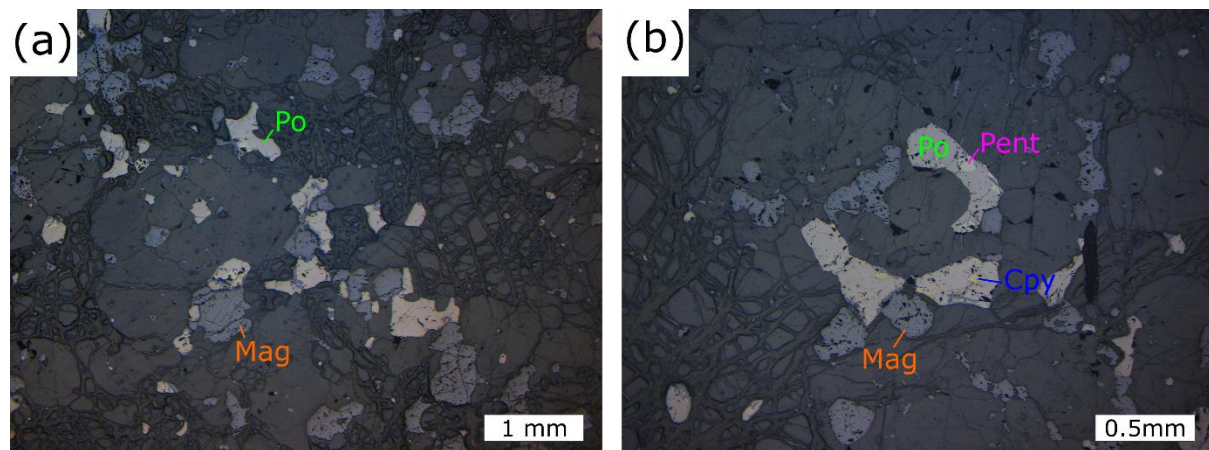
Figure 5.38: Reflected light photomicrographs of sulphides and oxides in wehrlite lithologies. (a) Sulphides are locally net textured and interstitial to sulphides. Magnetite is abundant and anhedral, commonly annealed to nearby grains (sample 81-1702). (b) Sulphides are locally restricted to interstitial patches (sample 81-1702).

5.3.3 Ti-rich Olivine Gabbro

The Ti-rich olivine gabbro consists of olivine, clinopyroxene, orthopyroxene, plagioclase and abundant oxides. Olivine and clinopyroxene appear to form interstitial phases with optical continuity suggesting crystal sizes on the order of several mm, containing rounded plagioclase inclusions 0.1-0.7 mm in size. Olivine and plagioclase are the most abundant phases representing 30% and 60% of the rock respectively in the fine-grained portions of the unit. Clinopyroxene and lesser orthopyroxene form a minor constituent (5-10% pyroxene) unevenly distributed throughout the rock (Figure 5.39). The rocks show a characteristic spotted texture, with spots varying in size from 0.5-2 cm. The spots consist of olivine oikocrysts containing chadacrysts of plagioclase. The whole unit has been strongly recrystallised with 120° triple junction grain boundaries being common (Figure 5.40).

Magnetite and ilmenite are abundant (several modal %) showing a wide range of grain sizes and are found either as inclusions within silicates or along grain boundaries. Larger grains (0.2-0.5 mm width) tend to occur along boundaries, whereas oxide inclusions in silicate phases are significantly smaller (~0.05 mm). Ilmenite is present as both a separate phase and, less commonly, as exsolution lamellae in magnetite. Sulphides are present as trace disseminated grains that are comprised equally of pyrrhotite, chalcopyrite and pentlandite and also contain magnetite-ilmenite.
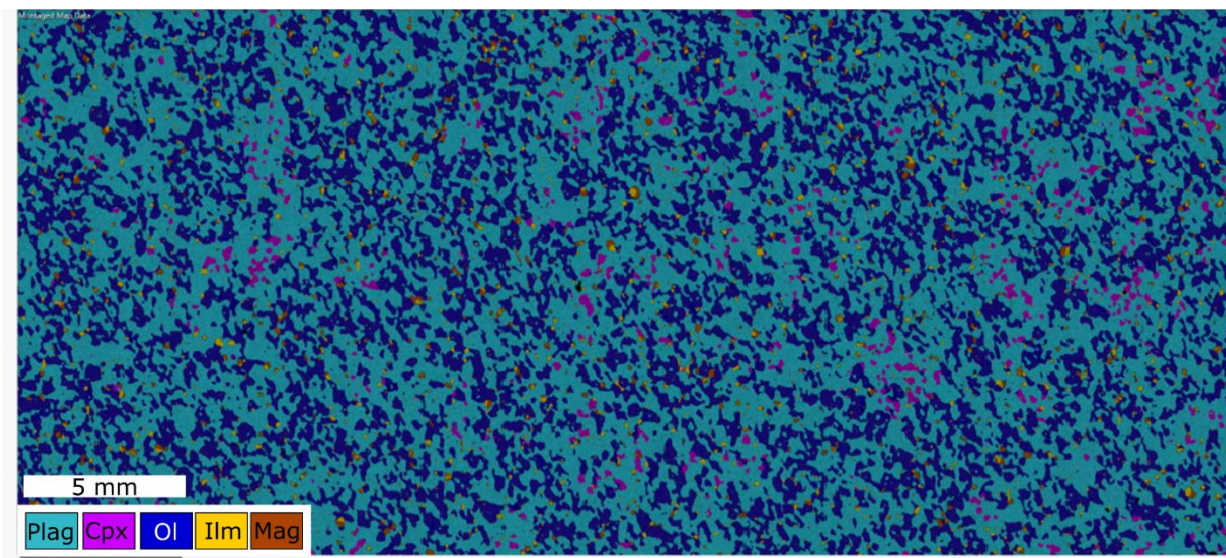
Figure 5.39: Element map of the Ti-rich olivine gabbro of an oikocryst-free thin section showing fine grained pyroxene, olivine and abundant plagioclase (sample 81-1720). Note that clinopyroxene tends to be concentrated in patches where olivine is absent
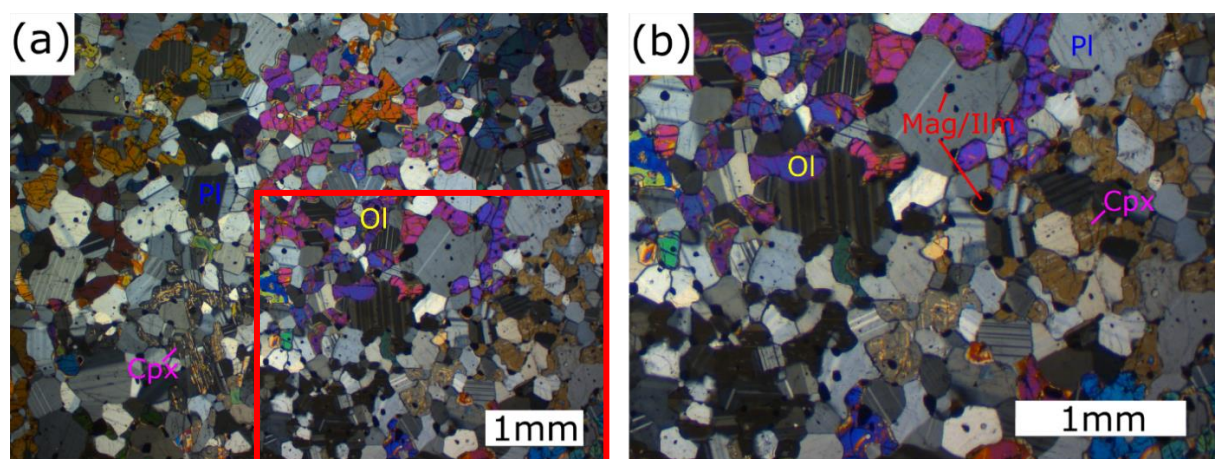
Figure 5.40: Photomicrographs of the Ti-rich olivine gabbro. (a) Large oikocrysts of olivine and clinopyroxene in a matrix of subhedral plagioclase. The rock is strongly recrystallised with most phases displaying 120° triple junction boundaries (sample 81-1720). (b) Enlarged view of (a) (see red box) showing abundant subhedral magnetite and ilmenite found as inclusions in all mineral phases and on grain boundaries (sample 81-1720).

5.3.4 Olivine Mela-Gabbronorite

Olivine mela-gabbronorite forms the lowermost lithological unit exposed in drill core UMT081, but the borehole has been terminated within 1.5 m of its upper contact. Orthopyroxene can form subhedral laths up to 3.5 mm in length and 0.5 mm in width forming 31% of the unit (modal %). There is no evidence of alignment of the orthopyroxene laths (Figure 5.41). Olivine (14 modal % of the rock) forms oikocrysts up to 4 mm in diameter that are commonly surrounded by a 'halo' of small clinopyroxene crystals (15 modal %; Figure 5.42), that are in

optical continuity with each other, suggesting these are part of larger oikocrysts surrounding the olivine oikocrysts (Figure 5.42d). Plagioclase generally forms stubby subhedral laths and occurs as both cumulus and intercumulus crystals (39 modal %). Plagioclase also forms small (0.1-0.4 mm) rounded inclusions within olivine.

Sulphides are present in trace quantities and are comprised either of monomineralic pyrrhotite or composite grains of pyrrhotite and chalcopyrite. The sulphides are generally found along grain boundaries and sometimes associated with subhedral phlogopite. Magnetite is subhedral and larger grains are closely associated with olivine oikocrysts. Smaller magnetite and ilmenite are found within other silicate phases or less commonly along grain boundaries.
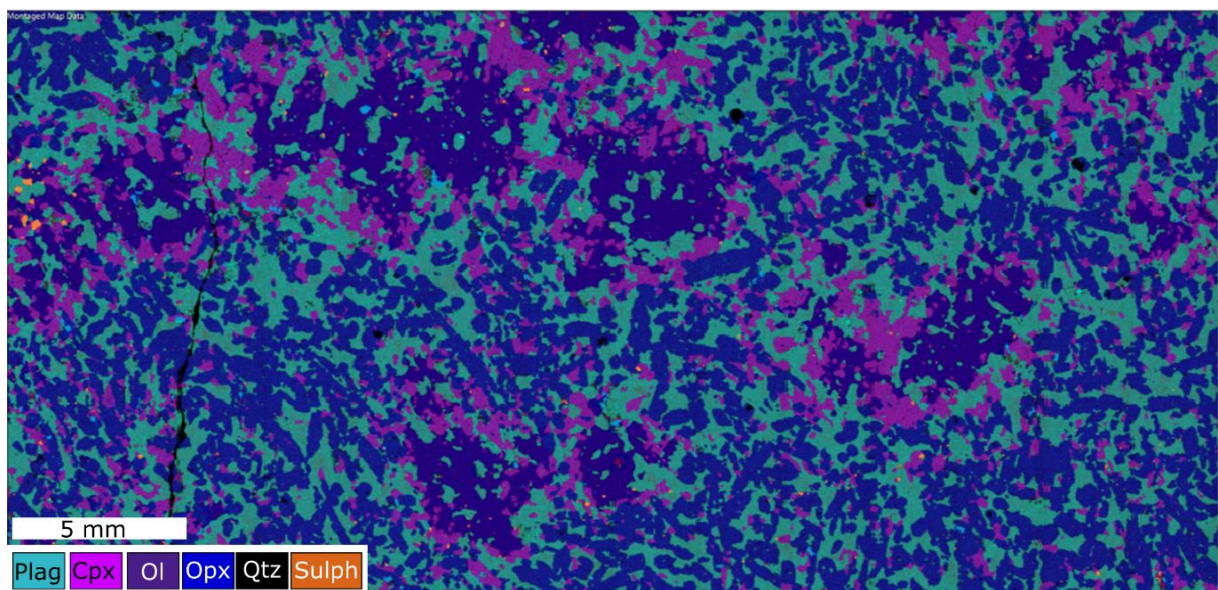
Figure 5.41: Element map of a thin section of olivine mela-gabbronorite (sample 81-1828) showing large oikocrysts of olivine with haloes of clinopyroxene within orthopyroxene and plagioclase.
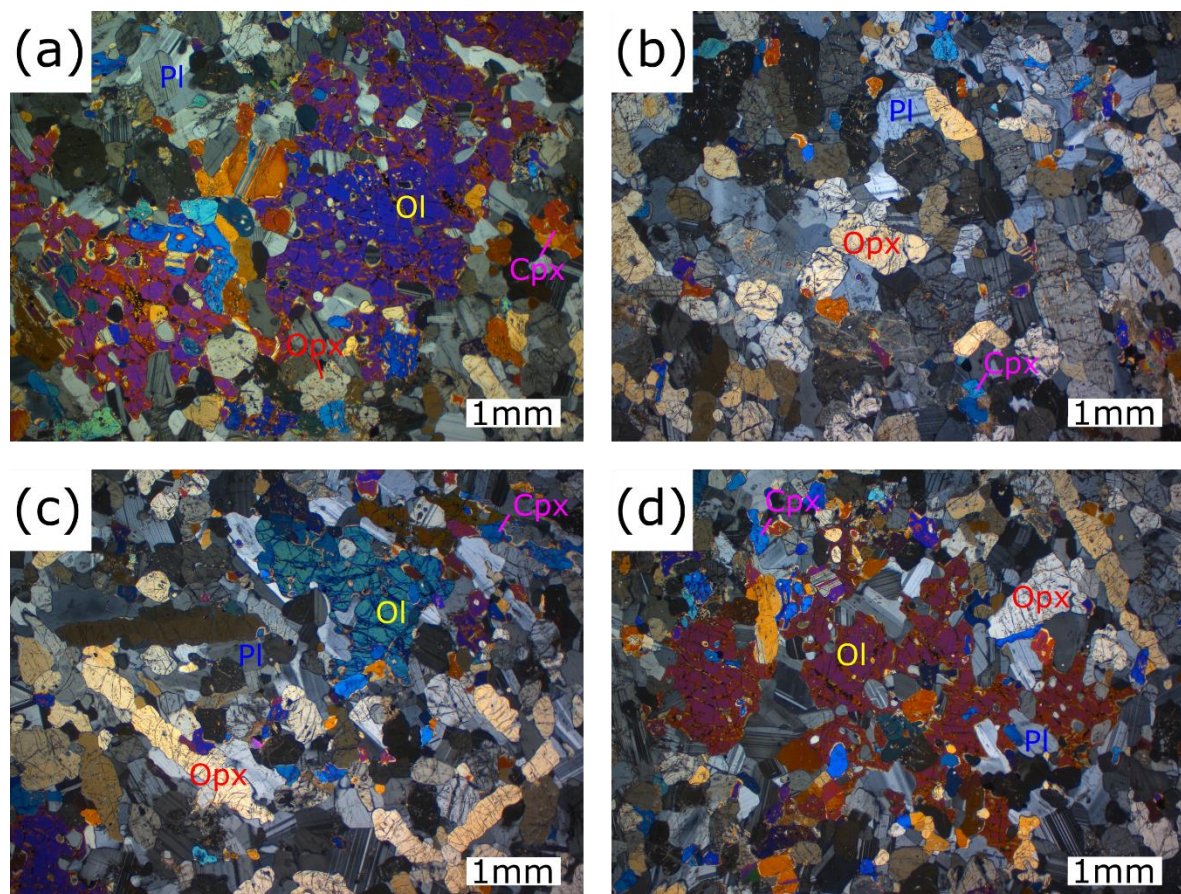
Figure 5.42: Photomicrographs of olivine mela-gabbronorite (sample 81-1828). (a) Large oikocrysts of olivine (≥ 1 cm) contain small chadacrysts of rounded plagioclase and clinopyroxene. Surrounding these large olivine oikocrysts are larger oikocrysts of clinopyroxene (orange) that are in optical continuity. (b) Orthopyroxene show no mineral alignment. (c) Elongate orthopyroxene with interstitial and cumulus plagioclase and anhedral olivine. (d) Large olivine oikocryst surrounded by larger clinopyroxene oikocryst that is in optical continuity (blue).

5.4 Transvaal Supergroup

5.4.1 Contact-Metamorphosed Footwall Rocks

Found at the base of drill core UMT094, the carbonaceous sedimentary footwall rocks have been variably contact-metamorphosed resulting in a wide range of minerals typically found in skarn assemblages including olivine, amphibole, brucite, perovskite, serpentine, versuvianite, monticellite, calcite, dolomite and various spinel (Figure 5.43). Sedimentary packages located within 50 m of the contact to the Bushveld intrusion typically show remnant layering (Figure 5.44). In drill core UMT094 the metamorphosed footwall is easily identified by the presence of sedimentary structures including stromatolites intersected 10-15 m below the magmatic contact. The rocks tend to be very fine grained making identification of minerals difficult. At the upper contact of the sedimentary package large crystals of clinopyroxene may form. With progressive distance from the contact, veins and clots of recrystallised carbonate are present but are volumetrically subordinate to calc-silicates.

At a depth of 50 to 100 m below the contact the rocks are characterised by a marked increase in their carbonate component. As expected, the protolith composition has a strong control on alteration mineral assemblage as epitomised by sample 94-1514 where a lithological change results in a sharp mineralogical change from predominantly brucite-serpentine to mainly carbonate and clay (Figure 5.45). There is also significant increase in magnetite locally, with euhedral magnetite grains (0.1-0.4 mm) constituting up to 20 % of the rock (sample 94-1468).

In the deepest portions of drill core UMT094, over 100 m below the magmatic contact, calcareous sediments have been metamorphosed to marble, showing porphyroblasts of euhedral olivine (0.1-0.5 mm). Locally, large biotite crystals (1-2 mm) are developed containing chadacrysts of olivine and calcite that are not in textural equilibrium with the biotite. Small subhedral spinel grains are also abundant and occur either along calcite crystal boundaries or more commonly within calcite crystals.
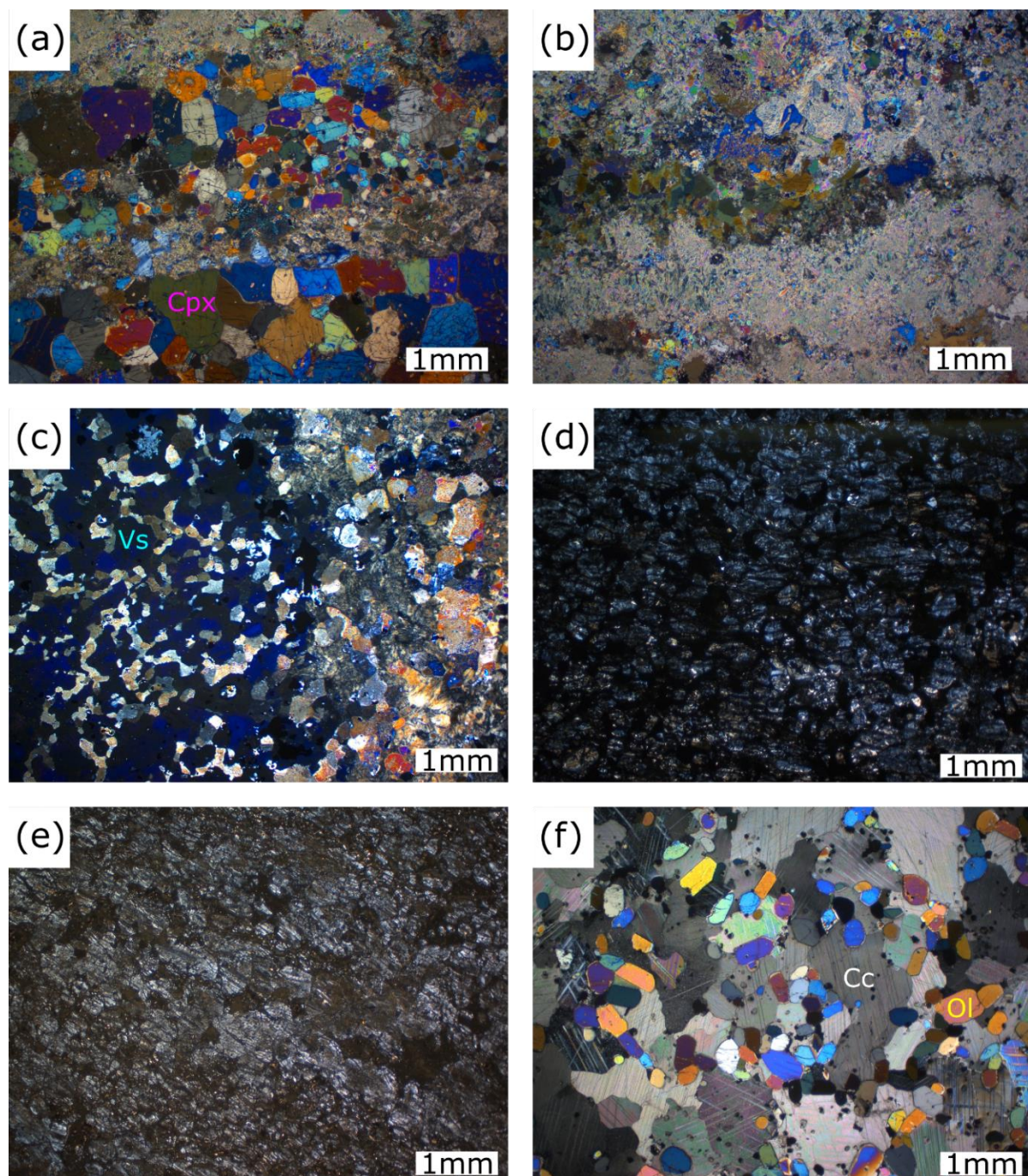
Figure 5.43: Photomicrographs of metamorphosed sedimentary footwall assemblages and calc-silicate xenoliths/rafts. (a) Calc-silicate xenolith with layering preserved forming a variety of alteration minerals including clinopyroxene (sample 81-1668). (b) Variable grain size and abundance of clays and fine-grained sheet silicates define protolith layering in calc-silicate xenolith (sample 81-1668). (c) Versuvianite is found in some calc-silicate xenoliths/rafts identified by its anomalous royal blue interference colour under crossed-polarisers (sample 81-1821). (d) Fine grained footwall rock that has undergone contact metamorphism resulting in brucite and serpentine crystals among clays and small iron oxides, crossed-polarisers (sample 94-1411). (e) Plane polarised image showing fine-grained nature of contact metamorphosed footwall in close proximity (< 15 m) to the overlying magmatic units (sample 94-1414). (f) Marble with euhedral olivine and spinel, 150 m below the magmatic contact (sample 94-1562).
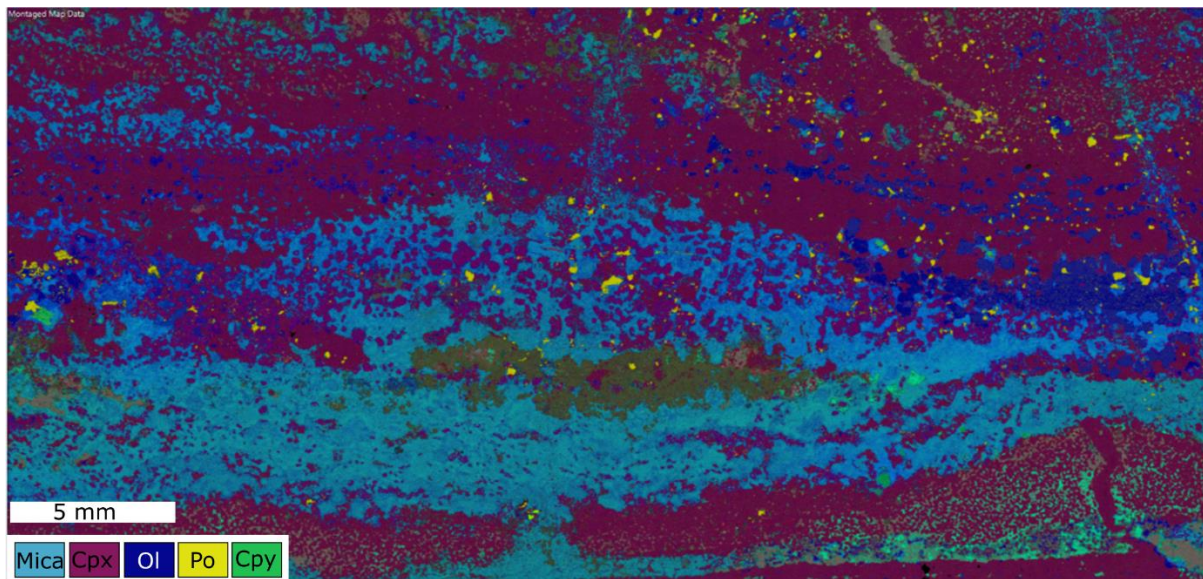
Figure 5.44: Element map of a carbonate xenolith (sample 81-1668) displaying mineralogy and protolithic structures of metamorphosed footwall and calc-silicate xenoliths. Layers of potassium and sodium rich minerals (light blue) are interlayered with calcium rich bands (pink). In places, metamorphic olivine (dark blue) forms within calcium rich domains (pink).
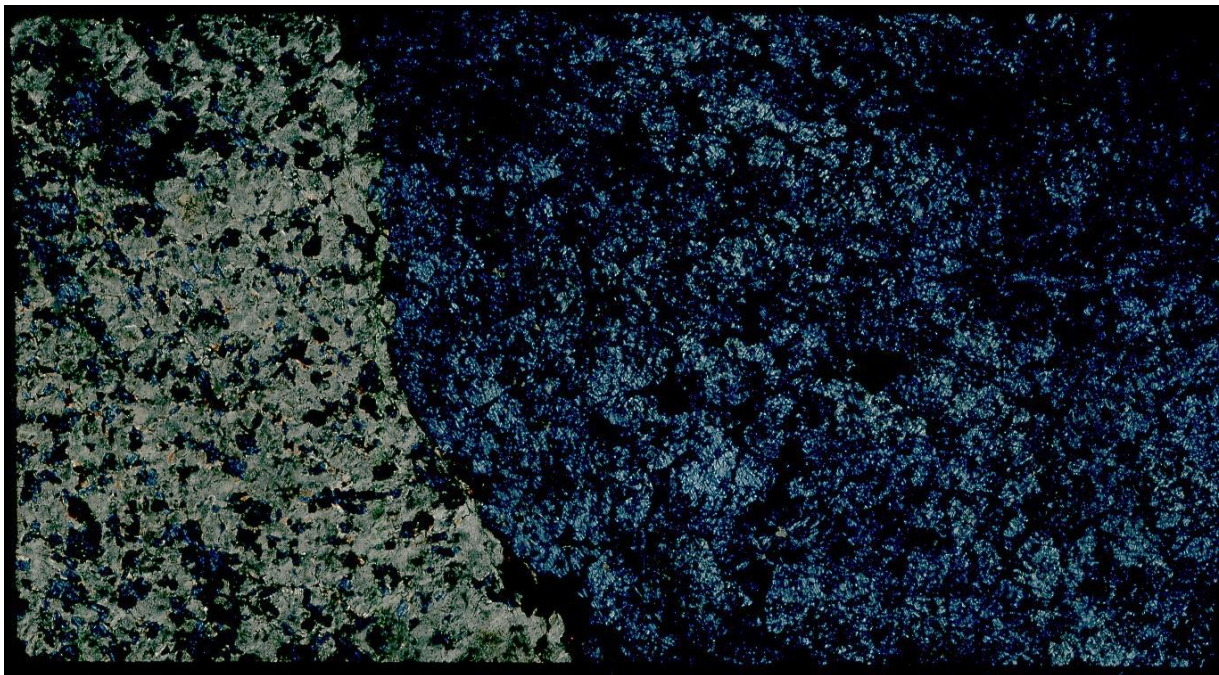
Figure 5.45: Photomicrograph of thin section (sample 94-1454) of lithological boundary between two metamorphosed units in the sedimentary footwall of drill core UMT094. The right hand side of the photomicrograph is dominated by brucite and serpentine whereas the left hand side is characterised by fine grained clay and carbonate minerals with minor oxide and brucite crystals.

5.4.2 Unmetamorphosed Footwall Rocks

Six samples of calcareous sediments from the Malmani and Duitschland Formations (Figure 5.46) collected outside the contact metamorphic aureole of the Bushveld Complex show

textural evidence of low level recrystallisation. The calcareous sediments are comprised mainly of fine-grained anhedral carbonate crystals (Figure 5.46). Fine grained clays and iron-staining of carbonates is restricted to certain strata.

5.4.2.1 Malmani Subgroup

The samples from the Malmani subgroup are dark grey in hand specimen. The rocks are comprised mainly of fine-grained (0.03-0.1 mm) dolomite and calcite grains which can be discoloured by iron-staining and fine clays. In some rocks small subrounded rip-up clasts of semi-consolidated carbonate are found. Quartz-rich strata are also present, particularly in sample Malmani 1 (MAL1) where quartz has replaced a stromatolite-like structure (Figure 5.46e) forming anhedral crystal aggregates with 120° triple junctions.

5.4.2.2 Duitschland Formation

Carbonate samples from the Duitschland Formation are more variable than those of the Malmani Subgroup. Sample Duitschland 1 (DUIT1) is dark grey and finely laminated whereas the remaining 3 (DUIT2, 3, 4) samples are rusty red in colour. DUIT1 comprises finely laminated carbonate grains (0.02-0.05 mm) with varying proportions of detrital quartz, fine-grained oxides and clays (all <0.015 mm) delineating layering. There is no evidence of rip-up structures or clasts that may indicate high energy events. Samples DUIT2 and DUIT3 are remarkably similar, comprised largely of carbonate grains (0.02-0.1 mm), trace detrital quartz grains and fine grained quartz aggregates (0.5 mm, 1% mod.). Staurolites are locally abundant (Figure 5.46b). DUIT4 contains abundant small spherical structures in a matrix of carbonates (0.05-0.1 mm). The spheres are 0.2-0.6 mm in size and vary in cross-section morphology from circular to oblate, reminiscent of ooids and largely comprised of fine grained oxides and quartz (Figure 5.44d). The 'walls' of the spheres are strongly iron stained, giving the rock its red-brown colour. REE-rich carbonates have also been identified in the walls.
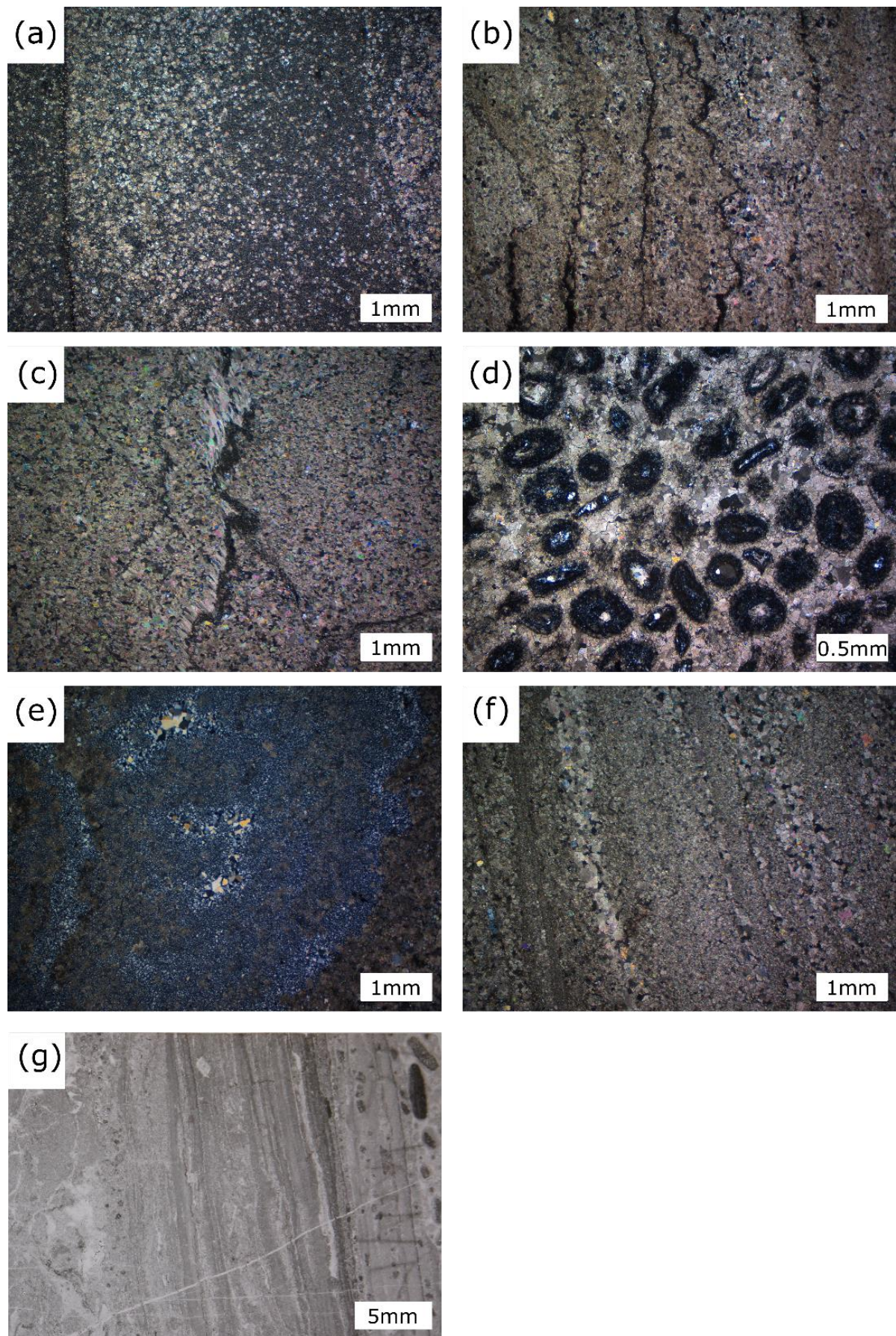
Figure 5.46: Photomicrographs of calcareous sediments from the Malmani Subgroup and Duitschland Formation. (a) Graded bedding of fine grained carbonate with variable proportions of detrital material,

crossed-polarisers (sample DUIT1). (b) Carbonate rich rock with abundant staurolites, crossed-polarisers (sample DUIT2). (c) Fine grained carbonates locally deformed around staurolite, crossed-polarisers (sample DUIT3). (d) Ellipsoid structures filled with quartz and carbonates set within a fine-grained carbonate matrix in sample DUIT4, crossed-polarisers. (e) Fine-grained carbonates with locally abundant quartz grains, showing some evidence of recrystallisation, crossed-polarisers (sample MAL1). (f) Fine-grained carbonates forming distinctive layering largely controlled by grain size, crossed-polarisers (sample MAL2). (g) Fine-grained layering overlain by sub-rounded carbonate clasts that are variably iron stained, plane-polarisers (sample MAL2).

Chapter 6 - Mineral Compositions of the lower Main Zone and Flatreef

The following chapter documents the mineral compositions of the main silicate minerals of the analysed igneous rocks of the Flatreef and lowermost rocks of the Main Zone, namely plagioclase, pyroxene and olivine. These data are essential to constrain processes including fractional crystallisation, magma mixing and contamination. In addition, the data can assist in determining potential correlations with the Platreef and the UCZ in the remainder of the Bushveld Complex.

6.1 Main Zone

Cumulus plagioclase in Main Zone norite has an average composition of An67 and a maximum of An72 in drill core UMT081 (sample 81-1238) plotting in the labradorite and bytownite compositional fields. The orthoclase component is variable between 1-5 molar %. Plagioclase from MZ norite in UMT094 is more anorthite rich with a maximum An content reaching 76 (Figure 6.1). Plagioclase in UMT094 is also more Al_2O_3 rich and SiO_2 poor with greater variability in K_2O and Fe_2O_3 contents.

Orthopyroxene is cumulus in the MZ and has compositions of clino-enstatite and pigeonite, with no difference between analyses from UMT081 and UMT094, and a narrow range of Mg# (71-73 Mg#, Figure 6.2). Orthopyroxene in UMT081 can have up to 5 wt.% CaO, likely representing exsolved clinopyroxene lamellae in the analysed spot. In contrast, interstitial clinopyroxene analyses have a greater compositional range, with Mg# varying between 73-81. Clinopyroxene in UMT094 is marginally more magnesian than clinopyroxene in UMT081 (Figure 6.2). Clinopyroxenes are mainly augitic in composition, with few grains with diopside composition and a single analysis of Ca-poor clinopyroxene that may result from inclusion of orthopyroxene lamellae in the analysed spot (UMT081).
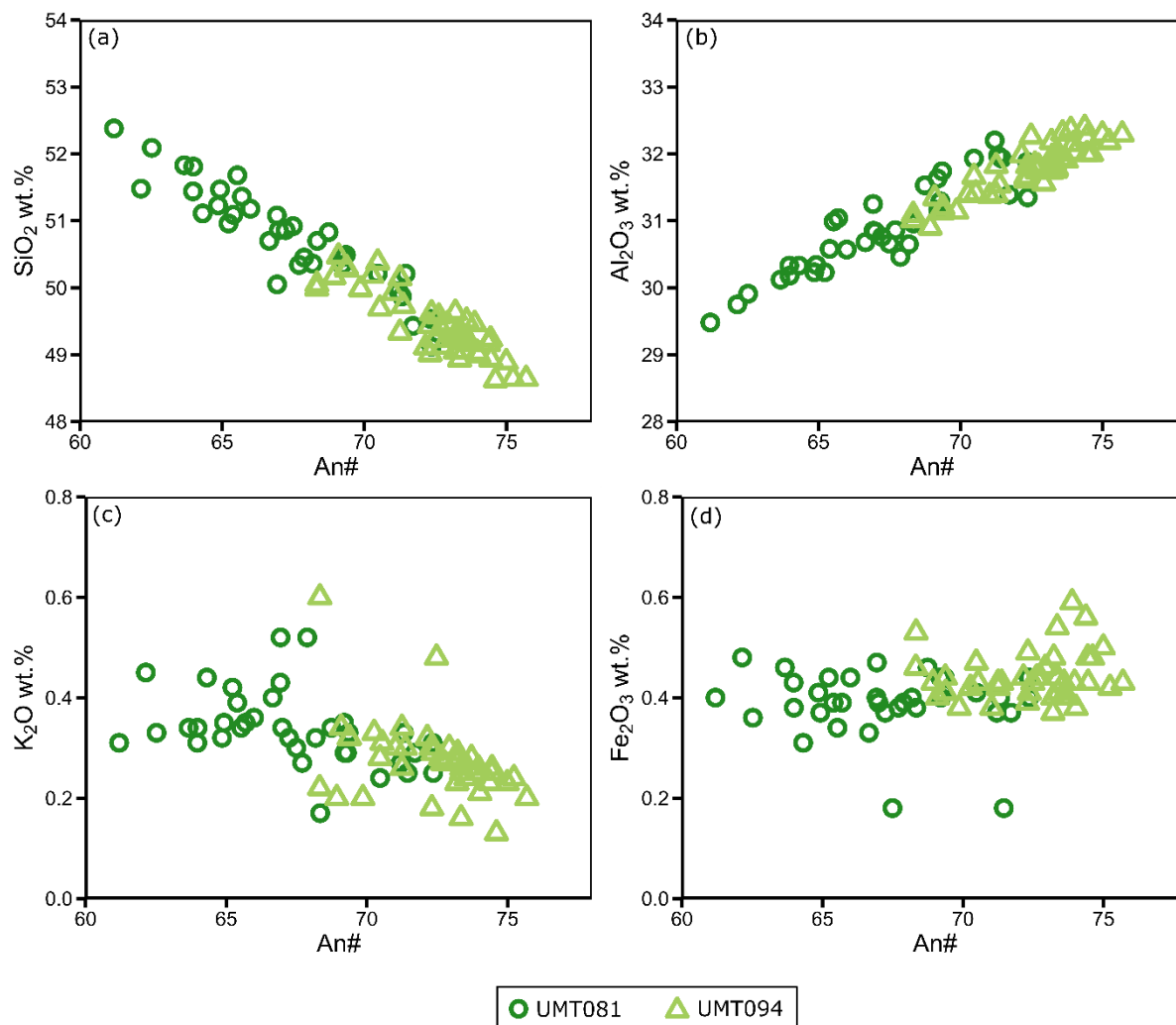
Figure 6.1: Binary variation plots against An content of Main Zone Plagioclase. (a) SiO_2, (b) Al_2O_3, (c) K_2O, (d) Fe_2O_3. Plagioclase in drill core UMT094 is more anorthite rich than in UMT081.
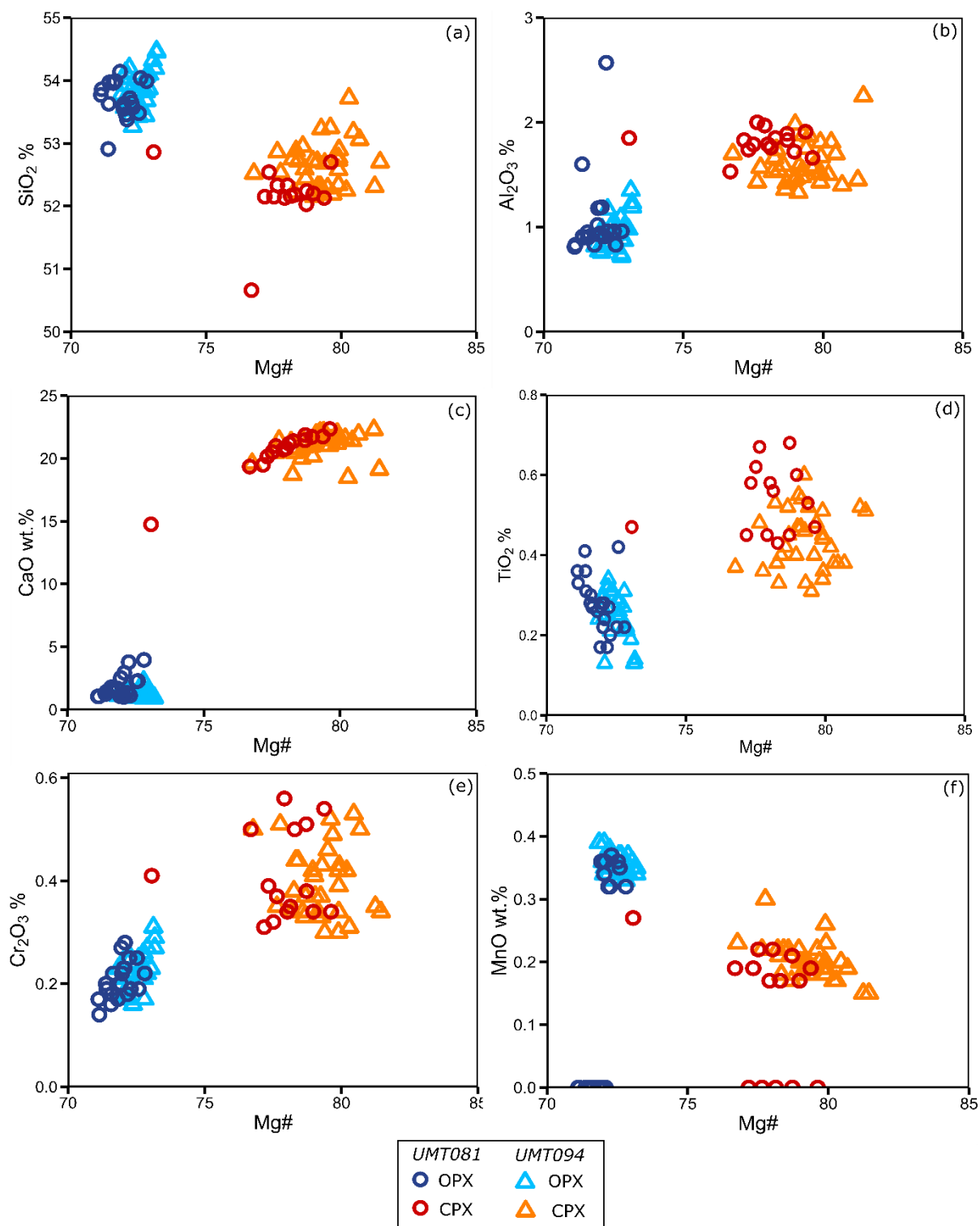
Figure 6.2: Binary variation diagrams against Mg# for pyroxenes from Main Zone norite. (a) SiO₂, (b) Al₂O₃, (c) CaO, (d) TiO₂, (e) Cr₂O₃, (f) MnO. Note that pyroxene compositions in the two drill cores broadly overlap.

6.2 Upper Flatreef

6.2.1 Upper Mottled Anorthosite

Plagioclase in the UMA is cumulus and dominantly of bytownitic composition, with some labradorite grains. Plagioclase displays moderate variability between the two drill cores, with UMT081 having more anorthite rich plagioclase (avg. An73) than UMT094 (avg. An69; Figure 6.3), the opposite of what is observed in the overlying Main Zone. Plagioclase in UMT094 shows greater variability in composition, with more variable K_2O, Al_2O_3 and Fe_2O_3 compositions.
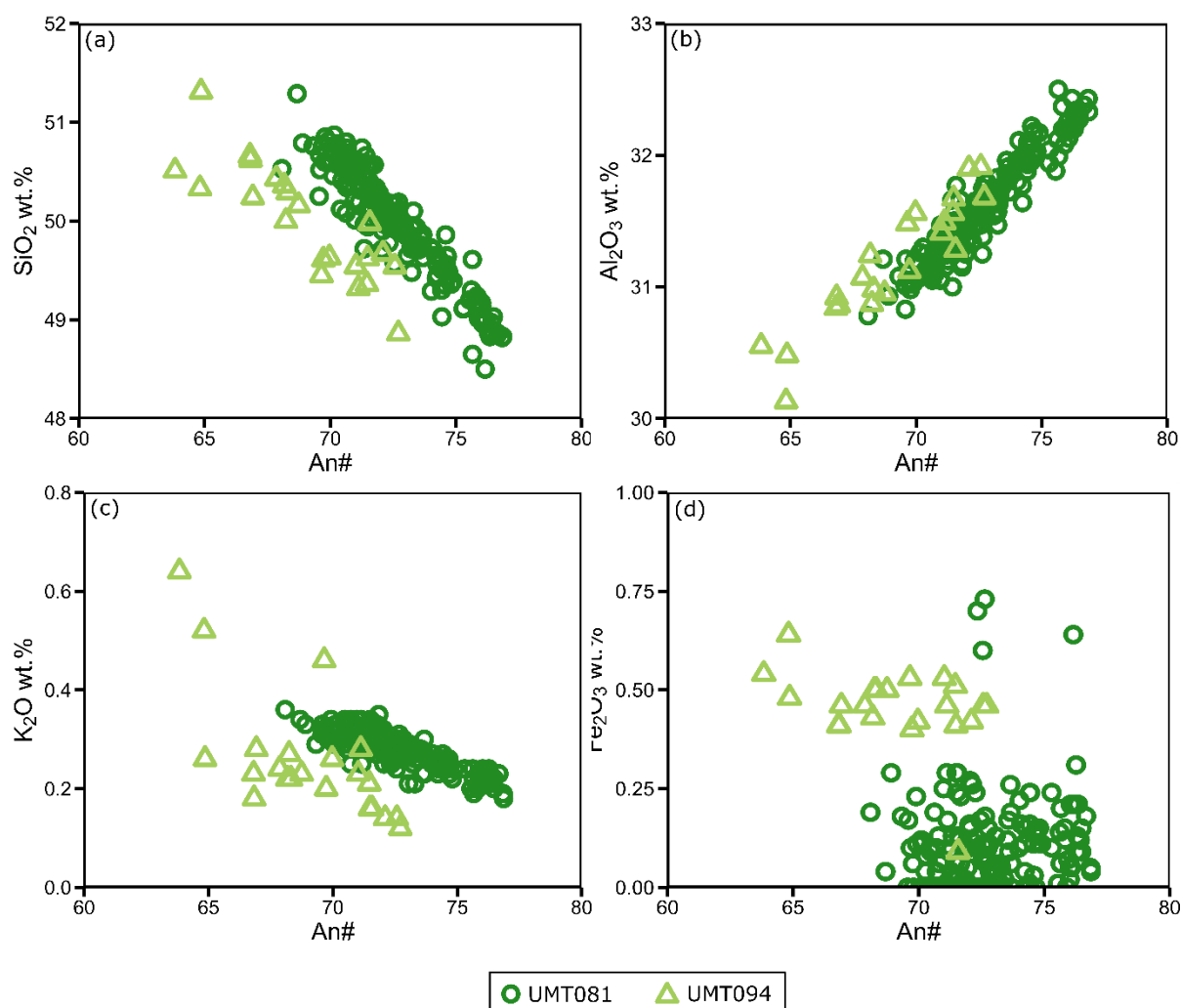
Figure 6.3: Binary variation plots against An content of plagioclase from the UMA. (a) SiO_2, (b) Al_2O_3, (c) K_2O, (d) Fe_2O_3. Note Plagioclase in UMT081 is more Ca-rich compared to UMT094.

There is more significant compositional variability in orthopyroxene between the two drill cores, which is interstitial in the UMA (Figure 6.4). Orthopyroxene in UMT081 is relatively more magnesian with a narrow range in Mg# (70.5-71.4) compared to orthopyroxene in UMT094 (67-69 Mg#). Orthopyroxene in UMT081 is also relatively more SiO_2 and Cr_2O_3 rich. Clinopyroxene compositions in both drill cores vary from diopside to augite. While the

compositional fields of clinopyroxene from both drill cores overlap, clinopyroxene analyses from drill core UMT094 show a markedly wider range of compositions, with Mg# varying from 69-79 compared to 76-80 in drill core UMT081.
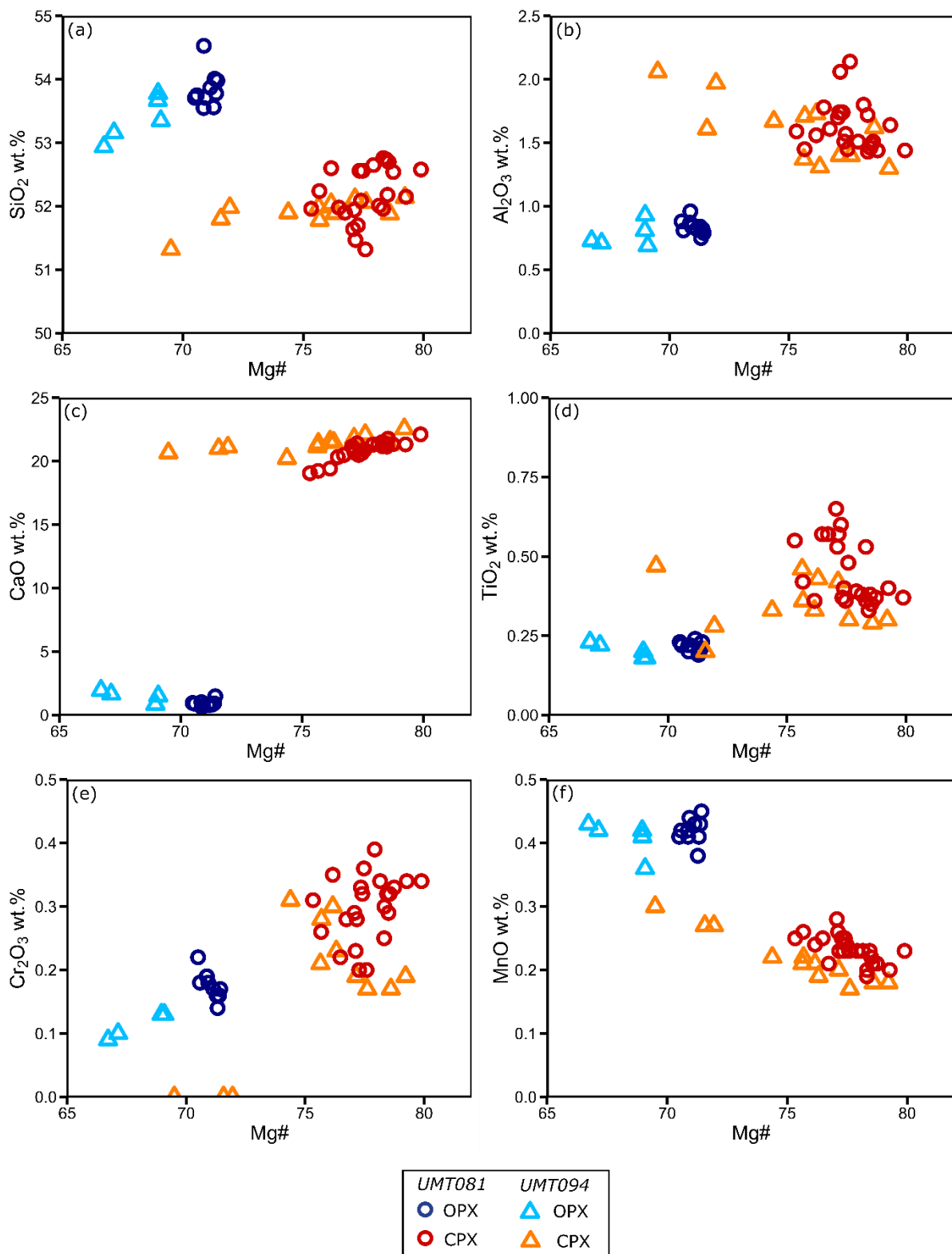
Figure 6.4: Binary variation plots against Mg# for the pyroxenes of the UMA. (a) SiO$_2$, (b) Al$_2$O$_3$, (c) CaO, (d) TiO$_2$, (e) Cr$_2$O$_3$, (f) MnO. Clinopyroxene from drill core UMT094 has a wider range of compositions compared to clinopyroxene from drill core UMT081.

6.2.2 Upper Pyroxenite

Interstitial plagioclase in the Upper Pyroxenite Unit has similar compositional ranges in drill cores UMT094 (avg. An64) and UMT081 (avg. An62). The grains are mainly comprised of labradorite with lesser bytownite (Figure 6.5). Plagioclase in clinopyroxenite is more Ca-rich (avg. An76) with bytownite compositions whereas plagioclase associated with the Main PGE Reef is more sodic (avg. An54), almost being of andesine composition. In contrast, plagioclase in the Upper PGE Reef is more calcic (An59-70). The composition of plagioclase in pegmatoidal pyroxenite overlaps with finer-grained pyroxenites.
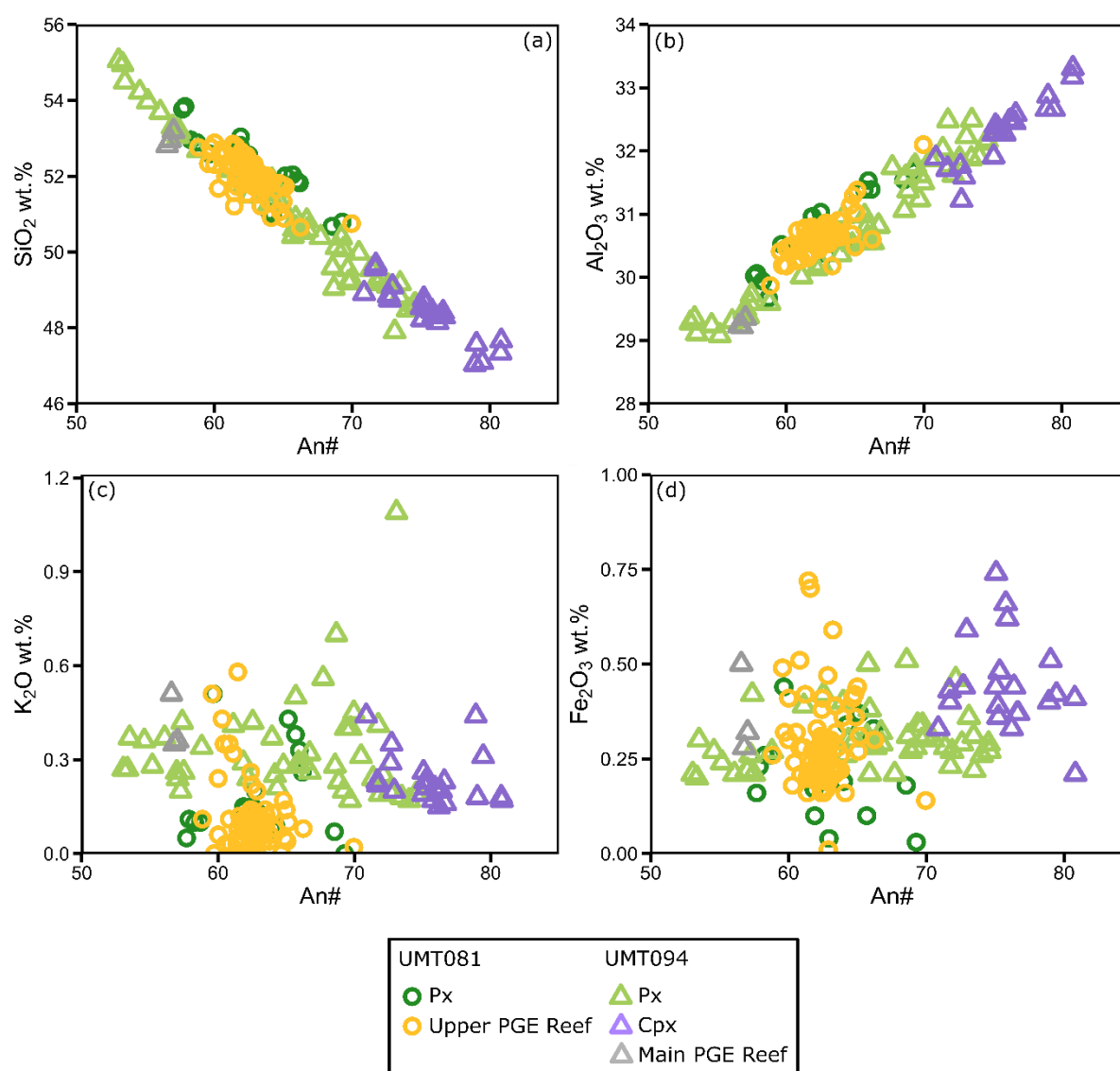
Figure 6.5: Binary variation diagrams of plagioclase compositions from the Upper Pyroxenite Unit including the Main PGE Reef. (a) SiO$_2$, (b) Al$_2$O$_3$, (c) K$_2$O, (d) Fe$_2$O$_3$.

There is no systematic difference in cumulus orthopyroxene composition of the Upper Pyroxenite from drill cores UMT081 and UMT094. Orthopyroxene is mainly clino-enstatite in composition, with some pigeonite present, that fall in a narrow range (79-86 Mg#).

Orthopyroxene compositions for the Main PGE Reef overlap with those from other orthopyroxenites (Figure 6.6; Figure 6.13) although the orthopyroxenes for both reefs plot in a narrow range of Mg# compared to the wider range of orthopyroxene compositions from the Upper Pyroxenite. Drill core UMT094 also contains a clinopyroxenite layer found beneath the olivine-bearing pyroxenite that hosts the Main PGE Reef. The composition of clinopyroxene in this clinopyroxenite layer is similar to that seen in other pyroxenite lithologies (Figure 6.6), but with a greater range in composition. Orthopyroxene compositions of reef samples in UMT081 show broad overlap with an average Mg# of 84 (Figure 6.7). The Main PGE Reef in drill core UMT094 has a distinctly different population of orthopyroxene with an average Mg# of 82. There is no overlap in compositions between the Main PGE Reef in drill cores UMT081 and UMT094. Orthopyroxene in the Upper PGE Reef has a narrow range (79-81 Mg#) and is less magnesian than the Main PGE Reef.

Olivine is only present in the olivine-bearing pyroxenite units associated with the Main PGE Reef. Olivine in drill cores UMT081 and UMT094 show subtle variation. In drill core UMT081 olivine has an average value of Fo content of 82, whereas the same layer in UMT094 has an average olivine composition of Fo 81.
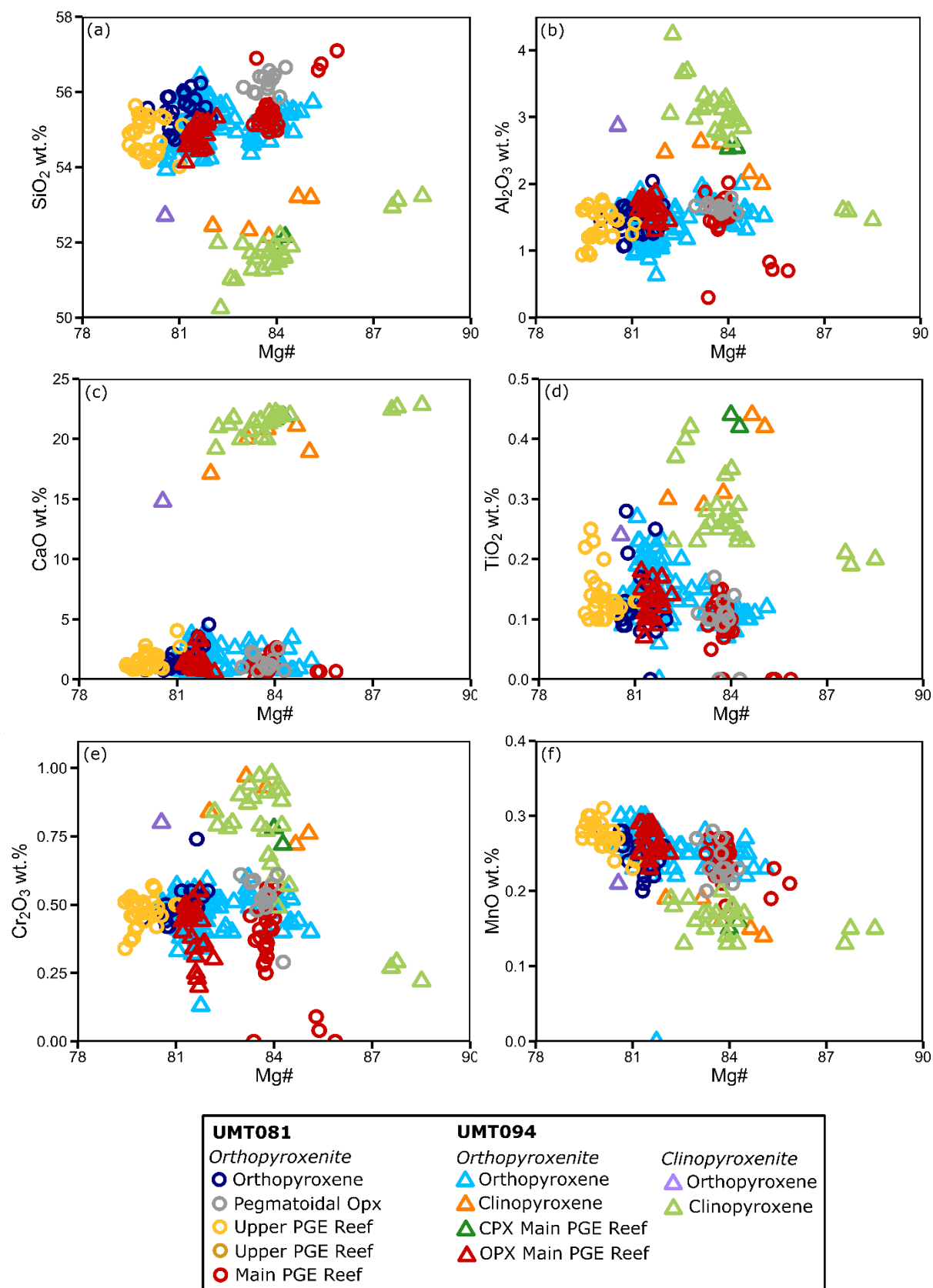
Figure 6.6: Binary variation plots of pyroxene compositions against Mg# from the Upper Pyroxenite Unit. (a) SiO_2, (b) Al_2O_3, (c) CaO, (d) TiO_2, (e) Cr_2O_3, (f) MnO. Note the pyroxene compositions of the Main PGE Reef broadly overlaps with pyroxenite compositions from the rest of the Upper Pyroxenite Unit.
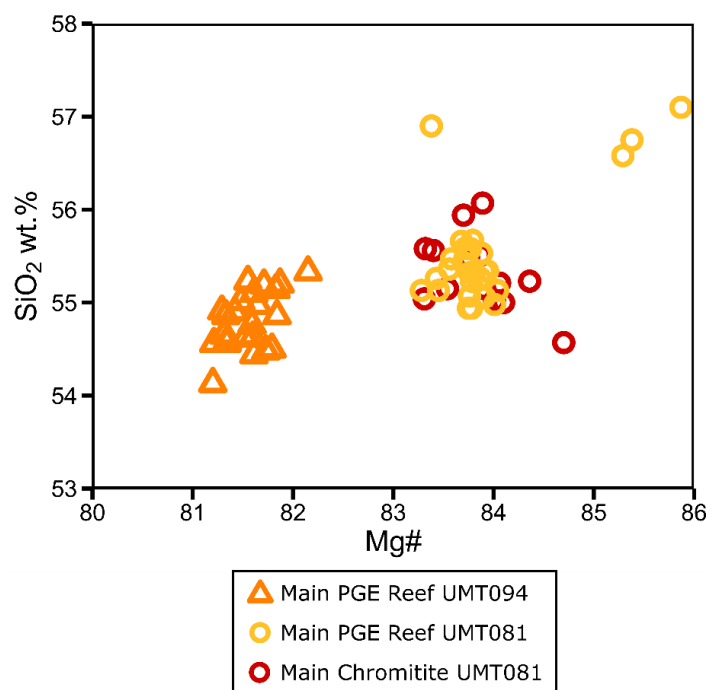
Figure 6.7: Graph of orthopyroxene analyses of the economic reefs. The Main PGE and Main Chromitite in UMT081 have very similar orthopyroxene compositions whilst the Main PGE Reef in UMt094 is less magnesian.

6.2.3 Central Norite

6.2.2.1 Norite

Cumulus plagioclase compositions show some variability between drill cores UMT094 and UMT081. UMT094 norite contains plagioclase of bytownitic compositions whereas UMT081 norites contain plagioclase with labradorite-bytownite compositions, with average An content of 74 and 69, respectively (Figure 6.8).

Orthopyroxene and clinopyroxene also show distinctly less evolved compositions in the Central Norite Unit of UMT094 compared to UMT081 (Figure 6.9). Thus, in drill core UMT081, orthopyroxene comprises clino-enstatite and pigeonite, with an average Mg# of 71, whereas in drill core UMT094 the average Mg# is 80. The range of Mg# of orthopyroxene in both drill cores is relatively small (68-74 Mg# in UMT081, 79-82 Mg# in UMT094). In addition, orthopyroxene in drill core UMT094 is marginally richer in Al_2O_3, SiO_2 and Cr_2O_3 and poorer in TiO_2 and MnO in comparison to orthopyroxene in drill core UMT081. Clinopyroxene in UMT081 has an average Mg# of 77 compared to Mg# 85 in UMT094. Clinopyroxene in UMT094 also has higher Cr_2O_3 and Al_2O_3 contents but lower SiO_2 contents than clinopyroxene in UMT081.
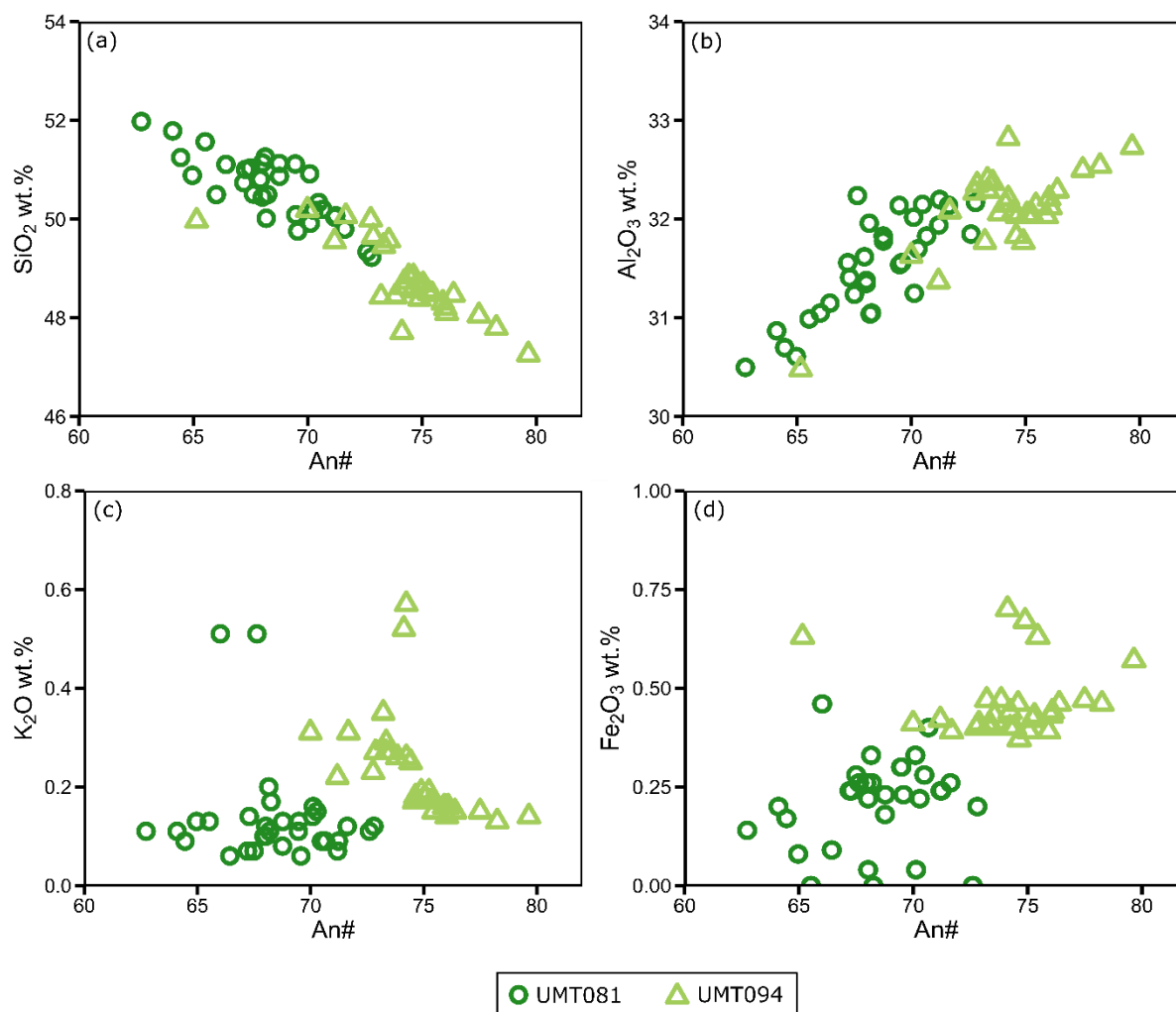
Figure 6.8: Binary variation plots against An content of Plagioclase from norite rocks of the Central Norite Unit. (a) SiO_2, (b) Al_2O_3, (c) K_2O, (d) Fe_2O_3. Plagioclase in UMT081 is distinctly more sodic relative to UMT094.
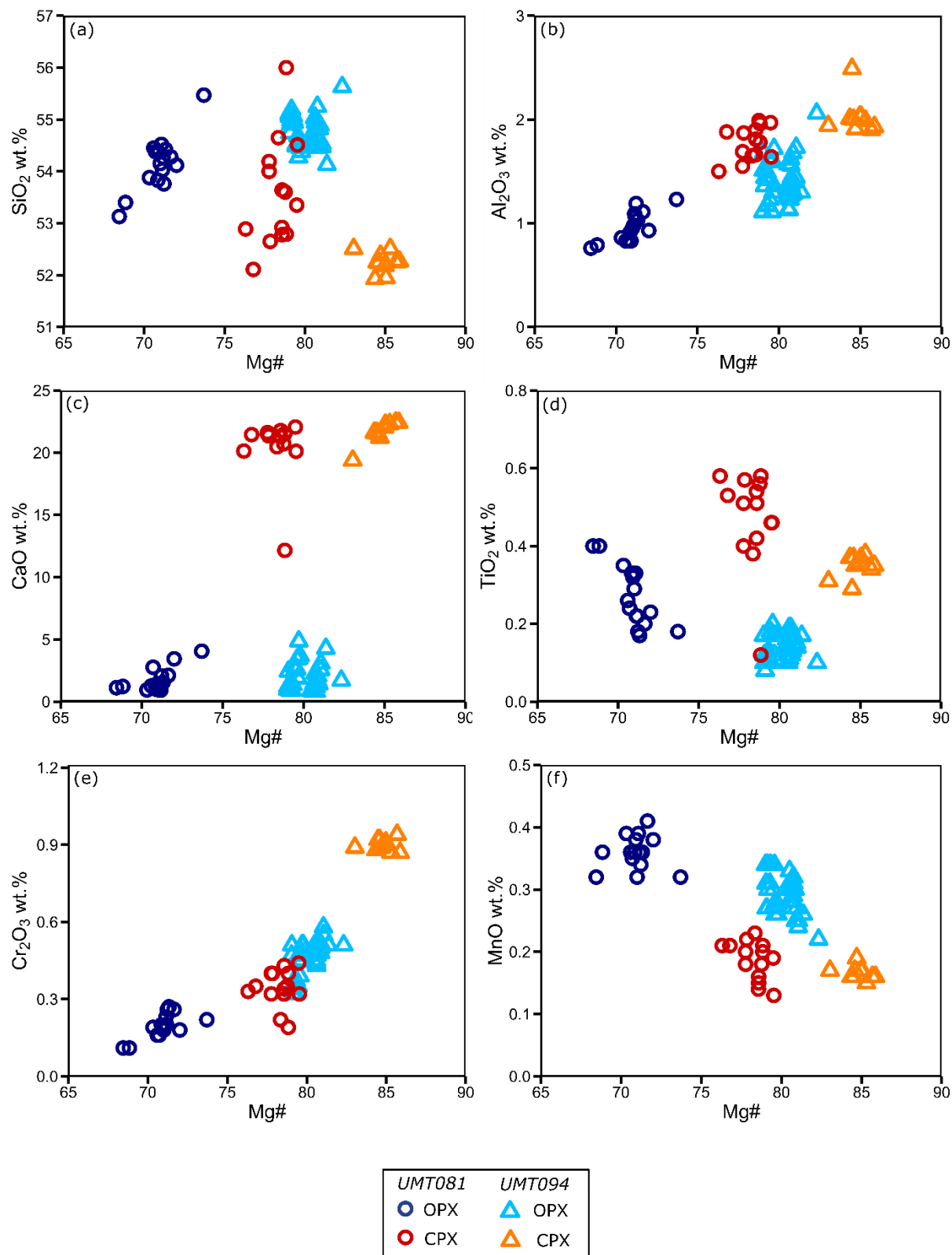
Figure 6.9: Binary variation plots against Mg# for pyroxenes in norite rocks of the Central Norite Unit. (a) SiO_2, (b) Al_2O_3, (c) CaO, (d) TiO_2, (e) Cr_2O_3, (f) MnO. Both clinopyroxene and orthopyroxene are more magnesian than pyroxenes in UMT081.

6.2.2.2 Anorthosite

Cumulus plagioclase in anorthite of the Central Norite is of bytownitic composition (avg. An76) in drill core UMT094 and labradoritic composition in UMT081 (avg. An68). Plagioclase in UMT094 has higher Al_2O_3 and lower SiO_2 content consistent with their higher An content (Figure 6.10). The intercumulus pyroxene compositions of the mottled anorthosite are less variable between drill cores UMT081 and UMT094 (Figure 6.8). Orthopyroxene is generally of clino-enstatite and pigeonite composition, but slightly more magnesian orthopyroxene is found in drill core UMT094 (avg. 78 Mg#) compared to UMT081 (avg. 73 Mg#). Orthopyroxene in drill core UMT094 is also slightly richer in Cr_2O_3 compared to UMT081 (Figure 6.11). Clinopyroxene comprises augite and diopside with significant disparity in composition between drill cores UMT081 and UMT094 (avg. Mg# 71 and 82, respectively). Clinopyroxene in UMT094 has a significantly higher calcium content (21.7 wt. % CaO) than that in UMT081 (12.3 wt. % CaO).
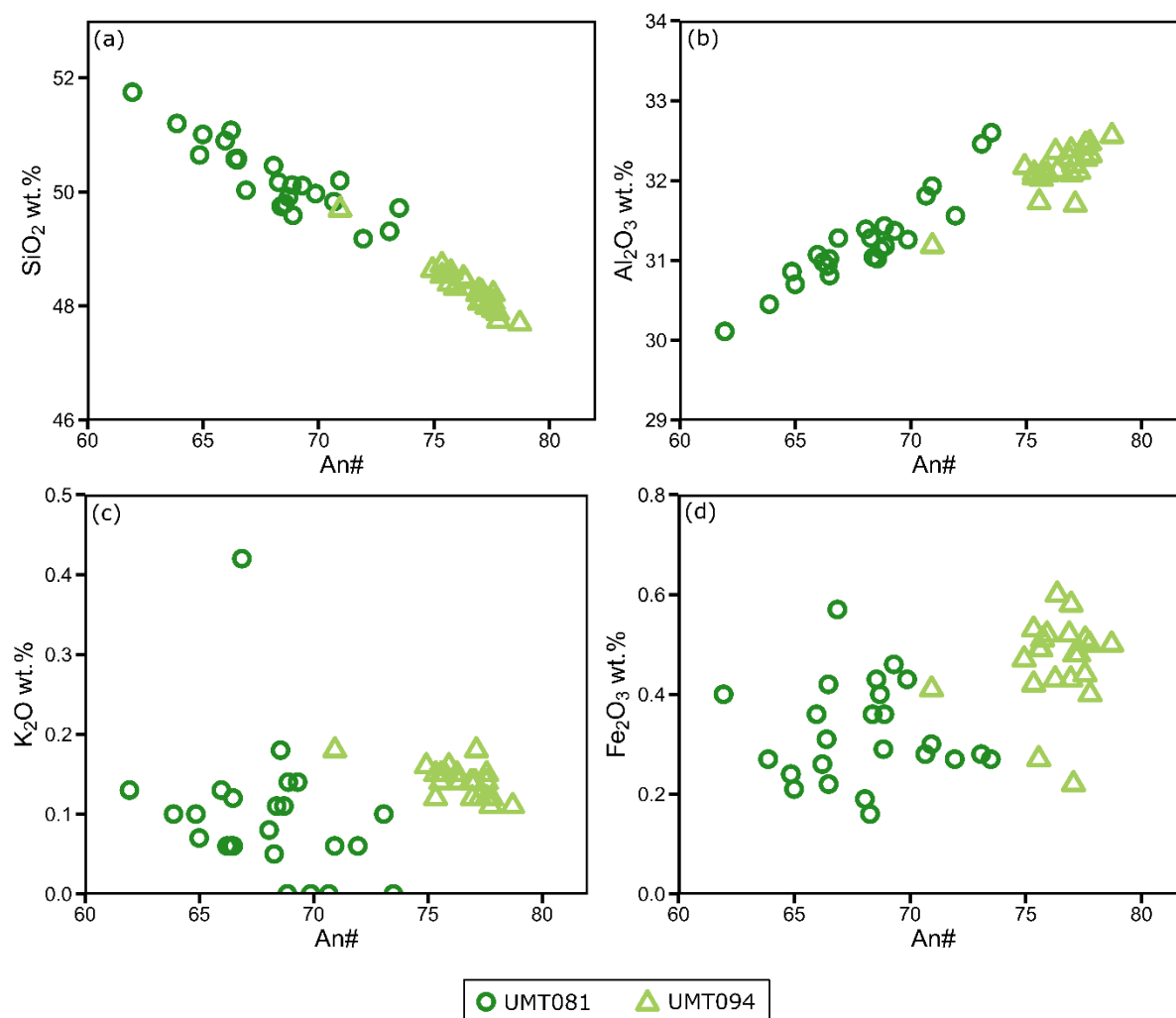
Figure 6.10: Binary variation plots against An# of Plagioclase from anorthosite rocks in the Central Norite Unit. (a) SiO₂, (b) Al₂O₃, (c) K₂O, (d) Fe₂O₃. Plagioclase in UMT094 anorthosite is more Ca-rich compared to UMT081.
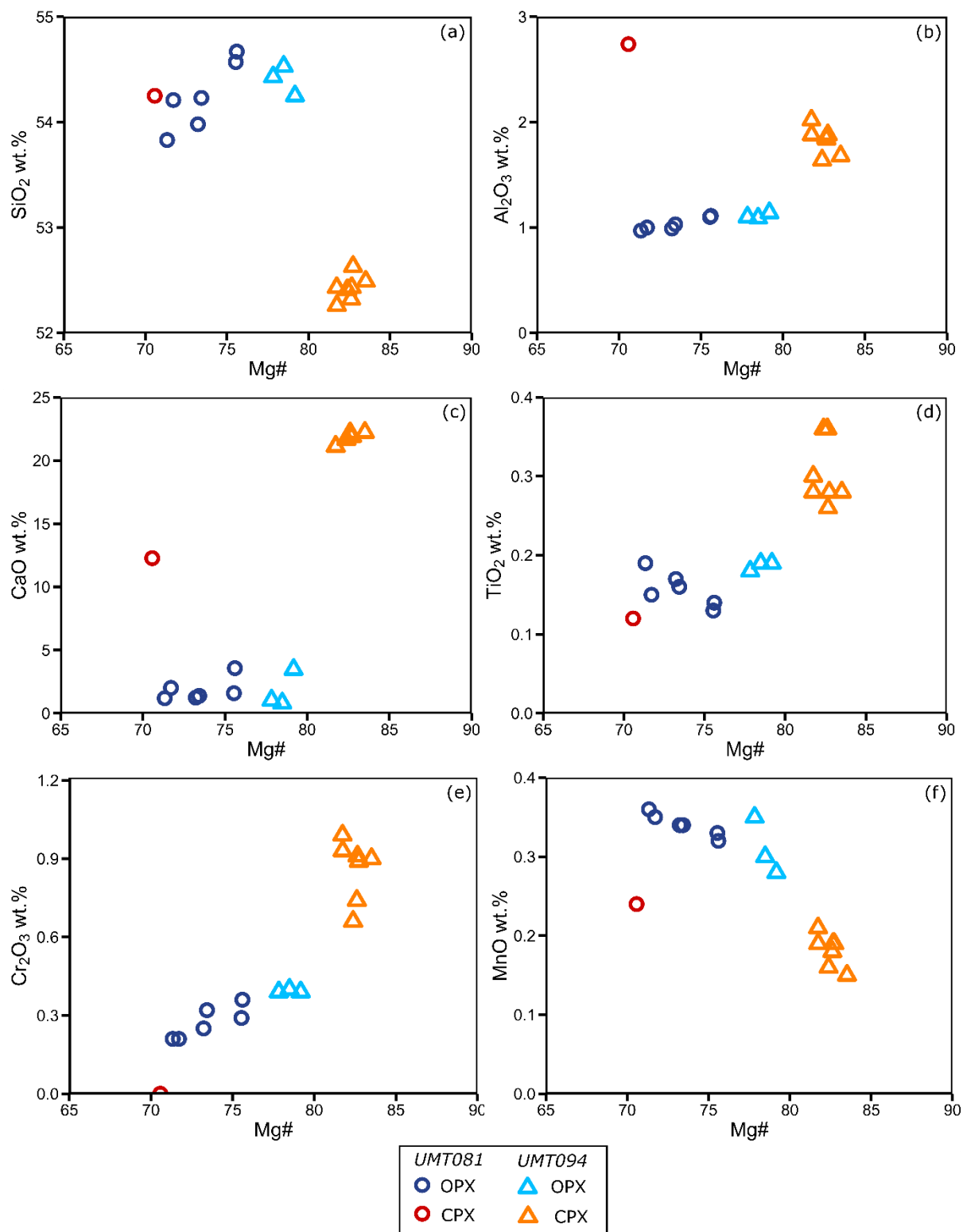
Figure 6.11: Binary variation plots of Mg# from pyroxenes in anorthosites of the Central Norite Unit. (a) SiO_2, (b) Al_2O_3, (c) CaO, (d) TiO_2, (e) Cr_2O_3, (f) MnO.

6.2.4 Lower Pyroxenite

In the Lower Pyroxenite Unit, intercumulus plagioclase in drill core UMT081 has a wide compositional range from andesine to labradorite (An47-67) and is more sodic than plagioclase in UMT094 which is largely labradoritic to bytownitic in composition (An67-72) (Figure 6.12). Orthopyroxene cumulates in the Lower Pyroxenite Unit has a narrow compositional range and is more magnesian in drill core UMT081 (Mg# 82-84) than orthopyroxene compositions in drill core UMT094 (Mg# 80-81). In addition, orthopyroxene composition of the pegmatoidal pyroxenite hosting the Main Chromitite shows the least evolved orthopyroxene composition (Mg# 83-85). Clinopyroxene is largely absent in drill core UMT081 with a single analysis (Mg# 90), whereas clinopyroxene in drill core UMT094 is less magnesian (Mg# 84-85).
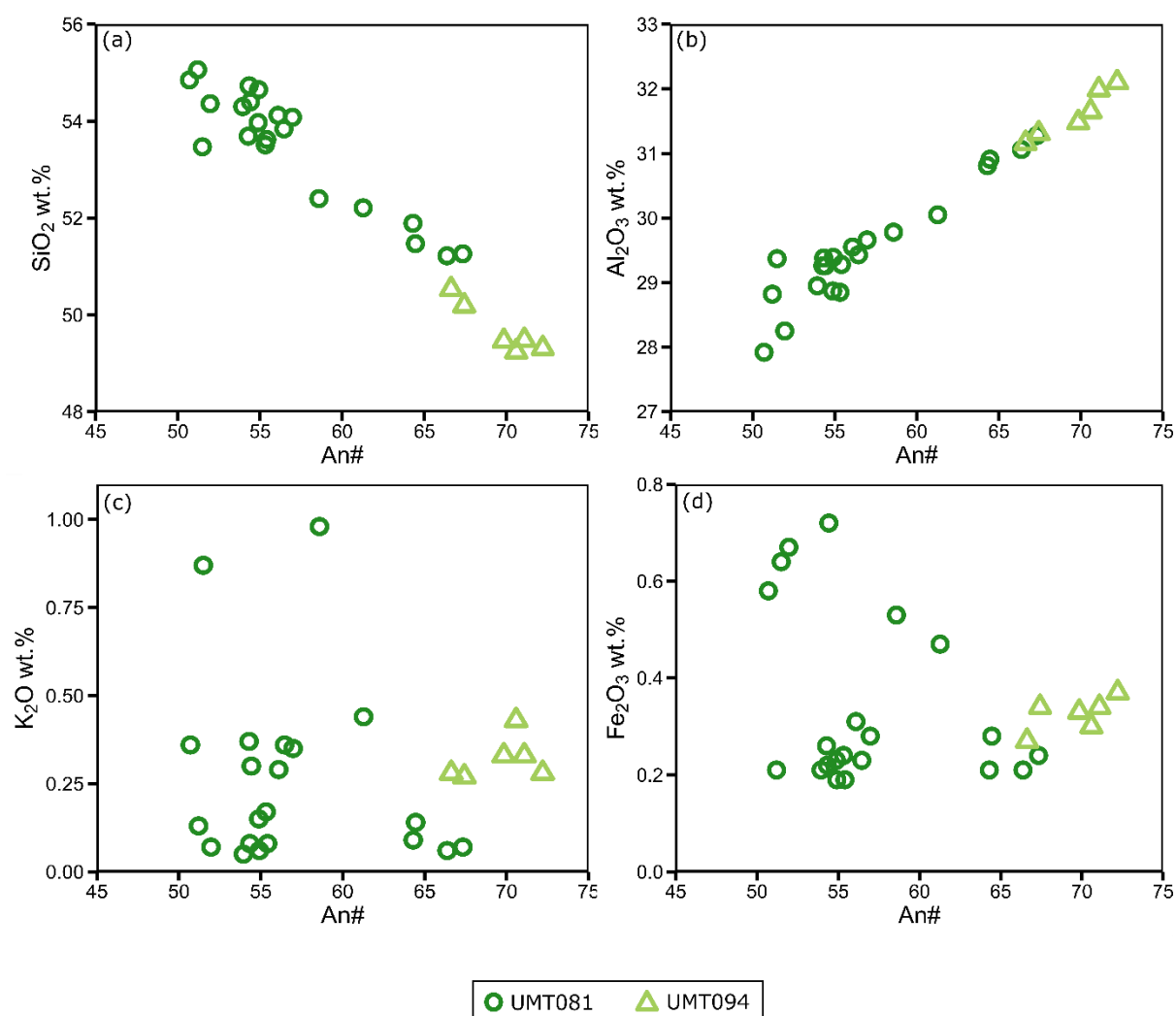
Figure 6.12: Binary variation diagrams of plagioclase compositions from the Lower Pyroxenite Unit. (a) SiO_2, (b) Al_2O_3, (c) K_2O, (d) Fe_2O_3. Note the more sodic composition of plagioclase in UMT081 relative to UMT094.
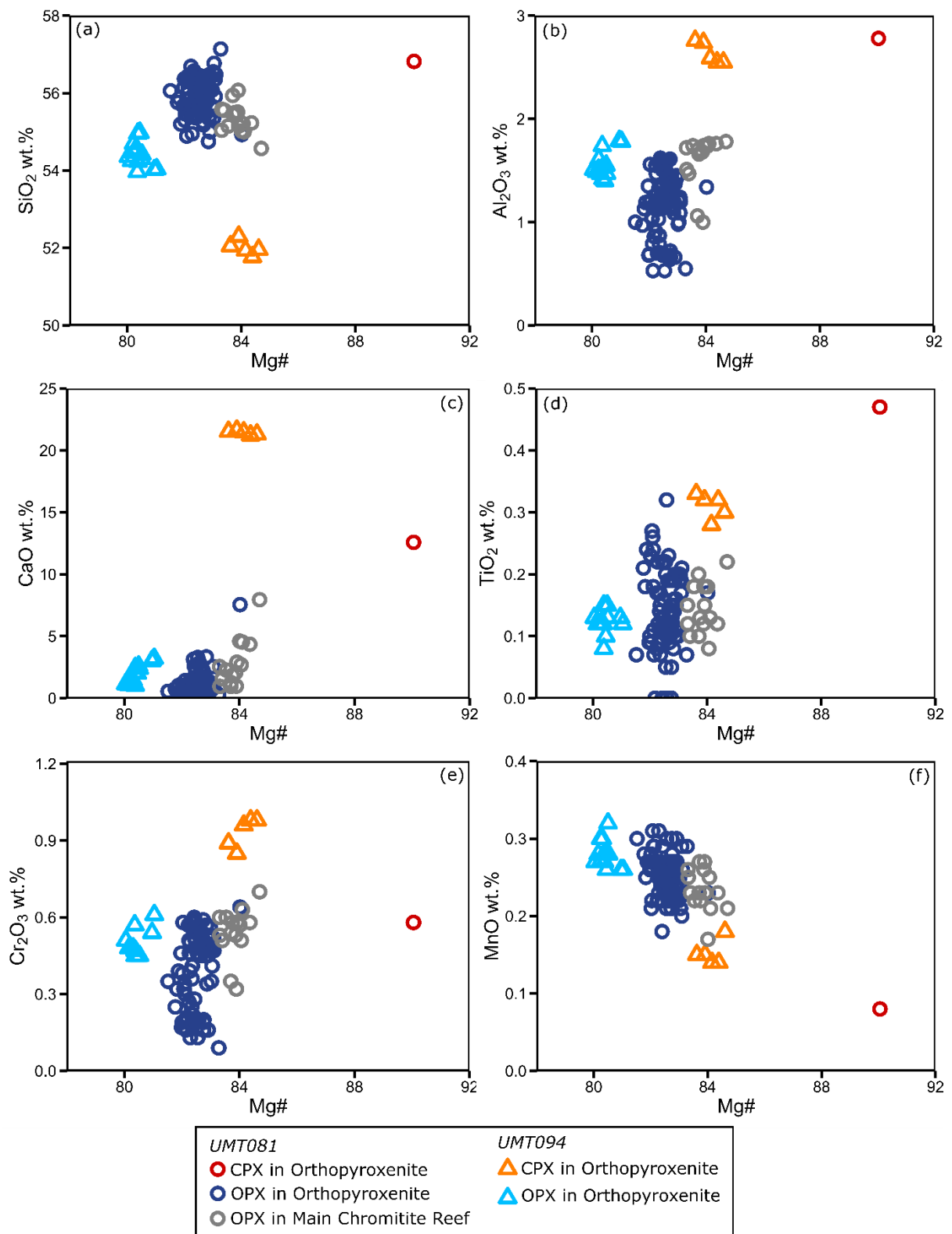
Figure 6.13: Binary variation plots of Mg# for pyroxenites from the Lower Pyroxenite Unit including the Main Chromitite Reef in UMT081. (a) SiO_2, (b) Al_2O_3, (c) CaO, (d) TiO_2, (e) Cr_2O_3, (f) MnO. Pyroxenite in the Main Chromitite is marginally more magnesian than the pyroxenites of the wider unit.

6.2.5 Lower Ultramafic Unit

6.2.5.1 Harzburgite

Interstitial plagioclase in harzburgite has a wide range of compositions from labradorite to bytownite. Plagioclase in drill core UMT081 has a narrower range of compositions compared to plagioclase in drill core UMT094 although they broadly overlap (An 58-72 vs An 56-78, respectively) (Figure 6.14). Pyroxene also has different compositions between drill cores UMT094 and UMT081. However, unlike orthopyroxene in norite and anorthosite that were more magnesian in UMT094, orthopyroxene in harzburgite is more magnesian in drill core UMT081 (Figure 6.29), (average Mg# of 84 compared to average Mg# 80 in UMT094) (Figure 6.15). Orthopyroxene in drill core UMT094 also has a marginally wider range of compositions with Mg# ranging from 79 to 82 Mg# compared to a range of 84-85 Mg# in UMT081. Clinopyroxene shows a similar variation with average Mg# of 87 and 84 for drill cores UMT081 and UMT094, respectively. Clinopyroxene in drill core UMT094 also has a lower CaO and TiO$_2$ content than samples in UMT081. Olivine compositions of harzburgite are forsteritic with more magnesian olivine present in drill core UMT081 compared to olivine in UMT094 (Fo 82-83 in UMT081 vs Fo 78-81 in UMT094;Figure 6.30). There is no zoning apparent in olivine.
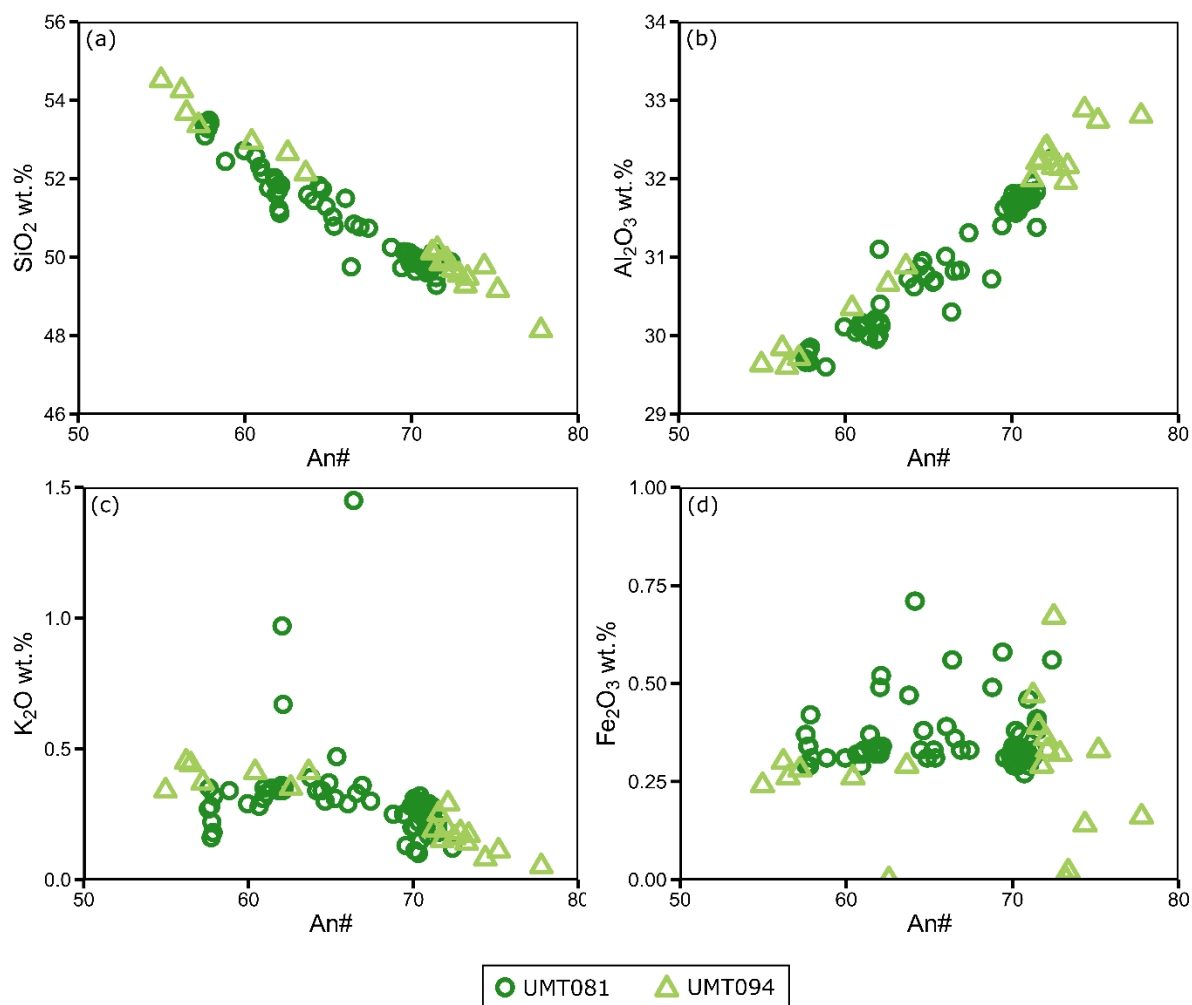
Figure 6.14: Binary variation plots against An content of plagioclase compositions from harzburgite of the Lower Ultramafic Unit. (a) SiO_2, (b) Al_2O_3, (c) K_2O, (d) Fe_2O_3. Note there is generally good overlap in plagioclase compositions in this lithology.
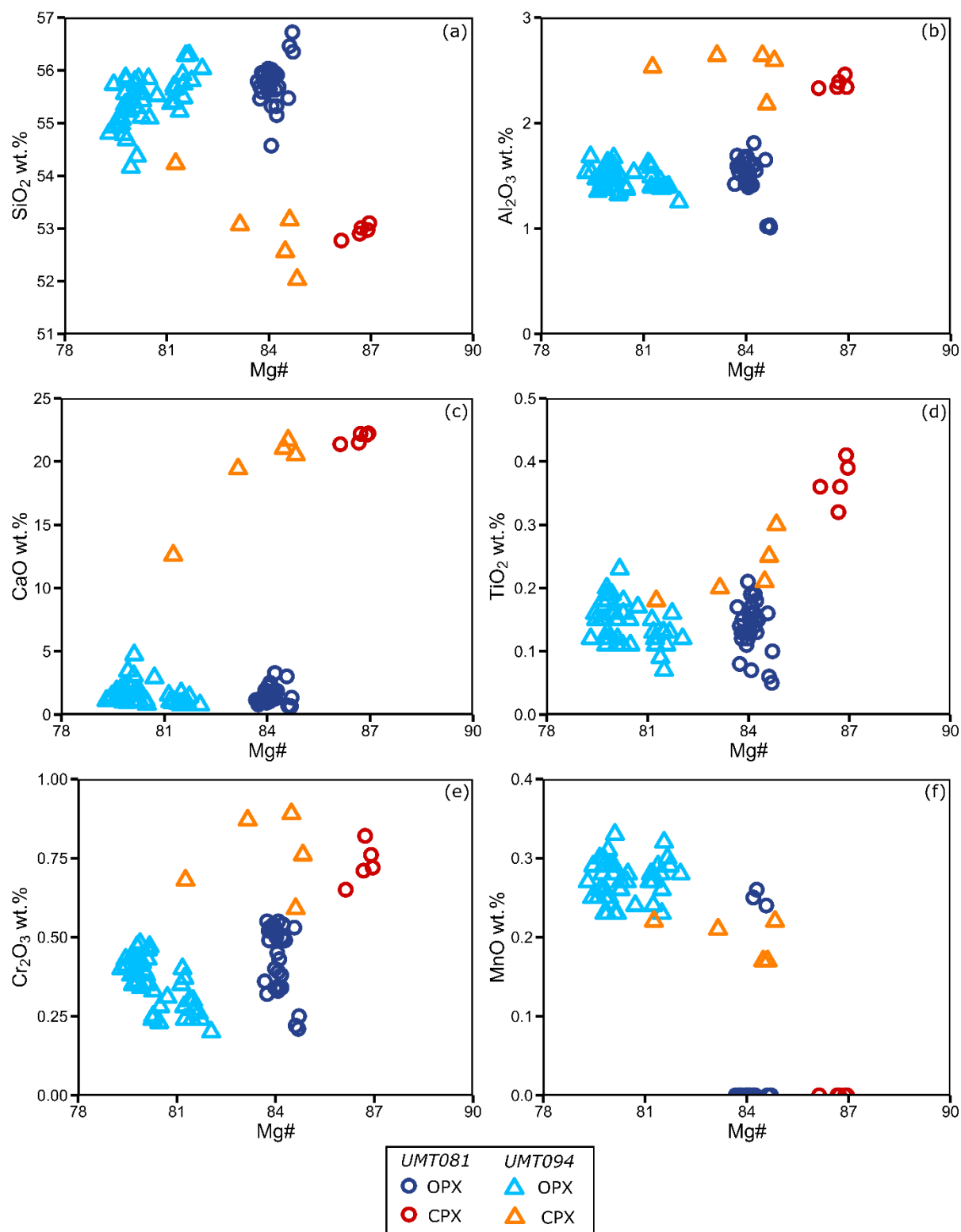
Figure 6.15: Binary variation plots of pyroxene compositions against Mg# in harzburgite rocks. (a) SiO_2, (b) Al_2O_3, (c) CaO, (d) TiO_2, (e) Cr_2O_3, (f) MnO. Pyroxene in UMT081 is distinctly more magnesian than pyroxene in UMT094.

6.2.5.2 Lherzolite

Intercumulus plagioclase compositions in lherzolite show distinct variability between drill cores UMT081 and UMT094. Plagioclase in drill core UMT081 is more anorthite rich, with compositions ranging between An 76-81, compared to An 55-71 in UMT094 (Figure 6.16). The lower An content in drill core UMT094 corresponds to higher SiO_2 and lower Al_2O_3 content.

Orthopyroxene compositions in lherzolite do not show systematic variation between drill cores, ranging between 80-84 Mg# (Figure 6.17). Orthopyroxene in drill core UMT094 has a marginally larger range extending to a slightly more magnesian composition (84 Mg#) compared to orthopyroxene found in drill core UMT081 (up to Mg# 82). Clinopyroxene composition in lherzolite is variable between drill cores with clinopyroxene in drill core UMT081 ranging from 81-85 Mg# whereas clinopyroxene in drill core UMT094 has a much wider range (78-87 Mg#). Clinopyroxenes found in lherzolite in drill core UMT094 fall into two distinct populations, one being highly magnesian (83-87 Mg#) and the other low magnesian (78-81 Mg#). This low magnesian clinopyroxene population is found in a single sample (94-1334).

There is a slight variation between olivine compositions in lherzolite between the two drill cores. Olivine in drill core UMT081 is slightly more magnesian on average compared to that of UMT094 (80 and 79 Mg#, respectively), although their ranges overlap. However, in drill core UMT094 there is a sub-population of significantly more magnesian olivine with compositions ranging 86-87 Mg# in a single sample, where clinopyroxene is notably magnesium poor (94-1334).
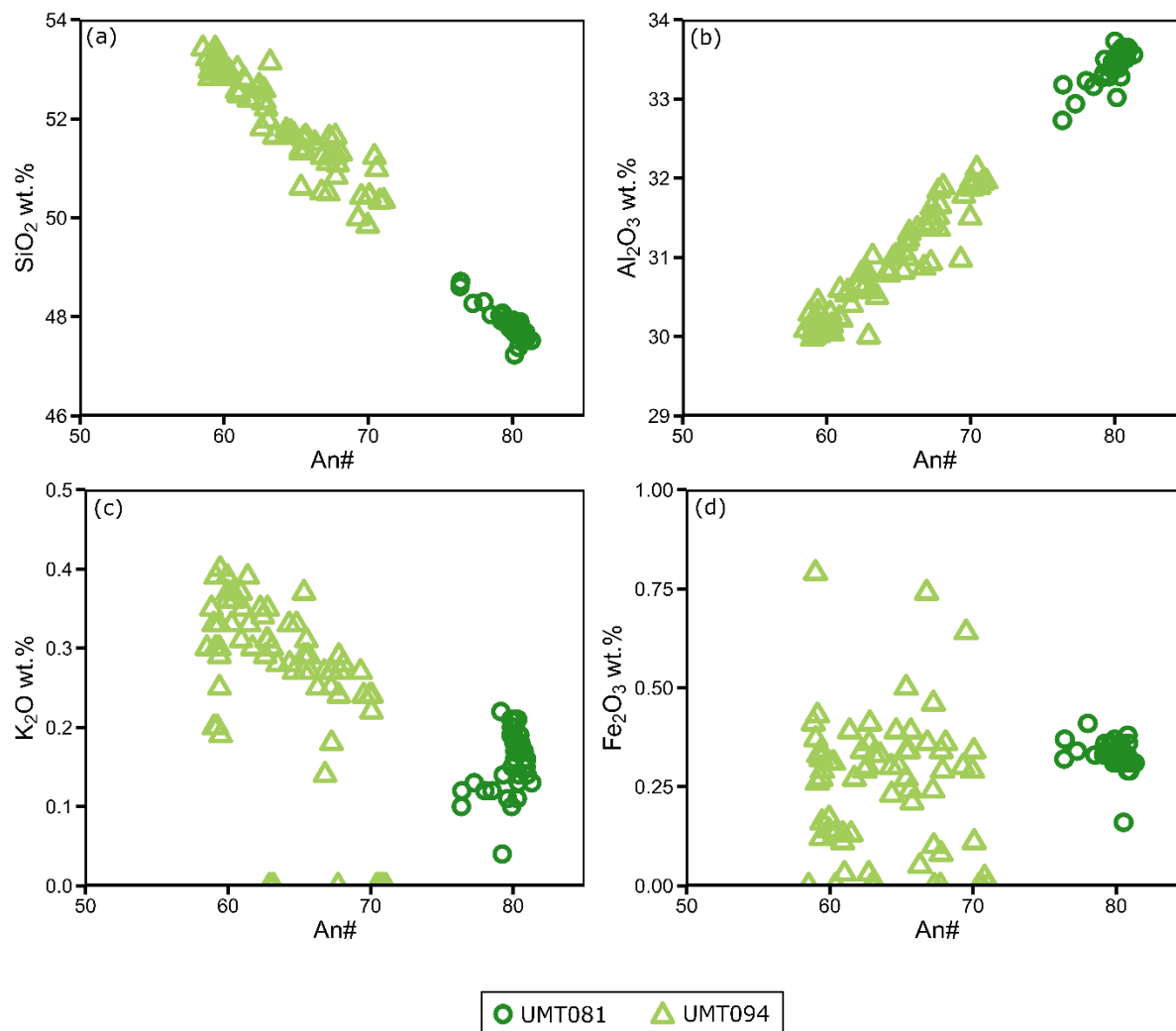
Figure 6.16: Binary variation plots of plagioclase composition against An content in lherzolite rocks. (a) SiO₂, (b) Al₂O₃, (c) K₂O, (d) Fe₂O₃. Note plagioclase is more sodic in UMT094 relative to UMT081.
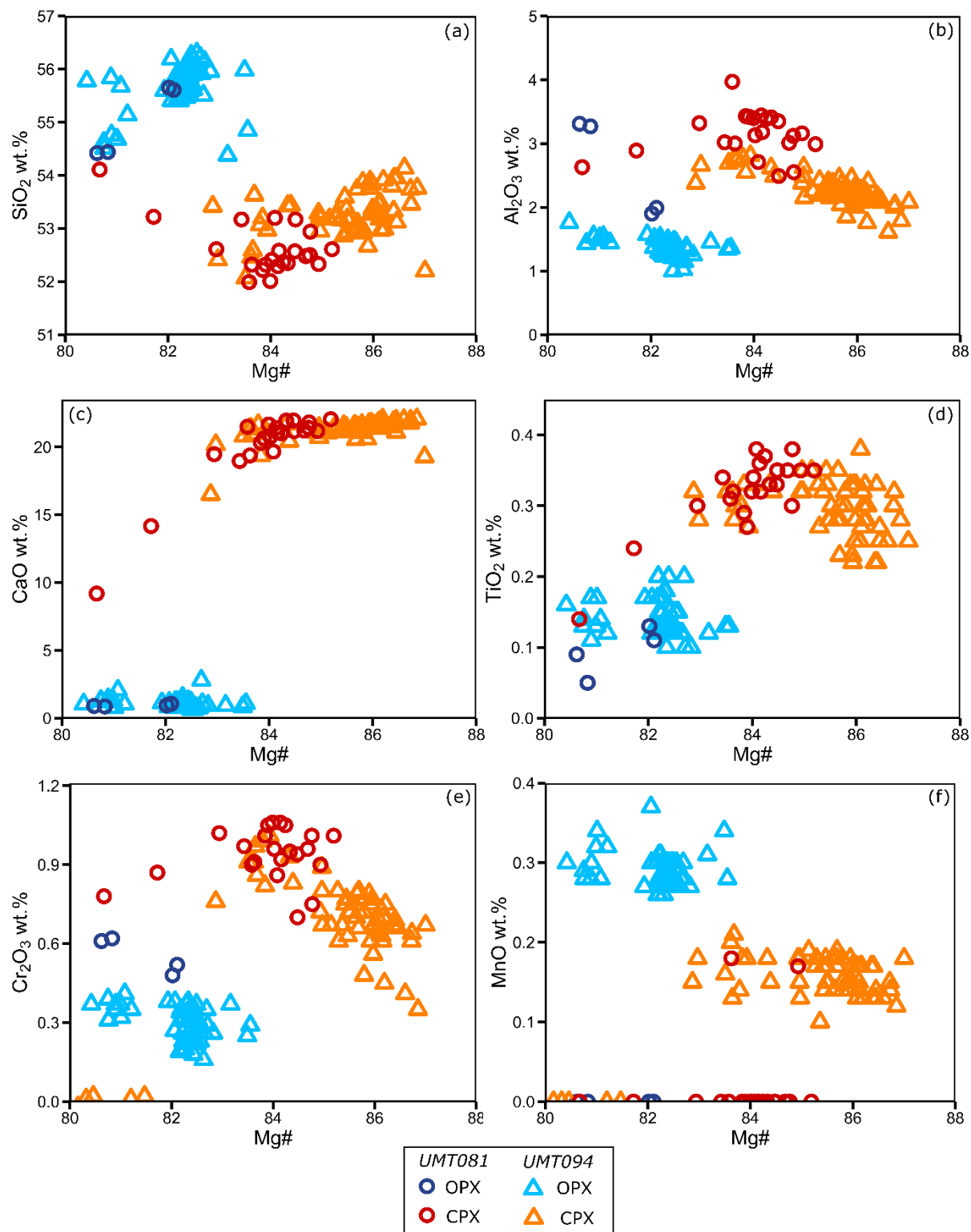
Figure 6.17: Binary variation plots against Mg# of pyroxene in lherzolite rocks. (a) SiO₂, (b) Al₂O₃, (c) CaO, (d) TiO₂, (e) Cr₂O₃, (f) MnO. Here pyroxene in UMT094 lherzolite is marginally more magnesian than pyroxene in UMT081.

6.2.5.3 Pyroxenite

In the Lower Ultramafic Unit, pyroxenite is only present in drill core UMT081. There is distinct variability in intercumulus plagioclase composition between fine-medium grained and pegmatoidal pyroxenites (Figure 6.18). Pegmatoidal pyroxenites are distinctly more sodic (An43-67) and comprise andesine and labradorite plagioclase compositions compared to other pyroxenites that are labradorite to bytownite in composition (An55-65, excluding 1 anomalous analysis at An12).

Both orthopyroxene and clinopyroxene show a wide range in mineral composition (Mg# 80-86 and 82-90, respectively). The compositions of orthopyroxene and clinopyroxene shows no systematic compositional difference between fine-medium grained and pegmatoidal pyroxenites, unlike the offset observed in accompanying plagioclase analyses (Figure 6.19). However, the composition of orthopyroxene is controlled by the sample analysed, with Mg# of orthopyroxene largely clustered according to their sample (Figure 6.20).
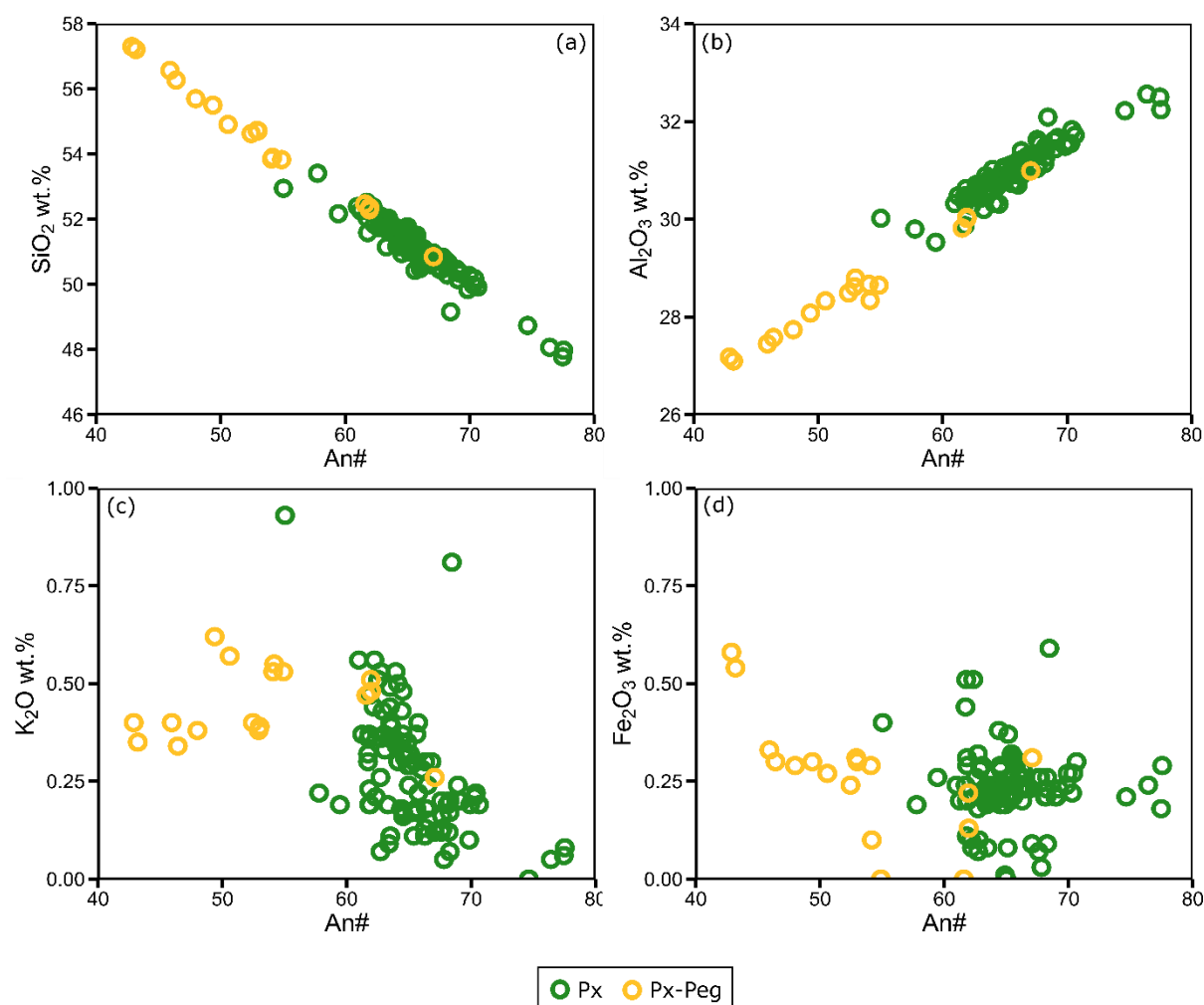
Figure 6.18: Binary variation plots of plagioclase compositions from pyroxenites in the Lower Ultramafic Unit. (a) SiO_2, (b) Al_2O_3, (c) K_2O, (d) Fe_2O_3. Pegmatoidal pyroxenite contains more sodic plagioclase compared to fine-medium grained pyroxenites.
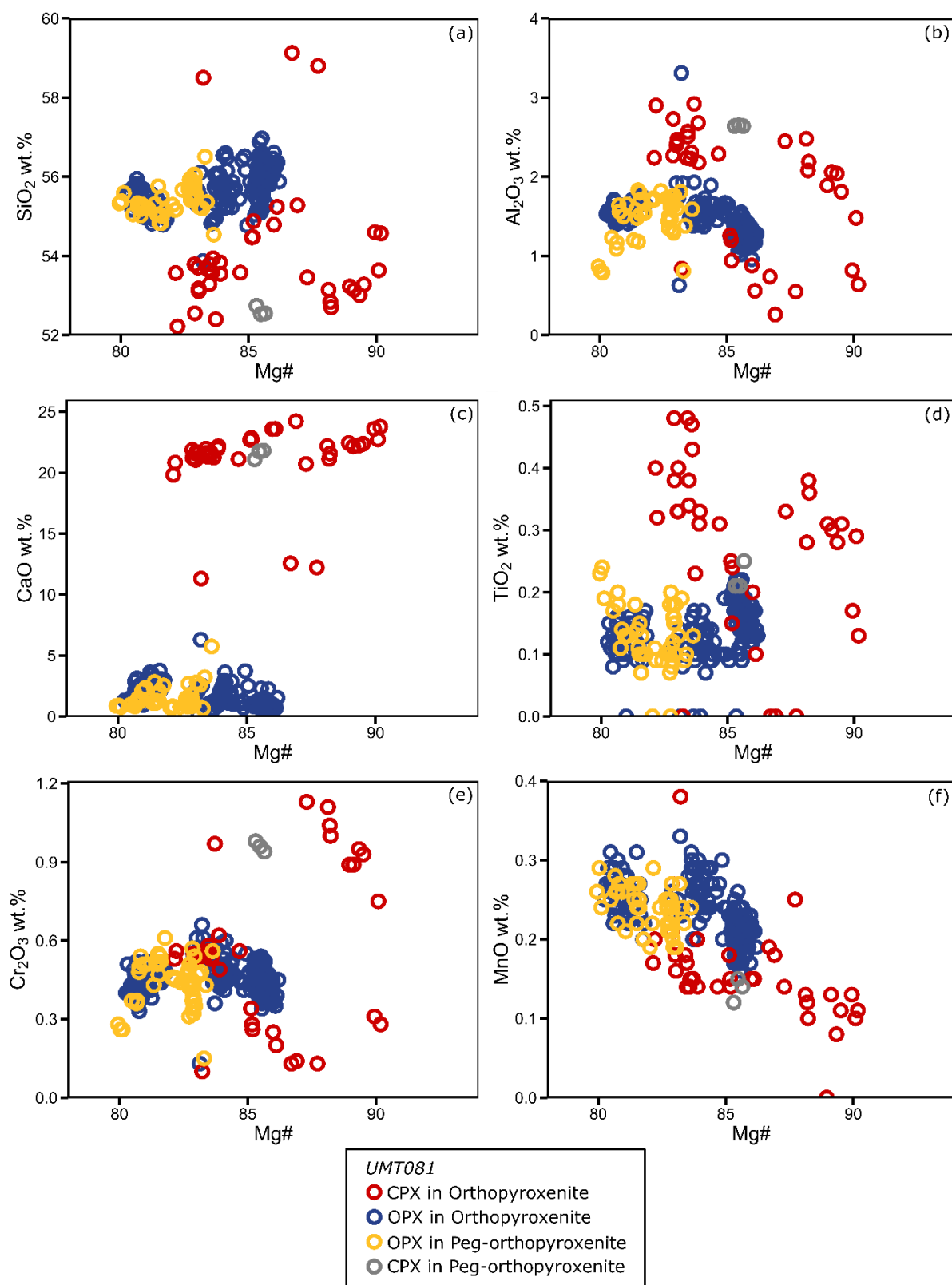
Figure 6.19: Binary variation plots of pyroxene composition against Mg# of pyroxenite from the Lower Ultramafic Unit. (a) SiO₂, (b) Al₂O₃, (c) CaO, (d) TiO₂, (e) Cr₂O₃, (f) MnO. Here there is little distinction in composition between pegmatoidal and fine-medium grained pyroxenites.
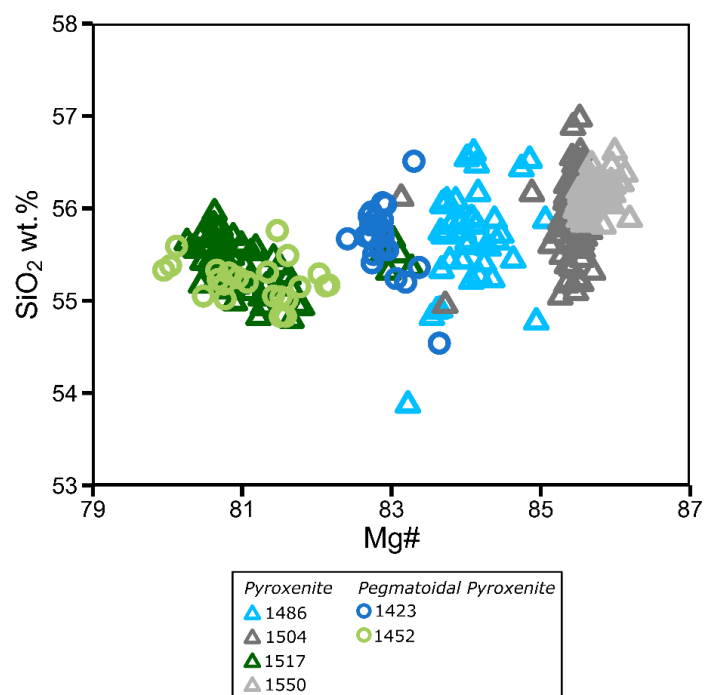
Figure 6.20: Graph of orthopyroxene analyses from pyroxenites of the Lower Ultramafic Unit in UMT081 categorized by sample. Each sample has a narrow and distinct compositional range.

6.3 Lower Flatreef

6.3.1 FAZ

In the FAZ, pyroxene composition varies between different lithologies forming distinct populations associated with each rock type (Figure 6.21). Clinopyroxene in parapyroxenite shows a wide range of Mg# from 69 to 90. Orthopyroxene has a significantly narrower range of Mg# (78-83). Orthopyroxene compositions in parapyroxenites can vary strongly on a localised scale. Orthopyroxene in parapyroxenite from drill core UMT081 is less magnesian (Mg# 69-86) than that in drill core UMT094 (Mg# 83-90).

Plagioclase also has distinct compositional ranges in different lithologies. Olivine gabbronorite has the most sodic plagioclase with compositions as low as An 46, although it covers a wide range of compositions including more calcium rich values up to An 76 (Figure 6.21). Plagioclase in olivine bearing pyroxenite is the most calcium-rich with compositions found between An 77-83. There is also a noticeable offset between parapyroxenite plagioclase compositions in drill cores UMT081 and UMT094. Plagioclase in UMT081 parapyroxenites has a more sodic range of values (An 54-72) compared to the narrow, but calcium rich, range found in UMT094 parapyroxenite (An 82-83).

Olivine compositions vary strongly according to the rock type. Parapyroxenites have the most magnesian olivines (Fo 77-80 in UMT081, Fo 83 in UMT094). Olivine gabbronorite and olivine

bearing pyroxenite have slightly less magnesian olivine compositions (Fo 77-78). Calc-silicate xenoliths/rafts in drill core UMT081 show the least magnesian compositions (Fo 76).
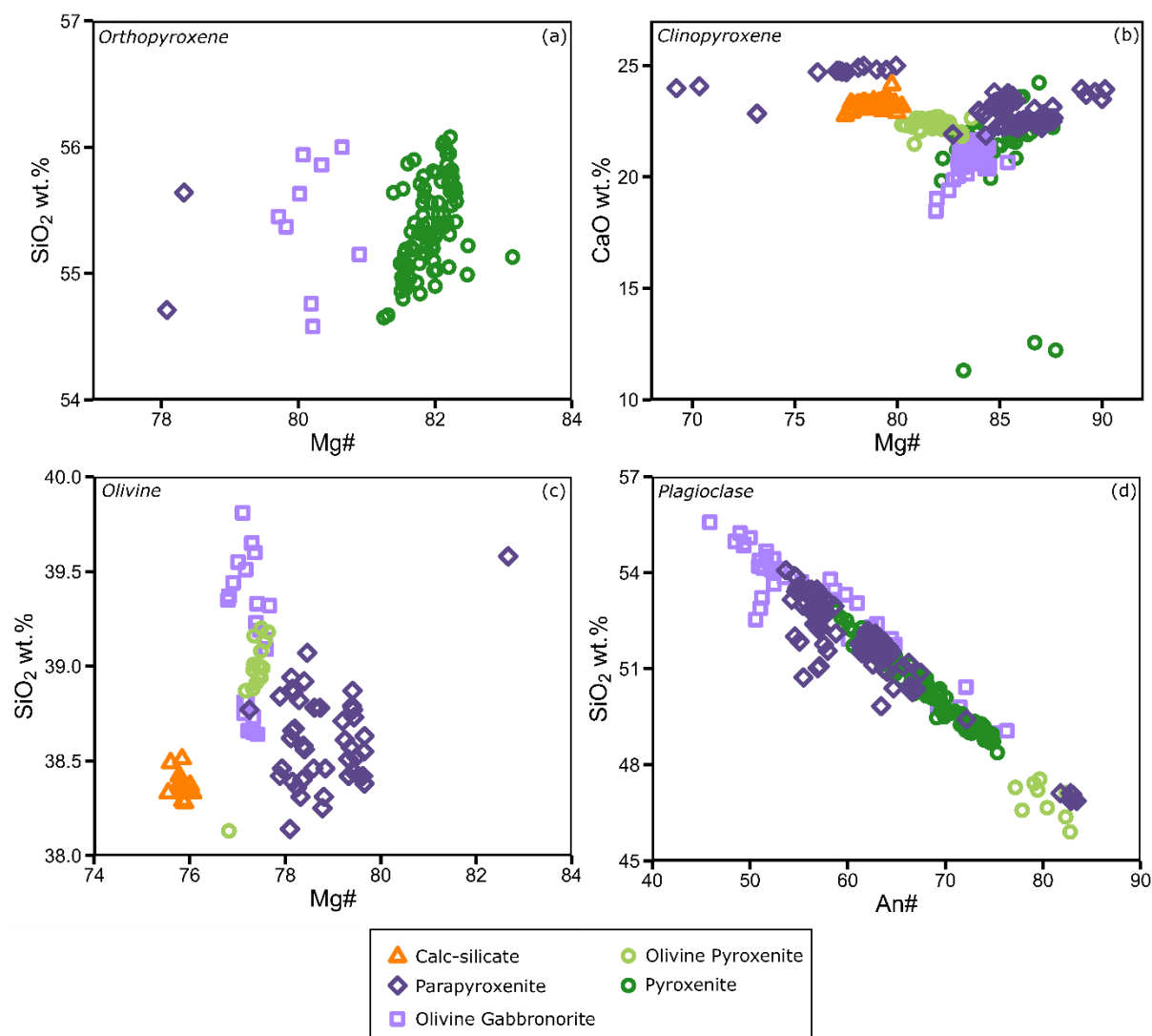
Figure 6.21: Graphs showing mineral chemistry of pyroxenes, plagioclase and olivine in the Footwall Assimilated Zone. Each rock type has a distinct mineral composition, especially apparent in pyroxene and olivine data.

6.3.2 Wehrlite

Clinopyroxenes in wehrlite forms two distinct compositional populations in drill cores UMT081 and UMT094 (Figure 6.22). Wehrlite in drill core UMT094 has more magnesium-rich clinopyroxenes (84 av. Mg#) with lower calcium content. In contrast, clinopyroxene in wherlite from drill core UMT081 has a lower average Mg# (82) but a greater range (79-90 Mg#) than in UMT094 (83-90 Mg#) and a higher average calcium content (23.11 wt. % av. UMT094; 23.76 wt. % avg. UMT081).

Olivine in wehrlite shows significant compositional variation between the two drill cores (Figure 6.30). In drill core UMT081, olivine is the most forsteritic of any rock type analysed, with an average composition of Fo 88 compared to Fo 84 in drill core UMT094. The range of olivine compositions in each drill core is small, resulting in two distinct populations with no overlapping values.
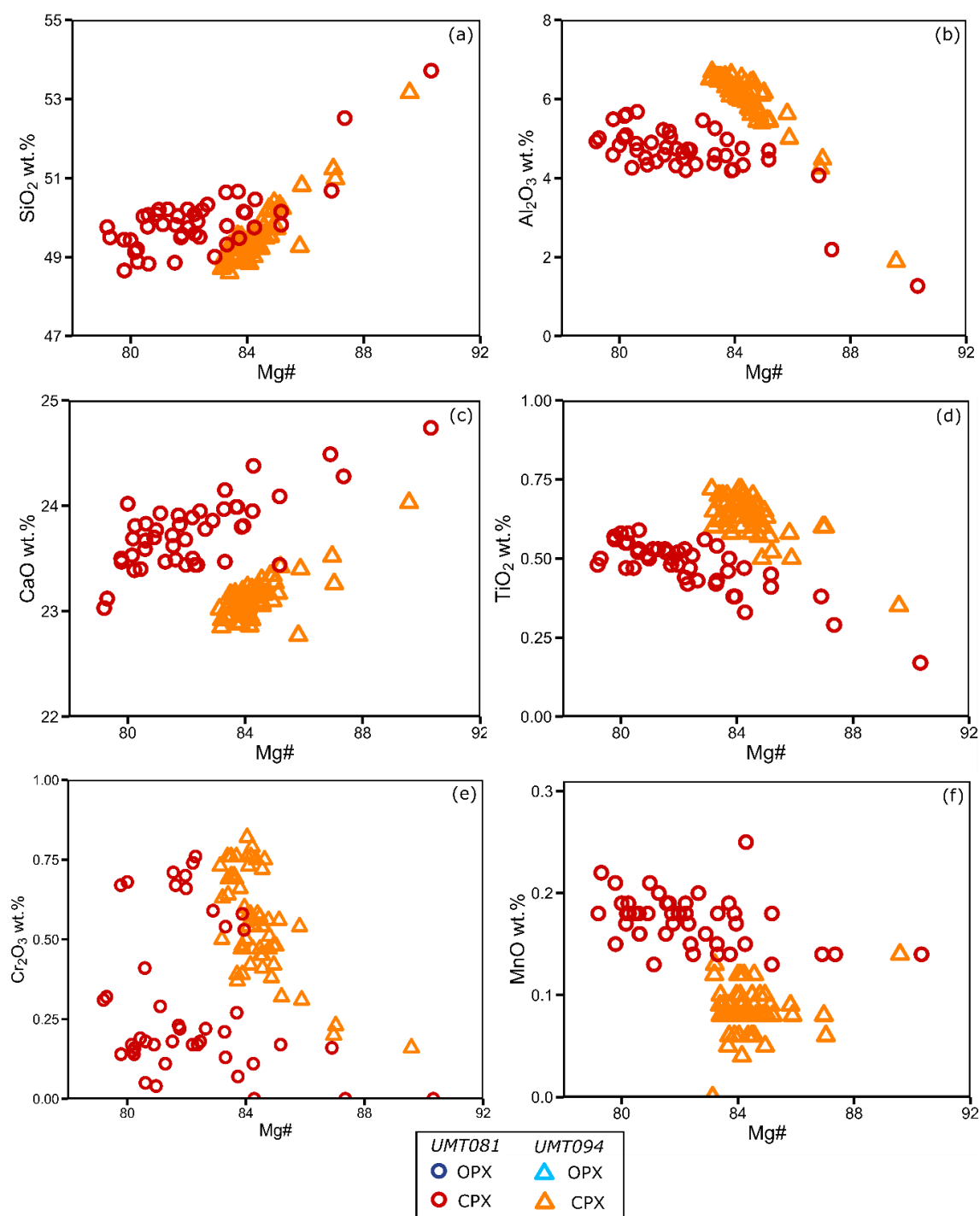
Figure 6.22: Binary variation plots of clinopyroxene compositions in wehrlite rocks. (a) SiO₂, (b) Al₂O₃, (c) CaO, (d) TiO₂, (e) Cr₂O₃, (f) MnO. Pyroxene in UMT094 is on average more magnesian than UMT081, although the latter has a wider range of compositions.

6.3.3 Ti-rich Olivine Gabbro

Plagioclase is significantly more sodium-rich in the Ti-rich olivine gabbro than in any other magmatic rock type studied here (min. An26). There is a subtle compositional variation between analysed samples. The upper sample (81-1720) is more evolved with a composition ranging between An26-28 compared to An32-36 for the lower sample (81-1787) (Figure 6.23). In contrast to the plagioclase data, there is no compositional difference in pyroxene between samples (Figure 6.24). Clinopyroxene in the Ti-rich olivine gabbro is slightly less calcium rich than in other rock types with all clinopyroxene in the sill comprised of augite. Clinopyroxene has a wide range of Mg# from 66-75, making it more iron-rich than clinopyroxene in other rock types. Orthopyroxene has a less magnesian composition with a narrow range of compositions (Mg# 64-66) comprising clino-enstatite and some pigeonite. Olivine in the Ti-rich olivine gabbro is the most fayalitic of any rock type analysed, with an average composition of Fo55 (Figure 6.30). There is a slight difference in olivine composition between the two Ti-rich olivine gabbro samples with average values of Fo53 (range Fo53-58) for the upper sample and Fo57 (range Fo56-58) for the lower sample.
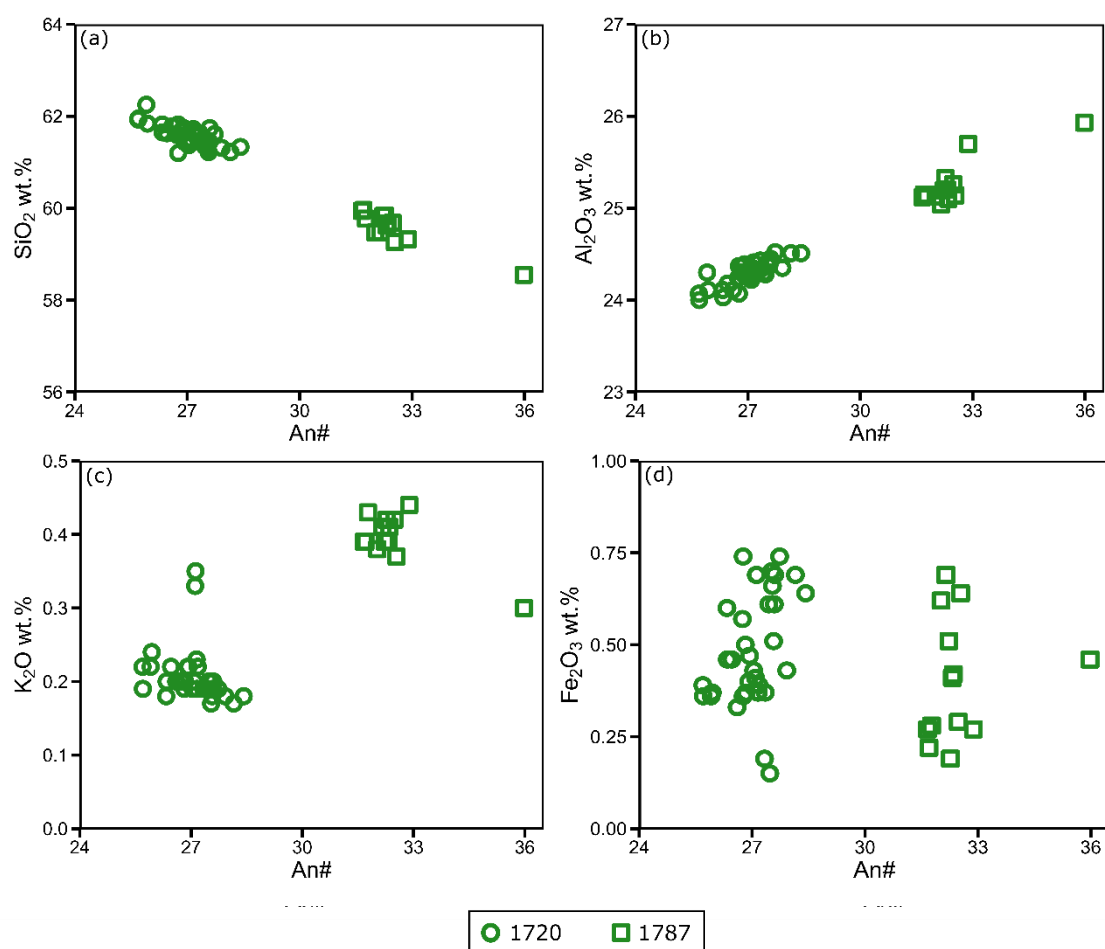
Figure 6.23: Binary variation plots against An# for plagioclase from the Ti-rich olivine gabbro. (a) SiO_2, (b) Al_2O_3, (c) K_2O, (d) Fe_2O_3. Plagioclase compositions from samples within the unit are distinct.
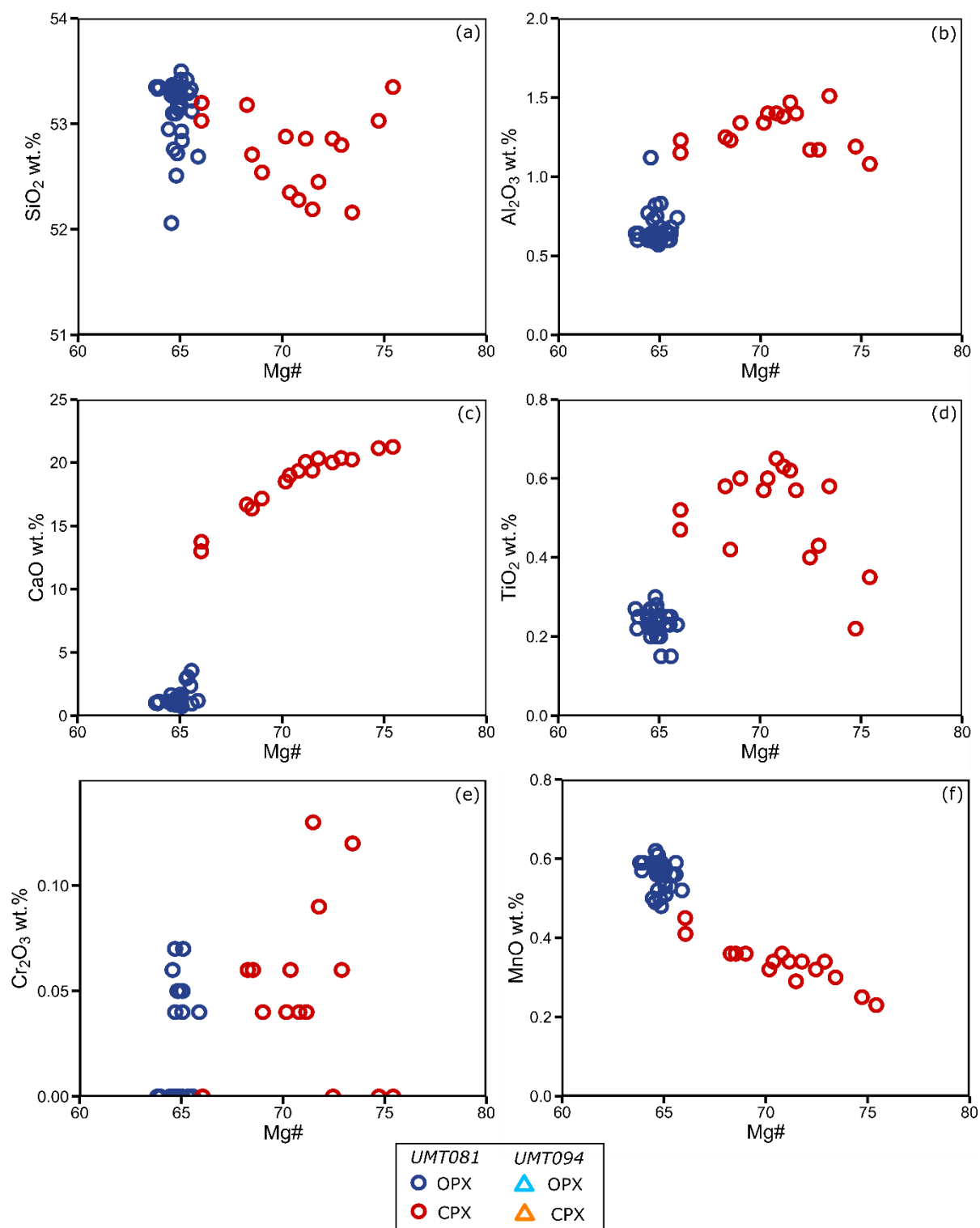
Figure 6.24: Binary variation plots against Mg# for pyroxenes from the Ti-rich olivine gabbro. (a) SiO_2, (b) Al_2O_3, (c) CaO, (d) TiO_2, (e) Cr_2O_3, (f) MnO. Clinopyroxene has a wider range of compositions relative to orthopyroxene.

6.3.4 Olivine Mela-Gabbronorite

Olivine mela-gabbronorite has evolved plagioclase compositions plotting in the andesine field ranging between An 35-42 (Figure 6.25). Pyroxene has a relatively magnesian composition with orthopyroxene values ranging between Mg# 79-80 and clinopyroxene ranging between Mg# 81-86 characterising the latter as clino-enstatite and augite, respectively (Figure 6.26). Clinopyroxene is less calcium-rich than seen in many other lithologies, with no diopside found. Olivine has a low magnesium content with an average composition of Fo 76 and no chemical zoning.
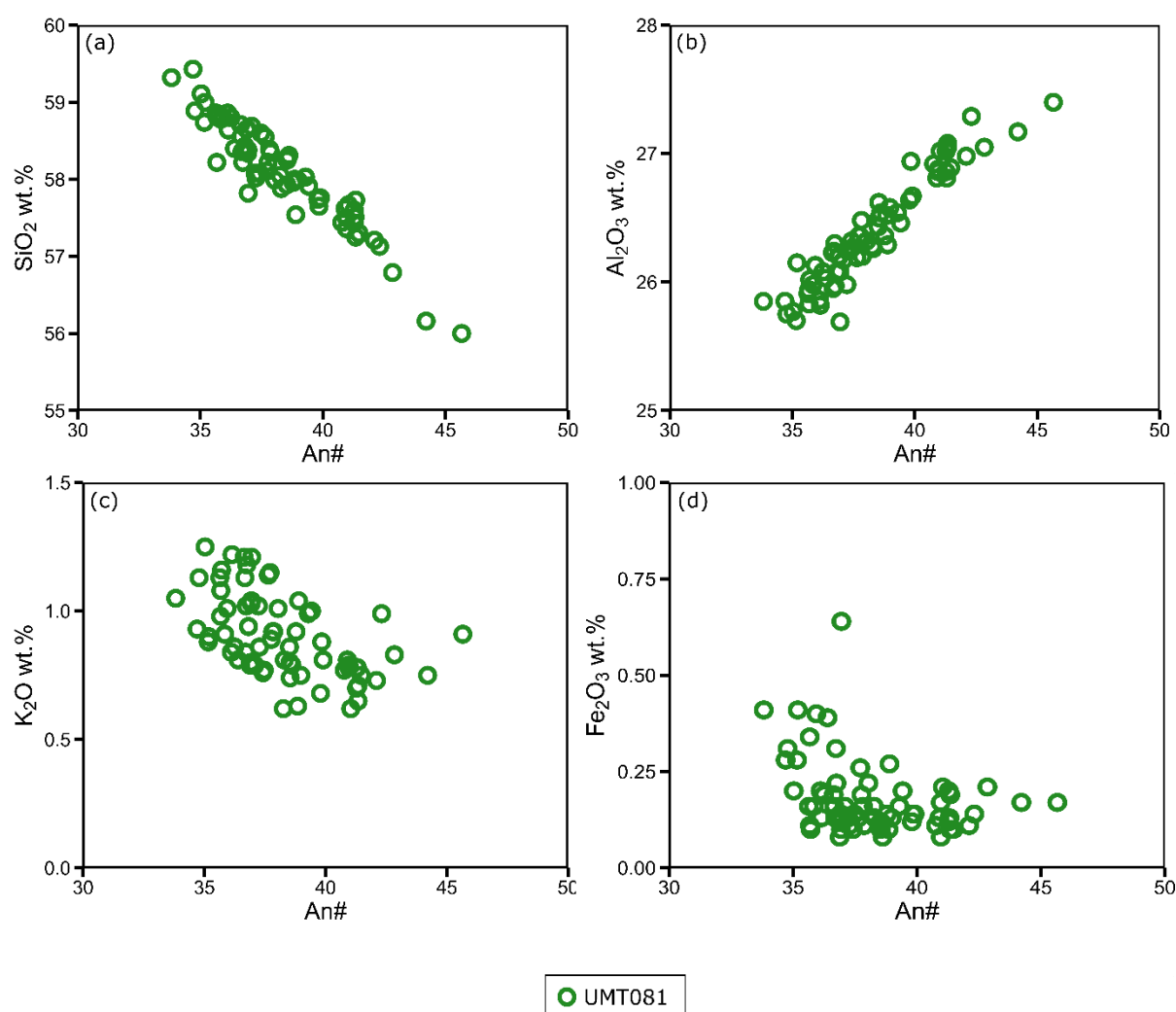
Figure 6.25: Binary variation plots against An# for plagioclase in the Olivine Mela-gabbronorite at the base of UMT081. (a) SiO₂, (b) Al₂O₃, (c) K₂O, (d) Fe₂O₃. These are among some of the most evolved plagioclase compositions observed in the Flatreef.
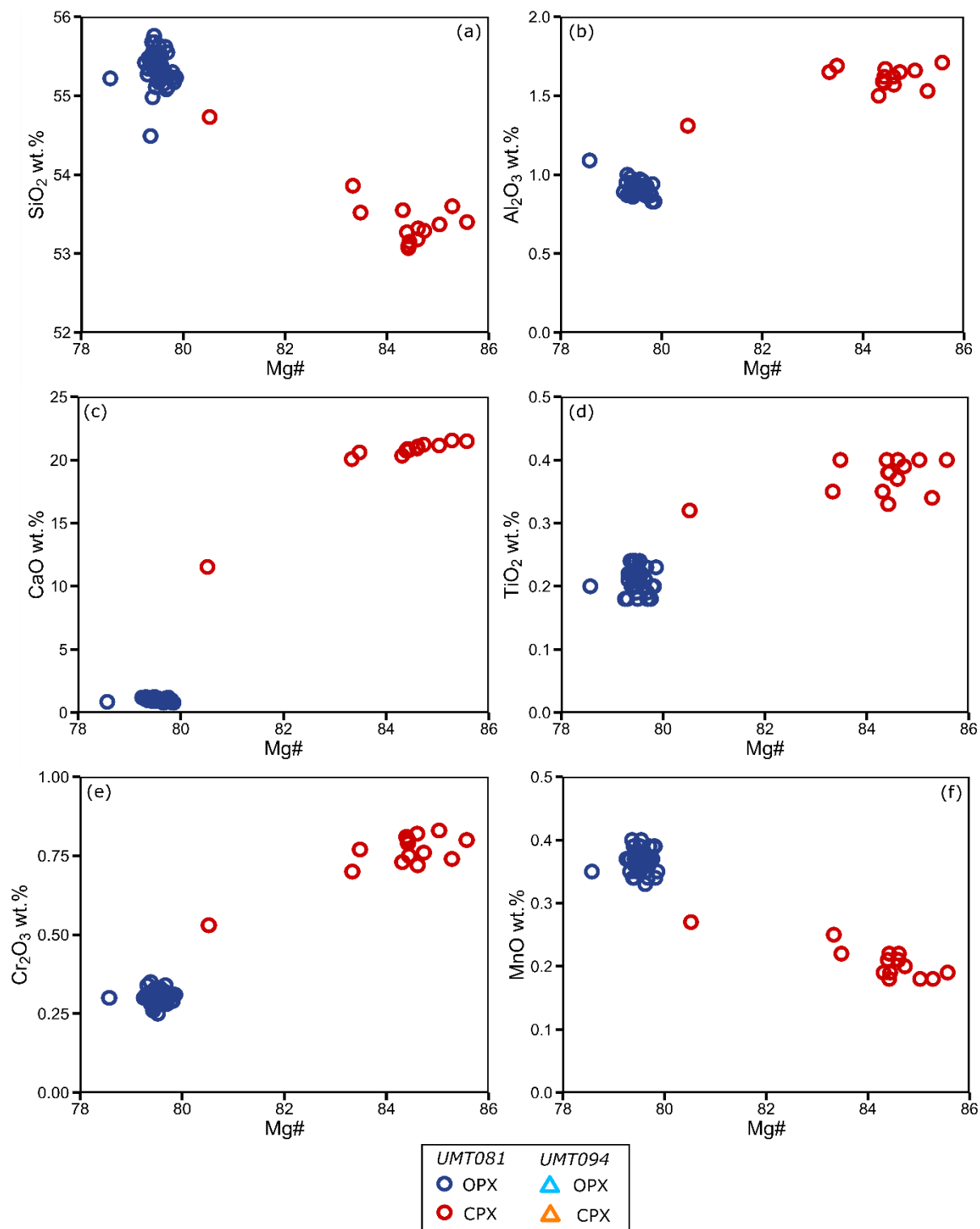
Figure 6.26: Binary variation plots of pyroxene compositions against Mg#. (a) SiO₂, (b) Al₂O₃, (c) CaO, (d) TiO₂, (e) Cr₂O₃, (f) MnO. Clinopyroxene has a wider compositional range than orthopyroxene, as also seen in the Ti-rich olivine gabbro.

6.4 Comparison of pyroxenite rocks through the Flatreef

A more detailed analysis of the different pyroxenite units (Upper Pyroxenite, Lower Pyroxenite and Lower Ultramafic Unit) shows there are subtle compositional differences between the units (Figure 6.27). Orthopyroxene in the Upper Pyroxenite Unit has the lowest range of Mg# values (79-85 Mg#) with the Lower Pyroxenite showing more magnesian values clustered around Mg# 80-84 in both UMT081 and UMT094. In the Upper Pyroxenite Unit pyroxenites in UMT094 are more magnesian than in UMT081 (avg. 82 and 80.5 Mg#, respectively) whereas in the Lower Pyroxenite Unit the opposite is true (avg. 80.4 and 83 Mg#, respectively). The orthopyroxene in pyroxenites from the Lower Ultramafic Unit (only present in UMT081) have Mg# ranging from 80-86 which represent the most magnesian orthopyroxene compositions of the analysed sequence. Orthopyroxene composition varies between samples, with each sample having a distinct and narrow range of Mg# (Figure 6.20). There is no relationship between depth and Mg# or between Mg# and grain size (i.e. pegmatoid vs non-pegmatoid).
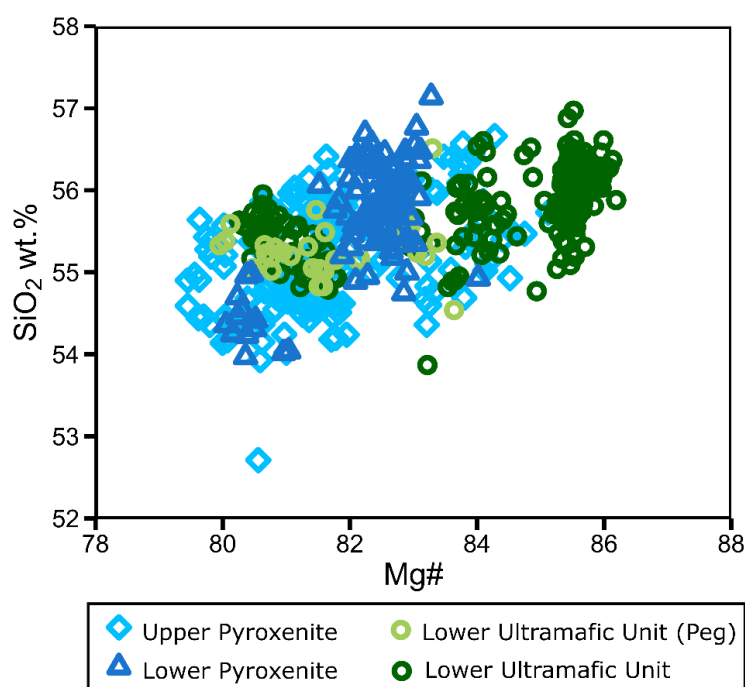
Figure 6.27: Graph of orthopyroxene compositions in pyroxenites from the Upper Pyroxenite Unit, Lower Pyroxenite Unit and Lower Ultramafic Unit including pegmatoidal layers

6.5 Plagioclase Zonation
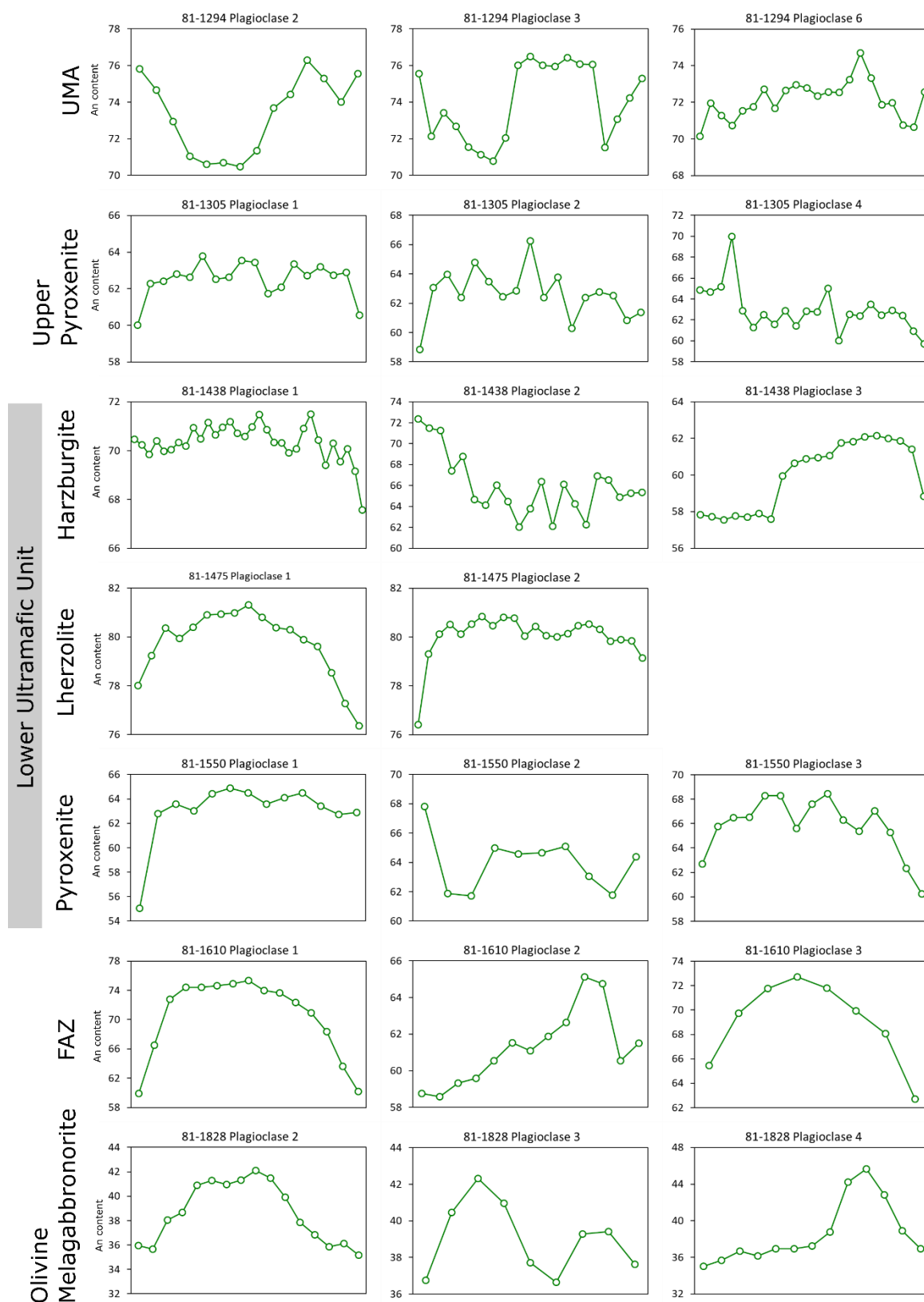
Figure 6.28: Graphs showing compositions of varying An content across transects of interstitial and cumulus plagioclase for different rock types within drill core UMT081. Note the wide variety of chemical zoning both within and between different lithologies.

Transects across plagioclase show a variety of zoning patterns across the studied sequence, including normal, cyclical and reversed (Figure 6.28). Within the UMA, cumulus plagioclase can show a several different types of zoning, with both normal and reversed zoning observed. In general, ultramafic rock types (pyroxenite, harzburgite, lherzolite), where plagioclase is of interstitial habit, tend to show patterns of anorthite-rich cores and more sodic rims. Intercumulus plagioclase from the Upper Pyroxenite and harzburgite in the LUU may show cyclical zoning forming a distinct sawtooth pattern Some plagioclase transects appear to show distinct plagioclase crystals with a compositionally different rim (e.g. 81-1438, plag. 3). There can be some cyclic variation within these distinct crystals, most pronounced in the Upper Pyroxenite. Olivine mela-gabbronorite shows calcium-rich patches that can be singular or multiple across a transect and surrounded by a more sodic rim.

6.6 Summary

Broad comparisons between analysed rock types show there are 3 main compositional groups of orthopyroxene (Figure 6.29). The first group occurs in pyroxenite, harzburgite, lherzolite and olivine mela-gabbronorite and consists of relatively magnesian orthopyroxene with Mg# between 79 and 86. The second group comprises orthopyroxene in rock types containing cumulus plagioclase (norites and anorthosites), which have less magnesian orthopyroxene (67-82 Mg#), whereas the third group comprises orthopyroxene in the Ti-rich olivine gabbro showing the most evolved orthopyroxene composition (64-66 Mg#). Notably, orthopyroxene in norites and anorthosites in UMT081 is significantly more evolved than in UMT094 (Figure 6.29). Conversely there is little difference in pyroxene composition between the 2 drill cores within ultramafic rocks (i.e. pyroxenite, harzburgite and lherzolite).
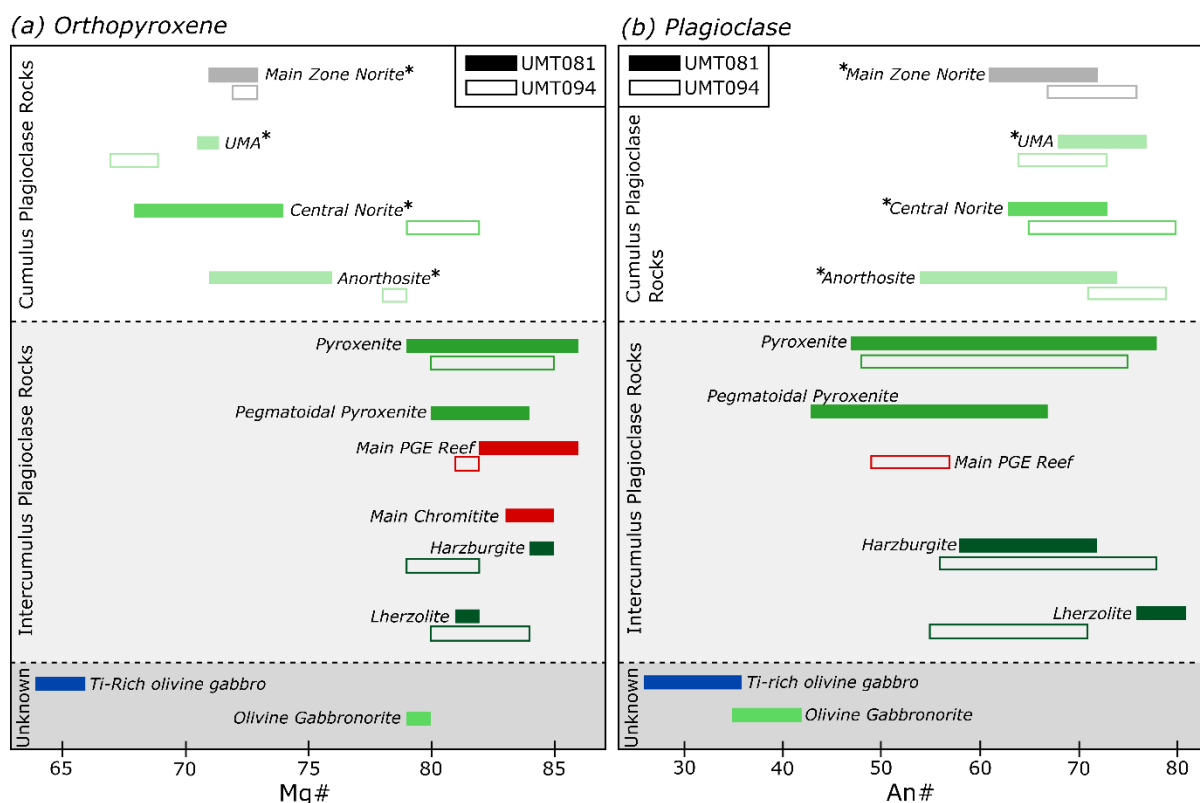
*Figure 6.29: Graphs showing the ranges of orthopyroxene and plagioclase compositions for the different major lithologies in UMT081 and UMT094. Certain lithologies show good correlation in composition between the two drill cores (e.g. pyroxenite), whereas others have contrasting mineral compositions, notably when plagioclase occurs as a cumulus phase (e.g. anorthosite). *denotes cumulus plagioclase lithologies.*

Plagioclase has a much wider range of compositions in each rock type than orthopyroxene. The widest range in An content occurs in pyroxenite and pegmatoidal pyroxenite (Figure 6.29). Norites and anorthosites have the most anorthite rich plagioclase compositions, whereas rocks from the base of the Lower Flatreef (i.e. the Ti-rich olivine gabbro and olivine mela-gabbronorite rocks) have the most sodic compositions. Plagioclase compositional ranges do not show significant variation between the two drill cores, except for lherzolite. The range of plagioclase compositions is larger in pyroxenites where plagioclase is largely interstitial, compared to cumulus plagioclase lithologies. Feldspathic lithologies (norite and anorthosite) tend to have lower Mg# in orthopyroxene but a slightly higher An content in plagioclase in comparison to pyroxenites. In contrast, the rocks of the Lower Flatreef (olivine mela-gabbronorite and the Ti-rich olivine gabbro) have a strikingly different mineral chemistry both from each other and all other rock types within the Flatreef analysed here. Olivine composition is strongly dependent on lithology with little range in olivine composition in individual rock types (Figure 6.30). The exceptions are olivine compositions in wehrlite, which forms 2 distinct

populations and olivine-bearing rocks in the Lower Ultramafic Unit (i.e. harzburgite and lherzolite).
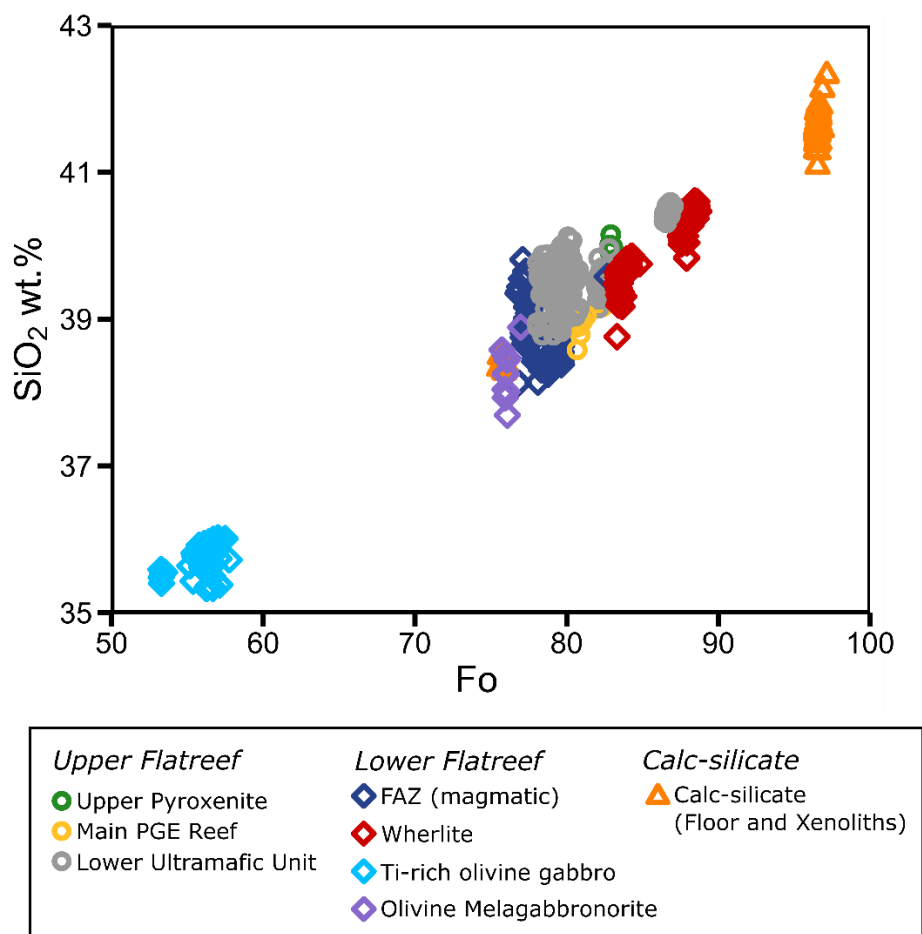
Figure 6.30: Graphs showing the composition of olivine in rocks across the Flatreef. Different rocks types form distinctive clusters of olivine compositions. Calc-silicate metamorphic olivines are the most magnesian whereas the Ti-rich olivine gabbro has the most evolved olivine compositions.

The average compositions of the major silicate minerals of the Upper Flatreef show little systematic variation with depth in the drill core UMT081 (Figure 6.31). The rocks beneath the FAZ show distinctly different mineral composition from each other and rocks of the Upper Flatreef. Pyroxenites in the Upper Pyroxenite Unit show a moderate decrease in Mg# with height. Olivine composition shows a reverse trend with increasingly forsteritic compositions with height, while plagioclase composition remains broadly constant over this sequence.

The composition of pyroxene is strongly dependent on the nature of co-existing plagioclase in the same sample. Where the rock comprises norite and anorthosite with predominantly cumulus plagioclase, the composition of orthopyroxene is significantly less magnesian (68-76 Mg#) than in ultramafic rocks where plagioclase is an intercumulus phase and orthopyroxene has Mg# 79-86 (Figure 6.29, 6.31), most notably in drill core UMT081. Less magnesian

orthopyroxene can occur as a result of fractional crystallisation or the trapped liquid shift effect, with the latter potentially having a greater influence on FeO/MgO ratios, as for example documented in the UCZ of the Bushveld Complex where trapped melt shift can lead to variations in Mg# of up to 10 molar % (Barnes, 1986). In contrast, plagioclase compositions show surprisingly little variation between cumulus and intercumulus domains (Figure 6.29b and 6.31d). Interstitial plagioclase tends to have wider compositional ranges whereas cumulus plagioclase has a narrower compositional range which tends to be marginally more calcic.
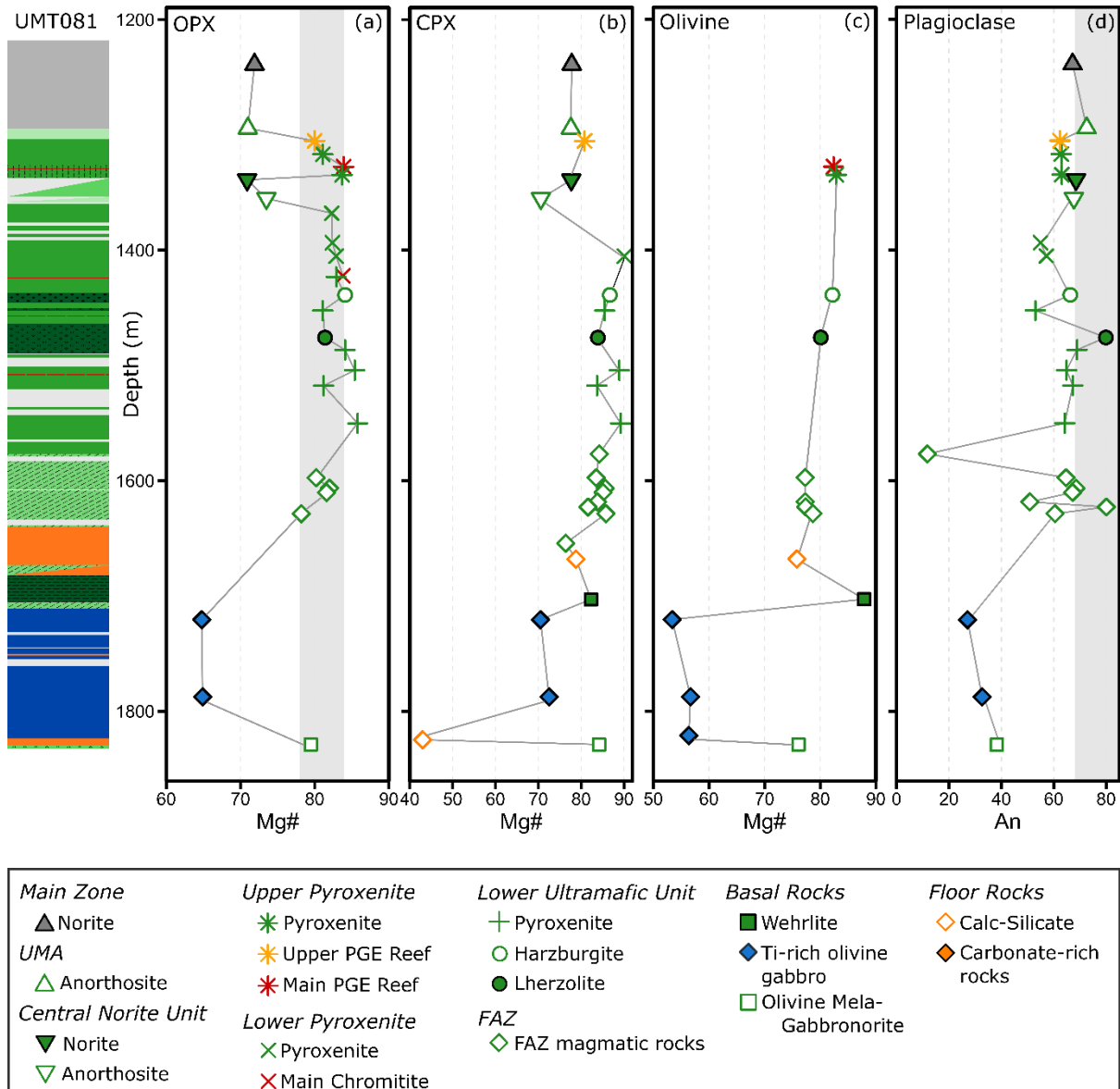
Figure 6.31: Graph of average silicate mineral compositions in drill core UMT081. There is little systematic difference in mineral composition downhole with rocks of the Lower Flatreef displaying more exotic compositions relative to the Upper Flatreef. Grey shading represents range of mineral compositions in the UCZ of the WBC (Eales and Cawthorn, 1996). Note rocks containing cumulus plagioclase are indicated by filled and open triangles.

Chapter 7 – Lithophile Elements of the lower Main Zone, Flatreef and sedimentary rocks

In this chapter the whole rock major and trace element compositions of 66 samples from the lithologies have been determined. These analyses cover igneous, sedimentary and metamorphic rocks. These data can be used to determine processes governing the formation of the Flatreef, including contamination by country rocks, magma mixing and fractional crystallisation. Whole rock geochemical data can also be applied to evaluating the correlation of the Flatreef with the Platreef in the northern limb and the remainder of the Bushveld Complex.

7.1 Compositional variation with depth

7.1.1 Drill Core UMT081

Rocks comprising the Upper Flatreef are characterised by cyclic downhole variations in major and trace element concentrations. Olivine and pyroxene rich rocks of the Upper Pyroxenite, Lower Pyroxenite and Lower Ultramafic Unit have higher MgO contents (but lower CaO, Al_2O_3, Na_2O and K_2O contents) than plagioclase rich norites and anorthosites. The Upper Pyroxenite shows increasing MgO with depth (and corresponding decreases in CaO, Al_2O_3, Na_2O and K_2O), whereas the Lower Pyroxenite has broadly constant major and minor element oxide contents. In contrast, the Lower Ultramafic Unit shows highly variable contents of MgO and other oxides (Figure 7.1, Figure 7.2).

Incompatible trace elements such as Zr and Sm show a broad trend of increasing contents upwards through the Flatreef. However, on a smaller scale there can be reversals such as the upward decrease in Zr within both the Upper and Lower Pyroxenites (Figure 7.4). Of particular note is that the Main PGE Reef contains the some of the highest Zr contents. Other trace elements show less systematic variation, either because they are largely controlled by cumulus minerals (e.g. Cr in pyroxene and chromite, and Sr in plagioclase) or because they are fluid mobile (e.g. Rb). Levels of LOI and CO_2 show no systematic trends (generally ≤ 2% and ~1%, respectively) (Figure 7.5).

The Lower Flatreef show relatively variable trace element contents, likely reflecting the enhanced contamination with crust, as reflected in the presence of abundant country rock xenoliths. Within the FAZ there is a broad upward increase in MgO, SiO_2, K_2O and Rb contents with corresponding decrease in CaO wt.% (Figure 7.1, Figure 7.2). Levels of Sr, Sm and Zr are highly erratic (Figure 7.4). The Ti-rich olivine gabbro has anomalously high concentrations of Na_2O, Fe_2O_3 and TiO_2, distinguishing these rocks from all other magmatic and sedimentary rocks analysed (Figure 7.2, Figure 7.3). In contrast to the overlying FAZ rocks, the Ti-rich

olivine gabbro shows a progressive downhole increase in Sm and Zr concentrations (Figure 7.4). The wehrlite and olivine mela-gabbronorite have major and minor oxide as well as trace element contents largely comparable to the overlying magmatic rocks of the Upper Flatreef, although wehrlite is significantly richer in MnO and Fe_2O_3. `
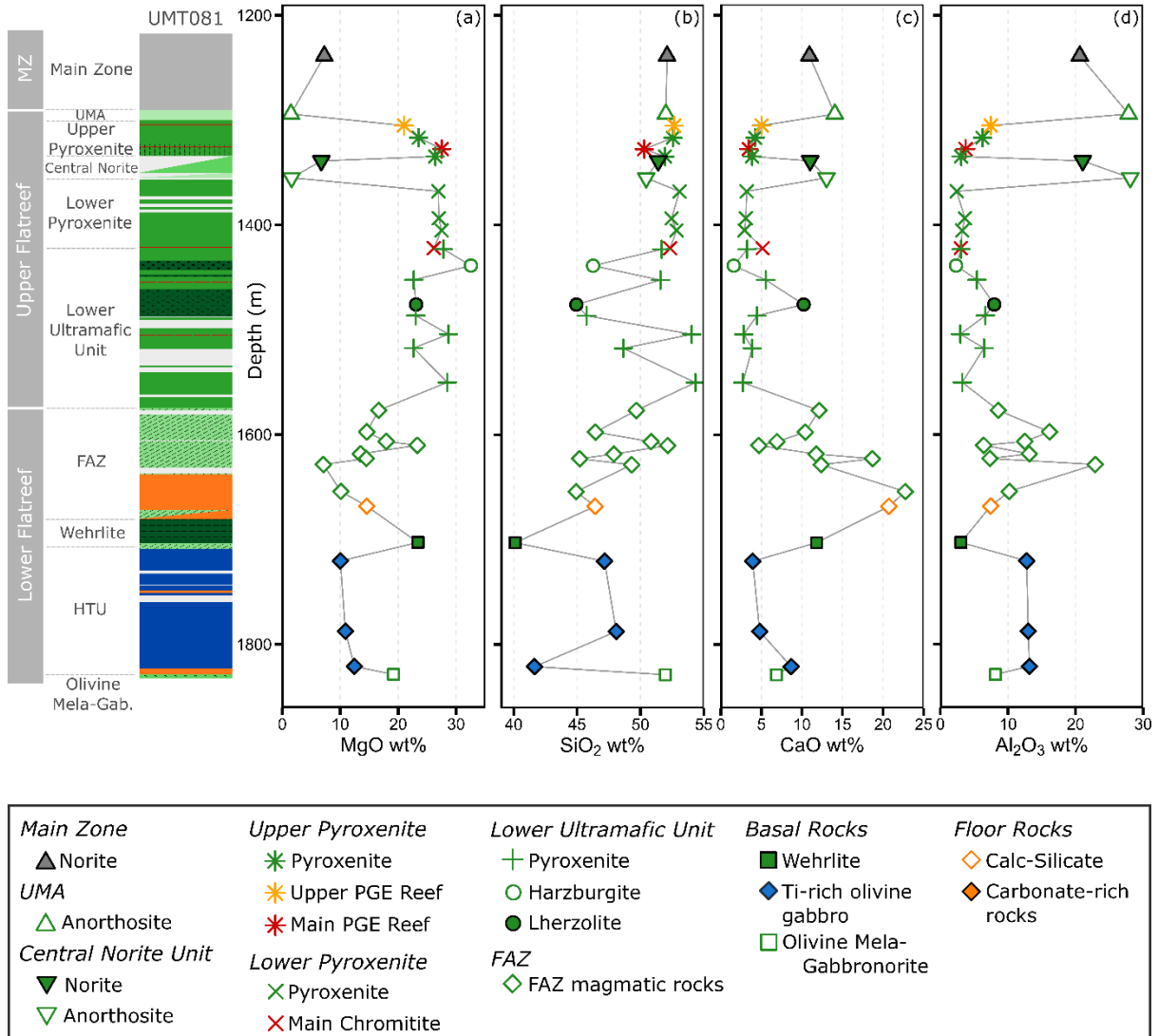
Figure 7.1: Downhole plots of drill core UMT081 of major element oxides. (a) MgO, (b) SiO_2, (c) CaO, (d) Al_2O_3.
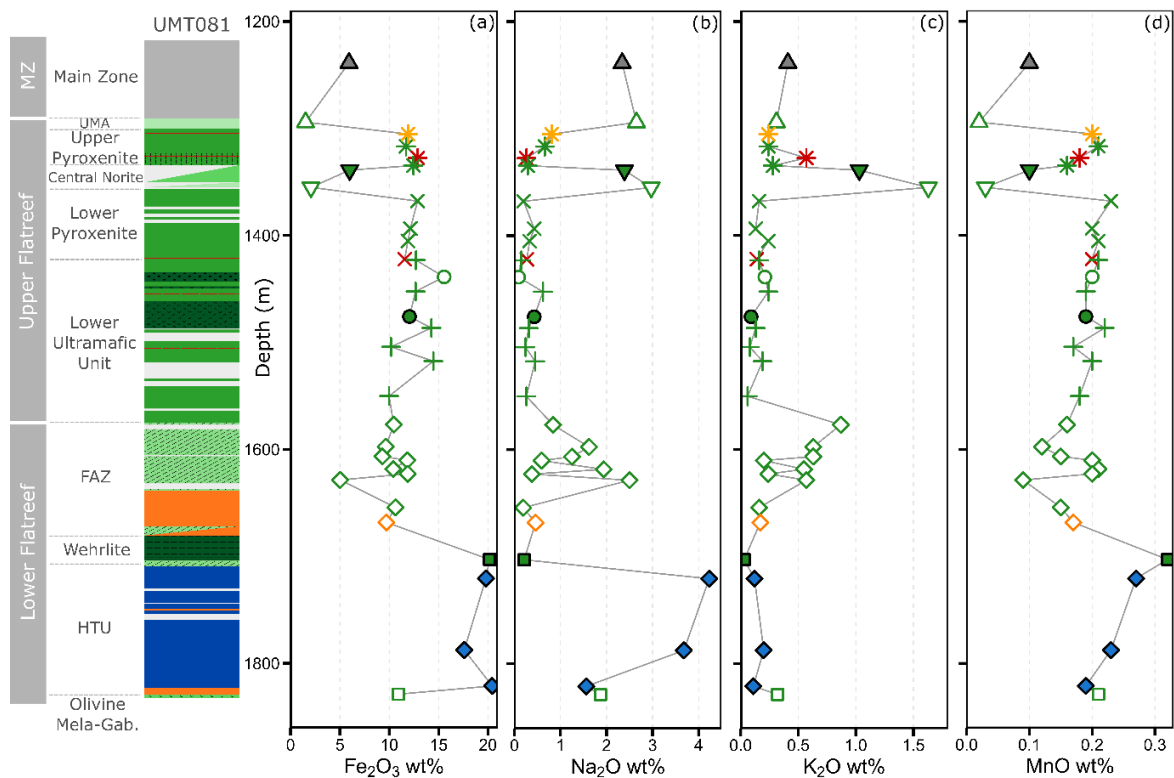
Figure 7.2: Downhole plots from drill core UMT081 of major oxides. (a) Fe_2O_3, (b) Na_2O, (c) K_2O, (d) MnO.
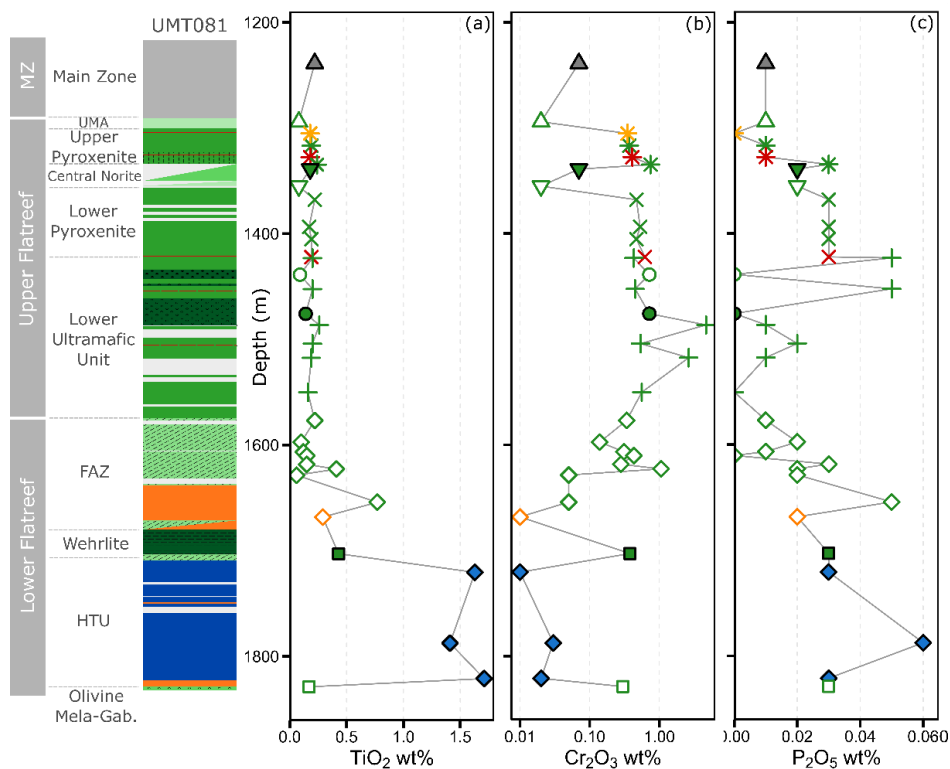
Figure 7.3: Downhole plots from drill core UMT081 of minor element oxides. (a) TiO_2, (b) Cr_2O_3, (c) P_2O_5.
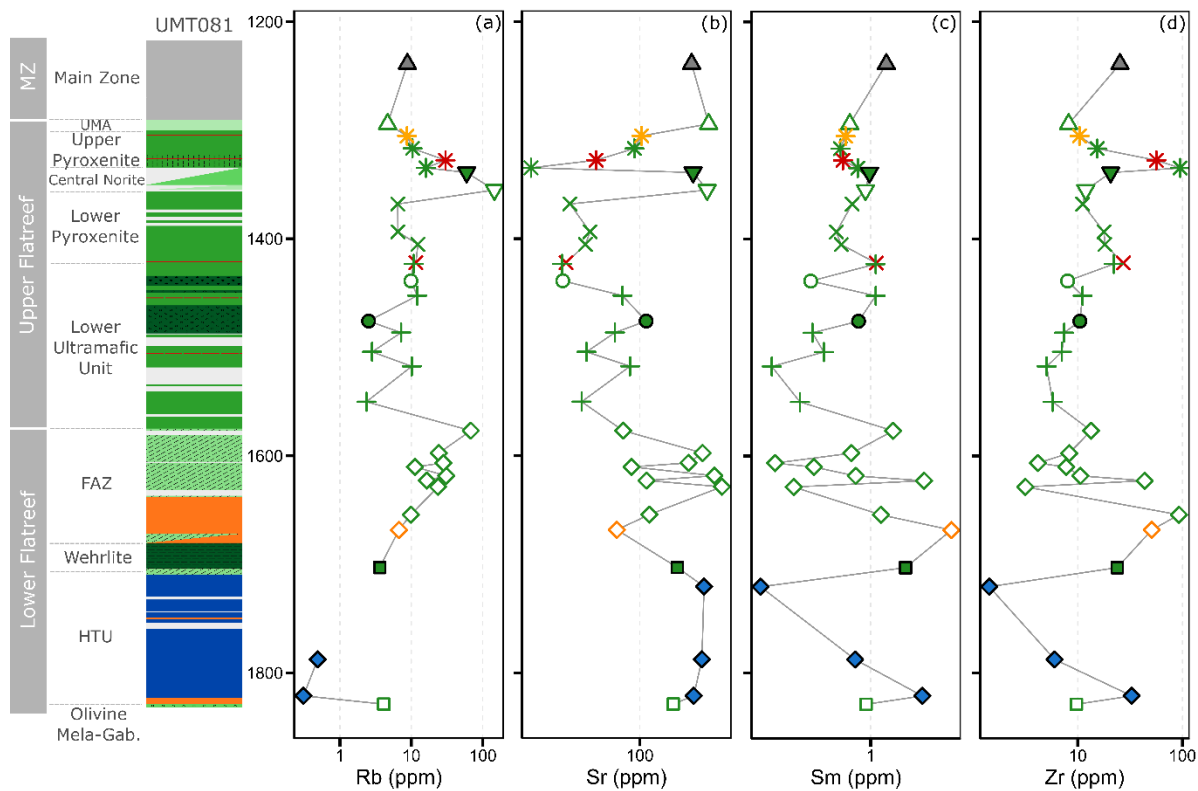
Figure 7.4: Downhole plots of trace elements in drill core UMT081. (a) Rb, (b) Sr, (c) Sm, (d) Zr.
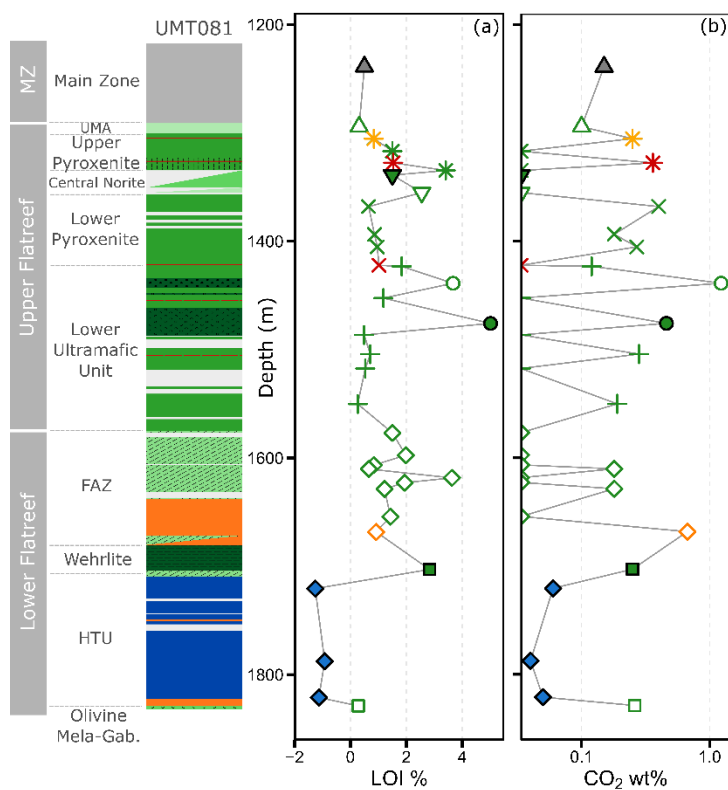
Figure 7.5: Downhole plots of volatile components in drill core UMT081. (a) LOI, (b) CO_2. Note that the negative LOI values for the Ti-rich olivine gabbro is likely due to FeO-Fe_2O_3 oxidation.

7.1.2 Drill Core UMT094

The data from drill core UMT094 show certain similarities to UMT081, such as the strong cyclicity in many elements, largely reflective cumulate control, the relatively constant MgO levels in the ultramafic rocks, and the upward increases in many incompatible elements such as K_2O, Na_2O, Rb, Zr and Sm (Figure 7.6, Figure 7.7, Figure 7.8).

The lower third of the drill core intersected carbonate floor rocks, which contain elevated MgO, CaO, LOI and CO_2 but low concentrations of most other oxides. The LOI of the carbonates increases downhole with increasing distance from the magmatic rocks, potentially reflecting progressively less metamorphism (Figure 7.9). One calc-silicate sample (94-1468) is anomalously rich in Fe_2O_3 and is also characterised by low LOI, CO_2 and CaO due to its magnetite content (Figure 7.10).
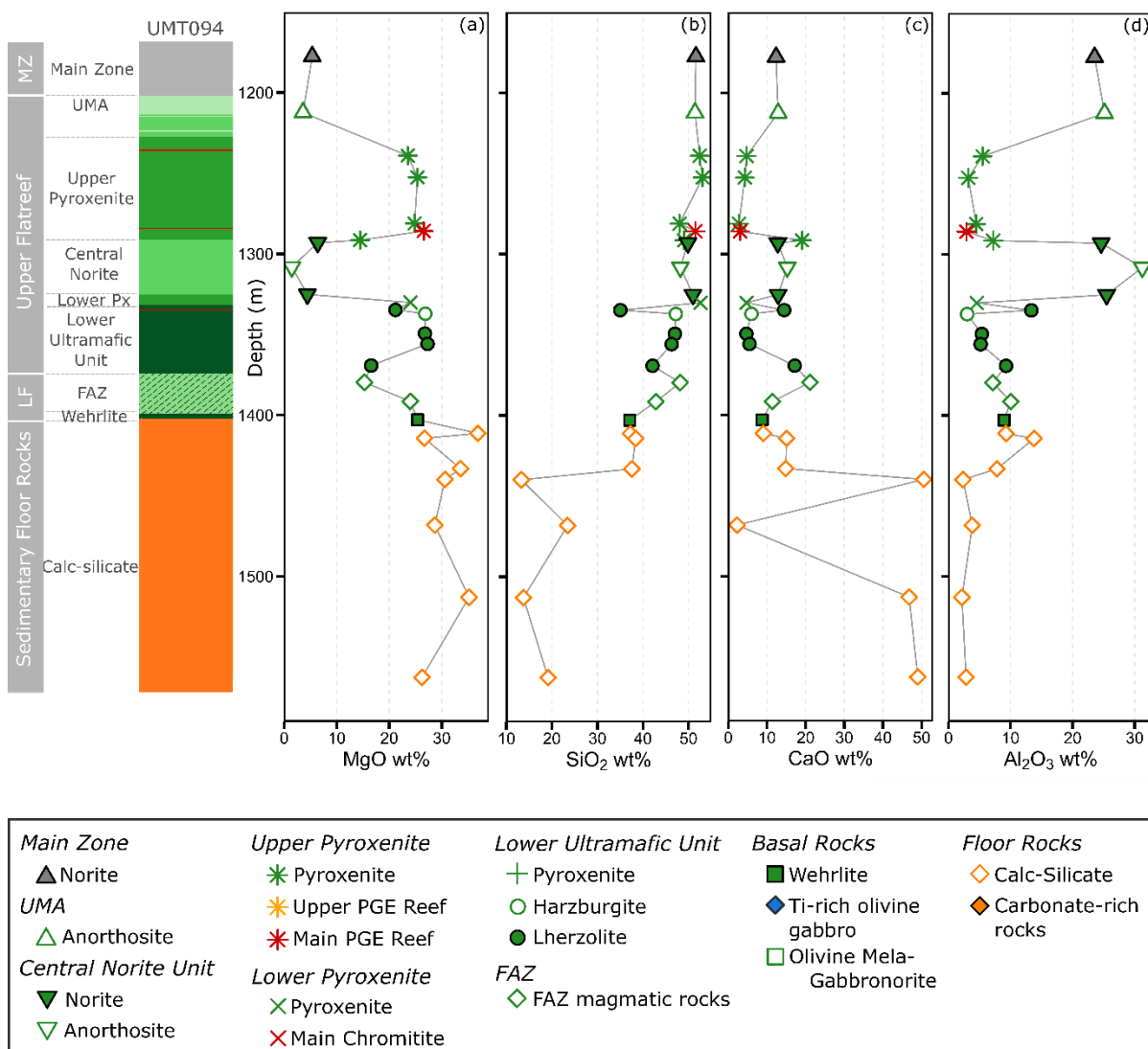
Figure 7.6: Downhole plots of data from drill core UMT094 of major element oxides. (a) MgO, (b) SiO₂, (c) CaO, (d) Al₂O₃.
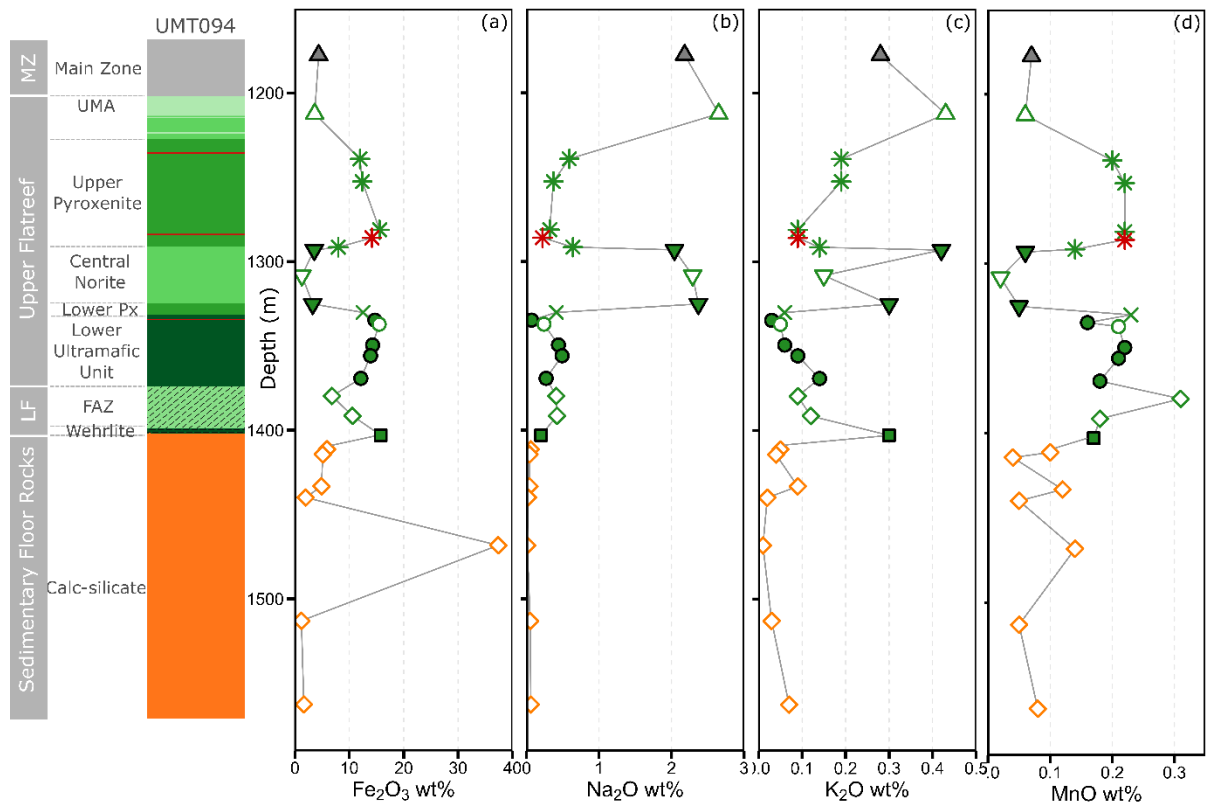
Figure 7.7: Downhole plots of major element oxides from drill core UMT094. (a) Fe_2O_3, (b) Na_2O, (c) K_2O, (d) MnO.
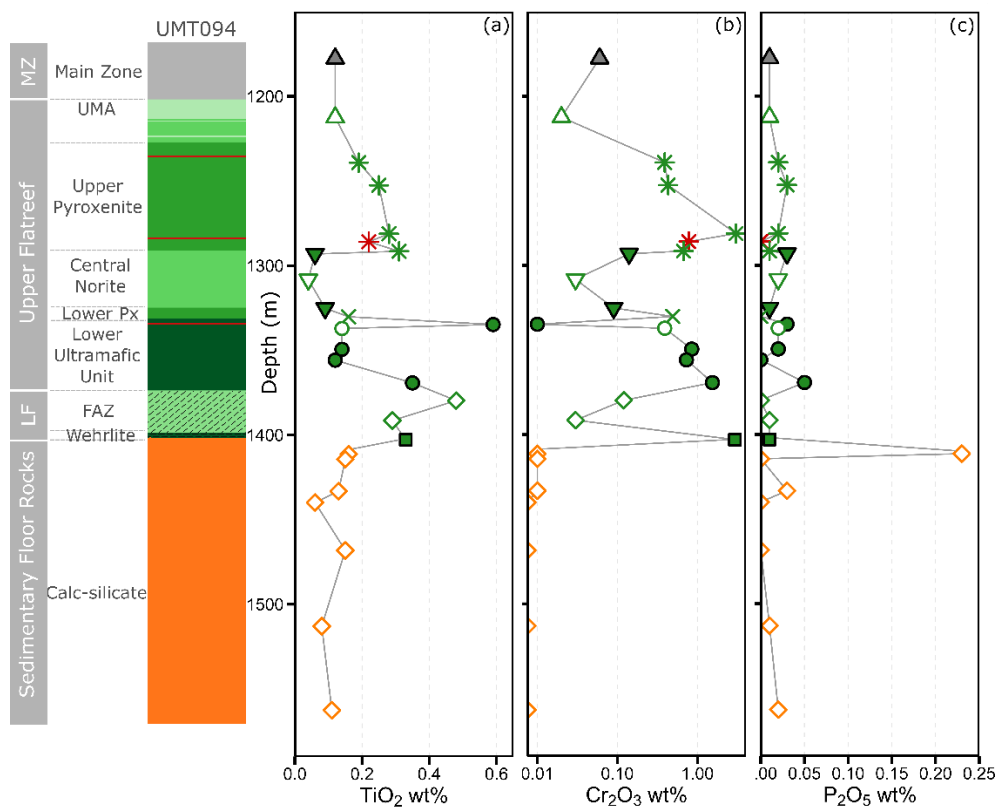
Figure 7.8: Downhole plots of minor element oxides from drill core UMT094. (a) TiO_2, (b) Cr_2O_3, (c) P_2O_5.
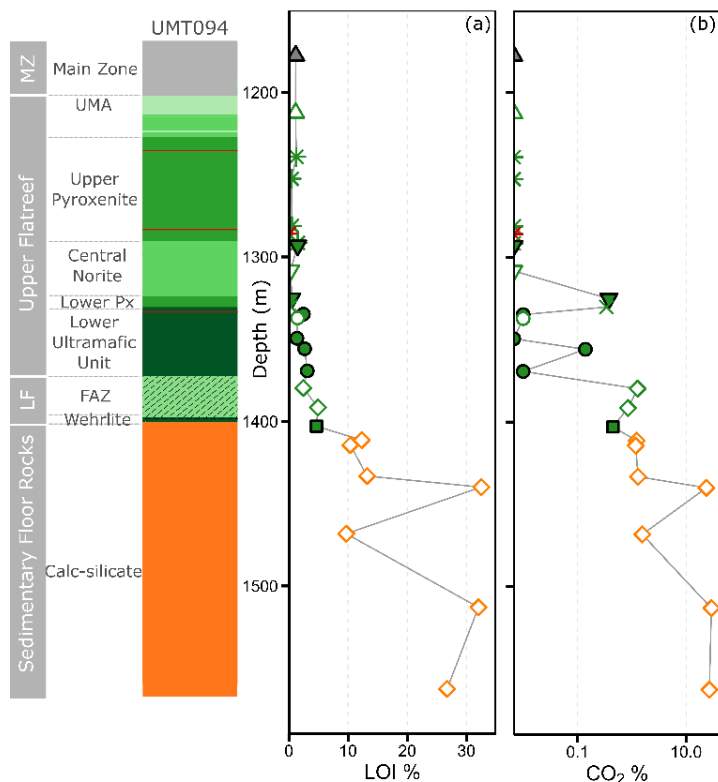
Figure 7.9: Downhole plots of volatile components of drill core UMT094. (a) LOI, (b) CO₂. Samples closest to magmatic rocks have the lowest LOI and CO₂ contents.
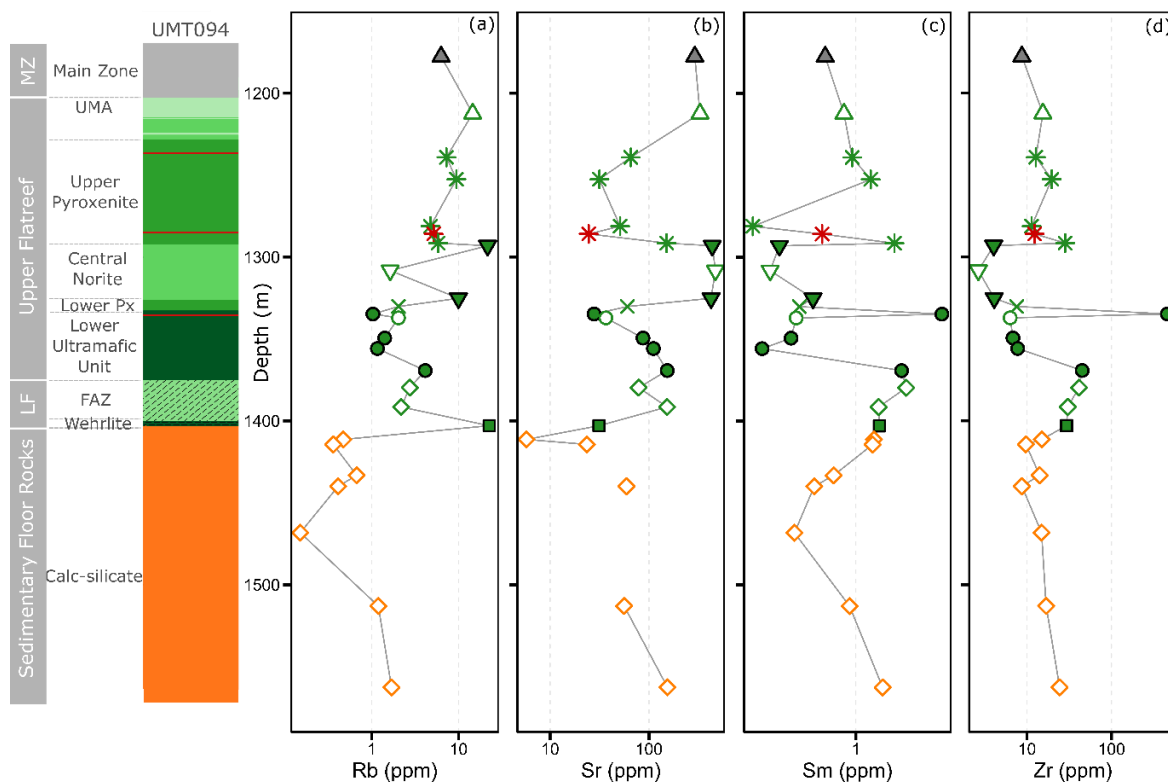
Figure 7.10: Downhole plots of trace elements from drill core UMT094. (a) Rb, (b) Sr, (c) Sm, (d) Zr. Note the similarities between Sm and Zr downhole.

7.2 Major and minor element oxides

Concentrations of major element oxides (Al_2O_3, CaO, MgO, SiO_2, Fe_2O_3, Na_2O, K_2O) plotted against MgO (wt.%) show large variability reflecting the different rock types in this study (Figure 7.11). In magmatic rocks, Al_2O_3, CaO and Na_2O decrease with increasing MgO, while Fe_2O_3 increases, which is largely a function of the relative modal proportions of plagioclase, pyroxene and olivine. Lherzolitic and wehrlitic rocks have relatively high CaO and low SiO_2 compared to other ultramafic rocks, resulting from the abundance of Ca-rich clinopyroxene and Si-poor olivine. Wehrlite is rich in Fe_2O_3 which is attributed to abundant sulphide and chromite. Ultramafic rocks generally show good positive correlations between MgO (wt.%) and Cr_2O_3 and MnO, with rocks from the Lower Ultramafic Unit particularly rich in Cr_2O_3 (Figure 7.12). Chromium readily partitions into clinopyroxene and orthopyroxene (K_D of 34 and 10, respectively; Table 7.1) as well as forming chromite, resulting in higher Cr_2O_3 contents in clinopyroxenite-rich wehrlite and lherzolite relative to orthopyroxenites. Ultramafic rocks are modestly rich in TiO_2 (max. 0.59 wt.%). Rocks from the FAZ have more variable compositions (e.g., MgO 7.08-24.01 %) than pyroxenites (Figure 7.12).

Plagioclase rich rocks (i.e., norite and anorthosite) have high Al_2O_3, Na_2O contents and sometimes K_2O relative to other magmatic rocks (Figure 7.11). The major oxide compositions of norite from the Main Zone and the Central Norite Unit overlap. Similarly, major oxide compositions of anorthosite from the UMA and the Central Norite Unit overlap, although the latter can have more variable K_2O and Na_2O composition. Norite and anorthosite from different units have similar minor oxide (Cr_2O_3, MnO, TiO_2, P_2O_5) compositions (Figure 7.12), with low but increasing Cr_2O_3, MnO and TiO_2 contents with increasing MgO (wt.%), due to control by pyroxene abundance. The Ti-rich olivine gabbro has distinct compositions, with elevated Fe_2O_3, Na_2O, MnO and TiO_2 and lower CaO contents compared to other magmatic units, due to elevated ilmenite-magnetite and sodic plagioclase contents (Figure 7.11).

Calcareous sediments and calc-silicate rocks have high MgO contents and significantly lower Fe_2O_3, SiO_2, Na_2O and K_2O contents than the magmatic rocks (Figure 7.11). The Al_2O_3, SiO_2 and CaO contents of these rocks are highly variable, with CaO rich rocks correspondingly poor in SiO_2, most likely as a function of the proportion of detrital material present. These rocks have the highest volatile component of any rock type in this study with a maximum weight loss on ignition (LOI) of 45.26 % (Figure 7.12). While there is no clear relationship between LOI and MgO, magmatic rocks with higher olivine contents (i.e., wehrlite, lherzolite and harzburgite) tend to have marginally higher LOI resulting from serpentinisation of olivine. Both calcareous sediments and calc-silicates are Cr_2O_3 poor. Calc-silicates are generally poor in MnO whereas calcareous sediments are rich in MnO and both rocks can be rich in P_2O_5 compared to magmatic rocks, although there is considerable in composition. Calc-silicate has

consistently low TiO₂ contents, whereas calcareous sediments can be variably richer and poorer in TiO₂ relative to the magmatic rocks.
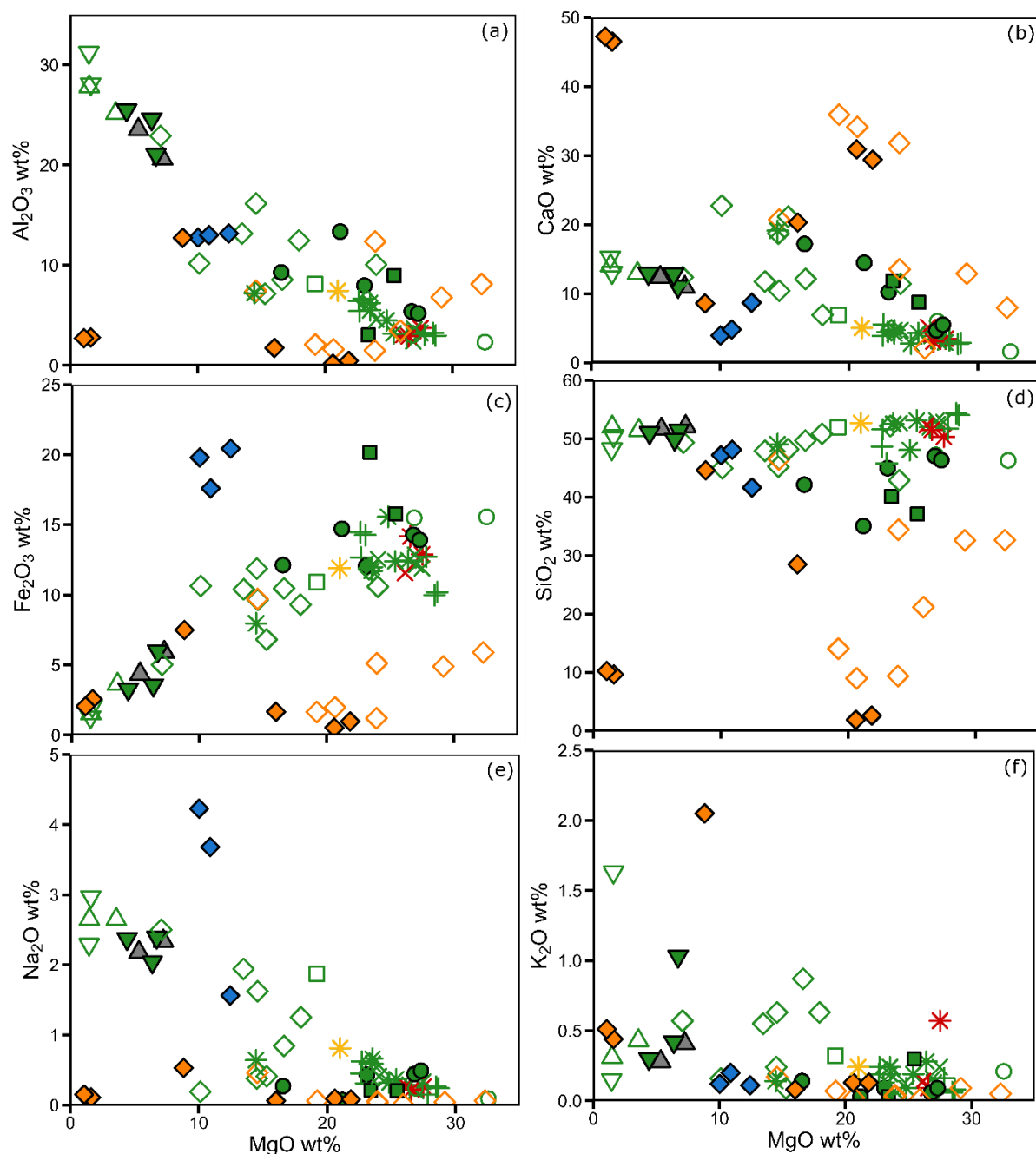
Figure 7.11: Bivariate plots of element oxides against MgO wt.%. (a) Al₂O₃, (b) CaO, (c) Fe₂O₃, (d) SiO₂, (e) Na₂O, (f) K₂O. Calc-silicate and especially calcareous sediments have a wide range of MgO contents and variable concentrations of all major element oxides.
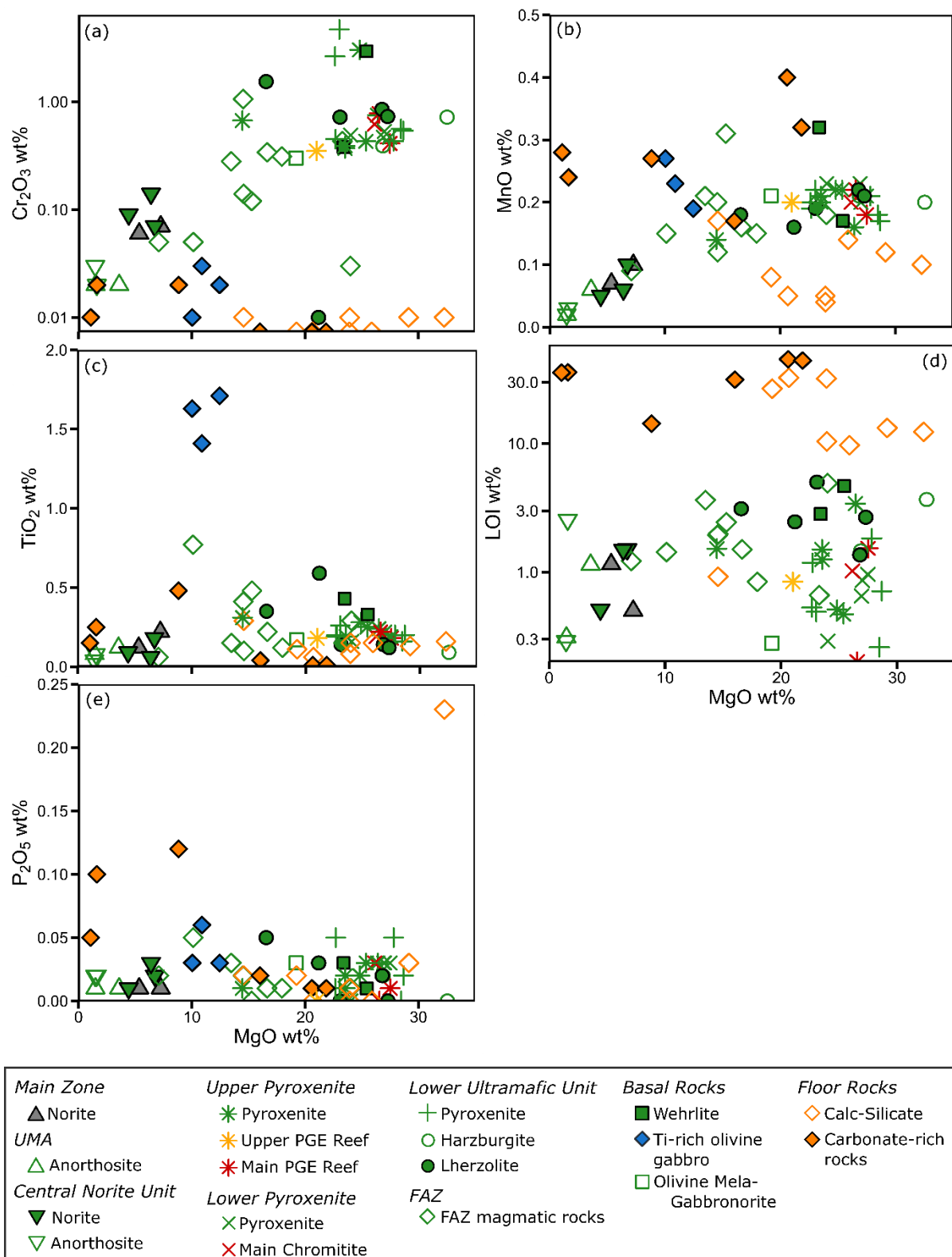
Figure 7.12: Bivariate plots of minor element oxides and LOI against wt.% MgO. (a) Cr$_2$O$_3$, (b) MnO, (c) TiO$_2$, (d) LOI, (e) P$_2$O$_5$. Calcareous sediments and calc-silicate samples are easily identified by their high LOI, an order of magnitude greater than in the magmatic rocks. Ti-rich olivine gabbro has significantly higher TiO$_2$ concentrations compared to magmatic rocks.

7.3 Trace elements

Magnesium concentration in magmatic Flatreef rocks is positively correlated with Sc, V and Zn, reflecting the control of these elements mainly by pyroxene (Figure 7.13). The Sc contents of olivine bearing rocks are slightly lower than those of pyroxenites, largely due to the higher D values of Sc for pyroxene over olivine (Table 7.1). In contrast, V, Pb and Zn contents broadly overlap.

Sr concentrations correlate negatively with increasing MgO (wt.%). Sr (and to a lesser degree La) partitions preferentially into plagioclase and is therefore richer in anorthosites and norites (Figure 7.14). In contrast, Zr, Rb and REE are incompatible in all major silicate minerals (with the exception of HREE into olivine) and therefore show no clear correlation with MgO content. In contrast, Zr and Y show a good positive correlation, likely reflecting control of both elements by trapped melt (Figure 7.14f, Table 7.1).

Partition Coefficients Basalt and Basaltic andesite liquids

	Olivine	Orthopyroxene	Clinopyroxene	Plagioclase	Magnetite
V	0.06	0.6	1.35		26
Sc	0.17	1.2	1.7-3.2	2.2-4.2	
Cr	0.7	10	34		153
Mn	1.45	1.4	0.3-1.2		
Rb	0.0098	0.022	0.031	0.071	
Sr	0.014	0.04	0.06	1.83	
Ti	0.02	0.1	0.4	0.04	7.5
Zr	0.012	0.18	0.1	0.048	0.1
La	0.0067		0.056	0.19	1.5-3
				0.1477	
Lu	0.0454	0.42	0.506	0.053	
	0.016		*0.56*	*0.067*	
				0.0232	

Table 7.1: Table of partition coefficients (Mineral/Melt) for basalt to basaltic-andesite melts (Rollinson, 1993). Numbers in italics represent alternative values.
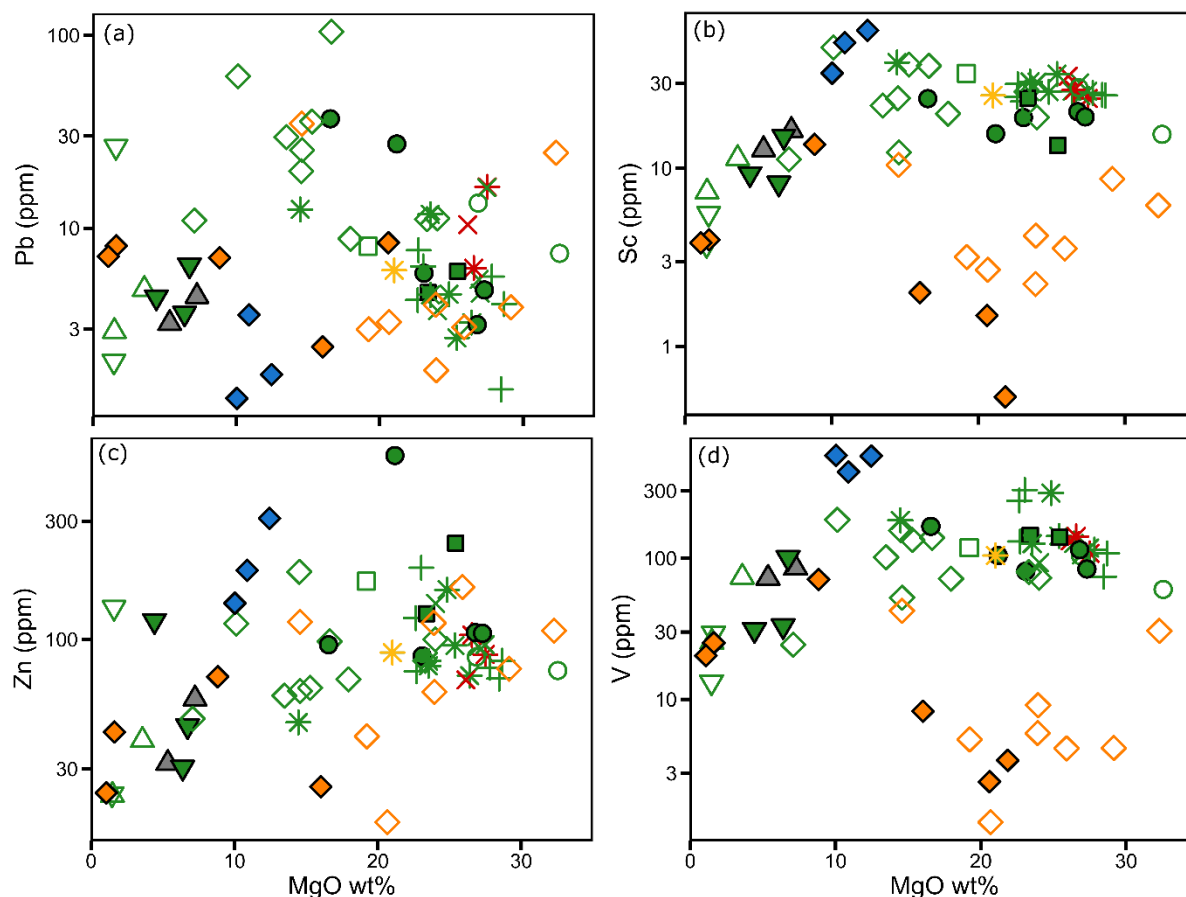
Figure 7.13: Bivariate plots of trace metals against MgO. (a) Pb, (b) Sc, (c) Zn, (d) V. Calcareous sediments and calc-silicate samples are generally poorer in trace metals compared to magmatic rocks.

The Ti-rich olivine gabbro has moderately elevated Zn, Sc and V relative to other magmatic rocks likely reflecting the presence of clinopyroxene. Lead and Rb are poor in the Ti-rich olivine gabbro relative to other lithologies, both elements are strongly mobile in fluids (Figure 7.13, Figure 7.14, Table 7.1). Calcareous sediments and calc-silicate rocks are poorer in V and Sc, but have variable concentrations of Zn, Sr and Pb.
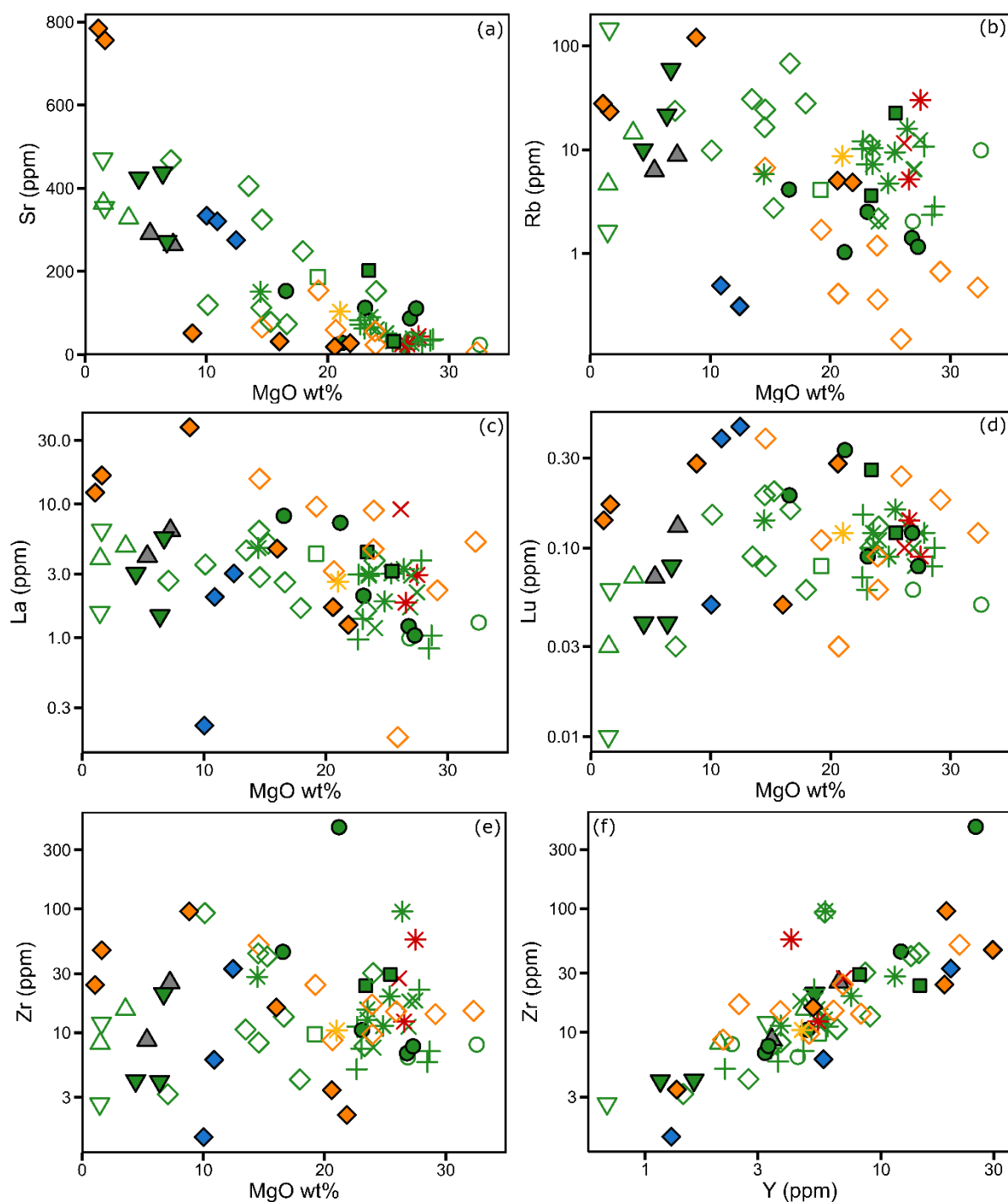
Figure 7.14: Bivariate plots of trace elements against MgO. (a) Sr, (b) Rb, (c) La, (d) Lu, (e) Zr, (f) Zr vs. Y. Note the strong correlation between Zr and Y. In contrast there is no concentration between La, Lu and MgO.

Rare earth element patterns of the rocks are plotted in Figure 7.15. Pyroxenite patterns show good overlap with equivalent rocks from the UCZ of the WBC (Maier et al., 2013). The patterns are moderately fractionated and slightly richer in LREE relative to HREE. The rocks of the Main PGE Reef overlap with other pyroxenites but the Main Chromitite is markedly richer in

LREE. Harzburgite and lherzolite have generally relative flat patterns, broadly similar to those of pyroxenites, but have strongly variable REE concentrations (Figure 7.15b).

Anorthosites and norites have broadly similar patterns with pronounced positive slopes from HREE to LREE and strong positive Eu anomalies. However, there is significant variability in their HREE patterns, most notably in anorthosite of the Central Norite Unit. Main Zone norite has similar REE and multi-element spider diagram patterns to norites in the Central Norite Unit, although the latter rocks can have lower overall concentrations of REE (Figure 7.15a,d; Figure 7.16a). Wehrlite and olivine mela-gabbronorite have broadly similar patterns to pyroxenites, albeit at shallower slopes. The Ti-rich olivine gabbro have highly variable REE concentrations with flat or trough-shaped REE patterns and a strong positive Eu anomaly. This is notable for a relatively differentiated rock. In addition, the Ti-rich olivine gabbro lacks a negative Nb-Ta anomaly in multi-element spider diagrams, which is characteristic of all other magmatic rocks studied (Figure 7.16).

Rocks from the FAZ have broadly similar REE patterns to pyroxenites although the former can have higher overall REE concentrations (max. Lu = 15.47 ppm). Calcareous sediments from the Duitschland Formation have the highest REE contents (max. Lu = 37.57 ppm) and have fractionated patterns similar to the calc-silicate rocks. In comparison, calcareous sediments from the Malmani subgroup has highly irregular REE patterns (Figure 7.15), but with generally lower REE contents. The high incompatible trace element contents of many calcareous sediments and calc-silicate rocks relative to most magmatic rocks is also apparent in multi-element spidergrams (e.g. U; Figure 7.16e, h).
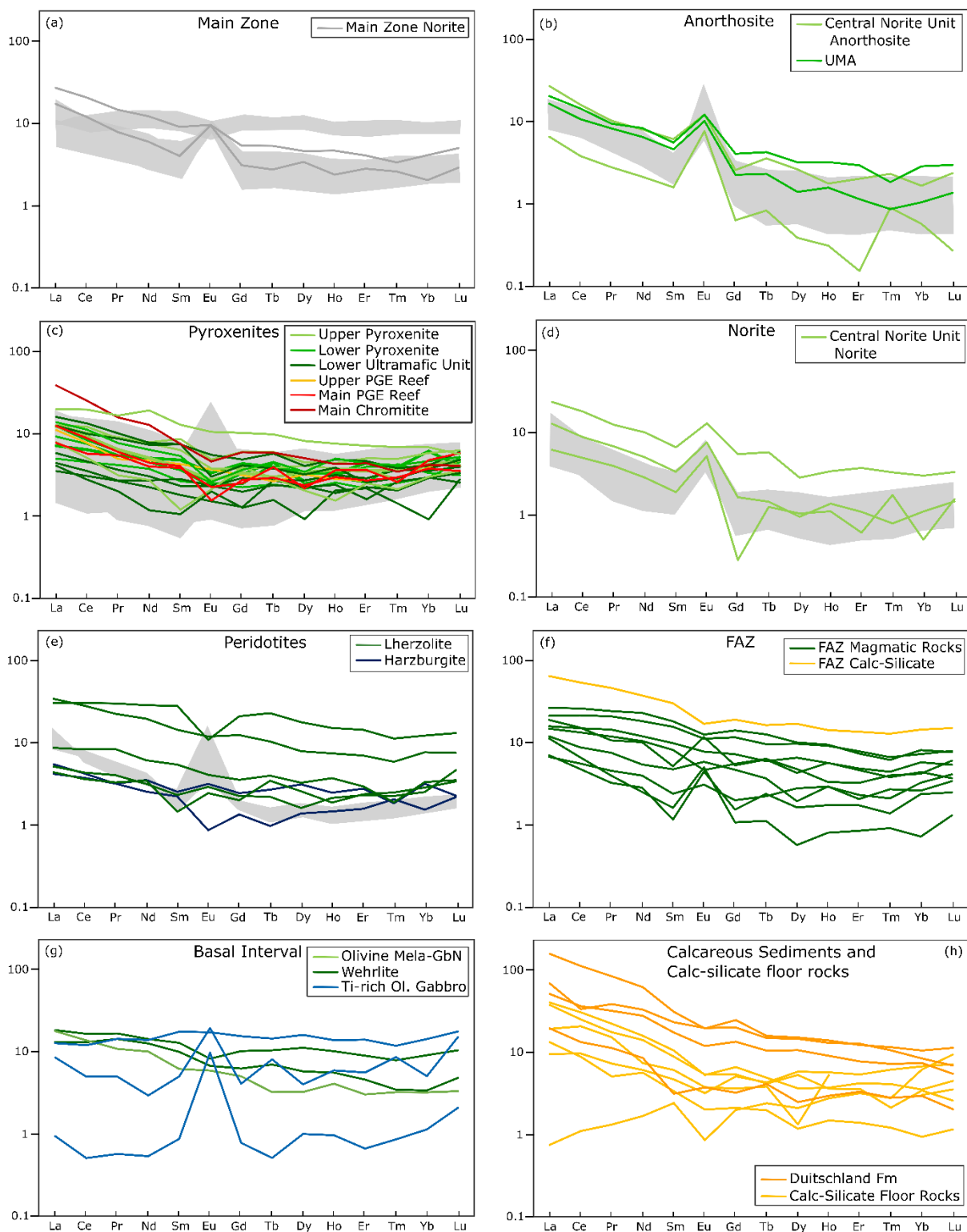
Figure 7.15: Chondrite normalized REE diagrams. Grey shaded areas are data from the WBC (Maier et al., 2013). Note that there is generally good overlap between data from this study and the WBC, except for harzburgite and lherzolite which show no resemblance to harzburgite data from the WBC. Normalized to CI Chondrite data from McDonough and Sun (1995).
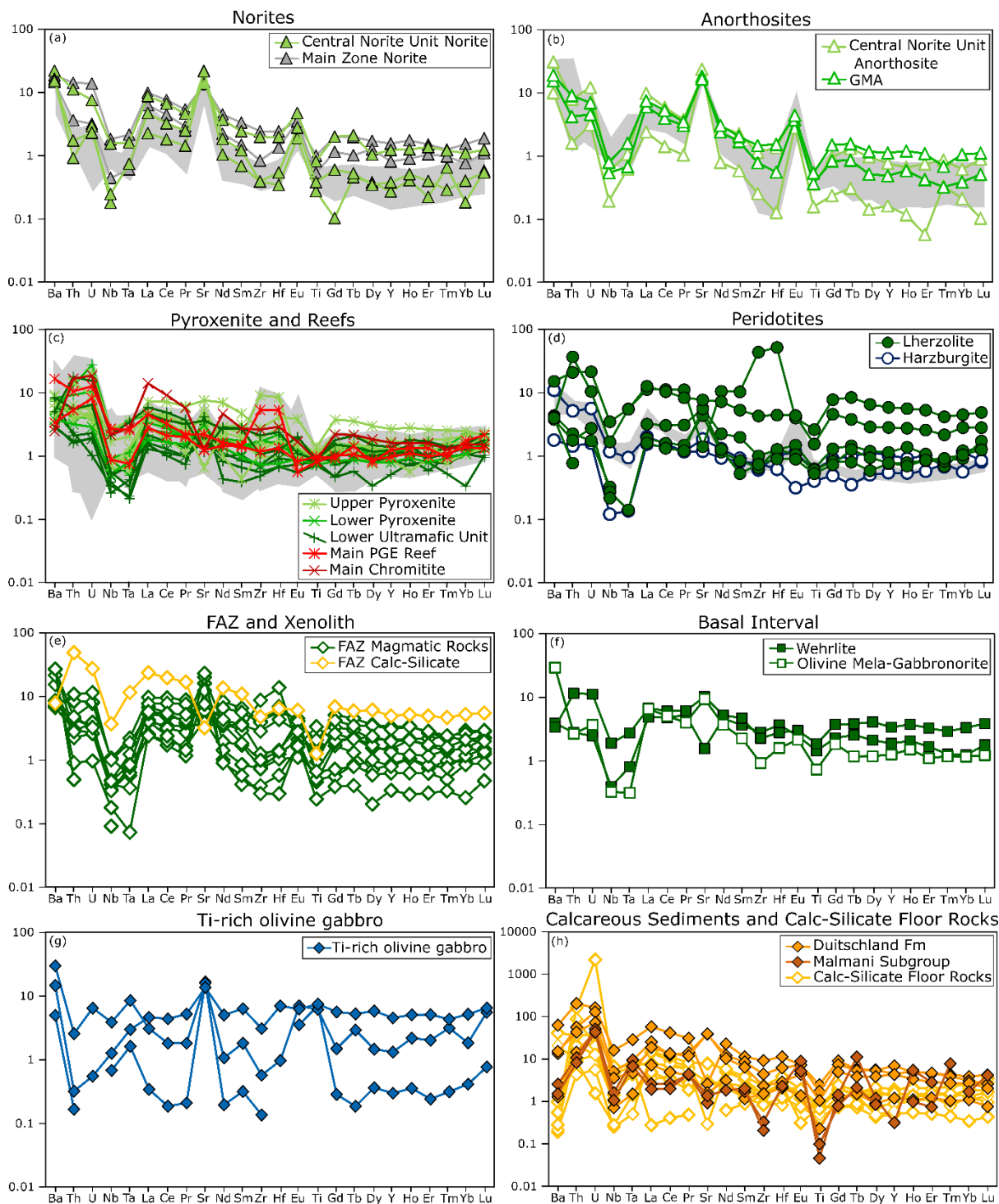
Figure 7.16: Multi-element spider diagrams of rocks from this study. Note the scale change of figure h, because calcareous sediments and calc-silicate rocks can be richer in trace elements by up to two orders of magnitude in comparison to magmatic rocks. Grey fields represent data from the UCZ of the Western Bushveld Complex (Maier et al., 2013). Data normalized to primitive mantle of McDonough and Sun (1995).

Chapter 8 - Chalcophile Elements of the lower Main Zone, Flatreef and sedimentary rocks

The Flatreef is one of the world's largest PGE resources and consequently it is imperative to document the variation in concentration of chalcophile elements both through the thickness of the Flatreef intrusion and along strike. The following chapter documents whole rock chalcophile element data acquired for the samples from drill cores UMT081 and UMT094. In addition, assessment of PGE concentrations across the Flatreef, in conjunction with other data presented in this thesis, will provide useful insight to build a model for the origin formation of the mineralization in the Flatreef.

8.1 Stratigraphic variation

8.1.1 Drill Core UMT081

There is a broad overall pattern of decreasing concentration downhole for all PGE, Au, Ni and Cu. The highest PGE concentrations found in the Main PGE Reef (max. 12,573 ppb Pt, 8377ppb Pd; Figure 8.1, Figure 8.2), with richer PGE contents in the Upper PGE Reef. The pyroxenite rocks that form the hangingwall of the Main PGE Reef are PGE poor compared to the pyroxenites in the footwall. The Central Norite Unit is PGE poor relative to the overlying pyroxenites, reflecting a general trend of poorer PGE contents in mafic rocks relative to ultramafic rocks seen in this drill core. The Ni and Co concentrations in these rocks are also significantly lower than in ultramafic rocks (Figure 8.4).

The Lower Pyroxenite Unit and the upper portion of the Lower Ultramafic Unit show a steady decrease in chalcophile element concentration downhole. In contrast to the Main PGE Reef, the Main Chromitite is only richer in IPGE+Rh relative to the surrounding pyroxenites which also manifests itself in relatively low Pd/Ir, Pt/Ir and PPGE/IPGE ratios compared to the rest of the Lower Pyroxenite unit (Figure 8.3, Figure 8.4). Pyroxenites in the lower portion of the Lower Ultramafic Unit have erratic PGE concentrations.

FAZ rocks have lower PGE contents than the overlying magmatic rocks, with a broad downhole decrease in PGE concentrations, albeit with more scatter than in the other units (221 ppb Pt at the top, 10 ppb Pt at the base, Figure 8.2). The FAZ Unit has the highest PPGE/IPGE ratios of any rocks in drill core UMT081, decreasing steadily downhole (Figure 8.2). The Ti-rich olivine gabbro has relatively low PGE concentrations. Samples from the lower section of the Ti-rich olivine gabbro have the highest Pt/Pd ratios (9.85) of all analysed rocks in drill core UMT081 and elevated Pt/Ir ratios (max. 101.29).

In contrast to the downhole decreases in PGE, Ni and Cu concentration, S concentration steadily increases downhole (Figure 8.4). In contrast, Pd/Ir decreases steadily downhole throughout the Upper Flatreef (Figure 8.3), but the top of the FAZ has higher Pd/Ir ratios than overlying magmatic rocks. The Ti-rich olivine gabbro and wehrlite rocks also show downhole decreases in Pd/Ir. Pt/Ir ratios show broadly the same downhole patterns as Pd/Ir, except for the FAZ and the Ti-rich olivine gabbro. PPGE/IPGE downhole plots also show broadly similar patterns to Pd/Ir. Pt/Pd progressively decreases downhole, with the exception of the Ti-rich olivine gabbro which shows sharply higher Pt/Pd. Downhole plots of Au/Pd show similar patterns, albeit with greater scatter.

Cu and Ni concentrations broadly decrease downhole, but with similarly erratic patterns in the Lower Ultramafic Unit and Upper Pyroxenite as seen in the S data. Cu/Ni ratios broadly increase downhole, although within the Lower Ultramafic Unit and Ti-rich olivine gabbro, greater variability in Cu/Ni ratios is accompanied by a localised decrease in Cu/Ni downhole (Figure 8.5). This overall trend of downward increasing Cu/Ni could reflect MSS fractionation, or enhanced mobility of Cu in fluids, as will be discussed in a later chapter. Cu/Pd shows contrasting trends across the studied interval, above the Main PGE the ratio shows an upward increasing trend but steadily decreases with depth below the Central Norite Unit (Figure 8.5).

The metal tenors of the sulphides (as represented by Cu/S and Ni/S ratios) decrease steadily downhole between the Main PGE Reef and the basal wehrlite layer. The most Cu rich sulphides occur at the top of the drill core in pyroxenites overlying the Main PGE Reef. Cu/S is anomalously rich in the Ti-rich olivine gabbro, but due to the low S and Cu contents these data are difficult to compare to the other rocks. Ni/S ratios show a less pronounced decrease with depth in the Upper Flatreef, likely reflecting partial control of Ni by olivine and pyroxene.
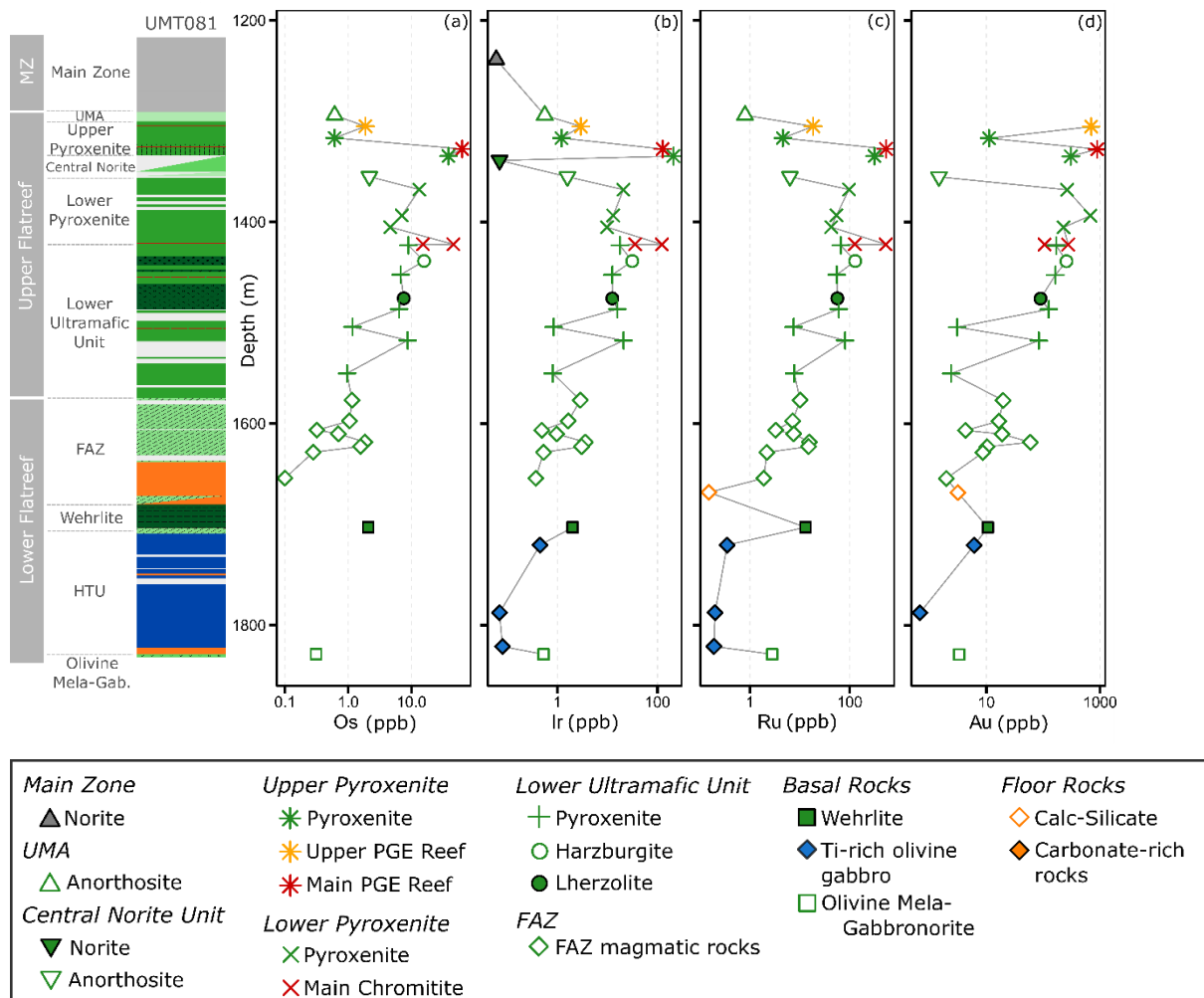
Figure 8.1: Downhole plots from drill core UMT081 of IPGE (ppb). (a) Os, (b) Ir, (c) Ru, (d) Au. Note all IPGE+Au show an overall decrease in concentration downhole.
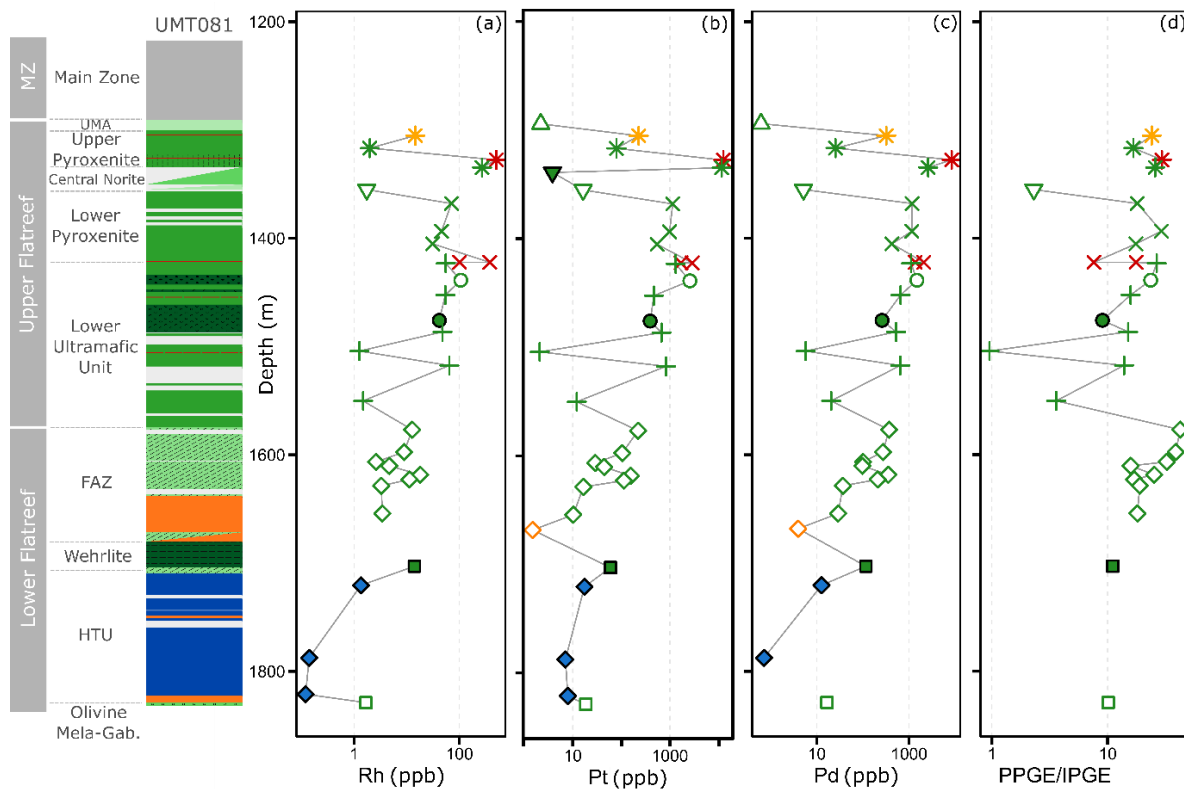
Figure 8.2: Downhole plots of PPGE and PPGE/IPGE from drill core UMT081. (a) Rh, (b) Pt, (c) Pd, (d) PPGE/IPGE. Note the decrease in all PPGE downhole.
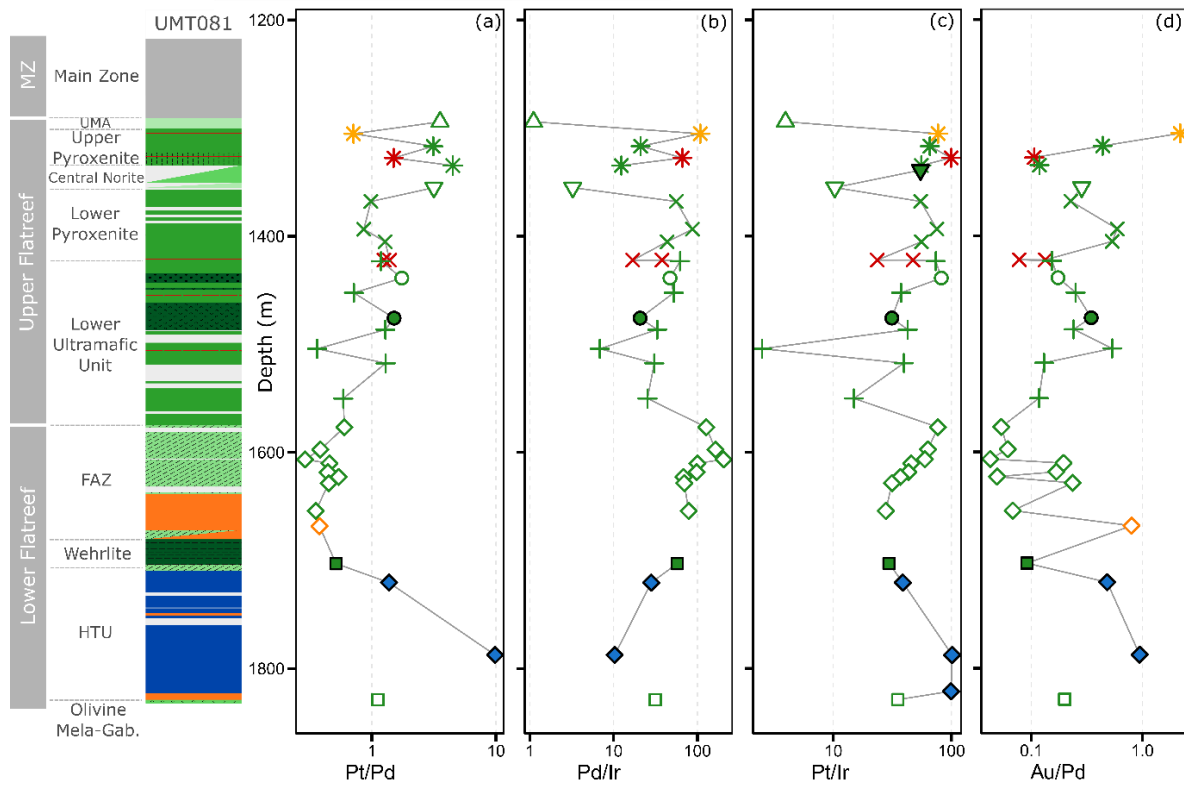
Figure 8.3: Downhole plots from drill core UMT081 of various PGE ratios (ppb). (a) Pt/Pd, (b) Pd/Ir, (c) Pt/Ir, (d) Au/Pd.
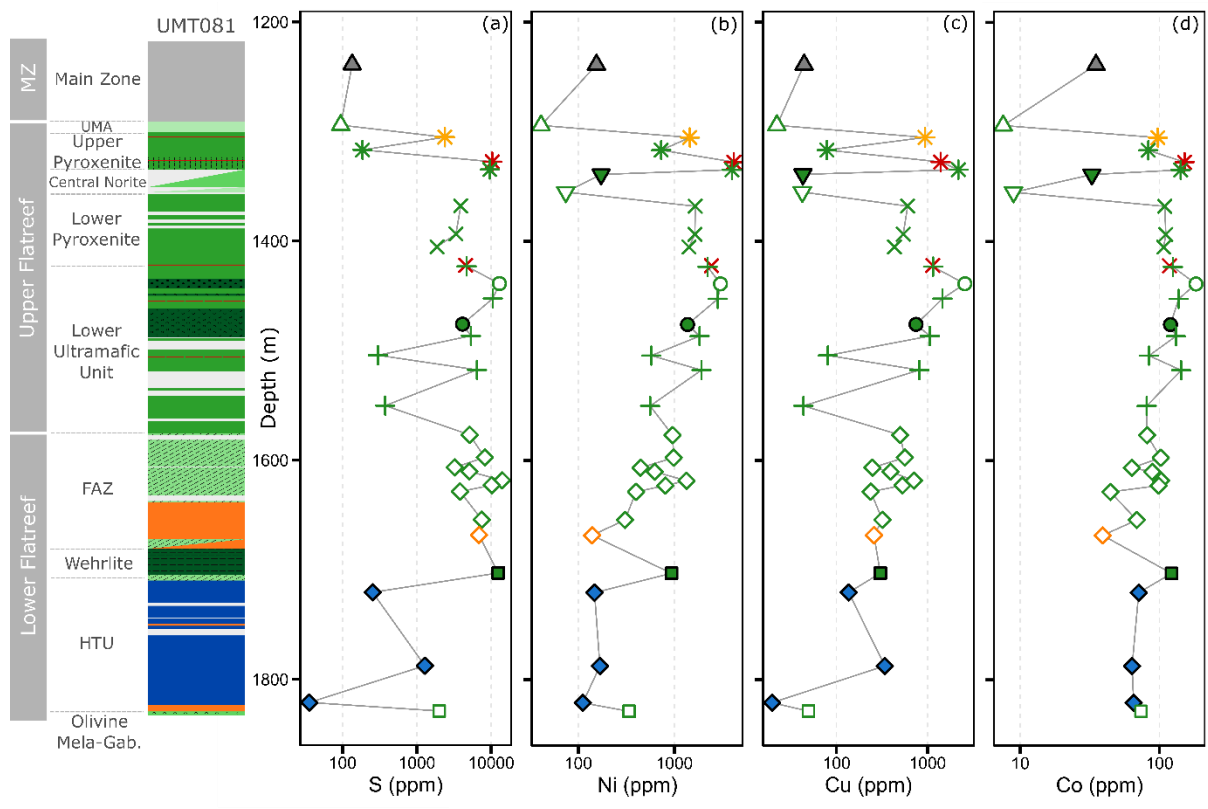
Figure 8.4: Downhole plots chalcophile elements (ppm). (a) S, (b) Ni, (c) Cu, (d) Co. Note the overall increase in S content downhole but the concurrent decrease in Ni and Cu.
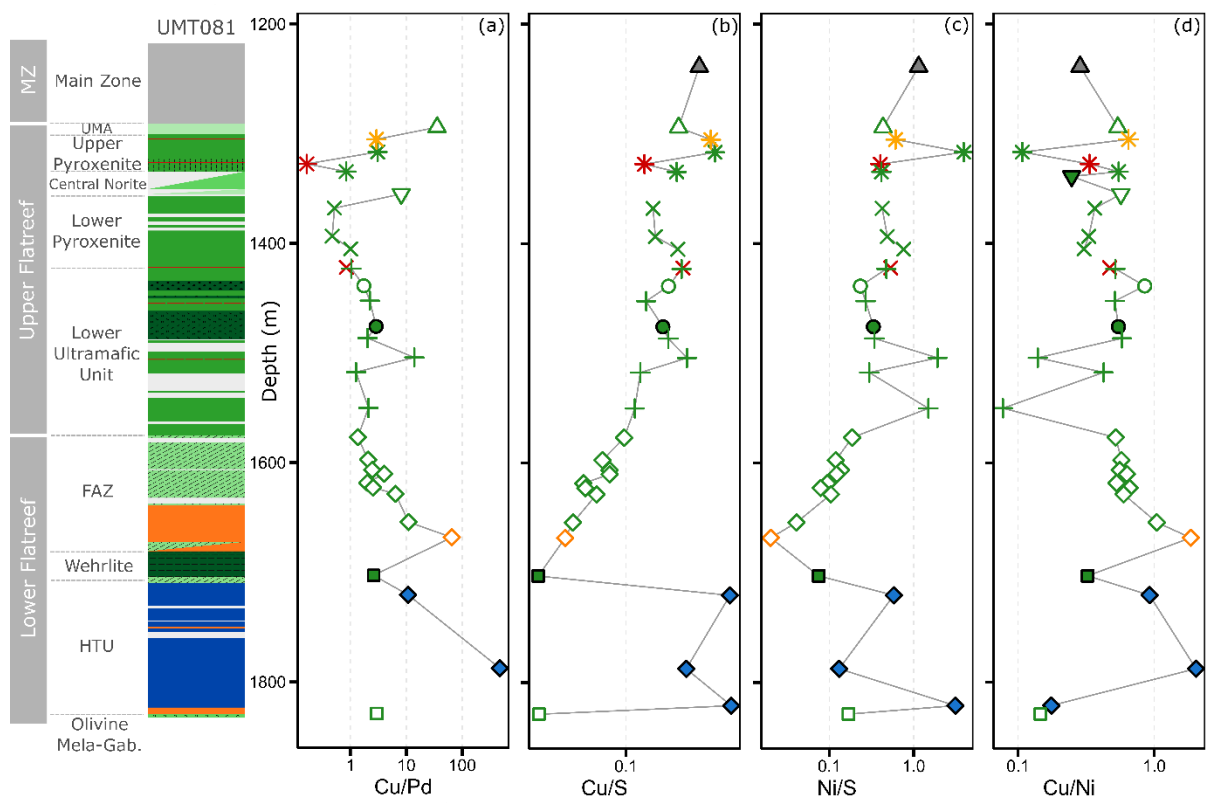
Figure 8.5: Downhole plots of chalcophile element ratios from drill hole UMT081. (a) Cu/Pd, (b) Cu/S, (c) Ni/S, (d) Cu/Ni. Note the decrease in metal tenor downhole, while Cu/Pd and Cu/Ni increase.

8.1.2 Drill Core UMT094

Drill core UMT094 shows more erratic trends of PGE, Au, Cu and Ni contents than UMT081, although the broad trend of decreasing PGE concentrations with depth is again evident (Figure 8.6, Figure 8.7). The concentrations of PGE in plagioclase rich rocks of the Central Norite Unit in drill core UMT094 is greater than seen in UMT081 (max. 213 ppb and 16 ppb Pt, respectively) and the decrease of PGE concentrations in the pyroxenitic hangingwall of the Main PGE Reef is less pronounced. Au contents are highest above the Main Reef. PGE contents in the Lower Ultramafic Unit are strongly variable, e.g., by up to two orders of magnitude in the case of Ir. The highest PGE contents are found in harzburgite of the Lower Ultramafic Unit (12682 ppb Pt, 6264 ppb Pd), with lherzolite layers directly beneath the harzburgite rocks containing low PGE contents. The calcsilicates have low but variable PGE contents.

As in drill core UMT081, Pt/Pd ratios show a well-defined downhole decrease below the Main PGE Reef which has a Pt/Pd ratio close to unity (1.27; Figure 8.8). Notably, while Pt/Ir ratios decrease downhole, as would be expected during magmatic fractionation, due to the compatible behaviour of IPGE in chromite and possibly olivine (Brenan et al., 2003; Righter et al., 2004), Pd/Ir in the Upper Flatreef shows no systematic downhole trends but is strongly variable. Au/Pd is variable below the Main PGE Reef, but shows a strong systematic increase with height above the reef, a trend also seen in UMT081 (Figure 8.8).

Concentrations of Ni, Cu and S show broadly similar erratic downhole trends. Ultramafic rocks are rich in Ni, Cu, Co and S, whereas the underlying calc-silicates are generally poorer in these elements, except the uppermost calc-silicate sample which contains magmatic concentrations of S, possibly suggesting S introduction from overlying rocks. Below this sample, Ni and Co show a broad decrease in concentration downhole in the calc-silicate package, while S and Cu have largely constant values (Figure 8.9).

Ni and Cu tenors in sulphides decrease slightly downhole but this is overprinted by significant localised variability, e.g., the Central Norite Unit norite has Cu/S and Ni/S ratios at least an order of magnitude greater than the surrounding rocks (Figure 8.10). Coupled with this is a weak trend of increasing Cu/Ni ratios downhole within the magmatic portions of the drill core, mirroring that seen in drill core UMT081. The uppermost sedimentary floor rocks (sample 94-1411) has the highest Cu/Ni ratio (1.72) of any rock in the drill core. Below this there is no systematic pattern of metal tenors within the country rocks.
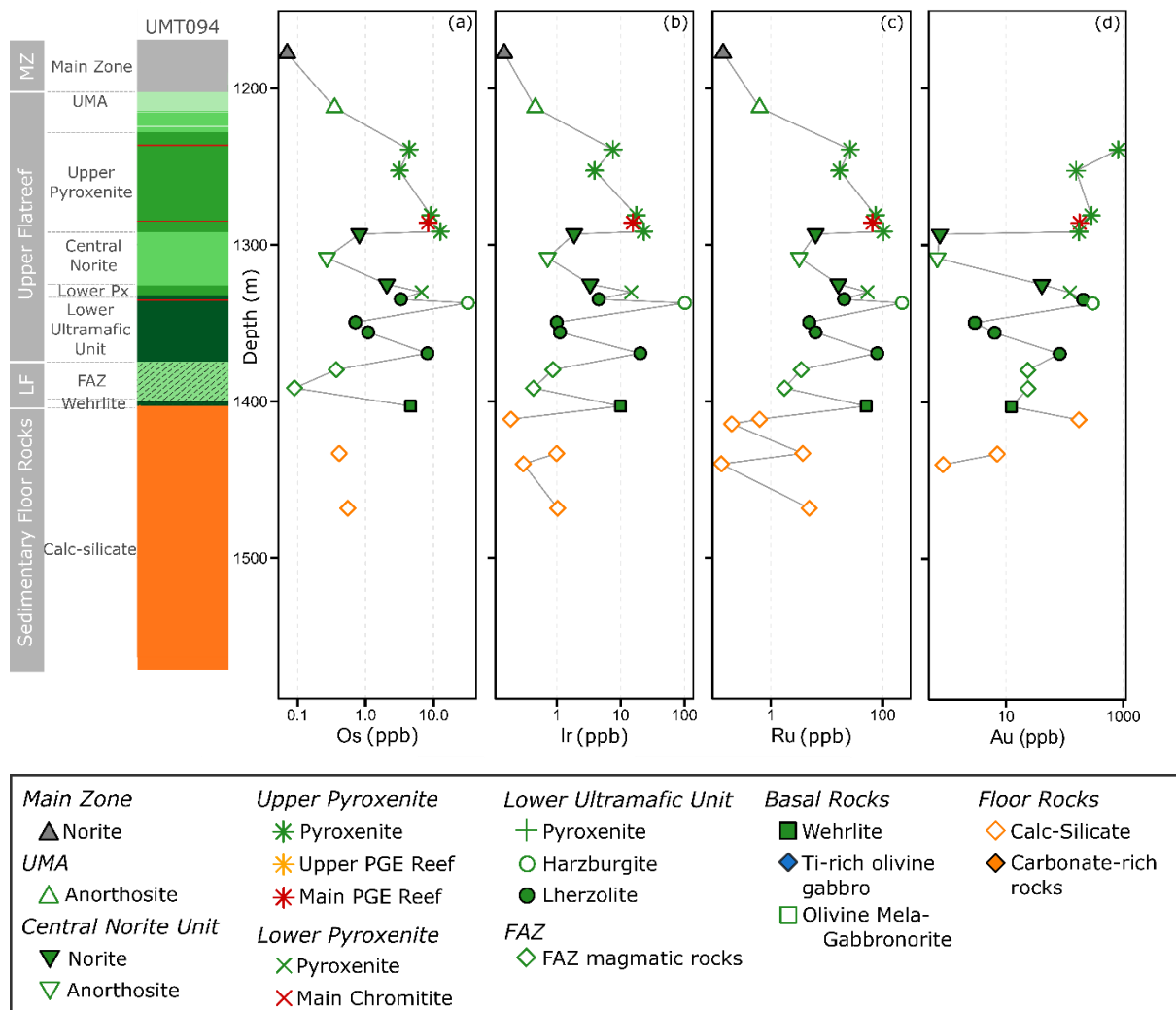
Figure 8.6: Downhole plots of IPGE and Au from drill core UMT094. (a) Os, (b) Ir, (c) Ru, (d) Au. Note the more erratic downhole pattern compared to UMT081 but showing an overall decrease in PGE concentration.
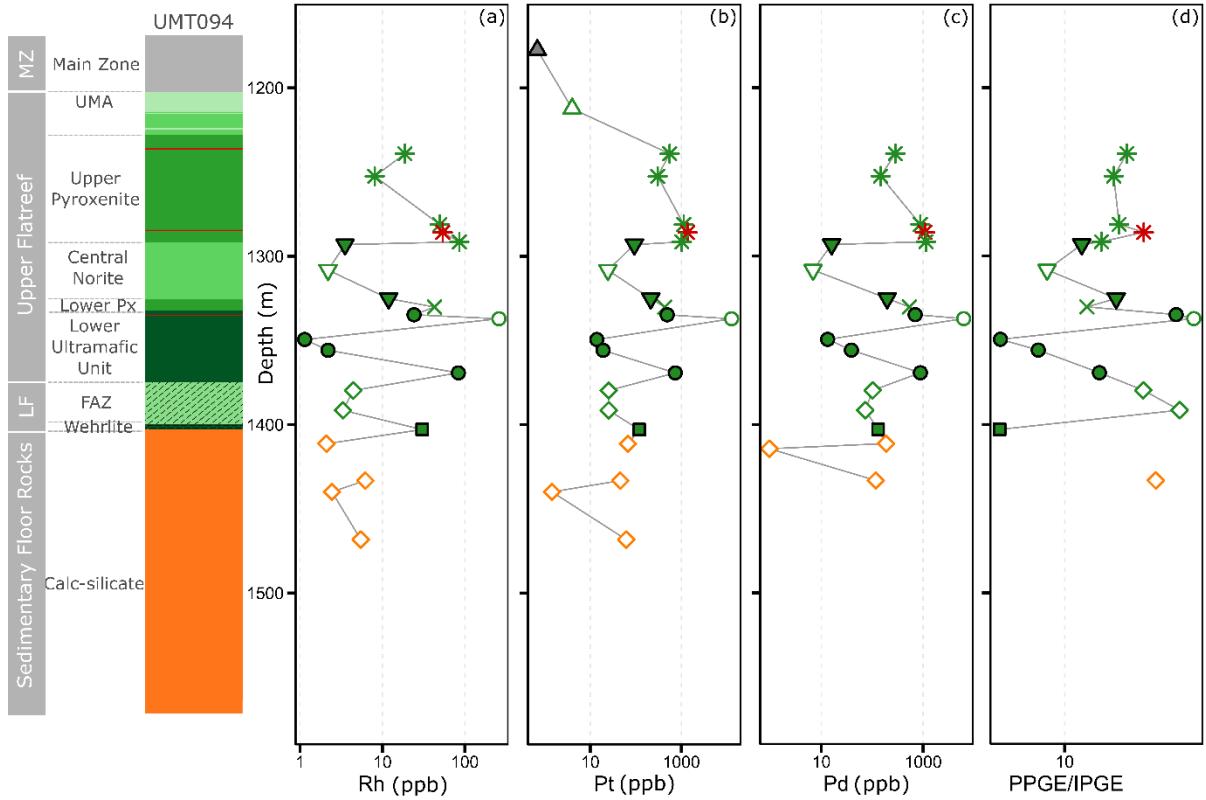
Figure 8.7: Downhole plots of PPGE and PPGE/IPGE from drill core UMT094. (a) Rh, (b) Pt, (c) Pd, (d) PPGE/IPGE. Note the decrease in PGE concentration downhole and higher PGE concentrations in harzburgite.
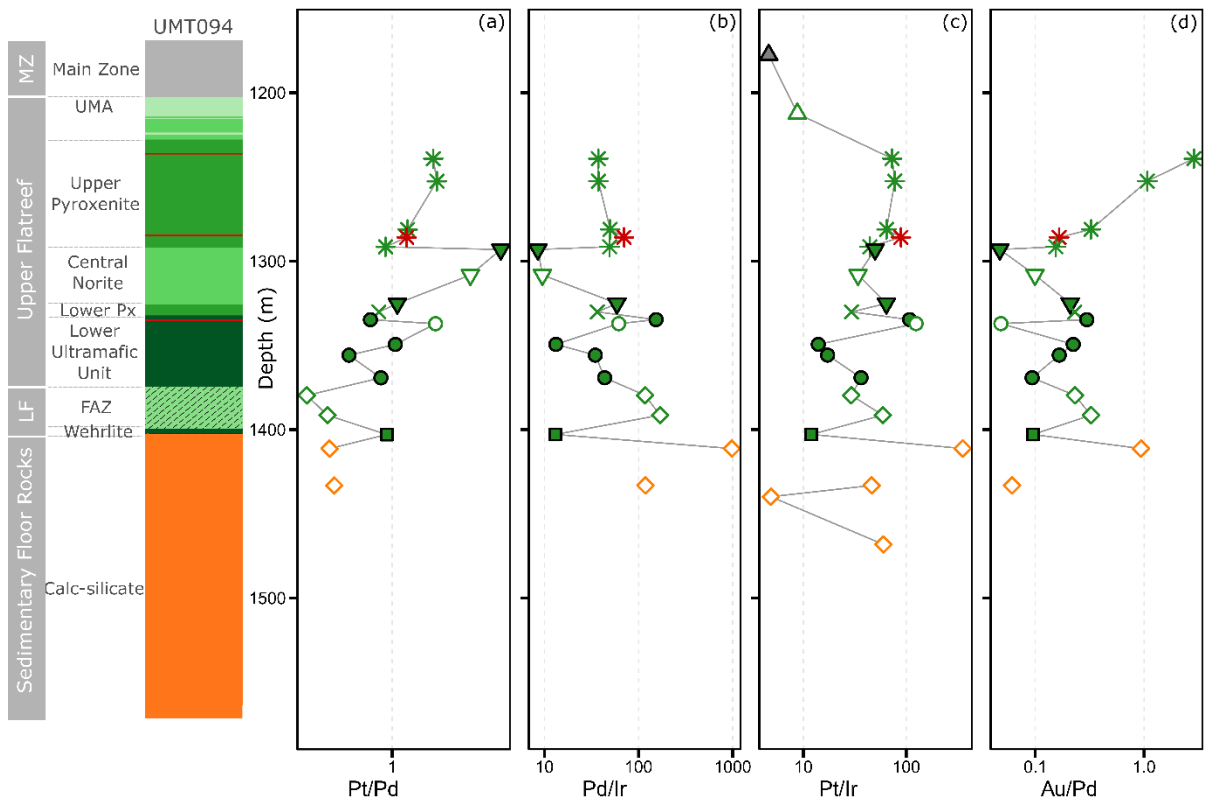
Figure 8.8: Downhole plots of PGE ratios from drill core UMT094. (a) Pt/Pd, (b) Pd/Ir, (c) Pt/Ir, (d) Au/Pd.
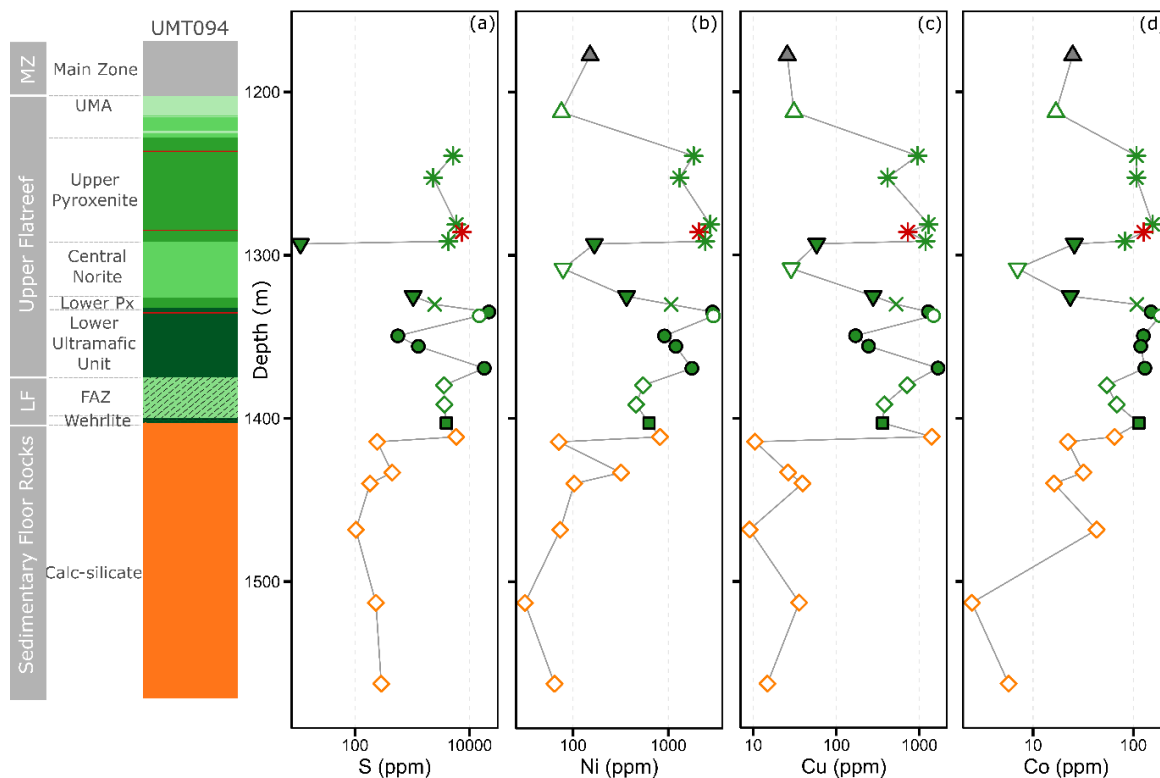
Figure 8.9: Downhole plots chalcophile elements in drill core UMT094. (a) S, (b) Ni, (c) Cu, (d) Co. Note the significantly poorer metal content in calc-silicate floor rocks relative to overlying magmatic units, except in the uppermost floor rock sample.
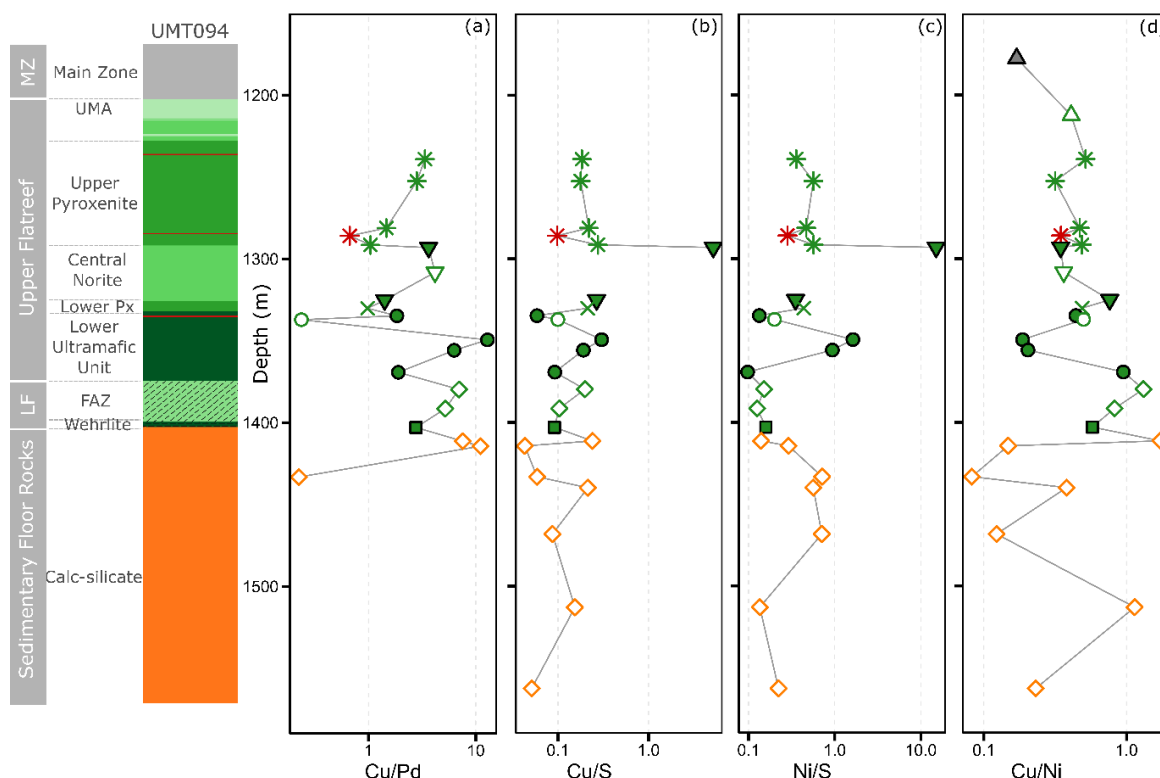
Figure 8.10: Downhole plots from drill core UMT094 of chalcophile element ratios. (a) Cu/Pd, (b) Cu/S, (c) Ni/S, (d) Cu/Ni.

8.2 Multi-element variation diagrams

Multi-element variation diagrams (Figure 8.11) show fractionated patterns in most rock types, with a progressive increase in content from Ni to Pt and decrease from Pd to Cu. Exceptions are the anorthosite rocks in both the UMA and Central Norite Unit, which show fairly flat patterns with only a slightly elevated PPGE relative to IPGE. In contrast, pyroxenite rocks show increasing chalcophile element contents from Ni to Pt and decrease from Pd to Cu although pyroxenites with lower overall chalcophile element content show flatter patterns. Pyroxenite rocks overlap in content with equivalent rocks from the UCZ of the WBC (Maier et al., 2013) but some pyroxenite rocks can be richer in the Flatreef, such as the Main PGE Reef and its pyroxenite footwall. Norite in the Central Norite unit shows fractionated patterns similar to those of the pyroxenite rocks, albeit at lower concentrations.

Harzburgite is generally richer in PGE than lherzolite with both showing a broad increase in chalcophile contents from Ni to Pt. Lherzolite overlaps with chalcophile contents and patterns of harzburgite rocks from the UCZ of the WBC, except for Cu; however, harzburgite in the Flatreef shows higher contents than equivalent rocks in the UCZ of the WBC (Maier et al., 2013). Harzburgite shows a decreasing content from Pd to Cu whereas in lherzolite rocks Pd to Cu is broadly constant. Olivine mela-gabbronorite and wehrlite rocks from the basal interval show similar patterns, although wehrlite shows higher chalcophile element contents than olivine mela-gabbronorite rocks. Both rock types show an increase in chalcophile element content between Ni and Pt but flat patterns between Pt and Cu. A similar pattern is also shown in magmatic FAZ rocks. Rocks from the Ti-rich olivine gabbro and Calc-silicate floor rocks show more erratic patterns but show an overall increase in content between Ni and Au. In addition, the Ti-rich olivine gabbro can be anomalously rich in Pt relative to other PGE.
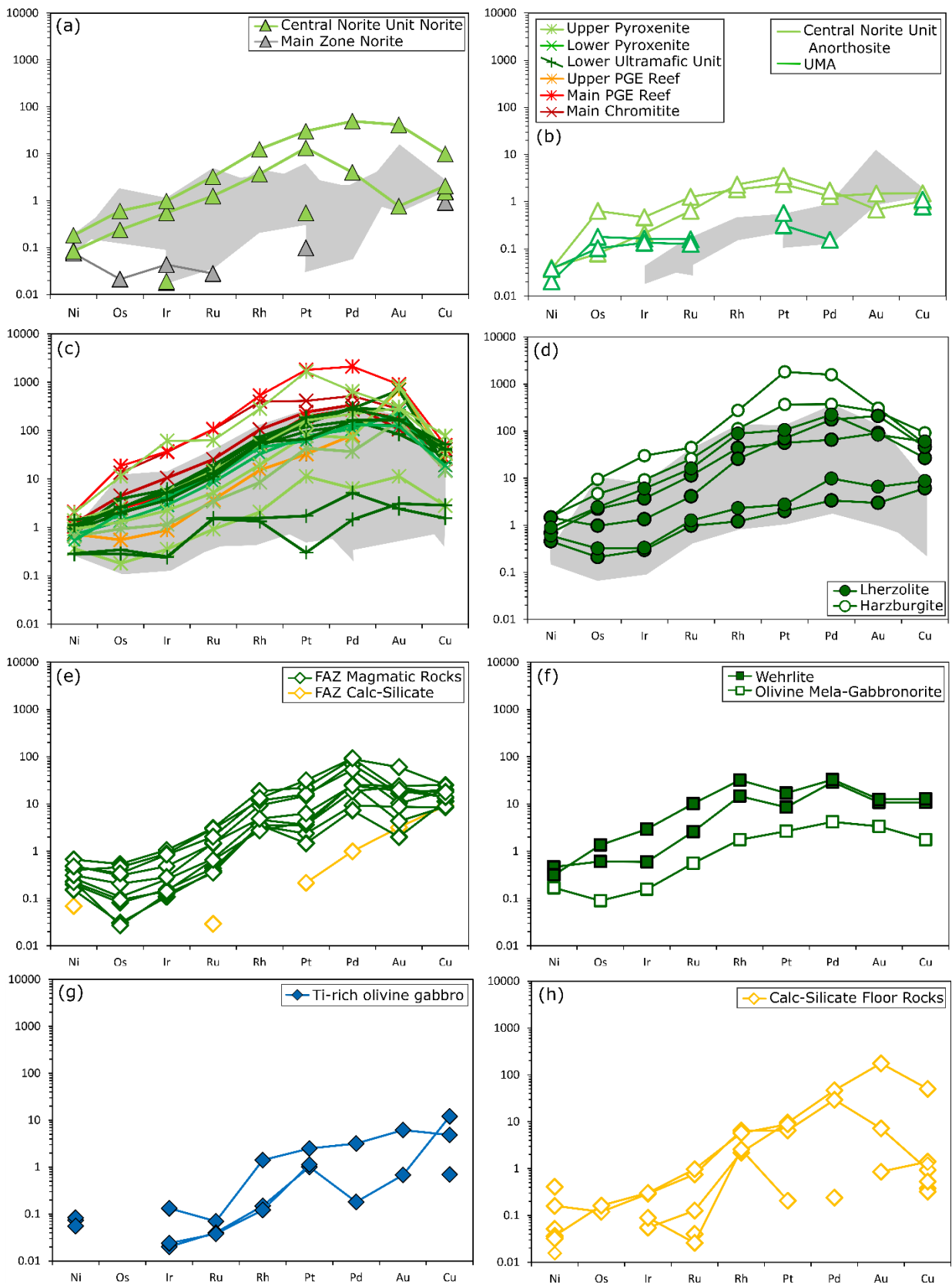
Figure 8.11: Multi-element variation diagrams of PGE-Ni-Cu-Au normalized to Primitive Mantle (Barnes and Maier, 1999). Shaded fields represent comparative data from equivalent rock types from the UCZ of the WBC (Maier et al., 2013). (a) Norites, (b) Anorthosites, (c) Pyroxenites including the Main PGE and Main Chromitite Reefs, (d) Peridotites, (e) FAZ and Calc-silicate xenolith, (f) Basal Interval rocks,

(g) Ti-rich olivine gabbro, (h) Calc-silicate floor rocks from UMT094. While Pyroxenites and peridotites share similar PGE patterns, other units have distinctive patterns with varying degrees of fractionation between IPGE and PPGE. Note the anomalously rich Pt found in the Ti-rich olivine gabbro. Also note that rocks deeper in the Flatreef sequence have lower Pt/Pd ratios, with relative rich Pd especially apparent in FAZ and Calc-silicate rocks.

8.3 Inter-element correlation matrices

PGE in the studied Flatreef rocks show good inter-element correlation in all magmatic rock types, although there is more scatter at low element concentrations, possibly due to more significant analytical errors at low concentrations (Figure 8.12). Scatter is most pronounced in the plots of Ir vs Pd with a correlation of 0.74 (Figure 8.12c; Table 8.1). This decoupling of Pd and Ir is particularly apparent in the Upper Pyroxenite where correlation is poorer than in other Upper Flatreef units (0.64). Correlation matrices for all PGE show that all other PGE correlate well with each other (Table 8.1).

In the Upper Flatreef where contamination appears to be limited, PGE show positive correlations with S, suggesting a strong sulphide control of PGE (Figure 8.13; Table 8.1). A similar pattern is observed in the FAZ, although this shows somewhat more scatter. FAZ rocks also have lower PGE/S ratios than most other Flatreef rocks (Figure 8.13). Calc-silicate rocks tend to have variable and generally low PGE contents but can be rich in S, at similar levels to the ultramafic rocks. The Ti-rich olivine gabbro has low S contents (36-1280 ppm) (Figure 8.13).

Other chalcophile elements, namely Cu, Ni and Co show similar trends as the PGE (Figure 8.14), with magmatic rocks containing high metal concentrations and showing positive correlation with S content, FAZ rocks containing significantly lower and more variable metal concentrations, and Ti-rich olivine gabbro and calc-silicate rocks containing low base metal concentrations, with considerable scatter in the latter. Gold shows the weakest positive correlation with S in all rocks.
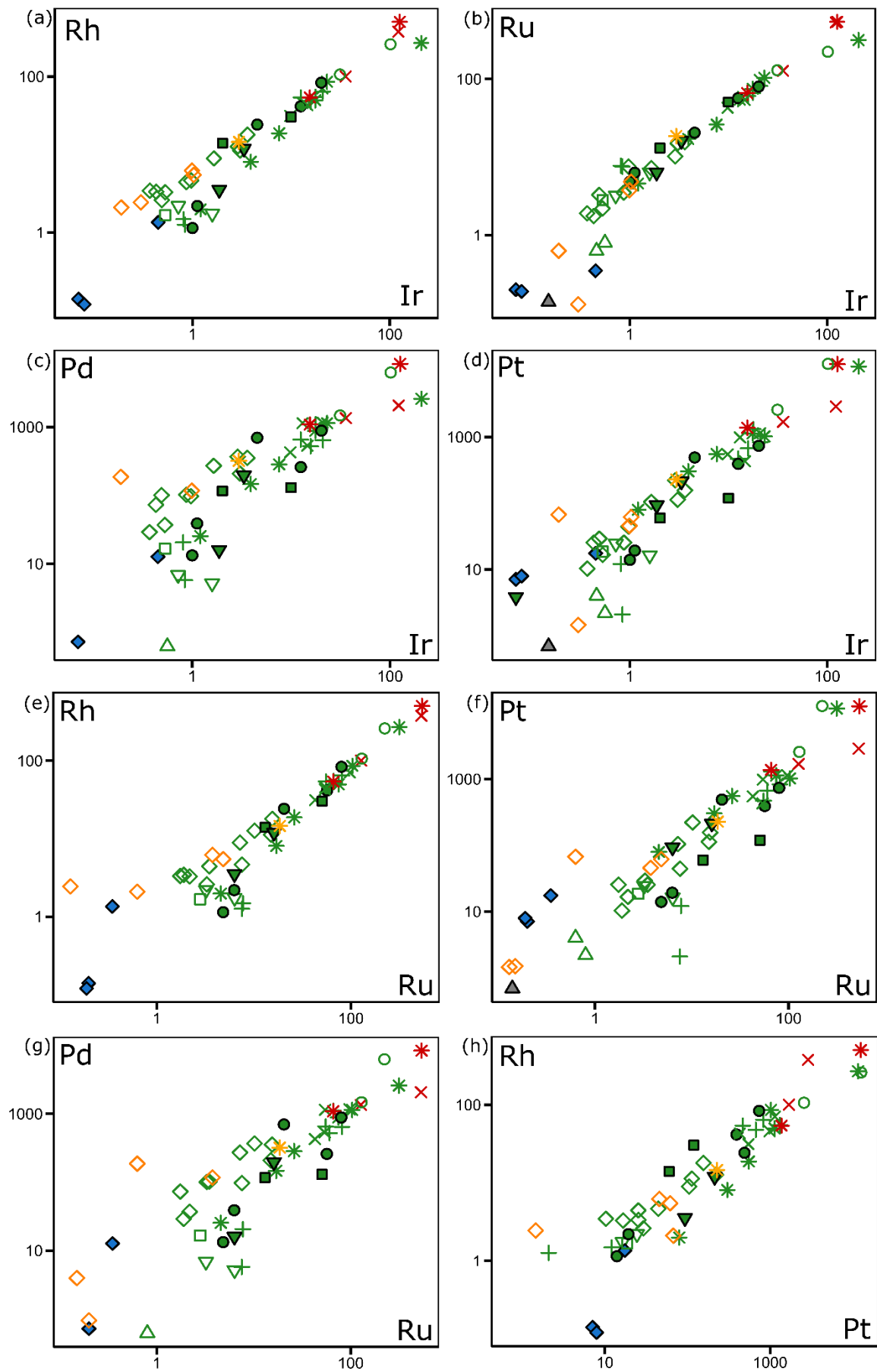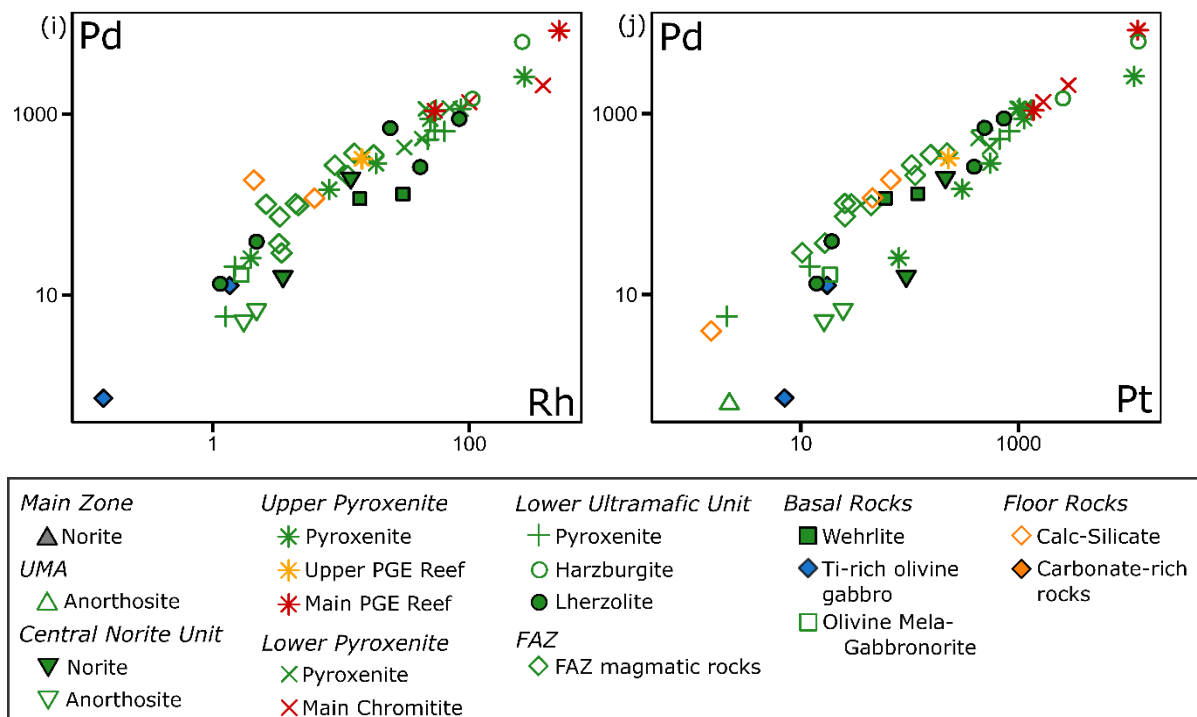
Figure 8.12: Bivariate plots of PGE concentrations against each other (all data in ppb). (a) Ir vs. Rh, (b) Ir, vs. Ru, (c) Ir vs. Pd, (d) Ir vs. Pt, (e) Ru vs. Rh, (f) Ru vs. Pt, (g) Ru vs. Pd, (h) Pt vs. Rh, (I) Rh vs. Pd, (j) Pt vs. Pd. Note there is good correlation between the individual PGE, with the exception of Pd that shows a weaker correlation with Ir and Ru.
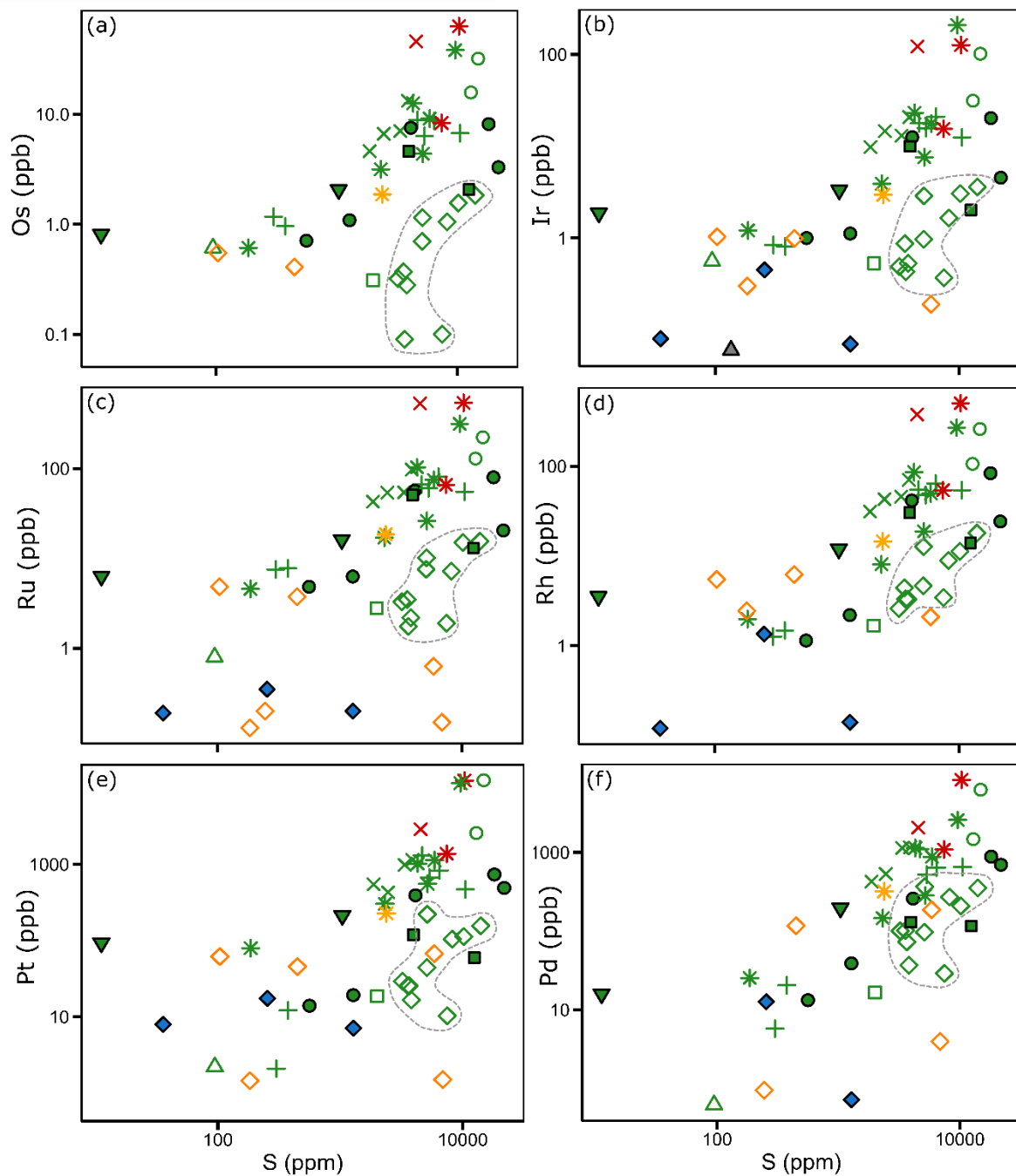
Figure 8.13: Bivariate plots of PGE against S. (a) Os, (b) Ir, (c) Ru, (d) Rh, (e) Pt, (f) Pd. Note the poor correlation in Calc-silicate and Ti-rich olivine gabbro between PGE and S. The FAZ is notably poor in PGE compared to magmatic rocks with similar S concentrations. Grey dashed fields denote the compositions of FAZ rocks.
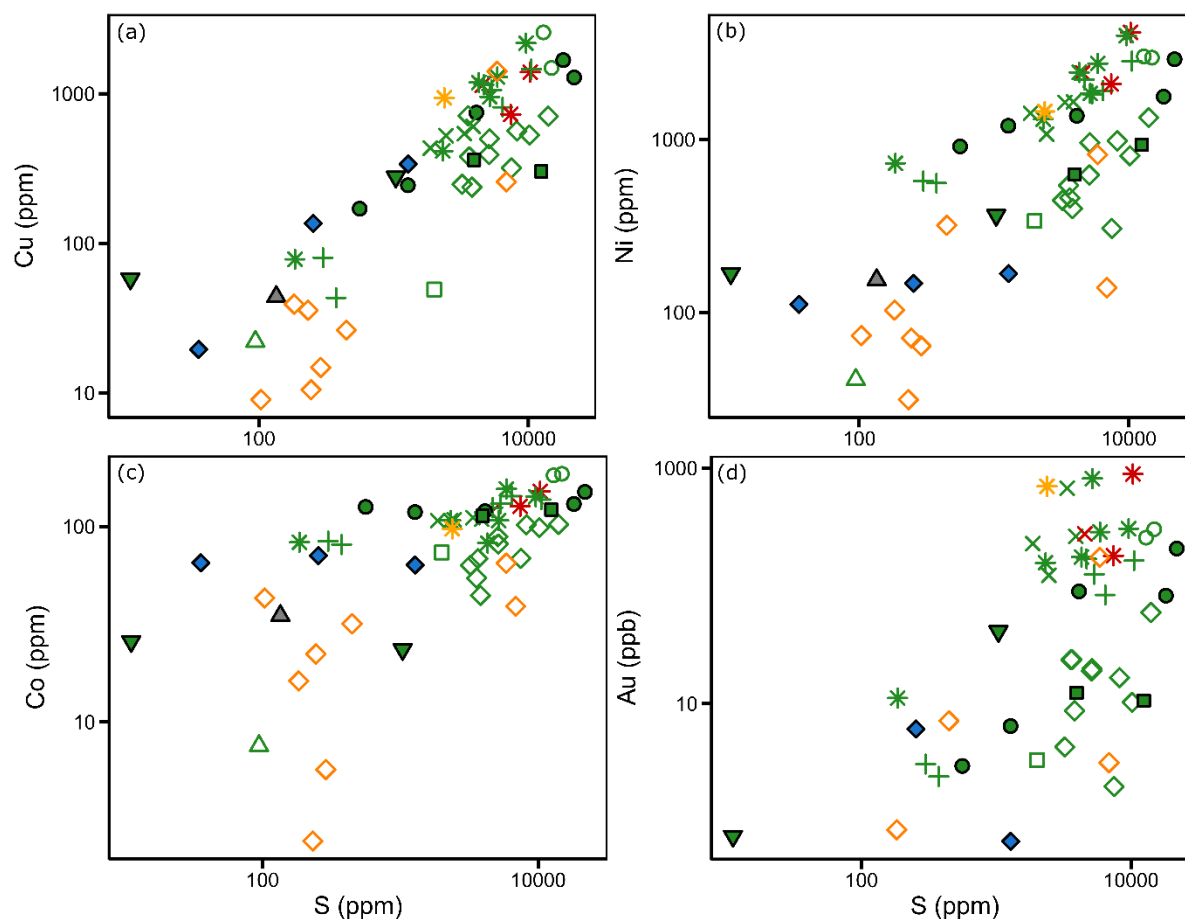
Figure 8.14: Bivariate diagrams of chalcophile metals against S. (a) Cu vs. S, (b) Ni vs. S, (c) Co vs. S, (d) Au vs. S. Note the poor correlation between Au and S. There is a better correlation between PGE and base metals than between base metals and S. FAZ rocks are generally poor in chalcophile metals relative to ultramafic rocks with similar S concentrations.

Correlation matrices for individual units indicate that the Central Norite Unit, despite being S poor, shows very good correlation between PPGE+Ru and Ni and Cu. Ni and Cu also show good correlation with S. The Upper Pyroxenite Unit shows good correlation between all PGE and Ni with significantly weaker correlation between PGE and Cu, most notably Pd-Cu (0.48), although Cu and Ir are strongly correlated (0.82; Table 8.1). Ni also has a significantly better correlation with S compared to Cu-S (0.93 and 0.79, respectively), although Ni and Cu are well correlated with each other in the Upper Pyroxenite Unit (0.89). Co is poorly correlated with all PGE except Ru and Rh where correlation is moderate (0.62 and 0.60, respectively), and with Cu and Ni. PGE show generally good correlations with S, except for Ir and Pd (0.77 and 0.74, respectively). There is no correlation between Cr and any PGE, Ni, Cu or S.

In the Lower Pyroxenite Unit Ni shows a better correlation with Pt and Pd (0.96 and 0.81, respectively) than Cu with Pt and Pd (0.89 and 0.71, respectively). All PGE within the Lower Pyroxenite Unit show better correlations with S (0.87-0.97) than Ni and Cu with S (0.83 and

0.82, respectively). Amongst the PGE, Ir shows the weakest correlation with S (0.87). There is a good correlation between Ni and Cu within this unit (0.90). Notably, the Lower Pyroxenite Unit is the only unit that shows good correlation between Cr and PGE, with values for Ir, Ru, Rh and Pt vs Cr being 0.83, 0.70, 0.77 and 0.80, respectively. Correlation between Os vs Cr and Pd vs Cr is weaker (0.60 and 0.66, respectively). Somewhat surprisingly, Cr also shows good correlations with Ni and Cu (0.86 and 0.92, respectively), but a moderate correlation with S (0.70).

Within the Upper Flatreef, the Lower Ultramafic Unit shows the poorest correlation between PGE and S, although there are good correlations between the various PGE (0.89-0.99). The correlations between PGE and Ni and Cu are moderate (0.45-0.68) with a particularly weak correlation between Pt and Cu (0.37). Sulphur is also less well correlated with PGE (<0.52), with only slightly better correlations between PGE and Ni and Cu (0.79 and 0.77, respectively), although Ni and Cu are well correlated with each other (0.87). There is no correlation between Cr and any of the PGE, Ni, Cu or S, but there is a very good correlation between Au and PGE, Ni, Cu and S, which is not observed in the other rocks of the Upper Flatreef (Table 8.1).

FAZ rocks show very good correlations between Ni and PGE (0.85-0.95), but less so between Cu and PGE (0.51-0.68). S shows good correlations with IPGE+Rh (0.77-0.82) but poorer correlation with Pt and Pd (0.52 and 0.60, respectively). The correlation of S with Ni and, especially, Cu is also poor compared to other Flatreef units (0.75 and 0.54, respectively). The correlation between Ni and Cu is the lowest of all units studied (0.72; Table 8.1). The Co concentration in FAZ rocks is significantly lower than in the overlying ultramafic units (Figure 8.14). Au shows moderate to good correlation with PGE, Ni and Cu, while Cr shows moderate correlation with IPGE and poor correlation to all other elements. Bivariate plots of Cu vs S and Ni vs S show that FAZ rocks have similar Cu/S to pyroxenite units but lower Ni/S values compared to the Upper Flatreef rocks.

All Rocks

	Os	Ir	Ru	Rh	Pt	Pd	Ni	Cu	Co	Au	S	Cr
Os	1.00											
Ir	0.90	1.00										
Ru	0.98	0.88	1.00									
Rh	0.99	0.89	0.99	1.00								
Pt	0.86	0.89	0.78	0.86	1.00							
Pd	0.89	0.74	0.82	0.89	0.92	1.00						
Ni	0.79	0.71	0.78	0.76	0.69	0.71	1.00					
Cu	0.63	0.61	0.62	0.59	0.56	0.52	0.88	1.00				
Co	0.53	0.47	0.54	0.52	0.48	0.51	0.85	0.76	1.00			
Au	0.56	0.43	0.53	0.55	0.50	0.59	0.63	0.49	0.44	1.00		
S	0.38	0.37	0.39	0.41	0.39	0.41	0.66	0.72	0.68	0.22	1.00	
Cr	0.10	0.12	0.17	0.11	0.05	0.04	0.36	0.33	0.49	0.04	0.20	1.00

n=60

Upper Pyroxenite Unit and Main PGE Reef

	Os	Ir	Ru	Rh	Pt	Pd	Ni	Cu	Co	Au	S	Cr
Os	1.00											
Ir	0.83	1.00										
Ru	1.00	0.82	1.00									
Rh	1.00	0.80	1.00	1.00								
Pt	0.96	0.94	0.96	0.95	1.00							
Pd	0.96	0.64	0.96	0.97	0.86	1.00						
Ni	0.90	0.85	0.89	0.87	0.89	0.79	1.00					
Cu	0.66	0.82	0.65	0.62	0.73	0.48	0.89	1.00				
Co	0.63	0.57	0.62	0.60	0.64	0.58	0.76	0.61	1.00			
Au	0.44	0.20	0.45	0.47	0.37	0.52	0.37	0.34	0.29	1.00		
S	0.82	0.77	0.82	0.80	0.83	0.74	0.93	0.79	0.81	0.40	1.00	
Cr	-0.09	-0.07	-0.09	-0.12	-0.11	-0.11	0.22	0.25	0.56	-0.20	0.16	1.00

n=9

Central Norite Unit

	Os	Ir	Ru	Rh	Pt	Pd	Ni	Cu	Co	Au	S	Cr
Os	1.00											
Ir	0.68	1.00										
Ru	0.67	0.98	1.00									
Rh	0.46	0.92	0.96	1.00								
Pt	0.38	0.92	0.93	0.97	1.00							
Pd	0.51	0.90	0.97	0.99	0.94	1.00						
Ni	0.42	0.71	0.95	0.99	0.90	0.96	1.00					
Cu	0.54	0.85	0.98	0.99	0.94	1.00	0.94	1.00				
Co	0.15	-0.01	0.61	0.62	0.25	0.53	0.56	0.25	1.00			
Au	0.54	0.90	0.97	0.99	0.92	1.00	0.95	0.99	0.49	1.00		
S	0.51	0.82	0.97	1.00	0.93	1.00	0.94	1.00	0.25	1.00	1.00	
Cr	-0.12	0.37	0.34	0.38	0.53	0.28	0.53	0.31	0.72	0.23	0.29	1.00

n=5

Lower Pyroxenite Unit and Main Chromitite

	Os	Ir	Ru	Rh	Pt	Pd	Ni	Cu	Co	Au	S	Cr
Os	1.00											
Ir	0.99	1.00										
Ru	0.99	1.00	1.00									
Rh	1.00	1.00	1.00	1.00								
Pt	0.95	0.94	0.93	0.94	1.00							
Pd	0.89	0.86	0.86	0.87	0.97	1.00						
Ni	0.79	0.87	0.85	0.87	0.96	0.81	1.00					
Cu	0.83	0.98	0.90	0.94	0.89	0.71	0.90	1.00				
Co	0.75	0.91	0.82	0.88	0.90	0.78	0.93	0.97	1.00			
Au	-0.09	-0.10	-0.07	-0.07	-0.02	0.15	-0.08	-0.37	-0.14	1.00		
S	0.94	0.87	0.91	0.93	0.95	0.97	0.83	0.82	0.83	0.00	1.00	
Cr	0.60	0.83	0.70	0.77	0.80	0.66	0.86	0.92	0.98	-0.12	0.70	1.00

n=6

Lower Ultramafic Unit

	Os	Ir	Ru	Rh	Pt	Pd	Ni	Cu	Co	Au	S	Cr
Os	1.00											
Ir	0.98	1.00										
Ru	0.99	0.96	1.00									
Rh	0.99	0.99	0.98	1.00								
Pt	0.94	0.98	0.89	0.94	1.00							
Pd	0.95	0.98	0.91	0.96	0.99	1.00						
Ni	0.65	0.57	0.67	0.64	0.50	0.57	1.00					
Cu	0.61	0.49	0.68	0.61	0.37	0.45	0.87	1.00				
Co	0.78	0.72	0.80	0.77	0.65	0.69	0.88	0.81	1.00			
Au	0.81	0.73	0.80	0.78	0.68	0.74	0.94	0.83	0.87	1.00		
S	0.47	0.43	0.50	0.52	0.37	0.46	0.79	0.77	0.69	0.72	1.00	
Cr	-0.06	-0.04	0.04	-0.03	-0.15	-0.15	-0.09	0.02	0.01	-0.11	-0.13	1.00

n=13

FAZ Magmatic Rocks Only

	Os	Ir	Ru	Rh	Pt	Pd	Ni	Cu	Co	Au	S	Cr
Os	1.00											
Ir	0.97	1.00										
Ru	0.98	0.96	1.00									
Rh	0.95	0.97	0.91	1.00								
Pt	0.82	0.89	0.79	0.89	1.00							
Pd	0.86	0.90	0.80	0.92	0.96	1.00						
Ni	0.92	0.90	0.86	0.95	0.85	0.94	1.00					
Cu	0.64	0.65	0.60	0.68	0.51	0.64	0.72	1.00				
Co	0.82	0.74	0.81	0.74	0.65	0.72	0.79	0.51	1.00			
Au	0.59	0.60	0.55	0.71	0.47	0.59	0.76	0.71	0.44	1.00		
S	0.82	0.77	0.80	0.82	0.52	0.60	0.75	0.54	0.77	0.58	1.00	
Cr	0.63	0.58	0.72	0.41	0.39	0.32	0.31	0.19	0.53	-0.06	0.39	1.00

n=10

Calc-Silicate Floor Rocks (UMT094)

	Os	Ir	Ru	Rh	Pt	Pd	Ni	Cu	Co	Au	S	Cr
Os	1.00											
Ir	1.00	1.00										
Ru	1.00	0.97	1.00									
Rh	-1.00	0.98	0.93	1.00								
Pt	1.00	0.28	0.49	0.27	1.00							
Pd	#DIV/0!	-1.00	0.25	-1.00	1.00	1.00						
Ni	-1.00	-0.54	-0.19	-0.45	0.53	0.94	1.00					
Cu	-1.00	-0.67	-0.33	-0.64	0.51	0.79	0.94	1.00				
Co	1.00	-0.18	0.20	-0.19	0.89	0.90	0.82	0.76	1.00			
Au	#DIV/0!	-0.59	-0.35	-0.54	0.77	1.00	0.96	1.00	0.96	1.00		
S	-1.00	-0.65	-0.32	-0.61	0.52	0.80	0.95	1.00	0.76	1.00	1.00	
Cr	-1.00	0.03	-0.34	0.20	0.38	-0.99	0.29	0.17	0.33	0.29	0.19	1.00

n=7

Table 8.1: Correlation matrices of various units from the Flatreef. (a) all rocks including MZ and carbonate footwall, (b) FAZ, (c) Central Norite Unit, (d) Upper Pyroxenite, (e) Lower Pyroxenite, (f) Lower Ultramafic Unit. Most units show good correlation between the PGE with variable correlation to base metals and S. The Lower Pyroxenite Unit is the only unit that has good correlation between PGE and Cr.

Chapter 9 – Isotopes of the lower Main Zone, Flatreef and sedimentary rocks

Isotope data were collected on whole rock samples for both radiogenic (Sr, Nd, Pb) and stable (O, Mg) isotope systems. These isotope systems were chosen because they can effectively discriminate between the potential contaminants of the Bushveld magmas. The Sr, Nd, O and Pb isotopes are particularly useful as they have been measured in rocks across the Bushveld Complex, thereby allowing assessment of processes such as contamination and magma mixing. Mg isotopes system has not been widely applied to magmatic rocks but was analysed in Bushveld rocks with the aim of quantifying the degree of contamination by dolomite rich rocks such as those of the Duitschland Formation and the Malmani Subgroup.

9.1 Radiogenic Isotopes

9.1.1 Neodymium Isotope Data

Samarium and Nd are considered to be relatively immobile in fluids and have broadly similar partitioning behaviour with regard to most rock forming minerals, making Nd isotope ratios less susceptible to alteration by syn- or post-magmatic fluids than, for example, Sr isotopes. Nd is marginally more incompatible than Sm into most major rock forming minerals due to its larger ionic radius and is thus concentrated in partial melts during melting of the mantle and the crust (Rollinson, 1993). These characteristics make the Sm-Nd isotope system suitable to track parental magma sources and contamination with crustal material. Nd data from this study is presented in Table 9.1.

Plotting $^{147}Sm/^{144}Nd$ against measured $^{143}Nd/^{144}Nd$ ratios for the present samples shows a strong positive correlation confirming closed system behaviour after crystallisation (Figure 9.1). Data from the UCZ of the WBC define a similar, but slightly elevated $^{143}Nd/^{144}Nd$ isochron relative to the magmatic Flatreef rocks from drill core UMT081 (Maier et al., 2000). The age calculated from the isochron constructed from all Flatreef data is 1921 ± 240 Ma (MSWD 0.57; Isoplot®) (Figure 9.1). This is younger than the age of the Bushveld Complex and therefore indicates addition of a non-magmatic component to the Nd budget of the Flatreef.

The data show no correlation between εNd and most major element oxides (including LOI). However, there is a positive correlation between εNd and K2O, P2O5 and Ba concentration (Figure 9.2). Trace element ratios of Ce/Sm and La/Nb show a no clear correlation, whereas La/Sm shows some positive correlation. The Ti-rich olivine gabbro is generally anomalous and plot outside these trends (except P_2O_5 and Ba). Concentrations and ratios of PGE show no clear correlation with εNd values.

Sample	Nd	Sm	Sm/Nd	$^{143}Nd/^{144}Nd_m$	2σ	$^{147}Sm/^{144}Nd$	$^{143}Nd/^{144}Nd_i$	ϵNd
Magmatic Rocks								
81-1238.81	5.61	1.22	0.22	0.511309	6.64E-06	0.131053	0.509534	-8.63
81-1294.6	2.74	0.53	0.19	0.511135	6.96E-06	0.116634	0.509555	-8.21
81-1305.23	1.95	0.47	0.24	0.511477	6.16E-06	0.145681	0.509504	-9.21
81-1327.62	2.70	0.62	0.23	0.511470	4.72E-06	0.139496	0.509581	-7.71
81-1438.8	0.91	0.21	0.23	0.511409	7.28E-06	0.140210	0.509510	-9.09
81-1475.85	3.12	0.82	0.26	0.511665	7.92E-06	0.158087	0.509524	-8.83
81-1550.22	1.97	0.60	0.31	0.512036	7.54E-06	0.184744	0.509534	-8.62
81-1610.25	1.63	0.41	0.25	0.511564	7.08E-06	0.150044	0.509532	-8.67
81-1628.6	1.67	0.32	0.19	0.511170	7.34E-06	0.115349	0.509607	-7.19
81-1787.55	1.03	0.32	0.31	0.512247	7.30E-06	0.187671	0.509706	-5.26
81-1828.87	3.33	0.76	0.23	0.511457	1.07E-05	0.138216	0.509585	-7.63
Variably Devolatized Carbonate Country Rocks								
94-1411.33	4.28	0.88	0.20	0.511261	6.44E-06	0.123869	0.509584	-7.65
94-1433.22	2.70	0.71	0.26	0.511746	5.50E-06	0.158724	0.509596	-7.41
94-1468.25	0.69	0.32	0.47	0.513323	6.50E-06	0.283834	0.509478	-9.72
94-1513.0	4.30	0.84	0.20	0.511254	7.02E-06	0.118334	0.509651	-6.33
94-1562.6	6.04	1.19	0.20	0.511319	6.44E-06	0.119443	0.509701	-5.34
Transvaal calcareous sediments								
Duit3	11.14	2.58	0.23	0.511478	7.50E-06	0.139769	0.509585	-7.62
Duit1	30.71	5.98	0.19	0.511151	6.36E-06	0.117710	0.509557	-8.17
Main Bushveld Complex, Merensky Reef								
B235-15A	1.43	0.29	0.20	0.511318	6.04E-06	0.121478	0.509673	-5.90

Table 9.1: Nd isotope data from the Flatreef, Main Zone, Carbonate Floor Rocks and Transvaal calcareous sediments. Age corrected for 2.05704 Ga.
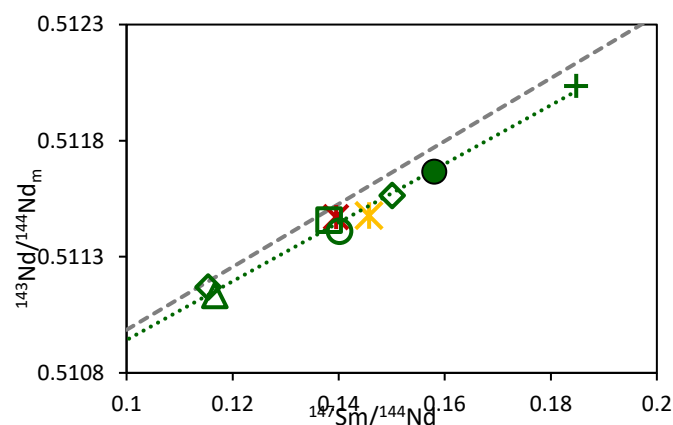
Figure 9.1: Isochron plots of Nd isotopes against parent isotope ratios. Grey line is the calculated isochron using UCZ average Nd isotopic values (line equation of UCZ isochron: y=0.0135x+0.5096; (Maier et al., 2000). Flatreef data plots on a trajectory with similar slope and intercept although slightly below the UCZ line. All Flatreef samples from UMT081 (except for Ti-rich olivine gabbro and olivine mela-gabbronorite rocks are plotted).
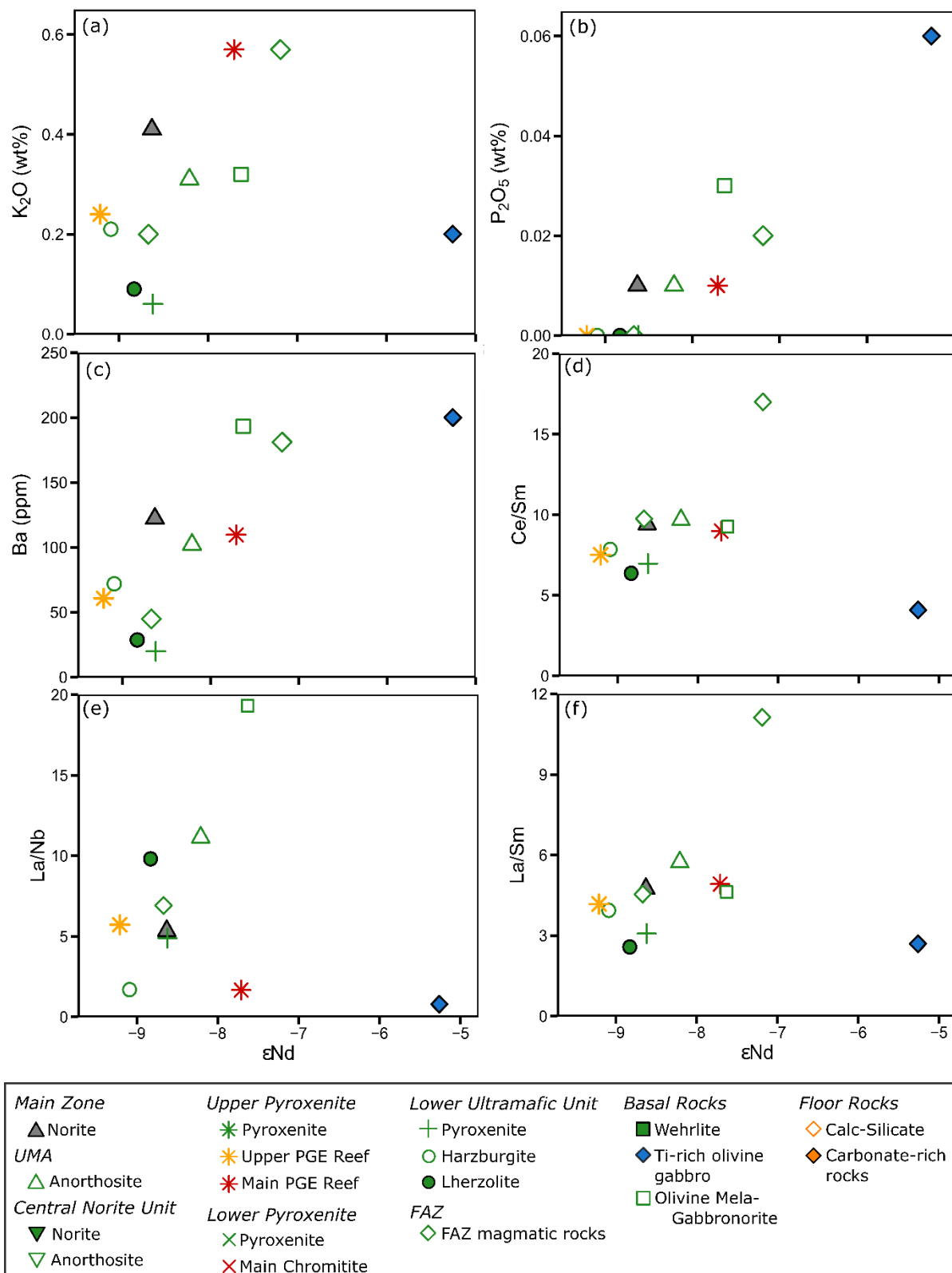
Figure 9.2: Trace element and trace element ratios plotted against εNd for Flatreef and Main Zone rocks. (a) K₂O (wt.%), (b) P₂O₅ (wt.%), (c) Ba (ppm), (d) Ce/Sm, (e) La/Nb, (f) La/Sm.

The downhole plot of drill core UMT081 shows that εNd is variable between approximately -7.5 to -9.5 (Figure 9.3). The highest value in the Upper Flatreef is found in the Main PGE Reef

(-7.71), while in the Lower Flatreef the FAZ has variable ratios between (-7.19 to -8.67). Flatreef rocks have significantly lower εNd values compared to the average UCZ (-6.6) and LCZ (-5.2) of the WBC apart from the Ti-rich olivine gabbro which has an εNd value of -5.26, overlapping with average LCZ values of the WBC. Olivine mela-gabbronorite at the base of drill core UMT081 has similar values to the Main PGE Reef (-7.63 and -7.71, respectively).
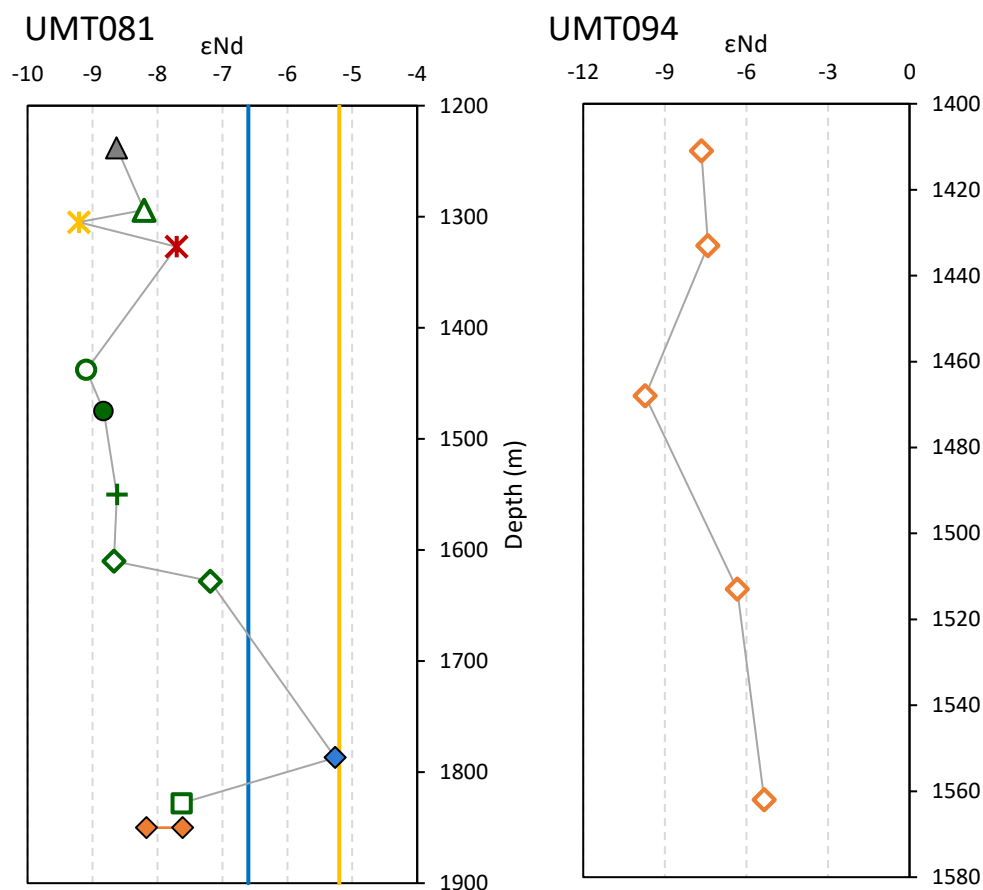
Figure 9.3: Downhole plots of εNd values for drill core UMT081 and UMT094. Duitschland calcareous sediment sample values are plotted at the base of drill core UMT081 for comparison. Blue line is the average UCZ εNd value from the WBC. yellow line is the average LCZ value from the WBC (Maier et al., 2000). Note calcareous sediments and partially devolatized calc-silicate floor rocks in drill core UMT094 have significantly higher εNd than magmatic samples.

Calcareous sediments and variably devolatized floor rocks from drill core UMT094 have variable isotope and trace element ratios and most samples have slightly higher εNd than in the magmatic rocks. Calcareous sediments from the Duitschland Formation has less radiogenic εNd values (-7.62 and -8.17) than Flatreef rocks (-7.71 to -9.21, Upper Flatreef) (Figure 9.3). Calc-silicate rocks the base of drill core UMT094 show a general decrease in εNd values with depth (-7.65 to -5.34 εNd) except sample 94-1468, a magnetite rich layer, which has an anomalously low εNd value (-9.72).

9.1.2 Strontium Isotope Data

In contrast to the Sm-Nd system, Rb and Sr have very different partition coefficients into the main rock forming minerals, with Rb significantly more incompatible than Sr resulting in greater element fractionation during partial melting. Rb and Sr are relatively mobile in fluids making them susceptible to alteration during and after magmatism (Rollinson, 1993). However, fluids will not affect the $^{87}Sr/^{86}Sr_i$ ratio as the isotopes have similar chemical behaviour. Data from this present study is presented in Table 9.2.

Sample	Rb (ppm)	Sr (ppm)	Rb/Sr	$^{87}Sr/^{86}Sr_m$	2σ	$^{87}Rb/^{86}Sr$	$^{87}Sr/^{86}Sr_i$
Magmatic Rocks							
81-1238.81	8.48	282.24	0.030	0.711967	1.08E-05	0.086975	0.709389
81-1294.6	4.09	358.22	0.011	0.709222	1.39E-05	0.033047	0.708242
81-1305.23	6.99	89.14	0.078	0.713717	1.07E-05	0.227095	0.706985
81-1327.62	37.10	56.09	0.661	0.738045	1.14E-05	1.918941	0.681166
81-1422.20	8.80	17.47	0.504	0.717598	1.13E-05	1.458038	0.674380
81-1438.80	8.07	16.21	0.498	0.728278	8.74E-06	1.442300	0.685528
81-1475.85	2.14	115.02	0.019	0.707707	1.35E-05	0.053863	0.706111
81-1550.22	4.73	69.70	0.068	0.711138	1.19E-05	0.196234	0.705321
81-1610.25	9.82	81.96	0.120	0.715418	1.57E-05	0.346744	0.705140
81-1628.6	27.17	580.10	0.047	0.709700	1.70E-05	0.135530	0.705683
81-1787.55	0.42	290.07	0.001	0.705941	1.13E-05	0.004191	0.705817
81-1828.87	2.65	140.78	0.019	0.705733	1.02E-05	0.054380	0.704121
Variably Devolatized Carbonate Country Rocks							
94-1433.22	0.04	1.57	0.026	0.715473	4.28E-05	0.076094	0.712808
94-1513.0	0.46	55.24	0.008	0.707492	1.13E-05	0.024057	0.706650
94-1562.6	0.78	124.21	0.006	0.707510	1.77E-05	0.018234	0.706871
Transvaal Calcareous sediments							
Mal1	2.37	15.95	0.149	0.725345	2.54E-05	0.431021	0.709896
Duit3	27.10	784.58	0.035	0.709211	3.04E-05	0.099921	0.705712

Table 9.2: Table of Sr isotope data for samples from this study. Note the very low (unrealistic) initial Sr ratios for samples 81-1327 to 81-1438 suggesting later fluid overprinting.

Bivariate plots of $^{87}Sr/^{86}Sr_m$ (i.e. present day) against $^{87}Rb/^{86}Sr$ show mostly good positive correlation suggesting there has been limited remobilisation of Rb and Sr after crystallisation (Figure 9.4). However, 3 samples (the Upper PGE Reef and Main Chromitite samples and LUU harzburgite, 81-1327, 81-1422 and 81-1438) have significantly higher $^{87}Rb/^{86}Sr$ relative to their $^{87}Sr/^{86}Sr_m$ values suggesting interaction with a fluid component which is confirmed by the presence of hydrous minerals including amphibole and phlogopite. These analyses are therefore excluded from further discussion. $^{87}Sr/^{86}Sr_i$ shows no significant correlation with any major element oxide (i.e. CaO, MgO, SiO_2, MnO, TiO_2). In addition, trace element ratios such

as La/Nb and Th/Nb do not show correlation with Sr isotope ratios (Figure 9.5). There is no correlation between Ce/Sm with increasing $^{87}Sr/^{86}Sr_i$ values.
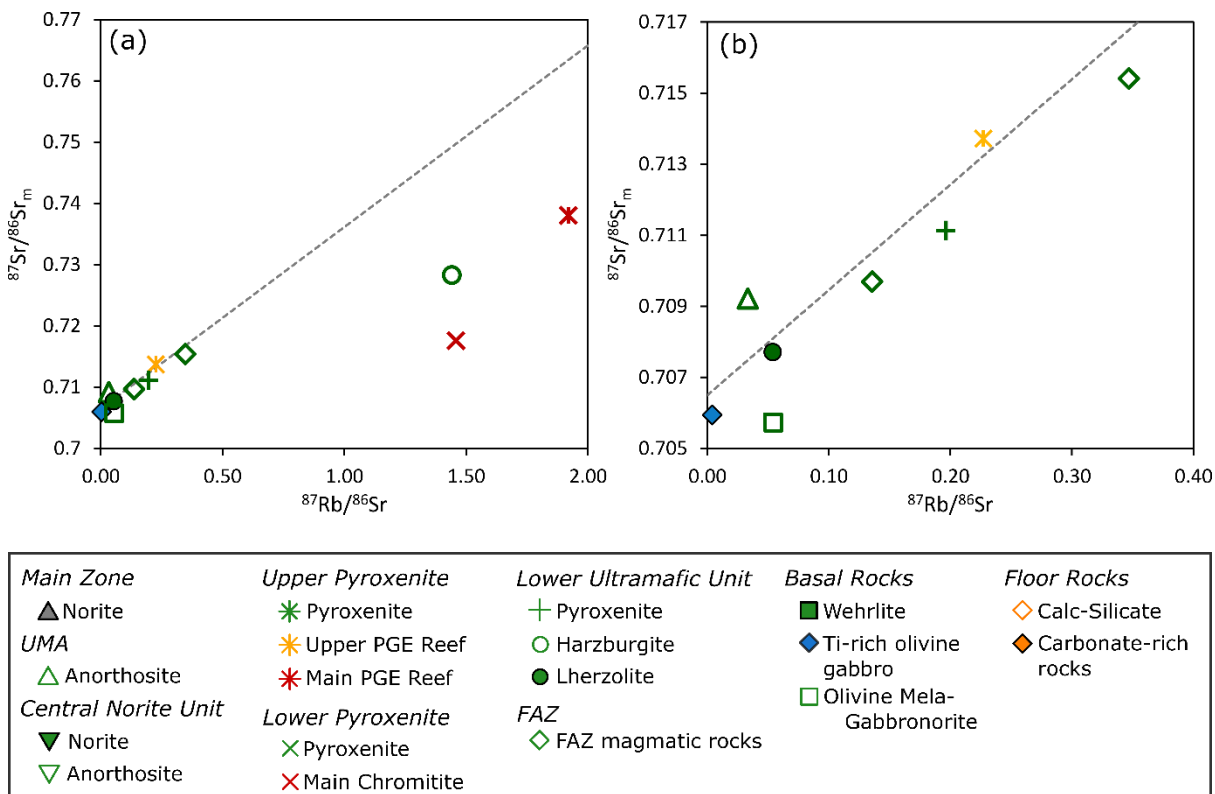
Figure 9.4: Bivariate plots of measured Sr isotope ratios against $^{87}Rb/^{86}Sr$ ratios. (a) All Flatreef data from drill core UMT081, (b) All conformable Flatreef data from drill core UMT081.
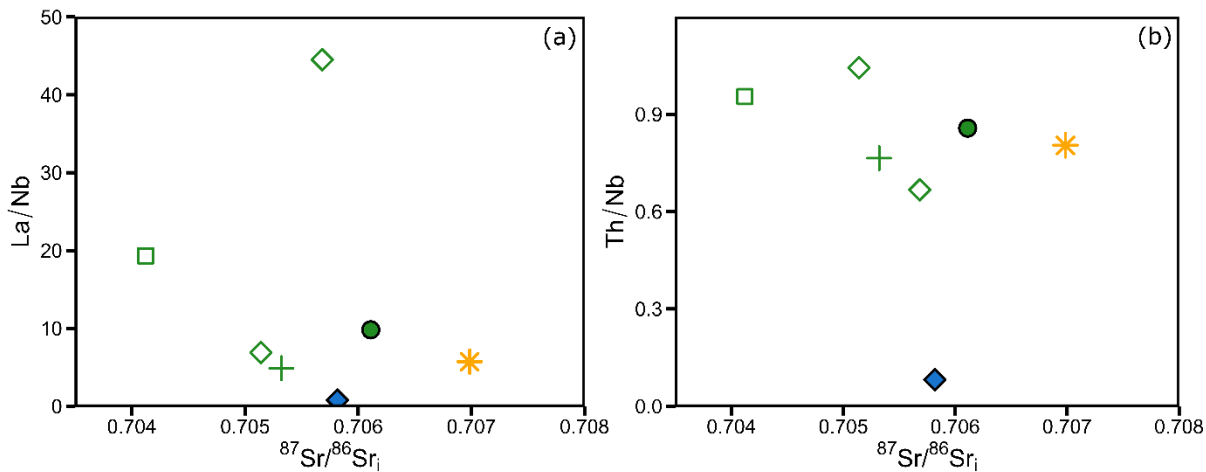
Figure 9.5: Trace element ratios and concentrations vs initial Sr ratios. (a) Ba (ppm), (b) Nb/Ta. Both Ba and Nb/Ta broadly increase with more radiogenic Sr isotope values.

The downhole plot of $^{87}Sr/^{86}Sr_i$ in drill core UMT081 shows an increase in values of the magmatic rocks with height, from 0.704121 at the base to 0.708242 at the top of the Flatreef (Figure 9.6). The overlying MZ has an $^{87}Sr/^{86}Sr_i$ ratio of 0.709389. This upward increase in

$^{87}Sr/^{86}Sr_i$ is a feature observed in many other Sr isotope studies of the Main Bushveld Complex (Kruger, 1994; Maier et al., 2000) and also documented in drill core UMT094 in the Flatreef (Mayer et al., 2018).
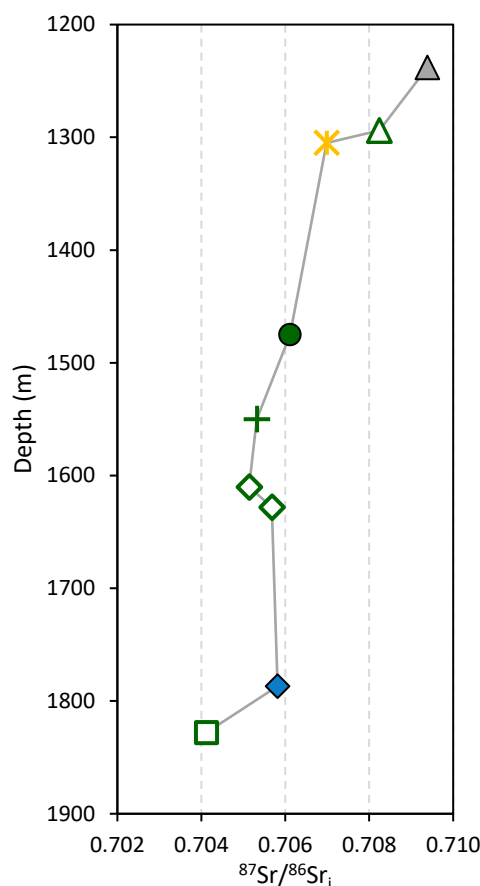
Figure 9.6: Downhole plots from drill core UMT081 of initial Sr ratios from drill core UMT081.

Bivariate plots of calcareous sediments and partially devolatized carbonate country rocks show a positive correlation between $^{87}Sr/^{86}Sr_i$ and several trace element ratios (Figure 9.7). There is a positive relationship between Rb/Sr and $^{87}Sr/^{86}Sr_i$ values, suggesting limited remobilization of trace elements since formation. Devolatized calc-silicate rocks also show a positive correlation but with much lower Rb/Sr ratios, suggesting that Rb has been preferentially removed post-2.05 Ga. Consequently, the Sr isotope ratios of calc-silicate rocks may be somewhat unreliable. Plots of Th/Nd and Th/La vs $^{87}Sr/^{86}Sr_i$ show positive correlation between the ratios and isotope ratios with all elements that are usually fluid immobile. Calc-silicate rocks also show strong negative correlation between LOI and $^{87}Sr/^{86}Sr_i$, with the lowest LOI (usually an indicator of the most strongly devolatized) having the highest $^{87}Sr/^{86}Sr_i$ values.
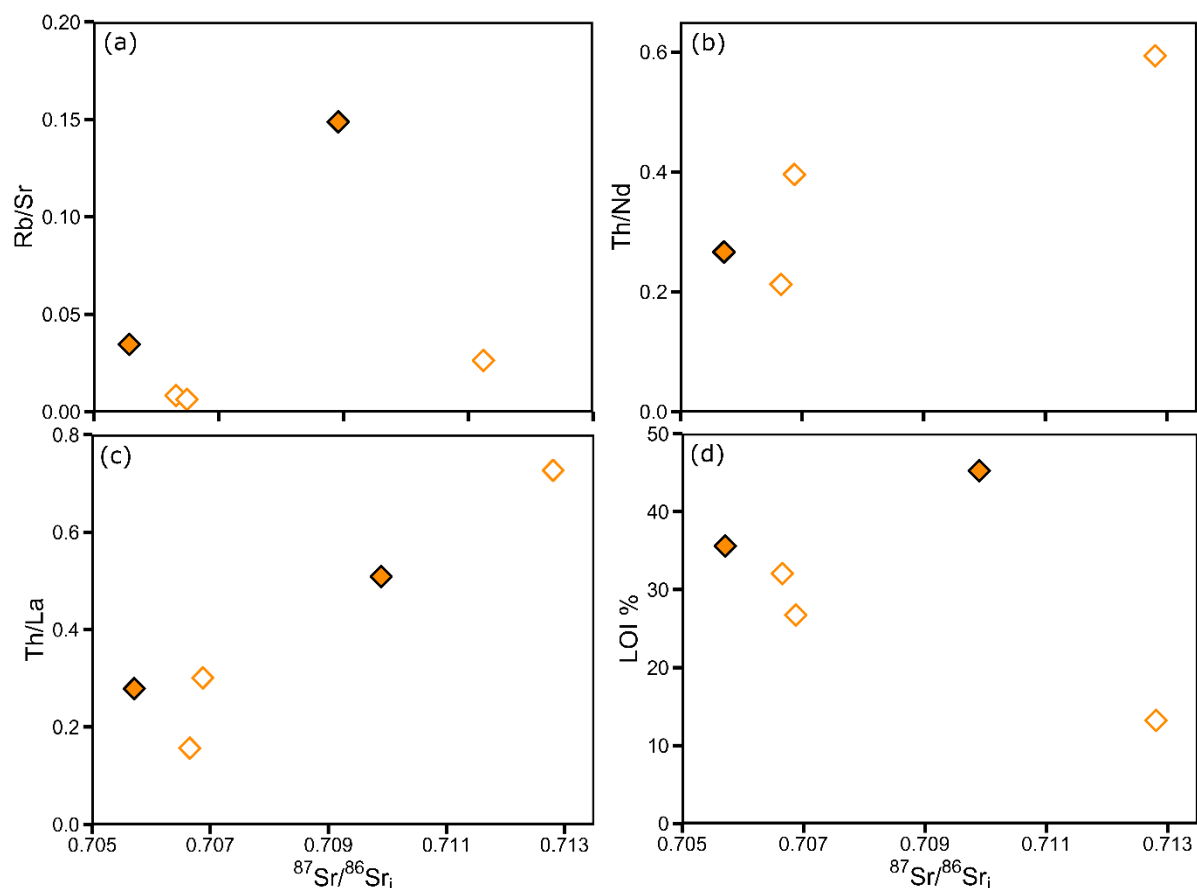
Figure 9.7: Bivariate plots of trace element ratios vs initial Sr isotope ratios of calc-silicate and calcareous sediments. (a) Rb/Sr, (b) Th/Nd, (c) Th/La, (d) LOI (%).

9.1.3 Lead Isotope Data

Few Pb isotope studies have been conducted on Bushveld rocks, but Pb isotopes are potentially useful in assessing contamination of magmas by calcareous sediments which can be significantly richer in U and Th. Pb isotopes are also used to determine magma provenance. While U, Th and Pb all have similar ionic charges and radii, U is highly soluble in aqueous fluids. Isochron diagrams show good correlation between measured $^{208}Pb/^{204}Pb$ against $^{232}Th/^{204}Pb$ suggesting little remobilisation of Pb isotopes post emplacement. Greater variability is present in $^{207}Pb/^{204}Pb$ vs $^{235}U/^{204}Pb$ suggesting some potential fluid mobilisation of isotopes, although this is somewhat limited by the diminutive proportion of isotope ^{235}U (<1%) within the overall U budget. In contrast, $^{238}U/^{204}Pb$ vs $^{206}Pb/^{204}Pb$ plots show significant scatter around the isochron suggesting fluid mobilisation of ^{238}U. This perturbation must have occurred significantly after emplacement of the Bushveld Complex, at a time when only minimal ^{235}U remained, so this event only had a noticeable impact on the more abundant ^{238}U portion. Consequently $^{206}Pb/^{204}Pb$ ratios are too disturbed to be of use in this study. $^{208}Pb/^{204}Pb$ and $^{207}Pb/^{204}Pb$ data are reported in Table 9.3. Figure 9.8 shows that Flatreef rocks plot with

lower ^{208}Pb/^{204}Pb ratios than the isochron compiled from UCZ data of Mathez and Kent (2007) (grey dashed line).

Sample	^{208}Pb/^{204}Pb$_m$	2σ	^{207}Pb/^{204}Pb$_m$	2σ	^{206}Pb/^{204}Pb$_m$	2σ
81-1305	35.552671	1.46E-03	15.373724	4.74E-04	16.129984	4.46E-04
81-1327	35.783713	1.19E-03	15.414578	4.60E-04	16.509200	4.56E-04
81-1422	35.921093	9.66E-04	15.499286	5.78E-04	16.795908	4.34E-04
81-1438	35.548727	1.46E-03	15.427145	5.70E-04	16.012763	5.10E-04
81-1475	35.343682	8.56E-04	15.356369	3.44E-04	15.625370	2.80E-04
81-1550	36.471015	1.34E-03	15.452129	4.70E-04	16.649413	4.80E-04
81-1610	35.040546	1.17E-03	15.293404	4.34E-04	15.348150	3.96E-04
81-1628	34.849177	1.42E-03	15.305734	4.96E-04	15.256639	4.66E-04
81-1787	35.126051	1.10E-03	15.440072	4.26E-04	15.514526	3.80E-04
81-1828	34.915282	1.69E-03	15.313963	5.78E-04	15.382978	4.60E-04
94-1411	36.356061	1.28E-03	15.306980	4.24E-04	15.504861	4.18E-04
94-1433	39.830373	2.42E-03	15.670217	7.12E-04	18.491663	6.94E-04
94-1513	37.727264	1.24E-03	15.337737	4.84E-04	15.550421	3.44E-03
94-1562	45.266431	2.28E-03	16.221721	7.14E-04	22.295130	7.98E-04
DUIT3	39.725862	1.46E-03	16.735434	4.98E-04	22.969038	5.70E-04
MAL1	40.284482	1.74E-03	16.357237	5.92E-04	23.061012	9.10E-04

Sample	^{232}Th/^{204}Pb	^{235}U/^{204}Pb	^{238}U/^{204}Pb	^{208}Pb/^{204}Pb$_i$	^{207}Pb/^{204}Pb$_i$	^{206}Pb/^{204}Pb$_i$
81-1305	4.8171	0.0080	1.1003	35.036334	15.314357	16.530724
81-1327	3.3867	0.0062	0.8552	35.420705	15.368435	15.811235
81-1422	8.9595	0.0172	2.3508	34.960741	15.372449	15.633033
81-1438	7.2300	0.0093	1.2720	34.773759	15.358518	16.321841
81-1475	2.1437	0.0033	0.4576	35.113907	15.331680	15.842217
81-1550	8.6441	0.0037	0.5088	35.544470	15.424677	15.435742
81-1610	1.3080	0.0023	0.3105	34.900346	15.276653	16.533702
81-1628	0.2663	0.0005	0.0744	34.820629	15.301722	15.320438
81-1787	0.8675	0.0014	0.1936	35.033061	15.429625	16.869353
81-1828	1.7754	0.0039	0.5346	34.724984	15.285119	15.315278
94-1411	21.6988	0.0095	1.3066	34.030209	15.236481	14.895986
94-1433	39.6607	0.0431	5.9003	35.579226	15.351873	13.305790
94-1513	22.4816	0.0102	1.3918	35.317508	15.262646	101.860233
94-1562	82.1656	0.1085	14.8545	36.459266	15.420260	10.014058
DUIT3	36.2399	0.1229	16.8268	35.841374	15.827561	16.023695
MAL1	26.5054	0.0876	11.9850	37.443423	15.710595	42.288345

Table 9.3: Pb isotope data from the Flatreef and country rocks.
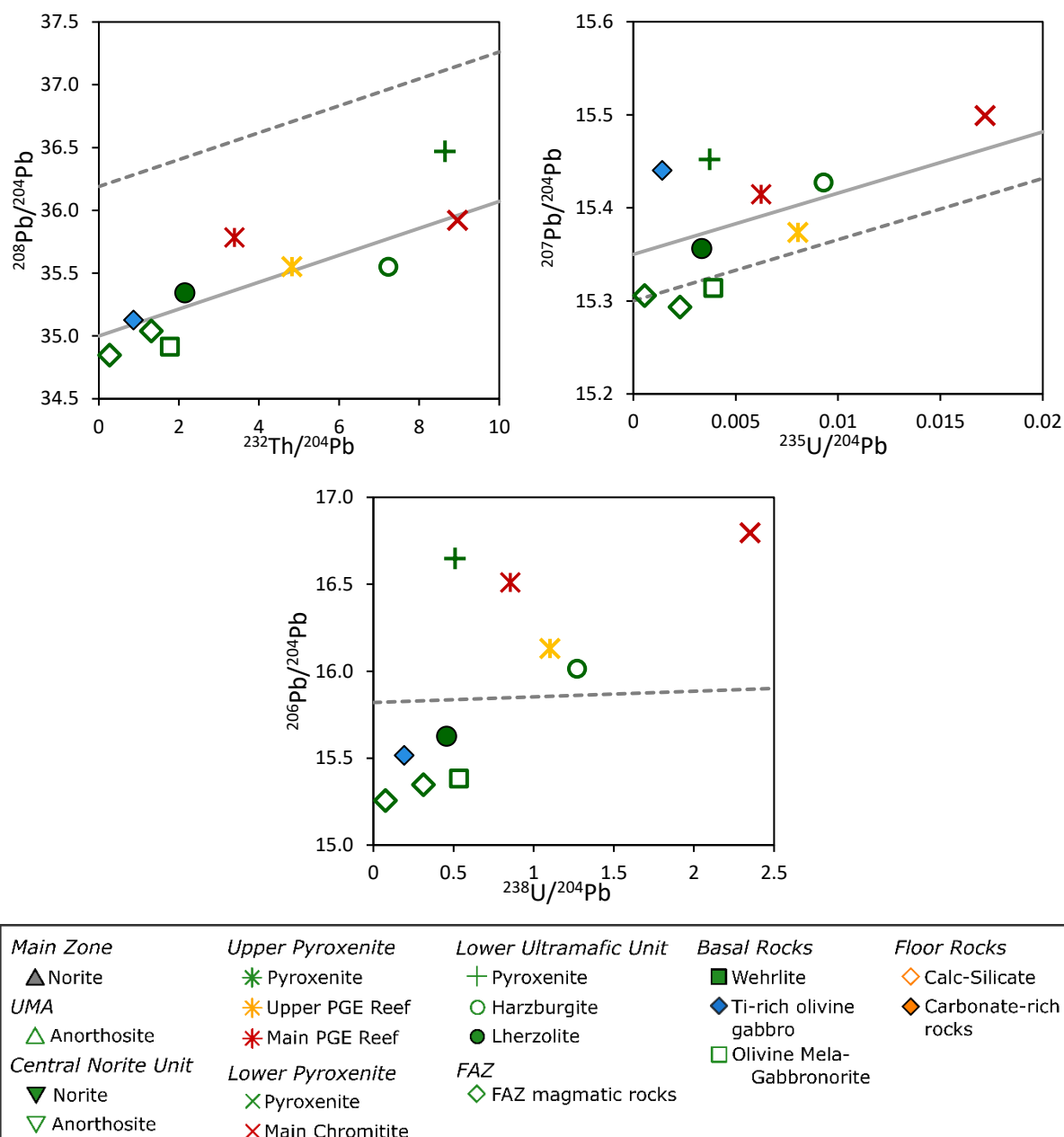
Figure 9.8: Isochron plots of measured Pb isotope ratios plotted against their parent ratios. (a) $^{208}Pb/^{204}Pb$ vs $^{232}Th/^{204}Pb$, (b) $^{207}Pb/^{204}Pb$ vs $^{235}U/^{204}Pb$, (c) $^{206}Pb/^{204}Pb$ vs $^{238}U/^{204}Pb$. Note the best correlation between measured and parent isotope ratios is within the Th-Pb decay system, with greatest scatter seen in ^{238}U-^{206}Pb space. Solid grey line – isochron constructed using data from this study. Dashed grey line – isochron constructed using UCZ data from Mathez and Kent (2007).

Bivariate plots of both $^{208}Pb/^{204}Pb$ and $^{207}Pb/^{204}Pb$ against various lithophile elements show broad similarities between the two isotope systems, although there is more scatter in $^{207}Pb/^{204}Pb$ compared to $^{208}Pb/^{204}Pb$ (Figure 9.9 and Figure 9.10). There is positive correlation between ^{208}Pb and ^{207}Pb isotopes and MgO and negative correlation with CaO, K_2O and MnO concentrations, although there is significant scatter.
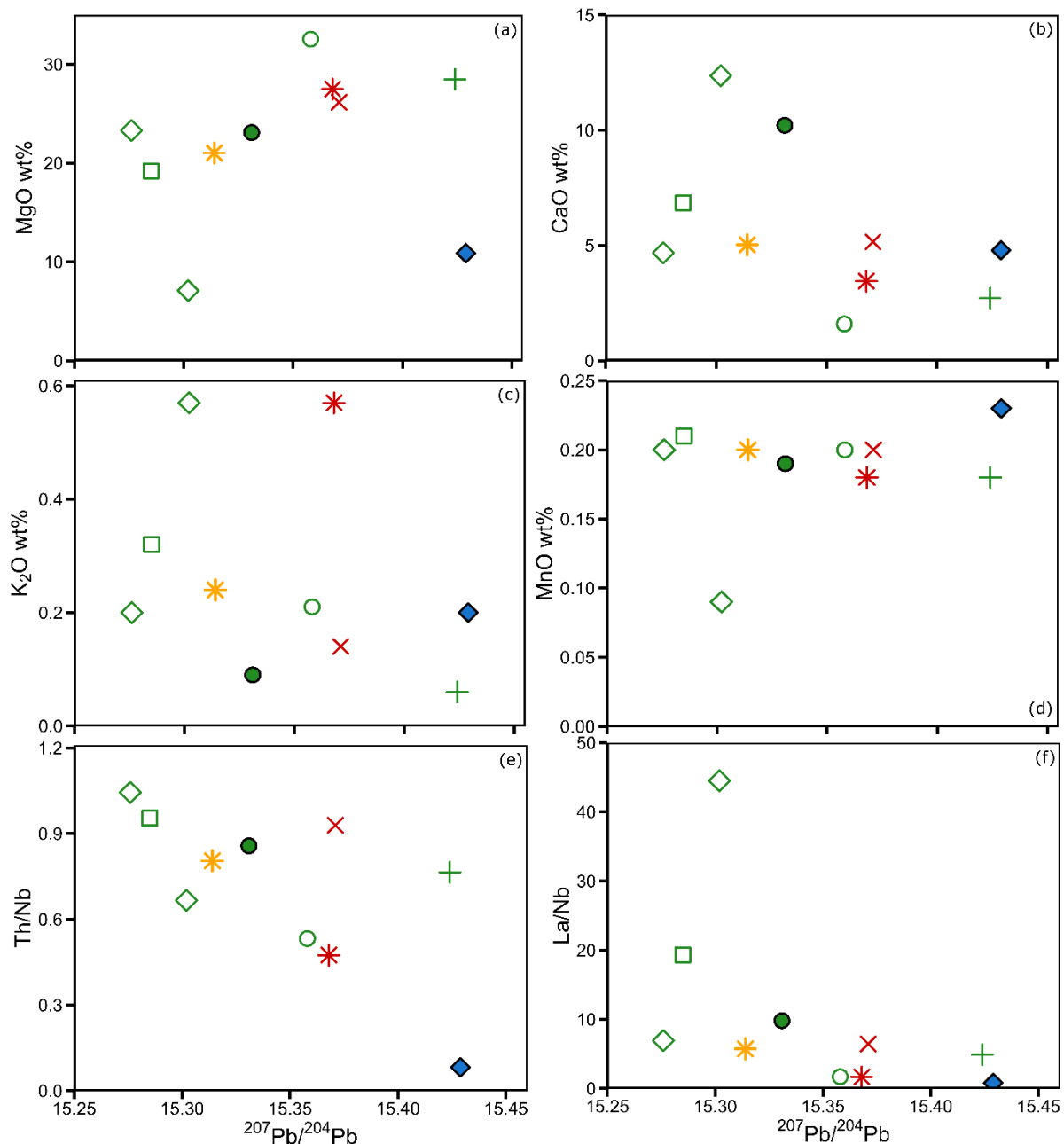
Figure 9.9: Bivariate plots of various lithophile elements and trace element ratios against $^{207}Pb/^{204}Pb$. (a) MgO, (b) CaO, (c) K_2O, (d) MnO, (e) Th/Nb, (f) La/Nb.
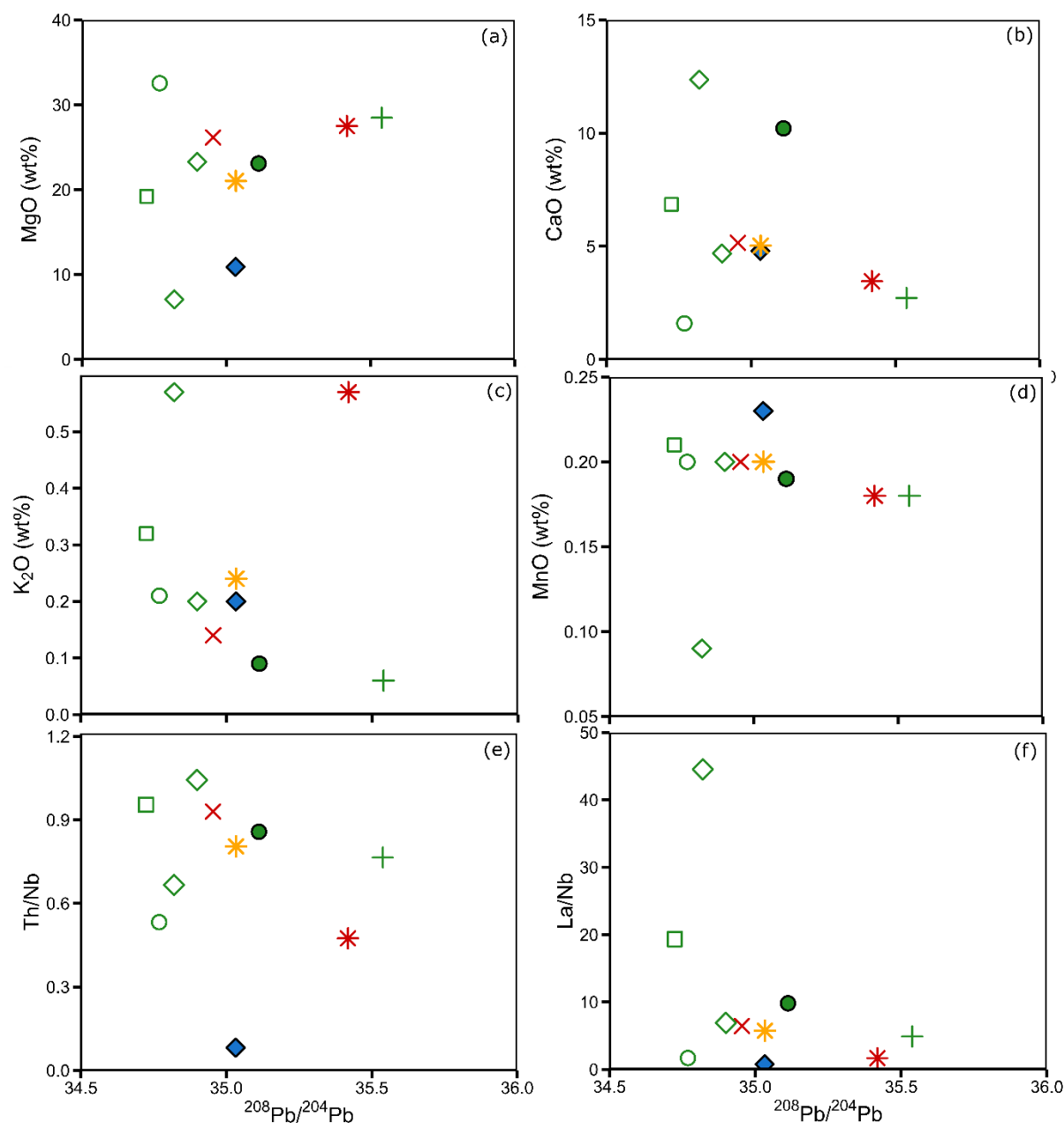
Figure 9.10: Bivariate plots of various lithophile elements and trace element ratios against $^{208}Pb/^{204}Pb$. (a) MgO, (b) CaO, (c) K_2O, (d) MnO, (e) Th/Nb, (f) La/Nb. Note there is a broad correlation with MnO with less scatter than seen in $^{207}Pb/^{204}Pb$ plots.

In trace elements and trace element ratios there is greater variability between the two isotope systems. Both $^{207}Pb/^{204}Pb$ and, to a lesser extent, $^{208}Pb/^{204}Pb$ show some negative correlation with Th/Nb and La/Nb ratios, albeit with significant scatter (Figure 9.9 and Figure 9.10). While $^{208}Pb/^{204}Pb$ shows no apparent correlation with PGE, $^{207}Pb/^{204}Pb$ values show some positive correlation with PGE, Cu and Ni concentrations (Figure 9.11). Neither Pb isotope system shows correlation with ratios of PGE.
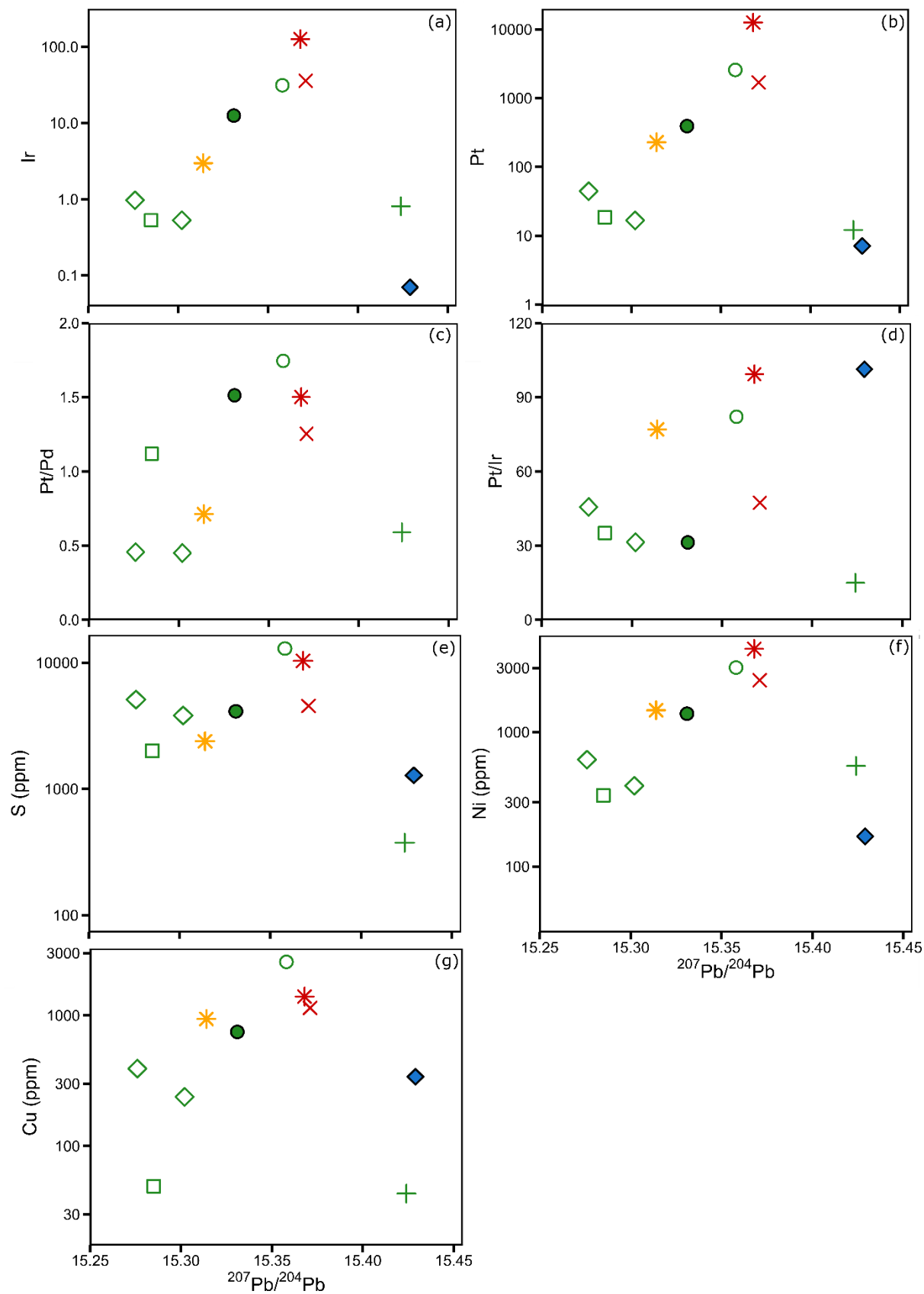
Figure 9.11: Bivariate plots of $^{207}Pb/^{204}Pb$ vs various PGE, PGE ratios and chalcophile elements.(a) Ir, (b) Pt, (c) Pt/Pd, (d) Pt/Ir, (e) S, (f) Ni, (g) Cu. Note the broadly positive correlation between increasing PGE, Cu, Ni, S concentrations and increasing $^{207}Pb/^{204}Pb$ values.

Downhole plots of Pb isotopes show that $^{208}Pb/^{204}Pb$ and $^{207}Pb/^{204}Pb$ are broadly coupled throughout drill core UMT081 (Figure 9.12). However, $^{208}Pb/^{204}Pb$ isotope values of the Main Chromitite and underlying harzburgite are relatively lower than their $^{207}Pb/^{204}Pb$ values. Downhole plots of the calc-silicate floor rocks at the base of drill core UMT094 show these rocks have broadly constant Pb isotope values and are less radiogenic than calcareous sediment samples (Figure 9.12). The uppermost sample of the calc-silicate floor rocks has marginally lighter $^{208}Pb/^{204}Pb$ values than underlying calc-silicate rocks.
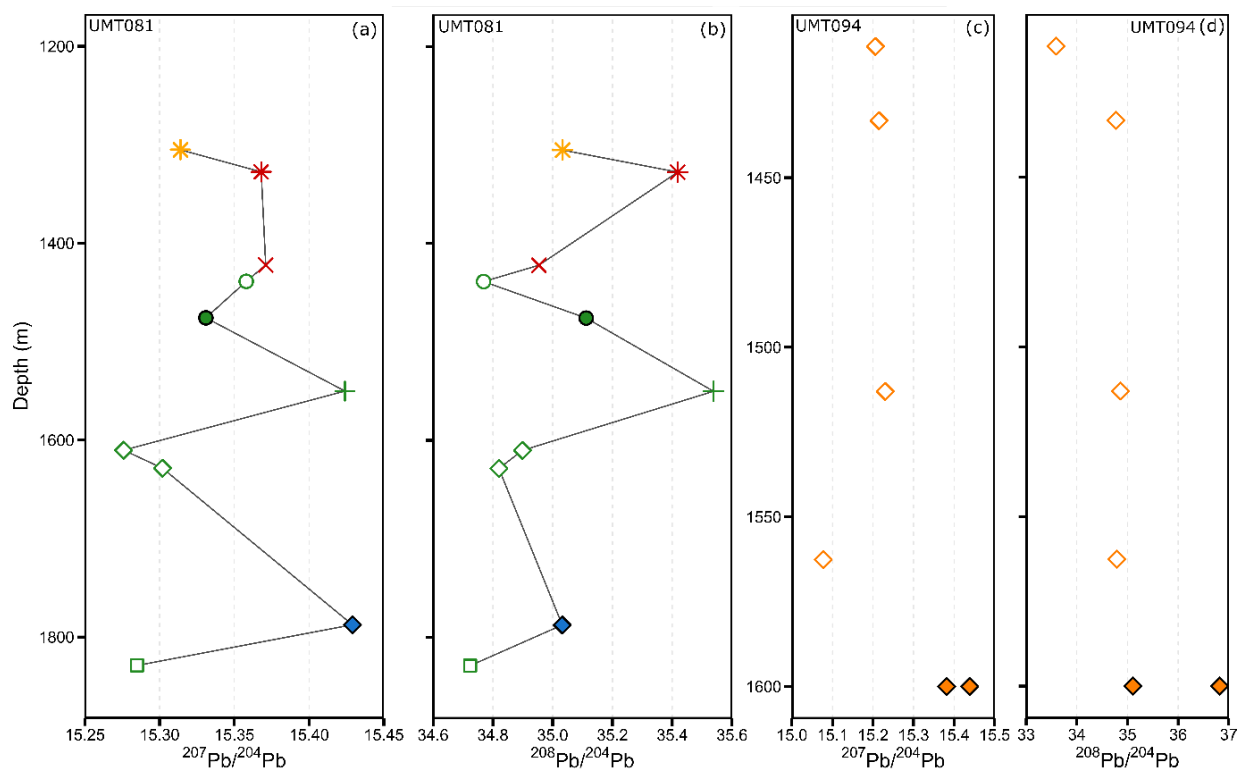
Figure 9.12: Downhole plots of Pb isotope ratios (a) $^{207}Pb/^{204}Pb$ and (b) $^{208}Pb/^{204}Pb$ in drill core UMT081 and (c) $^{207}Pb/^{204}Pb$ and (d) $^{208}Pb/^{204}Pb$ in drill core UMT094. UMT081 shows broadly similar downhole patterns for the two Pb isotope systems. Calc-silicate and calcareous sedimentary rocks (the latter arbitrarily plotted at 1600 m depth for comparison purposes) show broadly constant downhole isotope ratios, whilst calcareous sediments are richer in radiogenic Pb.

9.2 Stable Isotopes

9.2.1 Oxygen Isotope Data

Table 9.4 contains the stable isotope data (oxygen and carbon) presented in the following section. Unless otherwise specified, all $\delta^{18}O$ values are presented relative to Vienna Standard Mean Ocean Water (vSMOW) while $\delta^{13}C$ values are presented relative to Vienna Pee-Dee Belemnite (vPDB). Orthopyroxene and plagioclase analysed from the Main Zone (81-1238) give a $\Delta_{plagioclase-pyroxene}$ of 0.7. In the Flatreef, suitable plagioclase-pyroxene pairs were not available to measure. Therefore, partition offsets between $\delta^{18}O$ opx and plag are set at +0.55‰ and -0.2‰, after Harris et al. (2001). Flatreef rocks have generally heavy $\delta^{18}O_{WR}$ values (7.5-11.2‰) compared to mantle values (5.7‰ $\delta^{18}O_{WR}$; (Taylor, 1980). Downhole plots of $\delta^{18}O_{WR}$ show increasingly heavy values with depth below the Main PGE Reef, which has the lightest O isotope ratio in the Flatreef (7.55‰ $\delta^{18}O_{WR}$). Above the reef, $\delta^{18}O$ increases with height up to the top of the Flatreef. Lherzolite at 1475 m depth is anomalously light (7.4‰ $\delta^{18}O_{cpx}$) and does not fit the broad trends described here (Figure 9.13).

Sample	Unit	Rock Type	$\delta^{18}O_{Plag}$	$\delta^{18}O_{Px}$	$\delta^{18}O_{WR}$	$\delta^{18}O_{WR}$[a]
1238.81	MZ	No	8.80	8.06		8.61
1294.20	UMA	An	9.90			9.70
1305.23	Upper Pyroxenite	Px		8.44		8.99
1316.80	Upper Pyroxenite	Px		9.26		9.81
1327.62	Upper Pyroxenite	PGE Reef		7.00		7.55
1422.20	Lower Pyroxenite	Chromitite		8.80		9.35
1438.87	Lower Ultramafic	Hz		8.50		9.05
1475.85	Lower Ultramafic	Lz		7.40		7.95
1550.22	Lower Ultramafic	Px		8.90		9.45
1610.25	FAZ	Px		10.00		10.55
1787.55	High-Ti	High-Ti			10.73	10.73
1828.87	Basal Rocks	Ol Mela-Gab.		10.70		11.25
Duit 1	Transvaal	Dol			15.85	15.85
Duit 3	Transvaal	Dol			11.07	11.07
Mal 1	Transvaal	Dol			22.36	22.36

Table 9.4: Oxygen and carbon isotope data for Flatreef and calcareous sediment samples from this study. [a]oxygen isotope values have been converted into whole rock values using estimates from Harris et al. (2001).
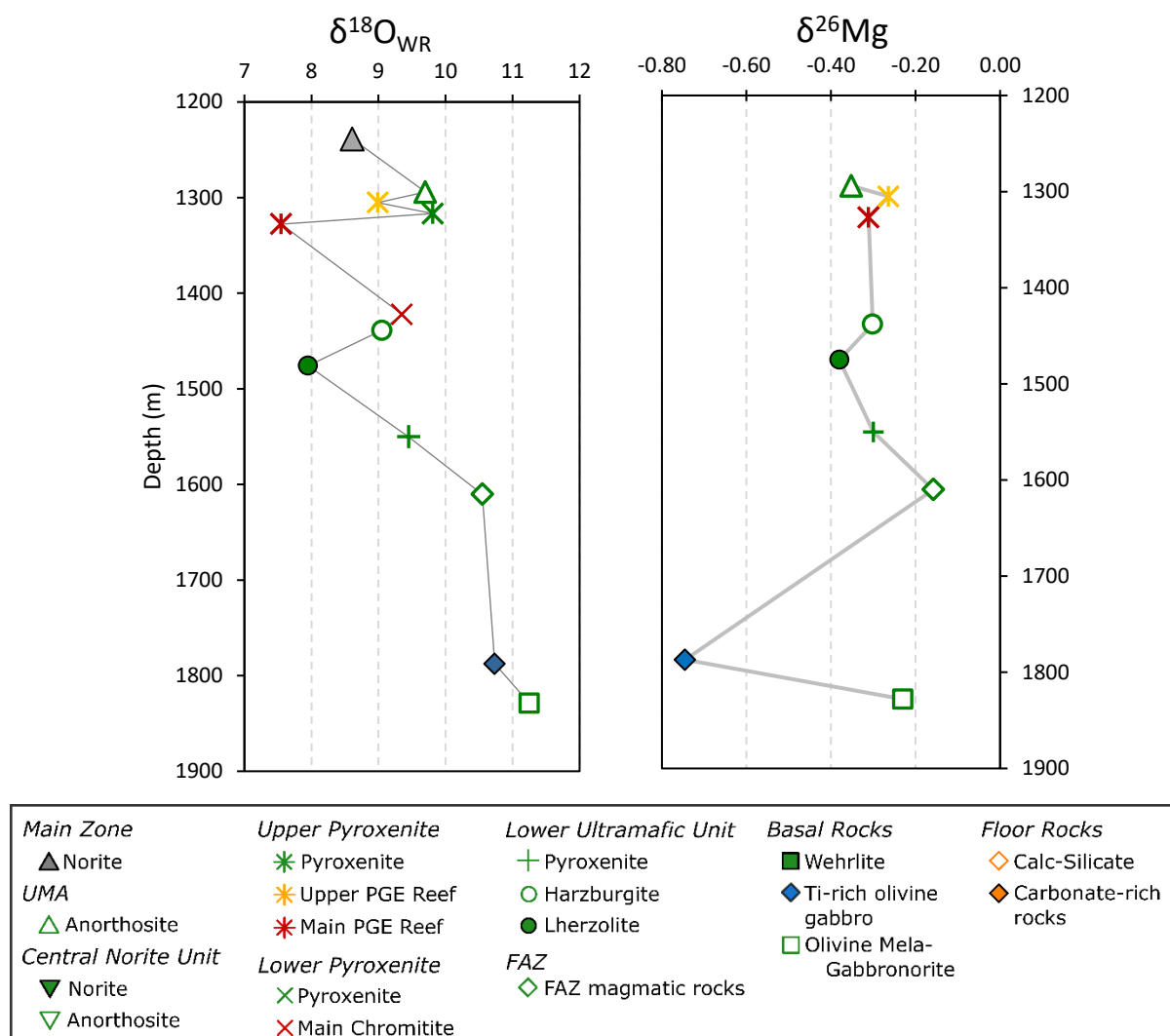
Figure 9.13: Downhole plots of stable isotopes from drill core UMT081. (a) $\delta^{18}O_{WR}$, (b) $\delta^{26}Mg$.

Bivariate plots of $\delta^{18}O$ against various major element oxides (CaO, MgO, SiO$_2$, TiO$_2$) show poor correlations (Figure 9.14). This is expected as oxygen is a major element in all rock types and consequently will not display mineralogical control. There is a weakly negative correlation between LOI and $\delta^{18}O$ (except for peridotite), where lower LOI correlate with heavier oxygen isotope signatures. In addition, heavier $\delta^{18}O$ shows a strong positive correlation with MnO concentration, except for in Main Zone norite and the UMA. There is a weak positive correlation between Sc and $\delta^{18}O$ but no clear relationship between chalcophile elements, S and $\delta^{18}O$. However, there are relationships between Cu, Ni, S and $\delta^{18}O$ within individual units (Figure 9.15). Pyroxenite from the Upper Pyroxenite Unit show increasing Cu/S and exponentially increasing Ni/S ratios correlated with heavier $\delta^{18}O$. This is in part a function of decreasing S contents with increasing $\delta^{18}O$. All pyroxenite rocks in drill core UMT081 show exponential increases in Ni/S and decreasing S with heavier $\delta^{18}O$ values.
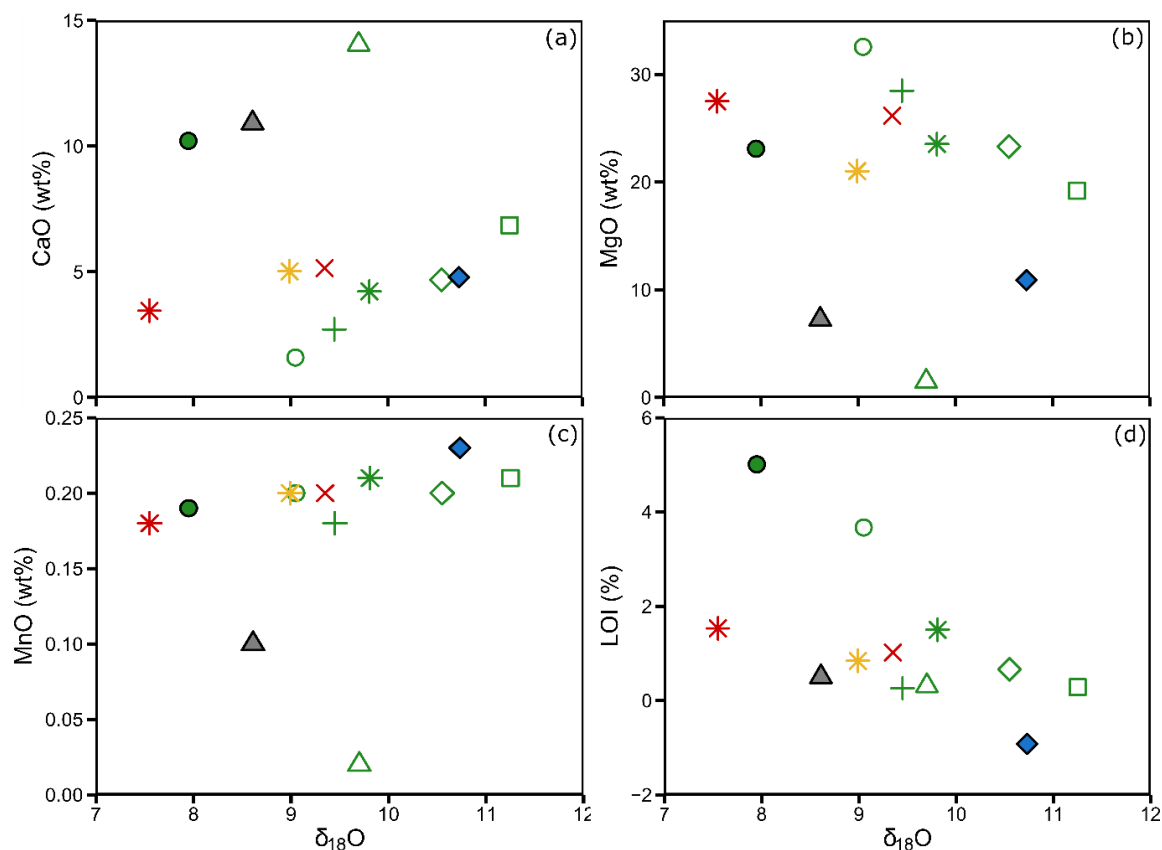
Figure 9.14: Bivariate plots of major element oxides (wt.%) against oxygen isotope data (whole rock). (a) CaO, (b) MgO, (c) MnO, (d) LOI. Note MnO has a positive correlation with δ¹⁸O.
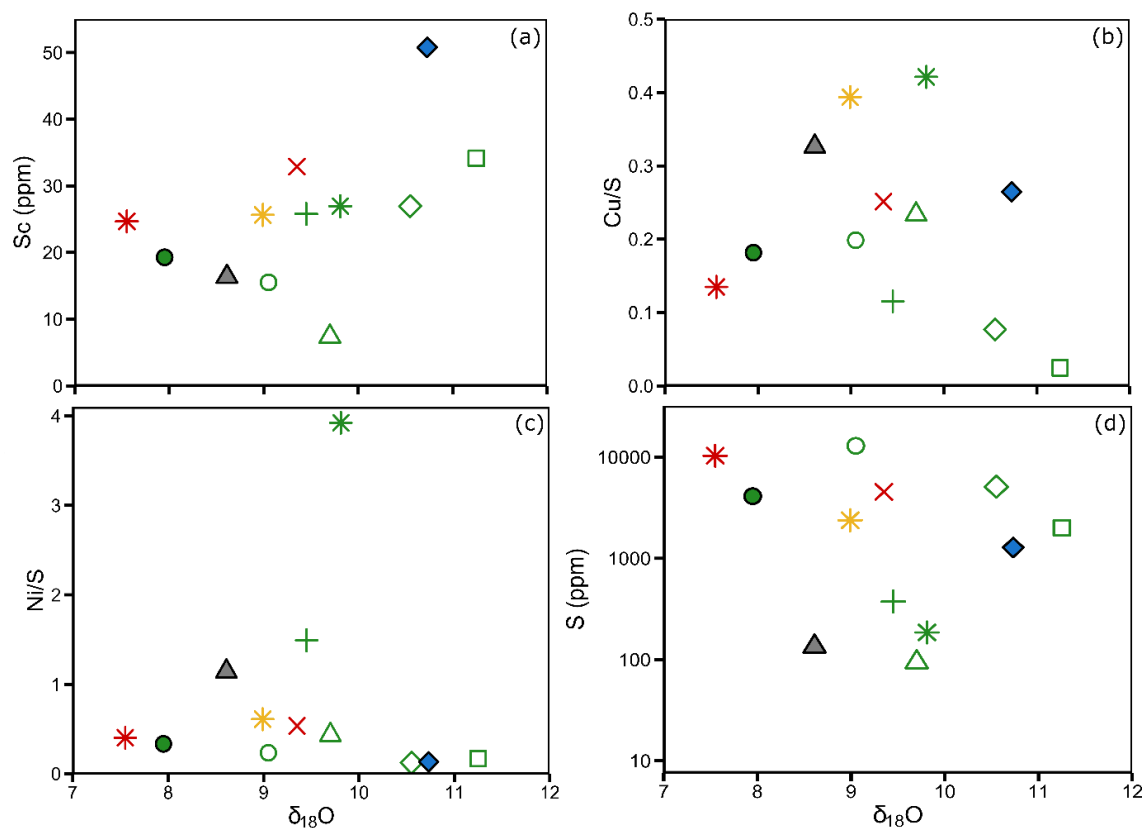
Figure 9.15: Bivariate plot of trace element and chalcophile element ratios against oxygen isotopes (whole rock). (a) Sc (ppm), (b) Cu/S, (c) Ni/S, (d) S (ppm).

The PGE show a negative correlation with $\delta^{18}O$, although there is considerable scatter (Figure 9.16). Apart from 2 samples in the Lower Ultramafic Unit, there is a negative correlation between $\delta^{18}O$ values and PPGE/IPGE content. There is no systematic relationship between Pt/Pd and $\delta^{18}O$.
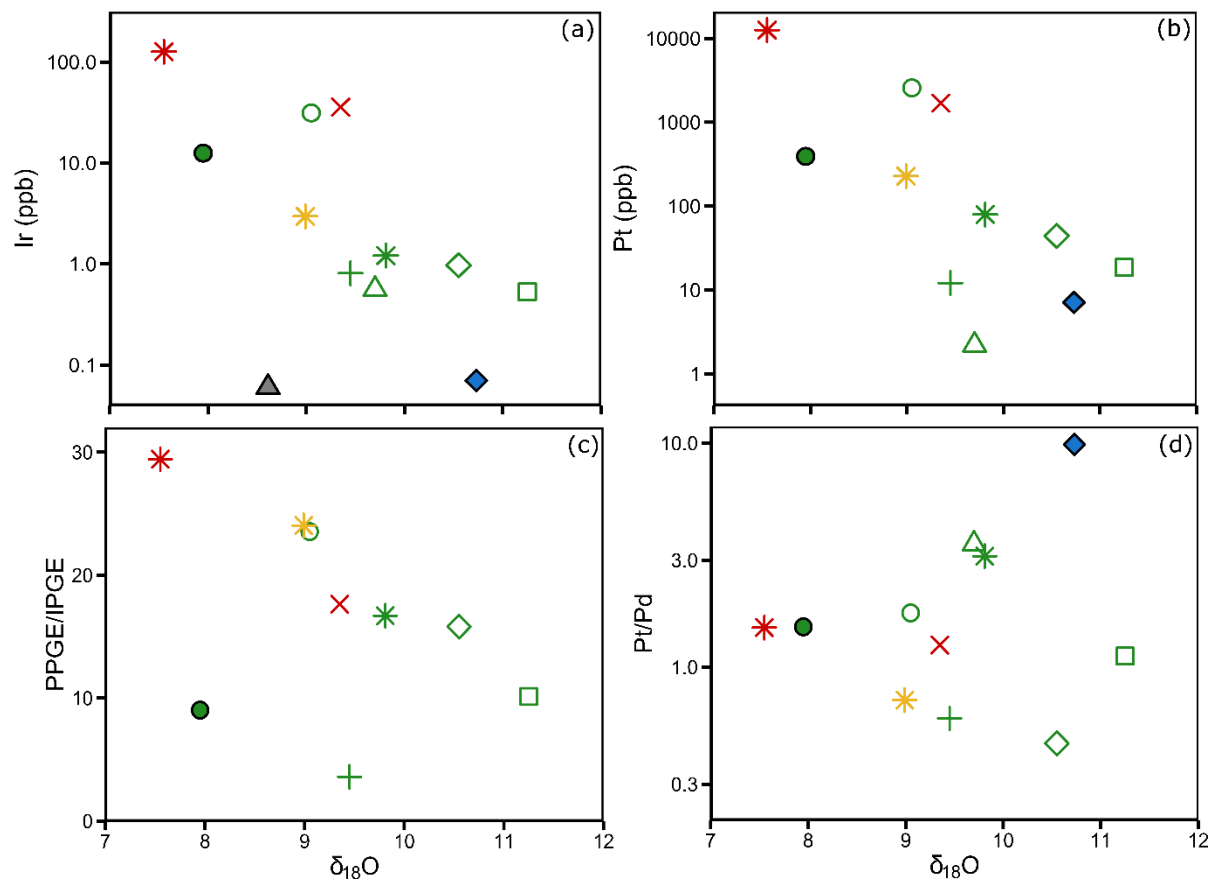
Figure 9.16: Bivariate plots of PGE data (ppb) against oxygen isotopes. (a) Ir, (b) Pt, (c) PPGE/IPGE, (d) Pt/Pd. Note there is a broadly negative relationship between $\delta^{26}Mg$ and PGE concentration as well as PPGE/IPGE ratios.

Whole-rock oxygen isotopes from calcareous sediment samples show a range of values (11.07-22.36‰ $\delta^{18}O$) with a wide range of $\delta^{13}C$ values also observed (-0.95 to 5.83‰). Other studies on Transvaal Supergroup carbonates have also shown a wide range of $\delta^{18}O$ and $\delta^{13}C$ values, which have been largely explained by fractionation during devolatization in response to contact metamorphism relating to intrusion of Bushveld magmas, driving isotope values of dolomite to +5‰ $\delta^{13}C$ and +9.4‰ $\delta^{18}O$ (Frauenstein et al., 2009). This process appears to apply to calcareous sediments from the Duitschland Formation in this study where lighter $\delta^{18}O$ is accompanied by lighter $\delta^{13}C$ (Figure 9.17). Malmani calcareous sediments, in contrast, has a light $\delta^{13}C$ value (-0.95‰) while maintaining heavy $\delta^{18}O$ (22.36‰ $\delta^{18}O$).
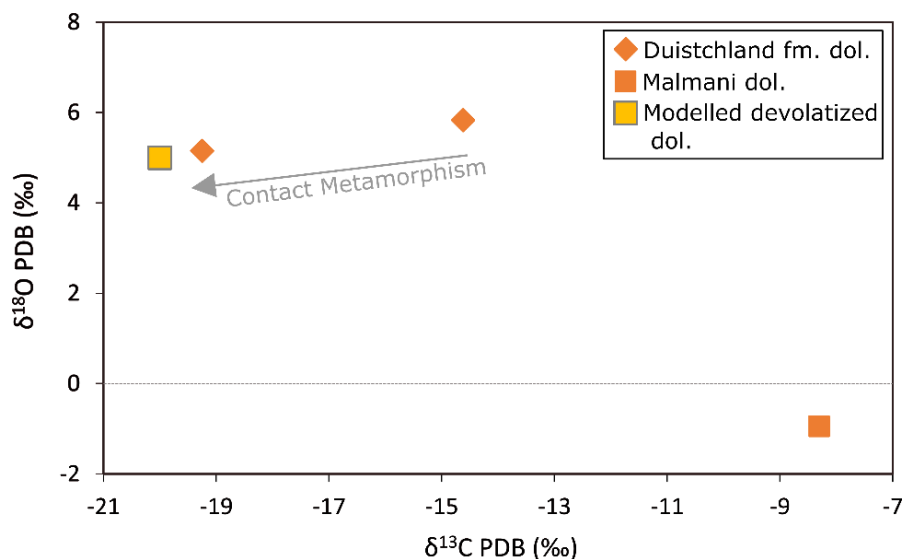
Figure 9.17: Bivariate isotope plot of oxygen and carbon isotopes demonstrating the devolatization pathway of Duitschland calcareous sediments in proximity to the Bushveld Complex.

9.2.2 Magnesium Isotope Data

Magnesium isotopes are being used increasingly to investigate magma provenance, alteration and contamination (Shen et al., 2013; Teng, 2017). As this is a non-traditional isotope system, it shall be briefly introduced before the data from this study is presented. Mantle composition (i.e. bulk earth) is -0.25‰ δ^{26}Mg ± 0.04, with mantle derived melts straddling this value (Figure 9.18) (Teng, 2017). In contrast, carbonate rocks can have very light Mg isotope signatures, a function of fractionation during their formation (-1.04 to -5.57‰ δ^{26}Mg in limestone and -0.38 to -3.25‰ δ^{26}Mg in dolomite) (Teng, 2017). Because of the large relative mass difference between Mg isotopes, low-temperature processes (such as carbonate formation) result in significantly lighter δ^{26}Mg values. However, low temperature (<350°C) metamorphism has been found to have no effect of Mg isotopic ratios, suggesting fluids produced during devolatization of dolomites have isotopic compositions akin to their protolith (Geske et al., 2012).
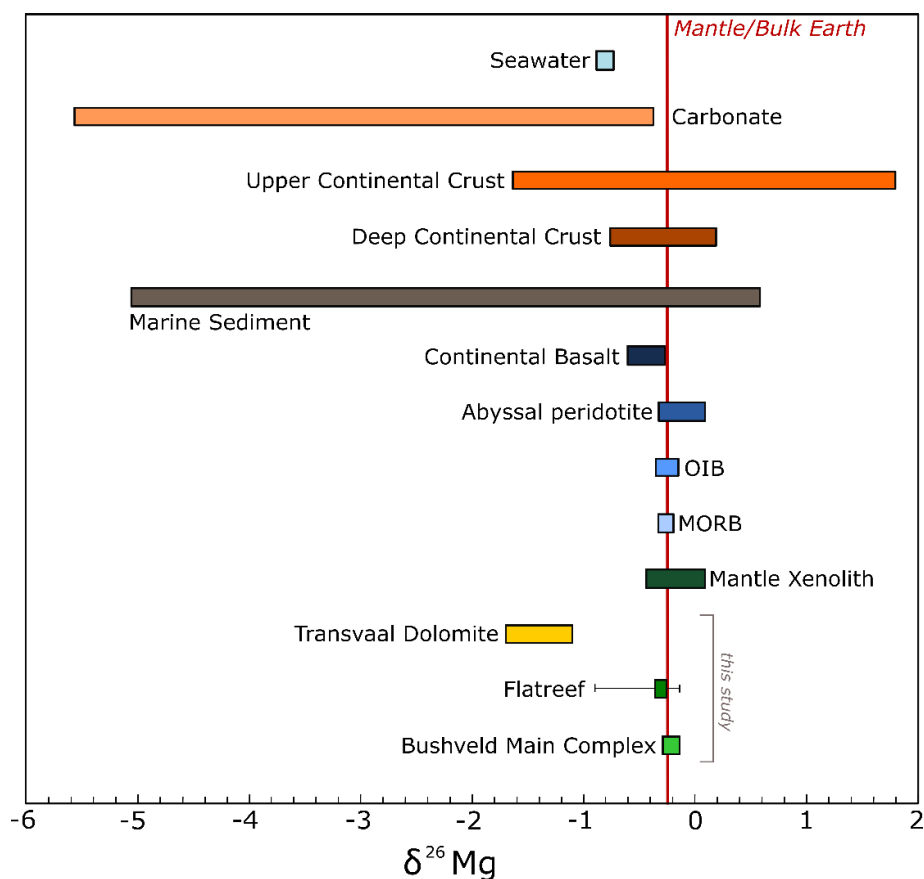
Figure 9.18: Range of δ²⁶Mg isotope values present in different reservoirs, compared to data from this study. Modified from Teng (2017).

Igneous rocks, formed at high-temperature, do not experience fractionation on the same order as in carbonate rock formation and this is reflected in the narrow range of δ^{26}Mg values. Olivine and pyroxenes have similar Mg isotope partitioning resulting in only small δ^{26}Mg fractionation (<0.2‰) (Teng, 2017). However, garnet and spinel have very different partition coefficients leading to elevated δ^{26}Mg values in spinel and lower values in garnet. In the Bushveld Complex, spinel is present as chromite and magnetite, both of which are Mg poor and consequently have no visible effect on δ^{26}Mg values.

As there are no previous Mg isotope data from the Bushveld Complex, two samples from the UCZ of the WBC were also analysed. Data for all Mg isotopes analysed in this study are presented in Table 9.5. The WBC Merensky Reef and its pyroxenitic hangingwall have δ^{26}Mg values of -0.16 and -0.28‰, respectively, the latter being within error of mantle values whereas the Merensky reef is heavier than both MORB (-0.31 to -0.19‰) and OIB (-0.35 to -0.18‰) data but overlaps with mantle xenolith data (Teng et al., 2010). The Upper Flatreef has a slightly lighter δ^{26}Mg signature, with most samples ranging between -0.26 to -0.37‰. The heaviest δ^{26}Mg signature occurs in the FAZ, overlapping with the Merensky Reef of the WBC. All other pyroxenites have Mg isotopic signatures similar to the UCZ pyroxenite (-0.28‰),

while lherzolite and UMA have lighter ratios (-0.37 and -0.35‰). The Ti-rich olivine gabbro is anomalously light (-0.75‰ δ^{26}Mg). Calcareous sediments from the Transvaal have strongly negative values (-1.10 and -1.70‰ δ^{26}Mg) that overlap with the global carbonate database (Teng, 2017). Plotting δ^{26}Mg vs δ^{25}Mg shows strong correlation between the two datasets and thus, negligible fractionation during sample preparation (Figure 9.19).

Sample	Unit	Rock Type	δ^{25}Mg$_{WR}$	2σ	δ^{26}Mg$_{WR}$	2σ
1294.20	*UMA*	*An*	-0.18	0.01	-0.35	0.02
1305.23	*Upper Pyroxenite*	*Px*	-0.14	0.06	-0.26	0.09
1327.62	*Upper Pyroxenite*	*PGE Reef*	-0.16	0.02	-0.31	0.03
1438.87	*Lower Ultramafic*	*Hz*	-0.16	0.01	-0.30	0.02
1475.85	*Lower Ultramafic*	*Lz*	-0.2	0.00	-0.38	0.01
1550.22	*Lower Ultramafic*	*Px*	-0.15	0.02	-0.30	0.02
1610.25	*FAZ*	*Px*	-0.08	0.02	-0.16	0.03
1787.55	*Ti-rich olivine gabbro*	*Ti-rich olivine gabbro*	-0.38	0.02	-0.75	0.02
1828.87	*Basal Rocks*	*Ol Mela-Gab.*	-0.12	0.02	-0.23	0.03
Duit 1	*Transvaal*	*Dol*	-0.57	0.04	-1.10	0.06
Mal 1	*Transvaal*	*Dol*	-0.89	0.04	-1.70	0.06
UA41	*UCZ WBC*	*Px*	-0.15	0.01	-0.28	0.02
B235-15A	*UCZ WBC*	*Merensky Reef Px*	-0.09	0.01	-0.16	0.02

Table 9.5: Table of magnesium isotope data collected for Flatreef and calcareous sediment samples from this study. In addition, 2 samples from the WBC were analysed, a pyroxenite of the UCZ and the Merensky Reef pyroxenite.
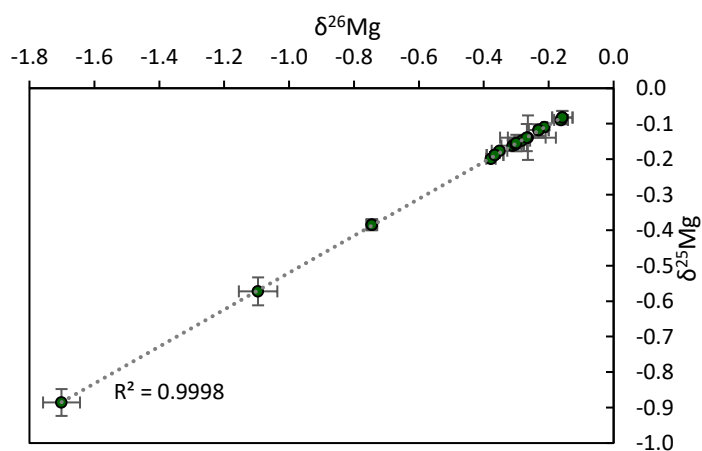
Figure 9.19: Bivariate plots of δ^{26}Mg vs δ^{25}Mg showing strong correlation indicating high quality data and no isotope fractionation during sample preparation.

Silicate rich sedimentary rocks formed in the same environment as carbonate rocks have heavier δ^{26}Mg compositions (Teng, 2017), which is also observed in this study. For example, sample DUIT1 is richer in detrital material and has a heavier δ^{26}Mg value (-1.10‰) compared to sample MAL1 (-1.70‰) which is a pure dolomite. These isotopic compositions are inversely correlated with δ^{18}O, i.e., heavier oxygen isotopes characterise samples with lighter Mg isotopes. The inverse is seen in magmatic samples, with heavier δ^{18}O samples correlating with heavier Mg isotopes (Figure 9.20). The Ti-rich olivine gabbro is an exception to this trend with strongly negative δ^{26}Mg values and heavy δ^{18}O.
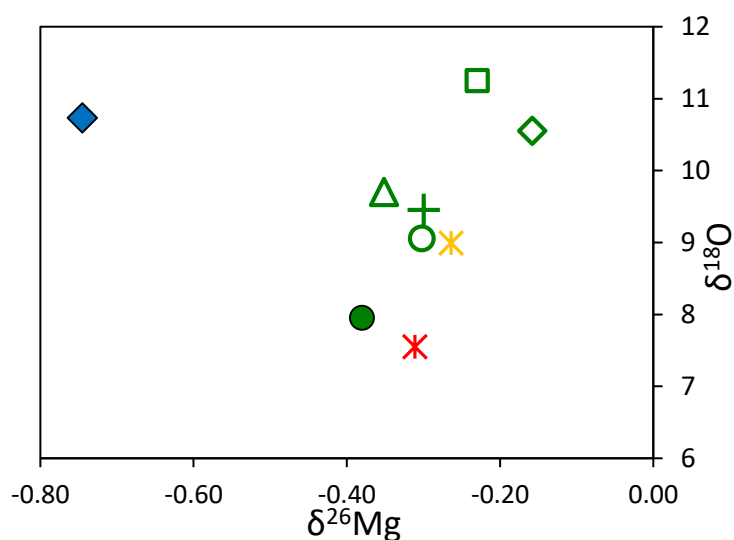
Figure 9.20: Bivariate diagram of the two studied stable isotope systems, oxygen and magnesium. Note the good positive correlation between these isotopes except for the Ti-rich olivine gabbro.

There does not appear to be any systematic relationship between major element oxides and δ^{26}Mg (Figure 9.21), but there is a positive relationship between MnO, which is richer in calcareous sediments, and δ^{26}Mg, albeit with some scatter. Lherzolite (sample 81-1475) has a lighter δ^{26}Mg isotope value (-0.37‰) than underlying pyroxenite and harzburgite above (both -0.30‰). This lighter δ^{26}Mg isotope signature is accompanied by elevated CaO (10.21 wt.%) and LOI (5.01%). As stated above, low temperature reactions, such as serpentinisation, can strongly fractionate Mg isotopes. However, serpentinised harzburgite (3.67% LOI) has the same δ^{26}Mg value as pyroxenite, suggesting weak serpentinisation in the Flatreef does not strongly influence δ^{26}Mg values. Pyroxenite from the Lower Ultramafic Unit and FAZ, while having very similar whole rock geochemistry have very different δ^{26}Mg (-0.30 and -0.16‰ δ^{26}Mg, respectively).
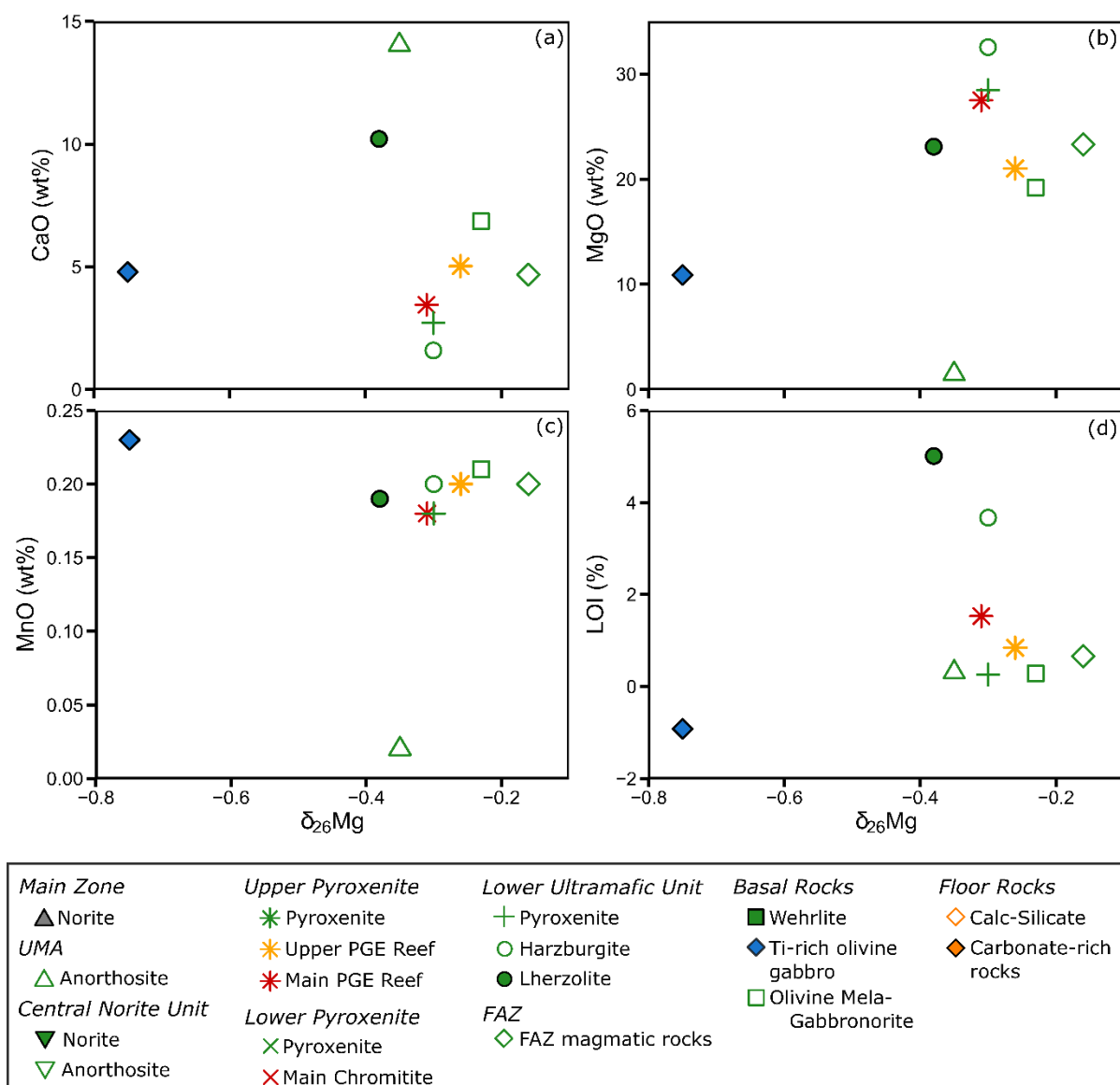
Figure 9.21: Bivariate plots of major element oxides (wt.%) against δ²⁶Mg. (a) CaO, (b) MgO, (c) MnO, (d) LOI. Note the positive correlation between MnO and δ²⁶Mg.

There is also a positive correlation between δ²⁶Mg and Sc concentration, except in the Ti-rich olivine gabbro (Figure 9.22). However, contrary to MnO, Sc is poorer in dolomitic rocks compared to the Flatreef. There is a positive relationship between S content and δ²⁶Mg; with olivine-bearing rocks richer S trends relative to olivine-poor rocks. Cu/S and Ni/S broadly decrease with lighter δ²⁶Mg values, although there is considerable scatter. There does not appear to be any systematic relationship between PGE concentrations and δ²⁶Mg except for a weakly negative correlation with Pt/Pd ratios (Figure 9.23). Mg isotope values broadly become less negative downhole from -0.35 in the UMA to -0.16 in the FAZ. However, the Ti-rich olivine gabbro and olivine mela-gabbronorite contravene this trend (-0.75 and -0.23, respectively) (Figure 9.13).
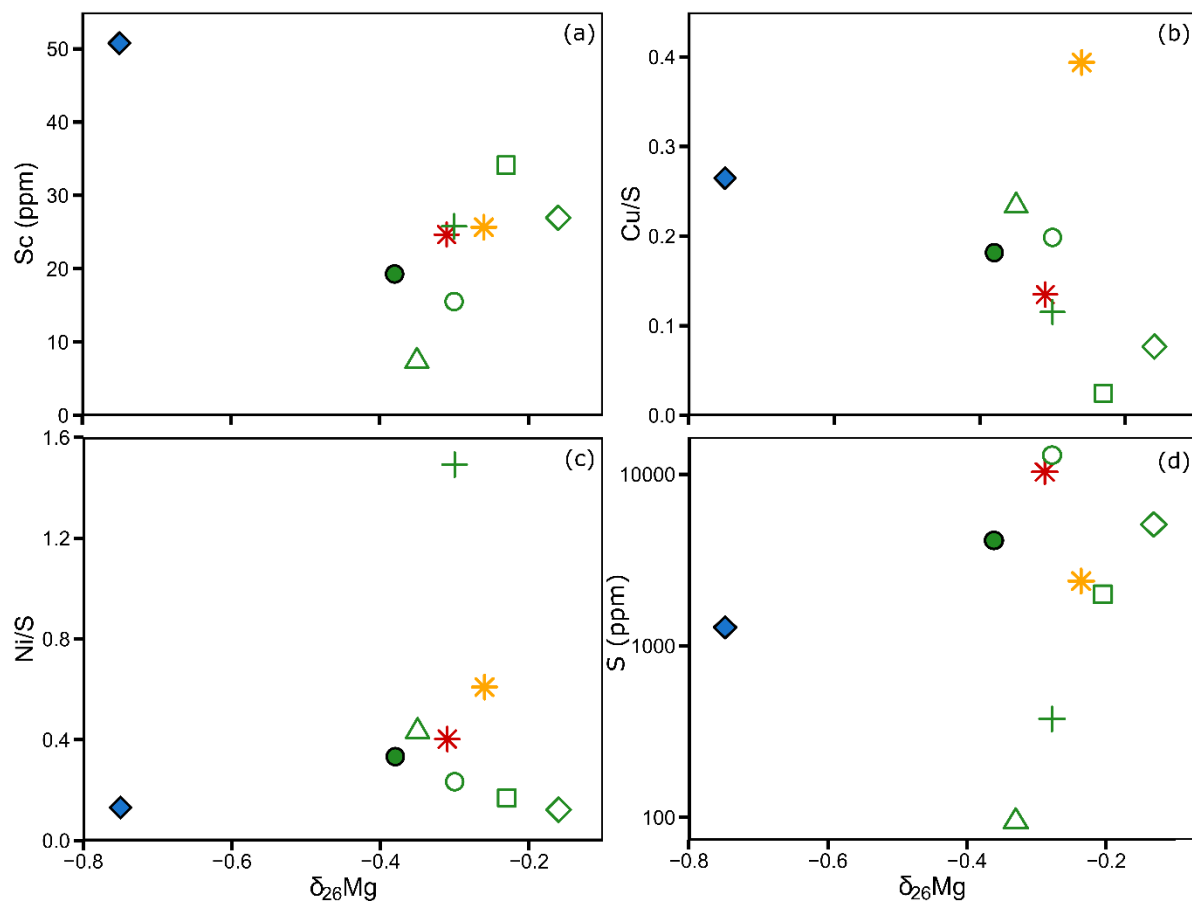
Figure 9.22: Bivariate plots of trace elements and chalcophile elements (ppm) against δ²⁶Mg. (a) Sc, (b) Cu/S, (c) Ni/S, (d) S. Note the weakly positive trend of δ²⁶Mg with Sc, but negative trends with sulphide tenors.
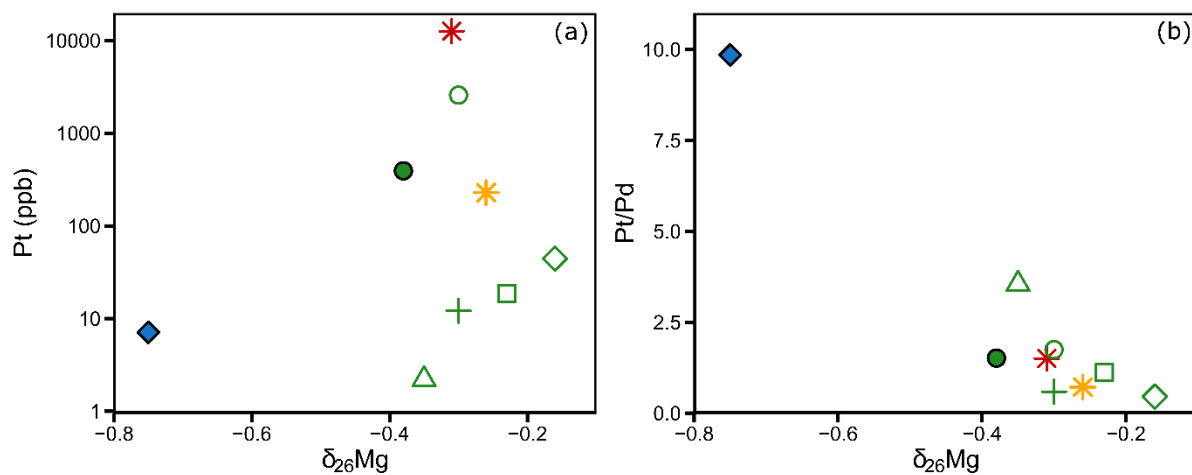
Figure 9.23: Bivariate plots of PGE (ppb) and PGE ratios against δ²⁶Mg. (a) Pt, (b) Pt/Pd. Note there is no clear relationship between Pt and δ²⁶Mg but there is a negative correlation between δ²⁶Mg and Pt/Pd.

Chapter 10 – Geochronology of the lower Main Zone, Flatreef and Merensky Reef

10.1 Introduction

Geochronological analysis of zircons and their leachates produced during chemical abrasion has been conducted on four samples from the studied sequence, namely the Main Zone (MZ), the Upper Reef, the Main PGE Reef (M2) and the Main Chromitite. These are important as they represent important lithological layers that can be easily recognised and correlated across the property. In addition, geochronological data for these layers across the western and eastern limbs of the Bushveld Complex have been provided by Mungall et al. (2016), Scoates and Wall (2015) and Zeh et al. (2015). In view of the relatively low zircon content of Bushveld cumulates, several decimetres of drill core were used for analysis in order to assess the relative temporal relationship between the different samples analysed, every effort was taken to source these samples from the same drill cores. In addition, in order to assess the results relative to the Merensky Reef of the WBC and eliminate issues of inter-laboratory variability, a sample from the Merensky Reef at Northam Mine (NORT) was also analysed.

U-Pb zircon data analysed here by CA-ID-TIMS are evaluated for data precision, reverse discordance and non-zero age Pb loss. Where there is evidence that these factors have affected analyses, the relevant zircon fraction may be rejected from the final age interpretation of the sample. Relatively imprecise data can result from a variety of issues during data collection including poor ionisation of the sample during analysis, high ^{204}Pb suggesting introduction of common Pb during sample preparation, the presence of inclusions, or low radiogenic Pb. Reverse discordance is identified when samples plot above the line of Concordia, resulting from significant fractionation of U-Pb, or Pb-gain, most likely during the chemical abrasion step of sample preparation.

The presence of open-system behaviour within a zircon crystal has important implications for interpreting the sample age. If the Pb-loss has a zero-age intercept the ^{207}Pb/^{206}Pb age will be the same as the age of crystallisation, but if non-zero Pb loss is present (i.e. open-system zircon remains) the ^{207}Pb/^{206}Pb age will be younger than the true age of crystallisation. Non-zero age Pb loss can be more difficult to identify. After zircon crystallisation, open-system behaviour can occur allowing Pb to diffuse out of the zircon grain (e.g. in response to later thermal events), deviating U-Pb and ^{207}Pb-^{206}Pb dates to give younger dates for the affected zircon. To account for this, chemical abrasion of zircons during sample preparation is used to remove damaged sections of the zircon, although this process is not always completely

effective and Pb-loss in chemically abraded zircons is reported in other Bushveld studies (Zeh et al., 2015). Zircons that still contain portions with non-zero age Pb loss after chemical abrasion can plot discordantly (i.e. $^{206}Pb/^{238}U$ and $^{207}Pb/^{235}U$ dates are not in agreement with each other) and in some cases zircon plots outside the uncertainty range of the Concordia. Where only a small, subordinate portion of zircon displaying open-system behaviour remains after chemical abrasion, the presence of non-zero age Pb loss could be difficult to detect. In this scenario the zircon measurement is dominated by closed-system U-Pb decay and still plots within the uncertainty of Concordia but will yield ages younger than the true crystallisation age.

This study has sought to identify zircons that contain subordinate domains of non-zero age open-system behaviour zircon by measuring the U-Pb dates of leachates, i.e. the portion of zircon dissolved during chemical abrasion. Closed system zircon and its corresponding leachates should intersect Concordia at zero age and the zircon $^{207}Pb/^{206}Pb$ date is deemed robust. Where leachates and the parent zircon form a discordia with non-zero age Pb loss, the interpretation of the zircon date within the wider context of the sample should be treated with lower confidence and in the case whereby the zircon date forms an anomalously younger outlier, its date is rejected from further consideration attributed to non-zero age Pb loss.

The interpreted ages deemed to represent the age of crystallisation are evaluated as weighted mean dates of single populations that yield a statistically acceptable Mean Square Weighted Deviate (MSWD) according to that population size (Wendt and Carl, 1991). If the MSWD is greater than the statistical limit of scatter the data either reflects real dispersion due to geological processes or uncertainties within the data have not been sufficiently propagated. Uncertainties are reported as 2σ x/y/z where x = analytical uncertainty only, y = uncertainty including tracer calibration and z = total uncertainty (including uncertainty on decay constants). X uncertainty can be used for direct comparison with data from Mungall et al. (2016) and Zeh et al. (2015) who also used the EARTHTIME 2535 tracer for analysing other localities in the Bushveld Complex.

Samples selected are briefly listed in chapter 3 but described in more detail here. The Main Zone sample (UMT232, 740.3-741.2 m) comprises a medium grained homogeneous gabbronorite and appears lithologically similar to the Main Zone sample from drill core UMT081. The Upper PGE Reef (UMT232, 804.7-805.9 m) consists of medium grained orthopyroxenite with approximately 3% interstitial sulphides and minor interstitial feldspar and is texturally similar to the equivalent sample in drillcore UMT081. However, the sample can contain patches of olivine with interstitial plagioclase which can be coarse grained over several cm. The Main PGE Reef (UMT232 838-839 m) is formed of medium grained olivine

bearing pyroxenite with ~5% interstitial sulphides. Domains of coarser grained pyroxenite occur locally. The sample from the Main Chromitite Pyroxenite (UMT345, 1518-1519 m) comprises medium-grained pyroxenite. Clinopyroxene makes up approximately 15% and is thus somewhat more abundant than in the overlying units. Interstitial plagioclase makes up ~15%. Both the Main PGE Reef and the Main Chromitite are similar in lithology and texture to the equivalent rocks in drill core UMT081. The Merensky Reef sample from Northam in the WBC is comprised of a medium grained pyroxenite with approximately 5% interstitial plagioclase. Clinopyroxene is a minor phase forming large oikocrysts (2-4 cm in diameter).

Th/U ratios, calculated from ^{208}Pb and an assumed concordancy between U-Pb and Th-Pb systems, are also presented as ranges within each sample. Th$_{(model)}$/U can represent fractionation within interstitial melt in a cumulate system such as the Bushveld Complex (Table 10.1).

Sample	Th/U range
Main Zone	0.79-0.89
Upper PGE Reef	1.84-5.51
Main PGE Reef (M2)	0.52-1.44
Main Chromitite	1.09-8.96
Merensky Reef Northam	0.96-4.58

Table 10.1: Record of Th/U ranges from the samples analysed. Note the low Th/U range of Main Zone zircons.

10.2 Analysed Samples

10.2.1 Main Zone

Limited cathodoluminescence (CL) images of zircons (sample had poor zircon yield) indicate a varied population with sector zoning (grains 1, 2 and 5) and largely featureless zircons (grains 4 and 5) present (Figure 10.1). Zircons in the Main Zone have a very narrow range of Th/U (0.79-0.89) suggesting minimal fractionation of interstitial melt.

Both z3 and z6 are rejected based on non-zero age Pb loss in leachates, which appears to have extended into the residual zircon cores. The remaining analyses do not form a single population with a statistically acceptable MSWD but can be represented by 2 populations that capture the dispersion of ages from this sample (Figure 10.2). The younger population (z1, z2, z7) has a ^{207}Pb/^{206}Pb age of 2056.002 ± 0.047/0.32/6.0 Ma (MSWD=2.5, n=3) and the older population (z4 and z5) has a ^{207}Pb/^{206}Pb age 2056.184 ± 0.081/0.32/6.0 Ma (n=2) (Figure 10.3). The resultant time span in dates is 0.182 ± 0.094 Myrs.

When all zircons are considered including the rejected fractions (except z1) they lie on a single discordia with a lower intercept of 1102 ± 110 Ma. When excluding z3 and z6, all other zircons and their leachates plot with zero-age Pb-loss (excluding z2L1) indicating the $^{207}Pb/^{206}Pb$ dates and associated dispersions in the dates are valid.
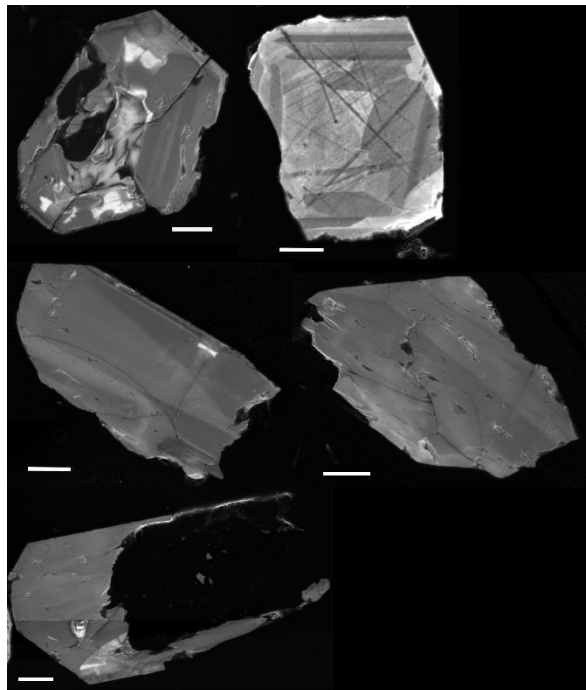
Figure 10.1: CL images of representative zircons from the Main Zone. Note the heterogeneity in zircon morphology within this small sample size. (white bar = 20 um).
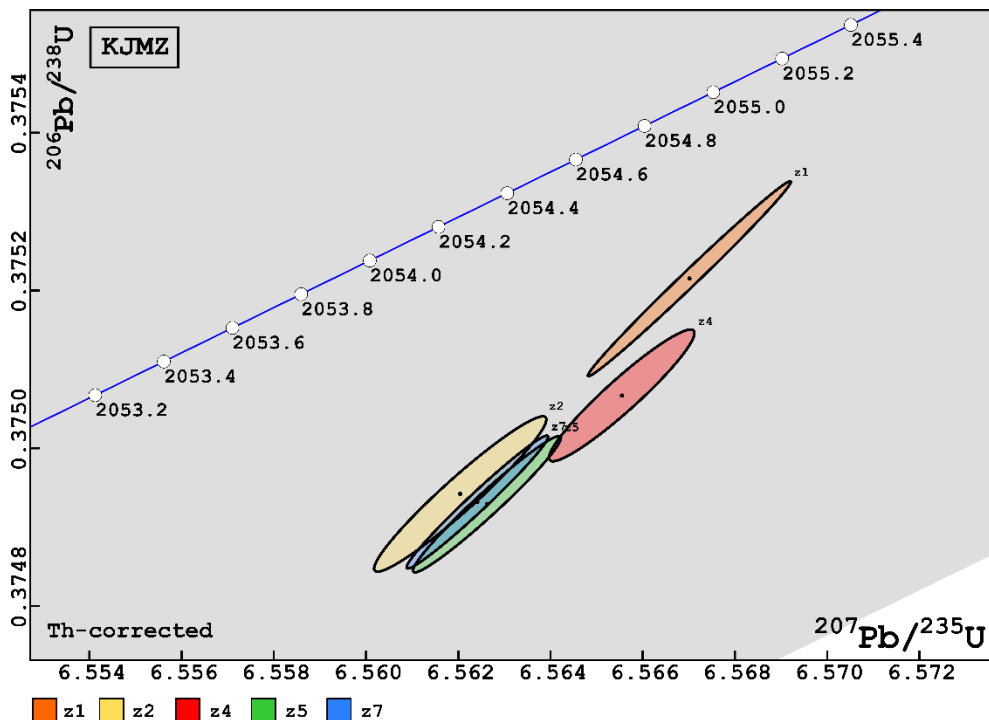
Figure 10.2: Concordia diagram of the dispersive zircon population from the Main Zone. All zircon lie within the uncertainty on concordia (grey shaded area) but do not form a single well defined population.
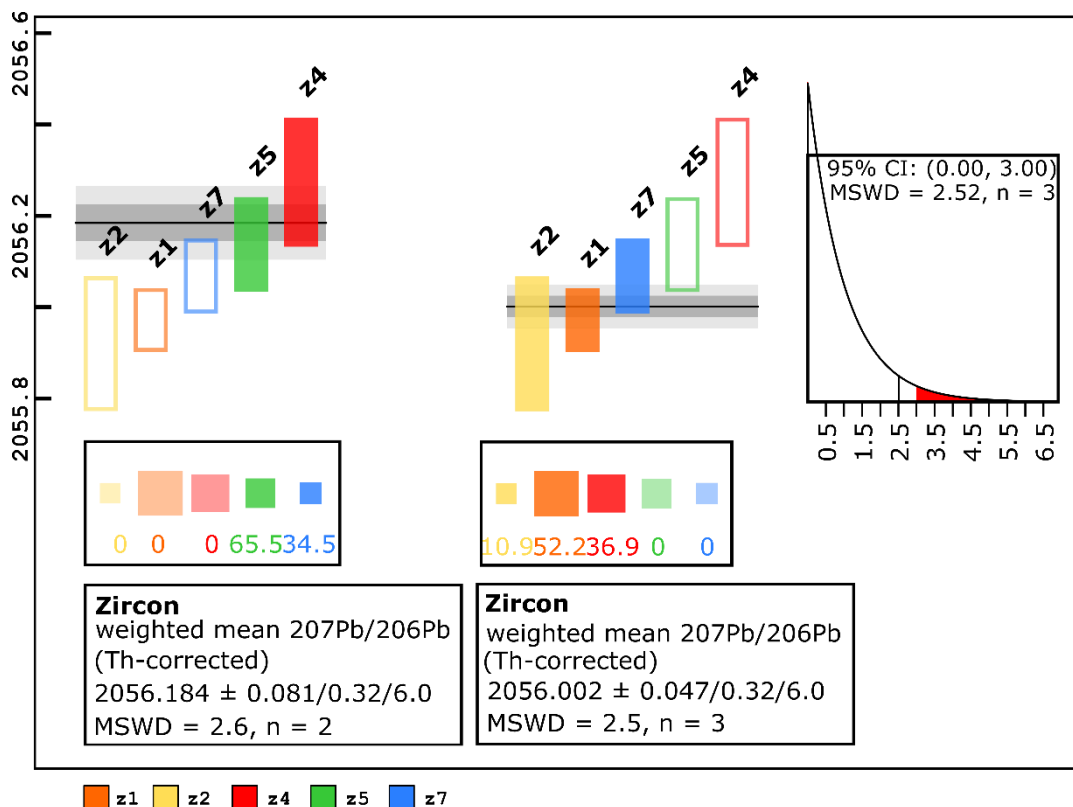
Figure 10.3: Weighted means diagrams for the two modelled age populations from the Main Zone. (a) Older zircon population age formed from two zircons, there is insufficient data to generate MSWD values. (b) younger zircon population.

10.2.2 Upper PGE Reef

CL images of zircons show a diverse population with some featureless zircons (grains 1-3) and abundant zoned and sector zoned crystals (grains 6-13) with some zircons displaying irregular bright patches (grain 14)(Figure 10.4). Zircons from the Upper Reef display some fractionation of Th/U (1.84 z1 to 5.51 z5) suggesting possible ongoing fractionation of the melt during crystallisation of zircon, although this is not temporally resolvable.

The Upper PGE Reef produces a consistent $^{207}Pb/^{206}Pb$ age 2055.566 ± 0.060/0.32/6.0 Ma (MSWD=0.35, n=4) (Figure 10.5, Figure 10.6). Rejected analyses include z3 and z7. Although both z3 and z7 plot within the decay uncertainty of Concordia, z3 is reversely discordant suggesting fractionation during chemical abrasion and z7 plots with a younger $^{207}Pb/^{206}Pb$ age suggesting non-zero age Pb loss. Both zircons also display non-zero age Pb-loss in their leachates. z2, z4 and z5 all have remarkably consistent $^{207}Pb/^{206}Pb$ ranges and all display zero-age Pb loss. While z1 leachates indicate non-zero age Pb loss (508 ± 45 Ma) the zircon overlaps with the main population and is included in the age interpretation.
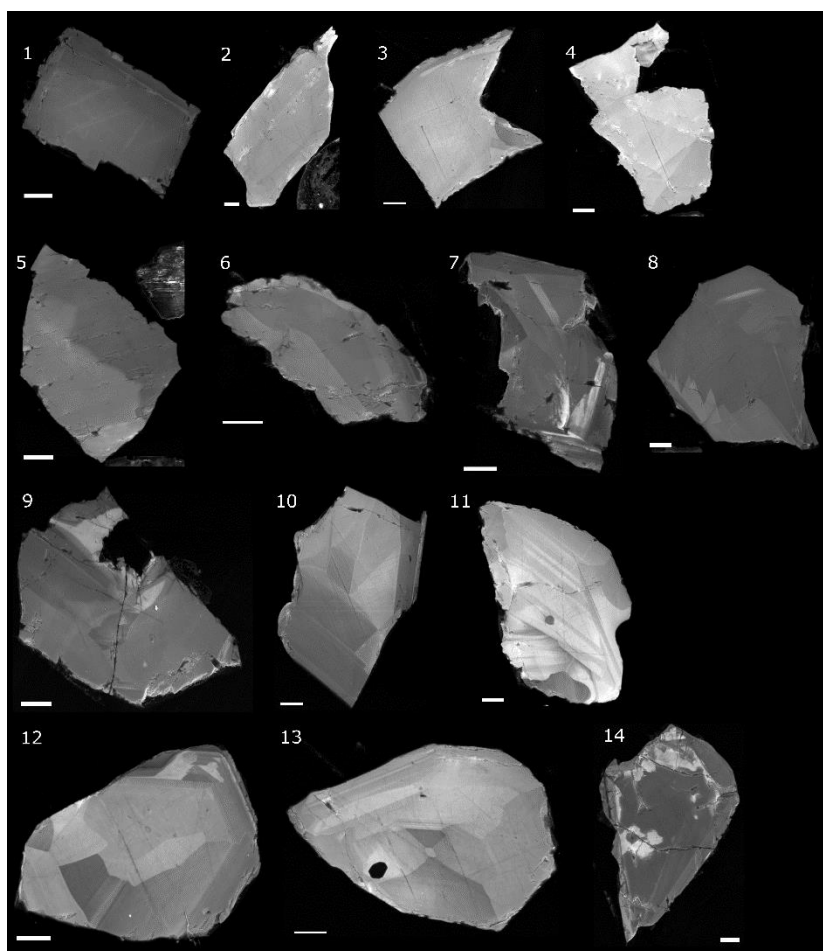
Figure 10.4: CL images of representative zircon grains from the Upper PGE Reef. (white bar = 20 um).
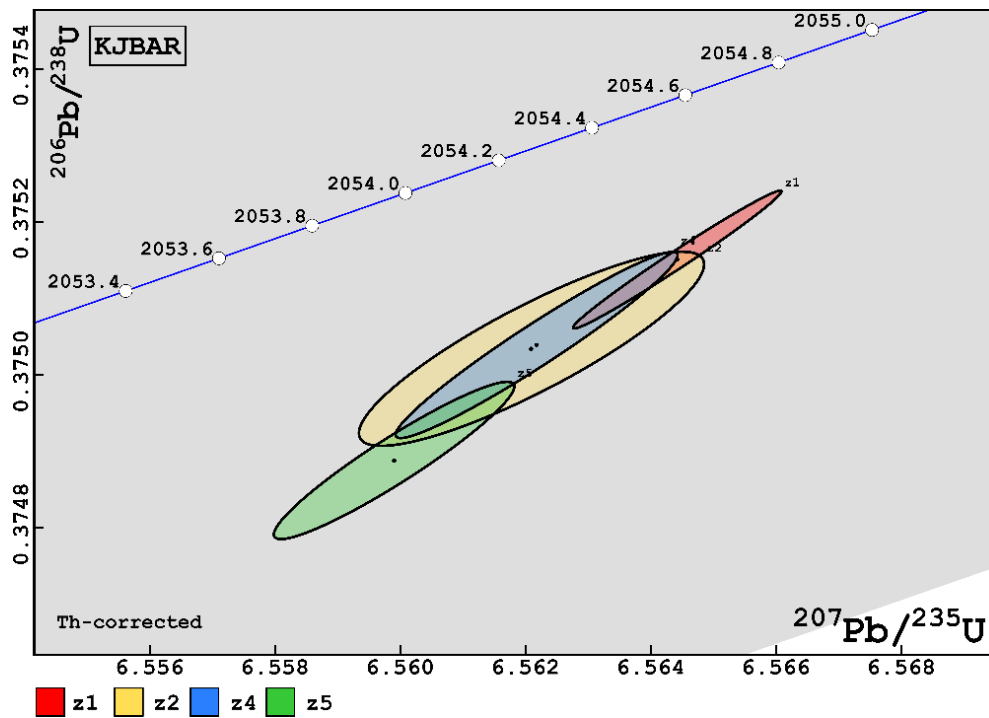
Figure 10.5: Concordia diagram of zircon fractions from the Upper PGE Reef. Note all zircons lie uncertainty of the concordia (grey shaded area) and form a single population.
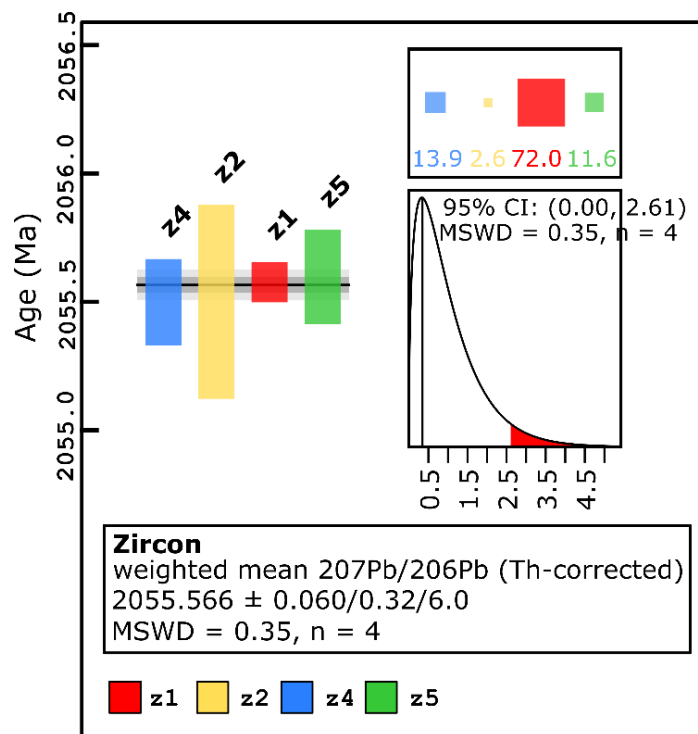
Figure 10.6: Weighted means diagram of the single age population of zircons from the Upper PGE Reef.

10.2.3 Main PGE Reef (M2)

CL imagery of the zircon population shows broadly featureless zircons with minor oscillatory zoning (grains 6, 7 and 13) and sector zoning (e.g. grains 9 and 10) (Figure 10.7). Several zircons also display bright irregular patches (e.g. grains 12, 15, 16). One subhedral zircon (grain 17) with oscillatory zoning was also present that appears anomalous with the remainder of the sampled population which is fragmented and anhedral. Zircons from the Main PGE Reef on the Flatreef have a narrow range of Th/U values (0.52-1.44) suggesting minimal fractionation of interstitial material.

The Main PGE Reef (M2) on the Flatreef contains a range of zircon ages that do not form a single population with a statistically acceptable MSWD, which was reproduced during 3 analytical sessions spanning 1 year. The younger population (z3a and z6) has a calculated $^{207}Pb/^{206}Pb$ age of 2055.656 ± 0.088/0.33/6.0 Ma (n=2). While z3a contains non-zero Pb loss in its leachates, the residual zircon overlaps with z6, which displays zero-age Pb loss in its leachates, suggesting z3a has not been reset by a significantly younger event. In contrast, zircons z2 and z2a display both non-zero Pb-loss and do not overlap with more robust zircon measurements and are therefore interpreted as containing a component of non-zero age Pb loss and rejected from age interpretations. The older zircon population is comprised of several fractions with remarkable overlap giving an older $^{207}Pb/^{206}Pb$ age of 2056.245 ± 0.053/0.095/6.0 Ma (MSWD=0.042, n=3). Fractions z1a and z7 plot between these 2 end-member populations (Figure 10.8, Figure 10.9). This gives a zircon age range of 0.589 ± 0.103 Myrs.
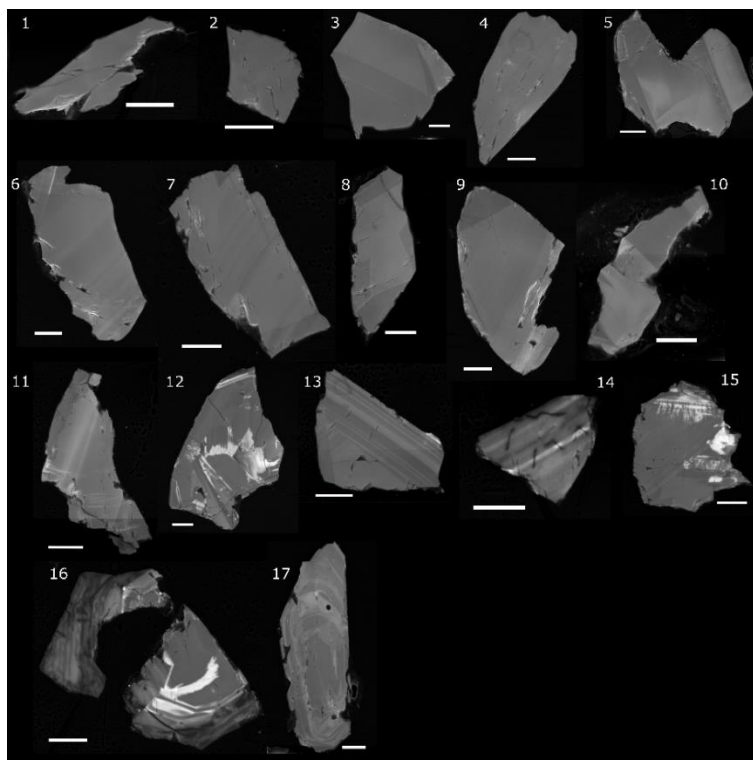
Figure 10.7: CL images of representative zircons from the Main PGE Reef (M2). Note the wide range of morphologies and presence of magmatic textures including oscillatory zoning. (white bar = 20 um).
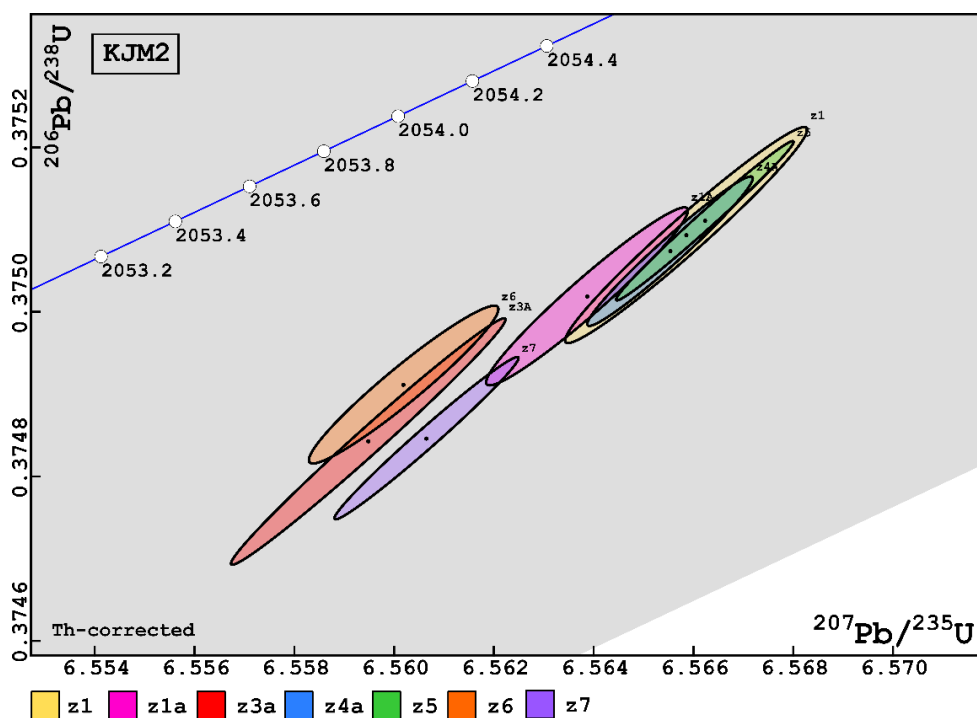
Figure 10.8: Concordia diagram of zircon fractions from the M2 Main PGE Reef on the Flatreef. All samples plot within the uncertainty on concordia (grey shaded area). Note the remarkable reproducibility of the older zircon population.
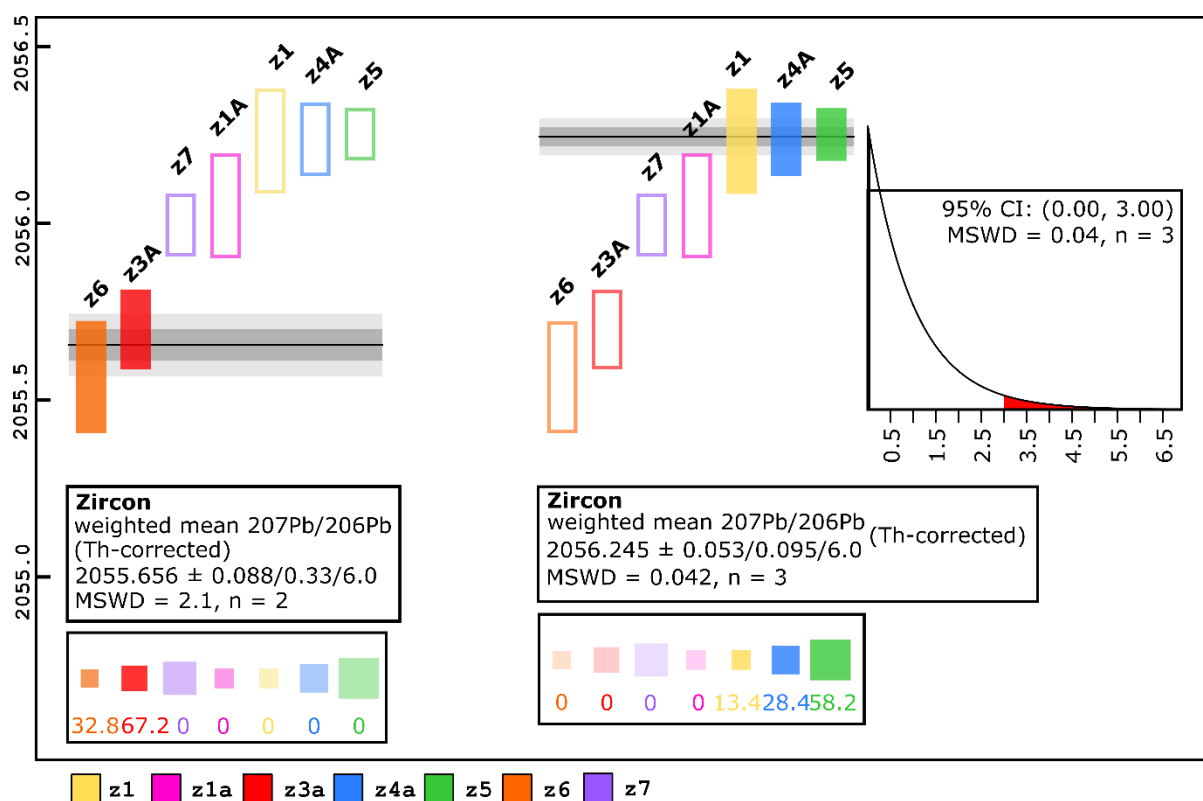
Figure 10.9: Weighted means diagrams of the two end-member populations of zircon from the Main PGE Reef, M2. (a) Younger population formed by 2 zircons is insufficient to generate MSWD statistics. (b) Older zircon population has remarkable reproducibility as indicated by its low MSWD value.

10.2.4 Main Chromitite

CL imaging of 16 zircon grains from the Main Chromitite show the main population comprises largely featureless zircon (grains 1-8) with some displaying oscillatory zoning (grains 10, 14-16) and some suggesting incorporated zircon cores (grain 13) (Table 10.1).

The zircons from the Main Chromitite have a robust and consistent single population ^{207}Pb/^{206}Pb age of 2055.834 ± 0.079/0.32/6.0 Ma (MSWD=0.46, n=5) (Figure 10.11, Figure 10.12). Leachates generally lie close to Concordia suggesting Pb-loss is not a dominant feature of the Main Chromitite layer, with calculated Pb-loss for most zircons at zero. Leachates from two zircons (z3 and z6) show non-zero age Pb-loss (lower intercepts at 312 ± 140 Ma and 605 ± 48 Ma, respectively) suggesting z3 and z6 leachates represent a mix of pan-African and zero-age Pb loss.

Main Chromitite zircons have the highest variability of Th$_{(model)}$/U of all zircon fractions analysed with a maximum value of 8.96 (z2) which indicates strong fractionation of interstitial melt (Zeh et al., 2015) (Table 10.1). However, lower values (1.09 z1) are also recorded suggesting fractionation may have been ongoing during zircon crystallisation and is not temporally resolvable.
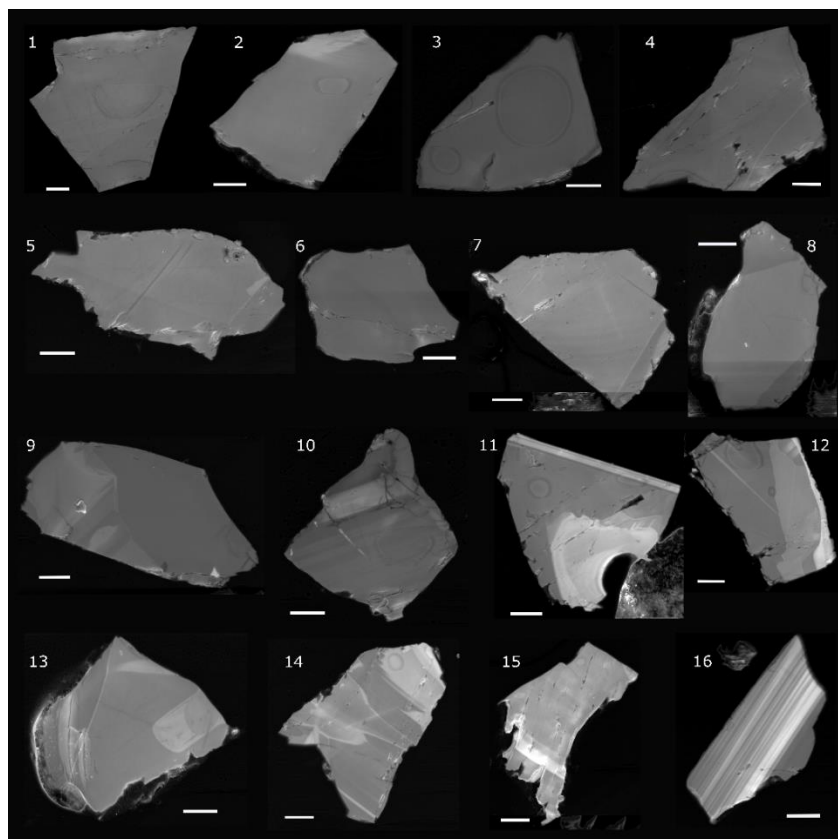
Figure 10.10: CL images of 16 representative zircon fractions from the Main Chromitite. (white bar = 20 µm).
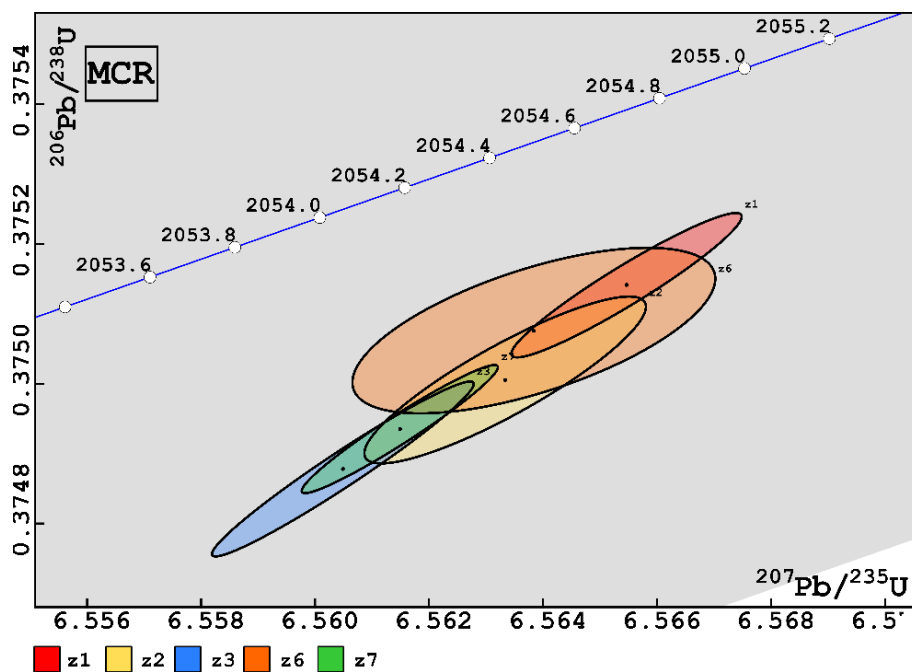
Figure 10.11: Concordia diagram for zircon from the Main Chromitite layer in the Flatreef. Note all samples plots within the uncertainty of the concordia (grey shaded area) and form a single population.
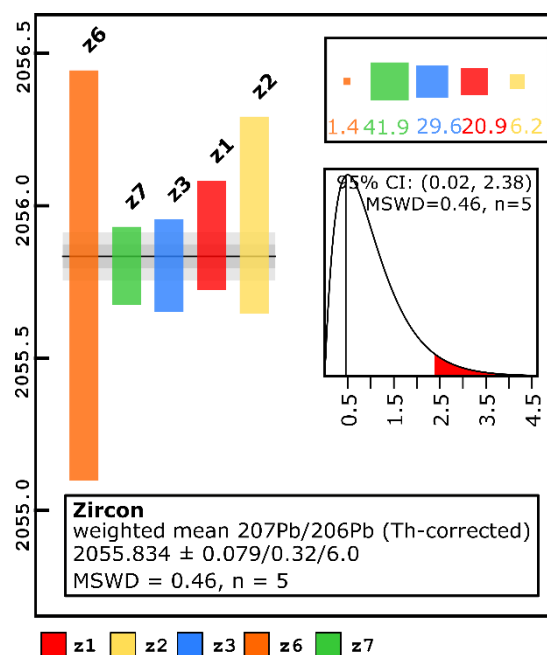
Figure 10.12: Weighted mean diagram for analysed zircon from the Main Chromitite layer with all zircon fractions forming a single age population.

10.2.5 Merensky Reef Northam (WBC)

Similar to the Main PGE Reef on the Flatreef, at Northam the zircon fractions from the Merensky Reef do not form a single population of statistical significance (Figure 10.13). The older population (z1, z3 and z8) gives a $^{207}Pb/^{206}Pb$ age of 2056.10 ± 0.16/0.36/6.0 Ma (MSWD=1.6, n=3) although z1 and z8 can also be combined with z9 and z4 to give a younger population $^{207}Pb/^{206}Pb$ age of 2055.79 ± 0.11/0.34/6.0 Ma (MSWD=2.2, n=4) giving a range of ages spanning 0.31 ± 0.194 Ma (Figure 10.14). In zircon from this sample there is no evidence of non-zero age Pb loss from leachate analyses.

Zircon data from the Merensky Reef at Northam shows a range of Th/U values (0.96-4.58) that suggest modest fractionation and possibly indicates fractionation of interstitial melt. This range is greater than that recorded in the sampled Main PGE Reef on the Flatreef (0.52-1.44).
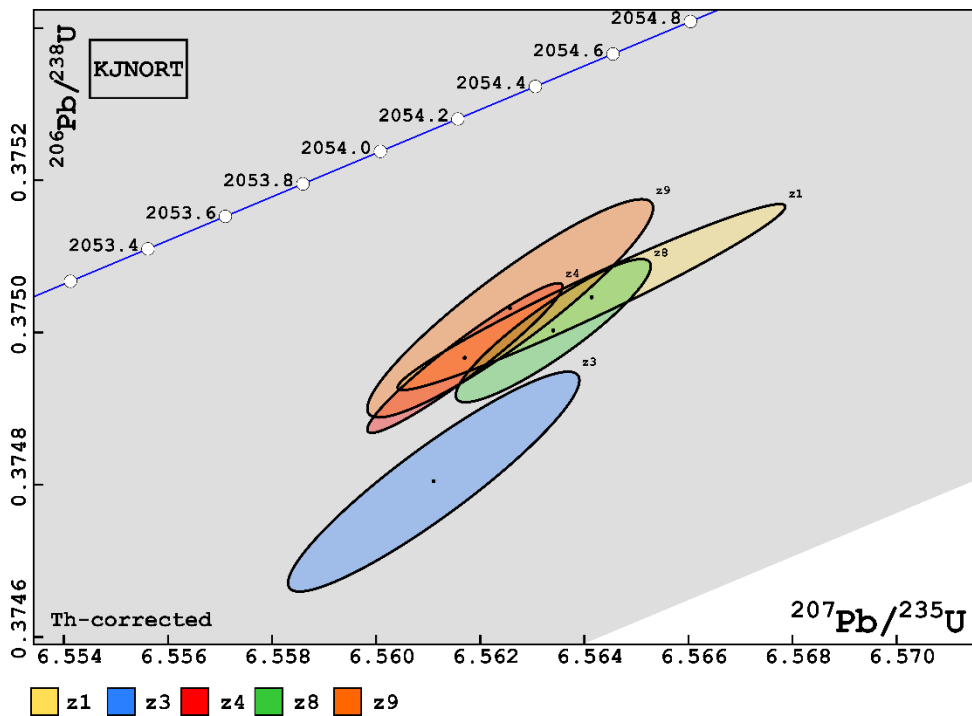
Figure 10.13: Concordia diagram of zircon population from the Merensky Reef on the farm Northam. All samples plot within uncertainty on the Concordia (grey shaded area).
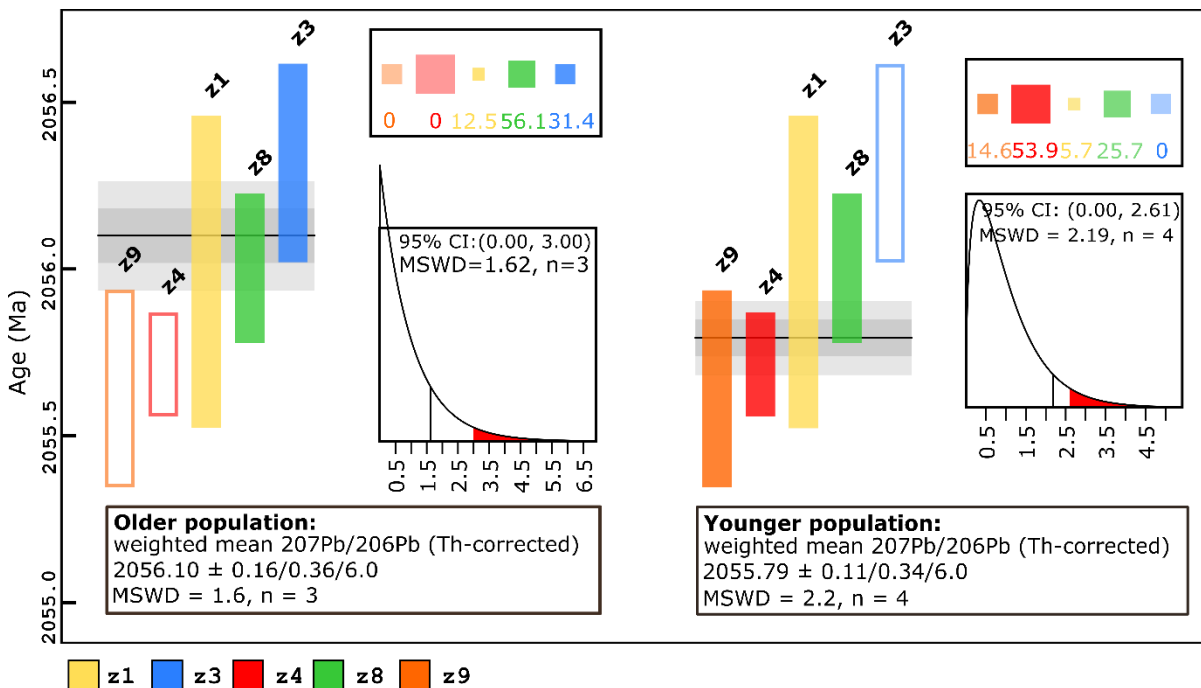
Figure 10.14: Weighted means diagram of the 2 modelled zircon populations from the Northam Merensky Reef sample. Z1 and z8 both statistically overlap with end-member zircons making them suitable for modelling both age populations.

10.3 Summary of ages of Flatreef units

Magmatism from across the Flatreef samples studied here spans nearly 800 kyrs (0.679 ± 0.08 Ma). The data presented here show a complex sequence of events that may contain multiple processes that will be discussed later. The data show that while some units have narrow age ranges (i.e. Upper PGE Reef, 2055.566 ± 0.060 Ma) others display a wide range (e.g. Main PGE Reef, 0.589 ± 0.103 Ma). Individual zircon analyses that represent the most extreme ages determined for units show that differences in crystallisation ages are clearly resolvable, such as the younger age of the Upper PGE Reef relative to the overlying Main Zone (Figure 10.15).
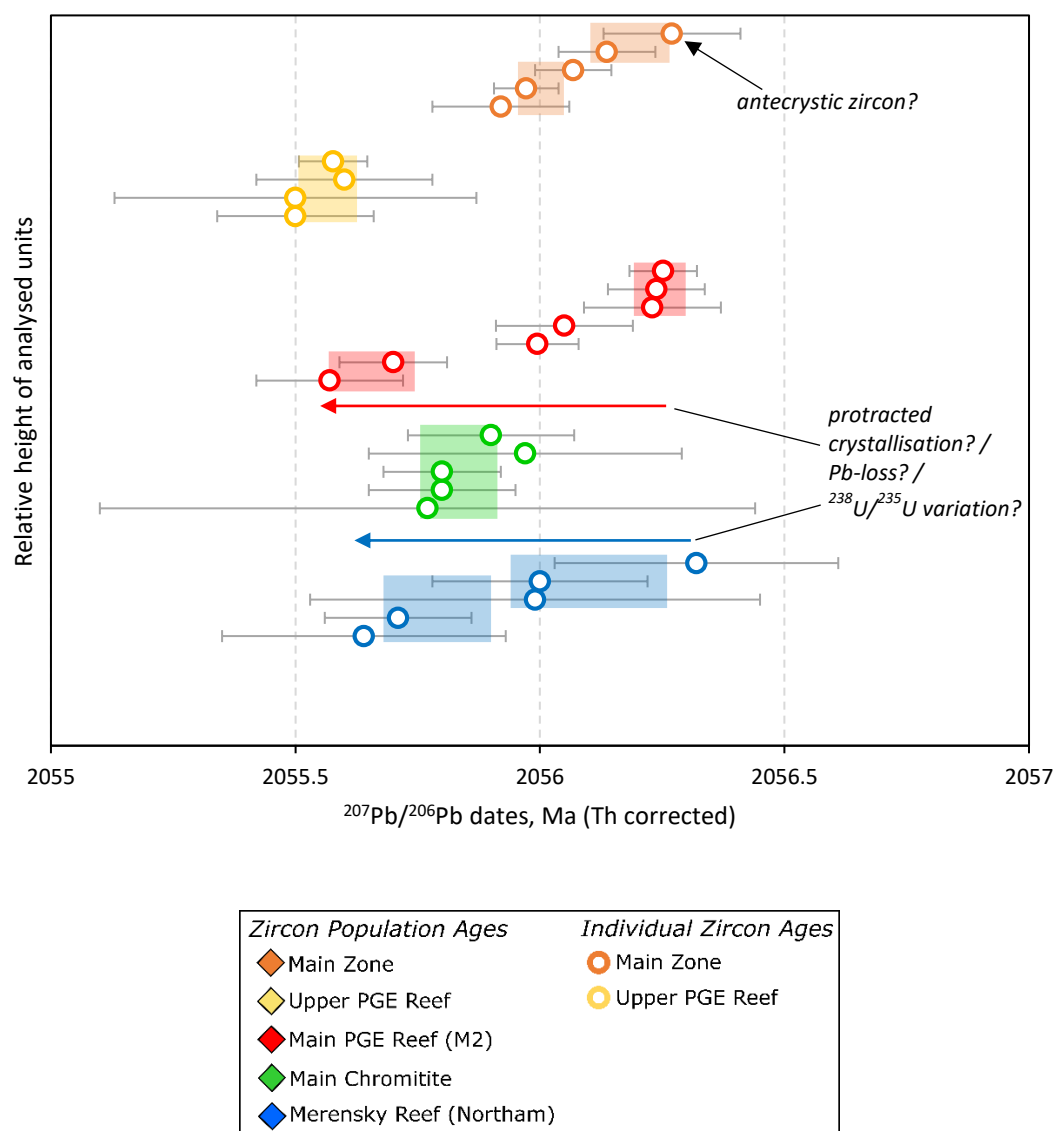
Figure 10.15: *Plot displaying zircon dates and favoured weighted means all displaying uncertainties of 2 sigma. Where zircon dispersion exceeds the range of weighted means, processes including protracted crystallisation or U isotope variability may have occurred and are discussed in section 10.4.*

10.4 Potential causes of zircon date dispersion within single samples

Improved data point precision of zircon data from CA-ID-TIMS analysis in this study reveals significant dispersion within zircon dates from individual units that was not determined in previous studies (Mungall et al., 2016; Zeh et al., 2015). As indicated from these data, apart from the Upper PGE Reef and Main Chromitite on the Flatreef, the range of $^{207}Pb/^{206}Pb$ ages in individual units can span 0.589 ± 0.103 Myrs (M2)(Figure 10.15). Reasons for this could include: (1) non-zero age Pb loss relating to post-Bushveld events; (2) U isotope variability within individual samples; (3) entrainment of antecrystic zircon during emplacement; (4) protracted crystallisation of zircon within a single unit; and (5) re-setting of the U-Pb system within zircon crystals during emplacement of the Bushveld Complex.

Careful evaluation of leachate and zircon data was undertaken to determine non-zero age Pb loss. If leachates yielded anomalously younger $^{207}Pb/^{206}Pb$ dates derived from chemically abraded zircon their associated zircon dates have been rejected unless these overlap with more robust zircon fractions. Therefore, post-Bushveld non-zero age Pb loss is not the sole factor in generating the protracted ages observed in the remaining zircon populations.

Fractionation of U isotopes ($^{238}U/^{235}U$) between zircon grains within an individual unit could potentially generate significant temporal differences. Data processed with the widely used legacy value of $^{238}U/^{235}U = 137.88$ compared to the consensus $^{238}U/^{235}U$ value of 137.8185 (Hiess et al., 2012) would generate temporal differences of ~0.8 Myrs within the $^{207}Pb/^{206}Pb$ dates, which can be expanded to almost 2 Myrs if the 2s.d. on the global range of $^{238}U/^{235}U$ is accounted for (137.8185 ± 0.045). To date, uranium isotope fractionation within a single intrusive unit has not been reported in any system, largely due to the analytical challenges of resolving isotopic variability at such low mass (~≤ 2 ng U) within single zircon analyses relative to that required to resolve isotopic variation in previous studies (~500 ng U). Consequently, this potential variability has not yet been evaluated. Within high-temperature magmatic systems, U isotopes are unlikely to vary significantly, but this cannot be discounted without single zircon crystal analysis of U isotope variation. With this caveat in mind, the age dispersion observed can be evaluated against the remaining 3 processes: entrainment of antecrystic zircon, protracted zircon crystallisation or re-setting of the U-Pb system in zircons in response to proximal thermal events.

Older zircon populations in samples displaying dispersed ages can either reflect initial crystallisation ages or entrainment of antecrystic zircon. This could be applied to the older population of the Main PGE Reef (M2) (2056.245 ± 0.045 Ma). However, the remarkable reproducibility of these dates (both $^{207}Pb/^{206}Pb$ and $^{206}Pb/^{238}U$) from 3 separate single zircon analyses suggests this is highly unlikely and these dates probably reflect the onset of zircon

crystallisation within the Main PGE Reef (M2) unit. Similar age dispersions observed from both the Merensky Reef in the western limb (Northam) and Main PGE Reef in the northern limb (M2) also suggest antecrystic zircon entrainment is unlikely and would require magma intrusions more than 200 kilometres apart to entrain older zircon of roughly the same age. However, poor reproducibility in the older dates of the MZ suggests antecryst entrainment could have occurred during MZ emplacement.

The final two processes (thermal re-setting and protracted crystallisation) would result in younger zircon dates. The dates derived from CA-ID-TIMS U-Pb analyses of zircon represent either an average of their initial crystallisation that occurred at a later stage and their continued growth below a closure temperature of ~900 °C (Lee et al., 1997) or capture partial or complete resetting of the U-Pb system in the zircon crystal (after chemical abrasion) in response to thermal events occurring above the closure temperature. Continued injection of magmas into the Flatreef may have locally raised temperatures of existing rocks (such as the Main PGE Reef or MZ) above the closure temperature (~900 °C) (Lee et al., 1997). This would have to occur within ~1 Myrs of the rocks reaching the closure temperature the first time to generate the dispersion observed without displaying detectable non-zero age Pb loss in their leachates. This process of non-zero age Pb loss due to syn-Bushveld resetting cannot be resolved from zero-age at the resolution of the leachate. Considering the dispersion in Main PGE Reef dates, re-heating of these rocks above the closure temperature may have been achieved by the later emplacement of the Upper PGE Reef Unit directly above the Main PGE Reef in drill core UMT232 (as also observed in drill core UMT081). Similarly, rocks within the lower portion of the MZ may also have experienced thermal resetting in reaction to emplacement of younger units such as the Upper PGE Reef rocks.

This leaves a model of protracted crystallisation to consider. Thermal modelling by Zeh et al. (2015) suggest the vast volumes of magma and consequent thermal energy associated with the emplacement of the Bushveld Complex may have sustained temperatures over the interval of zircon crystallisation temperatures (700-900 °C) for 0.3-0.65 Myrs. When accounting for the emplacement of the 4 km thick Lebowa granite suite above the Rustenburg layered suite, these temperatures could be sustained for up to 0.95 Myrs (Zeh et al., 2015). It is therefore possible that slow cooling of units could have sustained long periods of interstitial melt and result in protracted crystallisation of zircon over the longest interval of 0.589 ± 0.103 Myrs (Main PGE Reef, M2). Directly beneath the Main PGE Reef package lies a ~10 m thick pegmatoidal orthopyroxenite which suggests slow cooling. Small pockets of pegmatoidal material and felsic melt channels are also observed within the Main PGE Reef unit. Protracted crystallisation may also have occurred during cooling of the MZ.

Another factor to consider is the cumulus nature of rocks from the Bushveld Complex. Zircons are late-stage phases crystallising with other interstitial material. The occurrence and possible extent of vertical transport of interstitial melt is still debated in the Bushveld Complex and is strongly dependent on models for crystallisation and emplacement within the complex. It has been suggested by some to reach 4-40 m, broadly on the same scale as the vertical separation between units such as the Bastard Reefs and Merensky Reefs (Cawthorn, 1996; Hayes et al., 2017; Holness et al., 2017). Detailed studies on interstitial melts of the Lower Zone by Karykowski et al. (2017) also suggest significant melt migration. Zeh et al., (2015) suggested that Th/U ratios exceeding 6 indicate extreme interstitial melt fractionation. While our data shows a range of Th/U ratios (0.52-8.96) that overlap with other studies and are indicative of magmatic origin (i.e. > 0.1), further investigation would be required to determine the full implications of Th/U variation in zircons (Mungall et al., 2016; Zeh et al., 2015).

Chapter 11 Discussion

In this chapter the datasets presented in chapters 4-10 have been used to answer the main research questions set out in chapter 1. One of the key outstanding questions in the Bushveld academic community and in the mineral exploration industry concerns the relationship is between the northern limb and the remainder of the Bushveld Complex. Contamination of Bushveld magma by country rocks in the Platreef, and generally disrupted layering of the intrusion in the northern limb can make correlation with the UCZ of the WBC difficult. As the Flatreef represents a relatively less contaminated correlative of the Platreef the former is ideally placed to determine the degree of stratigraphic correlation with the wider Bushveld Complex. In addition, in this chapter I have placed some tighter constraints on the relative contribution of different contaminants to the Flatreef magmas and developed a geological model for formation of the Flatreef.

11.1 Towards a stratigraphic framework for the Flatreef

Grobler et al. (2018) proposed a model whereby the Flatreef is the down-dip extension of the Platreef in the northern limb which itself represents strongly contaminated UCZ. In the following chapter the data presented in chapters 4-10 will be compared with data from the remainder of the Flatreef, as well as the Platreef and the UCZ in the WBC in order to constrain the stratigraphy and petrogenesis of the rocks.

11.1.1 Comparison of data from across the Flatreef

11.1.1.1 Lithostratigraphic Comparisons

The Flatreef is defined here as a mafic-ultramafic package stratigraphically positioned between the Main Zone hangingwall and footwall of the Transvaal Supergroup. The Flatreef is further sub-divided into an upper portion (the Upper Flatreef) and a lower portion (the Lower Flatreef). The Upper Flatreef comprises all igneous units between and including the UMA down to and including the LUU. The Upper Flatreef is largely comprised of orthopyroxenite with lesser amounts of norite, anorthosite and peridotites. The underlying Lower Flatreef comprises heavily contaminated rocks of the FAZ and beneath this several distinctive magmatic sills comprised of wehrlite, the Ti-rich olivine gabbro and olivine mela-gabbronorite. The thickness of the Flatreef is variable, with the Upper Flatreef ranging from 180 m in drill core UMT094 to 280 m in drill core UMT081, and the Lower Flatreef from ~30 m in UMT094 to ~250 m in UMT081. The reduced thickness of the Flatreef in UMT094 may partly be a result of a localised topographic high in the dolomitic footwall. In addition, the relatively thick Lower Flatreef in UMT081 may, in part, be due to the exceptional length of this drill core intersecting magmatic rocks at depth that have not been documented previously in the Flatreef. Despite

this, both drill cores are broadly representative of the wider Flatreef deposit capturing both key lithological layers and the inherent variability of this deposit.

The uppermost layer of the Flatreef, consisting of the UMA, is developed across the property, albeit in variable thickness. It is commonly sheared although it is undeformed in the 2 drill cores that have been studied in detail. Across the rest of the Flatreef, the UMA has been correlated to the Giant Mottled Anorthosite (GMA), which is present in the remainder of the Bushveld Complex (Grobler et al., 2018; Mitchell and Scoon, 2012). Mitchell and Scoon (2012) reported that the GMA pinches out on the farm Akanani, approximately 20 km to the north of Turfspruit.

Below the UMA the various Flatreef layers show markedly less lateral continuity than the UMA, with individual layers showing localised thickening, while being absent elsewhere. For example, the UMA overlies an interlayered norite-anorthosite package in UMT094 which is absent in UMT081 (Grobler et al., 2018). Underlying this is the Upper PGE Reef, so termed by Yudovskaya et al. (2017b). It is present across most of the property and hosted in weakly mineralised orthopyroxenite.

In many parts of the property the Upper PGE Reef is underlain by norites and anorthosites, separating it from the Main PGE Reef (Grobler et al., 2018). However, in drill cores UMT081 and UMT094 these norites and anorthosites are absent and the Upper PGE Reef rests directly on pyroxenites associated with the Main PGE Reef. This results in a thick, relatively uniform pyroxenitic package hosting both the Upper and the Main PGE reefs, a feature generally more common in the shallow and eastern portions of the Flatreef i.e. with proximity to the proposed feeder zone at Mokopane (Grobler et al., 2018; van der Merwe, 1976). Vertical separation between mineralized layers also varies considerably between the two drill cores with the distance between the Upper PGE Reef and the Main PGE Reef ranging from ~41 m in UMT094 to ~23 m in UMT081 (Figure 11.1). However, in the up-dip extensions of the Flatreef there is a similar separation between the reefs (UMT383 14.5 m, UMT368 20 m, UMT073 19 m) (Figure 11.2).

The distance between the Main PGE Reef and Main Chromitite varies from ~62 m in UMT094 to ~95 m in UMT081. Up-dip and to the east of drill-core UMT081 the Central Norite Unit and the Main Chromitite are absent, which is in part due to the relatively elevated stratigraphic position of the FAZ (e.g. in drill core UMT368 and UMT073; Figure 11.2). The thickness of the FAZ in these drill cores is not clear due to termination of the drill cores within the FAZ. The Lower Pyroxenite Unit that hosts the Main Chromitite is significantly thinner in UMT094 compared to UMT081, accounting for the variable thickness of the Main PGE – Main Chromitite interval between these drill cores. Down-dip of UMT081, drill core UMT336 also

contains a Central Norite Unit and shows a similar distance between the Main PGE and Main Chromitite reefs (106 m) (Figure 11.2).

The Lower Ultramafic Unit in drill core UMT081 contains multiple chromitite lenses and is strongly mineralised, unlike most other equivalent intersections of the Flatreef on the farm Turfspruit. It is also anomalously thick (153 m in UMT081, compared to 42 m UMT094). The FAZ and wehrlite packages of the Lower Flatreef are also thicker in UMT081 (105 m and 23 m, respectively) compared to UMT094 (25 m and 3 m, respectively). The ~120 m thick package of Ti-rich olivine gabbro situated in the lowermost portions of drill core UMT081 has not been identified elsewhere on the property, possibly due to the fact that most other drill cores are shorter than UMT081. Olivine mela-gabbronorite at the base of UMT081 has not been intersected elsewhere on the property. It is possible that these rocks represent the MgZ or the uppermost portion of the LZ, as will be discussed later.
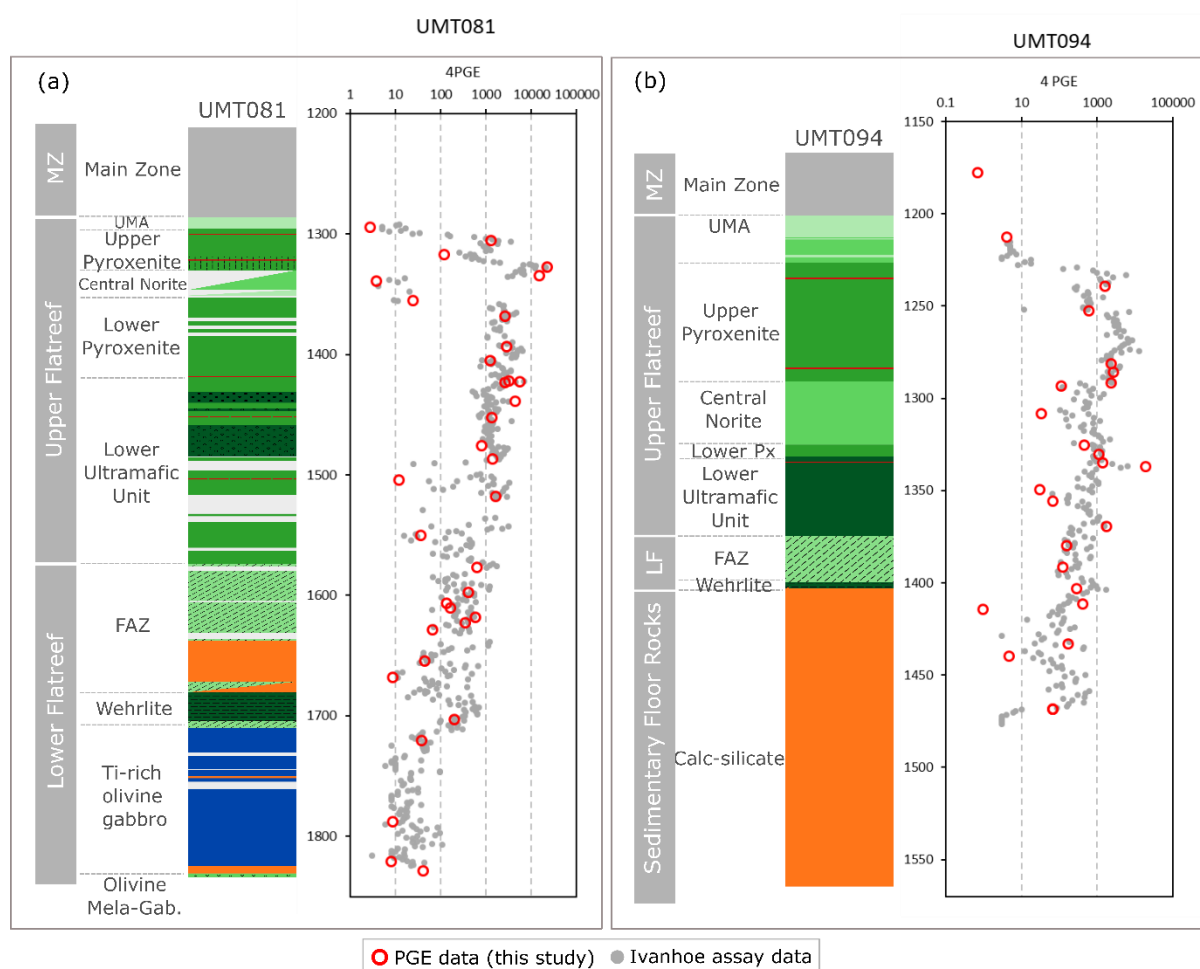
Figure 11.1: Assay data displaying downhole trends in PGE grade in drill core (a) UMT081 and (b) UMT094. Vertical separation between the Upper and Main PGE reefs in drill core UMT081 is smaller (23 m) than in drill core UMT094 (41 m).

The intersection of thick calc-silicate floor rocks in UMT094 is unique to this drill core. The absence of other magmatic units such as the Ti-rich olivine gabbro and olivine mela-

gabbronorite could suggest that the hole is not deep enough, or that these units are not developed in this area of the property. In both drill cores studied there is a distinct absence of hornfels xenoliths, which are abundant elsewhere on Turfspruit, particularly in the PNZ and the Platreef (Grobler et al., 2018; Kinnaird et al., 2005).
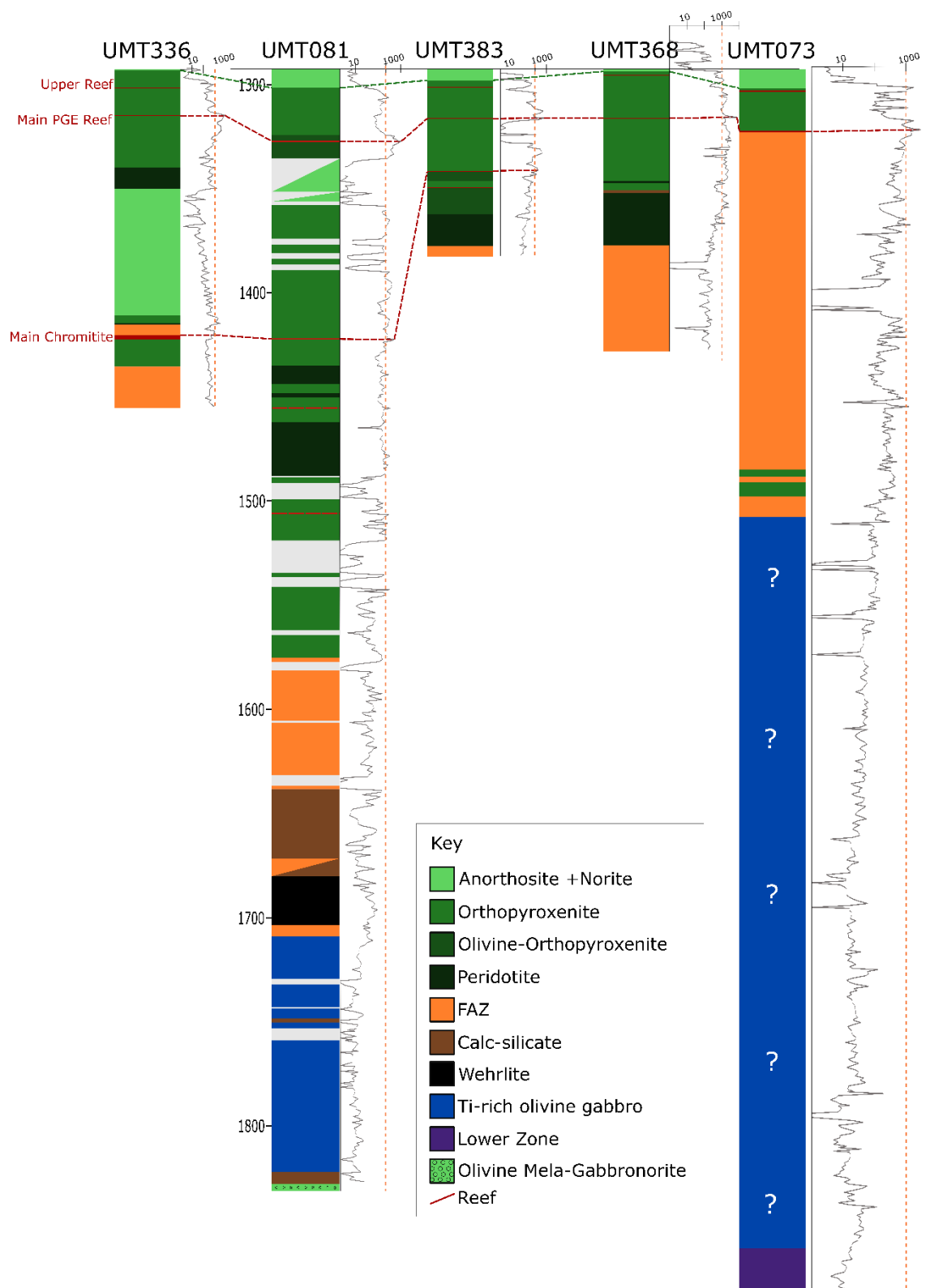
Figure 11.2: Stratigraphic cross-section with downhole Pt assay data (in ppb) broadly in NE-SW direction across the Flatreef deposit (section 2 in figure 3.1) illustrating both the remarkable depth of

UMT081 relative to other drill cores and broadly similar stratigraphy. Vertical orange dashed lines have been drawn to highlight 1000 ppb Pt (log data and photos supplied by Ivanhoe Mines Ltd.)

11.1.1.2 Mineral Chemistry

Mineral chemistry data from across the Flatreef are still relatively sparse but they generally overlap with compositions from UMT081 and UMT094 (Figure 11.3). Pyroxenites from this study show Mg# of opx 79-86 (UMT081 and UMT094) which is consistent with data of Marquis (2015) from drill core UMT083 (78-82 Mg#) (Figure 11.3). The relatively sodic range of plagioclase found in UMT081 (min. An 43) may reflect the infiltration of relatively evolved melt derived from the footwall cumulates at this locality. The UMA in the 2 analysed drill cores has broadly similar composition to that in drill core UMT083, although orthopyroxene is less magnesian in UMT081 compared to UMT083 (Mg# 70.5-71.4 Opx, An 68-77 in UMT081 and 78-84 Mg# Opx, An 66-79 in UMT083) (Marquis, 2015).

Mineral compositions are also available for the Flatreef in drill core UMT336, down-dip of drill core UMT081 (Opx 70-86 Mg#, Plag An 76-87 and Ol Fo 81-86), showing broad overlap with mineral compositions in the equivalent interval in UMT081 and UMT094 (Flatreef Opx 67-86 Mg#, An 43-81, Fo 78-87) (Figure 11.3) (Nodder, 2015). Further to the north, on the Farm Akanani where the Flatreef is termed 'Deep Platreef' (Yudovskaya et al., 2013), mineral compositions in harzburgite are Mg# 76-83 for orthopyroxene and Fo 82-84 for olivine, broadly overlapping with harzburgite in UMT081 and UMT094 (Opx Mg# 79-85, Olivine Fo 78-83).
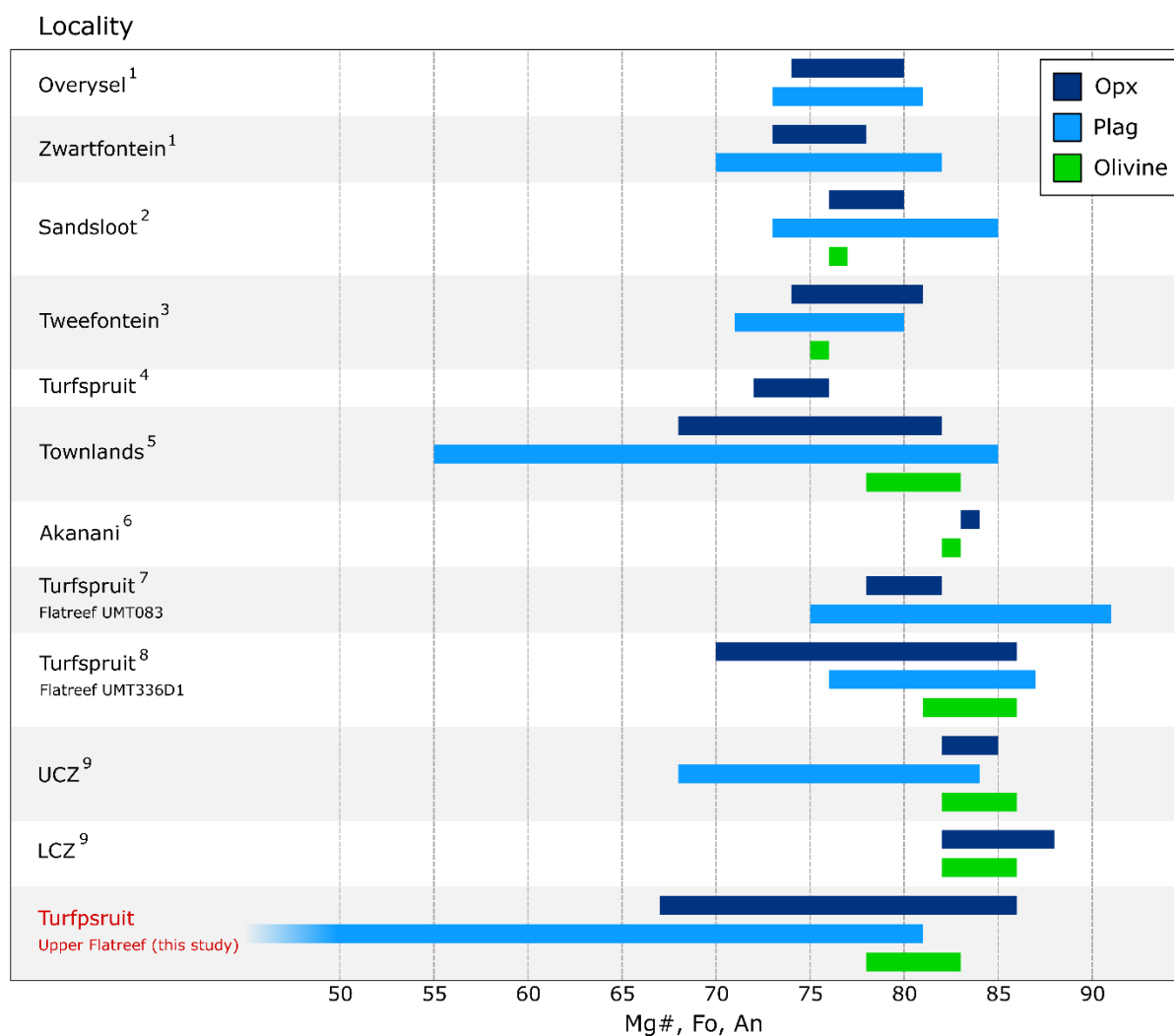
Figure 11.3: Summary of various silicate mineral compositional ranges across the Bushveld. (1) Holwell and McDonald (2006), (2) Harris and Chaumba (2001), Holwell and McDonald (2006), McDonald et al. (2005), (3,4) Buchanan and Rouse, (1984) in McDonald et al. (2011), (5) Manyeruke et al. (2005), (6) Yudovskaya et al. (2017b), (7) Marquis (2015), (8) Nodder (2015), (9) Eales and Cawthorn (1996). Data from this study from Upper Flatreef only.

11.1.1.3 Whole Rock Geochemistry

There is good overlap between whole-rock geochemical data from drill cores UMT081 and UMT094 and other drill cores intersecting the Flatreef (Figure 11.4) (Ivanhoe Mines Ltd, unpublished). The Lower Flatreef has more variable whole rock compositions than the Upper Flatreef and the former overlap with parapyroxenite and paraharzburgite units (so termed by Ivanhoe) from the wider Flatreef deposit. Similar variability in Lower Flatreef compositions is observed for various trace elements (Figure 11.5). The composition of the Upper Flatreef rocks analysed in this study broadly overlap with typical magmatic rocks of the Flatreef analysed by Ivanhoe (e.g. pyroxenite, norite, anorthosite etc.). Flatreef rocks sampled from UMT081 and UMT094 also exhibit CaO and K_2O enrichment observed in other Flatreef rocks, suggesting this is a general feature of the Flatreef.
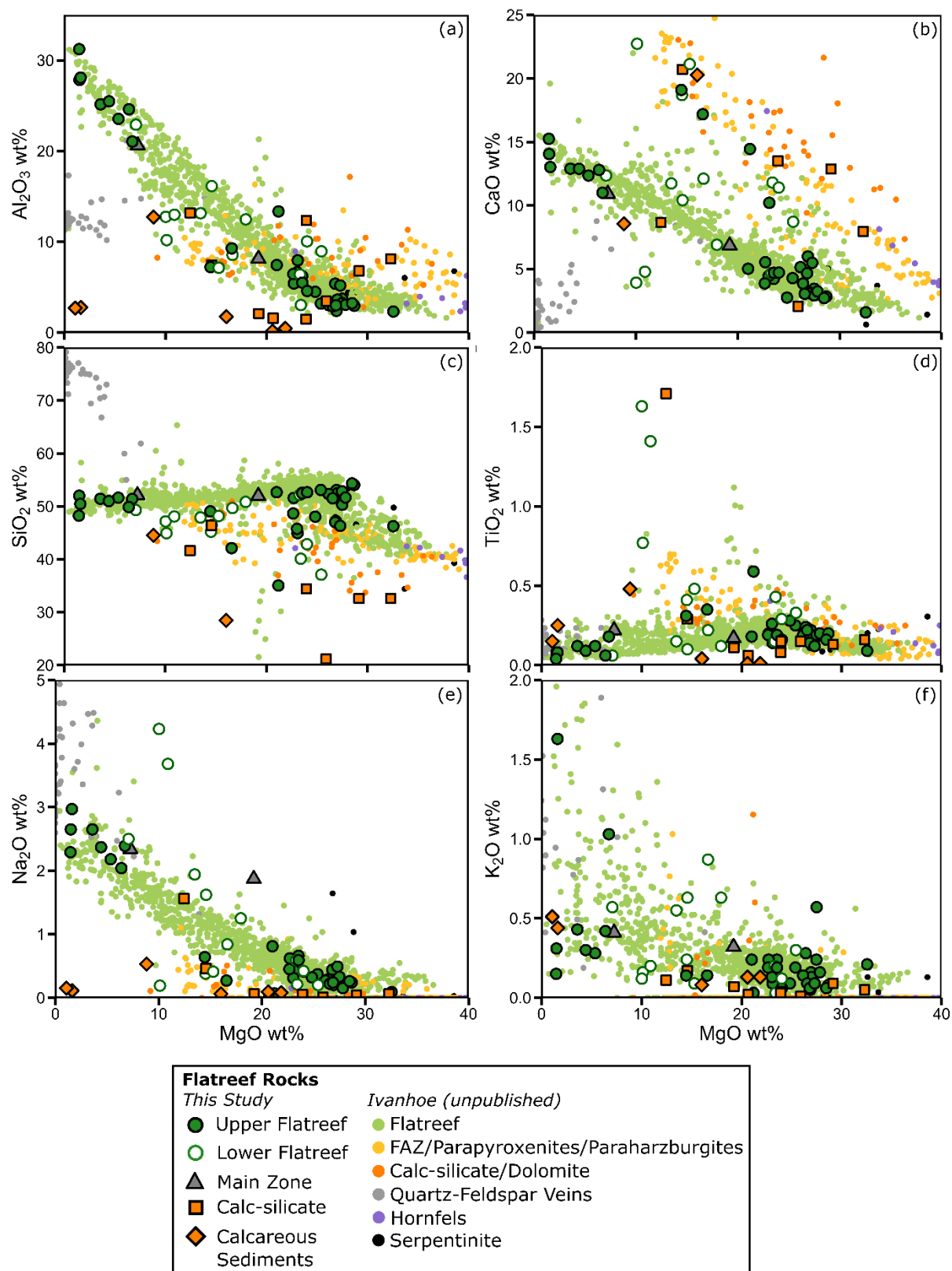
Figure 11.4: Bivariate plots of Flatreef data from this study and unpublished data of Ivanhoe of various oxides against MgO (wt.%). (a) Al₂O₃, (b) CaO, (c) SiO₂, (d) TiO₂, (e) Na₂O, (f) K₂O.
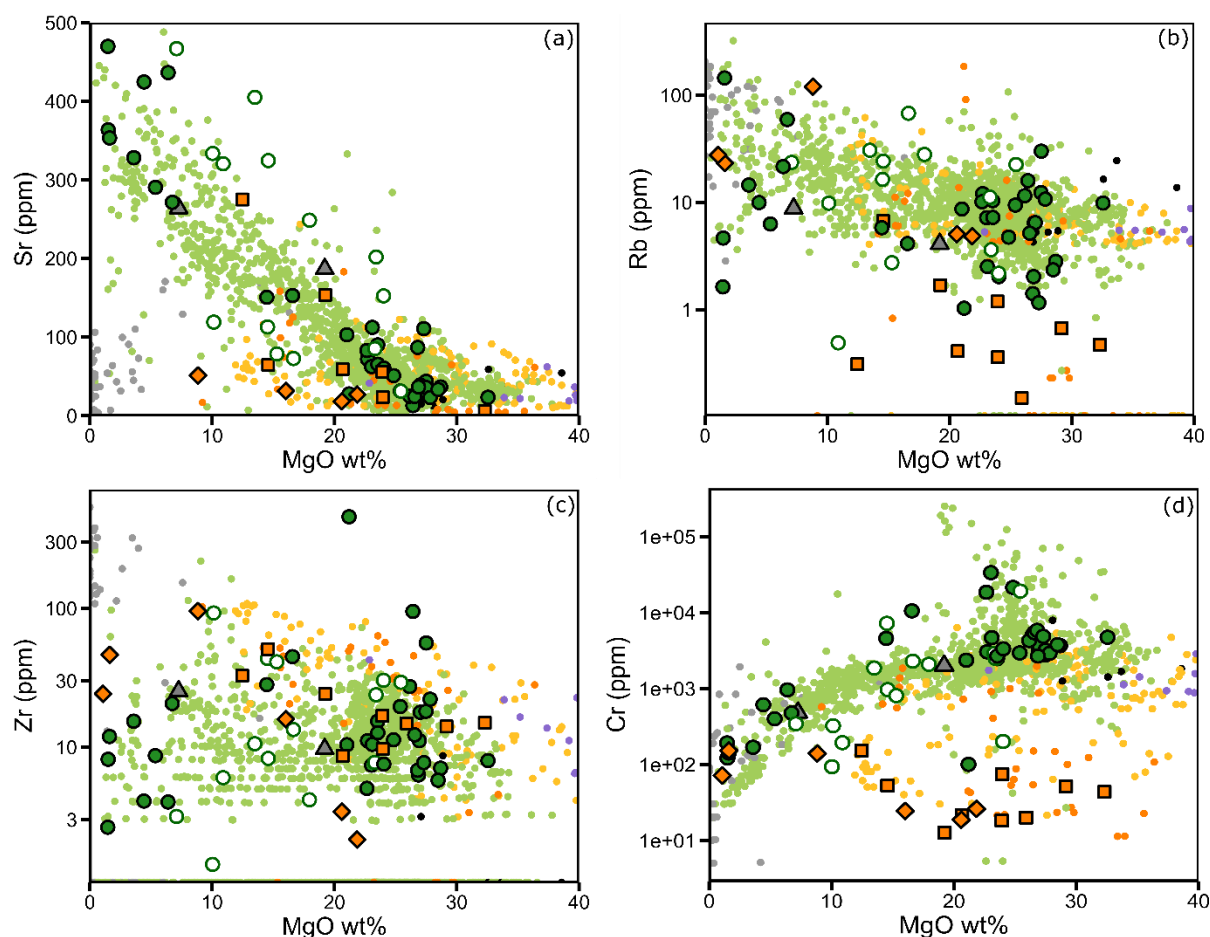
Figure 11.5: Bivariate plots of trace element data from the Flatreef against MgO (wt.%). (a) Sr, (b) Rb, (c) Zr, (d) Cr. Additional data from Ivanhoe (unpublished).

11.1.1.4 PGE

One of the most remarkable features of the Flatreef is the high PGE grades across intervals measuring several 10s of metres. Particularly rich intersections have been recorded in drill core TMT006 (4.5 g/t over 90m) (Grobler et al., 2018). Drill core UMT081 is also very well mineralized (>1 ppm PGE+Au over ~250 m, 1300-1550 m depth) although significant mineralization also occur in some other drill cores e.g., UMT368 (Figure 11.2).

In most drill cores in the Flatreef, PGE concentrations broadly decrease downhole (e.g. UMT081, UMT094, UMT383, UMT368 and UMT073, Figure 11.2). In addition, Pt/Pd ratios also decrease downhole in most drill cores on the property, including in both UMT081 and UMT094, but also in e.g., UMT 342d1, UMT378, UMT449, UMT345, TMT006, UMT383, UMT368, UMT073 (Figure 11.2) (Grobler et al., 2018; Maier et al., 2019 In Press). Typically the Main PGE Reef has grades of <4 g/t 3PGE (Yudovskaya et al., 2017b) and the Main Chromitite carries a grade of 3.2 g/t (Grobler et al., 2018). Cu/Pd ratios also show similar trends in all drill cores across the property with ratios increasing with height above the Main PGE Reef (lowest Cu/Pd layer) and increasing with depth below the reef.

208

11.1.1.5 Summary

Based on the comparisons drawn above, it can be confirmed that the Flatreef, while being characterised by significant contamination in its lower portions, shows more regular layering than the Platreef which can be correlated across the property. This is not withstanding the fact that some layers can be absent in parts of the property (feldspathic units separating the Upper and Main PGE Reefs), whereas others can show significant variation in thickness (e.g. Lower Ultramafic Unit in UMT081). In addition, certain layers show strong interaction with variable footwall topography (e.g. UMT094). However, within this framework there are many features that tie UMT081 and UMT094 with the remainder of the Flatreef deposit including overlapping whole rock compositions and similar downhole patterns of high PGE grade, Pt/Pd and Cu/Pd ratios. It is therefore reasonable to assume that drill cores UMT081 and UMT094 broadly capture the characteristics of the Flatreef and can thus be used to draw comparisons between the Flatreef and the Platreef, as well as the UCZ in the Main Bushveld Complex.

11.1.2 Comparison between the Flatreef and the Platreef

Since the Flatreef broadly represents the down-dip extension of the Platreef (Grobler et al., 2018), it is pertinent to review the definition of the Platreef. Kinnaird and McDonald (2005) proposed that the Platreef consists of "Mafic units enriched in Ni-Cu-PGE that occur between the Archean granite-gneiss basements or the Transvaal Supergroup and the gabbros [and] gabbronorites of the Main Zone, north of the Planknek Fault" (p196). In contrast Maier et al. (2008) proposed a definition whereby all contact-style Ni-Cu-PGE mineralisation in the northern limb is classified as Platreef, thus incorporating mineralization of interpreted Main Zone in the northern sector of the northern limb and also including contact-style mineralization on the farm Rooipoort.

11.1.2.1 Lithostratigraphic Comparisons

The Flatreef bears many similarities to the Platreef in terms of its lithostratigraphy, including the prevalence of feldspathic pyroxenites with lesser amounts of norite and anorthosite (

Figure 11.6) (Grobler et al., 2018; Kinnaird and Nex, 2015) and the abundant evidence for interaction of northern limb magmas with the country rocks. Extensive dolomite contamination of magmas on the farm Sandsloot resulted in lithologies that are exotic to the remainder of the Bushveld Complex including websterite, clinopyroxenite, lherzolite and wehrlite (McDonald et al., 2005). Some of these may also occur in the Flatreef, e.g. wehrlite in the Lower Flatreef (at ~1700 m depth, UMT081).

Contamination by the floor rocks in the Flatreef and Platreef is expressed by abundant xenoliths and felsic veins (Kinnaird, 2005; Maier et al., 2008; McDonald and Holwell, 2011; Pronost et al., 2008). However, the Platreef contains a wider array of country rock rafts and xenoliths than the Flatreef including dolomite, quartzite and hornfels, the latter being

209

particularly abundant throughout the Platreef on Turfspruit (e.g. ATS26, ATS67, ATS20, ATS46 by (Kinnaird et al., 2005). These abundant xenoliths and country-rock rafts can significantly increase the total thickness of the Platreef (Kinnaird and Nex, 2015). Hornfels xenoliths are also present in the Flatreef (Kvadsheim, 2017; Marquis, 2015) but are absent in drill cores UMT081 and UMT094 which instead contain calc-silicate xenoliths, generally located towards the base of the Flatreef (

Figure 11.6).

Across the northern limb the thickness of the Platreef varies considerably both within and between various locations, analogous to but on a far larger scale, than the Flatreef (Table 11.1;

Figure 11.6). On the farm Turfspruit the Platreef is generally somewhat thicker (up to 445 m) (Kinnaird et al., 2005) than the Flatreef (340 m in UMT081, Upper Flatreef + FAZ). While both the Flatreef and Platreef are bound by a hangingwall of Main Zone comprising gabbronorite, norite and anorthosite, and a footwall of variable country rock lithologies (Kinnaird and Nex, 2015), the Platreef shows less lateral continuity of lithostratigraphy than the Flatreef. For example, on Turfspruit the GMA and Norite Cycles are relatively rare in the Platreef (GMA 2/6 and Norite Cycles 1/6 cores logged) (Kinnaird et al., 2005). In addition, the latter has thick serpentinite intersections and layers of supposed Marginal Zone that are not observed in the Flatreef (Grobler et al., 2018; Kinnaird et al., 2005).
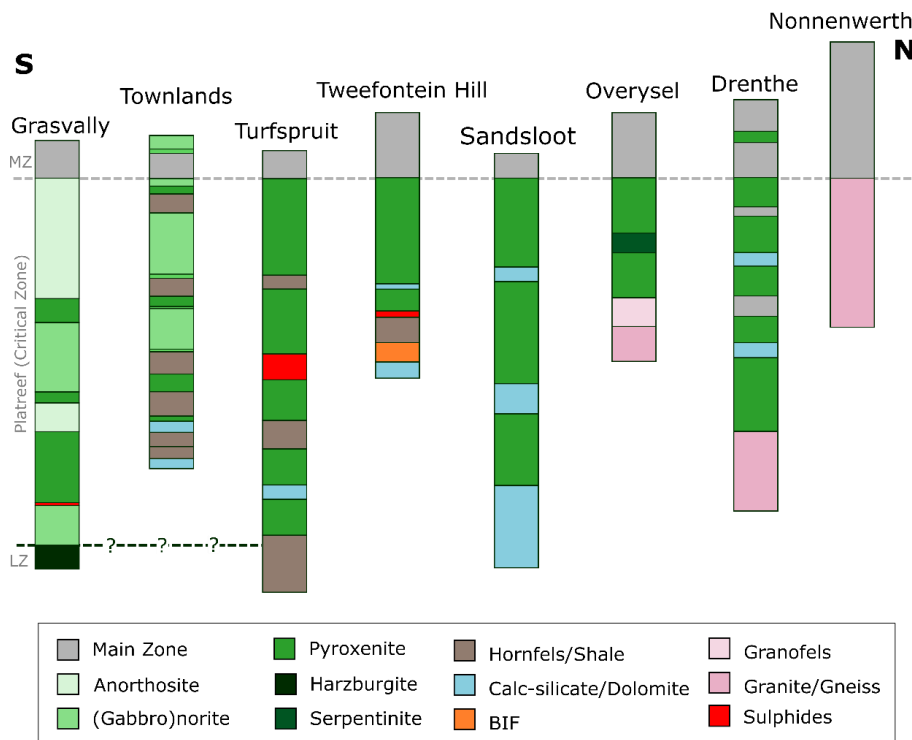
Figure 11.6: Representative stratigraphic logs from across the northern limb displaying the along-strike variability in Platreef lithologies, mineralization and footwall lithologies. Modified after (Kinnaird and Nex, 2015)

Farm	*Author*	**Platreef Thickness**	**Xenolith Population**
Overysel	*Holwell and McDonald 2006*	35-135	Calc-silicate Banded Gneiss
Sandsloot	*Armitage et al., 2002; McDonald et al., 2005*	Min. 12-15m	Calc-silicate
Turfspruit	*Kinnaird et al., 2005*	230-445	Dolomite, quartzite, hornfels
Townlands	*Manyeruke et al., 2005*	~150m	Quartzite, hornfels, calc-silicate
Rooipoort	*Maier et al., 2008*	Up to 700m	

Table 11.1: Variability of Platreef thickness and xenolith population along strike (Armitage et al., 2002; Holwell and McDonald, 2006; Kinnaird et al., 2005; Maier et al., 2008; Manyeruke et al., 2005; McDonald et al., 2005).

11.1.2.2 Mineral Chemistry

Past studies of mineral compositions on Platreef rocks indicate that the largest range of compositions, including the most evolved ones, are found on the farm Townlands (Opx Mg# 68-82 and Plag An 55-85) except for olivine which is more magnesian (Fo 78-83) than at most other Platreef localities (Figure 11.3) (Manyeruke et al., 2005). The remainder of the Platreef localities generally show a more restricted range of mineral compositions. Mineral compositions from the Flatreef broadly overlap with compositions across the Platreef, although Flatreef compositions show a wider range that is only matched by mineral compositions from the Platreef on the farm Townlands (Manyeruke et al., 2005). Of particular note is the wider range of plagioclase compositions relative to orthopyroxene within individual Platreef and Flatreef localities. While orthopyroxene is almost everywhere a cumulus phase, plagioclase is more commonly interstitial, except in feldspathic lithologies. The relatively wide range of plagioclase compositions from this study in particular is interpreted to reflect the more extensive analysis including traverses across plagioclase crystals, revealing zonation (Figure 6.28), which may reflect percolation of evolved liquids through the rocks, and reaction with the crystal mush.

There is petrographic evidence for significant interaction between sedimentary floor rocks and the Bushveld magmas in the Platreef that is not observed in the analysed Flatreef rocks. For example, in the Platreef on the farm Turfspruit, carbonate pseudomorphs within norite and strongly serpentinised rocks are documented (Kinnaird et al., 2005). McDonald et al. (2005) document fayalitic olivine forming a 'replaced reef' on the farm Sandsloot commonly accompanied by Fe-rich clinopyroxene after plagioclase where the Platreef abuts ironstone

formations. On the farm Overysel the Platreef pyroxenites contain accessory phlogopite and quartz, the latter becoming more abundant with proximity to the basement rocks (Cawthorn et al., 1985; Holwell and McDonald, 2006). In contrast, quartz is only observed in norite in drill cores UMT094 and UMT081 (but has been reported in pyroxenites by Yudovskaya et al. 2017 in drill core UMT314 on Turfspruit) and phlogopite is largely restricted to the interval between the Main PGE Reef and the Main Chromitite. Olivine in the Flatreef is consistently more magnesian than in 'replaced Platreef' and pervasive serpentinisation is absent in drill cores UMT094 and UMT081. However, the abundance of clinopyroxene, largely associated with strongly contaminated rocks is typical of both the Flatreef and the Platreef.

11.1.2.3 Whole Rock Geochemistry

Both the Flatreef and Platreef have highly variable lithophile element compositions (Figure 11.7) (Harris and Chaumba, 2001; Maier et al., 2008; McDonald et al., 2005; Pronost et al., 2008). The Platreef overlies and intruded a range of sedimentary and basement rocks; at Nonnenwerth, Sandsloot, Turfspruit, Townlands and Rooipoort these include Archean granite, Malmani dolomite, Duitschland carbonates, Timeball Hill shales and Magaliesberg quartzite, respectively (Kinnaird and Nex, 2015). In general, the Platreef at Sandsloot tends to have more variable compositions than the Platreef at other localities, including markedly higher CaO and MnO contents, but lower SiO_2, likely reflecting the contamination of the Platreef with dolomite at this locality. Another locality that has somewhat distinct composition is Rooipoort, which has lower CaO contents than other Platreef localities, but higher K_2O contents. The Platreef on Townlands is enriched in the same lithophile elements as Sandsloot Platreef, albeit at lower levels, while the Platreef on Nonnenwerth has a narrow range of MgO and is relatively rich in Fe_2O_3 and MnO. Rocks from the Flatreef show significant overlap with the Platreef, most notably on the farm Sandsloot, although the high MnO content is not observed in the Flatreef. The composition of calc-silicate rocks below the Flatreef overlaps with that of the most contaminated Sandsloot Platreef samples. Notably, the Ti-rich olivine gabbro in the Flatreef has no analogues elsewhere in the Platreef (Figure 11.7).
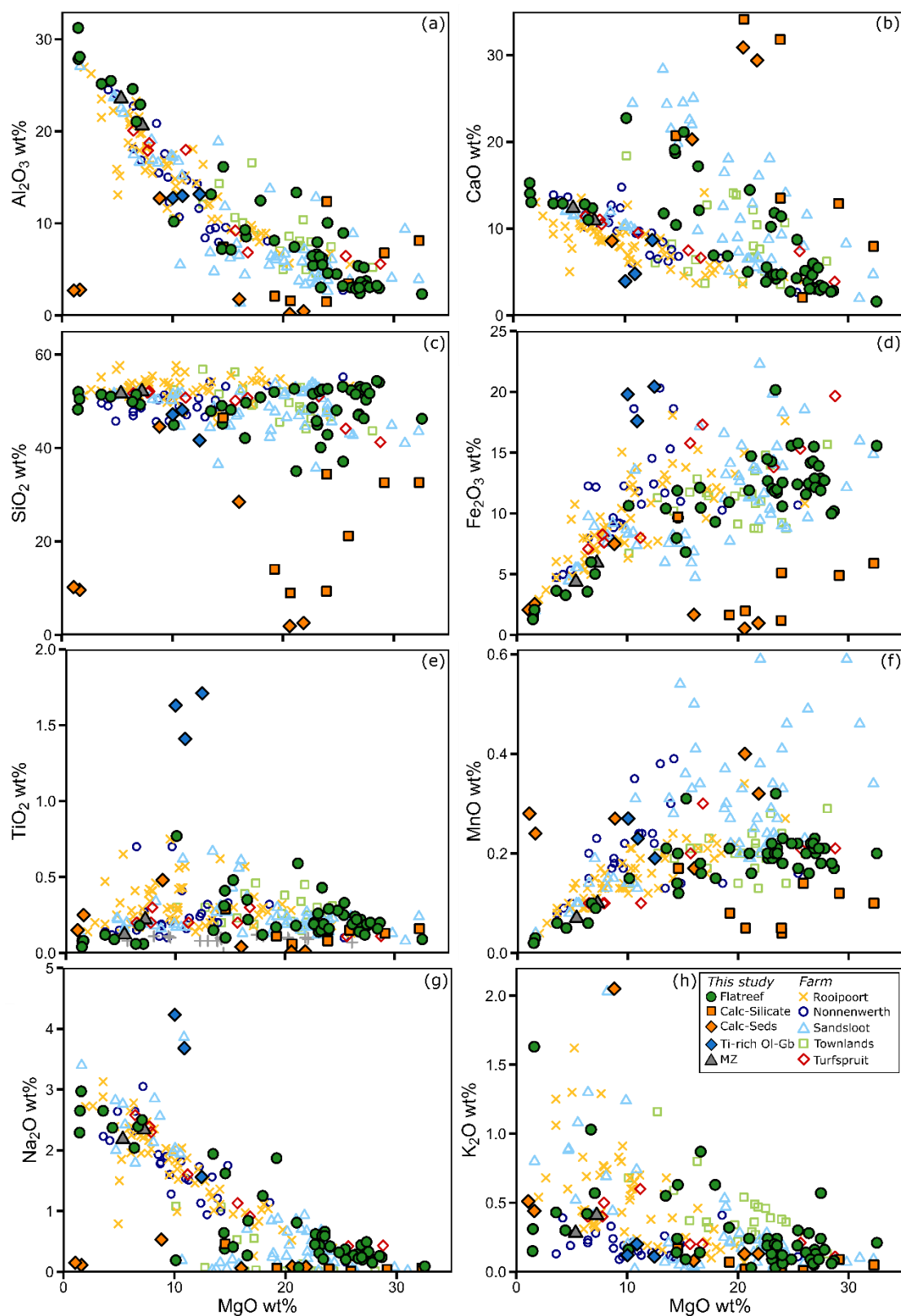
Figure 11.7: Bivariate plots of data plotted against MgO (wt.%) from this study compared to Platreef data from a range of localities in the Northern limb. (a) Al_2O_3, (b) CaO, (c) SiO_2, (d) Fe_2O_3, (e) TiO_2, (f) MnO, (g) Na_2O, (h) K_2O. Data from this study overlaps with data from the Platreef at Sandsloot, most notably in terms of the enhanced CaO content. (Harris and Chaumba, 2001; Maier et al., 2008; McDonald et al., 2005; Pronost et al., 2008).

Principal Component Analysis (PCA) of four major element oxides (MgO, SiO$_2$, Al$_2$O$_3$ and CaO) allow for easy visualization and separation of data trends not easily achievable through bivariate plots (Figure 11.8). The first and second principle components capture over 90% of the variability within the data from the Platreef. The direction (eigenvector) and length (eigenvalue) of each arrow shows the relative importance of specific major element oxides. When orthogonal these are independent of each other (i.e. SiO$_2$ and MgO; Figure 11.8). Al$_2$O$_3$ and MgO eigenvectors plot virtually 180° from each other, indicating that as concentration of one oxide increases the other decreases. This is typical of a fractionation trend from olivine-rich peridotites to plagioclase-rich anorthosites. The CaO eigenvector is orthogonal to the Al$_2$O$_3$-MgO fractionation trend and one can therefore assume that much of the CaO is derived from an external source (i.e., contamination by carbonate-rich country rocks). The majority of rocks plot along an Al$_2$O$_3$-MgO fractionation trend with some Sandsloot rocks plotting sub-parallel to the CaO vector. Rooipoort rocks generally plot above the main Al$_2$O$_3$-MgO trend signalling input by SiO$_2$ rich material and relatively less control by calcium contamination. The Flatreef data broadly plot along the Al$_2$O$_3$-MgO fractionation trend with localised contamination forming a secondary trend of elevated CaO contents, much like that seen at Sandsloot, in the FAZ and some rocks from Townlands (Figure 11.8).
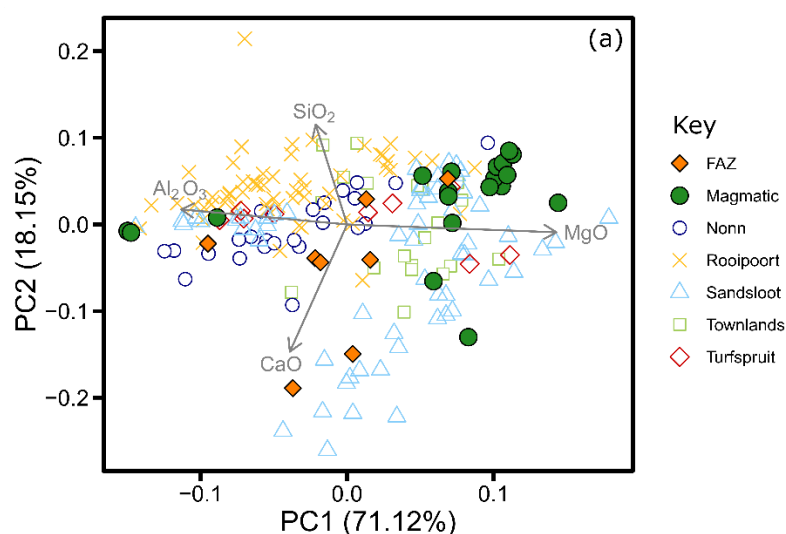
Figure 11.8: Plots of Principle Component Analysis of major element (MgO, CaO, SiO$_2$, Al$_2$O$_3$) data (wt.%) from across the Platreef. Note that the magmatic rocks of the Flatreef (UMT081) show good overlap with the Platreef on the farm Sandsloot. Data from present study and Harris and Chaumba (2001); Maier et al., (2008); McDonald et al., (2005); Pronost et al., (2008).

11.1.2.4 PGE

The PGE mineralisation in the Platreef shows strong similarities to that in the Flatreef, most notably the elevated PGE grade across much thicker intervals than in the remainder of the Bushveld Complex. Other similarities include the downward decrease in Pt/Pd ratio that has been previously documented in the central and southern sector of the northern limb (Kinnaird

and Nex, 2015). However, this pattern is not ubiquitous across the Platreef. The available data from Sandsloot and Zwartfontein show both constant and decreasing downhole Pt/Pd ratios while data from Tweefontein Hill show a downhole decrease in Pt/Pd in some, but not all drill cores (Kinnaird and Nex, 2015). On the farm Nonnenwerth, Pt/Pd decreases downhole in the upper 2/3 of the drill core but increases beneath this (Maier et al., 2008; Manyeruke, 2007). Other Platreef localities show no evidence of decreasing Pt/Pd downhole. On the farm Overysel the Pt/Pd ratio remains at 0.7-0.8 throughout the Platreef, except for massive sulphides within the footwall gneiss where Pt/Pd is 0.35 (Holwell and McDonald, 2007). In the southern Platreef on the farm Townlands, the data from Manyeruke et al. (2005) do not show a downhole decrease in Pt/Pd, while on the farm Drenthe Pt/Pd increases downhole (Gain and Mostert, 1982).

In both the Platreef and the Flatreef, PGE-mineralisation may extend into the footwall rocks (e.g. in the Platreef at the localities Tweefontein North, Tweefontein Hill and Sandsloot) and in calc-silicate floor rocks from the present study (sample 94-1411) (Kinnaird and Nex, 2015). Massive sulphides are also documented in the country rock footwall at several Platreef localities (e.g. Overysel and Turfspruit) and in the Flatreef (Holwell and McDonald, 2007; Kinnaird et al., 2005; Yudovskaya et al., 2017b).

Comparative chalcophile element data from across the northern limb indicate that the Flatreef is dissimilar to the Platreef in terms of average Pt/Pd and Ni/Cu ratios (Table 11.2). The Flatreef and specifically the Main PGE Reef have higher average Ni/Cu ratios than the Platreef (except on Townlands) and higher Pt/Pd ratios compared to the Platreef. The Flatreef also has higher (Pt+Pd)/Au ratios compared to the Platreef (except on Townlands and Uitloop).

The PGE tenors of the sulphides in most of the Flatreef show less variation compared to the Platreef, as expressed by stronger correlation between PGE and S in the Flatreef (Figure 5.19). However, scatter in the PGE-S plots increases towards the floor rocks, especially within the Lower Ultramafic Unit. In the Platreef, PGE and S show a relatively good positive correlation on the farms Townlands and Overysel, but a relatively poor correlation in the southern sector of the northern limb where the footwall rocks are dolomitic (Grobler et al., 2018; Kinnaird et al., 2005; Kinnaird and Nex, 2015).

Northern Limb	(2PGE+Au)	Ni/Cu	Pt/Pd	(Pt+Pd)/Au	Main Complex	(2PGE+Au)	Ni/Cu	Pt/Pd	(Pt+Pd)/Au
Aurora Project					**Northeastern Bushveld**				
					Lebowa Plats				
Kransplaats	1.17	0.73	0.73	6.62	Merensky	4.22		2.17	13.50
Nonnenwerth	1.36	0.64	0.60	5.98	Lesago Merensky	5.89	1.54	1.73	12.80
La Pucella-Altona	1.37	0.81	0.60	5.97	Lebowa Plats UG2	6.68		0.84	49.30
					GaPashaUG2	6.53		0.88	53.50
Platreef					Lesago UG2	6.27	2.00	1.15	44.50
Drenthe	1.05	1.50	0.83	12.10					
Drenthe**	1.14	2.03	1.32	6.05	**Southeastern Bushveld**				
					Booysendal				
Akanani P2 Unit	3.88	1.77	0.88	15.20	Merensky	4.28	2.36	1.86	11.20
Akanani P1 Unit	2.51	1.88	0.73	17.80	Booysendal UG2	4.24	9.00	1.68	112.00
Zwartfontein South	3.30	2.06	0.94	15.40					
Sandsloot	3.19	1.33	0.97	14.10	**Western Bushveld**				
					Frischgewaagd				
Tweefontein North	6.90	1.75	1.05	12.90	Merensky	5.70	3.28	2.38	23.70
					Amandebult				
Tweefontein Hill	5.00	1.21	0.62	7.21	Merensky	8.10		1.87	21.50
Townlands	0.55	1.72	0.67		RPM Merensky	7.33	2.25	2.76	18.60
Townlands**	0.99	10.81	1.24	18.37	Frischgewaagd UG2	4.51		2.43	100.00
Nonnenwerth**	1.00	1.81[a]	0.72	7.05	AmandebultUG2	5.21	11.00	2.23	125.00
Uitloop**	1.14	3.23	0.66	21.34	RPM UG2	5.36	9.00	1.60	128.00
					Union Section UZ†	0.27	1.18	1.56	61.33
Flatreef					Union Section MZ†	0.03	3.83	4.80	12.78
Turfspruit*	1.95	2.73	1.49	17.26	Union Section UCZ†	0.54	13.67	5.39	13.26
UMT081 Main PGE Reef*	21.84	2.99	1.50	23.53	Union Section LCZ†	0.20	19.78	2.73	23.44
					Union Section LZ†	0.03	33.68	1.19	16.90
GNPA Member									
War Springs (C Reef)	1.24	1.33	0.21	16.70					
War Springs (B Reef)	0.88	1.28	0.45	9.63	Av. B1 °	36.07	5.57	1.38	12.26
Rooipoort M2 (MANO)	1.34	1.70	0.51	13.10	Av. B2 °	16.65	1.39	1.83	7.76
Rooipoort L3 (LMF)	1.15	1.54	1.16	22.50	Av. B3 °	16.88	2.87	3.88	17.97

*Table 11.2: PGE data from various locations in the northern limb and the remainder of the Bushveld Complex, modified from (McDonald and Holwell, 2011). * This study excluding devolatized footwall and calcareous sediments, **Maier et al. (2008), †Maier et al. (2013), °Barnes et al., (2010), [a]Excluding 1 anomalous altered sample.*

11.1.2.5 Isotopes

Platreef rocks are generally characterised by a wide range of isotopic compositions, reflecting the variable degrees and types of contamination that occur across the northern limb (Figure 11.9). The isotopic data for the Flatreef rocks show broad overlap with those of the Platreef while showing considerable variation in detail. For example, while Flatreef rocks have similar $\delta^{18}O$ and $^{87}Sr/^{86}Sr_i$ to Sandsloot, the εNd of the former are more negative, overlapping with the Platreef on the farm Overysel (Barton et al., 1986; Harris and Chaumba, 2001; Pronost et al., 2008).

The $\delta^{18}O_{opx}$ of the Upper Flatreef plots in a similar range (7.0-9.3 $\delta^{18}O_{opx}$) to the Platreef data from Turfspruit (6.2-9.7 $\delta^{18}O_{opx}$) and Sandsloot (6.2-9.7 $\delta^{18}O_{opx}$), whereas the isotopic range on Overysel is somewhat lighter (5.1-8.1 $\delta^{18}O_{opx}$). In contrast, the Platreef on Overysel has a wider and generally more radiogenic $^{87}Sr/^{86}Sr_i$ signature compared to the Flatreef (Barton et al., 1986; Pronost et al., 2008). The Platreef on Turfspruit and Sandsloot also exhibit relatively more radiogenic Sr isotopes than the Flatreef, although the latter does overlap with the lower end of the Sandsloot data. However, the Platreef on Sandsloot has a less negative and narrower range of εNd (-6.9 to -7.3 εNd) compared to the Upper Flatreef (-7.71 to -9.21 εNd), which broadly overlaps with the Platreef on Overysel and the banded gneiss of the Archean basement (Pronost et al., 2008).
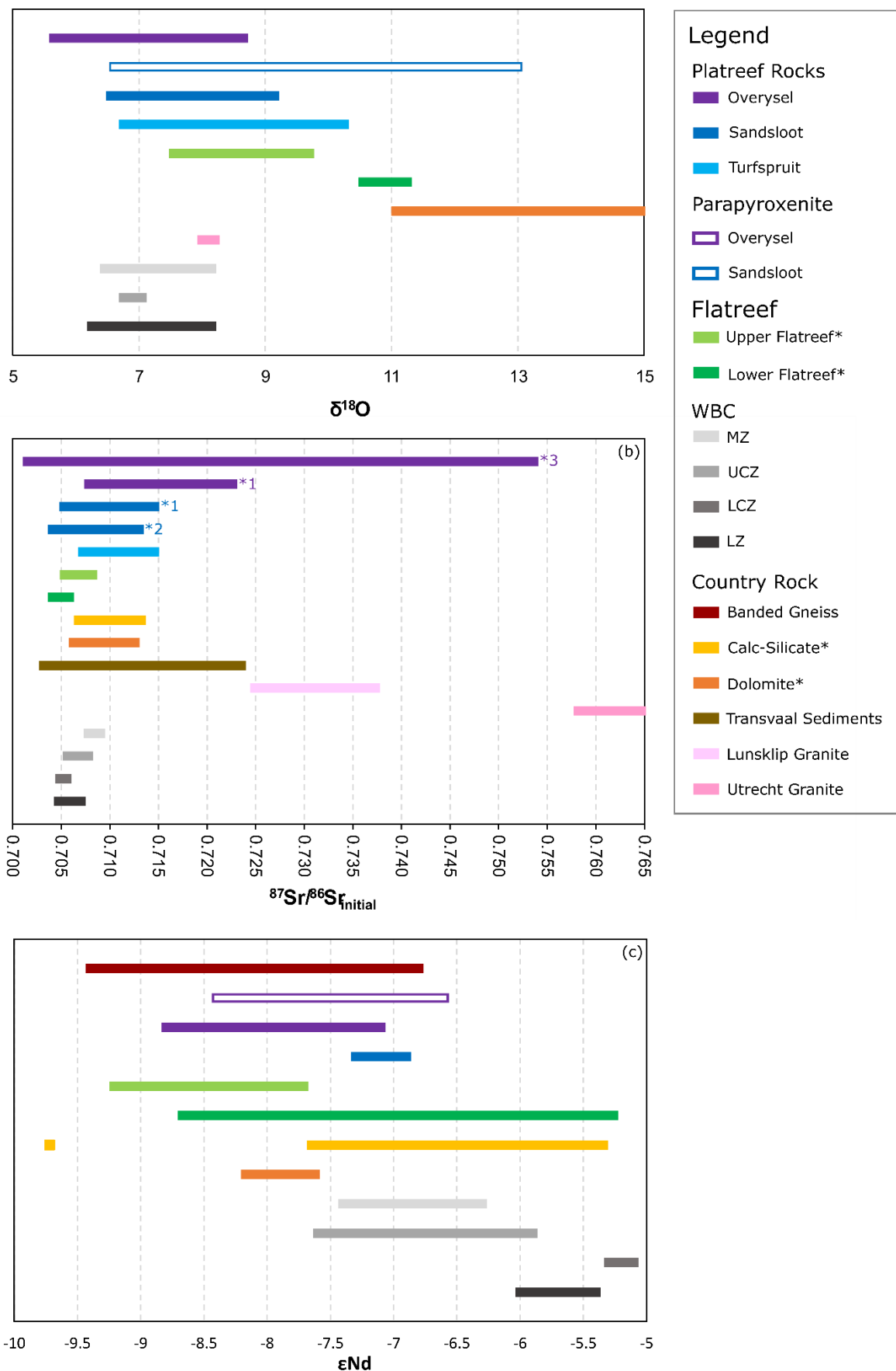
Figure 11.9: Range of isotopic values from various localities across the northern limb and zones of the WBC. (a) Oxygen isotope data, (b) Sr isotope data, (c) Nd isotope data. All δ¹⁸O opx data have been

converted to whole rock values using conversion of +0.55 for Opx and -0.2 for Plag according to Harris et al. (2001). All radiogenic isotope data presented are calculated for an age of 2.05704Ga)(Scoates and Wall, 2015), In the legend, * denotes data from this study. Where multiple isotope ranges are presented for the same farm numbered stars refer to*1 Barton et al. (1986), *2 Harris et al. (2001), *3 Pronost et al. (2008). (Flatreef data includes FAZ rocks, but not Ti-rich olivine gabbro and olivine gabbronorite rocks). (Barton et al., 1986; Cawthorn et al., 1985; Eales et al., 1990; Harris and Chaumba, 2001; Harris et al., 2005; Kruger, 1994a; Kruger, 2005; Maier et al., 2000; Mathez and Agrinier, unpublished; Pronost et al., 2008).

11.1.2.6 Summary

Data from Overysel, Sandsloot and Turfspruit confirm that the Platreef consists of feldspathic orthopyroxenite, gabbronorites, norites and anorthosites in the main instance but localised contamination gave rise to a range of exotic lithologies such as websterite and parapyroxenites (McDonald and Holwell, 2011). In places, this contamination can totally obliterate magmatic layering (i.e. on the farm Sandsloot) but elsewhere is restricted to the lower portions of the magmatic package, similar to what is observed in the Flatreef. It seems reasonable to suggest that the Platreef represents a more contaminated up-dip extension of the Flatreef, in agreement with the model proposed by Grobler et al. (2018), with extensive contamination overprinting distinctive layering and geochemical compositions, the nature of which varies strongly with changing footwall lithologies.

11.1.3 Comparison between the Flatreef and the UCZ of the WBC

11.1.3.1 Lithostratigraphic comparisons

Both the Flatreef and the UCZ of the WBC consist of mafic-ultramafic packages comprising multiple layers of cumulate rocks. The UCZ of the WBC shows strong lateral variability in lithology, but on average norites are the most common rock type, followed by pyroxenite, and with subordinate volumes of anorthosites and olivine-bearing rocks i.e. harzburgite, troctolite and olivine-norite (Maier et al., 2013; Maier and Eales, 1997). The Upper Flatreef is comprised mainly of feldspathic orthopyroxenites, whereas norites, anorthosites and harzburgites make up a relatively small proportion of the sequence in most drill cores. In both the Flatreef and the UCZ, the MZ boundary is demarcated by a mottled anorthosite layer with large (up to 10 cm) oikocrysts (mottles) of pyroxene, termed the Giant Mottled Anorthosite in the WBC (De Klerk, 1992). However, in the WBC evidence of interaction with floor rocks is much less prominent, and essentially confined to the southwestern sector on the farm Schietfontein, where the Main, Critical and Lower Zones contain major rafts or xenoliths of metasedimentary rocks, similar to rafts observed in the Platreef (Kinnaird, 2005; Maier and Bowen, 1996).

While layering is observed on both the Flatreef and UCZ, it is more regular and laterally continuous in the UCZ, forming the so-called cyclic units. The latter typically consist of a chromitite stringer at the base overlain by harzburgite and/or orthopyroxenite, norite and then

anorthosite, with individual cycles ranging in thickness from millimetres to >100 metres. The units can be truncated, in part explaining the variation in thickness, interpreted to result from thermal-mechanical-chemical erosion by overlying magma influxes (Eales et al., 1988; Eales et al., 1986; Gain, 1985; Maier et al., 2013). Kinnaird et al. (2005) have suggested that the norite cycles of the Platreef, which are also observed in the Flatreef, are reminiscent of the cyclic units observed in the Main Bushveld Complex. However, the norite cycles do not normally show regular cyclicity progressing from ultramafic bases to more feldspathic lithologies at the top of the cycles. Instead norite cycles in the Flatreef are characterised by alterations between more pyroxene-rich and pyroxene-poor layers.

As noted above, although the UCZ in the WBC contains laterally more continuous layering than in the Flatreef, the thickness of individual layers in the WBC is not consistent. For example, in the Merensky Reef cyclic unit the proportion of feldspathic rocks varies between 33% and 85% along strike (Eales et al., 1986; Vermaak, 1976). The total thickness of the UG2-Merensky Reef interval also varies between ~30 m at Union section to 205 m in the Brits area (Maier and Eales, 1997) with certain layers pinching out laterally. Similar variability occurs in the Flatreef where the Main PGE-Main Chromitite interval ranges between 62 and 95 m in drill cores UMT094 and UMT081, respectively. At the Amendelbult section of the northwestern Bushveld Complex there are multiple layers of anorthosite and norites between layers of pyroxenite that are absent in the same interval at Union section, and the base of the UG2 cyclic unit is interjected by multiple norite layers on the farm Schietfontein (Figure 11.10) (Eales et al., 1988; Maier and Bowen, 1996). This is reminiscent of the absence of feldspathic layers between the Upper and Main PGE Reefs in some Flatreef intersections. Other UCZ layers of the WBC only occur in close proximity to proposed feeder zones, such as the Tarentaal or Upper Pseudoreef harzburgite documented at the Union and Amendelbult sections (Figure 11.10). The Mg# of individual (especially feldspathic) layers is also variable across the WBC, largely in relation to distance from the proposed feeder zone at Union Section (Eales et al., 1988; Maier and Bowen, 1996; Maier and Teigler, 1995). Flatreef rocks also show laterally variable Mg# within specific layers, which is reflected in variable whole rock and mineral compositions between drill cores (chapter 6).
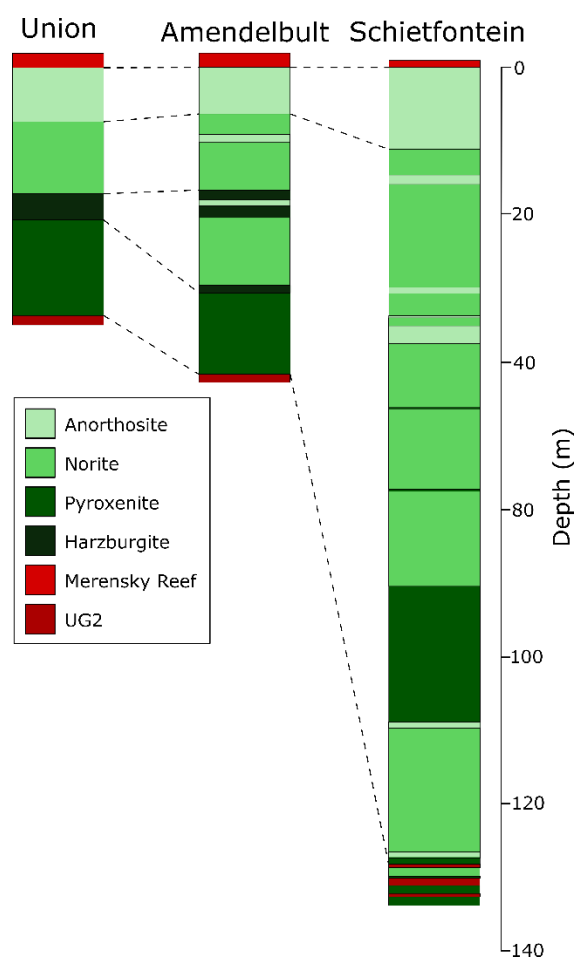
Figure 11.10: Variability in the Merensky reef – UG2 interval across the WBC. Compiled from(Maier and Bowen, 1996).

The most notable lithostratigraphic difference between the Flatreef and the UCZ is the contrasting thicknesses of the PGE reefs. The thickness of the Merensky Reef in the UCZ is generally 2 cm to 2 m although locally can reach up to 4 m (Arndt et al., 2005; Barnes and Maier, 2002a; Brynard et al., 1976). In contrast the overall thickness of the Main PGE Reef in the Flatreef is between 8.8 m (UMT081) and 26.1 m (UMT094), and in some drill cores (e.g. TMT006), PGE grade can exceed 4 g/t over nearly 100 m (Grobler et al., 2018).

11.1.3.2 Mineral chemistry

As evident from Figure 11.3, mineral compositions from the UCZ and LCZ in the WBC overlap with the most primitive mineral compositions in the Flatreef. However, the Flatreef also contains more evolved mineral compositions. Pyroxenites and norites in the upper half of the Flatreef have broadly similar orthopyroxene and plagioclase mineral chemistry (76-86 Mg#, An 43-81 UMT081) to the UCZ (78-84 Mg#, An 68-84) (Eales and Cawthorn, 1996). In contrast, the Main PGE Reef in the Flatreef is marginally more magnesian (Fo 82-83, Opx Mg# 83-86) than the Merensky Reef (Fo 79 and Opx Mg# 78-82) (Maier and Eales, 1994; Naldrett et al., 1986). Downhole plots of mineral compositions show that orthopyroxene in the Flatreef has a largely constant composition, a trend also observed in the UCZ (Cameron,

221

1982). However, both packages also show a decrease in Mg# of orthopyroxene with height above the Main PGE and Merensky Reefs, respectively (Cameron, 1982).

11.1.3.3 Whole Rock Geochemistry

A robust comparison between the Main Zone in the northern limb and the remainder of the Bushveld Complex is difficult as only 2 samples were analysed in the current study. These samples have similar Al_2O_3, Na_2O, CaO and MgO concentrations to the WBC MZ, except for K_2O, which is elevated in the Flatreef (up to 0.41 wt.% this study; Figure 11.11). Flatreef MZ also has elevated K_2O contents relative to other MZ studies in the northern limb where the lower MZ contains ~0.15 wt.% K_2O (Roelofse et al., 2015).

There is relatively good overlap in whole rock chemistry between Flatreef rocks and those of the UCZ of the main Bushveld Complex, although there is some variability in certain elements. In general, the Flatreef is variably rich in CaO, K_2O, MnO, Rb and Zr relative to UCZ rocks of the WBC (Figure 11.11, Figure 11.12). Plagioclase rich rocks from the Flatreef are relatively rich in K_2O but tend to be slightly poorer in Al_2O_3 and CaO compared to equivalent rocks from the UCZ of the WBC. Ultramafic Flatreef rocks broadly overlap with those trends in the WBC, but show greater variability, especially in CaO, SiO_2 and K_2O contents (Figure 11.11). Upper Flatreef rocks show better overlap with the UCZ rocks than the Lower Flatreef which tends to be more variable in composition. Principle component analysis further confirms the similarity between Flatreef and CZ rocks of the WBC (Figure 11.13). The near parallel arrows of Al_2O_3 and CaO indicate that addition of CaO from contamination is not a major feature of rocks from the UCZ of the main Bushveld Complex, unlike the Flatreef of the northern limb. UCZ rocks overlap with both the more MgO and Al_2O_3 rich rocks of the Flatreef whereas LCZ and LZ rocks lack more Al_2O_3 rich compositions (i.e. more feldspathic rocks) (Figure 11.13). There is also generally good major element compositional overlap between the Merensky Reef of the WBC and the Main PGE Reef of the Flatreef.
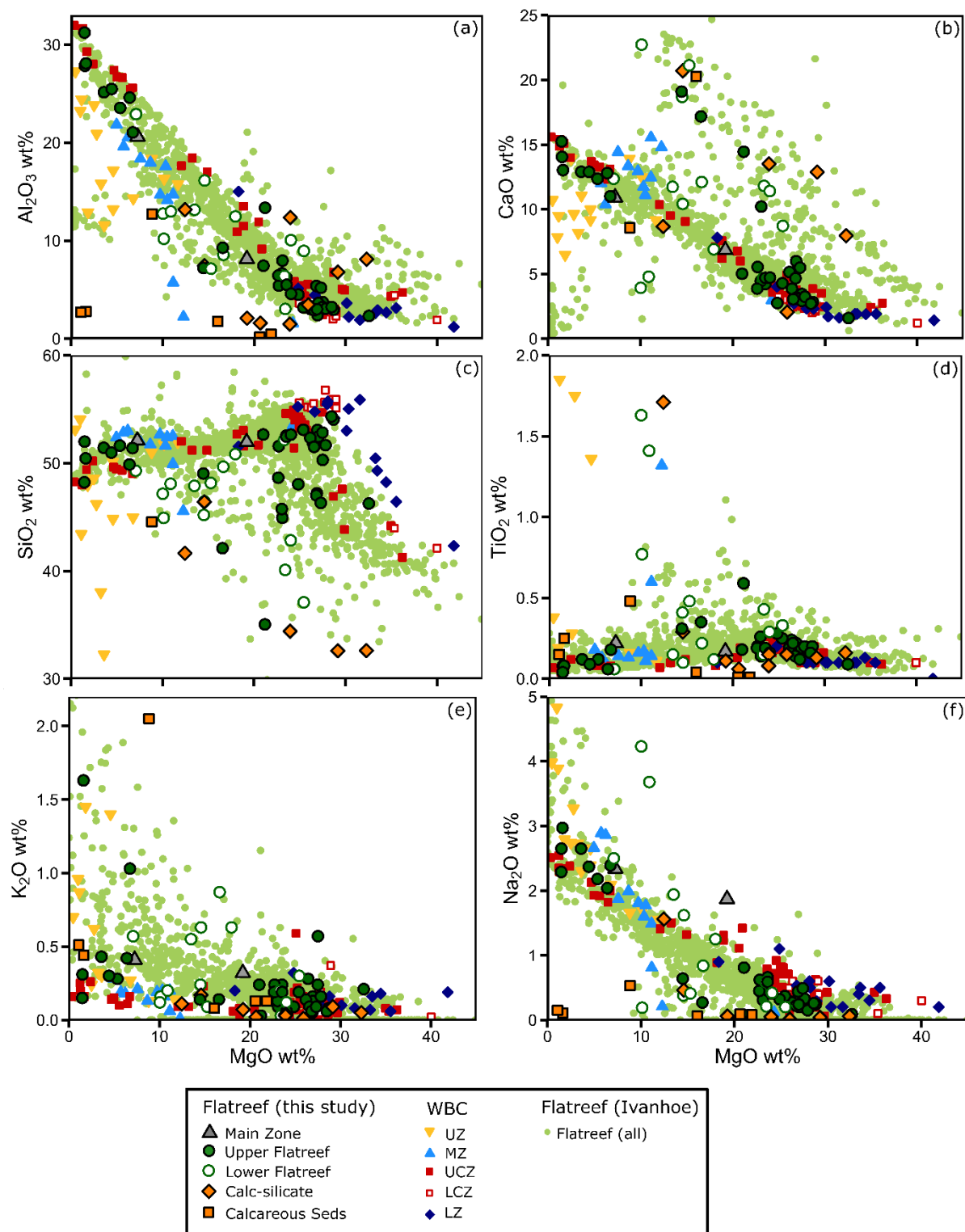
Figure 11.11: Bivariate plots of major and minor element data from this study and unpublished data of Ivanhoe mines, plotted with data from the WBC against MgO (wt.%). (a) Al$_2$O$_3$, (b) CaO, (c) SiO$_2$, (d) TiO$_2$, (e) Na$_2$O, (f) K$_2$O. There is good overlap between data from this study and the UCZ. However, the Flatreef can be variably rich in CaO, K$_2$O and poor in SiO$_2$, a trend also seen in other Flatreef data (Grobler et al., 2018; Maier et al., 2013).
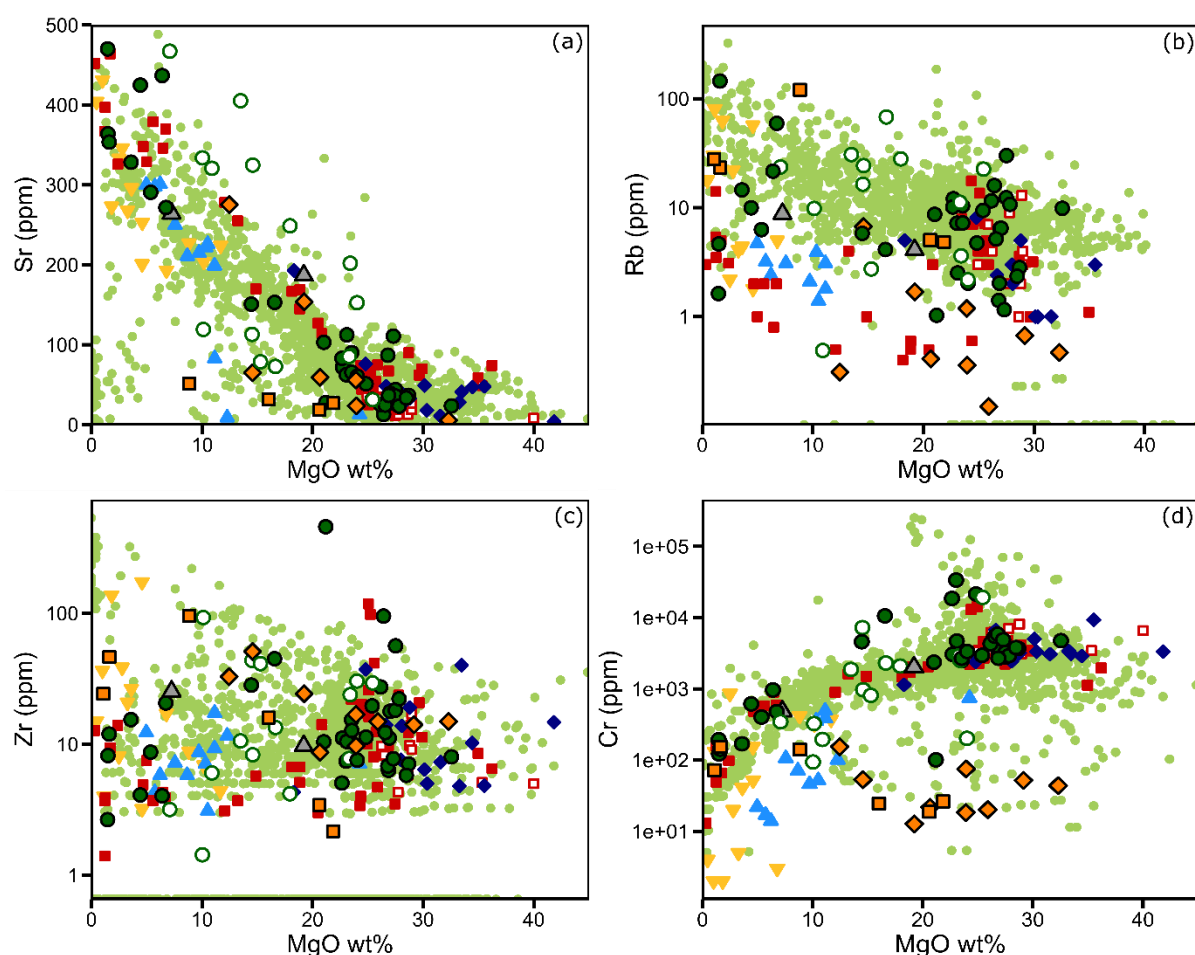
Figure 11.12: Bivariate plots of trace elements from this study compared to data from the WBC and Flatreef plotted against MgO wt.%. (a) Sr, (b) Rb, (c) Zr, (d) Cr.

The Main Zone norite above the Flatreef has broadly similar compositions and REE patterns to equivalent rocks in the WBC but can be marginally rich in absolute REE contents (Figure 5.5e). The MZ norites from this study are also rich in Zr (max. 25.34 ppm) and Rb (max. 8.80 ppm) relative to the WBC. Trace element concentrations in magmatic rocks from the Flatreef show considerable overlap with UCZ rocks of the WBC but tend to be more variable, especially in Lower Flatreef rocks (Figure 11.12). Trace element compositions and REE patterns of plagioclase rich rocks in the Flatreef (i.e. UMA and noritic units) mostly overlap with equivalent rocks in the WBC (Figure 7.15). REE patterns of pyroxenites also overlap (although none of the rocks analysed here show a positive Eu anomaly that is characteristic of pyroxenites from the UCZ in the WBC), whereas REE patterns of harzburgites bear little resemblance to equivalent rocks from the WBC (Figure 7.15). Flatreef rocks can also be relatively rich in HREE relative to the WBC rocks.
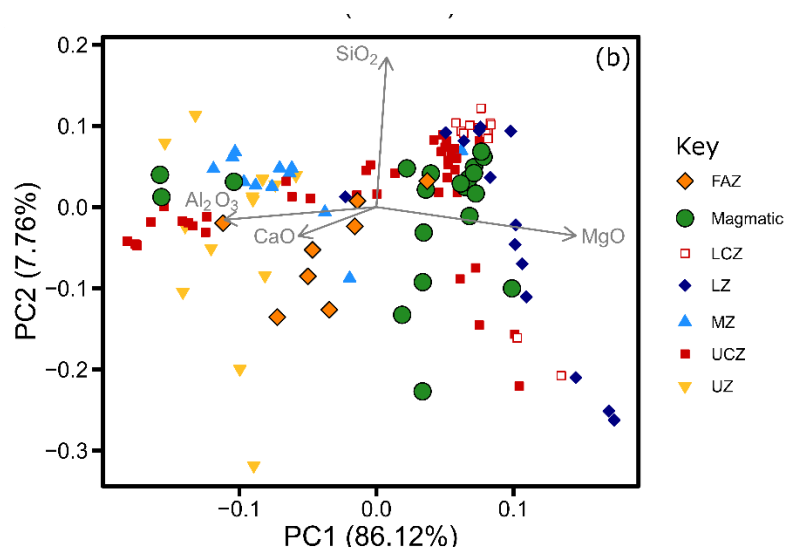
Figure 11.13: PCA of the major element oxides of silicate rocks from the Flatreef and the Bushveld Complex as well as calc-silicate floor rocks from UMT094.

11.1.3.4 PGE

One of the most notable differences between the Flatreef and the UCZ of the WBC is the much enhanced mineralization of the former (Figure 11.14) (Grobler et al., 2018; Maier et al., 2013). This is particularly striking in the Upper and Main PGE Reefs, which can be over 10 m thick. High PGE contents are also observed across the entire thickness of the Flatreef, whereas in the WBC PGE are largely concentrated in several strata-bound reefs (Table 11.3). Average Ni and Cu contents are also strongly elevated in the Flatreef relative to the WBC (Figure 11.14). In contrast, the 2 Main Zone samples analysed are poorer in PGE compared to the WBC (Maier and Barnes, 1999).

INTERSECTION	WBC	UPPER FLATREEF
Silicate rocks below UG2/Main Chromitite	PPGE 30-60ppb	PPGE avg. 881ppb
Bastard Pyroxenite	PPGE 220ppb	PPGE 2942ppb max.
Entire section excluding reefs	50-150ppm S *(LZ, CZ and MZ)*	1,000-10,000ppm
Bastard-UG2 intersection/ Upper-Main Chromitite intersection (all excluding reefs)	>200ppm S	Avg. 2654ppm S
Main Zone	<40 ppb PPGE	<0.69 ppb PPGE *or below detection limits*

Table 11.3: Comparative PGE and S concentrations from the WBC and Flatreef. Additional data from Ivanhoe (unpublished) and (Maier et al., 2013)

Downhole variability in overall PGE grade differs between the UCZ and the Flatreef. In the WBC, PGE contents define a pattern whereby Pt and Pd contents are much reduced

immediately below the UG2 and Merensky Reef, but show a steady upward decline in PGE grade above the reef (Figure 11.16). In contrast, in the Flatreef the footwall and hangingwall rocks of the reefs are mostly strongly mineralised, with grades commonly approaching those of the reefs. In both the Flatreef and the UCZ of the WBC, PGE generally show strong inter-element correlation and somewhat poorer correlation between PGE and Au (Barnes and Maier, 2002b).

Vertical trends in mineralization and chalcophile element ratios also show certain differences between the Flatreef and the UCZ in the WBC. Across much of the Flatreef, Pt/Pd decreases downhole. In contrast, Pt/Pd in the UCZ is more variable; in the rocks above the UG2 reef Pt/Pd increases downhole, whereas below the UG2 reef, Pt/Pd sharply increases (reaching a maximum value of 36) and remains elevated over 280 m before returning to values around 1.5 (Figure 11.15b) (Maier et al., 2013). However, over the entire stratigraphy of the western Bushveld CZ and LZ rocks, Pt/Pd ratios show an overall decrease downhole, analogous to the Flatreef (Figure 11.15a). The actual values of Pt/Pd are also comparable. Rocks above the UG2 in the WBC and the Main Chromitite in the Flatreef have similar average Pt/Pd (1.71 and 2.19, respectively) and ranges of Pt/Pd (0.28-4.64 and 0.71-4.49, respectively). In contrast, the Pt/Pd ratios of the Merensky Reef in the WBC are higher (2.01-2.42) than in the Main PGE Reef of the Flatreef (1.61 across the Flatreef, 1.5 in UMT081) but the latter overlaps with values from the EBC (1.47-2.10) (Grobler et al., 2018).
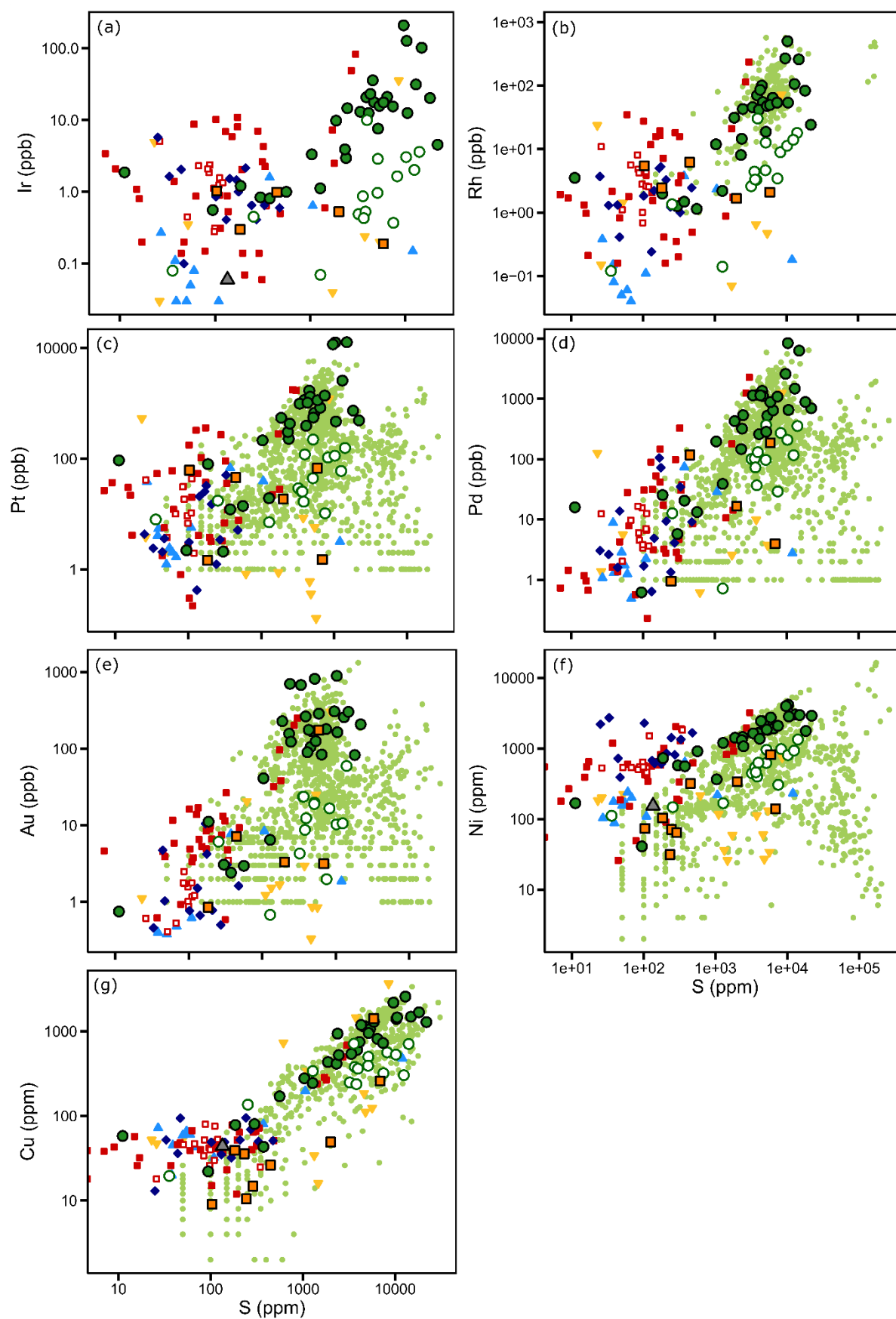
Figure 11.14: Bivariate plots of chalcophile elements against S (ppm). (a) Ir, (b) Rh, (c) Pt, (d) Pd, (e) Au. Comparative data from the WBC and Flatreef (Maier et al., 2013 and Ivanhoe Mines, unpublished).
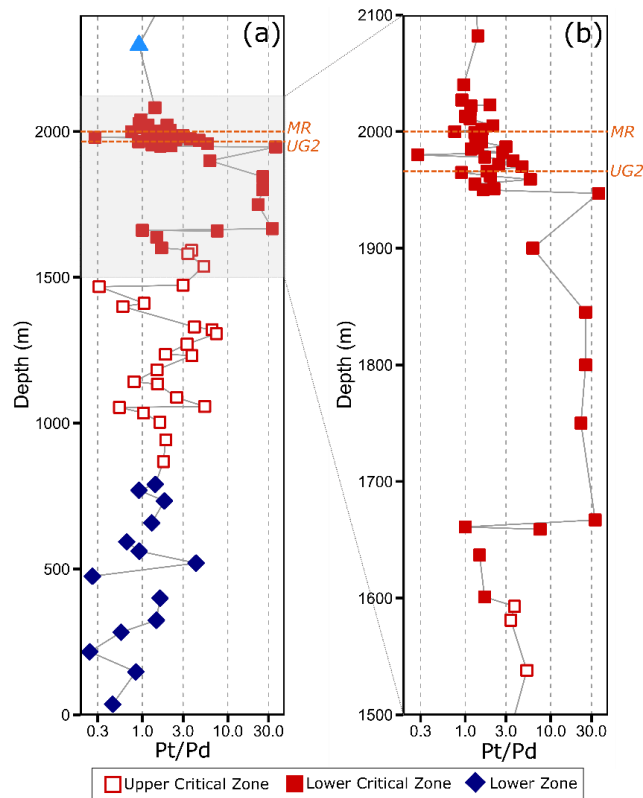
Figure 11.15: Downhole plots of Pt/Pd ratio within the WBC. (a) Pt/Pd ratios across the UCZ, LCZ and LZ of the WBC. (b) Pt/Pd ratios across the UCZ (Maier et al., 2013).
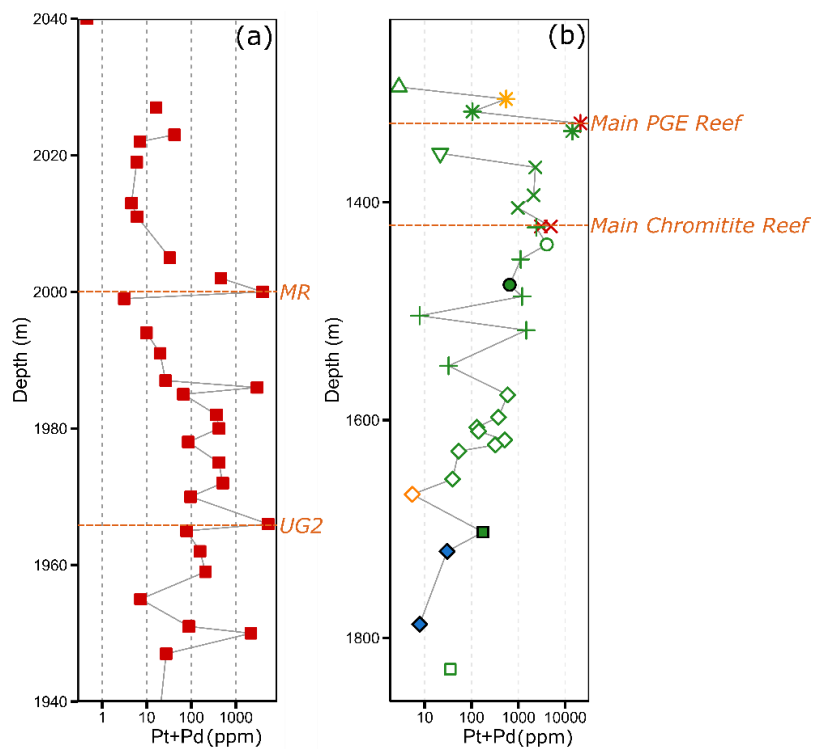
Figure 11.16: Downhole plots from the WBC (a) and UMT081 in the Flatreef (b) showing Pt+Pd grade. Note the clear cyclicity in PGE grade within the WBC that is largely absent in the Flatreef (Maier et al., 2013).

11.1.3.5 Isotopes

Isotopic data from the main Bushveld Complex (EBC and WBC) show broadly similar ranges in strontium and magnesium isotopes to the Flatreef, whereas oxygen, lead and neodymium isotope ranges are different to those of the Flatreef (Figure 11.9). Considering Sr first, the Flatreef shows good overlap with Sr_i data of the UCZ in the WBC from Eales (1990), with a marginally wider range observed in the Flatreef relative to the UCZ (0.70514-0.708242 and 0.70565-0.70779 $^{87}Sr/^{86}Sr_i$, respectively) (Figure 11.9). Mg isotopes from the WBC (2 samples from Union Section, this study) are at -0.16 and -0.28‰ $\delta^{26}Mg$ for Merensky Reef and its pyroxenitic hangingwall, respectively, overlapping in part with Upper Flatreef samples (-0.16 to -0.38‰ $\delta^{26}Mg$).

While there is substantial oxygen isotope data for the Main and Upper Zones of the Bushveld Complex, there is limited data from the UCZ. Harris et al. (2005) analysed 5 norites and pegmatoids from the Merensky reef with a range of 6.2 to 6.5 $\delta^{18}O_{opx}$ which is significantly lighter than Upper and Lower Flatreef samples (7.0-9.9 and 10-10.7 $\delta^{18}O_{opx}$, respectively). Limited Pb isotope data from the Bushveld complex shows that the Flatreef broadly overlaps with $^{208}Pb/^{204}Pb$ from UG2 chromitite but is generally more radiogenic than other WBC layers. The $^{207}Pb/^{204}Pb$ whole rock data from the UG2 footwall and mineral data from some UG2 plagioclase grains (Mathez and Kent, 2007) overlap with the Flatreef data. In contrast, the Flatreef $^{208}Pb/^{204}Pb$ and $^{207}Pb/^{204}Pb$ data are more radiogenic than Bastard Reef values from the WBC (Figure 11.17). However, Pb isotope data for the Western Bushveld Complex rocks were determined from whole rock suggesting that overlap with Flatreef data could result from remobilization of Pb, and that a reliable comparison is not possible (Harmer et al., 1995). The available Nd isotope data show little overlap between the Flatreef (-7.19 to -9.21 εNd) and the UCZ of the main Bushveld Complex (-5.9 to -7.6 εNd) (Figure 11.9). However, there is some overlap between the least radiogenic Flatreef and most radiogenic UCZ and MZ rocks (UCZ -7.6, MZ -7.4 εNd) (Maier et al., 2000).
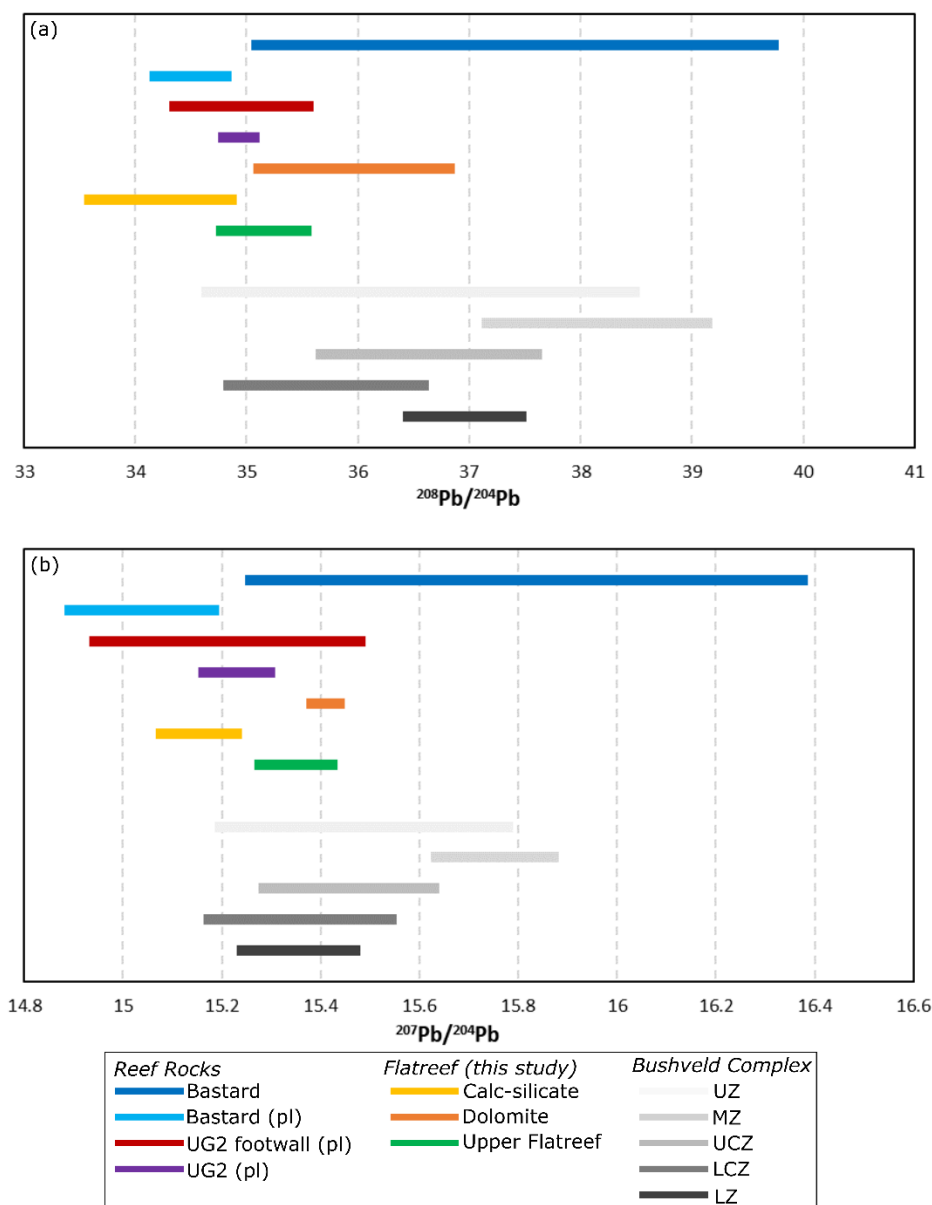
Figure 11.17: Bar graphs of Pb-isotopic ranges from various rocks across the Bushveld Complex. (a) $^{208}Pb/^{204}Pb$, (b) $^{207}Pb/^{204}Pb$. Comparative data from (Harmer et al., 1995; Mathez and Kent, 2007). Unless otherwise stated all data is from whole rock analyses.

11.1.3.6 Geochronology

The dispersed zircon dates from the Main PGE Reef (M2) in the northern limb and the Merensky Reef at Northam mine (NORT) in the western limb of the Bushveld Complex clearly overlap (Figure 11.18). The older age populations from these samples, considered to represent initial zircon crystallisation, place these reefs on each limb within 0.145 ± 0.169 Myrs of each other. Taking into account the relatively low sampling density of zircon at Northam (n=5) and the Flatreef (n=7), these data support a model that these units were emplaced broadly contemporaneously and their age dispersion resulted either from protracted crystallisation or resetting of the U-Pb system in pre-existing zircons.

When compared to other CA-ID-TIMS U-Pb data from the Bushveld Complex, the younger zircon population ages from M2 and NORT fall within uncertainty of Merensky Reef weighted mean dates from the western limb of Mungall et al. (2016), but are older than the eastern limb Merensky Reef data of Zeh et al. (2015) (Figure 11.18). The older zircon populations of M2 and NORT can be resolved as significantly older than the data from Zeh et al. (2015) and Mungall et al. (2016) and significantly younger than data from Scoates and Wall (2015). The lower Main Zone from the Flatreef also has 2 zircon age populations (2056.002 ± 0.047 and 2056.184 ± 0.081 Ma). This is older than the lower Main Zone from the EBC (2055.01 ± 0.44 Ma) (Zeh et al., 2015) by at least ~50 kyrs but overlaps (within error) with the age of the MZ from the WBC (2055.86 ± 0.15 Ma) (Figure 11.18) (Mungall et al., 2016).

The divergence between the different data sets could reflect a range of different laboratory, data reduction and geological interpretations. For example, Scoates and Wall (2015) and Zeh et al. (2015) measured Pb isotopes by a dynamic ion counting method, which are susceptible to issues in deadtime corrections (Richter et al., 2001). Scoates and Wall (2015) did not analyse data using the "EARTHTIME2535" tracer that Mungall et al. (2016), Zeh et al. (2015) and this study used, and thus do not fully account for mass fractionation. While Mungall et al. (2016) used a similar analytical setup to this work, a different reduction scheme was applied (in-house) whereas this study utilised the EARTHTIME Redux programme (Bowring et al., 2011). Mungall et al. (2016), also used up to 5 zircon fragments within a single analysis (i.e., multi-grain), whereas this study analysed single zircon crystals. The multi-grain approach of Mungall et al. (2016) has the potential to homogenise the dispersion of dates and miss the complexity observed in this study. Advances in single data point precision of zircons within a single magmatic unit has generated data with age dispersions not previously observed in the Bushveld Complex. Weighted means of previous data generated on samples from the Bushveld Complex will therefore be biased towards the younger dates that cannot be resolved at the stated precision achieved in these studies (Mungall et al., 2016; Zeh et al., 2015). Averaging the dispersion may introduce artificial patterns of out-of-sequence emplacement if units are treated as single date populations.

Due to these issues it is important not to over-interpret the small observed divergence in interpreted ages between different datasets for comparable units, and this was the main rationale behind analysing NORT Merensky Reef in this study, to allow for a more detailed comparison with the Flatreef samples. Broadly speaking, however, the previously analysed data are in broad agreement with data generated in this study, spanning ~2.5 Myrs (<0.1%), which is remarkable given the size of the Bushveld Complex (Figure 11.18).
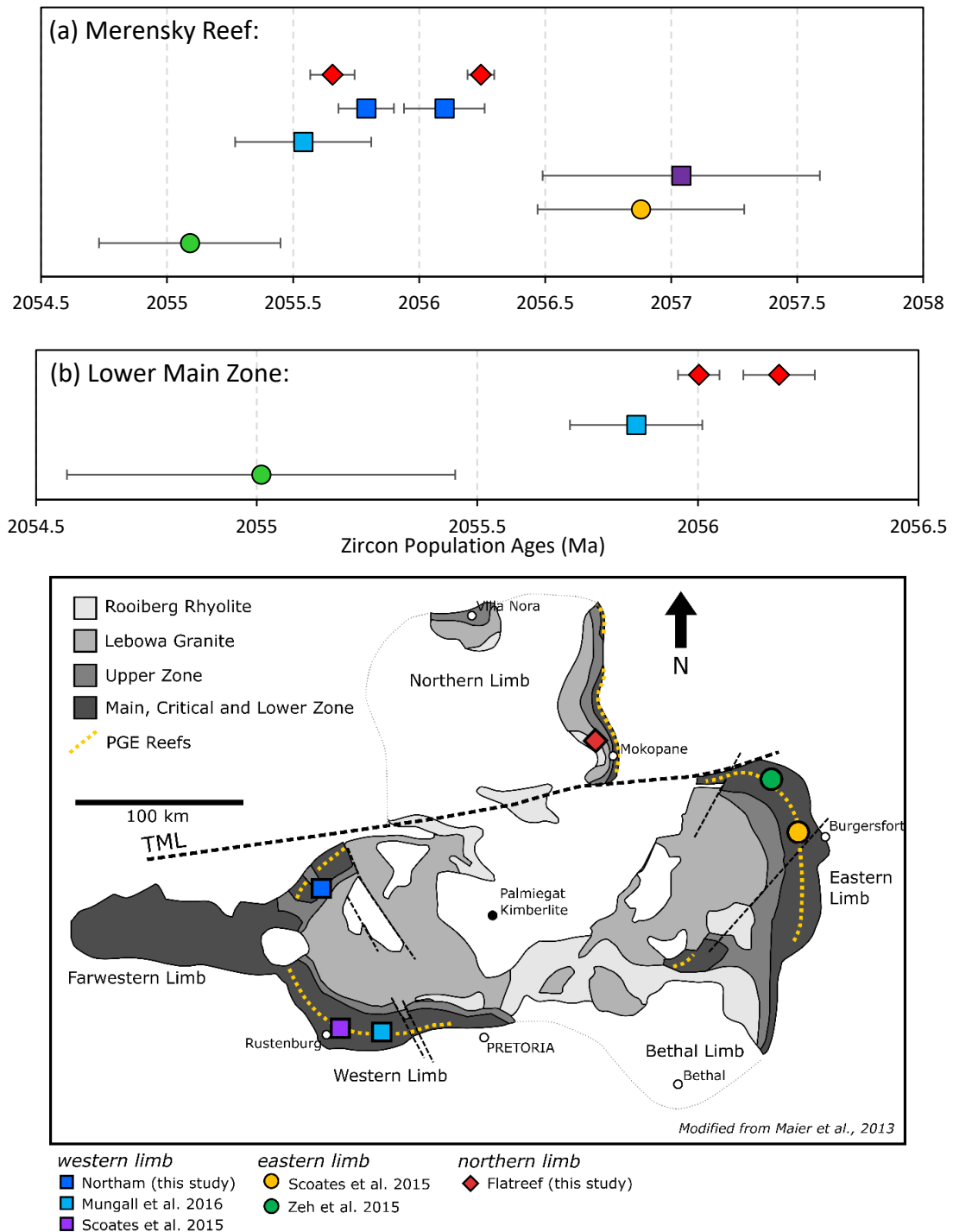
Figure 11.18: Comparative geochronological data from across the Bushveld Complex. (a) Graph comparing age-ranges of Merensky Reef and Main PGE Reef samples from across the Bushveld. Note that our data show some overlap with data from (Mungall et al., 2016; Scoates and Wall, 2015; Zeh et al., 2015). (b) Graph comparing age ranges of lower Main Zone from across the Bushveld Complex. Note MZ data from this study overlap with those of Mungall et al. (2016) but both are significantly older than the age determined by Zeh et al. (2015) from the eastern Bushveld Complex. (c) Map of sample locations.

11.1.3.7 Summary

The various lines of evidence summarised above suggest that the Upper Flatreef can be broadly correlated to the UCZ of the main Bushveld Complex, notwithstanding the considerable variability in the detailed stratigraphy of the western Bushveld UCZ and the Flatreef. This interpretation is supported by broadly overlapping whole rock compositions and PCA analysis of Flatreef and WBC rocks as well as U-Pb zircon ages of the Merensky Reef in the UCZ and the Main PGE Reef in the Flatreef. Localised contamination and variation in sampling manifest themselves in wider variability of isotopic signatures and mineral compositions in the Flatreef rocks compared to western Bushveld UCZ rocks. However, the Flatreef has a vastly larger chalcophile element budget than the western Bushveld UCZ and models for this enrichment will be discussed later.

11.1.4 Proposed stratigraphic terminology for the Flatreef

One of the main aims of this study was to comprehensively characterise the Flatreef using representative drill cores. The 2 drill cores selected (UMT081 and UMT094) are from the deepest bore holes on the property and intersect many key lithologies present in the Flatreef. In the preceding chapters the stratigraphic relationships between units in these drill cores were documented while largely avoiding genetic or correlative terms. These results are now considered with regard to the models proposed by Yudovskaya et al. (2017b) and Grobler et al. (2018).

The terminology for the stratigraphy of the Upper Flatreef and the resulting lithostratigraphic models has evolved over the last decade, undergoing several updates (i.e. Ivanplats, 2012 to Grobler et al. 2018) largely in response to more extensive drilling, modelling and academic research. In 2012 the Flatreef stratigraphy proposed by Ivanplats comprised 2 layers of norite cycles (NC1 and NC2) either side of the purported Bastard Reef (BAR) and the so-called Turfspruit Cyclic Units (T1, $T1_U$ and $T1_L$) (Figure 11.19). By 2017 more extensive drilling supported an updated stratigraphy wherein the NC1 was relabelled the Hangingwall Unit and GMA, the Bastard Reef was called Upper Reef, the upper sections of the T1 became the Middling Unit (MDU) and the lower Turfspruit Cyclic Units were regrouped into the Main Reef (Yudovskaya et al., 2017b). In 2018, Grobler et al. proposed that the Main Reef can be correlated to the Merensky Reef, which was further subdivided into the M2, $M1_U$ comprising orthopyroxenites, the latter of which is pegmatoidal, and $M1_L$ comprising pegmatoidal harzburgite (Grobler et al., 2018). Below the MCU, the NC2 and its footwall rocks were combined to create the Footwall Cyclic Unit (FCU), while classification of the UG2 cyclic unit remained unchanged.

Whereas the work by Grobler et al. (2018) was based largely on lithostratigraphic relationships with minor supporting whole rock geochemical data, the present study considers mineral

compositions and multiple isotopic systems in addition to more detailed lithophile and chalcophile element data and stratigraphic relationships. Comparisons of these datasets with those of the Platreef and UCZ support the model of Grobler et al. (2018) whereby the Upper Flatreef is a correlative of the UCZ of the WBC, while the Platreef represents strongly contaminated UCZ. Consequently, a new unified stratigraphic model is proposed below for the Flatreef, based on the accepted nomenclature of the UCZ (Figure 11.19).

The Upper Flatreef is separated into 5 units, namely the UMA, Upper Pyroxenite, Central Norite, Lower Pyroxenite and Lower Ultramafic Unit. Within the Upper Flatreef, the 3 mineralized reefs, previously termed the Upper PGE Reef, Main PGE Reef and Main Chromitite are now termed the Bastard, Merensky and UG2 reefs, respectively.

The mottled anorthosite (UMA) at the top of the Upper Flatreef is found across the Flatreef, the UCZ of the WBC and, sporadically, across the Platreef and has been named as the GMA in the northern limb by several previous studies (Grobler et al., 2018). Below this is the Bastard Cyclic Unit (BCU) hosting the Bastard Reef towards the base of the unit, and also typically containing interlayered norite and anorthosite, although the uppermost feldspathic portions of the BCU is not developed in all drill cores intersecting the Flatreef (e.g. in UMT081). While truncations and partial developments of cyclic units are common in the UCZ as well (Eales et al., 1988) this has not been described for the Bastard Unit (De Klerk, 1992).

Below the BCU is the Merensky Cyclic Unit (MCU). In drill cores UMT081 and UMT094 the unit lacks feldspathic upper portions but Grobler et al. (2018) showed that feldspathic rocks are present below the BCU in many other drill cores on the property. The Merensky Reef is much thicker in the Flatreef than the UCZ Merensky Reef, but Yudovskaya et al. (2017b) suggest similar formation processes for both occurrences of Merensky Reef. Underneath the MCU is the feldspathic Merensky Footwall Unit, previously termed either Norite Cycles 2 (Ivanhoe Mines Ltd, unpublished) or Footwall Cyclic Unit (Grobler et al., 2018) and Central Norite (this study). The Lower Pyroxenite is proposed to be renamed the UG2 unit, culminating in a thick chromitite at the base of the unit that is correlated to the UG2 chromitite by Ivanplats (2012) and Grobler et al. (2018). However, these earlier authors considered that the UG2 unit (UG2 CU) only spans the immediate hangingwall and footwall rocks of the UG2 chromitite. The new proposed stratigraphy assigns all orthopyroxenites between the UG2 chromitite and the feldspathic Merensky Footwall Unit (i.e. the entire Lower Pyroxenite) to the UG2 unit, in keeping with the stratigraphy of the WBC (e.g. Eales et al., 1998).

The correlation of the Lower Ultramafic Unit and the Lower Flatreef rocks remains somewhat less evident. The lithostratigraphy of the Lower Ultramafic Unit suggests it can be correlated to the Critical Zone, but whether it represents the UCZ or LCZ is unclear. The package is thus given the generic term "UG2 Footwall Unit". In the Lower Flatreef, in proximity to the footwall

calcareous sediments, contamination signatures in the magmatic rocks become more pronounced, commonly resulting in disturbed magmatic layering reminiscent of the Platreef. This has rendered correlation of these rocks with those of the WBC difficult.
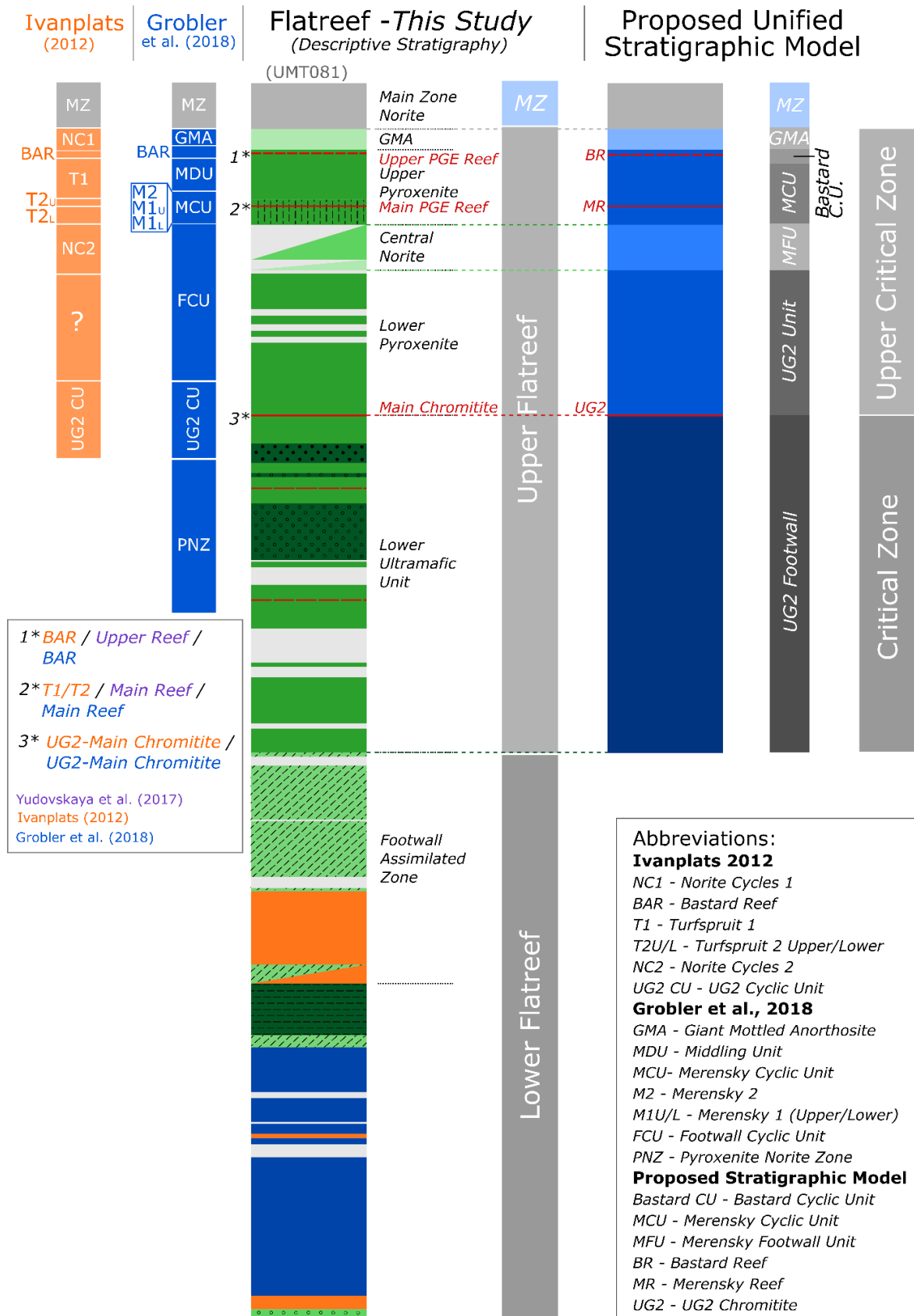
Figure 11.19: Proposed unified stratigraphic model correlating the Flatreef with the UCZ of the WBC, compared to earlier stratigraphic models of Grobler et al., (2018); Ivanhoe Mines Ltd., (unpublished) and Yudovskaya et al., (2017b).

11.2 Magma Composition and Contamination

11.2.1 Parental Magmas

The magmatic lineage of the Bushveld Complex can be traced to 3 main types of parent magma, named Bushveld magmas 1-3 (B1, B2 and B3) exposed in the form of fine grained marginal rocks that were intruded into the sedimentary country rocks that host the complex (Barnes et al., 2010; Sharpe, 1981). B1 is a Mg-rich basaltic andesite (avg. 12% MgO) (Barnes et al., 2010) and locally komatiite (18% MgO) (Maier et al., 2016a) that is believed to be parental to the Lower and Lower Critical Zones of the complex. B2 and B3 are tholeiitic basalts (avg. 8 and 9% MgO, respectively) (Sharpe, 1981), purported to be parental to the Upper Critical Zone and Main Zone, respectively. However, models of B2 magma indicate a crystallisation sequence at odds with the rocks observed in the UCZ, and it has thus been proposed that the UCZ formed from a mix of B2 and B1 magmas (Barnes et al., 2010; Maier et al., 2013).

All 3 magma types show evidence of crustal contamination expressed by the negative εNd and elevated $\delta^{18}O$ values (Harris et al., 2005; Maier et al., 2000; Schiffries and Rye, 1989). Comparisons between the Flatreef and WBC presented in the previous section suggest that the Flatreef can be correlated to the UCZ, based largely on stratigraphic and whole rock compositional grounds. Therefore, it is likely that the Flatreef crystallised from a mix of B1 and B2 magmas. However, the relatively enhanced levels of crustal contamination in the Flatreef make it difficult to establish the precise nature of its parental magmas.

Ratio plots of Ce vs Sm have been used previously to unravel the contribution of various magma types in cumulates, with B2/3 magmas being rich in Sm relative to Ce than B1 magma (Maier et al., 2008). Figure 11.20 shows that Flatreef rocks tend to be more Sm rich than UCZ rocks. This could suggest a smaller B1 contribution in the Flatreef compared to the UCZ. However, Ce/Sm ratios could also be affected by contamination from sedimentary rocks. It is worth noting however, that both Merensky Reef samples from the Flatreef plot within the field of Merensky Reef ratios from the WBC.
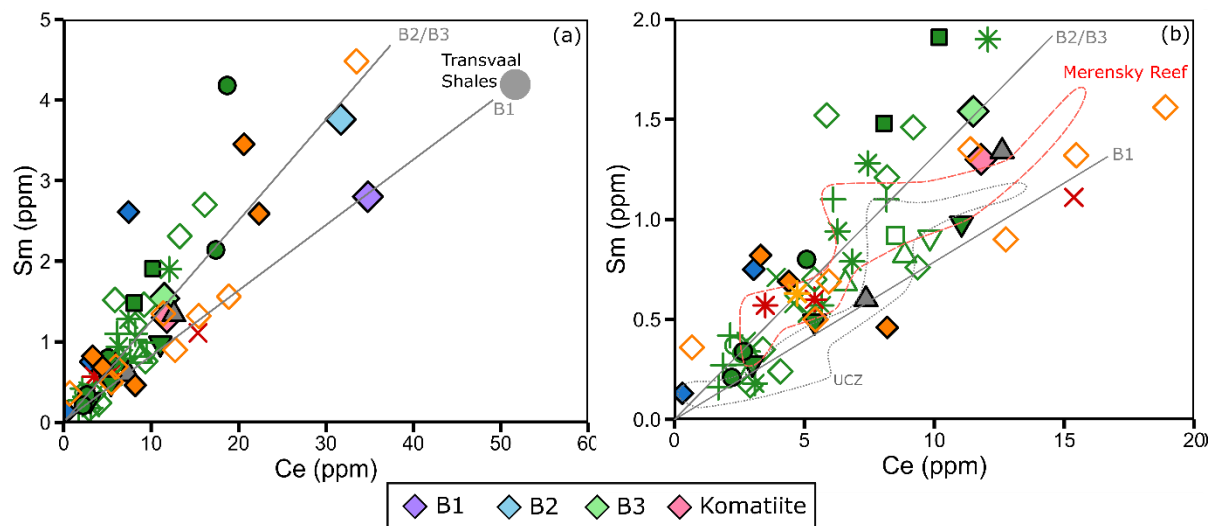
Figure 11.20: Bivariate plots of Sm vs Ce (ppm) separating different Bushveld Parental Magmas. (a) Plot of Sm/Ce for all rocks analysed in this present study. (b) Zoom in section of (a). Additional data from Barnes and Maier, (2002b); Barnes et al., (2010); Klein and Beukes, (1989); Maier et al., (2000); Maier and Barnes, (1998); Maier et al., (2016a). Modified after Maier et al. (2000).

11.2.2 Quantifying contamination of the Flatreef magma

Previous isotopic studies of the Bushveld Complex have suggested significant (10-40%) contamination of magma with crustal material (Davies et al., 1980; Harris et al., 2005; Maier et al., 2000; Schiffries and Rye, 1989). The lack of systematic changes in these isotopes with height in some intervals, similar isotopic signatures of certain marker layers across the entire complex, and crustal signatures in the fine grained sills believed to represent the parent magmas led to the suggestion that contamination occurred prior to intrusion, possibly in a well-mixed staging chamber (Curl, 2001; Harris et al., 2005; Maier et al., 2000; Schiffries and Rye, 1989). In addition, the northern limb shows evidence of significant in-situ contamination such as country rock xenoliths and parapyroxenites. Magmas in the northern limb were therefore likely contaminated both before and during emplacement. Across the northern limb granite, dolomite and shale are identified in previous studies as the main magma contaminants (Barton et al., 1986; Harris et al., 2005; Pronost et al., 2008; Reisberg et al., 2011). Below, I will attempt to unravel the relative importance and order of these events.

11.2.3 Field Evidence for Contamination

In the northern limb there is abundant evidence of in-situ contamination of intruding magmas by country rocks including the presence of numerous xenoliths of calc-silicate, hornfels and quartzite in the Flatreef, Platreef and Main Zone (Grobler et al., 2018; Kinnaird, 2005; Kinnaird et al., 2005; Manyeruke et al., 2005). Contamination by a range of different country rocks is expressed by the presence of exotic lithologies including websterite, wehrlite and parapyroxenite, and locally relatively high quartz contents (Cawthorn et al., 1985; McDonald et al., 2005; Yudovskaya et al., 2017b). Contamination may also have added significant S to

the magma (Holwell and McDonald, 2006; Sharman et al., 2013). In addition, abundant granitic veins cross-cut the Flatreef and Platreef (Kinnaird, 2005; Maier et al., 2008; McDonald and Holwell, 2011; Pronost et al., 2008).

11.2.4 Isotopic evidence for contamination

As evident from Figures 11.10 and 11.18, all isotope systems analysed in the present study show evidence for country rock contamination of Flatreef magmas. Several previous studies have utilised oxygen isotopes to understand dolomite contamination in the northern limb (Harris and Chaumba, 2001; Pronost et al., 2008). For example, on the farm Sandsloot dolomite contamination is interpreted to have resulted in variable, but generally relatively heavy $\delta^{18}O$ values (Harris and Chaumba, 2001). Rocks that are interpreted to have experienced significant interaction with post-magmatic fluids are characterised by relatively lighter $\delta^{18}O_{px}$ values (min 3.6 $\delta^{18}O_{px}$) and concurrently heavier $\delta^{18}O_{plag}$ (Pronost et al., 2008). The elevated $\delta^{18}O$ isotope values in the Flatreef samples also suggest contamination from isotopically heavy dolomitic floor rocks (max +22.4 $\delta^{18}O_{wr}$, sample MAL1), while the lack of isotopically lighter rocks in the Flatreef could suggest there was little alteration of $\delta^{18}O$ isotopes from post-magmatic fluids. Nd isotopes of the Flatreef are also strongly perturbed compared to the WBC (Maier et al., 2000). In contrast, Sr isotopes of the Flatreef have a less pronounced contamination signature, broadly overlapping with the UCZ. However, on the farm Overysel approximately 20 km north of Turfspruit, elevated Sr isotope values (max. 0.753578 $^{87}Sr/^{86}Sr_i$) are suggested to reflect contamination by granites (Barton et al., 1986; Cawthorn et al., 1985; Pronost et al., 2008). Mg isotopes are used in this study for the first time in the Bushveld Complex to model contamination. Mg isotopes are particularly effective at discriminating between calcareous sediments and granite contamination of magmas as they have significantly different $\delta^{26}Mg$ compositions to each-other and the magma (Table 11.4).

Of the potential contaminants identified (calcareous sediments, shale and granite), none alone fully satisfy all the observed isotopic contamination signatures in the Flatreef. For example, while calcareous sediments have elevated $\delta^{18}O$ and $^{87}Sr/^{86}Sr_i$ values and light $\delta^{26}Mg$, the Sr concentration in calcareous sediments is not sufficiently high to significantly perturb the Sr isotopic signature of the magma and εNd is not low enough to generate the observed Flatreef values. In contrast, granite broadly has a highly radiogenic Sr isotope signature and accompanying high Sr content in addition to strongly negative εNd values, but only marginally elevated $\delta^{18}O$ and heavy $\delta^{26}Mg$ (Barton et al., 1999; Pronost et al., 2008; Telus et al., 2012). Shale can have a wide range of isotopic values due to its detrital nature thus sampling a wide range of lithologies, but is broadly characterised by high $\delta^{18}O$, low $^{87}Sr/^{86}Sr_i$, low εNd, and heavy $\delta^{26}Mg$ (Beukes et al., 1990; Hunter and Hamilton, 1978; Jahn and Condie, 1995; Li et al., 2010). Below, I attempt to place some further constraints on the nature of the contaminants to the Flatreef.

11.2.5 Modelling of potential contaminants in the Flatreef

In order to model contamination, it is important to characterise the country rocks proposed to act as contaminants to the Flatreef magmas. The isotopic compositions and relevant element concentrations of footwall calcareous sediments were determined during the course of the present study, while granite and shale data were sourced from the literature (Barton et al., 1999; Barton et al., 1992; Beukes et al., 1990; Henderson et al., 2000; Hunter and Hamilton, 1978; Jahn and Condie, 1995; Li et al., 2010; Pronost et al., 2008; Stephenson, 2019; Telus et al., 2012). Figure 11.21 shows the wide variability of granite compositions from plutons surrounding the Bushveld Complex including the Baviaanskloof granite (near the Matok Granite) (Barton et al., 1992), Turfloop Batholith (Henderson et al., 2000) and the Johannesburg Dome (Barton et al., 1999). Banded Gneiss from the Archean basement on the farm Overysel was also included (Pronost et al., 2008). Average compositions of these granitic bodies are used as end-member contaminants for the first stage of modelling. Corresponding Sr and Nd isotope data are available for these granites and banded gneiss, but accompanying oxygen and magnesium isotopes have not been analysed. All granites were assigned a $\delta^{18}O$ of +8.1 averaged from granites analysed by Pronost et al. (2008) (range 8.0-8.2 $\delta^{18}O$) and an end member $\delta^{26}Mg$ granite value of -0.094 ± 0.065‰ (Telus et al., 2012).

There is no comprehensive isotopic dataset for shales in the Transvaal Supergroup but an approximation was compiled from several literature sources (Table 11.4) (Beukes et al., 1990; Hunter and Hamilton, 1978; Jahn and Condie, 1995; Li et al., 2010; Stephenson, 2019). While the modelled shale composition will have significant uncertainty due to both the mix of contributing literature data and inherent variability of shale compositions, it has sufficiently different isotopic compositions compared to granitic and dolomitic contaminants to be useful

in the model. All radiogenic isotopes were recalculated to a Bushveld age of 2057.04 Ma (Scoates and Wall, 2015) to represent their composition at the time of assimilation.
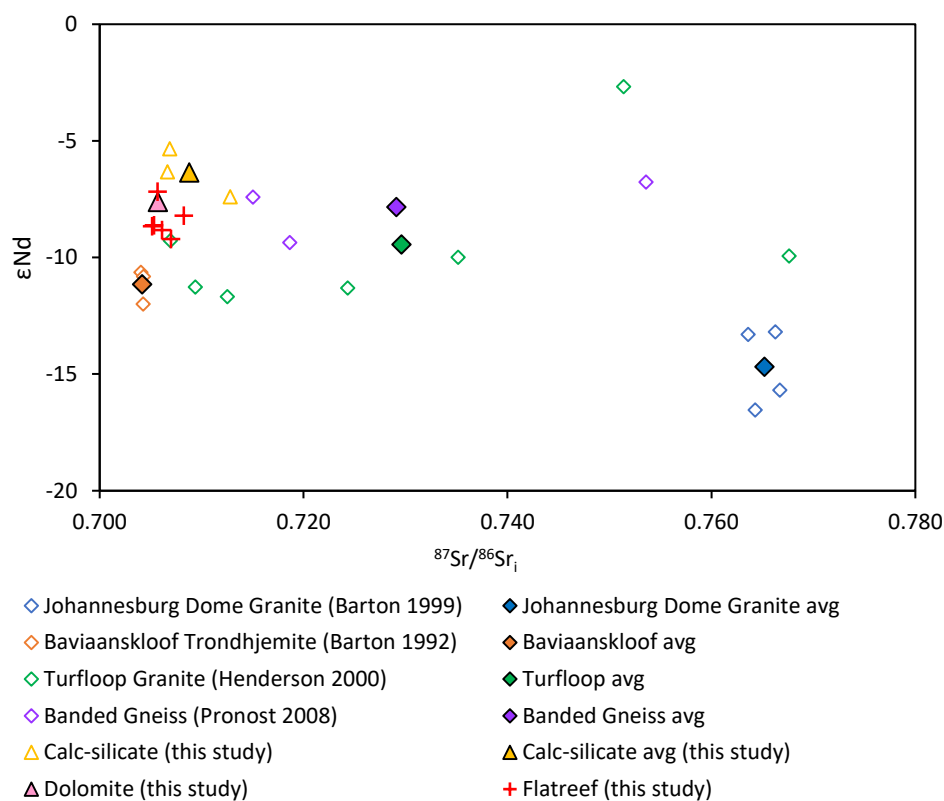
Figure 11.21: Plot of Nd and Sr isotopic data from the Flatreef and several possible contaminants including: calc-silicate and calcareous sedimentary floor rocks (this study); Banded Gneiss (Pronost et al., 2008) and Granitic bodies from the Johannesburg Dome (Barton et al., 1999), Baviaanskloof near Matok Granite (Barton et al., 1992), Turfloop Batholith (Henderson et al., 2000) and Utrecht Granite (Cawthorn et al., 1985; Pronost et al., 2008).

The style of assimilation may also vary for the different contaminants. Contamination is estimated by mixing models. Granites and banded gneisses are likely to form partial melts, with the incompatible Nd partitioning earlier into the melt than the more compatible Sr. Mg is mostly stored in biotite, which will melt early. In all melting scenarios oxygen is modelled with a partition coefficient of 1. Testing the relative importance of differing degrees of partial melting showed little sensitivity to reasonable ranges of melting (Figure 11.22). Therefore, a partial melt of 1% was used for modelling granite contamination. In contrast, shale and calcareous sediments are assumed to have been assimilated via batch melting or dissolution. While it is likely that calcareous sediments release a CO_2 rich fluid during interaction with the magma, additional isotopic systems required to constrain fluid activity, such as hydrogen and carbon, were not analysed in this study. However, the present approach will capture most of the contamination by direct assimilation observed in the Flatreef.

Rock Type	εNd	δ^{18}O	δ^{26}Mg
B1:B2 Magma	-5.76	5.1	-0.25 ±0.04
calcareous sediments (DUIT1)	-4.4	15.9	-1.1 ± 0.06
Shale	-7.01	18.86	+0.05
Granite (JD)	-14.69	8.1	-0.094 ± 0.065

Table 11.4: Isotopic data for the various country rocks that are used in the second-stage models for Flatreef magma contamination. Calcareous sediment data from this study. Additional data from Curl (2001), Teng et al. (2017), Jahn and Condie (1995), Beukes et al. (1990), Li et al. (2010), Barton et al. (1999), Pronost et al. (2008) , Telus et al. (2012).

Establishing the initial composition of Flatreef magmas prior to contamination is also required. The UCZ is purported to have crystallised from a mix of B1 and B2 magmas at a ratio of 60:40 in order to produce the observed crystallisation sequence (Barnes et al., 2010). Since the Flatreef has been correlated with the UCZ in the preceding chapter, this B1:B2 mix will be used in the current modelling. In order to assess whether the Flatreef underwent additional contamination relative to the WBC, the isotopic signatures of B1 and B2 magmas were also used in the modelling, which reflect the contamination purported to occur in a staging chamber prior to emplacement (Curl, 2001). Mg isotopic data from the WBC relies on just 2 samples (this study) showing a relatively wide range of δ^{26}Mg (-0.16 ‰ Merensky reef, -0.28 ‰ δ^{26}Mg UCZ pyroxenite). This suggests neither is reliable to represent the composition of initial magmas, therefore the mantle value of -0.25 ‰ δ^{26}Mg was used (Teng, 2017).
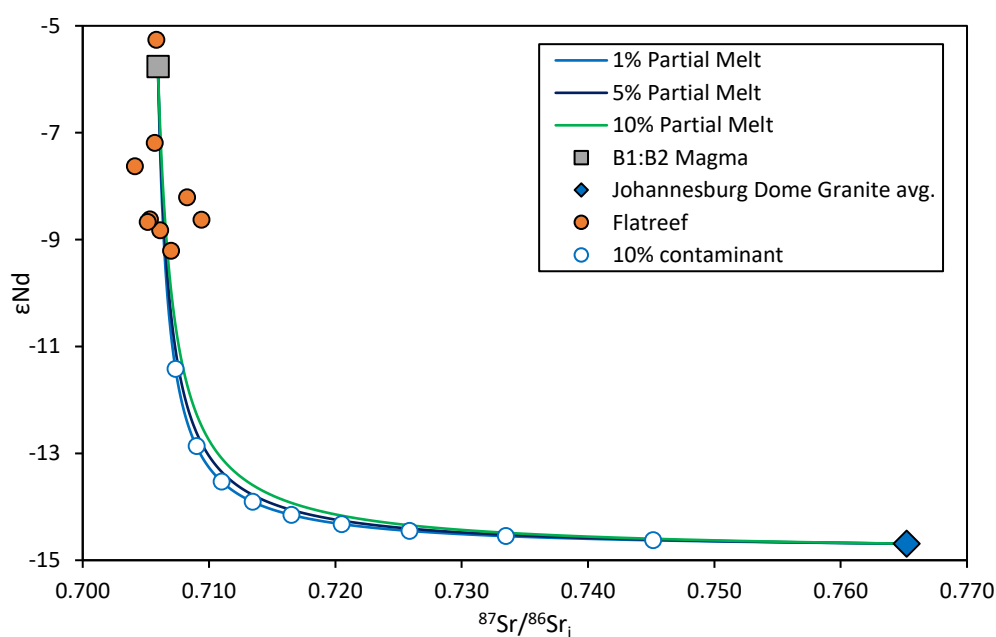
Figure 11.22: Initial models determining sensitivity to degrees of partial melting of granite. Dots mark 10% increments of contamination by a 1% granitic partial melt.

Using the starting compositions outlined above, the first set of models were generated. In these models contaminated magmas assimilate melts from a mix of granitic, shale and additional calcareous sediments. These 3 main contaminant sources have unique O-Nd-Mg isotope compositions and are used for modelling contamination of the Flatreef (Figure 11.23 d,e,f). In contrast, the Sr isotopic system shows little variability in the Flatreef samples relative to O-Nd-Mg isotopes. Additionally, the calcareous sediments and shale $^{87}Sr/^{86}Sr_i$ compositions overlap. Sr isotopes are therefore of little use for modelling potential contaminants (Figure 11.23 a,b,c,). The paucity of suitable Pb isotope data from both contaminants and parental magmas prevent Pb isotopes from being used in these models. The Ti-rich olivine gabbro plots anomalously to the remainder of the Flatreef samples (Figure 11.23).

The first-stage models show that samples from the Flatreef form a positive trend in $\delta^{18}O$ vs $\delta^{26}Mg$ space (Figure 11.24), that bisects the curved mixing line between calcareous sediments (samples DUIT1 and MAL1) and the Flatreef parent magma. The Flatreef intruded into Duitschland Formation rocks and consequently Duitschland calcareous sediments are the more likely contaminant instead of Malmani dolomite. A trend line (derived using *Isoplot®*) for the Flatreef samples intersects the calcareous sediments (DUIT1) mixing curve at 18% dolomite assimilation, implying all Flatreef magmas initially saw roughly 18% contamination by dolomite. The slope of the regression line is used to assess the degree of dolomite contamination for each Flatreef sample (Figure 11.24). This trend of Flatreef samples intersecting the calcareous sediments contamination curve suggests these sediments are the first country rock to be assimilated by the intruding magmas.
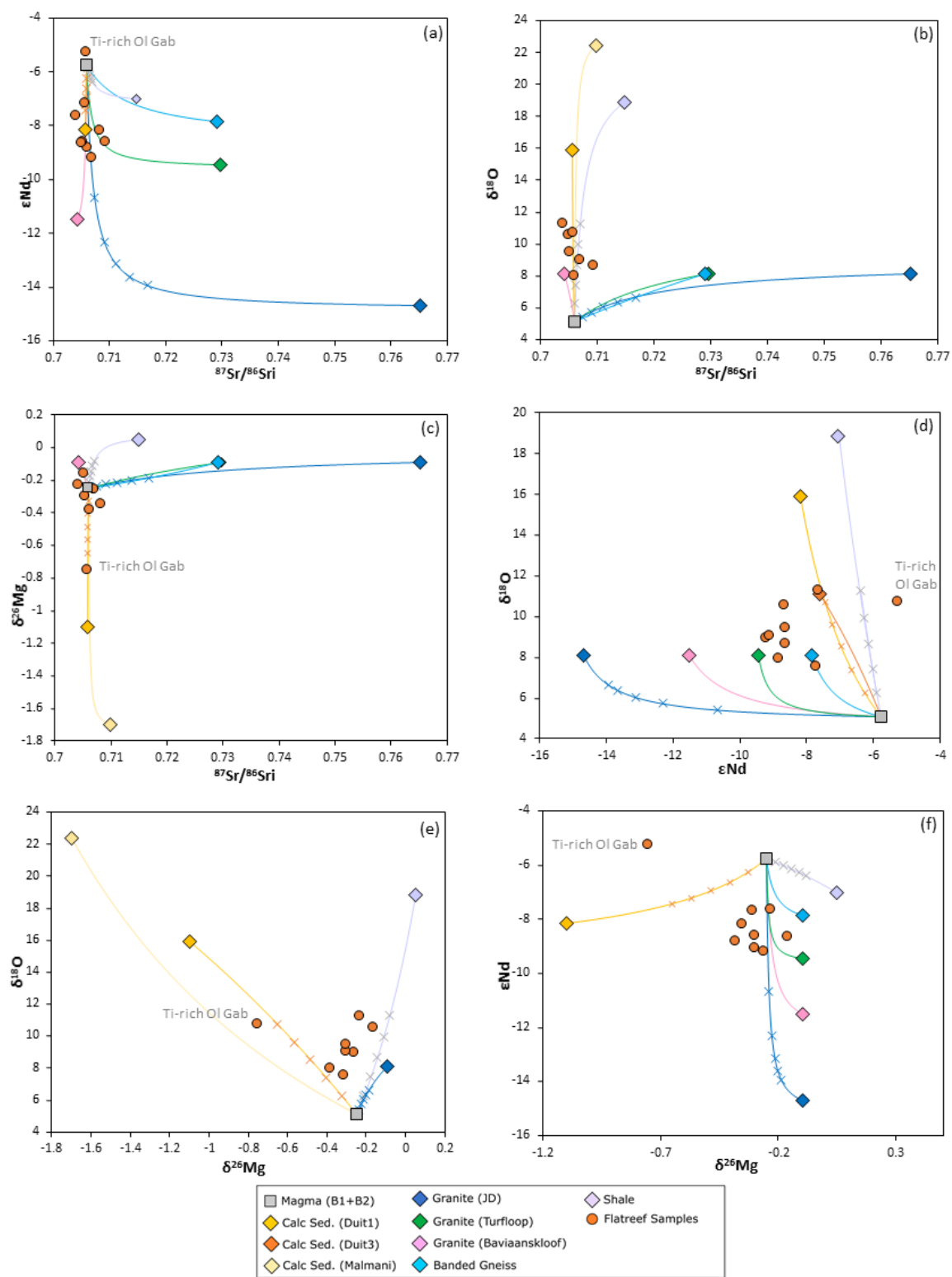
Figure 11.23: Modelling outputs of calcareous sediments, granite and shale contamination of a B1:B2 magma. Note the lower range of variability in Sr isotopes relative to O, Nd and Mg isotopes in Flatreef rocks. Crosses mark 10% mixing.
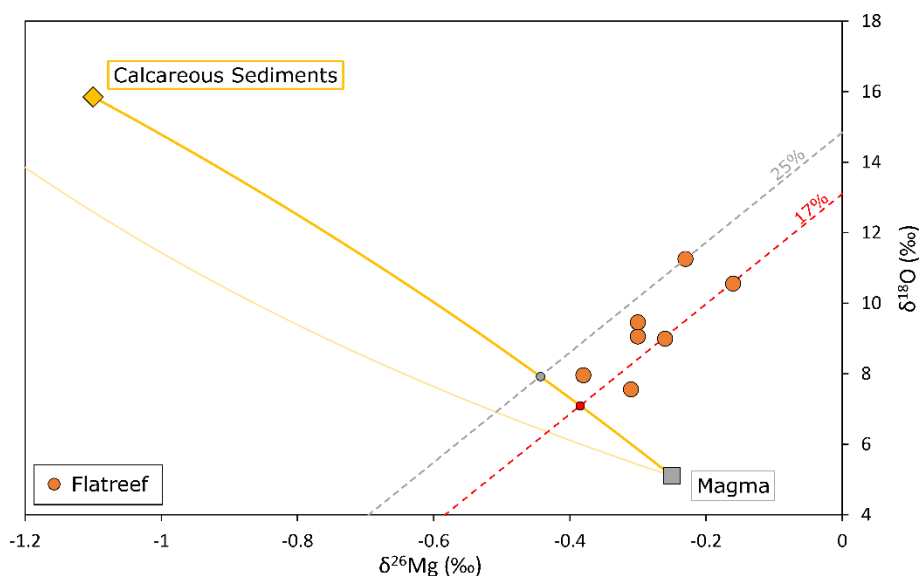
Figure 11.24: Mg-O isotope plot generated from the first-stage of modelling. Flatreef rocks plot along a trend perpendicular to the main mixing line from Flatreef magma to calcareous sediments (Duit1). The intersection of the regression and mixing lines is used to calculate the calcareous sediment contamination (%) of that sample.

It is unlikely that contamination by calcareous sediments occurred in a magma staging chamber as there is only approximately 2 km of dolomite (Malmani Subgroup) (Eriksson et al., 1993) underlying the Flatreef below which lies Archean basement. This Malmani dolomite is therefore unlikely to provide ample space to host a staging chamber. It is instead more likely that contamination of the magmas by calcareous sediments occurred during emplacement of the Flatreef into the Duitschland Formation. This is supported by the abundance of calc-silicate xenoliths that occur at broadly similar stratigraphic heights across the Flatreef, mainly within the FAZ. The calculated contamination by calcareous sediments for each Flatreef sample is used in the second-stage of contamination modelling to represent the starting composition of calcareous sediment-contaminated magma that were consequently additionally contaminated by shale and granite.

While the likely calcareous sediments and shale end-members have been identified, the first-stage models also include 3 granite and 1 banded gneiss contaminant. The absence of quartz throughout the Flatreef, except in feldspathic rocks, in drill cores UMT081 and UMT094 suggests that only small volumes of granitic material interacted with the magmas, in contrast to the Platreef on the farm Overysel, where quartz abundance increased with proximity to the granite floor rocks (Cawthorn et al., 1985). Therefore, Johannesburg Dome (JD) granite was selected as the granite contaminant for the next stage of modelling as this contains the most negative εNd values and thus can alter the Nd isotopic signature of the Flatreef magmas even if only small amounts of granitic melt were assimilated.

The second-stage contamination models are shown in Figure 11.26 and Figure 11.26. In these second stage models a fixed amount of contamination by calcareous sediments is included in the starting composition of the magmas, predetermined for each sample. From this contaminated starting point mixing models for contamination by granite and shale are calculated.

Figure 11.25 shows one-such model where the Flatreef magma has been contaminated by 17% calcareous sediments (as calculated from the first-stage model for samples 81-1610 and 81-1305). These pseudo-ternary diagrams can be read like traditional ternary plots where the relative % of granite and shale contamination as well as the % contribution of magma to the final isotope values of the sample can be determined. For each sample which has a different % calcareous sediments contamination, new pseudo-ternary diagrams are plotted (e.g. Figure 11.26). Consequently, the relative % of shale contamination, granite contamination and the percentage of calcareous sediments contaminated magma can be calculated for every sample for which there is O, Mg and Nd isotope data available.
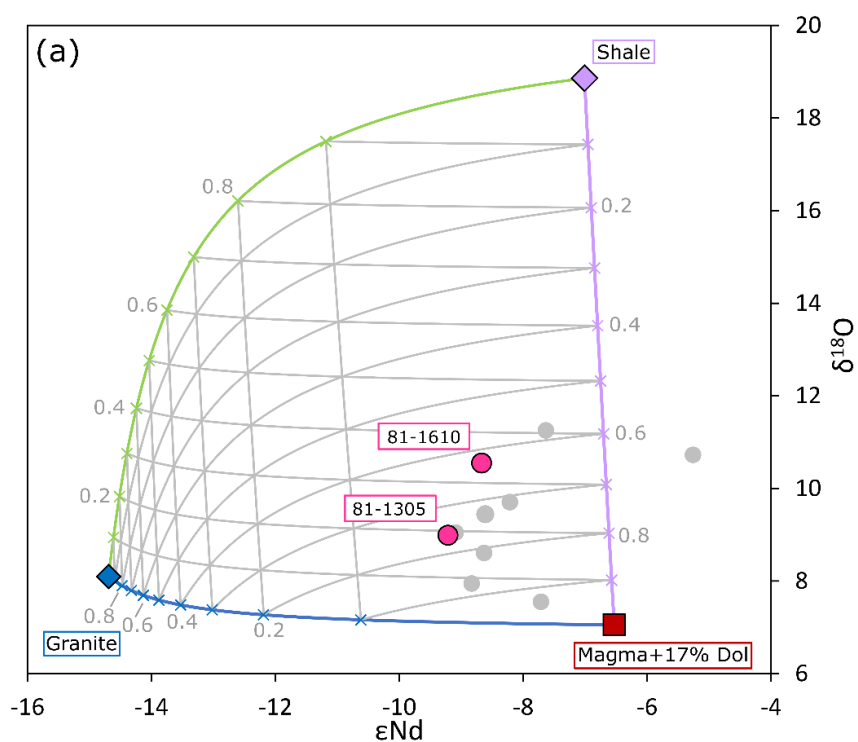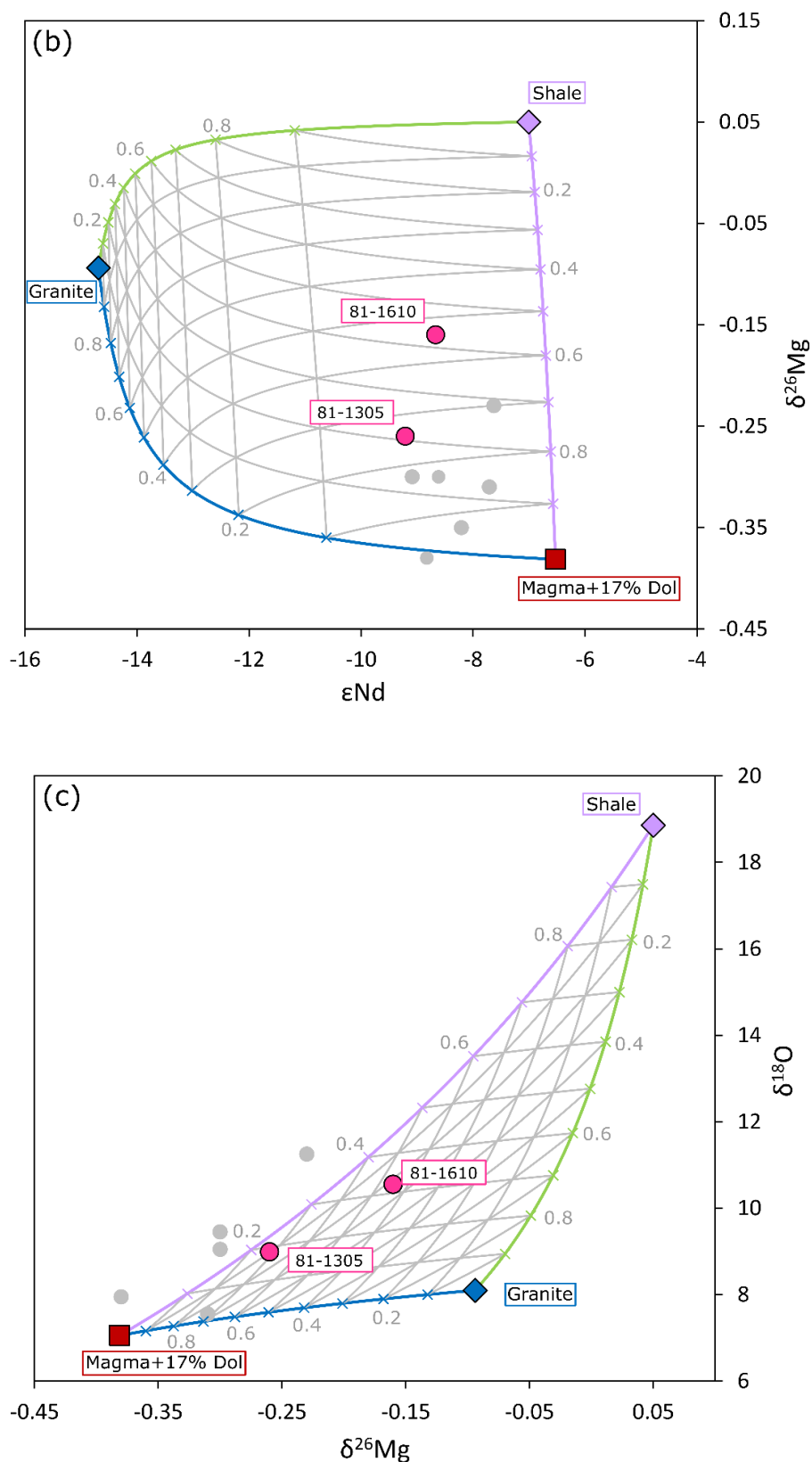
Figure 11.25: Second-stage models are plotted where pseudo-ternary diagrams represent the relative contribution of granite, shale and pre-contaminated magma to the isotopic signature of samples where magmas contain 17% calcareous sediments. (a) εNd vs δ¹⁸O, (b) εNd vs δ²⁶Mg, (c) δ¹⁸O vs δ²⁶Mg. Grey lines indicate 10% mixing lines.
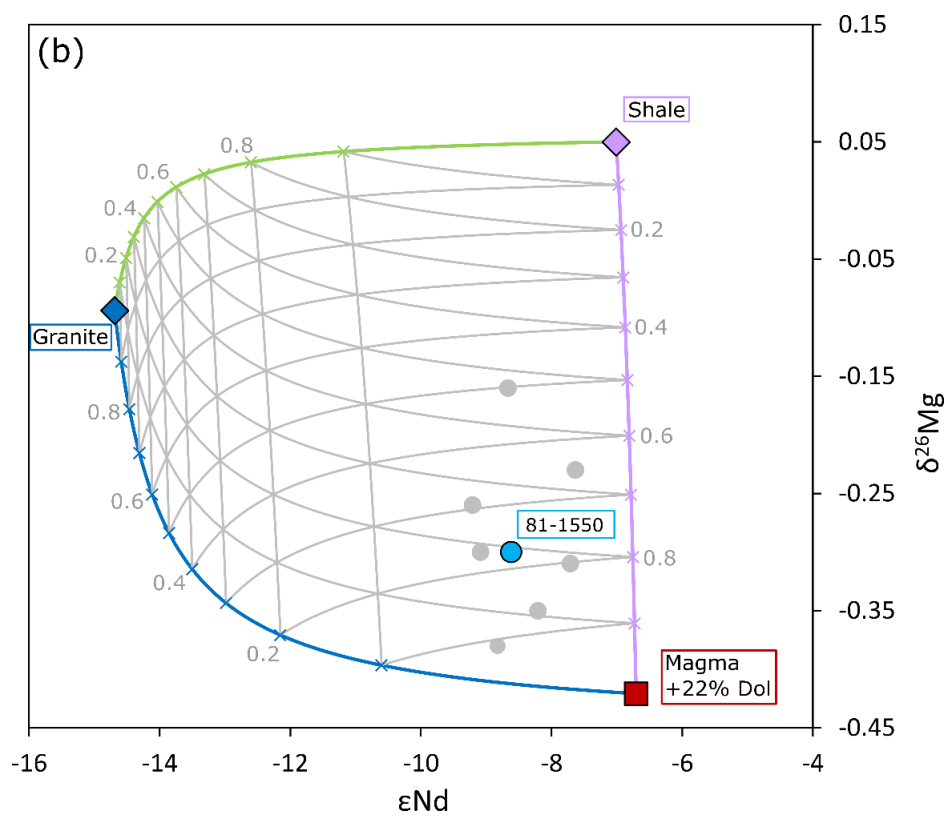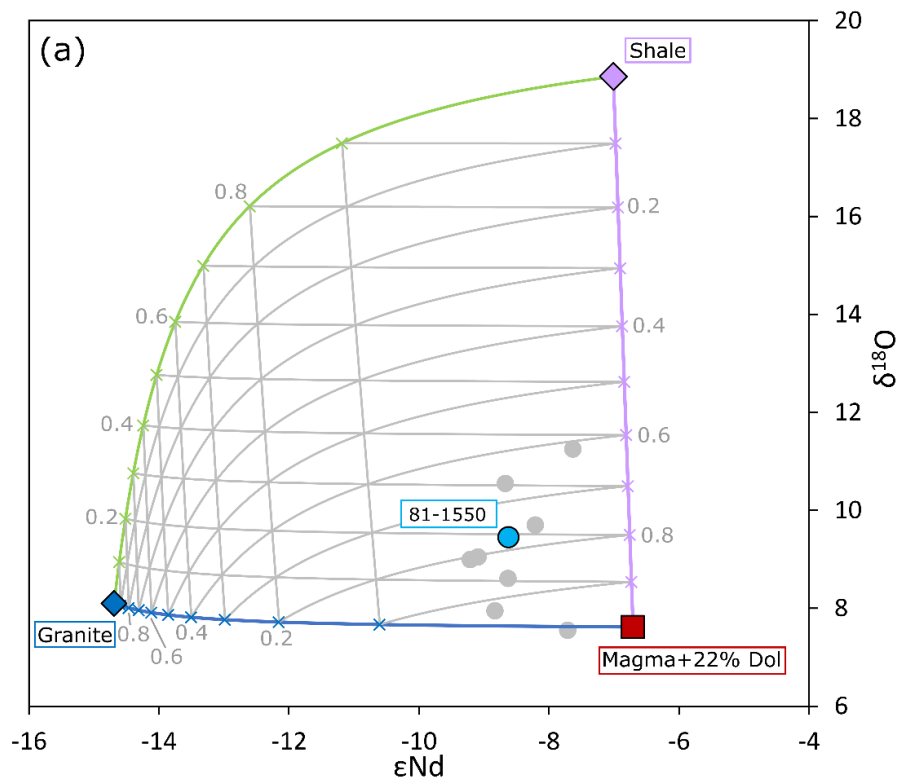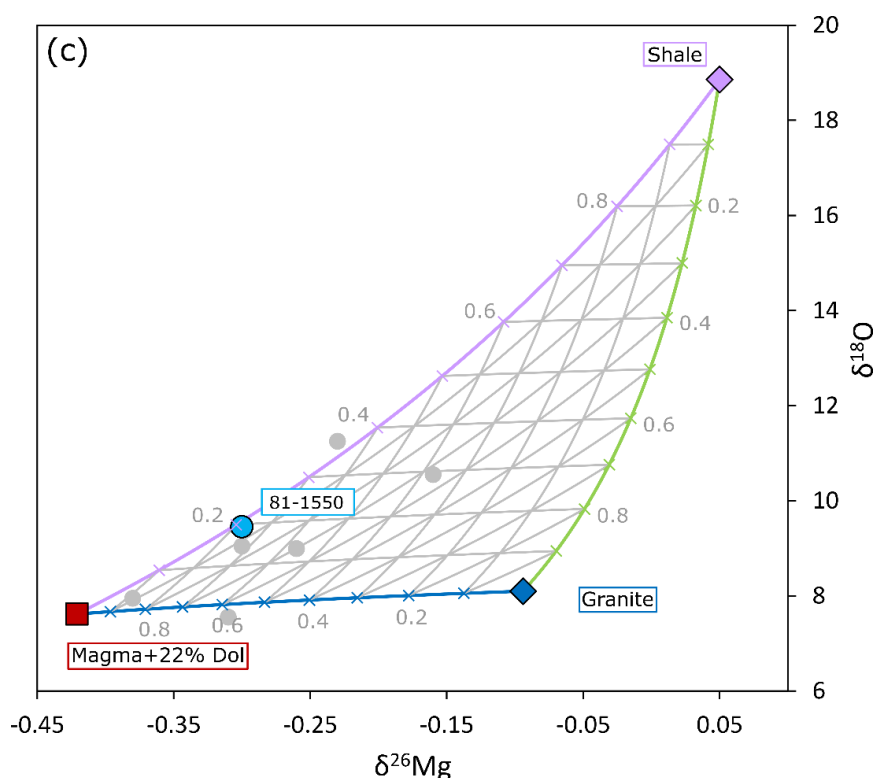
Figure 11.26: Second-stage models used to determine the amount of granite and shale contamination where Flatreef magmas experienced 22% contamination by calcareous sediments. (a) εNd vs δ¹⁸O, (b) εNd vs δ²⁶Mg, (c) δ¹⁸O vs δ²⁶Mg. Grey lines show 10% mixing.

The contribution of granite and shale to the isotopic composition of Flatreef samples was determined separately in O-Mg, O-Nd and Mg-Nd models. The relative contribution of granite and shale to the contamination signature of the Flatreef samples are plotted in Figure 11.27. There is good agreement between the different models for shale and magma contribution to the isotopic compositions of the Flatreef samples. However, while modelled contributions for granite agree well in Nd-Mg and Nd-O models, the values determined from Mg-O differ. This is likely because granite has similar $\delta^{18}O$ composition to the magma and similar $\delta^{26}Mg$ to shale and thus is difficult to discriminate effectively, especially where small percentages of contamination are concerned, as is the case with contamination by granite. Apart from this Mg-O granite contribution, all other data were averaged to give a mean contribution of shale, granite and magma (+ calcareous sediments) for each sample.

The calculated calcareous sediments contamination and combined granite and shale contamination is then used to calculate the total contamination experienced by magma intruding the Flatreef. Contamination by calcareous sediments is presumed to occur as the first stage of contamination of Flatreef magmas to explain the trend shown in Figure 11.24. The volatile rich nature of calcareous sediments combined with the abundant xenoliths and rafts of calcareous sediments in drill core UMT081 also attest to significant calcareous sediment assimilation. Beyond this there is no clear evidence for whether granite or shale

contamination occurred next. However, individually their relative contamination patterns downhole through the stratigraphy can be plotted and their combined contribution to the overall contamination of Flatreef magmas can be calculated. For example, sample 81-1305 contains 17% calcareous sediments contamination as determined from the first-stage models. This is then added to the magma for the second stage of modelling where magma + calcareous sediments was contaminated by 20% shale and 5% granite, leaving 74% magma + calcareous sediments, of which 17% is dolomite contamination and thus 83% magma. This therefore means that only 61% (i.e. 83% of 74) of the final rock is magmatic according to its isotopic composition, and therefore 39% represents the contaminant. Total contamination is calculated for all samples modelled here and reported in Table 11.5.

Sample	% calc. sediments	%magma+cal.sed	%shale	%granite	total contam.
1305	0.17	0.74	0.20	0.05	0.39
1327	0.14	0.89	0.08	0.02	0.23
1438	0.2	0.79	0.17	0.05	0.37
1475	0.21	0.92	0.05	0.04	0.28
1550	0.22	0.77	0.19	0.03	0.40
1610	0.17	0.54	0.36	0.03	0.55
1828	0.25	0.63	0.36	0.01	0.53

Table 11.5: Average model outputs for % attribution of each contaminant to the isotopic composition of samples in drill core UMT081. Note the % calcareous sediments is determined from the first stage models whereas the other percentages refer to second stage models. Total contamination accounts for calcareous sediments, granite and shale and corrects for the 2-stage process.

The total amount of contamination of the Flatreef rocks analysed in the present study ranges from 23% to 55%. The Lower Flatreef is significantly more contaminated (53-55%) than the Upper Flatreef (23-40%). The Upper Flatreef does not show systematic downhole trends of increasing contamination but erratic variation in contamination. However, the relative contamination by granite systematically increases upwards as the contamination by calcareous sediments decreases upwards.

There are 3 anomalous samples that do not follow this trend. Firstly sample 81-1610, an orthopyroxenite, shows significantly lower levels of calcareous sediments contamination than samples above and below, especially given its stratigraphic position within the FAZ (Figure 11.27). This orthopyroxenite shows little petrographic evidence of contamination, comprising fine grained orthopyroxene and interstitial plagioclase, clinopyroxene and locally net-textured sulphides (~5%). It is therefore proposed that this orthopyroxenite was intruded as a late stage sill into the strongly contaminated FAZ after assimilation and devolatization of calcareous sediments was largely completed.
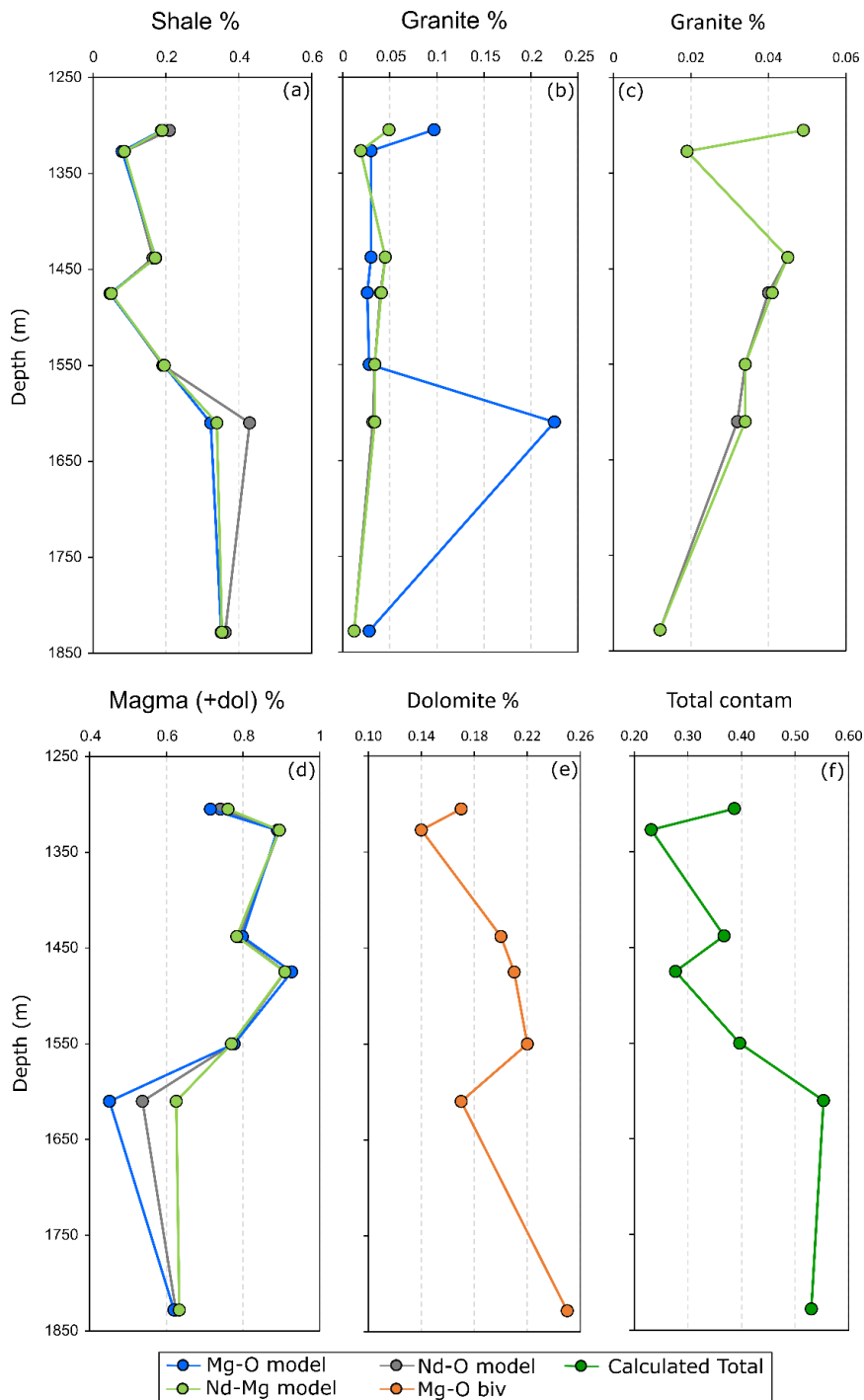
Figure 11.27: Downhole plots of contamination of rocks by granite, shale and calcareous sediments. (a) relative shale contamination, (b) relative granite contamination including anomalous results from Mg-O model. (c) granite contamination of successful models showing clear upwards increase in contamination. (d) relative proportion of calcareous sediments contaminated magmas in second-stage models. (e) relative contamination by calcareous sediments derived from first-stage Mg-O model. (f) Total contamination calculated from both model stages. The Lower Flatreef is significantly more contaminated than the Upper Flatreef.

Sample 81-1475 (lherzolite) shows a lower proportion of shale contamination relative to the overlying harzburgite and underlying orthopyroxenite (Figure 11.27). The lherzolite has

relatively lower Mg# in pyroxene than the harzburgite and lherzolite in drill core UMT094. In addition, it has higher An content in plagioclase than the harzburgite, and higher REE contents. It is therefore possible that it experienced additional contamination by a country rock not modelled here, such as BIF, to explain the lower Mg# of orthopyroxene.

The third anomalous sample is the Merensky Reef (81-1327) which shows a lower proportion of calcareous sediments and granite contamination than the surrounding rocks (Figure 11.27). Geochronological data presented earlier indicates that the Merensky Reef constitutes one of the earliest intrusives of the Upper Flatreef. This could suggest that the Merensky Reef magma was emplaced early into relatively cold country rocks, prior to significant contact metamorphism and partial melting of basement granite. In this scenario, protracted zircon crystallisation ages determined for the Merensky Reef could represent partial re-setting of zircon ages in response to thermal events from localised intrusions of Flatreef rocks. However, protracted zircon crystallisation ages could also suggest that the Merensky Reef contained a melt phase for 0.589 ± 0.103 Myrs. Yudovskaya et al. (2017b) proposed the Merensky Reef in the Flatreef formed by several injections of magma flowing through the reef, resulting in upgraded sulphides and formation of chromitites. This additional magma may have served to dilute and/or largely remove this granitic contaminant.

The downhole pattern of decreasing granitic contamination with depth is also observed in the Platreef on the farms Overysel and Sandsloot, most notably where the footwall is dolomitic (Barton et al., 1986). Barton et al. (1986) propose that granites beneath the calcareous sediments would have experienced delayed onset of partial melting in response to the progressive expansion of the thermal metamorphic aureole, with the lower Platreef largely consolidated before granitic partial melts could intrude. Therefore, granitic melts principally interacted with upper portions of the Platreef. The model also argues that increasing $^{87}Sr/^{86}Sr_i$ and Rb concentrations with height occur as a function of this ascending granitic melt, consistent with data from the present study. However, increasing $^{87}Sr/^{86}Sr_i$ with height is also a feature of the UCZ across the Bushveld Complex where it is suggested to result from progressive inmixing of radiogenic MZ magma, to be discussed later (Eales et al., 1986). Sr isotopes of the Upper Flatreef broadly overlap with the UCZ. The low concentration of Sr in calcareous sediments and granitic partial melts, the latter due to the strong affinity of Sr for plagioclase, suggests this isotopic system is not very sensitive to contamination and that the upward increase in $^{87}Sr/^{86}Sr_i$ could instead be a function of magma mixing. This may also explain the upward progression of $^{87}Sr/^{86}Sr_i$ in the Platreef on the farm Overysel. In contrast, the ϵNd, $\delta^{18}O$ and $\delta^{26}Mg$ values of the Flatreef exceed the ranges of all main rock types of the WBC and therefore cannot be generated from magma mixing. Instead, they are most readily explained as a product of crustal contamination. Another possibility is that granite contamination occurs at depth in a staging chamber, where earlier intrusions (i.e., Merensky

Reef) show little isotopic evidence for contamination and later intrusions (i.e., Bastard Reef) were more strongly contaminated in a staging chamber. More detailed geochronological studies are required to test this model.

11.2.6 Summary

In the preceding section, multiple lines of evidence have been presented indicating that the Flatreef magmas experienced significant contamination with sedimentary country rocks, both prior to and after emplacement into the northern limb. The evidence includes the highly variable lithophile composition of the rocks, the trend towards crustal isotopic signatures and the presence of abundant xenoliths and rafts of country rock material in the Flatreef. Modelling multiple isotope systems has successfully captured the complexity of a multi-contaminant system. While the entire Flatreef experienced substantial calcareous sediment assimilation (~18%) some rocks also reflect significant shale and granite contamination of the parent magma (up to 39%). The bulk of contamination by shale and calcareous sediments probably occurred in the form of a fluid in addition to direct assimilation, whereas granites likely release a partial melt which transported fluid immobile Nd into Flatreef magmas. Calcareous sediments and shale contamination are most pronounced in the Lower Flatreef whereas granite contamination increases with height through the Flatreef, likely due to delayed melting of granite in response to progression of the thermal metamorphic aureole through thick Transvaal sediments.

11.3 Magma emplacement and crystallisation of lithological units of the Flatreef

11.3.1 Constraints on the mode of magma emplacement

Models for emplacement of magmas into the Bushveld Complex proposed in the literature have been described in chapter 2 and will therefore only be briefly summarised here. Two fundamentally distinct models can be distinguished, (1) cumulate precipitation from a large, frequently replenished, magma chamber, and (2) magma emplacement in the form of multiple sills inflating an originally relatively small chamber. In the first model magmatic layering has been proposed to result from processes such as crystal settling by gravity, either directly from a convecting magma (Wager and Brown, 1967), from crystal slurries cascading along the chamber floor (Maier et al., 2013), or in-situ crystallisation at the top of the cumulate pile by supersaturation triggered by pressure fluctuations (Cawthorn, 2005). In addition, Boudreau (2008) proposed a model whereby layering formed in response to incongruent melting in the presence of fluids and precipitation of new silicate phases.

The second model discounts the need for a large convecting chamber. This model is consistent with the occurrence of numerous marginal sills into the country rocks surrounding the Bushveld Complex (Wabo, 2013), some of which measure up to 250 m thickness, and

intrude quartzites, shales and calcareous sediments (Button and Cawthorn, 2015). Wallmach et al. (1989) shows that mineral assemblages in calc-silicate xenoliths within the Marginal Zone, now overlain by >8 km of cumulates, originally equilibrated at depths of 3-5 km, consistent with inflation of a thinner original magma chamber. Kinnaird (2005) and Manyeruke et al. (2005) presented evidence for sill emplacement of the Platreef. Recent geochronological data from the WBC showing out-of-sequence units also supports a model of sill emplacement (Mungall et al., 2016).

In the present study of the Flatreef, there is abundant evidence to support the sill model. (1) The Ti-rich olivine gabbro forms a distinct igneous unit at the base of drill core UMT081 bound by dolomitic country rocks. (2) The occurrence of fine-grained orthopyroxenite layers within coarse-grained FAZ rocks. (3) The occurrence of LZ within the country rock footwall of the Flatreef (Yudovskaya et al., 2013). (4) Geochronological data indicating that the ages of some Flatreef units are out of sequence. For example, the analysed zircons in the Main Zone are older than those of the underlying Bastard Reef pyroxenite. The Merensky Reef in the Flatreef has the oldest dates of zircon crystallisation in the analysed samples and is significantly older than the underlying UG2 chromitite. The remarkable reproducibility of this older zircon population in the Merensky Reef suggests it is unlikely these zircons represent an older entrained fraction from underlying rocks. They are instead interpreted to represent the onset of initial crystallisation in the Merensky Reef. The second, younger zircon population of the Flatreef Merensky Reef (2055.656 ± 0.088 Ma) is interpreted to represent either protracted crystallisation pertaining to a prolonged melt phase, continued magmatism or partial re-setting of zircon ages in response to localised thermal events (assuming no $^{238}U/^{235}U$ variability). Yudovskaya et al. (2017b) suggest that continual flow of magma through the Merensky Reef could form the observed chromitite layering, which could explain the protracted zircon ages.

These data directly contradict the paradigm of sequential layering in the Bushveld Complex. However, it is important to remember that $^{238}U/^{235}U$ variability is assumed to be homogenous between units but could generate deviation on the order of 100s of kyrs to 2 Myrs over the globally observed range in zircon (Hiess et al., 2012). Latypov et al. (2017b) have argued against overinterpretation of geochronological data by showing that end-member zircons from other U-Pb zircon datasets overlap within uncertainty (Mungall et al., 2016). However, data from this study clearly indicate that zircon age populations from different units are resolvable with no overlap between single grain analyses (Figure 10.15). Therefore, a robust interpretation is that the Bastard Reef of the Flatreef is demonstrably younger than the overlying Main Zone, and the UG2 is younger than the overlying Merensky Reef.

A model of relatively early intrusion of MZ magma, prior to formation of the Bastard unit, was previously proposed by Eales et al. (1986). This model is potentially in agreement with zircon dates presented here. Mixing of Merensky and Bastard magmas with Main Zone magma was

cited as a potential mechanism for increasing $^{87}Sr/^{86}Sr_i$ upwards through this portion of the complex (Eales et al., 1986). Sr isotope data through the Upper Flatreef in drill core UMT094 shows a progressive increase in $^{87}Sr/^{86}Sr_i$ with height (Mayer et al., 2018). Therefore, the model suggested by Eales et al. (1986) can be broadly applied to the Flatreef.
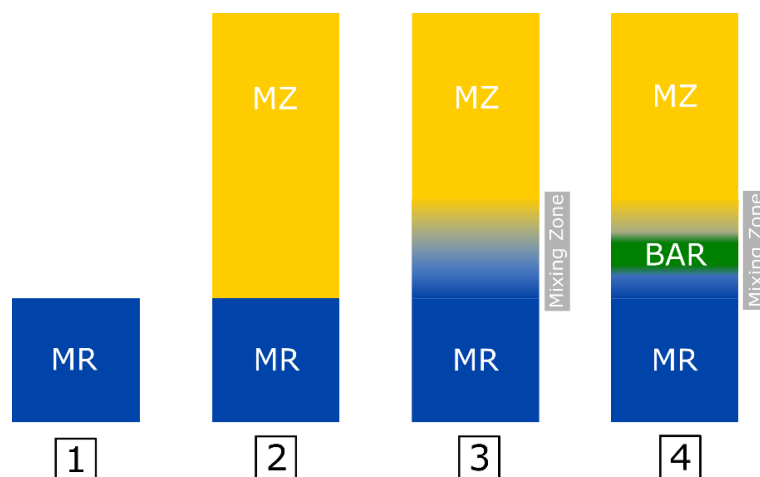
Figure 11.28: Model of formation of the Merensky Reef-Lower Main Zone intersection after (Eales et al., 1986). (1) Merensky Reef Cyclic Unit emplaced into the Flatreef. (2) Main Zone emplaced above Merensky Reef Cyclic Unit. (3) MZ and Merensky Magmas mix. (4) Intrusion of Bastard Reef Cyclic Unit magmas into the mixing zone.

Field evidence for cross-cutting relationships between the Bastard Reef in the Flatreef and the overlying Main Zone on the farm Turfspruit is unobtainable until completion of underground mine workings at Ivanplats. However, on the farm Akanani, Mitchell and Scoon (2012) document the Deep Platreef (Flatreef equivalent) intruding and intermingling with Main Zone. The authors argue that Platreef is also found intruding Main Zone further north on the farm Drenthe. In contrast, studies on the Platreef by Holwell and Jordaan (2006) have documented MZ cross-cutting the upper portions of the Platreef on the farms Sandsloot and Zwartfontein.

The Flatreef displays some systematic variability across the farm Turfspruit. This includes the absence of feldspathic sections of the Merensky Reef Cyclic Unit across the eastern areas of the Flatreef, and the northward pinching out of the GMA on the farm Akanani (Grobler et al., 2018; Mitchell and Scoon, 2012). This could be explained by a facies model, after Eales et al. (1988) and Maier and Teigler (1995), whereby the thickness and composition of intruding magmas is a function of distance from a feeder zone, with progressive magma pulses eroding previously formed layers. In the northern limb the proposed feeder zone lies to the west of Mokopane, several km to the south of the farm Turfspruit (van der Merwe, 1976).

11.3.2 Potential effects of recrystallisation

Recrystallisation primarily affects the textures of rocks and their mineral assemblages. Recrystallisation can occur as a result of addition of high-temperature fluids, volatile-rich

melts, or an elevation in temperature due to the intrusion of magma in close proximity to the rock. In the case of cumulus rocks the trapped or percolating intercumulus liquids can react with the cumulus crystals to form coronas and late-stage overgrowths. Evidence of recrystallisation is most readily identified by rock textures, whilst the composition of the minerals and bulk rock may also change. Recrystallisation textures can manifest themselves as mineral zoning in response to fluid interaction, coarsening of crystal sizes, becoming pegmatoidal in extreme cases, and equilibrium textures expressed as 120° triple crystal junctions. Recrystallisation has been documented throughout the Bushveld complex to explain igneous textures such as the zoning of olivine-pyroxene oikocrysts in mottled anorthosites (Maier, 1995). Pegmatoidal textures are relatively rare in the Bushveld Complex but are a prominent feature of the Merensky Reef. In the Flatreef they appear to be more common, appearing throughout ultramafic units.

11.3.3 Origin of the Olivine Mela-Gabbronorite

The olivine mela-gabbronorite forms the lowermost lithology exposed in drill core UMT081. It is located beneath a ~6 m thick dolomitic layer. It is comprised of elongate orthopyroxene laths (79-80 Mg#) with similar compositions to the overlying Flatreef rocks, but relatively more evolved olivine (Fo 76 avg.), the latter forming oikocrysts that are surrounded by haloes of clinopyroxene whose composition (81-86 Mg#) overlaps with clinopyroxene in the overlying Flatreef (Figure 6.31). Interstitial plagioclase is more sodic (35-42 An) than in the Flatreef but resembles that in the Ti-rich olivine gabbro. Olivine contains small, rounded plagioclase chadacrysts.

It is unclear whether the mineral assemblage of the olivine mela-gabbronorite is of primary origin or the result of recrystallisation. Oikocrysts of pyroxene and olivine in dolerites generally form because of their higher growth rate and lower nucleation rate compared to plagioclase, which tends to form multiple smaller crystals (Cox et al., 1979). However, the spatial relationship of olivine rich cores and clinopyroxene rims in the olivine mela-gabbronorite could suggest peritectic reaction or recrystallisation in the presence of Si-undersaturated fluids (Bourdreau, 2019). Recrystallisation could have been triggered by heat flux from the overlying Flatreef. In addition, certain disequilibrium textures (i.e. small plagioclase chadacrysts and embayed olivine surrounded by clinopyroxene haloes, in addition to ragged orthopyroxene laths) could be the result of recrystallisation, triggered by small amounts of late stage volatile rich trapped melt. Although hydrous phases are not observed, volatiles could have possibly escaped during crystallisation.

$\delta^{18}O_{opx}$ and $^{87}Sr/^{86}Sr_i$ are elevated (10.7 $\delta^{18}O_{opx}$ and 0.704121 $^{87}Sr/^{86}Sr_i$) compared to the Flatreef (7.0-9.3 $\delta^{18}O_{opx}$ and 0.705321-0.708242 $^{87}Sr/^{86}Sr_i$ Upper Flatreef), suggesting crystallisation of the rock from a contaminated magma. However, the rock does not display

the significantly contaminated δ^{26}Mg values of the Ti-rich olivine gabbro (-0.23 vs -0.75 δ^{26}Mg, respectively).

Interestingly, the whole rock composition of the olivine mela-gabbronorite (19.2 wt.% MgO, 8.13 wt.% Al_2O_3, 9.72 ppm Zr, 18.59 Pt, 16.61 Pd) shows considerable overlap with komatiitic chilled margin rocks documented by Maier et al. (2016a) (18.64-18.7 wt.% MgO, 10.04-10.11 wt.% Al_2O_3, 10-20 ppm Zr, 12.9-18.7 ppb Pt, 14.3-15.4 ppb Pd) (Figure 11.29). This could suggest that the olivine mela-gabbronorite is a recrystallised, unevolved B1 sill.

Alternatively, based on the stratigraphic position of the olivine mela-gabbronorite below the Flatreef, the rock may instead represent MgZ or a relatively evolved portion of LCZ or LZ rocks, documented to occur below the Flatreef, intrusive within the sedimentary footwall rocks (Yudovskaya et al., 2013). Comparative plots of olivine mela-gabbronorite against LCZ, LZ, MgZ, BUS and komatiite rocks shows some overlap with LZ, MgZ and komatiite but not in all major element oxide concentrations (Figure 11.29) (Maier et al., 2016a; Wilson, 2015).
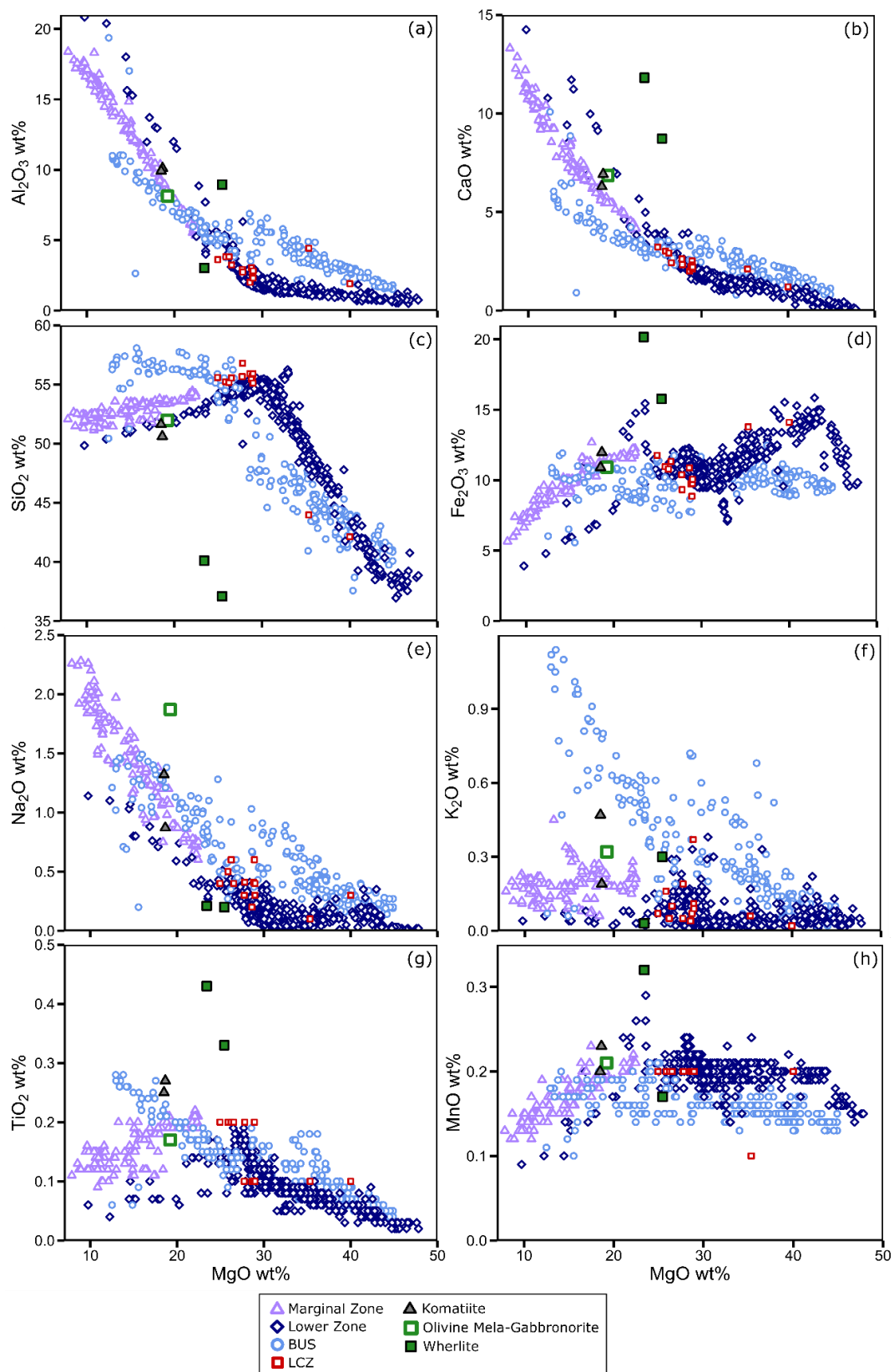
Figure 11.29: Bivariate plots of MgZ and LZ rocks from the main Bushveld complex compared to wehrlite and olivine mela-gabbronorite from the Flatreef. (a) Al$_2$O$_3$. (b) CaO, (c) SiO$_2$, (d) Fe$_2$O$_3$, (e) Na$_2$O, (f) K$_2$O, (g) TiO$_2$, (h) MnO. Comparative data from Maier et al., (2013); Maier et al., (2016a); Wilson (2015).

11.3.4 Nature and origin of the Ti-rich olivine gabbro

The Ti-rich olivine gabbro has been difficult to categorize due to its recrystallised texture. The rock was originally logged as hornfels by Ivanhoe geologists based on its fine-medium grain size, variable concentrations of dark mottles forming modally graded beds and the location of the rocks within dolomitic layers. However, these rocks lack cordierite and mica that are typical of hornfels elsewhere on Turfspruit (Kinnaird et al., 2005). Instead the rocks are solely comprised of olivine (30%), pyroxene (10%), plagioclase (55%), as well as magnetite and ilmenite (5%). Another possibility is that the textures of the rocks, including the poikilitic olivines, represent supercooling (Tegner and Wilson, 1995). More detailed mineral composition data is required to test this theory.

	$\delta^{18}O$	$^{87}Sr/^{86}Sr_i$	ϵNd
Ti-rich olivine gabbro	10.7	0.705817	-5.26
UZ	5.9-7.6 (MZ)	0.707305	
Shale	18.86	0.71487	-4.51 to -10.26
calcareous sediments	11.07-22.4	0.705712-0.709896	-4.4 to -4.9

Table 11.6: Isotopic data from both the Ti-rich olivine gabbro and potential contaminants across the northern limb. Additional data from Beukes et al., (1990); Harris et al., (2005); Hunter and Hamilton, (1978); Jahn and Condie, (1995); Kruger et al., (1987).

Geochemically, the Ti-rich olivine gabbro does not overlap with any other lithologies from the Flatreef, Platreef or UCZ. The only rocks in the Bushveld Complex that are rich in magnetite and ilmenite are within the UZ (Barnes et al., 2004). Elevated TiO_2 contents are also a common feature of shales and hornfels which are present in the Transvaal Supergroup, but other compositional evidence argues against a sedimentary origin. For example, the Ti-rich olivine gabbro has elevated $\delta^{18}O$ relative to the UZ but similar $^{87}Sr/^{86}Sr_i$ ratios (Table 11.6). In contrast, shale in the Transvaal Supergroup tends to have significantly higher $\delta^{18}O$ and $^{87}Sr/^{86}Sr_i$ values. These data thus favour a magmatic lineage of the Ti-rich olivine gabbro.

	An# (plag)	Mg# (opx)	Mg# (cpx)	Fo (ol)
Ti-rich olivine gabbro	26-36	64-66	66-75	53-58
MZ-UZ	21-78 (approx. UZ max 62)	26-80	27-86	6-59 (UZ only)

Table 11.7: Mineral composition from the MZ-UZ compared to the Ti-rich olivine gabbro (Ashwal et al., 2005).

There are several lines of evidence that favour correlation of the Ti-rich olivine gabbro specifically to the UZ of the main Bushveld Complex. The phases present in the Ti-rich olivine

gabbro and their composition overlap with UZ silicate rocks (Table 11.7). Both have strongly elevated V contents (avg. 490 ppm in Ti-rich olivine gabbro, avg. 395 ppm in UZ) (Maier et al., 2013) relative to typical Flatreef rocks (avg. 117 ppm). Chalcophile elements have broadly similar concentrations in the Ti-rich olivine gabbro and the UZ samples and are rich in PPGE relative to IPGE (Figure 11.30) (Barnes et al., 2004; Barnes et al., 2010).
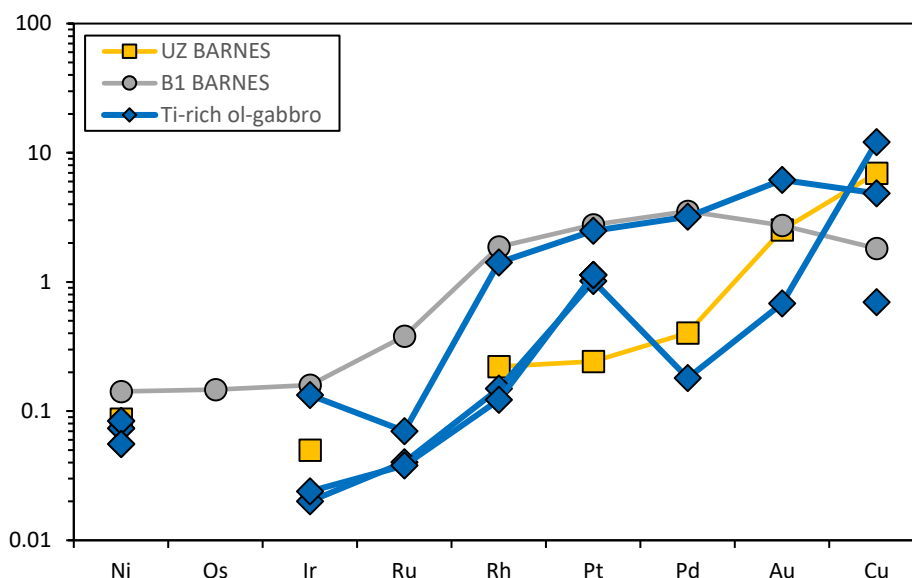
Figure 11.30: Chalcophile element diagram comparing the Ti-rich olivine gabbro with B1 magma (Barnes et al., 2010) and average UZ compositions (Barnes et al., 2004).

As the UZ may have crystallised from fractionated B1 magmas (Maier et al., 2013), an attempt was made to model the rocks using rhyolite-MELTS software (Ghiorso and Gualda, 2015; Gualda et al., 2012). However, fractionation of B1 magmas does not produce the composition and mineralogy of the Ti-rich olivine gabbro, including the high TiO_2 concentrations observed (Table 11.8). This suggests that the observed TiO_2 concentrations in the Ti-rich olivine gabbro is not solely the result of fractional crystallisation of B1 magma. Possibly, contamination with calcareous sediments increased the oxygen fugacity, resulting in oxide fractionation (Reynolds, 1985).

Model #	Starting composition	H_2O %	CO_2 %	fO_2	Pressure	Starting temp	Max. TiO_2 attained
6	B1	0.5	0	QFM-1	3000	1400	0.9639
8	B1	0.16	0.15	QFM	3000	1400	0.9579
10	B1	0.8	0.2	QFM	3000	1400	0.7216
14	B1	0.5	0.5	QFM	2500	1400	0.7952
23	B1	0.5	0.5	NNO	2500	1400	0.6921

Table 11.8: Table of selected MELTS modelling outputs for modelling the Ti-rich olivine gabbro.

The contamination model is consistent with $\delta^{18}O$, $^{87}Sr/^{86}Sr_i$ and $\delta^{26}Mg$ values of the rocks that consistently trend towards calcareous sediments compositions and away from magmatic values. Modelling of these 3 isotope systems suggests up to 59% contamination of B1 magma with calcareous sediments from the Duitschland Formation (sample DUIT1). Nd isotopes are less strongly influenced by calcareous sediment assimilation and are immobile in fluids. Because of the indicated high levels of contamination by calcareous sedimentary floor rocks, conclusive correlation between the Ti-rich olivine gabbro and rocks belonging to the UZ is not possible.

Variations in whole rock composition within the unit could reflect the specific origin of the Ti-rich olivine gabbro. The rocks are characterised by distinctive cycles grading from darker more mafic bases to more felsic tops, similar to the enigmatic Norite Cycles (Kinnaird et al., 2005). The samples analysed show compositional differences in plagioclase of ~6 An# (Figure 11.31). This could either be a function of primary fractional crystallisation, or the addition of Ca-rich contaminants such as the calcareous sediments. The analysed samples have similar whole rock MgO contents suggesting this difference in plagioclase composition is not a function of fractional crystallisation. Instead it is proposed that sample 81-1787, located proximal to the calcareous sediments of the Transvaal rocks (~20m), was more strongly contaminated than sample 81-1720.
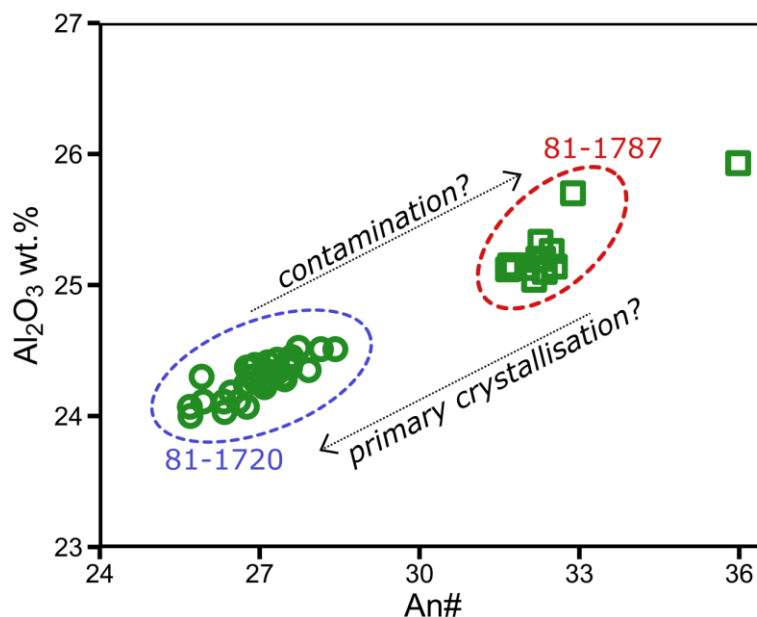
Figure 11.31*: Binary variation plot of plagioclase composition illustrating potential processes affecting plagioclase composition.*

11.3.5 Origin of the Wehrlite sill

In both drill cores UMT081 and UMT094 a wehrlite layer occurs directly above the calc-silicate footwall. The wehrlite is characterised by subhedral olivine and clinopyroxene grains with triple junctions around 120° and interstitial apatite (<1%). Triple grain junctions at 120° are indicative

of a high degree of textural equilibrium, possibly due to a prolonged cooling history. The euhedral nature of magnetite and chromite crystals found as inclusions within silicates suggests that spinel was the first mineral to crystallise, followed by olivine and clinopyroxene. At the same time, the presence of interstitial apatite, suggests that the parent magma was contaminated with crust, or that late stage fluids percolated through the rock.
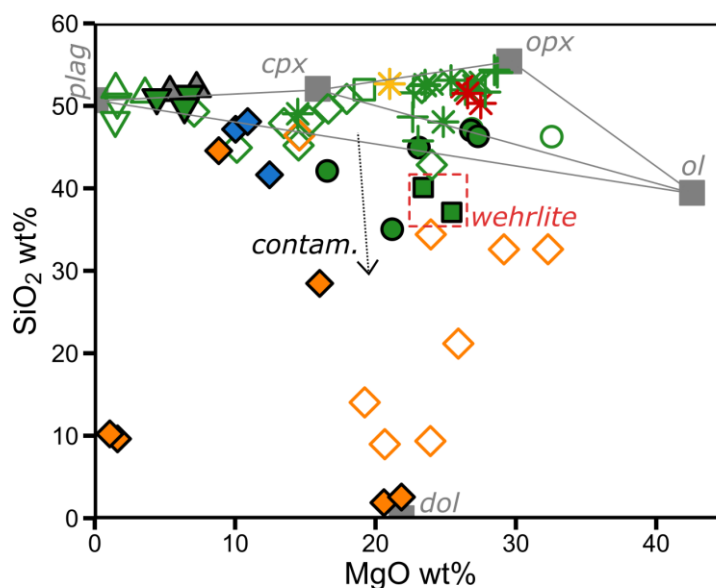
Figure 11.32: *Bivariate plot of SiO₂ against MgO (wt.%) illustrating the control of mineral composition on the composition of the whole rock, with wehrlite plotting outside these controls suggesting addition of a Si-poor contaminant.*

Both models are consistent with the fact that wehrlite is an exotic lithology only found the northern limb of the Bushveld Complex and is absent from UCZ, LCZ, LZ or MgZ of the WBC (Figure 11.29) (Maier et al., 2013; Maier et al., 2016a; McDonald et al., 2005; Wilson, 2015). The abundance of clinopyroxene and the elevated K_2O and CaO and low SiO_2 contents in whole rock compositional data are typical of rocks from the FAZ in the Flatreef, interpreted to result from contamination with dolomitic floor rocks. Figure 11.32 shows that the whole rock composition of the wehrlite rocks plots outside the expected compositions as defined by tie-lines between average mineral compositions of Flatreef silicates. Instead, wehrlites have lower SiO_2 concentrations and plot along a trend towards the composition of calcareous sediments. It is thus suggested that the analysed wehrlite rocks also formed from a strongly calcium contaminated magma. The wehrlite is locally rich in sulphides, magnetite and chromite (1.24% S, 2,506 ppm Cr), but PGE concentrations are relatively low (60 ppb Pt and 116 ppb Pd, sample 81-1702). Previous workers (Buchanan et al., 1981; McDonald et al., 2005) have suggested that wehrlite, lherzolite and harzburgite on the farms Sandsloot and Tweefontein formed through magma contamination with BIF. Notably, the mafic minerals within the rocks at Sandsloot are relatively Fe-rich whereas wehrlite in the Flatreef is relatively Mg-rich (i.e. olivine has Fo 88). It is therefore considered more likely that this rock formed in response to significant contamination of magmas by calcareous sediments.

11.3.6 Origin of the FAZ

The FAZ is comprised of variably contaminated igneous rocks and abundant calc-silicate xenoliths, the latter decreasing in abundance with height. FAZ rocks contain abundant clinopyroxene and olivine, the former often forming equigranular clinopyroxenites with 120° triple grain junctions (Figure 5.33d) indicative of recrystallisation, possibly in response to the emplacement of the overlying igneous units. Strong alteration increasing towards the base of the FAZ and contact with the footwall rocks likely reflects percolation of volatiles released from devolatizing carbonaceous sediments in response to the emplacement of the Flatreef.
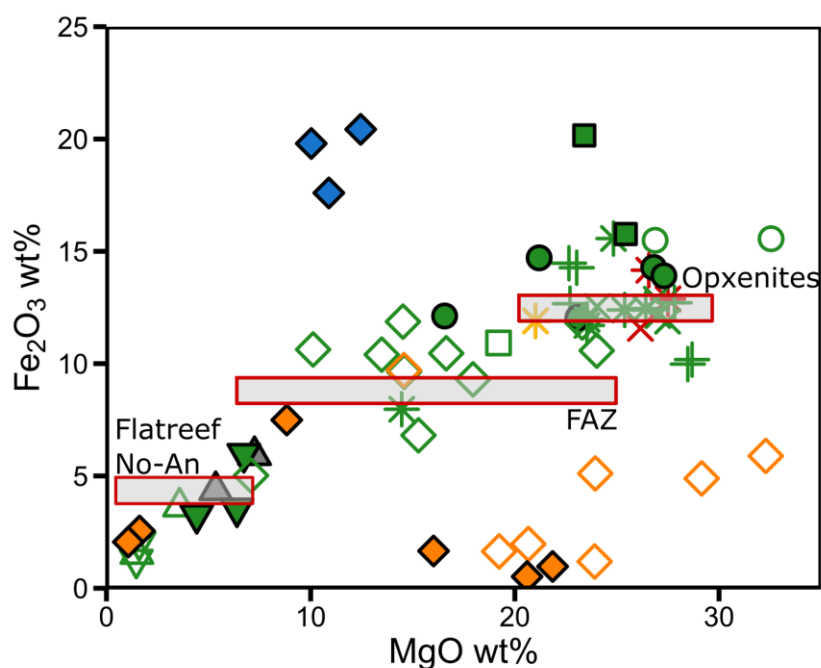
Figure 11.33: *Bivariate plot of Fe$_2$O$_3$ against MgO wt.% of whole rock compositional data. Red outlined bars show the range of MgO content in certain rock types. Note, for example, the wide range of FAZ compositions relative to norite-anorthosite and orthopyroxenite rocks of the Flatreef.*

The intense contamination of this unit precludes any attempt to correlate the rocks with those of the WBC. It likely crystallised from several magma injections with distinct compositions, each containing assimilated dolomitic material. This has manifested itself in a wide range of compositions as shown in Figure 11.33. The wide range of contaminated lithologies observed is also reflected by the variation in mineral compositions. Although the FAZ has highly variable lithophile element composition, there are some notable trends, such as the progressive upward increase in Rb and Cr contents. FAZ rocks with Cr contents significantly lower than magmatic rocks of similar MgO contents are interpreted to represent significant addition of crustal contaminant, which has negligible Cr concentrations (Figure 11.34).
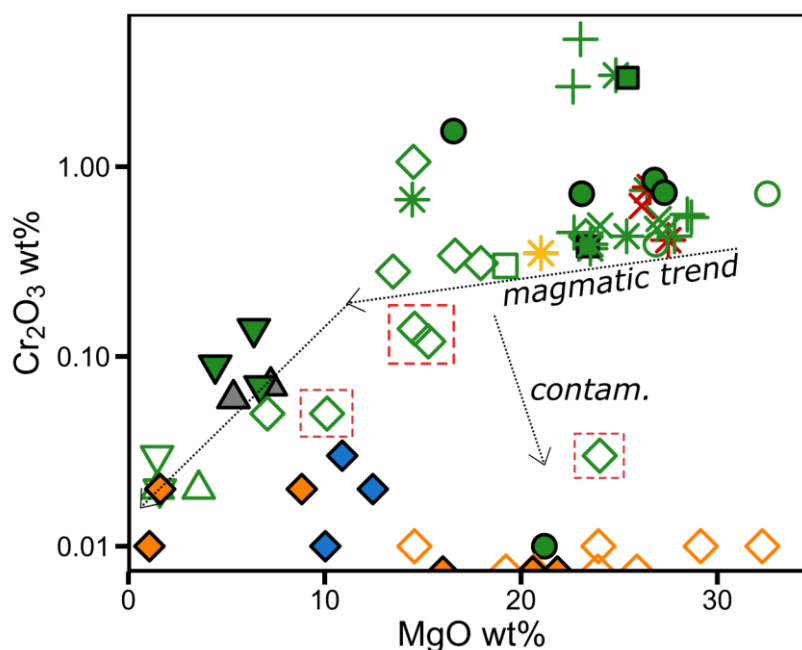
Figure 11.34*: Bivariate diagram of Cr_2O_3 against MgO illustrating the lower Cr_2O_3 concentrations detected in several FAZ rocks (highlighted by red boxes). This is interpreted to represent the addition of carbonaceous sediments.*

Thin (1-3 m) sills of fine-grained orthopyroxenite occur in the FAZ, whose major and trace element composition broadly overlaps with orthopyroxenites in the Upper Flatreef. Isotope data show that these orthopyroxenite sills also contain a crustal component, yielding lower εNd values (-8.67, sample 81-1610) than typical UCZ magma (-5.9 to -7.6 εNd) (Maier et al., 2000). However, these sills are less contaminated than the remainder of the FAZ.

Strong contamination of the FAZ by assimilation of calcareous sediments suggests emplacement of the bulk of this unit relatively early in the formation of the Flatreef, into relatively unmetamorphosed calcareous sediments of the Duitschland Formation.

11.3.7 Origin of the UG2 Footwall Unit

The UG2 Footwall Unit (UG2 FU, formerly the Lower Ultramafic Unit) located below the Main Chromitite in the Flatreef has not yet been satisfactorily correlated to stratigraphic units south of the TML (Grobler et al., 2018). Its unusual thickness in UMT081 allows for a more detailed inspection of the unit. The stratigraphic position of the UG2 FU suggests it could be of either UCZ or LCZ affinity, although its lithophile element and isotopic composition imply some degree of contamination which must be assessed before correlations with rocks from the main Bushveld Complex can be attempted. It is also necessary to determine the genesis of the olivine-rich rocks, as other studies have suggested they may not be of primary magmatic origin (Marquis, 2015; McDonald et al., 2005).

The UG2 contains lherzolite which is not present in the main Bushveld Complex. The presence of significant clinopyroxene in the UG2 FU, together with the proximity to dolomitic floor rocks suggests that the parent magma was contaminated with calcareous sediments. However, orthopyroxene compositions in lherzolite and harzburgite broadly overlap with each other (Mg# 80-84 and Mg# 79-85) and pyroxenite in UG2 FU pyroxenite (Mg# 80-86) that latter of which shows no lithological evidence of contamination. In addition, olivine composition of lherzolite (Fo 78-87) broadly overlaps with olivine in harzburgite (Fo 78-83). If the olivine in harzburgite and lherzolite was derived from contamination by magnesian floor rocks the olivine and pyroxene compositions could potentially be expected to be more magnesian than what is observed, due to addition of Mg (Wenzel et al., 2002). In addition, olivine in lherzolite and harzburgite is relatively Ca-poor (max. 0.07 and 0.13 wt.%, respectively), inconsistent with the assimilation of carbonate.

Petrographic observations of the UG2 FU, notably the amoeboidal shape of many olivine grains, suggest olivine may not be a primary phase crystallising from the melt but rather a secondary phase possibly from recrystallisation in response to fluid flow through the unit. Transects across interstitial plagioclase grains within lherzolite and harzburgite show a range of compositions with some plagioclase grains showing distinctive Ca-rich cores that could represent a core of cumulus plagioclase, with sharp transitions to sodic rims that could represent intercumulus overgrowth. There is no clear evidence of reverse zoning. However, lherzolite does have significantly higher plagioclase anorthite content (An80) compared to harzburgite and orthopyroxenite in the UG2 FU (An66 and 53, respectively).

The harzburgite layers are locally characterised by deformation, expressed by kink-banding in large olivine crystals and the presence of spindle twin lamellae in plagioclase (Figure 5.24). In contrast, in harzburgite minor clinopyroxene shows no evidence of deformation suggesting this phase represents the product of recrystallisation. Chromite is found as a phase within both olivine and pyroxene indicating it was the first to crystallise.

Boudreau (2016) suggested that much of the olivine in the Stillwater Complex was of secondary origin. This model could explain the amoeboidal morphology of olivine grains, reversely zoned plagioclase and elevated anorthite contents of plagioclase. However, while some olivine is amoeboidal in the UG2 FU it is not ubiquitous and plagioclase composition varies strongly between different rock-types in the UG2 FU with no reverse zoning detected. It is therefore proposed that most of the olivine in the lherzolite is of primary magmatic origin, in agreement with the conclusions of Mitchell and Scoon (2012) on the farm Akanani, although formation of some amoeboidal olivine and calcic plagioclase in response to localised fluid interaction cannot be ruled out. This does not explain the variable plagioclase compositions throughout the unit.
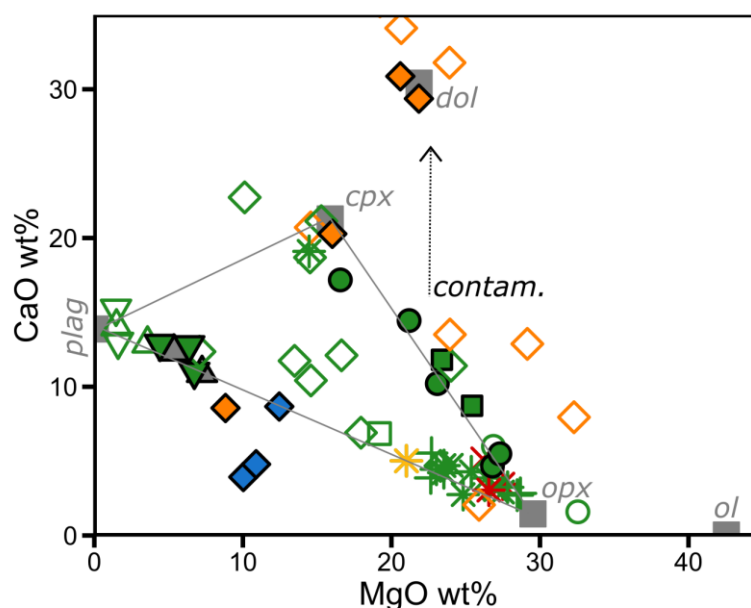
Figure 11.35*: Bivariate plot of CaO against MgO (wt%). Lherzolite (green filled circles) plots along tielines between olivine and orthopyroxene with clinopyroxene. Note other rocks that plot along or near these tielines are all contaminated FAZ or clinopyroxenites.*

Whole rock compositions of lherzolite and harzburgite plot above the plagioclase-orthopyroxene tielines along which rocks from the remainder of the uncontaminated Bushveld Complex plot (Figure 11.35). Instead lherzolite plots along clinopyroxene tielines with an overall increase in CaO contents plotting towards a contamination trend with calcareous sediments.

Isotopic evidence from drill core UMT081 is consistent with a model whereby the entire UG2 FU is variably contaminated, particularly the lherzolites. Sr isotopes of lherzolite are marginally more radiogenic (0.706111 $^{87}Sr/^{86}Sr_i$) relative to the underlying pyroxenite (0.705321 $^{87}Sr/^{86}Sr_i$). Lherzolite in UMT081 has a more negative $\delta^{26}Mg$ (-0.20‰) compared to overlying harzburgite (-0.16‰). The εNd isotopic values of harzburgite, lherzolite and pyroxenite from the LUU (-9.09, -8.83 and -8.62 εNd, respectively) all indicate a crustal component in the UG2 FU relative to the CZ rocks of the WBC (Maier et al., 2000)

In summary, the available data suggest that the UG2 FU has crystallised from variably contaminated magmas. Harzburgite and orthopyroxenite appear to be relatively less contaminated, based largely on their lithology, and their compositions resemble rocks from the UCZ of the WBC. Mineral compositions of the harzburgite (Mg# 79-85, Fo 78-83) and orthopyroxenite (Mg# 80-86) broadly overlap with compositional ranges from both the UCZ (Mg# 77-83, Fo 77-81) and LCZ (Mg# 82-85, Fo 82-86) but have slightly better overlap with the LCZ (Eales and Cawthorn, 1996). Most isotopic systems indicate an enhanced crustal component in the Flatreef rocks.

The reason for the unusual thickness of the UG2 FU in drill core UMT081 (153 m) remains unclear. The unit likely forms part of the UCZ, but due to the paucity of feldspathic rocks and the abundance of chromitite lenses hosted in orthopyroxenite it is somewhat reminiscent of the LCZ. The UG2 FU in drill core UMT081 comprises distinct layers of lherzolite and harzburgite hosted in feldspathic pyroxenite, whereas the thinner UG2 FU in drill core UMT094 is comprised of peridotite showing variability in the ratio of clinopyroxene to orthopyroxene, only sporadic chromitite lenses and no orthopyroxenite. Harzburgite and orthopyroxenite are prominent rock types in the LZ and LCZ, but Yudovskaya et al. (2013) found that in the Platreef, the LZ is usually separated from the CZ by the MgZ making correlation of the UG2 FU with the LZ unlikely.

Several models are considered here to explain the localised thickening of the UG2 FU in drill core UMT081 (Figure 11.36). Thickening may have occurred *in situ*, with intruding ultramafic magmas concentrated in a hydrodynamic trap such as a large pothole. Such traps could be formed in several ways:

(1) Graben faulting, e.g., through downfaulting of dolomitic floor rocks in response to crustal loading during emplacement of the Flatreef (Figure 11.36).

(2) Extension resulting from slumping of magmatic packages towards the centre of the Bushveld Complex. This could result in localised pull-apart structures within magmatic layers above which UG2 FU magmas intruded. Localised small scale extensional faulting has been suggested to form potholes in the UCZ of the EBC (Maier et al., 2016b). Extension along a detachment plane, e.g., the boundary between magmatic and country rocks, could also form pull-apart structures. This detachment plane could be further lubricated from volatile rich fluids produced by devolatizing floor rock calcareous sediments (Maier et al., 2019 In Press).

(3) Subsidence caused by devolatization of calcareous sediments or by folding of the dolomitic floor and development of localised depressions into which UG2 FU magmas pool and thicken. Folding of the Transvaal floor rocks is well documented across the northern limb and has been cited by many authors as a mechanism for controlling and compartmentalizing magmatic packages such as the LZ (Yudovskaya et al., 2013).

(4) Footwall up-doming and diapirism in response to heating from igneous intrusions (Scoon, 2002), between which Bushveld magmas pooled.

Grobler et al. (2018) reported an example of structural duplication of the Flatreef forming the so-called Bikkuri Reef. This was envisaged to have formed by detachment of a semi-consolidated section of layered cumulates along a low-angle fault in close proximity to dolomitic country rocks. UMT081 has been drilled on a relatively steep section of the Flatreef and thus may reflect cumulate instability along an inclined slope. In the drill core there is evidence for devolatization of calcareous sediments at depth and contamination within the

UG2 Footwall Unit. Structural duplication should be apparent in drill core geochemistry. While there is some repetition of lherzolite units with interspersed chromitite stringers the thickness of the lherzolite layers is not consistent (7 and 26m, respectively). More definitive compositional studies of the various chromitite stringers found throughout the UG2 FU would help constrain this model.

It is possible the orthopyroxenite of the UG2 FU in UMT081 is not part of this unit and rather intruded after emplacement, artificially thickening the UG2 FU. This would possibly imply down plunging sills of orthopyroxenitic material from the neighbouring UG2 Cyclic Unit (UG2 CU; formerly Lower Pyroxenite). Fine grained orthopyroxenite in the UG2 FU mostly overlaps in composition with orthopyroxenite of the UG2 CU (e.g. in MgO, Al_2O_3 and Cr_2O_3 contents) but orthopyroxene and plagioclase compositions differ. In places these orthopyroxenites can be pegmatoidal with mineral compositions that overlap with those of finer-grained rocks (Figure 6.20). This is interpreted to reflect recrystallisation of the orthopyroxenes, possibly in response to late sills intruding the cumulate package, or percolation of a volatile-rich melt.
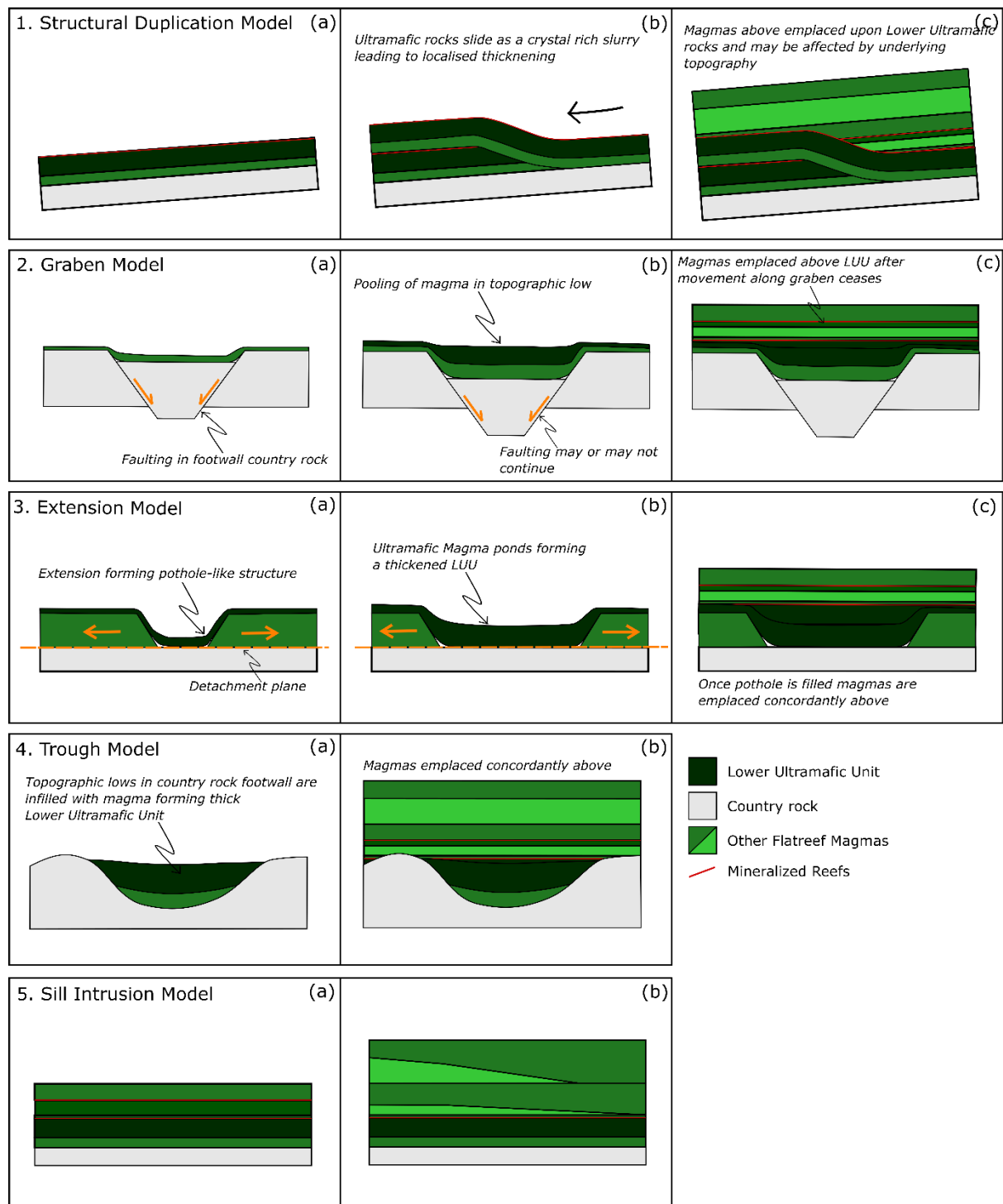
Figure 11.36: Sketch showing various models that could explain the anomalously thick UG2 Footwall observed in drill core UMT081. (1) Structural duplication model, (2) Graben model, (3) Extension model, (4) Trough model, (5) Sill Intrusion model.

11.3.8 Formation of the UG2 Cyclic Unit

The UG2 Cyclic Unit comprises medium grained to pegmatoidal orthopyroxenite with a thick chromite rich layer (the UG2) towards the base of the sequence. Variation in mineral composition of plagioclase and orthopyroxene and total unit thickness between drill cores UMT081 and UMT094 suggest lateral evolution of this unit with distance from the feeder zone, as is suggested in the WBC (Eales et al., 1988). The UG2 Cyclic Unit has remarkably consistent lithophile and chalcophile element contents throughout drill core UMT081. The consistent composition of the unit, as well as the lack of sharp contacts between medium-grained and pegmatoidal domains could suggest that the unit was intruded as a thick sill undergoing limited fractionation after emplacement. This model is consistent with deformation features of plagioclase such as bent and spindle-like twin lamellae, recording deformation during crystallisation. The bulk of the orthopyroxenites are medium grained. Domains of pegmatoidal material with diffuse transitions between grain sizes are interpreted to reflect localised recrystallisation of orthopyroxenite, likely in response to trapped pockets of volatile-rich fluids. There is no evidence of contamination in lithophile composition, with orthopyroxenites plotting along the defined trend of plagioclase to orthopyroxene (Figure 11.37). Consequently, these rocks are interpreted to reflect primary crystallisation, with localised recrystallisation in pegmatoidal domains.
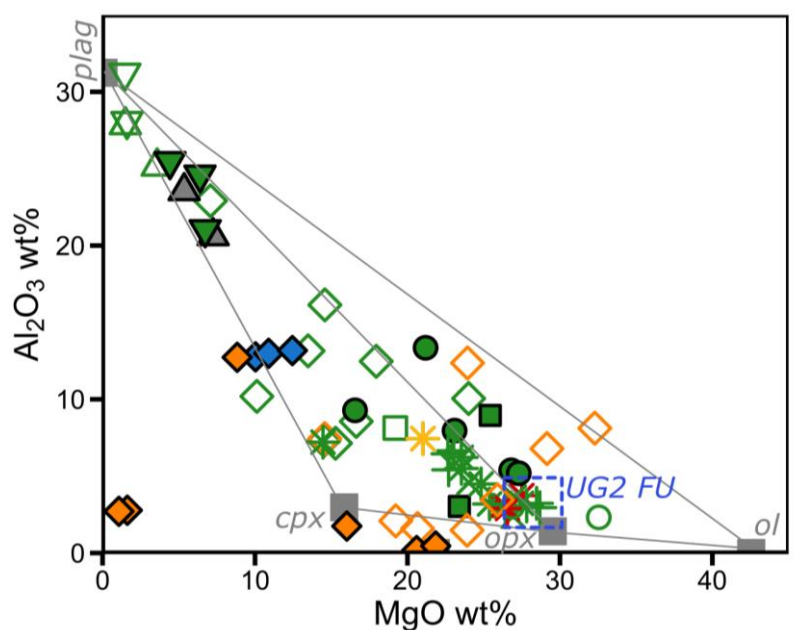
Figure 11.37*: Bivariate plot of Al₂O₃ vs MgO (wt.%). Orthopyroxenites of the UG2 Footwall Unit plot close to the Flatreef average composition of orthopyroxene and along the trend defined between plagioclase and orthopyroxene composition.*

The UG2 chromitite is approximately 1 m thick and contains PGE mineralisation of variable grade (2-6 ppm PGE; Grobler et al., 2018), whereas mineralisation of the UG2 is more consistent in the remainder of the Bushveld Complex (Naldrett et al., 2012). Several models

have been proposed to explain the formation of chromitite layers in the Bushveld Complex (see Maier et al., 2013 for a review). These include (1) crystal fractionation, (2) density currents, (3) magma mixing, (4) recrystallisation triggered by fluid flux, (5) pressure changes, (6) changing fO_2 and (7) injection of chromite slurries. Whilst crystal fractionation remains the most popular model (Naldrett et al., 2012), the mechanism to effectively remove small chromitite crystals from a viscous convecting magma remains unclear. Crystal slurries in which minerals segregate by density sorting, as proposed originally in the Skaergaard intrusion (Irvine et al., 1998), may offer a solution but cannot explain the presence of delicate elongate autoliths observed in the WBC (Maier and Barnes, 2008; Maier et al., 2013). Other models proposed, including pressure changes (Cameron, 1980) and recrystallisation in response to fluid flux (Boudreau, 2008), are not widely accepted in the Bushveld research community and do not explain the formation of thick chromitite seams. Triggering spinel crystallisation through oxidation of the magma (De Waal, 1977) is unlikely to occur across the magma chamber simultaneously (Naldrett et al., 2012).

With regard to the UG2 chromitite in the Flatreef, models of crystal fractionation or magma mixing that rely on large bodies of magma are at odds with geochronological data supporting a model of sill emplacement (chapter 10). This suggests that the intruding magma contained a significant chromite cargo, possibly in response to contamination in a staging chamber (Mondal and Mathez, 2007; Voordouw et al., 2009). This model would be consistent with the relatively high $\delta^{18}O$ in the host pyroxenite (9.35 $\delta^{18}O_{WR}$).

In contrast to the thick, well consolidated UG2 chromitite in the UCZ of the WBC, the Flatreef UG2 chromitite can form multiple lenses. This suggests that the UG2 chromitite in the Flatreef formed in a less quiescent environment than in the WBC, possibly due to large volumes of volatiles produced by devolatizing calcareous and pelitic sediments moving through the melt and disrupting the formation of chromitite.

Textural evidence suggests the chromitite layer, located at the base of the UG2 cyclic unit was a focus for deformation based on the presence of small pyroxene grains on the boundaries of larger pyroxene crystals, generally agreed to form under dynamic recrystallisation in response to deformation (Figure 5.21c). Deformation is commonly focussed along lithological boundaries, i.e. at the base of a cyclic unit, where the join between units represents a plane of weakness.

11.3.9 Formation of the Merensky Footwall Unit

In drill core UMT094 the Merensky Footwall Unit contains abundant well developed Norite Cycles, so termed by Kinnaird et al. (2005), while being largely overprinted by granite veining in drill core UMT081. The unit is largely absent in drill cores to the east of UMT094 and

UMT081, suggesting either that it was never formed here, or was eroded by later pulses of ultramafic magma, as proposed by Eales et al. (1988) in the UCZ of the WBC.
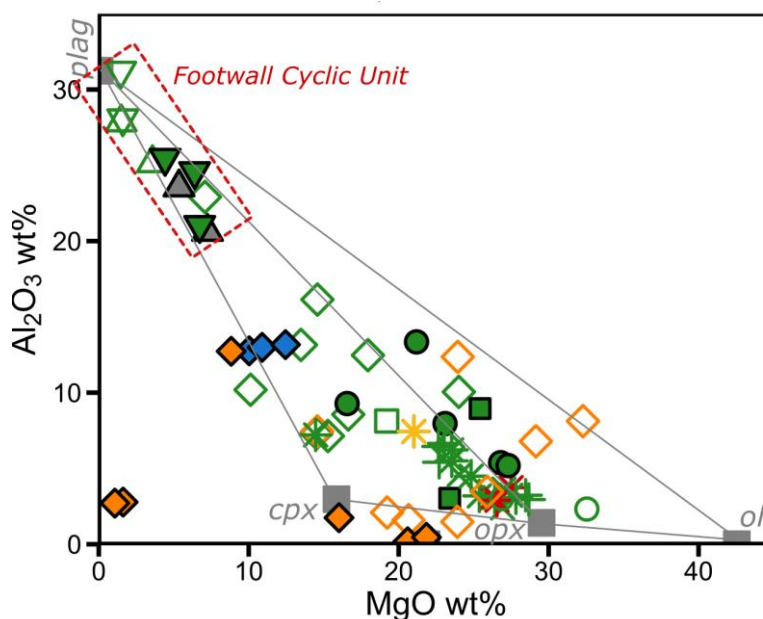
Figure 11.38: *Bivariate plot of Al_2O_3 against MgO (wt%) showing the compositions of norites and anorthosites from the Merensky Footwall Unit which plot close to the vectors of mineral composition demonstrating control of whole rock composition by these minerals.*

Element maps showing compositional variation within minerals highlights the zoned nature of pyroxene crystals in both norites and anorthosites. Figures 5.13 and 5.15 both show orthopyroxene rimmed by clinopyroxene. This is interpreted to reflect primary crystallisation in a progressively evolving magma as the melt becomes increasingly calcic, or possibly peritectic replacement of orthopyroxene by clinopyroxne. Plagioclase is interpreted to be the first crystallising phase forming subhedral laths whilst interstitial quartz represents the last phase to crystallise. The distinctly lower Mg# of orthopyroxene in these rocks compared to pyroxenites likely reflects the trapped liquid shift effect in which pockets of trapped melt re-equilibrate with pyroxene. Elsewhere in the Bushveld Complex this process can account for a compositional shift of up to 10 molar % (Barnes, 1986). Textural evidence in sample 81-1338 (Fig 5.13) shows orthopyroxene seemingly as a cumulus phase with later more ca-rich pyroxene surrounding individual crystals being interstitial to the plagioclase. These rocks show no compositional evidence of contamination and plot within the space defined by mineral composition vectors (e.g. Figure 11.38). However, the lack of isotopic data on this unit prevents a more detailed investigation of the scale of potential contamination.

Element mapping of a representative oikocryst suggests plagioclase laths within the pyroxene oikocryst are less sodic than outside the oikocryst where plagioclase are normally zoned. Relatively calcic plagioclase in the oikocryst may result from recrystallisation in response to fluids where sodic plagioclase is preferentially resorbed (Maier, 1995). This in turn would drive

plagioclase compositions towards more anorthite rich compositions. In order to assess this further, more detailed spatial studies of plagioclase compositions are required.
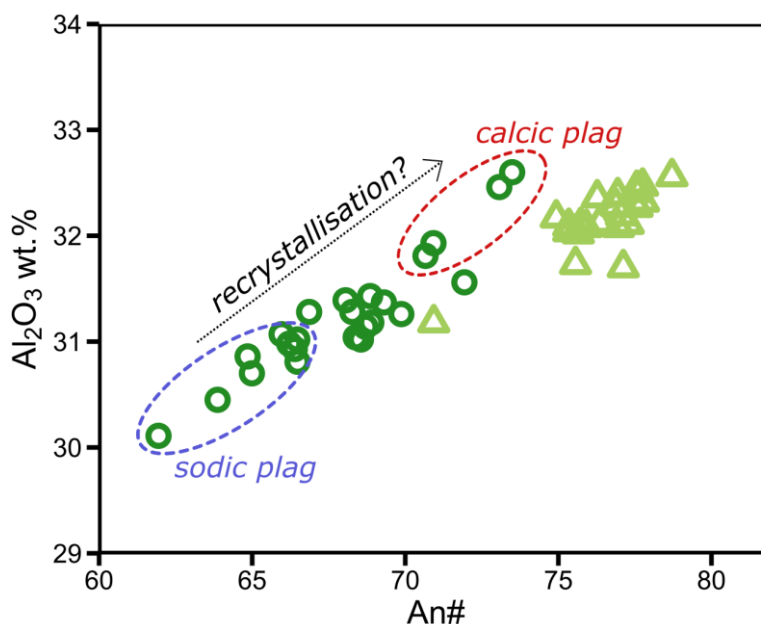
Figure 11.39: *Bivariate plot of plagioclase composition from Anorthosite rocks of the Merensky Footwall Unit. Wide variation in compositions in drill core UMT081 (dark green circles) could be the result of spatially restricted recrystallisation.*

In the absence of more detailed compositional studies, the formation of these norite cycles remains unresolved. All that can be said at the moment is that there is a discernible difference laterally in both plagioclase and pyroxene compositions of the unit, as exposed in the two studied drill cores (Figure 11.39), once again supporting a model of lateral evolution of magmas with distance from the feeder zone, originally proposed for the WBC (Maier and Teigler, 1995).

11.3.10 Formation of the Merensky Cyclic Unit

The Merensky Cyclic Unit comprises a thick sequence of medium-grained orthopyroxenites with a sulphide-rich olivine-bearing orthopyroxenite at its base containing the Merensky Reef. The composition of the unit varies along strike, with Merensky Reef orthopyroxene being more magnesian in drill core UMT081 than in UMT094. In addition, the thickness of the reef is also variable along strike (8.8 m in UMT081 vs 26.1 m in UMT094). The presence of chromitite seams bounding the pegmatoidal orthopyroxenites and harzburgites that host the bulk of the mineralization has been documented by Grobler et al. (2018) and Yudovskaya et al. (2017b). Both studies conclude that the reef is a correlative of the Merensky Reef in the WBC (Barnes and Maier, 2002b). It is therefore likely that the Merensky Reef in both the Flatreef and the WBC was formed by the same process(es). This is further supported by the contemporaneous crystallisation of the Merensky Reef in both limbs, and the protracted dates of zircon crystallisation found at both Northam and the Flatreef (chapter 10; figure 10.15).

As also observed at the base of the UG2 Cyclic Unit, there is evidence of dynamic recrystallisation at the base of the Merensky Cyclic Unit, manifested as orthopyroxene sub-grains along the boundaries of large orthopyroxene grains (Figure 11.40). While only documented here in reef rocks, it is likely that these recrystallisation textures occur close to contacts between many of the cyclic units discussed here.
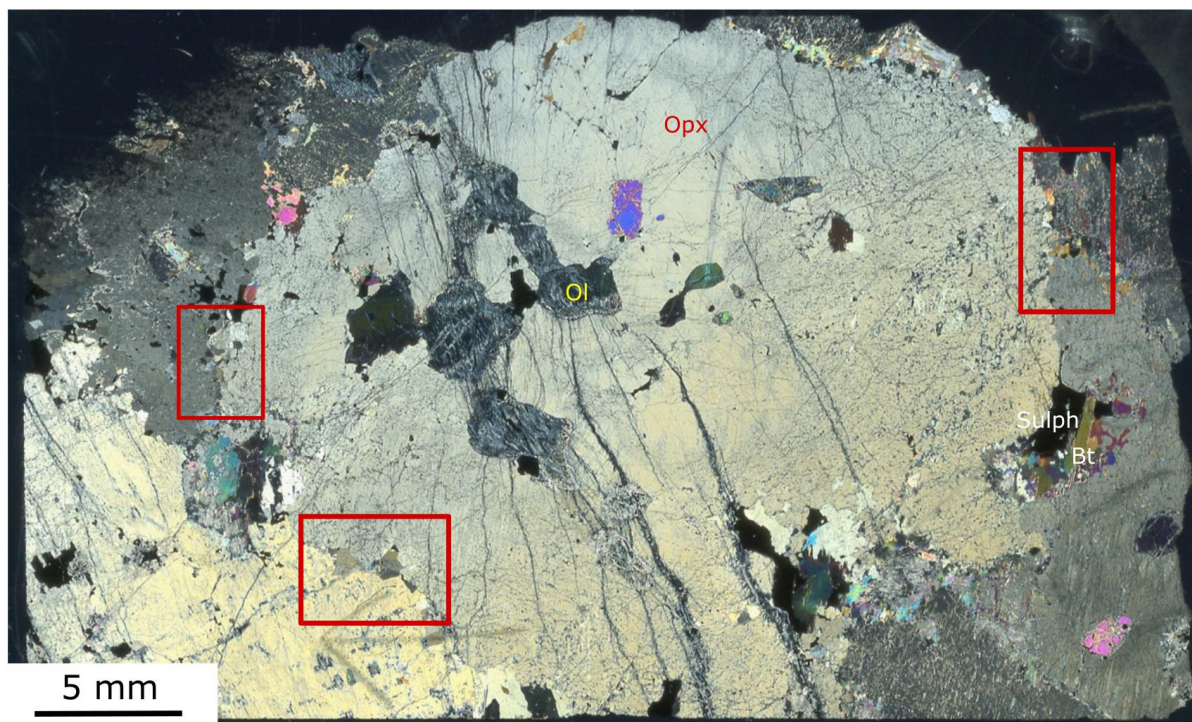
Figure 11.40: *Photomicrograph of sample 81-1327 showing areas where dynamic recrystallisation has formed small crystals along grain boundaries. Here such recrystallisation is restricted to small areas highlighted in red boxes, where the rest of the contact is either primary or altered to amphibole and biotite.*

As previously discussed, the protracted zircon crystallisation ages of the Merensky Reef are interpreted to either represent the continued presence of a melt component, or to result from nearby influxes of magma raising the temperature of the Merensky Reef above the zircon closure temperature. Yudovskaya et al. (2017b) suggested that the reef formed in response to continued magma injection, precipitating and upgrading PGE-rich sulphides. A similar model has been proposed for the Merensky Reef in the WBC (Latypov et al., 2015). Interestingly, the pyroxenite hangingwall to the reef shows more contaminated $\delta^{18}O_{WR}$ values (8.99-9.81) than the Merensky Reef (7.55 $\delta^{18}O_{WR}$).

In certain parts of the Turfspruit property, the upper portions of the MCU consist of feldspathic rocks but these are absent in drill cores UMT081 and UMT0984. In parts of the WBC, it was proposed that emplacement of hot unevolved magma effectively scoured feldspathic units and removed them (Eales et al., 1988). Alternatively, the feldspar rich rocks could represent discrete sills which did not develop in the studied area of the Flatreef.

11.3.11 Formation of the Bastard Cyclic Unit

The Bastard Cyclic Unit is comprised of fine-medium grained pyroxenite, resembling the underlying Merensky Cyclic Unit. In the Flatreef the Bastard Reef can be more strongly mineralized over a greater thickness (448-1670 ppb Pt, 338-1200 ppb Pd over 4m; Ivanhoe assay data) than in the WBC (up to 403 ppb Pt, 347 ppb Pd over several cm) (Maier and Barnes, 2008). The sample analysed in the present study (81-1305) is located >30 cm above the base of the Reef and contains 228 ppb Pt and 320 ppb Pd.

Pyroxenite in the hangingwall to the Flatreef Bastard Reef shows contaminated isotope signatures (-9.21 εNd, 8.99 $\delta^{18}O_{WR}$), reflecting one of the highest country rock components in the Upper Flatreef (5% granite, 20% shale). Models developed for the WBC by Eales et al. (1986) suggest that the Bastard Cyclic Unit was intruded as a sill into a hybrid melt of residual Merensky Reef magma and Main Zone magma (Figure 11.28). This model is consistent with the geochronological data acquired in this study (chapter 10) and the progressive upward increase in Sr isotope ratios (Mayer et al., 2019). However, the Bastard pyroxenite has relatively low $^{87}Sr/^{86}Sr_i$ (0.706985) relative to the MZ (0.709389), with the former overlapping UCZ values from the WBC (0.70565-0.70779) (Eales et al., 1990) suggesting only a minor (<10%) MZ component in this hybrid melt.

Both the Merensky Cyclic Unit and Bastard Cyclic Unit show an upward decrease in MgO (Figure 11.41) and an increase in CaO and Al_2O_3. However, the composition of plagioclase remains constant throughout these units. The origin of decoupling between pyroxene and plagioclase is unclear, possibly reflecting mixing between distinct magmas, which is consistent with geochronological data implying that the Bastard unit was intruded into a cumulate pile that was not fully crystallised.
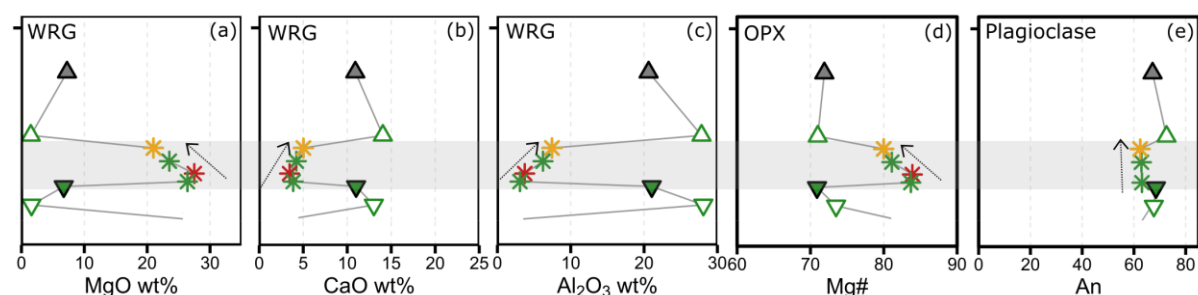
Figure 11.41: *Truncated downhole plots of lithophile composition (MgO, CaO and Al_2O_3 wt.%) and mineral compositions (orthopyroxene and plagioclase) showing downhole trends in both mineral and whole rock compositional data.*

11.3.12 Formation of the GMA

The Giant Mottled Anorthosite has mainly been described in the WBC where it forms the uppermost portion of the Bastard Cyclic Unit, separating the UCZ from the MZ (De Klerk,

1992). However, the relatively sharp magmatic contact between the GMA and BCU found in the Flatreef suggests that the GMA could be a distinct intrusion. The upper contact of the GMA in drill core UMT081 is diffuse over ~50 cm, whereas in drill core UMT094, the GMA contains several layers of more noritic material, likely belonging to the MZ. Isotopic data show that the GMA contains a significant crustal component expressed by negative εNd (-8.63), elevated $^{87}Sr/^{86}Sr_i$ (0.708242) and relatively heavy $\delta^{18}O$ (9.70$_{WR}$). Mitchell and Manthree (2002) proposed the GMA is in part derived from MZ magma, consistent with its elevated Sr isotope signature (MZ $^{87}Sr/^{86}Sr_i$ 0.709389). The GMA pinches out northwards on the farm Akanani (Mitchell and Scoon, 2012), supporting a model of emplacement from a feeder zone to the west of Mokopane. Petrographic evidence suggests the GMA has not been significantly recrystallised. Plagioclase forms euhedral cumulus laths whilst pyroxenes form large oikocrysts with pockets of orthopyroxene surrounded by clinopyroxene as the interstitial melt evolved. However, orthopyroxene within cumulus plagioclase rocks in the Flatreef is characterised by notably less magnesian composition that orthopyroxene in rocks where plagioclase is an interstitial phase. This is likely the result of the trapped liquid shift whereby the cumulus minerals equilibrate with evolved interstitial melt. Not only would this result in less magnesian orthopyroxene, but isolated pockets of melt can result in highly scattered compositional data as shown in Figure 11.42.
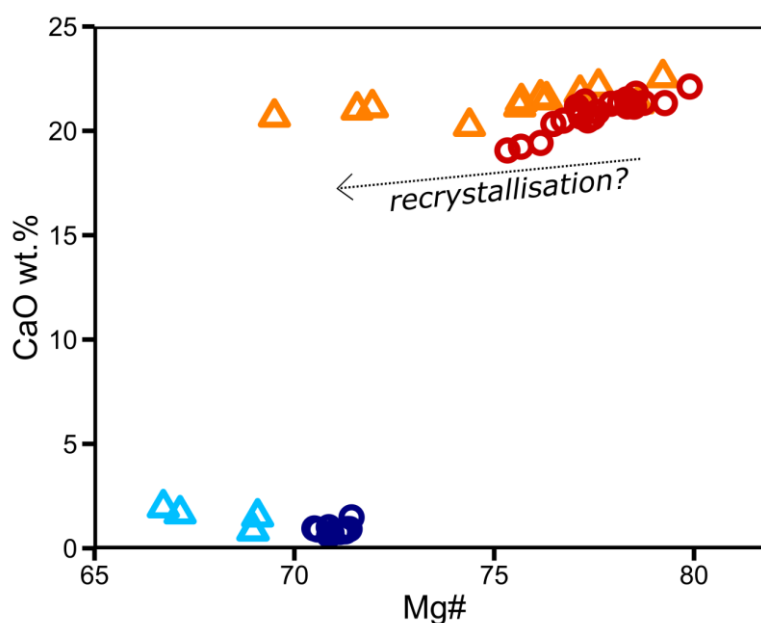
Figure 11.42: *Bivariate plot of pyroxene compositions in the GMA. Note the wide range of clinopyroxene compositions that may be a product of the trapped liquid shift effect.*

11.4 Origin of Sulphide Mineralization

114.1 Models for Reef formation

The laterally continuous PGE reefs of the Bushveld Complex are of particular interest largely on account of their global importance as Pt and Pd deposits. The formation of the Merensky Reef has remained the topic of research since its discovery in 1924 (Cawthorn, 1999b). These models can be divided into the following categories:

(1) In-situ sulphide saturation and segregation by magmatic processes including fractionation, magma mixing or pressure fluctuations. A model of magma fractionation is consistent with the global occurrence of PGE reefs in proximity to the ultramafic-mafic transition in layered intrusions (Maier, 2005). The role of magma mixing in triggering sulphide saturation in Bushveld magmas remains controversial (Cawthorn, 2002; Li et al., 2001, 2002; Naldrett et al., 1986; Seabrook and Cawthorn, 2005). For example, Li and Ripley (2005) found that sulphide melt saturation is only achievable in fractionated Bushveld magmas that are both close to sulphide saturation. However, sills of B1-B3 magmas are generally strongly sulphide undersaturated (Barnes et al., 2010). These models all envisage reef formation in a convecting magma chamber. If recent interpretation of new geochronological data is correct, it is likely the Bushveld Complex was instead constructed from a series of sill intrusions.

(2) In-situ sulphide saturation achieved by contamination of magma with crustal material, either through addition of crustal sulphur or altering the fO_2 of the magma. A contamination model with crustal sulphur has been proposed for the Platreef (Buchanan et al., 1981), implicating the same sulphur rich shales that underlie the Flatreef. Alternatively, sulphide saturation by contamination has been proposed to occur in response to changing the fO_2 of the magma, reducing sulphur solubility in the melt and triggering saturation (De Waal, 1977). However, the abundance of Fe and O within a magma would require significant addition of oxygen to change their ratio and thus alter the fO_2 of the magma.

(3) Concentration of magmatic sulphides in crystal slurries that slump towards the centre of the intrusion in response to subsidence from crustal loading (Maier et al., 2013). This model has been tested by analog tank experiments (Forien et al., 2015).

(4) Entrainment of sulphides from a staging chamber or conduit at depth. This has been proposed by several authors for mineralization in the WBC (Arndt et al., 2005; Maier, 2005) and the Platreef (McDonald and Holwell, 2007). In addition, some Bushveld sills stratigraphically beneath the EBC contain sulphides (Sharpe and Hulbert, 1985).

In addition to these primary models, Boudreau and co-workers have suggested that PGE were concentrated by fluids ascending through the cumulate pile (Boudreau, 2008; Boudreau and McCallum, 1992). Most Bushveld workers have remained sceptical of this model. For example, Cawthorn (1999a) argued that the proportions of various types of sulphides in the Merensky

Reef in the WBC are typical of magmatic assemblages. Furthermore, most Bushveld rocks contain few hydrous silicate minerals.

11.4.2 Mineralization Patterns in the Flatreef

There are two main mineralization features that are unique to the Flatreef, for which a satisfactory model has not yet been proposed. Firstly, the unusual thickness of mineralization in the Flatreef, (250 m in UMT081) relative to the main Bushveld Complex (typically up to 2 m), resulting in higher PGE budgets and average PGE contents across the Flatreef than in the UCZ in the WBC (836 ppb Pt vs. 313 ppb Pt, respectively) (present data and Maier et al., 2013). In addition, S concentrations are also significantly higher across the Flatreef. For example, in the Flatreef the Merensky-UG2 interval (95 m thick) averages 0.32 wt.% S, whereas in silicate rocks outside of the main PGE-bearing reefs in the UCZ of the WBC, S concentrations do not exceed 0.1 wt.% and are frequently as low as 0.01 wt.% (Naldrett et al., 2009). Second, the broad downhole decrease in both chalcophile element grades, Pt/Pd and Ni/Cu ratios, that are inconsistent with progressive magma fractionation.

The Flatreef shows a good correlation between S and the chalcophile elements suggesting that the concentration of the PGE and base metals are primarily controlled by sulphides, except in the FAZ and UG2 footwall where there is poorer correlation between PGE and S. However, it should be noted that Yudovskaya et al. (2017b) documented very low budgets of Pt in sulphides of the Flatreef Merensky and Bastard reefs, identifying PGM as their main host (97% of Pt in the Bastard Reef and 99% of Pt in the Merensky Reef). PGM formation could be due to late stage interaction with fluids (Kinloch and Peyerl, 1990).

11.4.3 Assessment of Models for Flatreef Mineralization

11.4.3.1 Primary magmatic processes

Magma chamber models in which processes of magma mixing, fractionation or pressure changes occur are attractive as they explain the high metal tenor of sulphides from interaction of immiscible sulphide melt with large volumes of magma (i.e. high R-factors). The new geochronological data from this study, places constraints on these models. If the Flatreef is formed by a series of discrete sills, the chalcophile budget of these sills must have been largely derived from within the sills. In a simplistic 2D model, the Bastard Cyclic Unit contains 693 ppb Pt over 8 m thickness, which exceeds that of the parental magma (B1 19 ppb Pt, B2 10 ppb Pt)(Barnes et al., 2010) by an order of magnitude. The same calculation shows the significant sulphide enrichment in the Bastard Cyclic Unit (2381 ppm S), relative to the proposed parental magmas (B1 438 ppm S, B2 177 ppm S)(Barnes et al., 2010).

The S mass balance problem could be satisfied through addition of crustal S from shale in the Duitschland and Timeball Hill formations. However, sulphur isotope studies in both the Platreef (Yudovskaya et al., 2017a) and the Flatreef (Keir-Sage et al., 2018) indicate that sulphides

throughout the mineralized units have S isotopes that overlap with magmatic ranges, and with those of the WBC. Some evidence of crustal S addition is found in strongly contaminated units at the base of the Platreef and Flatreef, but this is spatially restricted to their lowermost portions (Keir-Sage et al., 2018; Yudovskaya et al., 2017a). A model of limited crustal sulphur addition is also supported by Os isotopes, which only display evidence of significant crustal Os towards the base of the Platreef (Reisberg et al., 2011). Based on these considerations, it is unlikely S saturation in the Bastard Cyclic Unit, and possibly the remainder of the Flatreef, was achieved in situ. Instead it is proposed that sulphides were entrained by magmas during emplacement (McDonald and Holwell, 2011).

Petrographic examination of the Flatreef rocks shows that sulphides are largely found in patches of interstitial blebs which could be connected in 3D forming net texture ore (e.g. Figure 5.12b; 5.38a). Sulphides also show evidence of recrystallisation in the presence of hydrous alteration phases amphibole and biotite (e.g. Figure 5.19). Element maps in chapter 5 show that where significant sulphide is present it occurs as large interstitial blebs. Where only minor amounts of fine-grained sulphides are present, they can occur interstitially or sometimes within silicates, although the latter is somewhat rare.

11.4.3.2 Secondary Processes

Several workers have noted the correlation between high-PGE grade in the Platreef and a dolomitic footwall, which could suggest that interaction of Platreef magmas with calcareous sediments is a key ore forming process in the northern limb (De Waal, 1977; Hutchinson and Kinnaird, 2005; Maier et al., 2008; McDonald and Holwell, 2011). De Waal (1977) proposed that assimilation of dolomite can alter the fO_2 of the magma and trigger sulphide saturation. However, changing fO_2 in the magma can also stabilise sulphate and thus increase S solubility in the magma (Jugo, 2009; Jugo et al., 2005).

Some authors proposed that the high-grade mineralization of the Merensky Reef was formed from fluids introducing S and chalcophile elements that ascended through the crystal mush pile (Boudreau, 2008; Boudreau and McCallum, 1992). However, geochronological data from the WBC (Mungall et al., 2016) and the Flatreef (this study) support a model of sill emplacement, which is incompatible with a fluid flux model.

Nevertheless, the systematic downhole decreases in PGE grade and ratios such as Pt/Pd, Cu/Pd and Cu/Ni across the Flatreef imply that secondary processes have modified the distribution of sulphides after emplacement.

It is proposed that sulphides percolated downwards through a semi-consolidated cumulate mush (Maier et al., 2019 In Press). This model could explain the progressive downhole decrease in the chalcophile element contents of the Flatreef. Fractionation of percolating sulphides could explain the trend of increasing Cu/Ni downhole but does not explain the

decreasing PPGE/IPGE and Pd/Ir patterns downhole. Figure 11.43 shows sulphides occurring in patches and are interstitial to silicate minerals. Sulphides appear to show magmatic proportions that are typical of the Merensky Reef in the WBC (i.e., 50% Po, 30% Pent, 20% Cpy) (Barnes and Maier, 2002a). In addition, domains of sulphide free silicates are visible (orange circles). This suggests sulphides percolated downwards through a partially consolidated orthopyroxenite cumulate (Maier et al., 2019 In Press). In addition, the significant enrichment of sulphides in the uppermost sample of dolomitic floor rock in drill core UMT094 (5864 ppm S) also supports a model of downward percolation of sulphides.
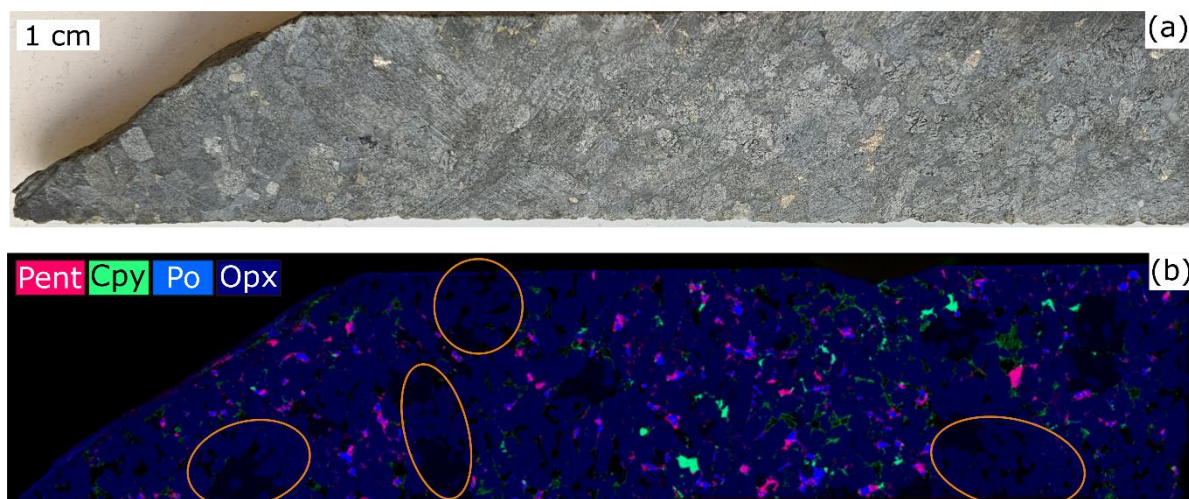
Figure 11.43: Images of the Merensky Reef from drill core TMT006 in the Flatreef. (a) Image of drill core showing medium-grained orthopyroxenite with visible sulphides. (b) False colour image of sulphide distribution through the Merensky Reef using microXRF element mapping (Barnes et al., 2017), orange circles denote patches where sulphides are absent. Modified after Maier et al. (2019 In Press).

11.4.3.3 Towards a model for the formation of Flatreef mineralization

Data presented in this thesis suggests that chalcophile element mineralization in the Flatreef formed from a combination of magmatic and hydrodynamic processes. Magmas emplaced into the Flatreef contained an immiscible sulphide component enriched in PGE. Sulphides were most likely entrained from a staging chamber, forming sulphide rich sills such as the Bastard Cyclic Unit, as supported by geochronological data and mass-balance calculations. A model of sill emplacement for the Bastard Reef implies that the PGE enrichment of this reef cannot be derived from a large volume of magma within a chamber forming the Flatreef. The intrusion of Flatreef magmas into the Transvaal Supergroup led to devolatization of calcareous sediments forming volatile rich fluids ascending through the Flatreef and triggering partial melting of cumulate rocks. This partial melting and recrystallisation formed pegmatoidal domains as well as facilitating the downward percolation of sulphides and thus redistributing mineralization throughout the Flatreef and resulting in the thick PGE rich intervals observed.

11.5 Implications for the Precambrian Atmosphere

The high level of calcareous sediment assimilation modelled for the Flatreef has potential implications for the Paleoproterozoic atmosphere. The period between 2.3-1.9 Ga saw significant change in the Precambrian atmosphere, including the Great Oxidation Event (GOE) at ~2.3 Ga (Holland, 2002; Lyons et al., 2014) and a change to deposition of organic carbon and phosphates. Among these is the termination of the Lomagundi-Jatuli event (LJE), a ~160-350 Myr positive $\delta^{13}C$ excursion (Karhu and Holland, 1996; Shields and Veizer, 2002) at around 2058 ± 2 Ma (Melezhik et al., 2007), and the onset of the Shunga Event (~2.05 Ga) (Hannah et al., 2008) which overlaps with the ages of the Bushveld Complex. The Shunga Event was a global event documented in America, Africa, Russia and Greenland. In northwest Russia, it was characterised by thick organic rich deposits covering 9,000 km^2 with a strongly negative $\delta^{13}C$ signature (down to -45‰), whose occurrence remains largely unexplained (Medvedev et al., 2009), although it has been suggested that such large amounts of organic material deposited contemporaneously around the world may represent a mass extinction event (Melezhik et al., 2003). With the end of the GOE at ~2.05 Ga proposed to represent a collapse in primary productivity (Hodgkiss et al., 2019). The remarkable overlap in ages of the end of the GOE, the LJE, the Shunga Event and the emplacement of the Bushveld Complex suggests a potential connection between them. Certainly, other large magmatic events have been related to mass extinction events, such as the Permian mass extinction and the formation of the Siberian Traps large igneous province, during which metamorphism of shale and evaporites added significant greenhouse gasses (>$1x10^6$ Gt CO_2) to the atmosphere, driving global warming and consequent mass extinction (Svensen et al., 2009). Svensen et al. (2007; 2009) also attribute global warming of the Triassic-Jurassic and the Toarcian to volcanism and consequent metamorphism of the sedimentary units they intrude.

The assimilation of large volumes of calcareous sediments in the Flatreef may have resulted in significant addition of CO_2 to the Paleoproterozoic atmosphere. The solubility of CO_2 within tholeiitic basalts is low, around 0.15% at 3 kbars (Shishkina et al., 2010) representing the suggested depth of emplacement for the Bushveld Complex (Cawthorn and Davies, 1983), and therefore most (99.85%) CO_2 produced from the calcareous sediments will form immiscible bubbles and ultimately be released into the atmosphere.
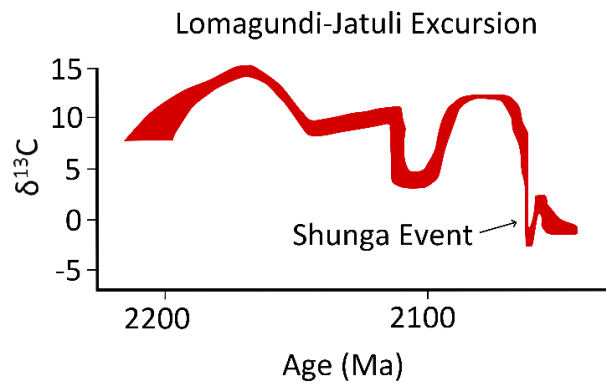
Figure 11.44: Graph of the positive $\delta^{13}C$ Lomagundi-Jatuli excursion and its rapid termination at the Shunga Event (2050 Ma). Modified after Melezhik et al. (2015).

The Flatreef deposit is on the order of 200-300 m thick and appears to extend to at least the farm Akanani (Mitchell and Scoon, 2012). The up-dip extension of the Flatreef, namely the Platreef can be traced along most of the length of the northern limb (Grobler et al., 2018). Geophysical data suggest that the northern limb extends for at least 160 km to the west of the outcropping northern limb, with a N-S length of 125 km (Finn et al., 2015). This gives a total Platreef/Flatreef volume of approximately 5,000 km^3. If all magmas experienced 18% contamination by calcareous sediments, then 900 km^3 of calcareous sediments was assimilated. Using a dolomite density of 2.83 g/cm^3 and a molecular weight of 47.7% CO_2 in dolomite, this gives a total value of 1.215x10^{15} kg (1,215 Gt) of CO_2, of which 99.85% is assumed to be released into the atmosphere (using CO_2 solubility in basalt of 0.15%). Thus, 1,213 Gt of CO_2 was released into the Precambrian atmosphere from direct assimilation of dolomite in the Flatreef and Platreef. This is equivalent to 1.2% of that released from the Siberian traps and associated country rock assimilation and metamorphism (>100,000 Gt CO_2) (Svensen et al., 2009).

Determining the atmospheric conditions of the Paleoproterozoic earth is somewhat trickier. Kaufman and Xiao (2003) suggest CO_2 levels were at least 20 times greater than present atmospheric levels (PAL) and thus a concentration of ~0.8% CO_2 (assuming ~400 ppm PAL), overlapping with estimates of Sheldon (2006). Using present day atmospheric mass (5.1x10^{18} kg) (Williams, 2019) gives an estimate of the total mass of CO_2 in the Precambrian atmosphere of 4.08x10^{16} kg or 4.08x10^4 Gt. The CO_2 contribution of assimilated Flatreef calcareous sediments to this Paleoproterozoic atmosphere is ~3%.

This may appear a small fraction of total carbon. However, to put it into a modern day context, the carbon contribution from assimilation in the Flatreef/Platreef alone is equivalent to ~33 years of current global CO_2 emissions from anthropogenic activity (37.1 Gt in 2018) (Le Quere et al., 2018). The calculated volume of CO_2 released represents the minimum CO_2 contribution from the Flatreef and ignores many other potentially significant carbon sources across the Bushveld Complex including; (1) assimilation of calcareous sediments by Lower Zone, Main

Zone and Upper Zone magmas in the northern limb, (2) assimilation of calcareous sediments underlying the remainder of the Bushveld Complex, (3) locally higher levels of assimilation such as in the 120 m thick Ti-rich olivine gabbro that saw up to ~59% dolomite assimilation, (4) devolatization in the wide contact metamorphic aureole of the northern limb (up to 18 km) (Frauenstein et al., 2009), (5) degassing of the magma releasing mantle derived CO_2 into the atmosphere from the entire Bushveld Complex (up to 1 million km^3 magma) (Cawthorn and Walraven, 1998), (6) Devolatization of calcareous sediments in the metamorphic aureole of the whole Bushveld Complex during which metamorphic reactions can produce significant volumes of CO_2 (Wallmach et al., 1989). Considering these factors, it is possible that the total CO_2 released following emplacement of the Bushveld Complex could be significantly larger than the amount calculated from Flatreef assimilation.

The potential mass extinction related to the Shunga Event is recorded by a large negative $\delta^{13}C$ excursion (Figure 11.44). While carbon in the Transvaal Supergroup calcareous sediments has negative $\delta^{13}C$ (as low as -6.26‰) the relatively small CO_2 contribution to the global budget estimated here is unlikely to have directly influenced the atmospheric $\delta^{13}C$ signature significantly (Frauenstein et al., 2009). However, the amount of carbon released into the atmosphere could potentially trigger feedback cycles and influence global climate.

While there is insufficient data and understanding of the Paleoproterozoic atmosphere to accurately calculate the contribution of CO_2 related to calcareous sediment assimilation in the Flatreef, these calculations highlight the potential importance of calcareous sediment devolatization in the Bushveld Complex on the wider Precambrian atmosphere. While unlikely to have single-handedly produced the negative $\delta^{13}C$ event of the Shunga Event, it's contribution may have triggered other processes and cycles operating in the Paleoproterozoic environment.

11.6 Summary: Petrogenetic model for the Flatreef

In the preceding sections key processes of magma emplacement, crustal contamination and mineralization that were instrumental to the formation of the Flatreef have been discussed. In the following section, a comprehensive genetic model for the Flatreef is proposed that accounts for the contamination and mineralization patterns presented in this study:

- Lower Zone material intruded into the Transvaal Supergroup, heating and metamorphosing the country rocks.
- The Ti-rich olivine gabbro was intruded as a sill into hot calcareous sediments causing a large degree of assimilation. The addition of calcareous sediments and volatiles (mainly CO_2 as well as H_2O, the latter possibly contributed from shale interlayers) to the magma significantly increased the fO_2 of the magma triggering ilmenite and

magnetite crystallisation. Any sulphur present was largely oxidized to sulphate which was then lost as a volatile phase.

- The FAZ rocks are intruded shortly thereafter into hot, partially devolatized calcareous sediments with resultant intermingling and mixing of calcareous sediments, calc-silicate and magma.

- Next, the Upper Flatreef and Lower Main Zone were intruded, firstly the Merensky Reef, then the Main Zone followed by the UG2 and finally the Bastard Cyclic Unit. With the exception of the Main Zone magma, these magmas contained entrained sulphides. These magmas all intruded into partially devolatized calcareous sediments and assimilated on average 18% calcareous sediments upon intrusion.

- Continued degassing of calcareous sediments formed vapour bubbles which possibly redistributed sulphide melt through the Flatreef or supressed crystallisation maintaining an interstitial melt through which sulphides could percolate downwards.

- Delayed partial melting of the basement granite released melts that pass largely undisturbed through the relatively consolidated Lower Flatreef but interacted with more molten Upper Flatreef.

Chapter 12 - Conclusions

This study has focussed on the Flatreef deposit in the northern limb of the Bushveld Complex. The two drill cores, UMT081 and UMT094, are amongst the deepest in the Flatreef and intersect lithologies not previously documented. The drill cores have been characterised in terms of their stratigraphy, petrography, mineral composition, geochemistry, PGE mineralization, radiogenic and stable isotope systems and zircon geochronology.

Based on the combined data accumulated, the Flatreef has been sub-divided into 2 sections. The Upper Flatreef is largely comprised of cyclic units dominated by orthopyroxenite with increasing abundance of feldspathic rocks (norite and anorthosite) with height. These cyclic units can be broadly correlated across the property, although the thickness and mineral composition of individual layers varies along strike and down-dip. The Lower Flatreef shows evidence for strong contamination of intruding magmas with sedimentary rocks of the Transvaal Supergroup, namely calcareous sediments. This has given rise to the Footwall Assimilation Zone (FAZ) characterised by numerous calc-silicate xenoliths as well as sills of exotic lithologies intruded into dolomitic floor rocks such as wehrlite. A further sill, intersected near the base of the Flatreef sequence in drill core UMT081, consists of the Ti-rich olivine gabbro, a rock type that has not been previously documented in the Flatreef and likely represents strongly contaminated UZ magmas. The deepest lithology intersected in drill core UMT081 (>1820 m depth) is olivine mela-gabbronorite.

Comparisons of stratigraphy, geochemistry, mineral composition, PGE mineralization and isotopic data show that the Flatreef is likely a less strongly contaminated down-dip extension of the Platreef in the northern limb. The latter has experienced significant interaction with various country rocks, disrupting magmatic layering. This has led many previous workers to reject a correlation of the Platreef to the UCZ of the western and eastern limbs.

However, in the present study, a new unified stratigraphic model has been proposed for the Flatreef. This model proposes that Flatreef layers can be correlated to stratigraphic packages of the UCZ in the remainder of the Bushveld Complex. In particular, the PGE-rich and chromite rich reefs of the Flatreef, originally termed the Upper PGE Reef, Main PGE Reef and Main Chromitite Reef have been shown to be correlative to the Bastard Reef, Merensky Reef and UG2 chromitite of the western and eastern Bushveld Complex, building on work done by Yudovskaya et al. (2017b) and Grobler et al. (2018).

Analysis of multiple isotope systems, namely Sm-Nd, O and Mg as well as Rb-Sr, U-Pb and Th-Pb, throughout a single drill core has enabled detailed modelling of the Flatreef rocks and

assessment of the relative contributions of calcareous sediments, granite and shale contaminants to the Flatreef. It is estimated that the Flatreef magmas were contaminated by ~18% calcareous sediments of the Duitschland Formation, most likely during final emplacement. The heat flux from continued intrusion of magma into the Flatreef eventually caused partial melting of the granitic basement beneath the Transvaal sediments as well as shales within the Transvaal Supergroup. Partial melts passed through the relatively consolidated Lower Flatreef and interacted with the incompletely consolidated upper portions of the Flatreef.

This study has provided constraints on the emplacement style and processes forming the magmatic layering and mineralization observed across the deposit. U-Pb dating of individual zircon grains has provided high precision ages for four zones of the Flatreef in the northern limb, namely the MZ, Bastard Reef, Merensky Reef, UG2 Reef. In addition, a sample of Merensky Reef at Northam Mine in the WBC was also dated. A key finding is the identification of protracted crystallisation ages for the Merensky Reef in both the western and northern limbs which have been interpreted to represent a sustained melt component. Most importantly the data suggests that magmatic layering in the Flatreef did not form sequentially from the bottom up. In the Flatreef U-Pb zircon geochronology dates show that Merensky Reef was the first of the analysed units to be emplaced into the Flatreef, shortly followed by Main Zone, both of which have protracted zircon ages. Below the Merensky Reef a younger intrusion of UG2 is emplaced before the final emplacement of Bastard Reef. In addition, the broad overlap in crystallisation ages between the Merensky Reef in the Flatreef and in the UCZ of the WBC implies these units were emplaced broadly contemporaneously and likely their protracted ages resulted from similar processes.

The geochronological data consequently support a model of Flatreef emplacement as a sill complex. This is supported by the presence of Lower Flatreef units emplaced into dolomitic floor rocks, namely the Ti-rich olivine gabbro and the olivine mela-gabbronorite, and fine-grained relatively uncontaminated orthopyroxenite sills injecting into the heavily contaminated FAZ rocks.

The origin of PGE mineralization in the Flatreef and the wider Platreef has remained unresolved. Geochronological data provides important constraints for Flatreef mineralization. For example, the rich PGE grades in the late-stage Bastard Reef sill indicates that sulphides could not have segregated from magma mixing, or percolate downwards from the unmineralized Main Zone. This suggests magmas entrained sulphides prior to emplacement, likely from a staging chamber. The significant mineralization beneath the Merensky Reef most likely reflects downward percolation of sulphides.

The timing of Bushveld Complex magmatism coincides with the end of the Lomagundi-Jatuli event and deposition of thick carbonaceous deposits forming the Shunga Event. These carbonaceous deposits have been suggested to reflect a mass extinction event. Consequently, the magmatic events pertaining to the Bushveld Complex and consequent devolatization of large volumes of sediments surrounding the intrusion could have played a pivotal role in the perturbations of the Precambrian atmosphere. As the Flatreef is postulated to extend for up to 160 km west and 125 km, the estimated volumes of CO_2 released into the atmosphere due to assimilation of calcareous sediments alone is 1213 Gt, which is fairly moderate in comparison to some more recent large igneous provinces.

References

Andersen, M. B., Vance, D., Morford, J. L., Bura-Nakic, E., Breitenbach, S. F. M., and Och, L., 2016, Closing in on the marine ^{238}U/^{235}U budget: Chemical Geology, v. 420, p. 11-22.

Armitage, P. E. B., McDonald, I., Edwards, S. J., and Manby, G. M., 2002, Platinum-group element mineralization in the Platreef and calc-silicate footwall at Sandsloot, Potgietersrus District, South Africa: Transactions of the Institution of Mining and Metallurgy Section B-Applied Earth Science, v. 111, p. B36-B45.

Arndt, N., Jenner, G., Ohnenstetter, M., Deloule, E., and Wilson, A. H., 2005, Trace elements in the Merensky Reef and adjacent norites Bushveld Complex South Africa: Mineralium Deposita, v. 40, p. 550-575.

Ashwal, L. D., Webb, S. J., and Knoper, M. W., 2005, Magmatic stratigraphy in the Bushveld Northern Lobe: continuous geophysical and mineralogical data from the 2950 m Bellevue drillcore: South African Journal of Geology, v. 108, p. 199-232.

Barnes, S.-J., and Maier, W. D., 1999, The fractionation of Ni, Cu and the Noble Metals in Silicate and Sulfide Liquids., Geological Association of Canada, Short Course Volume.

Barnes, S.-J., and Maier, W. D., 2002a, Platinum-group element distributions on the Rustenburg Layered Suite of the Bushveld Complex, South Africa, *in* Cabris, L., ed., The geology, geochemistry, mineralogy and mineral benefication of the platinum group elements., 54, CIM Special Volume, p. 431-458.

Barnes, S. J., Le Vaillant, M., and Lightfoot, P. C., 2017, Textural development in sulfide-matrix ore breccias in the Voisey's Bay Ni-Cu-Co deposit, Labrador, Canada: Ore Geology Reviews, v. 90, p. 414-438.

Barnes, S. J., and Maier, W. D., 2002b, Platinum-group elements and microstructures of normal Merensky Reef from Impala Platinum Mines, Bushveld Complex: Journal of Petrology, v. 43, p. 103-128.

Barnes, S. J., Maier, W. D., and Ashwal, L. D., 2004, Platinum-group element distribution in the main zone and upper zone of the Bushveld Complex, South Africa: Chemical Geology, v. 208, p. 293-317.

Barnes, S. J., Maier, W. D., and Curl, E. A., 2010, Composition of the Marginal Rocks and Sills of the Rustenburg Layered Suite, Bushveld Complex, South Africa: Implications for the Formation of the Platinum-Group Element Deposits: Economic Geology, v. 105, p. 1491-1511.

References

Barton, J. M., Barton, E. S., and Kroner, A., 1999, Age and isotopic evidence for the origin of the Archaean granitoid intrusives of the Johannesburg Dome, South Africa: Journal of African Earth Sciences, v. 28, p. 693-702.

Barton, J. M., Cawthorn, R. G., and White, J., 1986, The role of contamination in the evolution of the Platreef of the Bushveld Complex: Economic Geology, v. 81, p. 1096-1104.

Barton, J. M. J., Doig, R., Smith, C. B., Bohlender, F., and van Reenen, D. D., 1992, Isotopic and REE characteristics of the intrusive charnoenderbite and enderbite geographically associated with the Matok Pluton, Limpopo Belt, southern Africa: Precambrian Research, v. 55, p. 451-467.

Bedard, L. P., Savard, D., and Barnes, S. J., 2008, Total sulfur concentration in geological reference materials by elemental infrared analyser: Geostandards and Geoanalytical Research, v. 32, p. 203-208.

Bekker, A., Kaufman, A. J., Karhu, J. A., Beukes, N. J., Swart, Q. D., Coetzee, L. L., and Eriksson, K. A., 2001, Chemostratigraphy of the paleoproterozoic Duitschland Formation, South Africa: Implications for coupled climate change and carbon cycling: American Journal of Science, v. 301, p. 261-285.

Beukes, N. J., 1987, Facies relations, depositional environments and diagenesis in a major early proterozoic stromatolitic carbonate platform to basinal sequence, Campbellrand subgroup, Transvaal Supergroup, Southern Africa: Sedimentary Geology, v. 54, p. 1-46.

Beukes, N. J., Klein, C., Kaufman, A. J., and Hayes, J. M., 1990, Carbonate Petrography, Kerogen Distribution, and Carbon and Oxygen Isotope Variations in an Early Proterozoic Transition from the Limestone to Iron-Formation Deposition, Transvaal Supergroup, South Africa.: Economic Geology, v. 85, p. 663-690.

Boudreau, A. E., 2008, Modeling the Merensky Reef, Bushveld Complex, Republic of South Africa: Contributions to Mineralogy and Petrology, v. 156, p. 431-437.

Boudreau, A. E., 2016, The Stillwater Complex, Montana - Overview and the significance of volatiles: Mineralogical Magazine, v. 80, p. 585-637.

Boudreua, A.E., 2019, Hydromagmatic Processes and Platinum-Group Element Deposits in Layered Intrusions: Cambridge. Cambridge University Press.

Boudreau, A. E., and McCallum, I. S., 1992, Concentration of Platinum-Group Elements by Magmatic Fluids in Layered Intrusions: Economic Geology and the Bulletin of the Society of Economic Geologists, v. 87, p. 1830-1848.

Bowring, J. F., McLean, N. M., and Bowring, S. A., 2011, Engineering cyber infrastructure for U-Pb geochronology: Tripoli and U-Pb_Redux: Geochemistry Geophysics Geosystems, v. 12.

References

Brenan, J. M., McDonough, W. F., and Dalpe, C., 2003, Experimental constraints on the partitioning of rhenium and some platinum-group elements between olivine and silicate melt: Earth and Planetary Science Letters, v. 212, p. 135-150.

Brynard, H. J., de Villiers, J. P. R., and Viljoen, E. A., 1976, A Mineralogical Investigation of the Merensky Reef at the Western Platinum Mine, near Marikana, South Africa: Economic Geology, v. 71, p. 1299-1307.

Buchanan, D. L., Nolan, J., Suddaby, P., Rouse, J. E., Viljoen, M. J., and Davenport, J. W. J., 1981, The genesis of sulfide mineralization in a portion of the Potgietersrus limb of the Bushveld Complex: Economic Geology, v. 76, p. 568-579.

Buchanan, D. L., and Rouse, J. E., 1984, Role of contamination int he precipitation of sulfides in the Platreef of the Bushveld Complex, *in* Buchanan, D. L., and Jones, M. J., eds., Sulfide deposits in mafic and ultramafic rocks, London Institute of Mining and Metallurgy, p. 141-146.

Button, A., 1973, The stratigraphic history of the Malmani dolomite in the Eastern and North-Eastern Transvaal: Transactions of the Geological Society of South Africa, v. 76, p. 229-247.

Button, A., and Cawthorn, R. G., 2015, Distribution of mafic sills in the Transvaal Supergroup, northeastern South Africa: Journal of the Geological Society, v. 172, p. 357-367.

Cameron, E. N., 1978, Lower Zone of Eastern Bushveld Complex in Olifants river trough: Journal of Petrology, v. 19, p. 437-462.

Cameron, E. N., 1980, Evolution of the Lower Critical Zone, Central sector, Eastern Bushveld Complex, and its chromite deposits: Economic Geology, v. 75, p. 845-871.

Cameron, E. N., 1982, The upper Critical Zone of the Eastern Bushveld Complex - Precursor of the Merensky Reef: Economic Geology, v. 77, p. 1307-1327.

Campbell, I. H., and Naldrett, A. J., 1979, Influence of silicate-sulfide ratios on the geochemistry of magmatic sulfides: Economic Geology, v. 74, p. 1503-1506.

Cashman, K. V., Sparks, R. S. J., and Blundy, J. D., 2017, Volcanology Vertically extensive and unstable magmatic systems: A unified view of igneous processes: Science, v. 355.

Cawthorn, R. G., 1996, Models for incompatible trace-element abundances in cumulus minerals and their application to plagioclase and pyroxenes in the Bushveld Complex: Contributions to Mineralogy and Petrology, v. 123, p. 109-115.

Cawthorn, R. G., 1999a, Platinum-group element mineralization in the Bushveld Complex - a critical reassessment of geochemical models: South African Journal of Geology, v. 102, p. 268-281.

Cawthorn, R. G., 1999b, The discovery of the platiniferous Merensky Reef in 1924: South African Journal of Geology, v. 102, p. 178-183.

Cawthorn, R. G., 2002, The role of magma mixing in the genesis of PGE mineralization in the Bushveld Complex: Thermodynamic calculations and new interpretations - A discussion: Economic Geology and the Bulletin of the Society of Economic Geologists, v. 97, p. 663-666.

Cawthorn, R. G., 2005, Pressure fluctuations and the formation of the PGE-rich Merensky and chromitite reefs, Bushveld Complex: Mineralium Deposita, v. 40, p. 231-235.

Cawthorn, R. G., and Ashwal, L. D., 2009, Origin of Anorthosite and Magnetitite Layers in the Bushveld Complex, Constrained by Major Element Compositions of Plagioclase: Journal of Petrology, v. 50, p. 1607-1637.

Cawthorn, R. G., Barton, J. M., and Viljoen, M. J., 1985, Interaction of floor rocks with the Platreef on Overysel, Potgietersrus, Northern Transvaal: Economic Geology, v. 80, p. 988-1006.

Cawthorn, R. G., Cooper, G. R. J., and Webb, S. J., 1998, Connectivity between the western and eastern limbs of the Bushveld Complex: South African Journal of Geology, v. 101, p. 291-298.

Cawthorn, R. G., and Davies, G., 1983, Experimental data at 3-kbars pressure on parental magma to the Bushveld Complex: Contributions to Mineralogy and Petrology, v. 83, p. 128-135.

Cawthorn, R. G., Davies, G., Clubleyarmstrong, A., and McCarthy, T. S., 1981, Sills associated with the Bushveld Complex, South Africa - An estimate of the parental magma composition: Lithos, v. 14, p. 1-15.

Cawthorn, R. G., Meyer, P. S., and Kruger, F. J., 1991, Major addition of magma at the pyroxenite marker in the Western Bushveld Complex, South-Africa: Journal of Petrology, v. 32, p. 739-763.

Cawthorn, R. G., and Walraven, F., 1998, Emplacement and crystallization time for the Bushveld Complex: Journal of Petrology, v. 39, p. 1669-1687.

Charlier, B.L.A., Ginibre, C., Morgan, D., Nowell, G.M., Pearson, D.G., Davidson, J.P., Ottley, C.J., 2006, Methods for the microsampling and high-precision analysis of strontium and rubidium isotopes at single crystal scale for petrological and geochronological applications: Chemical Geology, v. 232, p. 114-133.

Cheney, E. S., and Twist, D., 1991, The conformable emplacement of the Bushveld mafic rocks along a regional unconformity in the Transvaal succession of South-Africa: Precambrian Research, v. 52, p. 115-132.

Cheng, H., Adkins, J., Edwards, R. L., and Boyle, E. A., 2000, U-Th dating of deep-sea corals: Geochimica Et Cosmochimica Acta, v. 64, p. 2401-2416.

Clarke, B., Uken, R., and Reinhardt, J., 2009, Structural and compositional constraints on the emplacement of the Bushveld Complex, South Africa: Lithos, v. 111, p. 21-36.

Clayton, R. N., and Mayeda, T. K., 1963, The use of bromine pentafluoride in the extraction of oxygen from oxides and silicates for isotopic analysis: Geochimica Et Cosmochimica Acta, v. 27, p. 43-52.

Clendenin, C. W., Henry, G., and Charlesworth, E. G., 1991, Characteristics of and influences on the Black Reef depositional sequence in the eastern Transvaal: South African Journal of Geology, v. 94, p. 321-327.

Cole, J., 2018, Three dimensional geometry of the Bushveld Complex derived from potential field modelling, University of Witswatersrand, 210 p.

Cole, J., Webb, S. J., and Finn, C. A., 2014, Gravity models of the Bushveld Complex - Have we come full circle?: Journal of African Earth Sciences, v. 92, p. 97-118.

Condon, D. J., Schoene, B., McLean, N. M., Bowring, S. A., and Parrish, R. R., 2015, Metrology and traceability of U-Pb isotope dilution geochronology (EARTHTIME Tracer Calibration Part I): Geochimica Et Cosmochimica Acta, v. 164, p. 464-480.

Cousins, C. A., 1959, The structure of the mafic portion of the Bushveld Igneous Complex: South African Journal of Geology, v. 62, p. 179-201.

Cousins, C. A., and Feringa, G., 1964, The Chromite Deposits of the Western Belt of the Bushveld Complex, in Haughton, S. H., ed., The geology of some ore deposits in Southern Africa, vol II: Johannesburg, Geological Society of South Africa, p. 183-202.

Cox, K.G., Bell, J.D., Pankhurst, R.J., 1979, The interpretation of igenous rocks: London, Allen and Unwin.

Curl, E. A., 2001, Parental magmas of the Bushveld Complex, South Africa, Monash University, 140 p.

Davies, G., Cawthorn, R. G., Barton, J. M., and Morton, M., 1980, Parental magma to the Bushveld Complex: Nature, v. 287, p. 33-35.

De Klerk, W. J., 1992, Petrogenesis of the Upper Critical zone in the western Bushveld Complex, with emphasis on the UG1 Footwall and Bastard units., Rhodes University, South Africa, 294 p p.

De Waal, S. A., 1977, Carbon Dioxide and Water from Metamorphic Reactions as Agents for Sulphide and Spinel Precipitation in Mafic Magmas: Transactions of the Geological Society of South Africa, v. 80, p. 193-196.

Du Plessis, A., and Kleywegt, R. J., 1987, A dipping sheet model for the mafic lobes of the Bushveld Complex: South African Journal of Geology, v. 90, p. 1-6.

du Toit, A. L., 1954, The Geology of South Africa: London, Oliver and Boyd.

Eales, H. V., and Cawthorn, R. G., 1996, The Bushveld Complex, in Cawthorn, R. G., ed., Layered Intrusions, Elsevier.

References

Eales, H. V., Deklerk, W. J., Butcher, A. R., and Kruger, F. J., 1990, The cyclic unit beneath the UG1 chromitite (UG1FW Unit) at RPM Union section platinum mine - rosetta stone of the Bushveld Upper Critical Zone: Mineralogical Magazine, v. 54, p. 23-43.

Eales, H. V., Field, M., Deklerk, W. J., and Scoon, R. N., 1988, regional trends of chemical variation and thermal erosion in the Upper Critical Zone, Western Bushveld Complex: Mineralogical Magazine, v. 52, p. 63-79.

Eales, H. V., Marsh, J. S., Mitchell, A. A., Deklerk, W. J., Kruger, F. J., and Field, M., 1986, Some geochemical constraints upon models for the crystallization of the Upper Critical Zone Main Zone interval, Northwestern Bushveld Complex: Mineralogical Magazine, v. 50, p. 567-582.

Engelbrecht, J. P., 1985, The Chromites of the Bushveld Complex in the Nietverdiend Area: Economic Geology, v. 80, p. 896-910.

Eriksson, K. A., and Truswell, J. F., 1974, Stratotypes from the Malmani Subgroup north-west of Johannesburg, South Africa: Transactions of the Geological Society of South Africa, v. 77, p. 211-222.

Eriksson, P. G., Altermann, W., Catuneanu, O., van der Merwe, R., and Bumby, A. J., 2001, Major influences on the evolution of the 2.67-2.1 Ga Transvaal basin, Kaapvaal craton: Sedimentary Geology, v. 141, p. 205-231.

Eriksson, P. G., Schweitzer, J. K., Bosch, P. J. A., Schereiber, U. M., Vandeventer, J. L., and Hatton, C. J., 1993, The Transvaal Sequence - An Overview: Journal of African Earth Sciences, v. 16, p. 25-51.

Eroglu, S., Schoenberg, R., Wille, M., Beukes, N., and Taubald, H., 2015, Geochemical stratigraphy, sedimentology, and Mo isotope systematics of the ca. 2.58-2.50 Ga-old Transvaal Supergroup carbonate platform, South Africa: Precambrian Research, v. 266, p. 27-46.

Finn, C. A., Bedrosian, P. A., Cole, J. C., Khoza, T. D., and Webb, S. J., 2015, Mapping the 3D extent of the Northern Lobe of the Bushveld layered mafic intrusion from geophysical data: Precambrian Research, v. 268, p. 279-294.

Forien, M., Tremblay, J., Barnes, S. J., Burgisser, A., and Page, P., 2015, The Role of Viscous Particle Segregation in Forming Chromite Layers from Slumped Crystal Slurries: Insights from Analogue Experiments: Journal of Petrology, v. 56, p. 2425-2444.

Frauenstein, F., Veizer, J., Beukes, N., Van Niekerk, H. S., and Coetzee, L. L., 2009, Transvaal Supergroup carbonates: Implications for Paleoproterozoic delta O-18 and delta C-13 records: Precambrian Research, v. 175, p. 149-160.

Gain, S. B., 1985, The geologic setting of the platiniferous UG2-chromitite layer on the farm Maandagshoek, Eastern Bushveld Complex: Economic Geology, v. 80, p. 925-943.

References

Gain, S. B., and Mostert, A. B., 1982, The geological setting of the platinoid and base-metal sulfide mineralization in the Platreef of the Bushveld Complex in Drenthe, north of Potgietersrus: Economic Geology, v. 77, p. 1395-1404.

Galy, A., Yoffe, O., Janney, P.E., Williams, R.W., Cloquet, C., Alard, O., Halicz, L., Wadhwa, M., Hutcheon, I.D., Ramon, E., Carignan, J., 2003, Magnesium isotope heterogeneity of the isotopic standard SRM980 and new reference materials for magnesium-isotope-ratio measurements: Journal of Analytical Atomic Spectrometry, v. 18, p. 1352-1356.

Gerstenberger, H., and Haase, G., 1997, A highly effective emitter substance for mass spectrometric Pb isotope ratio determinations: Chemical Geology, v. 136, p. 309-312.

Geske, A., Zorlu, J., Richter, D. K., Buhl, D., Niedermayr, A., and Immenhauser, A., 2012, Impact of diagenesis and low grade metamorphism on isotope (delta(26)mg, delta C-13, delta O-18 and Sr-87/Sr-86) and elemental (Ca, Mg, Mn, Fe and Sr) signatures of Triassic sabkha dolomites: Chemical Geology, v. 332, p. 45-64.

Ghiorso, M. S., and Gualda, G. A. R., 2015, An H2O-CO2 mixed fluid saturation model compatible with rhyolite-MELTS: Contributions to Mineralogy and Petrology, v. 169.

Godel, B., Barnes, S. J., and Maier, W. D., 2011, Parental magma composition inferred from trace element in cumulus and intercumulus silicate minerals: An example from the Lower and Lower Critical Zones of the Bushveld Complex, South-Africa: Lithos, v. 125, p. 537-552.

Good, N., and DeWit, M. J., 1997, The Thabazimbi-Murchison Lineament of the Kaapvaal Craton, South Africa: 2700 Ma of episodic deformation: Journal of the Geological Society, v. 154, p. 93-97.

Grobler, D. F., Brits, J. A. N., Maier, W. D., and Crossingham, A., 2018, Litho- and chemostratigraphy of the Flatreef PGE deposit, northern Bushveld Complex, Mineralium Deposita.

Gualda, G. A. R., Ghiorso, M. S., Lemons, R. V., and Carley, T. L., 2012, Rhyolite-MELTS: a Modified Calibration of MELTS Optimized for Silica-rich, Fluid-bearing Magmatic Systems: Journal of Petrology, v. 53, p. 875-890.

Hall, A. L., 1932a, The Bushveld Igneous Complex of the Central Transvaal: Geological Survey of the Union of South Africa, v. Memoir No. 28.

Hall, A. L., 1932b, The Bushveld Igneous Complex of the Central Transvaal: Pretoria, Geological Survey of the Union of South Africa.

Hamilton, J., 1977, Sr isotope and trace-element studies of Great Dyke and Bushveld Mafic phase and their relation to early Proterozoic magma genesis in Southern-Africa: Journal of Petrology, v. 18, p. 24-52.

Hannah, J. L., Stein, H. J., Zimmerman, A., Yang, G., Melezhik, V. A., Filippov, M. M., Turgeon, S. C., and Creaser, R. A., 2008, Re-Os geochronology of shungite: A 2.05 Ga fossil

References

oil field in Karelia: Goldschmidt Conference Abstracts Geochemica et Cosmochimica Acta.

Harmer, R. E., Auret, J. M., and Eglington, B. M., 1995, Lead isotope variations within the Bushveld complex, Southern Africa: A reconnaissance study: Journal of African Earth Sciences, v. 21, p. 595-606.

Harris, C., and Chaumba, J. B., 2001, Crustal contamination and fluid-rock interaction during the formation of the Platreef northern limb of the Bushveld complex, South Africa: Journal of Petrology, v. 42, p. 1321-1347.

Harris, C., Pronost, J., Ashwal, L. D., and Cawthorn, R. G., 2005, Oxygen and Hydrogen Isotope Stratigraphy of the Rustenburg Layered Suite, Bushveld Complex: Constraints on Crustal Contamination: Journal of Petrology, v. 46, p. 579-601.

Hayes, B., Ashwal, L. D., Webb, S. J., and Bybee, G. M., 2017, Large-scale magmatic layering in the Main Zone of the Bushveld Complex and episodic downward magma infiltration: Contributions to Mineralogy and Petrology, v. 172.

Henderson, D. R., Long, L. E., and Barton, J. M. J., 2000, Isotopic ages and chemical and isotopic composition of the Archaean Turfloop Batholith, Pietersburg granite-greenstone terrange, Kaapvaal Craton, South Africa: South African Journal of Geology, v. 103, p. 38-46.

Hiemstra, S. A., 1985, The distribution of some Platinum-Group Elements in the UG-2 Chromitite Layer of the Bushveld Complex: Economic Geology, v. 80, p. 944-957.

Hiess, J., Condon, D. J., McLean, N., and Noble, S. R., 2012, 238U/235U Systematics in terrestrial uranium-bearing minerals: Science, v. 335, p. 1610-1614.

Hodgkiss, M. S. W., Crockford, P. W., Peng, Y., Wing, B. A., and Horner, T. J., 2019, A productivity collapse to end Earth's Great Oxidation: PNAS, v. 116, p. 17207-17212.

Holland, H. D., 2002, Volcanic gases, black smokers, and the Great Oxidation Event: Geochimica Et Cosmochimica Acta, v. 66, p. 3811-3826.

Holness, M. B., Cawthorn, R. G., and Roberts, J., 2017, The thickness of the crystal mush on the floor of the Bushveld magma chamber: Contributions to Mineralogy and Petrology, v. 172.

Holwell, D. A., Armitage, P. E. B., and McDonald, I., 2005, Observations on the relationship between the Platreef and its hangingwall: Applied Earth Science, v. 114, p. 199-207.

Holwell, D. A., Boyce, A. J., and McDonald, I., 2007, Sulfur isotope variations within the platreef Ni-Cu-PGE deposit: Genetic implications for the origin of sulfide mineralization: Economic Geology, v. 102, p. 1091-1110.

Holwell, D. A., and Jordaan, A., 2006, Three-dimensional mapping of the Platreef at the Zwartfontein South mine: implications for the timing of magmatic events in the northern limb of the Bushveld Complex, South Africa: Applied Earth Science, v. 115, p. 41-48.

References

Holwell, D. A., and McDonald, I., 2006, Petrology, geochemistry and the mechanisms determining the distribution of platinum-group element and base metal sulphide mineralisation in the Platreef at Overysel, northern Bushveld Complex, South Africa: Mineralium Deposita, v. 41, p. 575-598.

Holwell, D. A., and McDonald, I., 2007, Distribution of platinum-group elements in the Platreef at Overysel, northern Bushveld Complex: a combined PGM and LA-ICP-MS study: Contributions to Mineralogy and Petrology, v. 154, p. 171-190.

Holwell, D. A., McDonald, I., and Armitage, P. E. B., 2006, Platinum-group mineral assemblages in the Platreef at the Sandsloot Mine, northern Bushveld Complex, South Africa: Mineralogical Magazine, v. 70, p. 83-101.

Holzer, L., Frei, R., Barton, J. M., and Kramers, J. D., 1998, Unraveling the record of successive high grade events in the Central Zone of the Limpopo Belt using Pb single phase dating of metamorphic minerals: Precambrian Research, v. 87, p. 87-115.

Horwitz, E.P., Chiarizia, R., Deitz, M.L., 1992, A novel strontium-selective extraction chromatographic resin: Solvent Extraction and Ion Exchange, v. 10, p. 313-336.

Hulbert, L. J., and Vongruenewaldt, G., 1982, Nickel, copper, and platinum mineralization in the Lower Zone of the Bushveld Complex, south of Potgietersrus: Economic Geology, v. 77, p. 1296-1306.

Hulbert, L. J., and Vongruenewaldt, G., 1985, Textural and compositional features of chromite in the Lower and Critical Zones of the Bushveld Complex south of Potgietersrus: Economic Geology, v. 80, p. 872-895.

Hunter, D. R., and Hamilton, P. J., 1978, The Bushveld Complex, in Tarling, D. H., ed., Evolution of the Earth's Crust: London, Academic Press.

Hutchinson, D., and Kinnaird, J. A., 2005, Complex multistage genesis for the Ni–Cu–PGE mineralisation in the southern region of the Platreef, Bushveld Complex, South Africa: Applied Earth Science, v. 114, p. 208-224.

Huthmann, F. M., Yudovskaya, M. A., Frei, D., and Kinnaird, J. A., 2016, Geochronological evidence for an extension of the Northern Lobe of the Bushveld Complex, Limpopo Province, South Africa: Precambrian Research, v. 280, p. 61-75.

Irvine, T. N., 1982, Terminology for Layered Intrusions: Journal of Petrology, v. 23, p. 127-162.

Irvine, T. N., Andersen, J. C. O., and Brooks, C. K., 1998, Included blocks (and blocks within blocks) in the Skaergaard intrusion: Geologic relations and the origins of rhythmic modally graded layers: Geological Society of America Bulletin, v. 110, p. 1398-1447.

Irvine, T. N., Keith, D. W., and Todd, S. G., 1983, The J-M Platinum-Palladium Reef of the Stillwater Complex, Montana: II. Origin by Double-Diffusive Convective Magma Mixing and Implications for the Bushveld Complex: Economic Geology, v. 78, p. 1287-1334.

References

Ivanhoe Mines Ltd, unpublished.

Jahn, B. M., and Condie, K. C., 1995, Evolution of the Kaapvaal-craton as viewed from geochemical and Sm-Nd isotopic analyses of intracratonic pelites: Geochimica Et Cosmochimica Acta, v. 59, p. 2239-2258.

Jugo, P. J., 2009, Sulfur content at sulfide saturation in oxidized magmas: Geology, v. 37, p. 415-418.

Jugo, P. J., Luth, R. W., and Richards, J. P., 2005, Experimental data on the speciation of sulfur as a function of oxygen fugacity in basaltic melts: Geochimica Et Cosmochimica Acta, v. 69, p. 497-503.

Karhu, J. A., and Holland, H. D., 1996, Carbon isotopes and the rise of atmospheric oxygen: Geology, v. 24, p. 867-870.

Karykowski, B. T., and Maier, W. D., 2017, Microtextural characterisation of the Lower Zone in the western limb of the Bushveld Complex, South Africa: evidence for extensive melt migration within a sill complex: Contributions to Mineralogy and Petrology, v. 172.

Karykowski, B. T., Yang, S. H., Maier, W. D., Lahaye, Y., Lissenberg, C. J., and O'Brien, H., 2017, In situ Sr Isotope Compositions of Plagioclase from a Complete Stratigraphic Profile of the Bushveld Complex, South Africa: Evidence for Extensive Magma Mixing and Percolation: Journal of Petrology, v. 58, p. 2285-2308.

Kaufman, A. J., and Xiao, S. H., 2003, High CO_2 levels in the Proterozoic atmosphere estimated from analyses of individual microfossils: Nature, v. 425, p. 279-282.

Keir-Sage, E., Leybourne, M. I., Jugo, P. J., and Grobler, D. F., 2018, Sulphur isotope variations across the Platreef, northern limb of the Bushveld Igneous Complex, 13th International Platinum Symposium: Polokwane, South Africa.

Kinloch, E. D., 1982, Regional trends in the Platinum-Group Mineralogy of the Critical Zone of the Bushveld Complex, South-Africa: Economic Geology, v. 77, p. 1328-1347.

Kinloch, E. D., and Peyerl, W., 1990, Platinum-Group Minerals in Various Rock types of the Merensky Reef: Genetic Implications: Economic Geology, v. 85, p. 537-555.

Kinnaird, J. A., 2005, Geochemical evidence for multiphase emplacement in the southern Platreef: Applied Earth Science, v. 114, p. 225-242.

Kinnaird, J. A., Hutchinson, D., Schurmann, L., Nex, P. A. M., and de Lange, R., 2005, Petrology and mineralisation of the southern Platreef: northern limb of the Bushveld Complex, South Africa: Mineralium Deposita, v. 40, p. 576-597.

Kinnaird, J. A., and McDonald, I., 2005, An introduction to mineralisation in the northern limb of the Bushveld Complex: Applied Earth Science, v. 114, p. 194-198.

Kinnaird, J. A., and Nex, P., 2015, An overview of the Platreef, in Hammond, N. Q., and Hatton, C., eds., Platinum-group element (PGE) mineralisation and resources of the Bushveld Complex: Pretoria, South Africa, Council for Geoscience.

References

Kinnaird, J. A., Yudovskaya, M., McCreesh, M., Huthmann, F., and Botha, T. J., 2017, The Waterberg Platinum Group Elemeut Deposit: Atypical Miueralization Mafic-Ultramafic Rocks of the Bushveld Complex, South Africa: Economic Geology, v. 112, p. 1367-1394.

Klein, C., and Beukes, N. J., 1989, Geochemistry and sedimentology of a facies transition from limestone to iron-formation deposition in the early Proterozoic Transvaal Supergroup, South Africa.: Economic Geology, v. 84, p. 1733-1774.

Krogh, T. E., 1973, A low-contamination method for hydrothermal decomposition of zircon and extraction of U and Pb for isotopic age determinations: Geochimica et Cosmochimica Acta, v. 37, p. 485-494.

Kruger, F. J., 1994a, The Sr-isotopic stratigraphy of the western Bushveld Complex: South African Journal of Geology, v. 97, p. 393-398.

Kruger, F. J., 1994b, The Sr-isotopic stratigraphy of the western Bushveld Complex, 97: South African Journal of Geology, p. 393-398.

Kruger, F. J., 2005, Filling the Bushveld Complex magma chamber: lateral expansion, roof and floor interaction, magmatic unconformities, and the formation of giant chromitite, PGE and Ti-V-magnetitite deposits: Mineralium Deposita, v. 40, p. 451-472.

Kruger, F. J., Cawthorn, R. G., and Walsh, K. L., 1987, Strontium isotopic evidence against magma addition in the Upper Zone of the Bushveld Complex: Earth and Planetary Science Letters, v. 84, p. 51-58.

Kvadsheim, A., 2017, Origin and development of sulphide-bearing norites in the basal Platreef, Turfspruit Northern Bushveld., Cardiff University, 184 p.

Latypov, R., Chistyakova, S., Barnes, S. J., and Hunt, E. J., 2017a, Origin of Platinum Deposits in Layered Intrusions by In Situ Crystallization: Evidence from Undercutting Merensky Reef of the Bushveld Complex: Journal of Petrology, v. 58, p. 715-761.

Latypov, R., Chistyakova, S., and Kramers, J., 2017b, Arguments against syn-magmatic sills in the Bushveld Complex, South Africa: South African Journal of Geology, v. 120, p. 565-574.

Latypov, R., Chistyakova, S., Page, A., and Hornsey, R., 2015, Field Evidence for the In Situ Crystallization of the Merensky Reef: Journal of Petrology, v. 56, p. 2341-2372.

Le Quere, C., Andrew, R. M., Friedlingstein, P., Sitch, S., Hauck, J., Pongratz, J., Pickers, P. A., Korsbakken, J. I., Peters, G. P., Canadell, J. G., Arneth, A., Arora, V. K., Barbero, L., Bastos, A., Bopp, L., Chevallier, F., Chini, L. P., Ciais, P., Doney, S. C., Gkritzalis, T., Goll, D. S., Harris, I., Haverd, V., Hoffman, F. M., Hoppema, M., Houghton, R. A., Hurtt, G., Ilyina, T., Jain, A. K., Johannessen, T., Jones, C. D., Kato, E., Keeling, R. F., Goldewijk, K. K., Landschutzer, P., Lefevre, N., Lienert, S., Liu, Z., Lombardozzi, D., Metzl, N., Munro, D. R., Nabel, J., Nakaoka, S., Neill, C., Olsen, A., Ono, T., Patra, P.,

References

Peregon, A., Peters, W., Peylin, P., Pfeil, B., Pierrot, D., Poulter, B., Rehder, G., Resplandy, L., Robertson, E., Rocher, M., Rodenbeck, C., Schuster, U., Schwinger, J., Seferian, R., Skjelvan, I., Steinhoff, T., Sutton, A., Tans, P. P., Tian, H. Q., Tilbrook, B., Tubiello, F. N., van der Laan-Luijkx, I. T., van der Werf, G. R., Viovy, N., Walker, A. P., Wiltshire, A. J., Wright, R., Zaehle, S., and Zheng, B., 2018, Global Carbon Budget 2018: Earth System Science Data, v. 10, p. 2141-2194.

Lee, C. A., 1996, A Review of Mineralization in the Bushveld Complex and some other Layered Intrusions, *in* Cawthorn, R. G., ed., Layered Intrusions: Amsterdam, Elsevier, p. 103-145.

Lee, J. K. W., Williams, I. S., and Ellis, D. J., 1997, Pb, U and Th diffusion in natural zircon: Nature, v. 390, p. 159-162.

Letts, S., Torsvik, T. H., Webb, S. J., and Ashwal, L. D., 2009, Palaeomagnetism of the 2054 Ma Bushveld Complex (South Africa): implications for emplacement and cooling: Geophysical Journal International, v. 179, p. 850-872.

Li, C. S., Maier, W. D., and de Waal, S. A., 2001, The role of magma mixing in the genesis of PGE mineralization in the Bushveld Complex: Thermodynamic calculations and new interpretations: Economic Geology and the Bulletin of the Society of Economic Geologists, v. 96, p. 653-662.

Li, C. S., Maier, W. D., and de Waal, S. A., 2002, The role of magma mixing in the genesis of PGE mineralization in the Bushveld Complex: Thermodynamic calculations and new interpretations - A reply: Economic Geology and the Bulletin of the Society of Economic Geologists, v. 97, p. 667-667.

Li, C. S., and Ripley, E. M., 2005, Empirical equations to predict the sulfur content of mafic magmas at sulfide saturation and applications to magmatic sulfide deposits: Mineralium Deposita, v. 40, p. 218-230.

Li, W. Y., Teng, F. Z., Ke, S., Rudnick, R. L., Gao, S., Wu, F. Y., and Chappell, B. W., 2010, Heterogeneous magnesium isotopic composition of the upper continental crust: Geochimica Et Cosmochimica Acta, v. 74, p. 6867-6884.

Lyons, T. W., Reinhard, C. T., and Planavsky, N. J., 2014, The rise of oxygen in Earth's early ocean and atmosphere: Nature, v. 506, p. 307-315.

Maier, W. , 1995, Olivine Oikcrysts in Bushveld Anorthosite: Some Implications for Cumulate Formation: The Canadian Mineralogist, v33, p. 1011-1022.

Maier, W., and Barnes, S. J., 2008, Platinum-group elements in the UG1 and UG2 chromitites, and the Bastard reef, at Impala platinum mine, western Bushveld Complex, South Africa: Evidence for late magmatic cumulate instability and reef constitution: South African Journal of Geology, v. 111, p. 159-176.

References

Maier, W. D., 2005, Platinum-group element (PGE) deposits and occurrences: Mineralization styles, genetic concepts, and exploration criteria: Journal of African Earth Sciences, v. 41, p. 165-191.

Maier, W. D., Abernethy, K. E. L., Grobler, D. F., and Moorhead, G., 2019 In Press, Formation of the Merensky and Bastard reefs in the Flatreef deposit, northern Bushveld, by hydrodynamic and hydromagmatic processes.: Mineralium Deposita.

Maier, W. D., Arndt, N. T., and Curl, E. A., 2000, Progressive crustal contamination of the Bushveld Complex: evidence from Nd isotopic analyses of the cumulate rocks: Contributions to Mineralogy and Petrology, v. 140, p. 316-327.

Maier, W. D., and Barnes, J., 2004, Pt/Pd and Pd/Ir ratios in mantle-derived magmas: A possible role for mantle metasomatism: South African Journal of Geology, v. 107, p. 333-340.

Maier, W. D., Barnes, S.-J., and van der Merwe, M. J., 2001, Platinum-group elements in the Pyroxenite Marker, Bushveld Complex: implications for the formation of the Main Zone: South African Journal of Geology, v. 104, p. 301-308.

Maier, W. D., and Barnes, S. J., 1998, Concentrations of rare earth elements in silicate rocks of the Lower, Critical and Main Zones of the Bushveld Complex: Chemical Geology, v. 150, p. 85-103.

Maier, W. D., and Barnes, S. J., 1999, Platinum-group elements in silicate rocks of the Lower, Critical and Main Zones at union section, western Bushveld Complex: Journal of Petrology, v. 40, p. 1647-1671.

Maier, W. D., Barnes, S. J., DeKlerk, W. J., Teigler, B., and Mitchell, A. A., 1996, Cu/Pd and Cu/Pt of silicate rocks in the Bushveld complex: Implications for platinum-group element exploration: Economic Geology and the Bulletin of the Society of Economic Geologists, v. 91, p. 1151-1158.

Maier, W. D., Barnes, S. J., and Groves, D. I., 2013, The Bushveld Complex, South Africa: formation of platinum-palladium, chrome- and vanadium-rich layers via hydrodynamic sorting of a mobilized cumulate slurry in a large, relatively slowly cooling, subsiding magma chamber: Mineralium Deposita, v. 48, p. 1-56.

Maier, W. D., Barnes, S. J., and Karykowski, B. T., 2016a, A chilled margin of komatiite and Mg-rich basaltic andesite in the western Bushveld Complex, South Africa: Contributions to Mineralogy and Petrology, v. 171.

Maier, W. D., and Bowen, M. P., 1996, The UG2-Merensky Reef interval of the Bushveld complex northwest of Pretoria: Mineralium Deposita, v. 31, p. 386-393.

Maier, W. D., de Klerk, L., Blaine, J., Manyeruke, T., Barnes, S. J., Stevens, M. V. A., and Mavrogenes, J. A., 2008, Petrogenesis of contact-style PGE mineralization in the

References

northern lobe of the Bushveld Complex: comparison of data from the farms Rooipoort, Townlands, Drenthe and Nonnenwerth: Mineralium Deposita, v. 43, p. 255-280.

Maier, W. D., and Eales, H. V., 1994, Facies model for interval between UG2 and Merensky Reef, Western Bushveld Complex, South Africa: Transactions of the Institution of Mining and Metallurgy, v. 103, p. 22-30.

Maier, W. D., and Eales, H. V., 1997, Correlation within the UG2-Merensky Reef interval of the Western Bushveld Complex, based on geochemical, mineralogical and petrological data: Bulletin of the Geological Survey of South Africa, v. 120.

Maier, W. D., Karykowski, B. T., and Yang, S. H., 2016b, Formation of transgressive anorthosite seams in the Bushveld Complex via tectonically induced mobilisation of plagioclase-rich crystal mushes: Geoscience Frontiers, v. 7, p. 875-889.

Maier, W. D., and Teigler, B., 1995, A facies model for the western Bushveld Complex: Economic Geology and the Bulletin of the Society of Economic Geologists, v. 90, p. 2343-2349.

Manyeruke, T. D., 2007, Geochemical variation of the Platreef in the norhtern limb of the Bushveld Complex: Implications for the origin of the PGE mineralization, University of Pretoria.

Manyeruke, T. D., Maier, W. D., and Barnes, S. J., 2005, Major and trace element geochemistry of the Platreef on the farm Townlands, northern Bushveld Complex: South African Journal of Geology, v. 108, p. 381-396.

Marquis, E., 2015, Petrogenesis of the Harzburgitic to Troctolitic Units in the Turfspruit Cyclic Unit, Northern Bushveld Complex, South Africa, Cardiff University, 256 p.

Mathez, E. A., and Agrinier, P., unpublished, In: Harris et al., (2005) Oxygen and Hydrogen Isotope Stratigraphy of the Rustenburg Layered Suite, Bushveld Complex: Constraints on Crustal Contamination.

Mathez, E. A., Hunter, R. H., and Kinzler, R., 1997, Petrologic evolution of partially molten cumulate: the Atok section of the Bushveld Complex: Contributions to Mineralogy and Petrology, v. 129, p. 20-34.

Mathez, E. A., and Kent, A. J. R., 2007, Variable initial Pb isotopic compositions of rocks associated with the UG2 chromitite, eastern Bushveld Complex: Geochimica Et Cosmochimica Acta, v. 71, p. 5514-5527.

Mathez, E. A., and Mey, J. L., 2005, Character of the UG2 chromitite and host rocks and petrogellesis of its pegmatoidal footwall, northeastern Bushveld Complex: Economic Geology, v. 100, p. 1617-1630.

Mattinson, J. M., 2005, Zircon U-Pb chemical abrasion ("CA-TIMS") method: Combined annealing and multi-step partial dissolution analysis for improved precision and accuracy of zircon ages: Chemical Geology, v. 220, p. 47-66.

References

Mayer, C. C., Jugo, P. J., Leybourne, M. I., and Grobler, D. F., 2018, Strontium isotope stratigraphy across the Platreef and comparison with the rest of the Bushveld: Abstract Volume, 13th International Platinum Symposium, Polokwane.

McCoy-West, A.J., Millet, M.-A., Burton, K.W., 2017, The neodymium stable isotope composition of the silicate Earth and chondrites: Earth and Planetary Science Letters. v. 480, p. 121-132.

McDonald, I., Harmer, R. E., Holwell, D. A., Hughes, H. S. R., and Boyce, A. J., 2017, Cu-Ni-PGE mineralisation at the Aurora Project and potential for a new PGE province in the Northern Bushveld Main Zone: Ore Geology Reviews, v. 80, p. 1135-1159.

McDonald, I., and Holwell, D. A., 2007, Did lower zone magma conduits store PGE-rich sulphides that were later supplied to the Platreef?: South African Journal of Geology, v. 110, p. 611-616.

McDonald, I., and Holwell, D. A., 2011, Geology of the Northern Bushveld Complex and the Setting and Genesis of the Platreef Ni-Cu-PGE Deposit: Reviews in Economic Geology, v. 17, p. 713-722.

McDonald, I., Holwell, D. A., and Armitage, P. E. B., 2005, Geochemistry and mineralogy of the Platreef and "Critical Zone" of the northern lobe of the Bushveld Complex, South Africa: implications for Bushveld stratigraphy and the development of PGE mineralisation: Mineralium Deposita, v. 40, p. 526-549.

McDonough, W. F., and Sun, S. S., 1995, The composition of the Earth: Chemical Geology, v. 120, p. 223-253.

McLean, N. M., Bowring, J. F., and Bowring, S. A., 2011, An algorithm for U-Pb isotope dilution data reduction and uncertainty propagation: Geochemistry Geophysics Geosystems, v. 12.

McLean, N. M., Condon, D. J., Schoene, B., and Bowring, S. A., 2015, Evaluating uncertainties in the calibration of isotopic reference materials and multi-element isotopic tracers (EARTHTIME Tracer Calibration Part II): Geochimica Et Cosmochimica Acta, v. 164, p. 481-501.

Medvedev, P. V., Melezhik, V. A., and Filippov, M. M., 2009, Palaeoproterozoic Petrified Oil Field (Shunga Event): Paleontological Journal, v. 43, p. 972-979.

Melezhik, V. A., Fallick, A. E., Brasier, A. T., and Lepland, A., 2015, Carbonate deposition in the Palaeoproterozoic Onega basin from Fennoscandia: a spotlight on the transition from the Lomagundi-Jatuli to Shunga events: Earth-Science Reviews, v. 147, p. 65-98.

Melezhik, V. A., Filippov, M. M., and Romashkin, A. E., 2003, Shunga Event - Was it a case of Palaeoproterozoic mass extinction?: Goldschmidt Conference Abstracts, Geochemica et Cosmochimica Acta.

References

Melezhik, V. A., Huhma, H., Condon, D. J., Fallick, A. E., and Whitehouse, M. J., 2007, Temporal constraints on the Paleoproterozoic Lomagundi-Jatuli carbon isotopic event: Geology, v. 35, p. 655-658.

Mitchell, A. A., 1990, The stratigraphy, petrography and mineralogy of the Main Zone of the northwestern Bushveld Complex: South African Journal of Geology, v. 93, p. 818-831.

Mitchell, A. A., and Manthree, R., 2002, The giant mottled anorthosite: a transitional sequence at the top of the Upper Critical Zone of the Bushveld Complex: South African Journal of Geology, v. 105, p. 15-24.

Mitchell, A. A., and Scoon, R. N., 2012, The Platreef of the Bushveld Complex, South Africa: A new hypothesis of multiple, non-sequential magma replenishment based on observations at the Akanani project, north-west of Mokopane: South African Journal of Geology, v. 115, p. 535-550.

Molyneux, T. G., 1974, A Geological Investigation of the Bushveld Complex in Sekhukhuneland and part of the Steelpoort Valley: Transactions of the Geological Society of South Africa, v. 77, p. 329-338.

Mondal, S. K., and Mathez, E. A., 2007, Origin of the UG2 chromitite layer, Bushveld Complex: Journal of Petrology, v. 48, p. 495-510.

Mungall, J. E., Brenan, J. M., Godel, B., Barnes, S. J., and Gaillard, F., 2015, Transport of metals and sulphur in magmas by flotation of sulphide melt on vapour bubbles: Nature Geoscience, v. 8, p. 216-219.

Mungall, J. E., Kamo, S. L., and McQuade, S., 2016, U-Pb geochronology documents out-of-sequence emplacement of ultramafic layers in the Bushveld Igneous Complex of South Africa: Nature Communications, v. 7.

Naldrett, A. J., Gasparrini, E. C., Barnes, S. J., Vongruenewaldt, G., and Sharpe, M. R., 1986, The Upper Critical Zone of the Bushveld Complex and the origin of Merensky-type ores: Economic Geology, v. 81, p. 1105-1117.

Naldrett, A. J., and Von Gruenewaldt, G., 1989, Association of Platinum-Group Elements with Chromitite in Layered Intrusions and Ophiolite Complexes: Economic Geology, v. 84, p. 180-187.

Naldrett, A. J., Wilson, A., Kinnaird, J., and Chunnett, G., 2009, PGE Tenor and Metal Ratios within and below the Merensky Reef, Bushveld Complex: Implications for its Genesis: Journal of Petrology, v. 50, p. 625-659.

Naldrett, A. J., Wilson, A., Kinnaird, J., Yudovskaya, M., and Chunnett, G., 2012, The origin of chromitites and related PGE mineralization in the Bushveld Complex: new mineralogical and petrological constraints: Mineralium Deposita, v. 47, p. 209-232.

Nicholson, D. M., and Mathez, E. A., 1991, Petrogenesis of the Merensky Reef in the Rustenburg section of the Bushveld Complex: Contributions to Mineralogy and Petrology, v. 107, p. 293-309.

Nodder, S. M., 2015, Correlating the Bushveld's northern limb with the western and eastern limbs: a geochemical and petrological study, Cardiff University, 257 p.

Olsson, J. R., Soderlund, U., Hamilton, M. A., Klausen, M. B., and Helffrich, G. R., 2011, A late Archaean radiating dyke swarm as possible clue to the origin of the Bushveld Complex: Nature Geoscience, v. 4, p. 865-869.

Pogge von Strandmann, P.A.E., Elliott, T., Marschall, H.R., Coath, C., Lai, Y.-J., Jeffcoate, A.B., Ionov, D.A., 2011, Variations of Li and Mg isotope ratios in bulk chondrites and mantle xenoliths: Geochimica et Cosmochimica Acta. v. 75, p. 5247-5268.

Pronost, J., Harris, C., and Pin, C., 2008, Relationship between footwall composition, crustal contamination, and fluid-rock interaction in the Platreef, Bushveld Complex, South Africa: Mineralium Deposita, v. 43, p. 825-848.

Reisberg, L., Tredoux, M., Harris, C., Coftier, A., and Chaumba, J., 2011, Re and Os distribution and Os isotope composition of the Platreef at the Sandsloot-Mogolakwena mine, Bushveld complex, South Africa: Chemical Geology, v. 281, p. 352-363.

Reynolds, I. M., 1985, The nature and origin of titaniferous magnetite-rich layers in the Upper Zone of the Bushveld Complex - a review and synthesis: Economic Geology, v. 80, p. 1089-1108.

Richardson, S. H., and Shirey, S. B., 2008, Continental mantle signature of Bushveld magmas and coeval diamonds: Nature, v. 453, p. 910-913.

Richter, S., Goldberg, S. A., Mason, P. B., Traina, A. J., and Schwieters, J. B., 2001, Linearity tests for secondary electron multipliers used in isotope ratio mass spectrometry: International Journal of Mass Spectrometry, v. 206, p. 105-127.

Righter, K., Campbell, A. J., Humayun, M., and Hervig, R. L., 2004, Partitioning of Ru, Rh, Pd, Re, Ir, and Au between Cr-bearing spinel, olivine, pyroxene and silicate melts: Geochimica Et Cosmochimica Acta, v. 68, p. 867-880.

Roelofse, F., and Ashwal, L. D., 2012, The Lower Main Zone in the Northern Limb of the Bushveld Complex - a > 1.3 km Thick Sequence of Intruded and Variably Contaminated Crystal Mushes: Journal of Petrology, v. 53, p. 1449-1476.

Roelofse, F., Ashwal, L. D., and Romer, R. L., 2015, Multiple, isotopically heterogeneous plagioclase populations in the Bushveld Complex suggest mush intrusion: Chemie Der Erde-Geochemistry, v. 75, p. 357-364.

Rollinson, H. R., 1993, Using geochemical data: evaluation, presentation, interpretation: Harlow, England, Routledge.

References

Rowling, R., van der Walt, E., and Pakiam, R., 2019, Why Palladium's Suddenly an Especially Precious Metal, 2019: www.bloomberg.com.

Savard, D., Barnes, S. J., and Meisel, T., 2010, Comparison between Nickel-Sulfur Fire Assay Te Co-precipitation and Isotope Dilution with High-Pressure Asher Acid Digestion for the Determination of Platinum-Group Elements, Rhenium and Gold: Geostandards and Geoanalytical Research, v. 34, p. 281-291.

Scharer, U., 1984, The effect of initial Th-230 disequilibrium on young U-Pb ages - The Makalu Case, Himalaya: Earth and Planetary Science Letters, v. 67, p. 191-204.

Schiffries, C. M., and Rye, D. M., 1989, Stable isotopic systematics of the Bushveld Complex. 1. Constraints of magmatic processes in layered intrusions: American Journal of Science, v. 289, p. 841-873.

Scoates, J. S., and Friedman, R. M., 2008, Precise age of the platiniferous Merensky reef, Bushveld Complex, South Africa, by the U-Pb zircon chemical abrasion ID-TIMS technique: Economic Geology, v. 103, p. 465-471.

Scoates, J. S., and Wall, C. J., 2015, Geochronology of layered intrusions, in Charlier, B., Namur, O., Latypov, R., and Tegner, C., eds., Layered Intrusions, Springer, p. 3-74.

Scoon, R. N., 2002, A new occurrence of Merensky reef on the flanks of the Zaaikloof dome, northeastern Bushveld Complex: Relationship between diapirism and magma replenishment: Economic Geology and the Bulletin of the Society of Economic Geologists, v. 97, p. 1037-1049.

Scoon, R. N., and Teigler, B., 1994, Platinum-Group Element Mineralization in the Critical Zone of the Western Bushveld Complex: I. Sulfide Poor-Chromitites below the UG-2: Economic Geology, v. 89, p. 1094-1121.

Seabrook, C. L., and Cawthorn, R. G., 2005, The Merensky Reef, Bushveld Complex: Mixing of Minerals Not Mixing of Magmas: Economic Geology, v. 100, p. 1191-1206.

Sharman, E. R., Penniston-Dorland, S. C., Kinnaird, J. A., Nex, P. A. M., Brown, M., and Wing, B. A., 2013, Primary origin of marginal Ni-Cu-(PGE) mineralization in layered intrusions: Delta S-33 evidence from the Platreef, Bushveld, South Africa: Economic Geology, v. 108, p. 365-377.

Sharpe, M. R., 1981, The chronology of magma influxes to the eastern compartment of the Bushveld Complex as exemplified by its marginal border groups: Journal of the Geological Society, v. 138, p. 307-326.

Sharpe, M. R., Bahat, D., and von Gruenewaldt, G., 1981, The concentric elliptical structure of feeder sites to the Bushveld Complex and possible economic implications: Transactions of the Geological Society of South Africa, v. 84, p. 239-244.

Sharpe, M. R., and Hulbert, L. J., 1985, Ultramafic Sills beneath the Eastern Bushveld Complex: Mobilized Suspensions of Early Lower Zone Cumulates in a Parental Magma with Boninitic Affinities: Economic Geology, v. 80, p. 849-871.

Sheldon, N. D., 2006, Precambrian paleosols and atmospheric CO2 levels: Precambrian Research, v. 147, p. 148-155.

Shen, B., Wimpenny, J., Lee, C.-T. A., Tollstrup, D., and Yin, Q.-Z., 2013, Magnesium isotope systematics of endoskarns: Implications for wallrock reaction in magma chambers: Chemical Geology, v. 356, p. 209-214.

Shields, G., and Veizer, J., 2002, Precambrian marine carbonate isotope database: Version 1.1: Geochemistry Geophysics Geosystems, v. 3.

Shishkina, T. A., Botcharnikov, R. E., Holtz, F., Almeev, R. R., and Portnyagin, M. V., 2010, Solubility of H2O- and CO2-bearing fluids in tholeiitic basalts at pressures up to 500 MPa: Chemical Geology, v. 277, p. 115-125.

Silver, P. G., Fouch, M. J., Gao, S. S., and Schmitz, M., 2004, Seismic anisotropy, mantle fabric, and the magmatic evolution of Precambrain southern Africa: South African Journal of Geology, v. 107, p. 45-58.

Stear, W. M., 1977, The stratigraphy and sedimentation of the Pretoria Group at Rooiberg, Transvaal: Transactions of the Geological Society of South Africa, v. 80, p. 53-65.

Stephenson, H., 2019, The Platreef Magmatic Event on Turfspruit, Cardiff University, 336 p.

Svensen, H., Planke, S., Chevallier, L., Malthe-Sorenssen, A., Corfu, F., and Jamtveit, B., 2007, Hydrothermal venting of greenhouse gases triggering Early Jurassic global warming: Earth and Planetary Science Letters, v. 256, p. 554-566.

Svensen, H., Planke, S., Polozov, A. G., Schmidbauer, N., Corfu, F., Podladchikov, Y. Y., and Jamtveit, B., 2009, Siberian gas venting and the end-Permian environmental crisis: Earth and Planetary Science Letters, v. 277, p. 490-500.

Tanner, D., Mavrogenes, J. A., Arculus, R. J., and Jenner, F. E., 2014, Trace Element Stratigraphy of the Bellevue Core, Northern Bushveld: Multiple Magma Injections Obscured by Diffusive Processes: Journal of Petrology, v. 55, p. 859-882.

Tanner, D., McDonald, L., Harmer, R. E. J., Muir, D. D., and Hughes, H. S. R., 2019, A record of assimilation preserved by exotic minerals in the lowermost platinum-group element deposit of the Bushveld Complex: The Volspruit Sulphide Zone: Lithos, v. 324, p. 584-608.

Taylor, H. P., 1980, The effects of assimilation of country rocks by magmas on O-18-O-16 and Sr-87-SR-86 systematics in igneous rocks: Earth and Planetary Science Letters, v. 47, p. 243-254.

References

Tegner, C., Cawthorn, R. G., and Kruger, F. J., 2006, Cyclicity in the main and upper zones of the Bushveld Complex, South Africa: Crystallization from a zoned magma sheet: Journal of Petrology, v. 47, p. 2257-2279.

Tegner, C., and Wilson, J. R., 1995, Textures in a poikilitic olivine gabbro cumulate - evidence for supercooling: Mineralogy and Petrology, v. 54, p. 161-173.

Teigler, B., 1990, Mineralogy, Petrology and Geochemistry of the Lower and Lower Critical Zones, Northwestern Bushveld Complex, Rhodes University, 339 pp p.

Teigler, B., and Eales, H. V., 1996, The Lower and Critical Zones of the Western Limb of the Bushveld Complex as intersected by the Nooitgedacht Boreholes: Bulletin of the Geological Survey of South Africa, v. 111, p. 121.

Teigler, B., Eales, H. V., and Scoon, R. N., 1992, The cumulate succession in the Critical Zone of the Rustenberg Layered Suite at Brits, western Bushveld Complex: South African Journal of Geology, v. 95, p. 17-28.

Telus, M., Dauphas, N., Moynier, F., Tissot, F. L. H., Teng, F. Z., Nabelek, P. I., Craddock, P. R., and Groat, L. A., 2012, Iron, zinc, magnesium and uranium isotopic fractionation during continental crust differentiation: The tale from migmatites, granitoids, and pegmatites: Geochimica Et Cosmochimica Acta, v. 97, p. 247-265.

Teng, F.-Z., 2017, Magnesium Isotope Geochemistry: Reviews in Mineralogy and Geochemistry, v. 82, p. 219-287.

Teng, F. Z., Li, W. Y., Ke, S., Marty, B., Dauphas, N., Huang, S. C., Wu, F. Y., and Pourmand, A., 2010, Magnesium isotopic composition of the Earth and chondrites: Geochimica Et Cosmochimica Acta, v. 74, p. 4150-4166.

van der Merwe, M. J., 1976, The Layered Sequence of the Potgietersrus Limb of the Bushveld Complex: Economic Geology, v. 71, p. 1337-1351.

van der Merwe, M. J., 2008, The geology and structure of the Rustenburg Layered Suite in the Potgietersrus/Mokopane area of the Bushveld Complex, South Africa: Mineralium Deposita, v. 43, p. 405-419.

Vermaak, C. F., 1976, The Merensky Reef - Thoughts on its Environment and Genesis: Economic Geology, v. 71, p. 1270-1298.

Viljoen, M. J., 1999, The nature and origin of the Merensky Reef of the western Bushveld Complex based on geological facies and geophysical data: South African Journal of Geology, v. 102, p. 221-239.

Von Gruenewaldt, G., Sharpe, M. R., and Hatton, C. J., 1985, A special issue devoted to the Bushveld Complex - The Bushveld Complex - Introduction and Review: Economic Geology, v. 80, p. 803-812.

Voordouw, R., Gutzmer, J., and Beukes, N. J., 2009, Intrusive origin for Upper Group (UG1, UG2) stratiform chromitite seams in the Dwars River area, Bushveld Complex, South Africa: Mineralogy and Petrology, v. 97, p. 75-94.

Wabo, H., 2013, Paleomagnetism of post-Transvaal sill complexes, selected dykes and the Uitkomst Complex - relation to the Bushveld Complex, University of Johannesburg, 273 p.

Wager, L. R., and Brown, G. M., 1967, Layered Igneous Rocks: Edinburgh, Oliver and Boyd Ltd.

Wager, L. R., and Brown, G. M., 1968, Layered Igneous Rocks: Edinburgh, Oliver and Boyd.

Wallmach, T., Hatton, C. J., and Droop, G. T. R., 1989, Extreme facies of contact-metamorphism developed in calc-silicate xenoliths in the Eastern Bushveld Complex: Canadian Mineralogist, v. 27, p. 509-523.

Walraven, F., and Hattingh, E., 1993, Geochronology of the Nebo Granite, Bushveld Complex: South African Journal of Geology, v. 96, p. 31-41.

Webb, S., Cawthorn, R. G., Nguuri, T., and James, D. E., 2004, Gravity modelling of Bushveld Complex connectivity supported by Southern African Seismic Experiment results: South African Journal of Geology, v. 107, p. 207-208.

Webb, S. J., Ashwal, L. D., and Cawthorn, R. G., 2011, Continuity between eastern and western Bushveld Complex, South Africa, confirmed by xenoliths from kimberlite: Contributions to Mineralogy and Petrology, v. 162, p. 101-107.

Wenzel, T., Baumgartner, L. P., Brugmann, G. E., Konnikov, E. G., and Kislov, E. V., 2002, Partial melting and assimilation of dolomitic xenoliths by mafic magma: the Ioko-Dovyren intrusion (North Baikal region, Russia): Journal of Petrology, v. 43, p. 2049-2074.

White, J. A., 1994, The Potgietersrus prospect - Geology and exploration history: Proceedings Xvth Cmmi Congress, Vol 3: Geology, v. 14, p. 173-181.

Willemse, J., 1964, A Brief Outline of the Geology of the Bushveld Igneous Complex, *in* Haughton, S. H., ed., The Geology of Some Ore Deposits in Southern Africa, volume II: Johannesburg, The Geological Society of South Africa.

Williams, D. R., 2019, Earth Fact Sheet, 2019, nssdc.gsfc.nasa.gov/planetary/factsheet/earthfact.html.

Wilson, A. H., 2012, A Chill Sequence to the Bushveld Complex: Insight into the First Stage of Emplacement and Implications for the Parental Magmas: Journal of Petrology, v. 53, p. 1123-1168.

Wilson, A. H., 2015, The Earliest Stages of Emplacement of the Eastern Bushveld Complex: Development of the Lower Zone, Marginal Zone and Basal Ultramafic Sequence: Journal of Petrology, v. 56, p. 347-388.

Wilson, J. R., Cawthorn, R. G., Kruger, F. J., and Grundvig, S., 1994, Intrusive origin for the unconformable Upper Zone in the Northern Gap, western Bushveld Complex: South African Journal of Geology, v. 97, p. 462-472.

www.infomine.com, 2019.

Yudovskaya, M., Belousova, E., Kinnaird, J., Dubinina, E., Grobler, D. F., and Pearson, N., 2017a, Re-Os and S isotope evidence for the origin of Platreef mineralization (Bushveld Complex): Geochimica Et Cosmochimica Acta, v. 214, p. 282-307.

Yudovskaya, M. A., Kinnaird, J. A., Grobler, D. F., Costin, G., Abramova, V. D., Dunnett, T., and Barnes, S. J., 2017b, Zonation of Merensky-Style Platinum-Group Element Mineralization in Turfspruit Thick Reef Facies (Northern Limb of the Bushveld Complex): Economic Geology, v. 112, p. 1333-1365.

Yudovskaya, M. A., Kinnaird, J. A., Sobolev, A. V., Kuzmin, D. V., McDonald, L., and Wilson, A. H., 2013, Petrogenesis of the Lower Zone Olivine-Rich Cumulates Beneath the Platreef and Their Correlation with Recognized Occurrences in the Bushveld Complex: Economic Geology, v. 108, p. 1923-1952.

Zeh, A., Ovtcharova, M., Wilson, A. H., and Schaltegger, U., 2015, The Bushveld Complex was emplaced and cooled in less than one million years - results of zirconology, and geotectonic implications: Earth and Planetary Science Letters, v. 418, p. 103-114.